Transactions of the ASME

Technical Editor, L. B. FREUND

APPLIED MECHANICS DIVISION

Chairman, CHARLES R. STEELE
Secretary, J. D. ACHENBACH
Associate Editors, S. T. ARIARATNAM
T. BELYTSCHKO
D. B. BOGY
M. M. CARROLL
R. J. CLIFTON
L. B. FREUND
MAURICE HOLT
W. D. IWAN
W. G. KNAUSS
A. S. KOBAYASHI
L. E. MALVERN
R. P. NORDGREN
R. H. PLAUT
R. T. SHIELD
C. T. SUN
J. S. WALKER
G. A. WEMPNER
S. E. WIDNALL

BOARD ON COMMUNICATIONS
Chairman and Vice-President
M. J. RABINS

Members-at-Large
W. BEGELL
W. G. GOTTENBERG
H. C. REEDER
D. KOENIG
M. KUTZ
F. LANDIS
J. W. LOCKE
J. E. ORTLOFF
C. PHILLIPS
K. REID

President, FRANK M. SCOTT
Exec. Dir.
PAUL ALLMENDINGER
Treasurer, ROBERT A. BENNETT

PUBLISHING STAFF
Mng. Dir., Pub., J. J. FREY
Dep. Mng. Dir., Pub.
JOS. SANSONE
Managing Editor,
CORNELIA MONAHAN
Production Editor, SUZANNE MAGIDA

The Journal of Applied Mechanics (ISSN 0021-8936) is published quarterly for $72 per year by The American Society of Mechanical Engineers, 345 East 47th Street, New York, NY 10017. Second class postage paid at New York, NY and additional mailing offices. POSTMASTER: Send address changes to The Journal of Applied Mechanics, c/o THE AMERICAN SOCIETY OF MECHANICAL ENGINEERS, P.O. Box 3199, Grand Central Station, New York, NY 10163. **CHANGES OF ADDRESS** must be received at Society headquarters seven weeks before they are to be effective. Please send old label and new address.

PRICES: To members, $36.00, annually; to nonmembers, $90.00. Single copies, $24.00 each. Add $6.00 for postage to countries outside the United States and Canada.

STATEMENT from By-Laws. The Society shall not be responsible for statements or opinions advanced in papers or . . . printed in its publications (B7.1, Par. 3).

COPYRIGHT © 1983 by the American Society of Mechanical Engineers. Reprints from this publication may be made on condition that full credit be given the TRANSACTIONS OF THE ASME, JOURNAL OF APPLIED MECHANICS, and the author, and date of publication be stated.

INDEXED by the Engineering Index, Inc.

Journal of Applied Mechanics

Published Quarterly by The American Society of Mechanical Engineers

VOLUME 50 • NUMBER 4a • DECEMBER 1983

TECHNICAL PAPERS

707 **Fluid Flow Through a Crack Network in Rocks**
R. Englman, Y. Gur, and Z. Jaeger

712 **Ablation by Frictional Heating**
L. N. Tao

717 **Compression of Fluid-Filled Spherical Shells by Rigid Indenters**
L. A. Taber

723 **Blast Loading of a Spherical Container Surrounded by an Infinite Elastic Medium** (83-WA/APM-17)
L. A. Glenn and R. E. Kidder

727 **On the Crushing Mechanics of Thin-Walled Structures** (83-WA/APM-12)
T. Wierzbicki and W. Abramowicz

735 **Small Deflections of Linear Elastic Circular Membranes Under Lateral Pressure**
B. Storåkers

740 **A Viscoelastic Correspondence Principle for Plane Membranes Subjected to Lateral Pressure**
B. Storåkers

743 **Variation Principles and Bounds for the Approximate Analysis of Plane Membranes Under Lateral Pressure** (83-WA/APM-18)
B. Storåkers

750 **Effects of Geometric Imperfections on Vibrations of Biaxially Compressed Rectangular Flat Plates** (83-WA/APM-20)
David Hui and A. W. Leissa

757 **Vibration of a Thick-Walled Pipe or a Ring of Arbitrary Shape in Its Plane**
K. Nagaya

765 **Numerical Simulation of Transient Finite Deformations of Thin Beams** (83-WA/APM-21)
J. J. A. Rodal, D. J. Steigmann, and E. A. Witmer

770 **The Penny-Shaped Interface Crack With Heat Flow, Part 2: Imperfection Contact** (83-WA/APM-13)
J. R. Barber and Maria Comninou

777 **Analysis of the Optical Shadow Spot Method for a Tensile Crack in a Power-Law Hardening Material**
A. J. Rosakis, C. C. Ma, and L. B. Freund

783 **On the Approach to Steady State for Frictional Contact Under Moving Loads**
J. Dundurs and A. K. Gautesen

789 **Endochronic Analysis of Cyclic Elastplastic Strain Fields in a Notched Plate** (83-WA/APM-14)
K. C. Valanis and J. Fan

795 **Strain-Hardening Topography of Elastic-Plastic Materials** (83-WA/APM-8)
J. Casey and H. H. Lin

802 **Ultrasonic Wave Scattering by a Subsurface Flaw in Joined Fluid-Solid Half Spaces** (83-WA/APM-22)
V. V. Varadan, T. A. K. Pillai, and V. K. Varadan

807 **The Stress Field in an Elastic Half Space Having a Spheroidal Inhomogeneity Under All-Around Tension Parallel to the Plane Boundary**
E. Tsuchida and T. Mura

817 **Finite Element Analysis of Dynamic Coupled Thermoelasticity Problems With Relaxation Times** (83-WA/APM-9)
J. H. Prevost and D. Tao

823 **The Lumped Parameter Method for Elastic Impact Problems** (83-WA/APM-10)
Y. Lee, J. F. Hamilton, and J. W. Sullivan

828 **Effective Properties of Fiber-Reinforced Materials** (83-WA/APM-16)
U. Tzadka and K. Schulgasser

835 **A Hybrid Finite Element Approach to Composite Laminate Elasticity Problems With Singularities** (83-WA/APM-15)
S. S. Wang and F. G. Yuan

845 **Stress Concentrations in a Hybrid Composite Sheet** (83-WA/APM-11)
H. Fukuda and T. W. Chou

849 **A Periodically Forced Impact Oscillator With Large Dissipation** (83-WA/APM-23)
S. W. Shaw and P. J. Holmes

858 **Index Evaluation for Dynamical Systems and Its Application to Locating All the Zeros of a Vector Function** (83-WA/APM-19)
C. S. Hsu and R. S. Guttalu

863 **An Alternative Analysis of the Plane Stick-Slip Problem**
A. Dutta

869 **A New Method for Holonomic Constraints**
J. W. Baumgarte

871 **Incremental Harmonic Balance Method With Multiple Time Scales for Aperiodic Vibration of Nonlinear Systems** (83-WA/APM-7)
S. L. Lau, Y. K. Cheung, and S. Y. Wu

(Contents continued on Inside Back Cover)

Downloaded 04 May 2010 to 171.66.16.34. Redistribution subject to ASME license or copyright; see http://www.asme.org/terms/Terms_Use.cfm

CONTENTS (CONTINUED)

877 **The Role of Cavitation in Whirl Instability in a Rotor Bearing, 1 The π-Film Model** (83-WA/APM-24)
J. Brindley, L. Elliott, and J. T. McKay

886 **The Role of Cavitation in Whirl Instability in a Rotor Bearing, 2 Effect of Oil Inlet Position and Supply Pressure** (83-WA/APM-25)
J. Brindley, L. Elliott, and J. T. McKay

BRIEF NOTES

891 Optimum Quasi-Rectangular Holes in Infinite Orthotropic Plates Under Inplane Loading
K. Rajaiah and N. K. Naik

892 Minimum-Weight Thin-Walled Cylinders of Given Torsional and Flexural Regidity
B. L. Karihaloo and W. S. Hemp

894 On the Hypoelastic Formulation of Plasticity Using the Past Maximum of Stress
M. E. Gurtin

896 Evaluation of Finite Element Calculations in a Cracked Cylinder Under Internal Pressure by Speckle Photography
G. J. Kaufmann, A. M. Lopergolo and S. Idelsohn

897 Closed-Form Axisymmetric Solution of the von Karman Plate Equations for Poisson's Ratio One-Third
J. G. Simmonds

898 On the Elastoplastic Stress Concentration at Reentrant Corners of Thin-Walled Cross Sections Subjected to Pure Torsion
D. Durban

901 Spectral Moments Calculation of Linear System Output
P.T. D. Spanos

903 Exact Periodic Solutions of Long Wave Equations for a Rotating Fluid
P. L. Sachdev and M. C. Singh

905 A Treatment of Rigid Body Dynamics
J. Casey

907 An Extended Weight-Function Method for Mixed-Mode Elastic Crack Analysis
Y. Bortman and L. Banks-Sills

DISCUSSION

910-911 Discussion on previously published paper by **Bottega** and **Maewal**

BOOK REVIEWS

912 ***Introduction to the Theory of Thin Shells*** by **H. Mollman**. . .Reviewed by **A. Kalnins**

Nonlinear Problems: Present and Future edited by **A. Bishop, D. Campbell,** and **B. Nicolaenko**. . .Reviewed by **P. Holmes**

913 ***Finite Element Flow Analysis*** edited by **T. Kawai**. . .Reviewed by **P. M. Pinsky**

914 ***Viscoplasticity*** by **N. Cristescu** and **I. Suliciu**. . .Reviewed by **J. L. Bassani**

The Finite Element Method in Engineering by **S. S. Rao**. . .Reviewed by **S. N. Atluri**

Fracture of Composite Materials edited by **G. C. Sih** and **V. P. Tamuzs**. . .Reviewed by **C. T. Herakovich**

915 ***Strömungsmechanik Nicht-Newtonscher Fluide*** by **G. Bohme**. . .Reviewed by **D. D. Joseph**

ERRATA

915 Erratum on "The Determination of the Elastodynamic Fields of an Ellipsoidal Inhomgeneity," by **L. S. Fu** and **T. Mura,** and published in the June, 1983 issue

---

788, 794, 827	Worldwide Mechanics Meeting List
716, 734, 739, 749, 776	Applied Mechanics Symposium Proceedings
816, 862, 885, 890, 911	Applied Mechanics Symposium Proceedings
726	Change of Address Form
918	New Books from MIT
916-917	Authors Index

Downloaded 04 May 2010 to 171.66.16.34. Redistribution subject to ASME license or copyright; see http://www.asme.org/terms/Terms_Use.cfm

R. Englman

Y. Gur

Z. Jaeger

Israel Atomic Energy Commission,
Soreq Nuclear Research Centre,
Yavne, Israel

Fluid Flow Through a Crack Network in Rocks[1]

A network of cracks pervading a rock is modeled by a random distribution of two-dimensional intersecting, complex, narrow cracks. The percolation properties of the resulting network are studied as functions of the crack-area density and size of the medium. Gas flow commences at a finite value of the crack density which in Arkansas Novaculite rocks amounts according to our model to 670 cracks per cm^2. The mean probability of finding at least one crack intersecting another is 0.57 at the threshold density. Above that, the rock gas-flow permeability increases superlinearly with crack density due to the enhancement of short percolative paths.

1 Introduction

In a rock containing cavities (faults, pores, cracks, etc.) a fluid injected at one end will emerge at the other end by flow inside the cavities [1–3]. For small values of the applied fluid pressure, the shape of the cavities will not change during fluid flow. We will analyze the flow process in terms of percolation of the fluid along the cracks in the rock. Typical crack widths for percolative flow of moderately viscous gases are a micron or larger.

Past works have treated fluid flow mainly in terms of the permeability K, a quantity with dimensions of an area (essentially the crack cross section). In a porous medium, K depends on the porosity in a way for which various (mainly empirical) suggestions have been made [4, 5]. Regarding the flow as proceeding along a set of winding channels and being of the laminal-Poiseuille type, K depends also on the tortuosity of the channels [2]. The variation of K is generally regarded as smooth, analytic; e.g., initially as the third power of the porosity [5]. Nonanalytic, sudden variation of K, e.g., in sand with water saturation, was found: this has been traced to physical processes rather than to geometrical causes [2].

There are several statistical type theories. In one, flow along straight cylindrical pores of varying length, width, and orientation is considered [6], in another, the probability of intersection of pores determines the speed of the flow [7]. Statistical relationships linking K with pore or crack dimensions have been derived [8]. Models of bond percolation in several two-dimensional networks were used to derive the threshold pore density at which the medium becomes permeable [9, 10]. (Bond percolation theory treats the transmission probability across a network in which the bond positions between the junctions are occupied with a given probability p. Threshold or critical occupation probabilities p_c as function of network type or size are calculated numerically or analytically, as well as distribution of sizes of bond clusters as function of p, etc. [11]). Percolation theory was also applied to flow along conduits connecting bulky pores [12, 13].

In this work we employ a two-dimensional percolative model having a *continuous*, rather than discrete, distribution of crack positions, orientations, etc. Parameters of the model are determined empirically. Not only is the continuum crack model more realistic for fluid flow in brittle rocks than previous models based on pores or discrete networks, but it also introduces new concepts (e.g., the effective bond occupation probability ζ, size dependence of the permeability), reaches new results (Section 3), and raises new problems (Sections 4 and 5). The model is defined in the next section, where a phenomenological derivation of the permeability is also given.

2 Description of the Model

Let us suppose a cube-shape rock of linear dimension R, a net fluid flow along the x-direction (such as is caused by a pressure gradient dP/dx in the rock), and assume that all normals to the planes of the cracks lie in a plane, say the x-y plane. The extension of the cracks in the perpendicular z-direction is supposed to be very long compared to their extension along x or y. Then the rate of x-directional flow will depend on the flow in the x-y plane, since the progress of gas molecules along z will not advance them along x.

The flow will proceed by penetration of gas into a crack originating at the high-pressure face, traversal along the crack, subsequent transfer to another intersecting crack, flow along the second crack, eventual transfer, and so on. The process terminates either by the gas molecules having been delivered by a crack to the low-pressure x-face or by their having gotten into a dead-end, nonintersecting crack. We shall regard the physical process of the flow within a straight or nearly straight portion of a crack as a laminal Poiseuille flow between boundaries separated by a small distance d [2, 5,

[1]Research supported partly by a grant from the Directorate of Geoscience Research, Ministry of Energy and Infrastructure, Jerusalem.

Contributed by the Applied Mechanics Division for publication in the JOURNAL OF APPLIED MECHANICS.

Discussion on this paper should be addressed to the Editorial Department, ASME, United Engineering Center, 345 East 47th Street, New York, N.Y. 10017, and will be accepted until two months after final publication of the paper itself in the JOURNAL OF APPLIED MECHANICS. Manuscript received by ASME Applied Mechanics Division, February, 1982; final revision, May, 1983.

Copyright © 1983 by ASME
Downloaded 02 May 2010 to 171.66.16.250. Redistribution subject to ASME license or copyright; see http://www.asme.org/terms/Terms_Use.cfm

14]. Transfers between intersecting cracks and sudden changes in directions of flow around sharp bends in a crack are presumed to be of such short duration as not to affect the total flow rate.

An important quantity in our work is the area density ρ_A of cracks, i.e., the number of crack intersections with a representative x-y plane, per unit area. In our model (in which all crack normals lie in the x-y plane) we assume a coarse-grained spatial uniformity on the average along z and relate ρ_V, the number of cracks per unit volume (or volume density of cracks) to ρ_A, by

$$\rho_A = \rho_V \bar{l}_z \tag{1}$$

where $\bar{l}_z$ is the mean crack length along z. This is a special case of the more general relation, established by Dienes [8, 14],

$$\rho_A = \alpha \rho_V \bar{l}_c' \tag{2}$$

where $\bar{l}_c'$ is a mean crack length and α is a numerical constant.

To represent the crack shapes in the x-y plane in a physically realistic form, we have resorted to photographs in solids, [15-17]. Photos of cracks taken in concrete by Stroeven [16] indicate that each crack consists of several thin straight segments. Each segment may taken as randomly oriented and having a variable length l_s which is very long compared to the width of the crack (in the x-y plane) but is much shorter than the cube-shaped sample size R. Altogether we have

$$d << l_s << l_z \sim R. \tag{3}$$

We have computer-generated distributions of four-segmented cracks in a plane, the positions and orientations of cracks being taken as continuously varying random variables. For the segment lengths l_s a gaussian distribution was assumed with the following values of the mean $\bar{l}_s$ and variance σ_s.

$$\bar{l}_s = 0.02 \text{ cm}$$
$$\sigma_s = 0.013 \text{ cm}.$$

These figures were derived from flaw size-distribution found by Shockey et al. in Arkansas Novaculite-rocks [18]. For comparison, the linear sample size in our calculations was 1 cm or larger.

Each two-dimensional distribution (Fig. 2) has (or has not) the mathematical property of percolativeness, along x or y, depending on whether there is at least one continuous pathway across the picture in the x or y-direction. The significance of percolativeness for the physical process of gas-flow permeability enters our model through a factor Π introduced presently and described in Section 3.

The flux Φ of gas at a point y in a thin straight crack of thickness d, length l, and height l_z is given as

$$\Phi = \frac{d}{\mu} y(d-y) \frac{\partial p}{\partial l} l_z \tag{4}$$

where μ is the gas viscosity and $\partial p/\partial l$ is the pressure drop per unit length along the crack.

For the special case of parallel cracks, all of which are oriented alongside the flow direction x, the contributions are additive and the total flux Φ_T is gotten by multiplying Φ by the number N_x of cracks intersecting a planar cross section of the cube perpendicular to x. In terms of the cube length R, the crack height l_z, and mean crack length (along x) $\bar{l}_c$

$$N_x = \rho_A \bar{l}_c R^2 / l_z \tag{5}$$

(Derivation of this result: The number of cracks in a characteristic xy-plane is $\rho_A R^2$. A fraction $\bar{l}_c/R$ of these cracks will intersect a line in the xy-plane lying along y and therefore perpendicular to the cracks. The number of *different* cracks intersecting a yz cross section of the cube is obtained by further multiplication by the number R/l_z.) More generally, for cracks oriented at an angle θ to the x-direction the contribution to the total flux is reduced by $\cos^2\theta$, one factor of $\cos\theta$ coming from the pressure drop and another from the reduction in the number of cracks crossing a plane perpendicular to x.

To calculate the mean total flux $\bar{\Phi}_T$ one averages over the positions y inside the crack, then over the crack width d and crack height l_z, and finally over the crack orientation θ. In addition, one must multiply by a statistical factor Π which measures the effectiveness of a typical crack to contribute to the flow: cracks that are isolated or form part of an isolated cluster or lead to a cul-de-sac, will not contribute. Those on a "backbone" cluster (namely, one that cuts across the sample, without its dangling parts) will contribute, but here again a network comprising several short parallel backbones will be more efficient than one (or a few) long, tortuous backbone [19].

Thus we have

$$\bar{\Phi}_T = \bar{\Phi} \overline{\cos^2\theta} \cdot N_x \cdot \Pi$$
$$= -\frac{\overline{d^3} R^2}{6\mu} \overline{\cos^2\theta} \frac{\partial p}{\partial x} \bar{l}_c \rho_A \Pi \tag{6}$$

Using (1) to replace the surface density ρ_A by $\rho_V \bar{l}_z$ and assuming uniformly distributed orientations in the x-y plane so that $\overline{\cos^2\theta} = 1/2$, we find for the specific permeability

$$K \equiv \frac{\bar{\Phi}_T \mu}{(-\partial p/\partial x)} \frac{1}{R^2} = \frac{1}{12} \overline{d^3} \bar{l}_c \bar{l}_z (\rho_V \Pi) \tag{7}$$

3 Parameters of Percolation

Equation (7) is our main result. It expresses the permeability K in terms of the volume density ρ_V of the cracks, the small dimension d and the large dimensions $\bar{l}_c$ and $\bar{l}_z$. For the distinction between d, l_z, and l (which is of the order of l_s) see Fig. 1.

Given any fixed d, $\bar{l}_z$, $\bar{l}_c$, etc. that characterize the type of cracks that form in the rock, the factor $\rho_V \Pi$ in equation (7) determines the gas flow in the rock as function of the crack population. We will now describe how the analysis of our crack distributions leads to the determination of this factor. We will temporarily ignore the model dependence of Π (e.g., its variation with the dimensionality (here equal to 2), with the segment number (4) or with the width (here taken as constant $d << \bar{l}_s$)). Instead, we will concentrate on:

(*i*) the dependence of Π on the total crack length (equal to $4\rho_A R^2 \bar{l}_s$) and on the sample size R; and

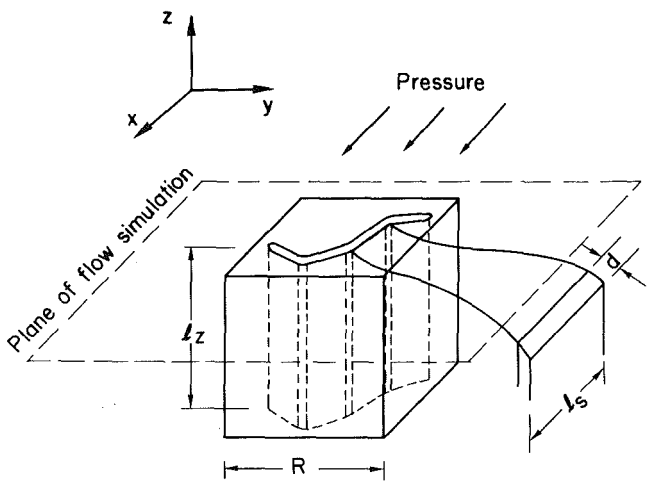


Fig. 1 Geometry of a complex crack, consisting of four segments, in a cube, representing the rock. In the figure the rock dimension R is drawn not to scale (too small).

Downloaded 02 May 2010 to 171.66.16.250. Redistribution subject to ASME license or copyright; see http://www.asme.org/terms/Terms_Use.cfm

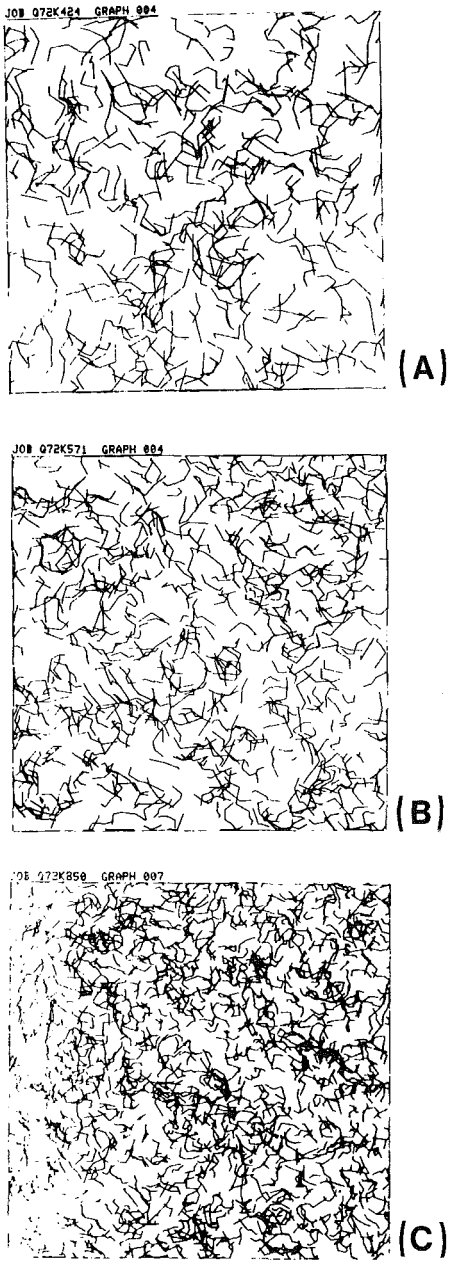


Fig. 2 Samples of crack distributions near the percolation threshold. The parameters of the drawing are: *L* [the sum of all segment lengths (in units such that the edges of the picture frame are about 10)] = 420 (*a*), 576 (*b*), 850 (*c*). *AVRGE* [the mean segment length, $\bar{l}_s$ (~0.02 cm in a typical rock)] = 30 (*a*), 22 (*b*), 15 (*c*). *SIGMA* [mean deviation of segment lengths, σ_s (~0.013 cm)] = 0.20 (*a*), 0.15 (*b*), 0.10 (*c*). The number of segments in a crack = 4. The spread of angles between one segment and the previous one in the forward direction = ±90 deg. In Figs. 2(*a*), (*b*), and (*c*) *AVRGE* and *SIGMA* are successively reduced: the figures can be so rescaled that they represent successively larger sample sizes.

(*ii*) the percolation threshold as function of sample size. In studies of critical behavior this is called finite-size scaling [20, 21].

For each value of the parameters (appearing in the caption of Fig. 2) several graphs (about 100) of crack distributions were generated by random sampling and were then scanned on a Tektronix screen and/or on a photographic record. The percolativity of each distribution was visually determined by tracing a continuous path of cracks across each graph. The relative percolation frequency ν is the ratio of percolative graphs to the total number. The visual method was adopted in preference to some counting algorithm [21] because of the availability of a reproducible Monte-Carlo procedure. After some practice the determination of percolativity took no longer than half a minute per graph and was child's play.

For any given parameter (which significantly includes the sample size) we got a sigmoidal frequency distribution as function of the total crack length L defined by

$$L = \sum_s l_s \quad (>>R) \tag{8}$$

being the sum of the lengths of all segments (Fig. 3). By rescaling the segment-length parameters, $\bar{l}_s$ and σ_s, and the sample size we find that the percolation frequency ν can be expressed as function of two independent parameters: R, the sample size, and

$$\zeta = (4\ \rho_A R^2)\pi(\bar{l}_s/2)^2/R^2 = \pi\rho_A \bar{l}_s^2 \tag{9}$$

As here defined, ζ has the meaning of the relative effective area of the crack segments, being the number of segments times the circular area swept out by an average rotating segment divided by the sample size. The sweeping-out of the effective area is linked to the random orientation of the segments: it represents an average effective region for each segment within which the intersection with another crack, approaching it from outside the region, is likely. Therefore ζ is the *effective bond-occupation probability* in our continuum model. Our numerical simulations yield ν as function of ζ and the sample size R.

Taking the model of circular regions literally, one obtains the probability p of one crack intersecting at least one other crack in terms of the geometric probability that on a plane, on which circular disks of constant radii $\bar{l}_s/2$ have been randomly thrown, one disk will be partially or fully overlapped by at least one other disk [22, 23]

$$p = 1 - e^{-\zeta} \tag{10}$$

with ζ given in equation (9), provided ρ_A is taken to be the surface density of disks.

Returning to the sigmoidal curves in Fig. 3, we will define the percolation threshold value $\zeta_T(R)$ in a sample of finite size R as the value of ζ where the relative percolation frequency $\nu = 1/2$. Alternative definitions for $\zeta_T(R)$, e.g., when $d\nu/d\zeta$ is maximum, give very similar results. As R increases, the threshold value $\zeta_T(R)$ apparently decreases and presumably reaches a limiting value $\zeta_T(\infty) = \zeta^*$.

The slope of the frequency curve, ν versus ζ, at ζ_T also rises with sample size and becomes according to the current notions of critical phenomena absolutely vertical for an infinite sample. In the limit $R \to \infty$ one anticipates having one (or possibly, but not likely, an infinite number of) infinite-size clusters of cracks; it has been shown that statistical weight of finite-size clusters shrinks to zero [24].

Thus one expects that a large rock will be impervious to gas flow up to a certain density of cracks, since no continuous pathway along cracks is available to the gas: $\nu = 0$. Then at a critical crack density, depending on the shapes of the cracks, the rock will necessarily become percolative: $\nu = 1$. The relation of the probability Π, introduced in equation (7), to ν will form the subject of the next section.

4 The Backbone Probability

From experiments and numerical simulations of electrical conductions in random networks [25–27] it has been known for some time that conductivity σ behaves differently from the relative percolation frequency (or, simply, percolation probability) ν, as function of the site or bond occupation probability p. Both σ and ν are initially zero, become nonzero at the critical occupation probability $p = p_c$ and rise to 1 at $p = 1$. However, their growths with $p - p_c$ take different forms, the curvatures of σ and ν being, respectively, positive

Downloaded 02 May 2010 to 171.66.16.250. Redistribution subject to ASME license or copyright; see http://www.asme.org/terms/Terms_Use.cfm

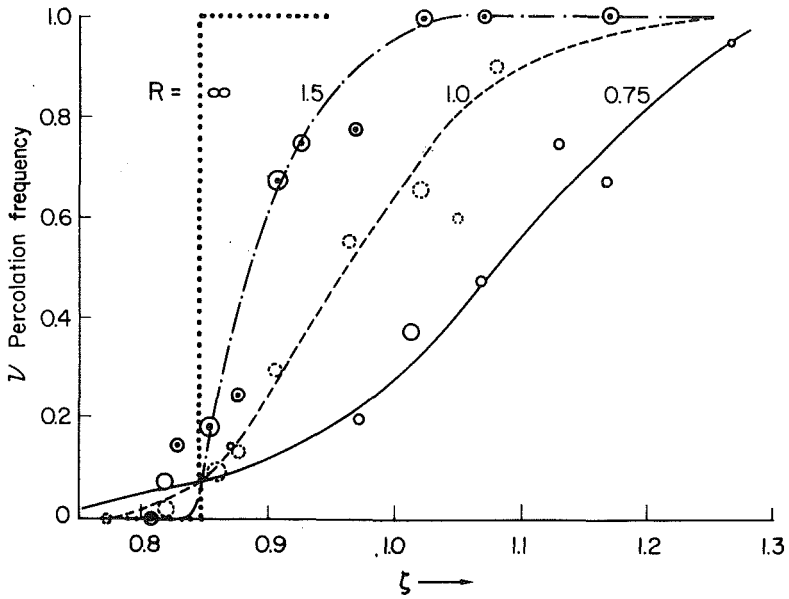


Fig. 3 Percolation frequency ν against ζ for different sample sizes R. ($\zeta \equiv \pi\rho_A l_s^2$, where ρ_A is the area density of cracks and l_s the mean segment length). The three sizes are: 0.7 cm: data points ◯ curve—— 1.0 cm: data points ◯ curve --- 1.5 cm: data points ◉ curve -·-·-. The dotted line is the asymptotic, infinite sample extrapolation. The diameters of the circles indicate the confidence weight of each data point: the largest circles are data points from about 120 simulation runs, smaller circles from less numerous runs.

and negative (for finite discrete networks) [25–27]. Clearly both $\nu \neq 0$ and $\sigma \neq 0$ are due to the backbone structure (namely, the set of cracks that cut across the medium) and are unaffected by isolated clusters or cul-de-sacs. On the other hand, the lengths of backbones are irrelevant to ν (which registers only the probability of passage) whereas they affect the conductivity σ.

The term "backbone probability" (short for probability of belonging to backbones) is used (in discrete-lattice structures) for the ratio

$$\sigma(p)/\sigma(p=1) \quad p>p_c \tag{11}$$

On the basis of the analogy [2] between the physical processes involved in conduction and in lamina gas flow, we propose to identify the scaled conductivity in equation (11) with the corresponding scaled permeability and a scaled quantity involving the probability Π introduced in Section 2 [equation (7)]. We expect the following equalities to be correct up to a factor of the order unity:

$$\frac{\rho_V}{\rho_{VT}}\Pi = \frac{K(p)}{K(p=1)} = \frac{\sigma(p)}{\sigma(1)}$$

where ρ_{VT} is the threshold value of the crack density and, in the context of gas flow across cracks, p has been defined in equation (10).

Determinations of the backbone probability have been made in two and three dimensions [25–27, 19], especially for p being in the neighborhood of p_c. In that region the principles of universality for critical phenomena [14], envisage a limiting behavior of the form

$$\frac{\rho_V}{\rho_{VT}}\Pi \propto (p-p_c)^t$$

According to different ways of determinations in finite size specimens, the critical exponent t varies between 0.9 and 1.5 in two dimensions and between 1.6 and 2 in three dimensions. (Reference [19] gives references and details).

From the point of view of measured permeabilities more significant is the broad variation of $\rho_V\Pi$ for p taking values from p_c up to 1. Numerical simulation of conductivity in finite samples throughout the range of p indicate the following dependence in three dimensions

$$\frac{\rho_V}{\rho_{VT}}\Pi = \frac{(p-p_c)^2}{(1-p_c)^2} \tag{12}$$

and a lower, but not clearly determinate, power dependence in two dimensions.

Our results for crack distributions in finite size two-dimensional specimens can be extrapolated to infinite samples (Fig. 3). We then obtain for the dimensionless parameter ζ, defined in equation (9), at the threshold

$$\zeta^* = \zeta(R=\infty) = 0.845 \pm 0.005$$

Assuming four segments in a crack, one can express this in terms of the following area density of cracks

$$\rho_{AT} = 0.269\,(\bar{l}_s)^{-2}$$

For the experimental parameter $\bar{l}_s = 0.02$ cm in Arkansas-Novaculite [18], there are 670 cracks per cm^2, at the gas-flow threshold.

The crossing point of the percolation frequencies at differing sample sizes, from which the limiting parameter ζ^* was derived (Fig. 3), occurs at

$$\left.\begin{aligned} \nu &= 0.08 \pm 0.0005 \\ p = p_c &= 0.570 \pm 0.0005 \end{aligned}\right\} \tag{13}$$

where equation (10) connects p_c and $\zeta = \zeta^*$.

Let it be noted that in a two-dimensional *discrete* square network being filled with nodes that are conducting with a probability p, there exists a complete homology between the conductive properties of this network and the blocking property of the network with occupation probability $1 - p$. Then by symmetry $p_c = 1/2$ and the crossing point occurs at $\nu = 1/2$. The homology also holds for percolation in continuous networks provided that the conductive and blocking channels have the same topological properties, e.g., seas and islands. In the present crack model the symmetry is lacking between flow along cracks and the blocking property of the rock. For this reason the values in (13) differ from those $(\frac{1}{2}, \frac{1}{2})$ in a topologically symmetric network.

Downloaded 02 May 2010 to 171.66.16.250. Redistribution subject to ASME license or copyright; see http://www.asme.org/terms/Terms_Use.cfm

5 Discussion and Conclusion

A semiquantitative expression has been proposed in equation (7) relating the fluid-flow permeability K in a rock to the characteristics of the crack network in it. The expression contains parameters of individual cracks, such as the small dimensions (d, the crack width) and its large dimensions (l_z, l_s). The statistical characterizations of the crack distribution included in the formula are the volume density ρ_v and the backbone probability Π (expressing the statistical efficiency of the crack system to facilitate gas flow).

The presence of the last quantity is apparently novel in the context of gas flow, though it is familiar in the related field of electrical conduction in random networks. Indeed we suggest that experimental and numerical determinations of Π in that field should be utilized in our expression. To a considerable extent those determinations should be independent of the details of the network (or of the model). On the other hand there are properties of Π that are model sensitive and our numerical investigations should provide estimates of these. Thus we have derived within our model a critical crack concentration beyond which flow is possible. We have also indicated the dependence of flow on sample size (Fig. 3).

Further work is required to broaden the significance of our numerical approach. An obvious need is the extension to three dimension. The dimension dependence of critical phenomena [20] can provide a guide near the permeability threshold and the results of Adler et al. [27] even beyond that. (It is noted that equation (7) is written in a form that applies to three-dimensional crack distributions.) Studies have been made to test computer models for cracks with segment numbers differing from 4. It is found that if one uses a smaller segment number (e.g., single segment cracks in place of four-segment cracks) one must use a larger segment length $\bar{l}_s$ (or $\bar{l}_c$), to get the same percolative properties. As expected, a larger deviation σ_s acts as though $\bar{l}_s$ were increased. The variation of widths (which forms the basis of previous work, e.g., in reference [6]) also needs to be investigated and so does the higher-order effect of width change due to application of pressure, as in hydraulic fracturing. Finally, one should study distributions of cracks such that include correlations between them in the course of their creation.

Acknowledgment

We have received useful advice from Professors A. Aharony, C. Domb, E. Domany, Y. Gefen, J. Gillis, and L. S. Schulman.

References

1 Scheidegger, A. E., *The Physics of Flow through Porous Media*, University of Toronto Press, Toronto, 1974.

2 Bear, I., *Dynamics of Fluids in Porous Media*, Elsevier, New York, 1972.

3 Lamb, H., *Hydrodynamics*, University Press, Cambridge, 1932.

4 Dullien, F. A. L., *Porous Media Fluid Transport and Pore Structure*, Academic Press, New York, 1979.

5 Carman, P. C., *Flow of Gases through Porous Media*, Butterworths, London, 1956.

6 Harring, R. E., and Greenkorn, R. A., "A Statistical Model of a Porous Medium With Nonuniform Pores," *Journal of the American Institute of Chemical Engineers*, Vol. 16, 1970, pp. 477–483.

7 Millington, R. J., and Quirk, J. P., "Permeability of Porous Solids," *Transactions of the Faraday Society*, Vol. 57, 1961, pp. 1200–1207.

8 Dienes, J. K., "Percolation Theory and the Permeability of Fractured Oil Shale," Los Alamos National Laboratory Report LA-8553-PR, Mar. 1981.

9 Fatt, I., "The Network Model of Porous Media," *Transactions of the American Institute of Mechanical Engineers, Petroleum Transactions*, Vol. 207, 1950, pp. 160–163.

10 Chatzis, I., and Dullien, F. A. L., "Modelling Pore Structure by 2-D and 3-D Network With Application to Sandstone," *Journal of Canadian Petrol Technology*, Vol. 16, 1977, pp. 97–108.

11 Essam, I. W., "Percolation Theory," *Reports on Progress in Physics*, Vol. 43, 1980, pp. 833–910.

12 De Gennes, P., and Guyon, E., "Lois Générales pour l'Injection d'un Fluide dans un Milieu Poreux Aléatoire," *Journal de Mécanique*, Vol. 17, 1978, pp. 403–432.

13 Dienes, J. K., "On the Permeability of Explosively Fractured Oil Shale," Los Alamos National Laboratory Report LA-87-69-PR, July 1981, pp. 21–25.

14 Dienes, J. K., "On the Inference of Crack Statistics From Observation on an Outcropping," *Proceeding of the 20th U.S. Symposium on Rock Mechanics*, Austin, Texas, 1979, pp. 390–399.

15 Watson, A. J., and Sanderson, A. J., "The Resistance of Concrete to Explosive Shock," *Institute of Physics Conference Series*, No. 47, Chapter 3, 1979, pp. 307–317.

16 Stroeven, P., "Geometric Probability Approaches to the Examination of Microcracking in Plain Concrete," *Journal of Materials Science*, Vol. 14, 1979, pp. 1141–1151.

17 Bowles, R., "The Effect of Grinding and Polishing on the Strength of Annealed Soda-Lime-Silica Glass," in *The Science of Ceramic Machining and Surface Finishing II*, National Bureau of Standards Special Publication No. 562, U.S. Government Printing Office, Washington, D.C., 1979, pp. 489–500.

18 Shockey, D. A., Petersen, C. F., Curran, D. R., and Rosenberg, J. T., "Failure of Rock Under High Rate Tensile Loads," in *New Horizons in Rock Mechanics*, Hardy, H. R., and Stefanko, R., eds., Fourteenth U.S. Symposium on Rock Mechanics, Pennsylvania, 1972, pp. 709–738.

19 Gefen, Y., Aharony, A., Mandelbrot, B. B., and Kirkpartick, S., "Solvable Fractal Family and its Possible Relation to the Backbone at Percolation," *Physical Review Letters*, Vol. 47, 1981, pp. 1771–1774.

20 Gawlinski, E. T., and Stanley, H. E., "Continuum Percolation in Two Dimensions: Monte Carlo Tests for Scaling and Universality for Noninteracting Discs," *Journal of Physics A*, Vol. 14, 1981, pp. L291–L299.

21 Hoshen, J., and Kopelman, R., "Percolation and Cluster Distribution. *I* Cluster Multiple Labeling Technique and Critical Concentration Algorithm," *Physical Review B*, Vol. 14, 1976, pp. 3438–3445.

22 Kendall, M. G., and Moran, P. A. P., *Geometrical Probability*, C. Griffin, London, 1963.

23 Vicsek, T., and Kertesz, J., "Monte Carlo Renormalization Group Approach to Percolation on a Continuum: Test of Universality," *Journal of Physics*, Vol. 14, 1981, pp. L31–L37.

24 Newman, C. M., and Schulman, L. S., "Number and Density of Percolating Clusters," *Journal of Physics A*, Vol. 14, 1981, pp. 1735–1743.

25 Last, B. I., and Thouless, D. J., "Percolation Theory and Electrical Conductivity," *Physical Review Letters*, Vol. 27, 1971, pp. 1719–1721.

26 Kirkpatrick, S., "Classical Transport in Disordered Media: Scaling and Effective-Medium Theories," *Physical Review Letters*, Vol. 27, 1971, pp. 1722–1725.

27 Adler, D., Flora, L. P., and Senturia, S. D., "Electrical Conductivity in Disordered Systems," *Solid-State Communications*, Vol. 12, 1973, pp. 9–12.

Downloaded 02 May 2010 to 171.66.16.250. Redistribution subject to ASME license or copyright; see http://www.asme.org/terms/Terms_Use.cfm

Ablation by Frictional Heating

L. N. Tao
Professor of Mechanics,
Department of Mechanical Engineering,
Illinois Institute of Technology,
Chicago, Ill. 60616
Fellow ASME

The ablation problem of a semi-infinite solid, moving at a constant speed parallel to its surface, is investigated. The study includes all induced motions caused by the density differences of various phases of the materials. Some appropriate transformations are introduced to reduce the problem to one where all phases behave as if they had the same density. The reduced problem is then solved by similarity transformations. It is found that the exact solution exists if and only if an inequality is satisfied. The physical interpretation of the inequality is examined. A numerical example is given to illustrate the result.

1 Introduction

An important feature of ablation problems is the occurrence of phase change. Surfaces that separate different phases are not at fixed locations. They are unknown a priori and depend on the state of materials adjacent to them. These problems fall into the general classification of moving boundary problems or Stefan problems.

Moving boundary problems have been investigated since the nineteenth century by the early works of Neumann, Stefan, and many others. The classical moving boundary problem is concerned with melting or freezing of a semi-infinite material initially at a constant temperature, which is in contact with a different temperature at its surface. A change of phase takes place immediately. The exact solution of this moving boundary problem was established by Neumann (see [1]) in the 1860s and by Stefan [2] in 1889. The solution is elegant and simple. The temperatures of both phases are expressed in error functions of a similarity variable $x/\sqrt{t}$ and the position of the interfacial boundary is proportional to $\sqrt{t}$. This means that the problem is solvable by a similarity transform, i.e., the partial differential equations of the problem are reducible to ordinary differential equations. Reduction to ordinary differential equations is possible only when the domain is infinite or semi-infinite and the prescribed initial and boundary conditions are of some special forms. To extend or generalize the solutions to problems with other boundary and initial conditions has been the objective of many investigations. Since similarity solutions to more general problems are usually not possible, many different mathematical techniques and approximate methods have been devised and applied to find the solutions to these moving boundary problems. Specific references may be found in many books [3–8] and survey papers [9–11]. There have also been numerous studies intended to find exact solutions to problems with more general initial and boundary conditions or to problems with more complicated differential equations. Only recently, some exact solutions of the classical Stefan problems with arbitrarily prescribed initial and boundary conditions in a semi-infinite region have been found [12–17]. The solutions of temperatures are expressed in series of functions and polynomials in the error integral family and time t, and the position of the interfacial boundary is an infinite series of $\sqrt{t}$.

The problem of ablation by frictional heating is more complex than the classical Stefan problem. In addition to temperatures, there are velocity components to be considered; the number of unknowns is greatly increased. Another difficulty is the presence of energy dissipations, generated by friction, which are proportional to squares of the velocity gradients. Also, there are convective motions induced by the density differences of various phases.

There are many studies of the ablation problems. References to these studies may be found in the foregoing cited books and survey papers. Most of these solutions are approximate ones. There is, however, an exact solution [18]. It adopts a commonly used assumption in moving boundary problems that the densities of all phases are equal. This assumption eliminates convective motions induced by those density jumps during phase transitions. A consequence of this assumption is the disappearance of nonlinear terms in the momentum and energy equations.

In this paper, we study the ablation problem of a semi-infinite solid moving at a constant speed parallel to the surface of contact. The solid is adjacent to a viscous incompressible fluid. The convective terms caused by density differences at the interfaces are included. Because of these added terms, a direct application of similarity transformation to these equations is no longer possible. However, we have found that by some appropriate transformations of the independent variables the equations are reducible to those without convective motions. In other words, we have found a reduced problem in which all phases behave as if they had the same density. With proper initial and boundary conditions we can then apply similarity transformations to study the problem.

In the next section we first formulate the problem and introduce the necessary transformations by which the original partial differential equations are reducible to a set of ordinary differential equations. These equations are then solved. The

Contributed by the Applied Mechanics Division for publication in the JOURNAL OF APPLIED MECHANICS.

Discussion on this paper should be addressed to the Editorial Department, ASME, United Engineering Center, 345 East 47th Street, New York, N.Y. 10017, and will be accepted until two months after final publication of the paper itself in the JOURNAL OF APPLIED MECHANICS. Manuscript received by ASME Applied Mechanics Division, January, 1983.

Copyright © 1983 by ASME
Downloaded 02 May 2010 to 171.66.16.250. Redistribution subject to ASME license or copyright; see http://www.asme.org/terms/Terms_Use.cfm

existence and uniqueness of the solution are then discussed in Section 3. We find that a unique solution exists if and only if an inequality is satisfied. Physical interpretation of this inequality is explored. Its implication agrees with the physics of the problem. In Section 4, we then give a numerical example which compares the result of interfacial positions with and without the assumption of equal densities.

2 Similarity Solutions

Consider a solid body occupying the half space $x<0$ and a viscous incompressible fluid occupying the half space $x>0$. The solid is moving at a constant speed parallel to the surface of contact. The surface of the solid, due to the effect of frictional heating, reaches the melting temperature at $t=0$. Subsequently, there coexist three different phases: a solid in the domain $-\infty<x<s$, a newly formed melt in $s<x<0$, and a flowing liquid, relative to the solid, in $0<x<\infty$, where $s(t)$ is the position of the interface between the solid and the melt. Also, we assume that the material properties of these three phases are different but constant. Let us denote these three phases: solid, melt, and liquid by subscripts 0, 1, and 2, respectively. Then, in the one-dimensional case the temperatures and the velocity components are at most functions of x and t. They must satisfy

(i) Differential Equations:

Solid:

$$\frac{\partial T_0}{\partial t}=\alpha_0\frac{\partial^2 T_0}{\partial x^2} \qquad -\infty<x<s(t)$$

Melt:

$$\frac{\partial v_1}{\partial t}+u_1\frac{\partial v_1}{\partial x}=\nu_1\frac{\partial^2 v_1}{\partial x^2}$$

$$\frac{\partial T_1}{\partial t}+u_1\frac{\partial T_1}{\partial x}=\alpha_1\frac{\partial^2 T_1}{\partial x^2}+\frac{\nu_1}{c_1}\left(\frac{\partial v_1}{\partial x}\right)^2 \qquad s(t)<x<0 \tag{2.1}$$

Liquid:

$$\frac{\partial v_2}{\partial t}+u_2\frac{\partial v_2}{\partial x}=\nu_2\frac{\partial^2 v_2}{\partial x^2}$$

$$\frac{\partial T_2}{\partial t}+u_2\frac{\partial T_2}{\partial x}=\alpha_2\frac{\partial^2 T_2}{\partial x^2}+\frac{\nu_2}{c_2}\left(\frac{\partial v_2}{\partial x}\right)^2 \qquad 0<x<\infty$$

(ii) Initial Conditions:

$$T_0(x,0)=\psi_0(x)$$
$$v_2(x,0)=\phi_2(x), \quad T_2(x,0)=\psi_2(x) \tag{2.2}$$

(iii) Boundary Conditions:

$$T_0(-\infty,t)=\psi_0(-\infty)$$
$$v_2(\infty,t)=\phi_2(\infty), \quad T_2(\infty,t)=\psi_2(\infty) \tag{2.3}$$

(iv) Interface Conditions at $x=s$:

$$v_1(s,t)=0, \quad T_0(s,t)=T_1(s,t)=T_m=0$$
$$k_0\frac{\partial T_0}{\partial x}\bigg|_{x=s}-k_1\frac{\partial T_1}{\partial x}\bigg|_{x=s}=\rho_1 L\frac{ds}{dt} \tag{2.4}$$

Here we have taken the melting temperature T_m of the solid to be the reference temperature.

(v) Interface Conditions at $x=0$:

$$v_1(0,t)=v_2(0,t), \quad T_1(0,t)=T_2(0,t)$$
$$\mu_1\frac{\partial v_1}{\partial x}\bigg|_{x=0}=\mu_2\frac{\partial v_2}{\partial x}\bigg|_{x=0}, \quad k_1\frac{\partial T_1}{\partial x}\bigg|_{x=0}=k_2\frac{\partial T_2}{\partial x}\bigg|_{x=0} \tag{2.5}$$

The symbols in these equations have their usual meanings: k = conductivity, α = diffusivity, μ = viscosity, ν = kinematic viscosity, ρ = density, c = specific heat, and L = latent heat.

In addition to the preceding equations and conditions, we also need continuity equations,

$$\partial u_1/\partial x=0 \quad \text{and} \quad \partial u_2/\partial x=0 \tag{2.6}$$

These two equations show that the velocity components perpendicular to the surface are functions of t only,

$$u_1=u_1(t) \quad \text{and} \quad u_2=u_2(t) \tag{2.7}$$

Therefore, applying the law of conservation of mass to the elements of interfaces at $x=s$ and $x=0$, we obtain

$$\rho_0\frac{ds}{dt}=\rho_1\left(\frac{ds}{dt}-u_1\right)$$
$$\rho_1 u_1=\rho_2 u_2 \tag{2.8}$$

or

$$u_1=\frac{\rho_1-\rho_0}{\rho_1}\frac{ds}{dt}=-\epsilon r_1\frac{ds}{dt}$$
$$u_2=(\rho_1/\rho_2)u_1=-\epsilon r_1 r_2\frac{ds}{dt} \tag{2.9}$$

where

$$r_i=\frac{\rho_{i-1}}{\rho_i}, \quad \epsilon=\frac{\rho_0-\rho_1}{\rho_0}=1-\frac{1}{r_1} \tag{2.10}$$

The preceding system is a set of nonlinear equations for determination of the unknowns T_i, v_i, and s. Fortunately, these nonlinear equations can be transformed, by some appropriate changes of the independent variables, to a system of linear ones. Introducing

$$\xi_1=\frac{x+(r_1-1)s}{r_1}=\frac{x}{r_1}+\epsilon s$$
$$\xi_2=\frac{x}{r_2}+\epsilon s \tag{2.11}$$

and

$$\beta_0^2=1/\alpha_0, \ \beta_i^2=r_i^2/\alpha_i, \ \gamma_i^2=r_i^2/\nu_i$$
$$\sigma_i=\nu_i/\alpha_i=\beta_i^2/\gamma_i^2=\text{Prandtl number} \quad (i=1,2) \tag{2.12}$$

we obtain

$$\beta_0^2\frac{\partial T_0}{\partial t}=\frac{\partial^2 T_0}{\partial x^2}$$
$$\gamma_i^2\frac{\partial v_i}{\partial t}=\frac{\partial^2 v_i}{\partial \xi_i^2}$$
$$\beta_i^2\frac{\partial T_i}{\partial t}=\frac{\partial^2 T_i}{\partial \xi_i^2}+\frac{\sigma_i}{c_i}\left(\frac{\partial v_i}{\partial \xi_i}\right)^2 \tag{2.13}$$

The new domains of the three phases are $(-\infty, s)$, $(s, \epsilon s)$, and $(\epsilon s, \infty)$, respectively. The initial and boundary conditions remain unchanged, but the interface conditions are now

(i) At $x=s$ and $\xi_1=s$:

$$v_1=0, \quad T_0=T_1=0$$

and

$$k_0(\partial T_0/\partial x)-(k_1/r_1)(\partial T_1/\partial \xi_1)=\rho_1 L(ds/dt) \tag{2.14}$$

(ii) At $x=0$ or $\xi_1=\xi_2=\epsilon s$:

$$v_1=v_2, \quad T_1=T_2$$
$$\frac{\mu_1}{r_1}\frac{\partial v_1}{\partial \xi_1}=\frac{\mu_2}{r_2}\frac{\partial v_2}{\partial \xi_2}, \quad \frac{k_1}{r_1}\frac{\partial T_1}{\partial \xi_1}=\frac{k_2}{r_2}\frac{\partial T_2}{\partial \xi_2} \tag{2.15}$$

In this study we are looking for a similarity solution. Similarity solutions exist only when the initial and boundary conditions are of some special forms. We assume that all

Downloaded 02 May 2010 to 171.66.16.250. Redistribution subject to ASME license or copyright; see http://www.asme.org/terms/Terms_Use.cfm

prescribed functions ψ_0, ϕ_2, and ψ_2 are constant. Introducing the similarity variables,

$$\zeta_0 = x/2\sqrt{t}, \quad \zeta_i = \xi_i/2\sqrt{t} \quad (i=1,2) \tag{2.16}$$

we obtain

$$\begin{aligned} &T_0''(\zeta_0) + 2\beta_0^2 \zeta_0 T_0'(\zeta_0) = 0 \\ &v_i''(\zeta_i) + 2\gamma_i^2 \zeta_i v_i'(\zeta_i) = 0 \\ &T_i''(\zeta_i) + 2\beta_i^2 \zeta_i T_i'(\zeta_i) + (\sigma_i/c_i)[v_i'(\zeta_i)]^2 = 0 \end{aligned} \tag{2.17}$$

subject to the conditions

(i)

$$\begin{aligned} &T_0(-\infty) = \psi_0 \\ &v_2(\infty) = \phi_2, \quad T_2(\infty) = \psi_2 \end{aligned} \tag{2.18}$$

(ii) **At** $\zeta_0 = \zeta_1 = s/2\sqrt{t}$

$$\begin{aligned} &v_1 = 0, \quad T_0 = T_1 = 0 \\ &k_0(\partial T_0/\partial\zeta_0) - (k_1/r_1)(\partial T_1/\partial\zeta_1) = 2\rho_1 L\sqrt{t}(ds/dt) \end{aligned} \tag{2.19}$$

(iii) **At** $\zeta_1 = \zeta_2 = \epsilon s/2\sqrt{t}$

$$\begin{aligned} &v_1 = v_2, \quad T_1 = T_2 \\ &(\mu_1/r_1)(\partial v_1/\partial\zeta_1) = (\mu_2/r_2)(\partial v_2/\partial\zeta_2) \\ &(k_1/r_1)(\partial T_1/\partial\zeta_1) = (k_2/r_2)(\partial T_2/\partial\zeta_2) \end{aligned} \tag{2.20}$$

It is clearly seen that a similarity solution exists only when the position of the interface $s(t)$ is proportional to $\sqrt{t}$. Accordingly, we introduce

$$s(t) = 2\lambda\sqrt{t} \tag{2.21}$$

The solutions of these ordinary equations are

$$\begin{aligned} &T_0 = C_0 + D_0 \operatorname{erfc}(-\beta_0\zeta_0) \\ &v_i = A_i + B_i \operatorname{erfc}(\gamma_i\zeta_i) \\ &T_i = C_i + D_i \operatorname{erfc}(\beta_i\zeta_i) \\ &\quad + \frac{\sqrt{\pi}}{2}\frac{\sigma_i}{c_i\beta_i}\int_{b_i}^{\zeta_i} e^{\beta_i^2 y^2}[v_i'(y)]^2[\operatorname{erfc}(\beta_i\zeta_i) - \operatorname{erfc}(\beta_i y)]dy \end{aligned} \tag{2.22}$$

where erfc(z) is the complimentary error function. The particular integrals in the preceding solutions can be found by direct integrations. Complimentary error functions of negative arguments are related to those of positive arguments by

$$\operatorname{erfc}(-z) = 2 - \operatorname{erfc}(z)$$

Since ζ_1 and ζ_2 are only defined in $(\lambda, \epsilon\lambda)$ and $(\epsilon\lambda, \infty)$, we choose

$$b_1 = \lambda, \quad b_2 = \epsilon\lambda \tag{2.23}$$

An alternate choice of b_2 could be ∞. This choice would simplify the determination of some constants. However, it might lead to some divergent integrals in later computations, particularly when β_2 is larger than β_1 or, more specifically, when the difference of Prandtl numbers between the liquid and the melt is larger than 2.

To complete the solutions, we need to find all 11 constants A_i, B_i, C_i, D_i, and λ. From the initial conditions, we obtain

$$\begin{aligned} &C_0 = \psi_0, \quad A_2 = \phi_2 \\ &C_2 = \psi_2 + \frac{\sqrt{\pi}}{2}\frac{\sigma_2}{c_2\beta_2}\int_{\epsilon\lambda}^{\infty} e^{\beta_2^2 y^2}[v_2'(y)]^2\operatorname{erfc}(\beta_2 y)dy \end{aligned} \tag{2.24}$$

It is noted that the integral in C_2 is always bounded since $v_2'(z)$ is of the exponentially decaying type and

$$\exp(\beta_2^2 y^2)\operatorname{erfc}(\beta_2 y)$$

is bounded between 0 and 1. From the interface conditions at $\zeta_0 = \zeta_1 = \lambda$, we obtain

$$\begin{aligned} &D_0 = -\psi_0/\operatorname{erfc}(-\beta_0\lambda) \\ &A_1 = -B_1\operatorname{erfc}(\gamma_1\lambda) \\ &C_1 = -D_1\operatorname{erfc}(\beta_1\lambda) \end{aligned} \tag{2.25}$$

and

$$k_0\beta_0\psi_0\frac{e^{-\beta_0^2\lambda^2}}{\operatorname{erfc}(-\beta_0\lambda)} - (k_1\beta_1 D_1/r_1)e^{-\beta_1^2\lambda^2} + \rho_1 L\sqrt{\pi}\lambda = 0$$

From the interface conditions at $\zeta_1 = \zeta_2 = \epsilon\lambda$, we obtain, though somewhat lengthy,

$$\begin{aligned} B_1 &= \phi_2[\operatorname{erfc}(\epsilon\gamma_1\lambda) - \operatorname{erfc}(\gamma_1\lambda) \\ &\quad - r_1(\gamma_2/\gamma_1)e^{\epsilon^2\lambda^2}(\gamma_2^2 - \gamma_1^2)\operatorname{erfc}(\epsilon\gamma_2\lambda)]^{-1} \\ B_2 &= r_1(\gamma_2/\gamma_1)e^{\epsilon^2\lambda^2(\gamma_2^2-\gamma_1^2)}B_1 \\ D_1 &= \left[\operatorname{erfc}(\epsilon\beta_1\lambda) - \operatorname{erfc}(\beta_1\lambda) \right. \\ &\quad \left. - \frac{k_1}{k_2}\left(\frac{\alpha_2}{\alpha_1}\right)^{\frac{1}{2}} e^{\epsilon^2\lambda^2(\beta_2^2-\beta_1^2)}\operatorname{erfc}(\epsilon\beta_2\lambda)\right]^{-1} \\ &\quad \times\left\{\psi_2 + \frac{\sqrt{\pi}}{2}\frac{\sigma_1}{c_1\beta_1}\int_{\lambda}^{\epsilon\lambda} e^{\beta_1^2 y^2}[v_1'(y)]^2\left[\operatorname{erfc}(\beta_1 y) - \operatorname{erfc}(\epsilon\beta_1\lambda)\right.\right. \\ &\quad \left.\left. + \frac{k_1}{k_2}\left(\frac{\alpha_2}{\alpha_1}\right)^{\frac{1}{2}} e^{\epsilon^2\lambda^2(\beta_2^2-\beta_1^2)}\operatorname{erfc}(\epsilon\beta_2\lambda)\right]dy \right. \\ &\quad \left. + \frac{\sqrt{\pi}}{2}\frac{\sigma_2}{c_2\beta_2}\int_{\epsilon\lambda}^{\infty} e^{\beta_2^2 y^2}[v_2'(y)]^2\operatorname{erfc}(\beta_2 y)\,dy\right\} \\ D_2 &= \frac{k_1}{k_2}\left(\frac{\alpha_2}{\alpha_1}\right)^{\frac{1}{2}} e^{\epsilon^2\lambda^2(\beta_2^2-\beta_1^2)}\left\{D_1 \right. \\ &\quad \left. + \frac{\sqrt{\pi}}{2}\frac{\sigma_1}{c_1\beta_1}\int_{\lambda}^{\epsilon\lambda} e^{\beta_1^2 y^2}[v_1'(y)]^2 dy\right\} \end{aligned} \tag{2.26}$$

Thus all 10 constants are uniquely determined when the value of λ is known.

We also note that the preceding solution is equally valid when the effect of density differences is ignored. In that case, $r_1 = 1$ and $\epsilon = 0$ which imply $u_1 = u_2 = 0$. We recover the case considered in [18]. However, due to different choices of integration limits as discussed previously, the two solutions are equivalent but not the same.

3 Existence and Uniqueness

In the preceding section we have established the solution of the problem if the value of λ can be found. It is the purpose of this section to show that the value of λ exists if and only if an inequality is satisfied. This inequality is definitely necessary from the physics of the problem. Furthermore, when λ exists, it is unique. This in turn shows that the special similarity solution is unique.

The value of λ satisfies

$$k_0\beta_0\psi_0\frac{e^{-\beta_0^2\lambda^2}}{\operatorname{erfc}(-\beta_0\lambda)} - (k_1\beta_1 D_1/r_1)e^{-\beta_1^2\lambda^2} + \rho_1 L\sqrt{\pi}\lambda = 0 \tag{3.1}$$

This transcendental equation has both positive and negative roots. However, a positive root is physically inadmissible, since it corresponds to an unrealistic case where an increase of solid material would appear by ablation. We thus ignore the positive root of this equation.

Downloaded 02 May 2010 to 171.66.16.250. Redistribution subject to ASME license or copyright; see http://www.asme.org/terms/Terms_Use.cfm

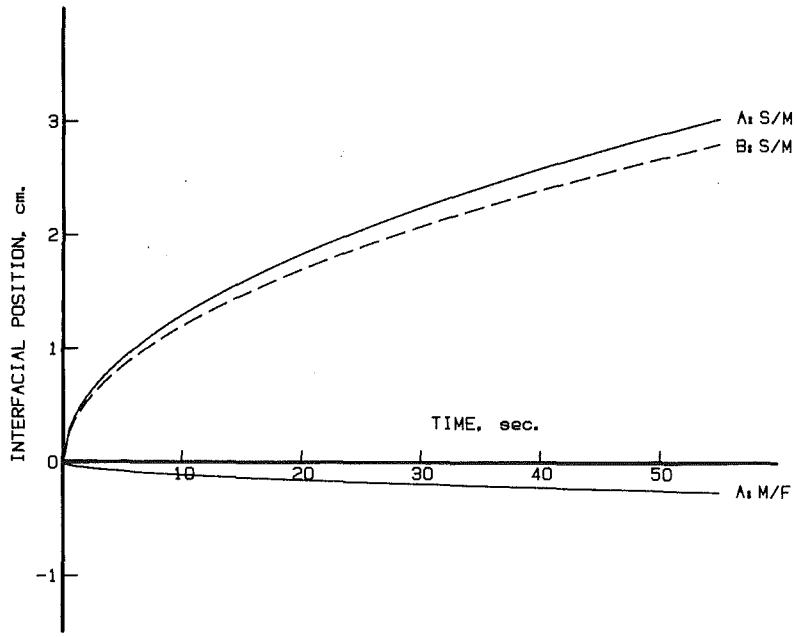


Fig. 1 Interfacial positions. A: Different densities; B: equal density. *S/M* = solid/melt, *M/F* = melt/fluid.

For negative λ, let us introduce $\lambda = -\omega$ and rewrite the equation,

$$k_1 e^{(\beta_0^2-\beta_1^2)\omega^2}\,\mathrm{erfc}(\beta_0\omega) = 1 + K_2\sqrt{\pi}\beta_0\omega e^{\beta_0^2\omega^2}\,\mathrm{erfc}(\beta_0\omega) \qquad (3.2)$$

where

$$K_1 = (k_1\beta_1/k_0\beta_0 r_1)(D_1/\psi_0), \quad K_2 = -\rho_1 L/k_0\beta_0^2\psi_0$$

We assume that all material constants are positive and $\psi_0 < 0$. From $\epsilon < 1$, we observe that D_1 is negative, since both complimentary error integrals and exponential functions are positive and

$$\mathrm{erfc}(-z) > \mathrm{erfc}(-\epsilon z)$$

for positive z. This in turn shows that K_1 and K_2 are positive.

To examine the existence of ω, we first note that for positive ω,

$$\exp[(\beta_0^2-\beta_1^2)\omega^2]\mathrm{erfc}(\beta_0\omega)$$

is monotone decreasing bounded between 1 and 0 since

$$\exp[(\beta_0^2-\beta_1^2)\omega^2]\mathrm{erfc}(\beta_0\omega)\,|_0 = 1$$

$$\exp[(\beta_0^2-\beta_1^2)\omega^2]\mathrm{erfc}(\beta_0\omega)\,|_\infty = 0$$

$$\frac{d}{d\omega}\{\exp[(\beta_0^2-\beta_1^2)\omega^2]\mathrm{erfc}(\beta_0\omega)\}$$

$$= -2\omega\exp[(\beta_0^2-\beta_1^2)\omega^2][\beta_1^2\,\mathrm{erfc}(\beta_0\omega) + \beta_0\, i\mathrm{erfc}(\beta_0\omega)] < 0$$

where $i\mathrm{erfc}(z)$ is the first repeated error integral. Also,

$$\sqrt{\pi}xe^{x^2}\,\mathrm{erfc}(x)$$

is monotone increasing [19] bounded between 0 and 1, since

$$\sqrt{\pi}xe^{x^2}\,\mathrm{erfc}\,x\,|_0 = 0$$

$$\sqrt{\pi}xe^{x^2}\,\mathrm{erfc}\,x\,|_\infty = 1$$

$$\frac{d}{dx}[\sqrt{\pi}xe^{x^2}\,\mathrm{erfc}\,x] = 2e^{x^2}\int_x^\infty\left(1-\frac{x^2}{z^2}\right)e^{-z^2}\,dz > 0$$

Thus the left-hand side of (3.2) is monotone decreasing from K_1 to 0 and the right-hand side is monotone increasing from 1 to $1+K_2$, where both K_1 and K_2 are positive. Hence a unique solution of ω or a negative λ exists if and only if

$$K_1 = (k_1\beta_1/k_0\beta_0 r_1)(D_1/\psi_0) > 1 \qquad (3.3)$$

This inequality is satisfied by a large absolute value of D_1 or a small absolute value of ψ_0, where both D_1 and ψ_0 are negative. Physically, it means that a unique solution exists when (*i*) the relative motion between the solid and the fluid is high, (*ii*) the initial temperature of the solid is close to the melting temperature, or (*iii*) the initial temperature of the fluid is high above the melting temperature. From a physical point of view, these effects are expected to be the dominant factors of ablation problems.

4 Illustrative Example

Let us consider a solid of ice that is in contact with sea water. The initial temperatures are $-5°C$ and $10°C$, respectively. The initial speed is 10 m/sec. Using the following numerical data in CGS units,

Ice:

$\rho_0 = 0.92$, $k_0 = 0.0053$, $c_0 = 0.502$, $L = 73.6$

Water:

$\rho_1 = 1$, $k_1 = 0.00144$, $c_1 = 1$, $\mu_1 = 0.018$

Sea Water:

$\rho_2 = 1.03$, $k_2 = 0.00144$, $c_2 = 1$, $\mu_2 = 0.018$

we may proceed to evaluate the position of the interfacial boundary, which is the solution of (3.2). It is noted that this example is used for illustration purpose. Any additional factors, which were not discussed in the previous sections, for example, mixing of two liquids, are not considered in this example.

Newton-Raphson's method is used to find the root of (3.2) and the integrals in these calculations are evaluated by Gaussian and Laguerre quadratures. The positive root of ω or negative λ is found to be 0.20435. The value is then used to calculate positions of the interfacial boundaries which are given in Fig. 1. They are labeled as Curves A: Curve A:*S/M* is the position of the interfacial boundary between the solid and the melt and Curve A:*M/F* is that between the melt and the fluid. For comparison, the value of ω for the same material combinations but with equal densities, i.e., $\rho_0 = \rho_1 = \rho_2 = 1$, is also evaluated. The result is shown as Curve B. The interfacial boundary between the solid and the melt is depicted by Curve B:*S/M*. Clearly there is only one curve, since the interfacial boundary between the melt and the fluid

Downloaded 02 May 2010 to 171.66.16.250. Redistribution subject to ASME license or copyright; see http://www.asme.org/terms/Terms_Use.cfm

remains at $x=0$. It is seen that the assumption of equal density underestimates the formation of the melt at both interfacial boundaries. Finally, we remark that even when the melt has the same density as the fluid, the interfacial boundary between them is not at $x=0$ if the solid and the melt are not of the same density.

Acknowledgment

This research is based on work supported by the National Science Foundation under Grant MEA 79-21350.

References

1 Riemann, G. F. B., and Weber, H., "Die Partiellen Differentialgleichungen der Mathematischen Physik," Bd. 2, 5-fl Aufl., Braunschweig, 1912.

2 Stefan, J., "Über Einige Probleme der Theorie der Wärmeleitung," *S.-B. Wien. Akad. Mat. Natur.*, Vol. 98, 1889, pp. 473-484.

3 Rubinstein, L. I., "The Stefan Problem" (English translation), *Am. Math. Soc.*, 1971.

4 Carslaw, H. S., and Jaeger, J. C., *Conduction of Heat in Solids*, 2nd ed., Clarendon Press, Oxford, 1959.

5 Crank, J., *The Mathematics of Diffusion*, 2nd ed., Clarendon Press, Oxford, 1975.

6 Ockendon, J. R., and Hodgkins, W. R., eds., *Moving Boundary Problems in Heat Flow and Diffusion*, Clarendon Press, Oxford, 1975.

7 Wilson, D. G., Solomon, A. D., and Boggs, P. T., eds., *Moving Boundary Problems*, Academic Press, New York, 1978.

8 Özisik, M. N., *Heat Conduction*, Wiley, New York, 1980.

9 Bankoff, S. G., "Heat Conduction or Diffusion With Change of Phase," *Adv. Chem. Eng.*, Vol. 5, 1964, pp. 75-150.

10 Muehlbauer, J. C., and Sunderland, J. E., "Heat Conduction With Freezing or Melting," *Appl. Mech. Rev.*, Vol. 18, 1965, pp. 951-959.

11 Boley, B. A., "Survey of Recent Developments in the Fields of Heat Conduction in Solids and Thermo-Elasticity," *Nuclear Eng. Des.*, Vol. 18, 1972, pp. 377-399.

12 Tao, L. N., "The Stefan Problem With Arbitrary Initial and Boundary Conditions," *Quart. Appl. Math.*, Vol. 36, 1978, pp. 223-233.

13 Tao, L. N., "On Free Boundary Problems With Arbitrary Initial and Flux Conditions," *ZAMP*, Vol. 30, 1979, pp. 416-426.

14 Tao, L. N., "Free Boundary Problems With Radiation Boundary Conditions," *Quart. Appl. Math.*, Vol. 37, 1979, pp. 1-10.

15 Tao, L. N., "The Analyticity of Solutions of the Stefan Problem," *Arch. Rational Mech. Anal.*, Vol. 72, 1980, pp. 285-301.

16 Tao, L. N., "On Solidification Problems Including the Density Jump at the Moving Boundary," *Quart. J. Mech. Appl. Math.*, Vol. 32, 1979, pp. 175-185.

17 Tao, L. N., "The Exact Solutions of Some Stefan Problems With Prescribed Heat Flux," ASME JOURNAL OF APPLIED MECHANICS, Vol. 48, 1981, pp. 732-736.

18 Grigorjan, S. S., "On Heating and Melting of a Solid Body Owing to Friction," *Prikl. Mat. Meh.*, Vol. 22, 1958, pp. 577-585; also, English translation, *J. Appl. Math. Mech.*, Vol. 22, 1958, pp. 815-825.

19 Tao, L. N., "The General Solution and Its Analyticity for Growth or Dissolution of a Gas Bubble," *J. Chem. Phys.*, Vol. 71, 1979, pp. 3455-3461.

Downloaded 02 May 2010 to 171.66.16.250. Redistribution subject to ASME license or copyright; see http://www.asme.org/terms/Terms_Use.cfm

Compression of Fluid-Filled Spherical Shells by Rigid Indenters

L. A. Taber
Assistant Professor,
Department of Mechanical Engineering,
University of Rochester,
Rochester, N.Y. 14627
Assoc. Mem. ASME

Two variational solutions were studied for large deflection of a fluid-filled hemispherical shell by a rigid cylindrical indenter. One solution is based on shell theory (including bending and stretching energy) and the other on a membrane model (stretching only). To study the transition from bending to membrane action, calculations are compared to load and fluid pressure data from experiments on water-filled rubber shells of various thicknesses. While bending effects dominate deflection as large as 20 percent of the radius for very thick shells ($R/t \lesssim 10$), the results indicate that membrane stress is significant in thinner shells even when the deflection is small.

Introduction

Bending often dominates large deflection of a thin shell. By taking advantage of this fact, Ashwell [1] and Ranjan and Steele [2] obtained analytical solutions to the problem of large deflection of an empty spherical shell due to a concentrated load applied at the apex. The dimpling of a spherical shell under a flat plate was studied in detail by Updike and Kalnins [3, 4]. And through asymptotic analysis, Wan [5] found that the inextensional bending solution dominates the axisymmetric dimpling of spherical shells under a variety of surface loadings. The pressure distributions he investigated were inward near the apex and outward near the equator for a complete shell, similar to the loading studied in this paper for the compression of a fluid-filled shell. Here, however, the constraint due to the incompressible fluid forces significant stretching of the middle surface.

Related membrane and shell problems have appeared in the literature. Using a theory that includes the effects of material nonlinearity for large strain, Feng and Yang [6] analyzed an inflated spherical membrane compressed between two flat plates, and Lardner and Pujara [7] extended their analysis to a membrane filled with an incompressible fluid. The effects of significant bending rigidity were studied by Taber [8], who extended the work of Ranjan and Steele [2] to a fluid-filled hemispherical shell. Experiments and calculations for a thick shell ($R/t = 6$) under a point load showed that bending stress governs the behavior for deflection less than 20 percent of the shell radius, but membrane stress dominates larger deflection. Part of the present paper is based on extension of the work in [8].

The purpose of this investigation is to determine the conditions under which a membrane model adequately describes the behavior of a fluid-filled shell. While bending effects are initially important during deformation of a thick shell [8], obviously a balloon can be considered a membrane even when the deflection is small. But where is the transition point and how does it depend on the geometry? Here, we study two analytic models that are based on moderately large rotation theory (small strain). One model is a fluid-filled membrane (membrane model) while the other includes both bending and stretching energy (shell model). After both models are analyzed by strain energy approaches, calculations and experimental results are compared for water-filled hemispherical shells of various thicknesses being compressed by rigid cylindrical indenters of several diameters.

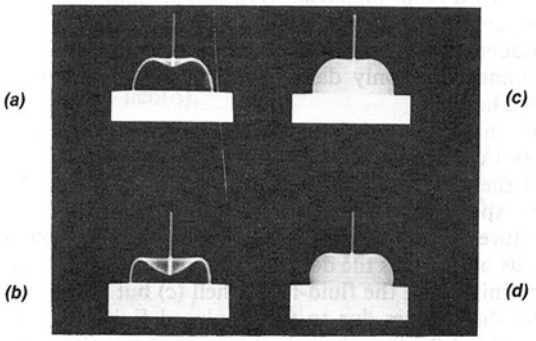


Fig. 1 X-rays of Shell 4 when empty (left) and fluid-filled (right) for $\Delta/R = 0.4$ and 0.8 ($r_0 = 1.25$ mm)

Experiment

Compression tests were conducted on four rubber shells, i.e., commercially manufactured racquetballs, with the following properties:

Shell 1: $R = 25.8$ mm, $t = 4.5$ mm ($R/t = 5.7$)
Shell 2: $R = 25.0$ mm, $t = 2.7$ mm ($R/t = 9.3$)

Contributed by the Applied Mechanics Division for publication in the JOURNAL OF APPLIED MECHANICS.
Discussion on this paper should be addressed to the Editorial Department ASME, limited Engineering Center, 345 East 47th Street, New York, N.Y. 10017, and will be accepted until two months after final publication of the paper itself in the JOURNAL OF APPLIED MECHANICS. Manuscript received by ASME Applied Mechanics Division, November, 1982; final revision May, 1983.

Copyright © 1983 by ASME
Downloaded 02 May 2010 to 171.66.16.250. Redistribution subject to ASME license or copyright; see http://www.asme.org/terms/Terms_Use.cfm

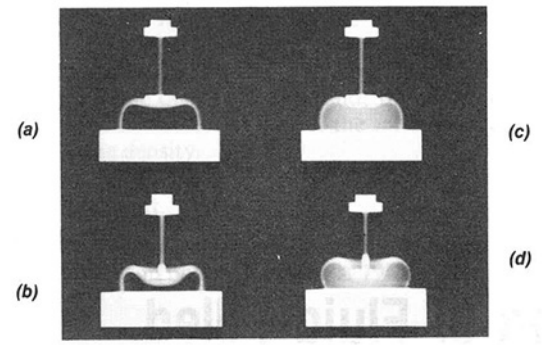


Fig. 2 X-rays of Shell 1 when empty (left) and fluid-filled (right) for $\Delta/R = 0.4$ and 0.8 ($r_0 = 10.0$ mm)

Shell 3: $R = 24.6$ mm, $t = 2.3$ mm ($R/t = 10.7$)
Shell 4: $R = 24.6$ mm, $t = 1.8$ mm, ($R/t = 13.7$)
$E = 4000$ kPa, $\nu = 0.5$

where R is the radius of the middle surface, t is the thickness, E is Young's modulus for small strain, and ν is Poisson's ratio for the homogeneous, isotropic material. Shell 1 represents original racquetball geometry; each of the other shells was formed by machining the outside of the upper half of a ball to the thickness indicated. Details of the experimental procedure are described in Taber [8]. Briefly, after the lower half of the shell was glued into a rigid hemispherical support, a hydraulic testing machine applied a slow displacement at the apex through cylindrical aluminum indenters of sizes ranging from essentially a point load (radius $r_0 = 1.25$ mm) to a flat plate. Both empty and water-filled shells were tested with displacement, load, and fluid pressure recorded simultaneously. Only data from the loading phase is considered here.

The character of deformation is illustrated through x-rays. Figure 1 compares the deformed shape of an empty to a fluid-filled shell (Shell 4) under a point load. In agreement with other experimental observations [1, 8, 9], a dimple of reversed curvature forms under the load in the empty shell (*a*) and spreads outward as the deflection increases (*b*). A dimple also forms initially in the fluid-filled shell (*c*) but begins to distort as the shell bulges due to the displaced fluid. At very large deflection (*d*), the shell looks like a membrane with a singularity under the load. So, consistent with the results in [8], in the fluid-filled shell there apears to be a transition from shell-like to membrane-like behavior, similar to that discussed by Reissner [10] for a hinged spherical cap with internal pressure.

The deformation of a thicker shell (Shell 1) under a larger indenter is shown in Fig. 2. Although a dimple again forms in the empty shell (*a*, *b*) the increasing fluid pressure eventually pushes the water-filled shell flat against the indenter (*c*). And even this very thick shell ($R/t = 5.7$) takes the form of a membrane at very large deflection (*d*).

Shell Model

With slight modification, the analysis of the shell model is that developed for a point load in Taber [8] and is only briefly described here. Since deformation is restricted to the upper hemisphere, the model reduces to a fluid-filled hemispherical cap clamped around its edge. The total deformation is divided into four steps (see Fig. 3 of [8]), which represent (*a*) formation of a dimple of reversed curvature, (*b*) bulging due to fluid pressure, (*c*) bending the edges to conform to continuity and boundary conditions, and (*d*) the local displacement under the load. The flattening of the shell against the indenter (Fig. 2 *c*, *d*) was not considered.

Significant contributions to the strain energy are due to stretching the middle surface in (*b*) and bending the edges in (*c*); step (*d*) is initially neglected. The modified total potential energy is

$$\Pi = U_M + U_B + U_L - p\Delta V \qquad (1)$$

where U_M and U_B are the strain energies due to membrane and bending stress (shear deformation is neglected), respectively, U_L is the potential of the applied load, and the last term represents the work due to the fluid. Since there is no change in enclosed volume ΔV for an incompressible fluid, the fluid pressure p acts as a Lagrange multiplier. With the nonlinear edge zone solution of Ranjan and Steele [2], Π can be expressed as a function of five displacement parameters and the multiplier. Equilibrium requires that the variation of Π with respect to each of these parameters vanish; variation with respect to p yields the fluid incompressibility condition $\Delta V = 0$. After the resulting six nonlinear algebraic equations were solved by successive approximation, adding the linear solution for a ring load on a shallow shell (step (*d*)) provided the total deflection.

To incorporate an indenter of finite radius, the analysis of [8] is slightly modified. The fourth deflection mode (see Fig.

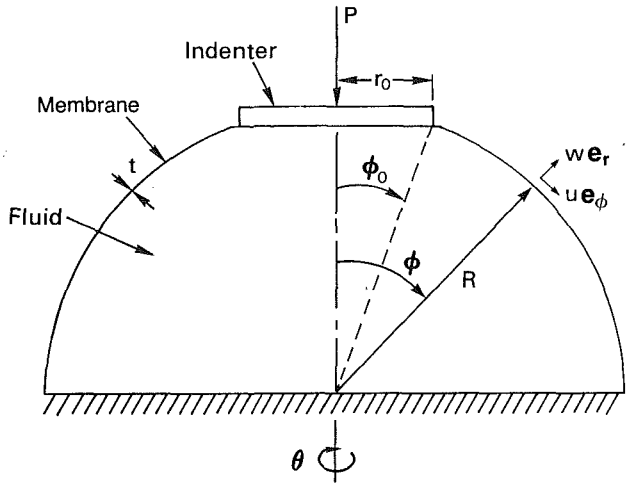


Fig. 3(*a*) Geometry of membrane model

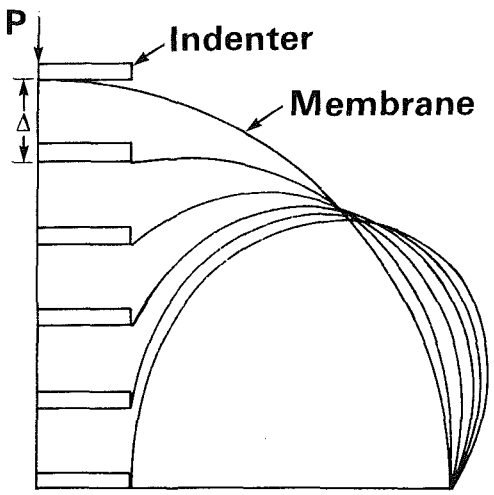


Fig. 3(*b*) Typical computed deformation shapes

Fig. 3

Downloaded 02 May 2010 to 171.66.16.250. Redistribution subject to ASME license or copyright; see http://www.asme.org/terms/Terms_Use.cfm

3(*d*) of [8]) is approximated by a ring load of radius r_0 on a shallow spherical shell segment, similar to a problem studied by Wan [11]. Here, the linear solution was obtained through the shallow shell theory of Reissner [12]. Another modification affects the deflection of the first mode ([8], Fig. 3(*a*)), which becomes

$$\Delta_1/R = 1 - 2\cos\alpha + [1-(r_0/R)^2]^{1/2} \tag{2}$$

for a ring load.

In the case of a flat plate, the deflection Δ_1 is half that for a point load and the ring load represents a rough approximation to the actual load, which is distributed over a small annular area at the edge of the dimple (see [3, 4]). In addition, the results in this paper include the effects of the deflection Δ_2, which was neglected along with Δ_3 in [8] in comparison with Δ_1. As in [8], results for the empty shell were obtained by setting $U_M = p = 0$.

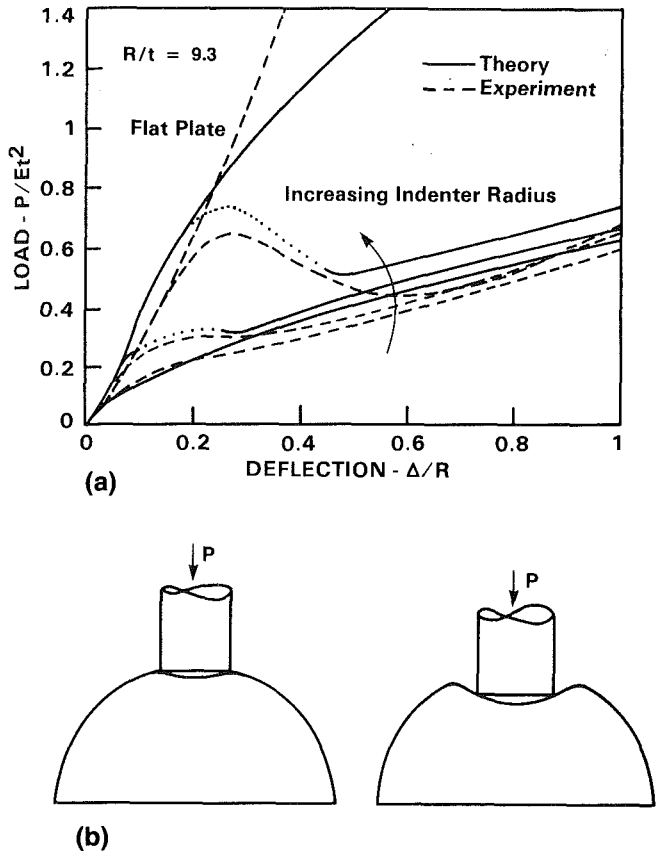


Fig. 4(*a*) Experimental and calculated load-deflection curves for empty Shell 2 (r_0 = 1.25, 3.75, 10.0, ∞ mm); (*b*) transition from flat-plate-type (left) to point-load-type behavior (right)

Membrane Model

For relatively small indenters, the membrane model (Fig. 3(*a*)), like the shell model, can neglect the deformation directly beneath the indenter. With no slipping allowed between the indenter and the membrane, the model, therefore, consists of a segment of a fluid-filled spherical membrane clamped at its lower edge to a rigid support and at its upper edge to the indenter.

Potential Energy. The strain energy stored in the spherical membrane due to stretching is

$$U_M = \frac{\pi E t R^2}{1-\nu^2}\int_{\phi_0}^{\pi/2}(\epsilon_\phi^2 + \epsilon_\theta{}^2 + 2\nu\epsilon_\phi\epsilon_\theta)\sin\phi d\phi \tag{3}$$

where the nonlinear membrane strains are

$$\epsilon_\phi = \frac{1}{R}\left(w + \frac{du}{d\phi}\right) + \frac{1}{2}\left(\frac{dw}{Rd\phi}\right)^2$$

$$\epsilon_\theta = \frac{1}{R}(w + u\cot\phi), \tag{4}$$

which are consistent with those used in the shell model and correspond to the nonlinear membrane theory of Bromberg and Stoker [13] for moderately large rotation. After sub-

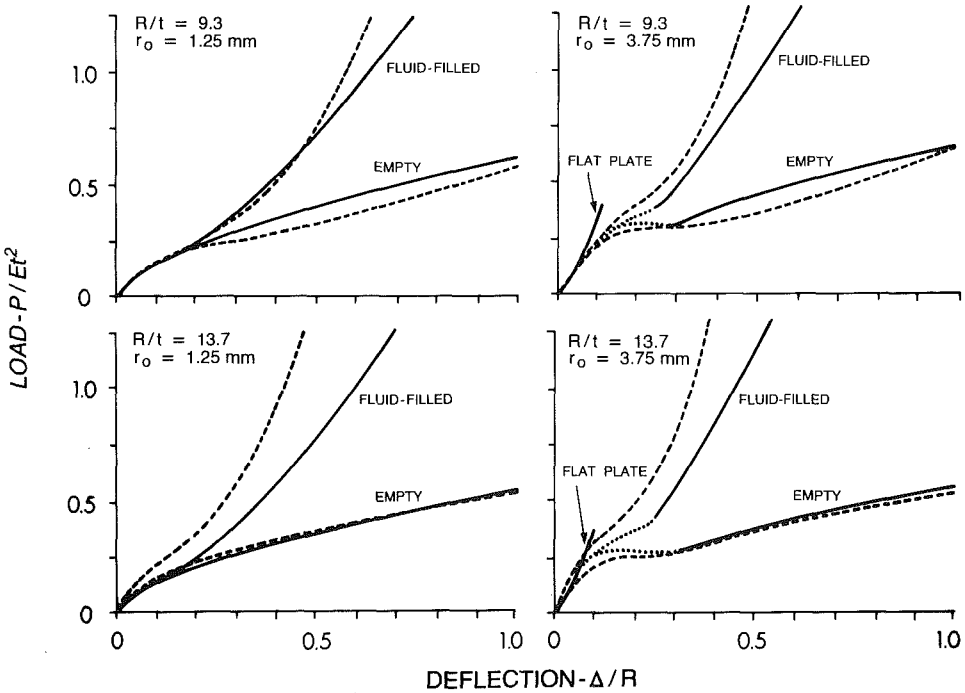


Fig. 5 Comparison of empty and fluid-filled response for Shells 2 and 4 under two indenter sizes(– shell model theory; – – – experiment)

Downloaded 02 May 2010 to 171.66.16.250. Redistribution subject to ASME license or copyright; see http://www.asme.org/terms/Terms_Use.cfm

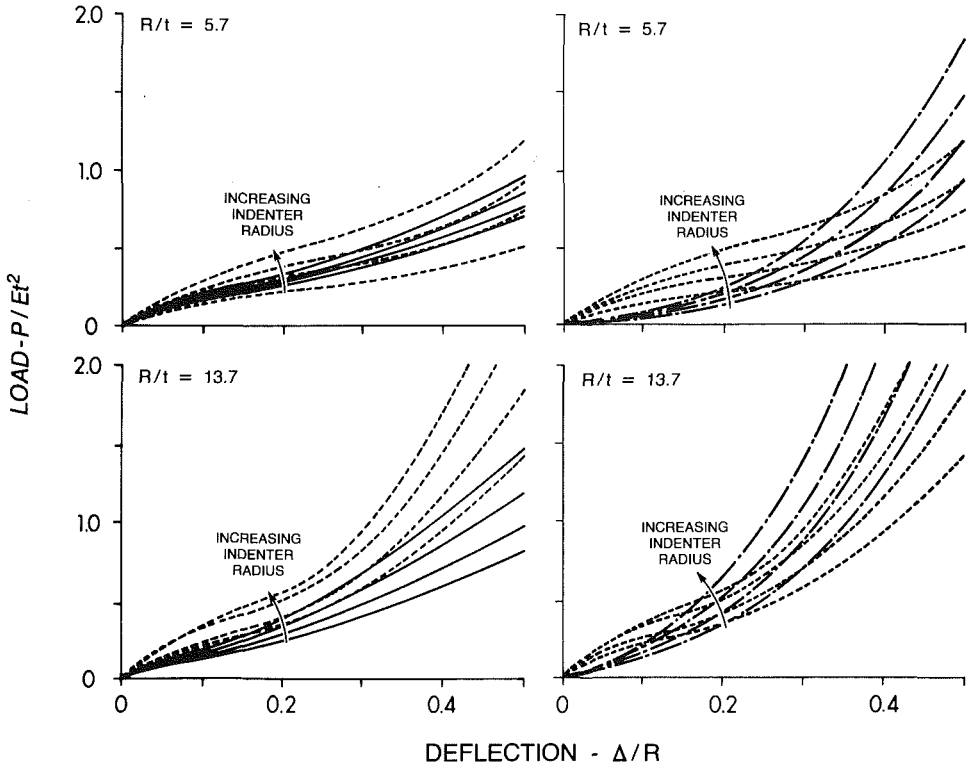


Fig. 6 Comparison of experimental load-deflection curves to calculations from shell model (left) and membrane model (right) for fluid-filled Shells 1 and 4 (r_0 = 1.25, 2.5, 3.75, 5.0 mm) (– shell model; – – – membrane model; – – – – experiment)

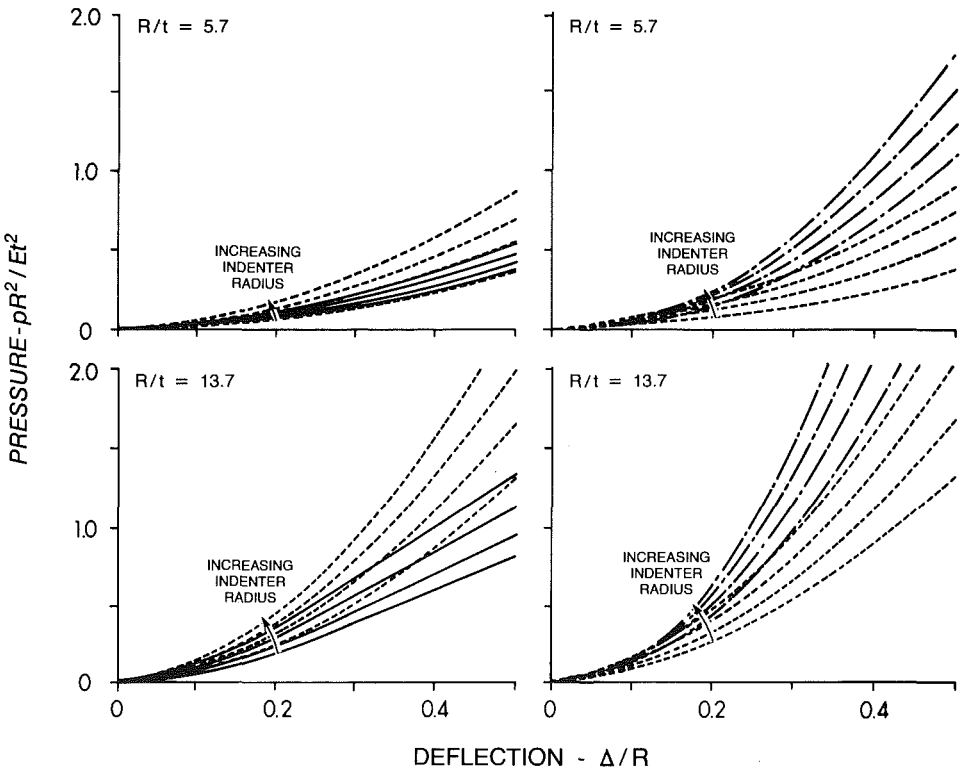


Fig. 7 Comparison of experimental fluid pressure-deflection curves to calculations from shell model (left) and membrane model (right) for Shells 1 and 4 (r_0 = 1.25, 2.5, 3.75, 5.0 mm) (– – shell model; – – · – – membrane model; – – – experiment)

stitution of equation (4) into equation (3), U_M becomes a function of the tangential and normal displacement components u and w, respectively.

Since the solution begins when the indenter makes full contact with the membrane, the potential of the applied load is

Downloaded 02 May 2010 to 171.66.16.250. Redistribution subject to ASME license or copyright; see http://www.asme.org/terms/Terms_Use.cfm

$$U_L = Pw(\phi_0)/\cos\phi_0 \tag{5}$$

where ϕ_0 is the meridional angle at the edge of the indenter, and the total downward displacement of the indenter is

$$\Delta = -w(\phi_0)/\cos\phi_0 + R(1-\cos\phi_0). \tag{6}$$

The modified total potential energy for the system is written

$$\Pi = U_M + U_L - p\Delta V + \lambda\epsilon_\theta(\phi_0), \tag{7}$$

which is essentially equation (1) with $U_B = 0$. The contribution involving a Lagrange multiplier λ is added to enforce the geometric constraint of zero horizontal displacement at the edge of the indenter, i.e., $\epsilon_\theta(\phi_0) = 0$. Through equations (3), (4), and (5) and the development in the Appendix for the computation of ΔV, Π becomes a function of u, w, p, and λ for a given applied load P.

Method of Solution. The Rayleigh-Ritz technique provides an approximate solution to the problem. The displacement components were taken in the form of series

$$\begin{aligned} w(\phi) &= \sum_{n=0}^{\infty} a_n \alpha_n(\phi) \\ u(\phi) &= \sum_{n=0}^{\infty} b_n \beta_n(\phi) \end{aligned} \tag{8}$$

where a_n and b_n are amplitude parameters and the shape functions

$$\begin{aligned} \alpha_0(\phi) &= -\cos[\pi(\phi-\phi_0)/(\pi-2\phi_0)] \\ \beta_0(\phi) &= -\alpha_0(\phi)\tan\phi_0 \\ \alpha_n(\phi) &= \beta_n(\phi) \\ &= \sin[2n\pi(\phi-\phi_0)/(\pi-2\phi_0)], \quad n=1,2,\ldots \end{aligned} \tag{9}$$

were chosen to satisfy the boundary condition $u = w = 0$ at the lower edge ($\phi = \pi/2$) and to allow satisfaction of the other geometric constraints through the Lagrange multipliers p and λ.

After substitution of equation (8) into the displacement form of equation (7), equilibrium requires

$$\frac{\partial\Pi}{\partial a_n} = \frac{\partial\Pi}{\partial b_n} = 0, \; n=0,1,2,\ldots \tag{10}$$

and the constraint relations are given by

$$\begin{aligned} \frac{\partial\Pi}{\partial p} &= -\Delta V = 0 \\ \frac{\partial\Pi}{\partial\lambda} &= \epsilon_\theta(\phi_0) = 0. \end{aligned} \tag{11}$$

These relations provide a system of nonlinear algebraic equations which was solved by successvie approximations for a_n, b_n, p, and λ with the integrals evaluated numerically. Note that while the actual deformation (see Figs. 1 and 2) initially resembles the assumed deformation of the shell model ([8], Fig. 3), at larger deflection, the actual deformation looks like the computed shape of the membrane model (Fig. 3(*b*)).

Discussion of Results

The behavior of an empty shell is illustrated by the experimental load-deflection curves of Fig. 4(*a*) for several indenter sizes ranging from a point load ($r_0 = 1.25$ mm) to a flat plate ($r_0 = \infty$). For all of the indenters of finite radius, the load initially follows that of the flat plate, may reach a peak depending on the indenter size, and then falls toward the curve for the point load. As found by Evan-Iwanowski et.al. [9] in experiments with ring loads on spherical shells, there is a minimum indenter radius, below which no peak occurs, i.e., the load increases monotonically. But unlike the ring load results, for larger indenters there is no sharp jump in load past the peak, which would indicate local buckling. Instead, there is a smooth transition from the stiff flat-plate-type to the point-load-type response.

A possible explanation for this behavior is portrayed in Fig. 4(*b*). For small deflection (left), the indenter looks like a flat plate to the shell, but when the dimple grows large enough (right), the indenter looks more like a point load. The computed curves in Fig. 4(*a*) correspond to these two cases; the transition, approximated by dotted curves, has not yet been studied analytically. Note that the load for $r_0 = 10.0$ mm falls below that for $r_0 = 3.75$ near $\Delta/R = 0.7$, possibly indicating the onset of asymmetric buckling [4], which is difficult to observe experimentally.

The effects of an internal fluid are studied next. Figure 5 compares experimental results from Shells 2 and 4 to computations based on the shell model. Curves for both the empty and fluid-filled shells are given for two indenter sizes. These and similar curves for the other shells illustrate several points:

1 As the shell grows thinner, the analytical results for the empty shell move into closer agreement with the experimental data, indicating that shear deformation probably accounts for much of the error in the results from the thicker shells.

2 A region of predominant bending is indicated for the fluid-filled Shell 2 where the loads of the empty and fluid-filled shells coincide ($\Delta/R \lesssim 0.15$ for $r_0 = 1.25$ mm). As discussed in [8] and consistent with observations mentioned earlier, a transition then occurs from behavior dominated by shell bending to behavior dominated by membrane stretching, and the load begins to rise rapidly. For all indenters, this transition takes place before the load is able to drop as it does in the empty shell.

3 As the fluid-filled shell grows thinner, the bending region grows smaller and virtually disappears in the experimental curves for Shell 4. Thus, although Shell 4 is still quite thick ($R/t = 13.7$), membrane stress is significant even for relatively small deflection.

4 Since the larger indenters displace more fluid, stretching becomes significant at smaller deflection. Therefore, the size of the bending region decreases as the indenter size increases. For compression by a flat plate, bending effects are small (see [7]).

5 In contrast to the empty shell, as the fluid-filled shell grows *thicker*, the computed results generally move into closer agreement with experiment. Apparently, this is due to the difference in the membrane-like deformation of the thinner shells (Fig. 1) from the assumed deformation of the shell model ([8], Fig. 3). The membrane model (Fig. 3) would, therefore, be expected to provide more accurate results in regions of predominant membrane stress.

6 At very large deflection, the experimental stiffness of the fluid-filled shell is higher than the calculations indicate. The use of a linear solution for the fourth deflection mode in the shell analysis may account for much of the discrepancy [8].

The load curves of Fig. 6 compare the behavior of the shell and membrane models to test data from two fluid-filled shells. The membrane model results are based on including three and six terms in the series for w and u, respectively [equation (8)]. As expected from the previous discussion, while the shell model predicts the form of the response more accurately for the very thick Shell 1, the membrane model is more accurate in the membrane region ($\Delta/R \gtrsim 0.2$) for the

Downloaded 02 May 2010 to 171.66.16.250. Redistribution subject to ASME license or copyright; see http://www.asme.org/terms/Terms_Use.cfm

thinner Shell 4; including material nonlinearity may further increase the accuracy of the membrane model. The reason the shell and membrane models do not agree even when membrane stress dominates is that the approximate solution methods differ. In the transition region for Shell 4, where both bending and membrane stress are important ($\Delta/R \lesssim 0.2$), a more exact analysis is required.

Although both models correctly predict the shape of the fluid pressure-deflection curves (Fig. 7), the membrane model substantially overestimates the pressure at large deflection. This error is probably due to the unreliability of using the Rayleigh-Ritz method to compute stress. And again, the shell model loses accuracy as the shell becomes thinner.

Conclusions

The large deflection behavior of fluid-filled spherical shells under rigid indenters was studied by comparing experimental data to calculations from two analytical models. The results indicate that, as the deflection increases, a transition from predominant bending to predominant stretching occurs. As the shell becomes thinner or the indenter size increases, the region of bending grows smaller. In particular, the results suggest that while bending effects dominate deflection up to 20 percent of the radius of thick shells ($R/t \lesssim 10$), membrane stress is significant in thinner shells even when the deflection is quite small. Nonlinear membrane theory is generally adequate for large deflection of thinner fluid-filled spherical shells ($R/t \gtrsim 15$). Although these conclusions are valid in the present study, care must be taken in extension to other geometry and loading conditions.

Acknowledgment

This study was begun while the author was an employee of the General Motors Research Laboratories in Warren, Mich. The author would like to thank Mary E. Pope for her help with the experimental portion of this work.

References

1 Ashwell, D. G., "On the Large Deflection of a Spherical Shell With an Inward Point Load," *Proceedings of I.U.T.A.M. Symposium on the Theory of Thin Elastic Shells*, Delft, Aug. 1959, North Holland, Amsterdam, 1960, pp. 43–63.

2 Ranjan, G. V., and Steele, C. R., "Large Deflection of Deep Spherical Shells Under Concentrated Load," *Proceedings, AIAA/ASME 18th Structures, Structural Dynamics, and Materials Conference*, San Diego, Mar. 21-23, 1977, pp. 269—278.

3 Updike, D. P., and Kalnins, A., "Axisymmetric Behavior of an Elastic Spherical Shell Compressed Between Rigid Plates," ASME JOURNAL OF APPLIED MECHANIC, Vol. 37, 1970, pp. 635–640.

4 Updike, D. P., and Kalnins, A., "Axisymmetric Postbuckling and Nonsymmetric Buckling of a Spherical Shell Compressed Between Rigid Plates," ASME JOURNAL OF APPLIED MECHANICS, Vol. 39, 1972, pp. 172–178.

5 Wan, F. Y. M., "Polar Dimpling of Complete Spherical Shells," *Proceedings of Third I.U.T.A.M. Symposium on Shell Theory*, Tbilisi, U.S.S.R., Aug. 22–28, 1978, North Holland, Amsterdam, 1980, pp. 589–605.

6 Feng, W. W., and Yang, W.-H., "On the Contact Problem of an Inflated Spherical Nonlinear Membrane," ASME JOURNAL OF APPLIED MECHANICS, Vol. 40, 1973, pp. 209–214.

7 Lardner, T. J., and Pujara, P., "Compression of Spherical Cells," *Mechanics Today*, Vol. 5, Nemat-Nasser, S., ed., Pergamon, 1980, pp. 161–176.

8 Taber, L. A., "Large Deflection of a Fluid-Filled Spherical Shell Under a Point Load, ASME JOURNAL OF APPLIED MECHANICS, Vol. 49, 1982, pp. 121–128.

9 Evan-Iwanowski, R. M., Loo, T. C., and Tierney, D. W., "Local Buckling of Shells," in *Developments in Mechanics*, Vol. 2, Ostrach, S., and Scanlan, R. H., eds., Pergamon, 1963.

10 Reissner, E., "Symmetric Bending of Shallow Shells of Revolution," *Journal of Mathematics and Mechanics*, Vol. 7, 1958, pp. 121–140.

11 Wan, F. Y. M., "Shallow Caps With a Localized Pressure Distribution Centered at the Apex," I.A.M.S. Technical Report No. 79-44, University of British Columbia, Vancouver, B.C., Canada, Aug. 1979.

12 Reissner, E., "Stresses and Small Displacements of Shallow Spherical Shells," *Journal of Mathematics and Physics*, Vol. 25, 1946, pp. 80–85, 279–300; also, Vol. 27, 1948, p. 240.

13 Bromberg, E., and Stoker, J. J., "Nonlinear Theory of Curved Elastic Sheets," *Quarterly of Applied Mathematics*, Vol. 3, 1945, pp. 246–265.

14 Flügge, W., *Tensor Analysis and Continuum Mechanics*, Springer, Berlin, 1972.

APPENDIX

Volume Displacement

The fluid volume displaced by the motion of the membrane model (Fig. 3) is computed through differential geometry[1]. Consider a spherical surface and let $\mathbf{r}$ and $\mathbf{r}' = \mathbf{r} + \mathbf{v}$ represent position vectors to a point on the surface before and after deformation, respectively. Any point along the displacement vector $\mathbf{v}$ is given by

$$\mathbf{R} = \mathbf{r}(\phi,\theta) + z\mathbf{v}(\phi,\theta) \tag{12}$$

which is a function of the surface coordinates (ϕ,θ) and the coordinate z, which ranges from 0 to 1 along $\mathbf{v}$.

For a spherical surface, $\mathbf{r} = R\mathbf{e}_r$ and $\mathbf{v} = w\mathbf{e}_r + u\mathbf{e}_\phi$, and the base vectors for the nonorthogonal coordinate system (ϕ,θ,z) are [14]

$$\mathbf{G}_\phi = \frac{\partial \mathbf{R}}{\partial \phi} = z\left(\frac{\partial w}{\partial \phi} - u\right)\mathbf{e}_r + \left[R + z\left(\frac{\partial u}{\partial \phi} + w\right)\right]\mathbf{e}_\phi$$

$$\mathbf{G}_\theta = \frac{\partial \mathbf{R}}{\partial \theta} = [R\sin\phi + z(w\sin\phi + u\cos\phi)]\mathbf{e}_\theta$$

$$\mathbf{G}_z = \frac{\partial \mathbf{R}}{\partial z} = \mathbf{v} = w\mathbf{e}_r + u\mathbf{e}_\phi \tag{13}$$

in terms of the displacement components u and w and the unit vectors $\mathbf{e}_r$, $\mathbf{e}_\phi$, and $\mathbf{e}_\theta$. The differential volume element is [14]

$$dV = (\mathbf{G}_\phi d\phi \times \mathbf{G}_\theta d\theta)\cdot\mathbf{G}_z dz, \tag{14}$$

so the total volume displaced by the membrane is

$$\Delta V_1 = \int_{\phi_0}^{\pi/2}\int_0^{2\pi}\int_0^1 (\mathbf{G}_\phi \times \mathbf{G}_\theta)\cdot\mathbf{G}_z dz d\theta d\phi. \tag{15}$$

Finally, with the additional fluid displaced by the indenter

$$\Delta V_2 = \pi r_0^2 w(\phi_0)/\cos\phi_0, \tag{16}$$

the total increase in enclosed volume is $\Delta V = \Delta V_1 + \Delta V_2$. Note that the small volume displaced before the indenter makes full contact with the membrane is neglected here, while in the shell model, the alteration in volume due to the flattening of the shell against the indenter was neglected.

[1] I am indebted to Professor Charles R. Steele of Stanford University for suggesting this approach to the problem.

Downloaded 02 May 2010 to 171.66.16.250. Redistribution subject to ASME license or copyright; see http://www.asme.org/terms/Terms_Use.cfm

L. A. Glenn
Associate Division Leader for
Theoretical and Applied Mechanics,
(H Division),
Physics Department.

R. E. Kidder
Senior Staff Scientist,
Theoretical Division,
Physics Department.

University of California,
Lawrence Livermore National Laboratory,
Livermore, Calif. 94550

Blast Loading of a Spherical Container Surrounded by an Infinite Elastic Medium

Closed-form solutions are derived for the response of a spherical elastic shell, surrounded by a different elastic medium of infinite extent, and subjected to Heaviside or impulsive loading. The results are compared with earlier solutions in which the surrounding medium was a fluid. The importance of interfacial separation is also investigated by comparing the impulsive loading results with finite difference calculations in which it was possible for the shell to decouple from the surroundings when radial tensile stresses occurred at the shared boundary.

1 Introduction

A useful system for containing explosions is obtained by immersing the containment vessel, assumed to be a shell of revolution, in a fluid medium. Exact solutions for the response of spherical and cylindrical elastic shells, so employed, were obtained by Forrestal and Sagartz [1] for Heaviside loading. Subsequently, Duffey [2] obtained solutions for impulsive loading of spherical shells, including also viscoelastic and viscoplastic behavior of the shell material. Duffey's work was applied by Karpp, Duffey, and Neal [3] to estimate the improved performance to be derived by surrounding the containment vessel with concrete or rock, instead of, say, water. Their results were derived based on inertial and impedance properties and ignored strength effects, i.e., the surrounding medium could not support shear.

In the present work, we reformulate the problem with the surroundings assumed to obey Hooke's law. In exact analogy with the earlier work we obtain closed-form solutions for both Heaviside and impulsive loading. These solutions collapse on the previous results when the shear modulus of the surrounding medium vanishes. For Heaviside loading, the peak hoop stress in the containment vessel decreases sharply with only small reduction in the Poisson's ratio of the surroundings. The marginal hoop stress decrease is less important when the loading is impulsive, a large decrease already occurring as a result of inertial and impedance effects. However, we demonstrate, via numerical solution of the full field equations, that the assumption of continuity of radial stress and displacement at the interface between shell and surroundings is not entirely valid for this case. This is especially significant when the surrounding medium is a fluid, and interfacial separation occurs well before the peak shell displacement is attained. The results derived with the simplified model then represent only an upper bound to the actual situation.

Work performed under the auspices of the U.S. Department of Energy by Lawrence Livermore National Laboratory under contract #W-7405-Eng-48.

Contributed by the Applied Mechanics Division and presented at the Winter Annual Meeting, Boston, Mass., November 13–18, 1983 of THE AMERICAN SOCIETY OF MECHANICAL ENGINEERS.

Discussion on this paper should be addressed to the Editorial Department, ASME United Engineering Center, 345 East 47th Street, New York, N.Y. 10017, and will be accepted until two months after final publication of the paper itself in the JOURNAL OF APPLIED MECHANICS. Manuscript received by ASME Applied Mechanics Division, October, 1982; final revision, April, 1983. Paper No. 83-WA/APM-17.

Copies will be available until July, 1984.

2 Model Equations and Solution

We assume the medium surrounding the containment shell to be infinite, inviscid, and compressible. The equation of motion is:

$$-\rho\frac{\partial^2 u}{\partial t^2}=\frac{\partial \sigma_R}{\partial r}+\frac{2}{r}(\sigma_R-\sigma_T) \tag{1}$$

σ_R is the radial stress, σ_T the tangential (hoop) stress, ρ the density, and u the displacement. The constitutive relations, with spherical symmetry, are:

$$-\sigma_R=\left(k+\frac{4}{3}\mu\right)\frac{\partial u}{\partial r}+2\left(k-\frac{2}{3}\mu\right)\frac{u}{r} \tag{2}$$

$$-\sigma_T=\left(k-\frac{2}{3}\mu\right)\frac{\partial u}{\partial r}+2\left(k+\frac{1}{3}\mu\right)\frac{u}{r} \tag{3}$$

where k and μ are, respectively, the bulk and shear moduli. The motion being irrotational, it is permissible to express the displacement in terms of a scalar potential function, i.e.,

$$u\equiv-\frac{\partial \phi}{\partial r}=\frac{1}{r^2}\psi(\theta)+\frac{1}{cr}\psi'(\theta) \tag{4}$$

$$\psi=r\phi \tag{5}$$

satisfies the one-dimensional plane-wave equation, and we have introduced the retarded time

$$\theta=t-(r-R)/c\geq 0 \tag{6}$$

where c is the velocity of dilatation waves in an unbounded medium and R is the cavity radius. Substituting (2)–(6) into (1), the interface motion can be described by

Copyright © 1983 by ASME
Downloaded 02 May 2010 to 171.66.16.250. Redistribution subject to ASME license or copyright; see http://www.asme.org/terms/Terms_Use.cfm

$$\rho\ddot{u}(R,\theta)=\rho\ddot{u}(R,t)=\left[\left(k+\frac{4}{3}\mu\right)/cR\right](\psi'''/c^2+\psi''/cR) \tag{7}$$

The equation of motion of the shell itself is:

$$\rho_L h[\ddot{u}(R,t)+\omega_0^2 u(R,t)]=P(t)-\sigma_R(R,t) \tag{8}$$

where

$$\omega_0^2=2E_L/\rho_L(1-\nu_L)R^2=2c_L^2/R^2. \tag{9}$$

P is the cavity pressure, h the thickness of the spherical liner, E the Young's modulus, and ν the Poisson's ratio. Symbols appended with the subscript L refer to the elastic liner; otherwise reference is to the surrounding elastic medium. Equation (8) implies continuity of displacement and stress at the fluid-shell interface, $r = R$, and also that $R/h >> 1$.

We now introduce the nondimensional displacement

$$w=2uE_L h/P_0R^2(1-\nu_L) \tag{10}$$

where

$$P_0=P(0), \tag{11}$$

and let

$$\bar{t}=ct/R=c_L t/\eta R \tag{12}$$

(Subsequent dot notation refers to derivatives with respect to $\bar{t}$). It can then be shown that

$$\ddot{w}+[1+\rho R/\rho_L h]\ddot{w}+\dot{w}/\alpha+w/\alpha=(1/\beta P_0)(P+\dot{P}_0) \tag{13}$$

where

$$\beta=1/2\eta^2 \tag{14}$$

and

$$(1/\alpha)=(1/\beta)+2(1-2\nu)\rho R/(1-\nu)\rho_L h \tag{15}$$

Equation (13) is subject to the initial conditions

$$w(0)=\dot{w}(0)=0 \tag{16}$$

$$\ddot{w}(0)=1/\beta \tag{17}$$

It is identical with that employed in [1] and [2] when $\nu = 0.5$.

The solution is obtained using Laplace transforms. For Heaviside loading,

$$P=P_0H(t). \tag{18}$$

The result is:

$$(\sigma_T)_L=-E_L u/(1-\nu_L)R=-(P_0R/2h)w$$

$$=-(P_0R/2h)\left\{\alpha/\beta+\frac{(1+z)e^{z\bar{t}}}{\beta z[(x-z)^2+y^2]}\right. \tag{19}$$

$$\left.+e^{x\bar{t}}/\beta y\left[\frac{y(z-2x-x^2-y^2)\cos y\bar{t}+(x^3+y^2x-zx^2-zy^2+x^2-y^2-xz)\sin y\bar{t}}{(x^2+y^2)[(x-z)^2+y^2)]}\right]\right\}$$

where x, y, and z are obtained from the zeros of:

$$(s-z)(s-x+iy)(s-x-iy)=s^3$$

$$+[1+\rho R/\rho_L h]s^2+s/\alpha+1/\alpha \tag{20}$$

We note that the leading term in (19),

$$\alpha/\beta=1/(1+A),\ A=\frac{R}{h}\frac{\mu}{\mu_L}\left(\frac{1-\nu_L}{1+\nu_L}\right) \tag{21}$$

is precisely the static result obtained from the equations of equilibrium, when continuity of radial stress and displacement are prescribed at the interface.

For impulsive loading,

$$P=I_0\delta(t) \tag{22}$$

and

$$(\sigma_T)_L=-E_L u/(1-\nu_L)R=-(P_0R/2h)w$$

$$=-(I_0c_L\eta/h)[(x-z)^2+y^2]^{-1}[(1+z)(e^{z\bar{t}}-e^{x\bar{t}}\cos y\bar{t})$$

$$+(e^{x\bar{t}}/y)(x^2+y^2+x-z-xz)\sin y\bar{t}] \tag{23}$$

This is exactly Duffey's result [2], except that the zeros of the cubic, equation (20), are obtained from equation (15).

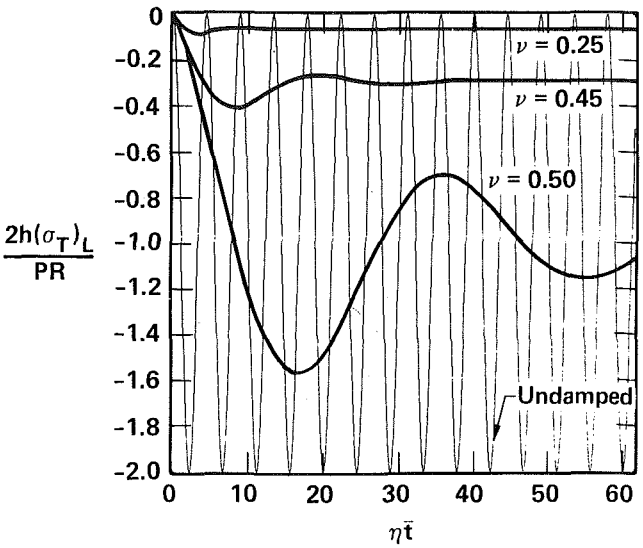


Fig. 1 Hoop stress in steel liner for Heaviside loading ($\rho/\rho_L = 0.35$, $R/h = 200, k_L/k = 9.7, \nu_L = 0.29$)

3 Discussion of Results

3.1 Heaviside Loading. Figure 1 illustrates the importance of the surrounding medium's ability to support finite shear stress. The hoop stress in the linear is plotted as a function of time for the physically interesting parameter set: $\rho/\rho_L = 0.35$, $R/h = 200$, $k_L/k = 9.7$, and $\nu_L = 0.29$. This corresponds to a large steel shell bounded by a granitic rock mass. Equation (19) was evaluated for three different values of the Poisson's ratio: 0.5, 0.45, and 0.25, the latter actually representative of the rock. In the background we outline the undamped solution, trivially obtained by setting $\sigma_R(R, t)$ to zero in equation (8). Taking the rock to be a fluid ($\nu = 0.5$) results in a fractional peak stress of 0.785 relative to the undamped result whereas the $\nu = 0.25$ surroundings yields 0.042, almost 20 times less. Just reducing the Poisson's ratio from 0.5 to 0.45 cuts the fractional peak stress to 0.205.

Figure 2 explicitly shows the decrease in peak stress with decreasing Poisson's ratio. Also depicted is the static stress ratio (equation (21)).

We note that in order for these results to retain physical significance the surrounding medium must support modest tensile stress. In particular, at equilibrium, corresponding to equation (21), the ratio of (hoop) tensile stress in the surrounding medium at the liner interface to that in the liner itself is:

$$\sigma_T|_{r=R}/(\sigma_T)_L=\frac{\mu}{\mu_L}\left(\frac{1-\nu_L}{1+\nu_L}\right) \tag{24}$$

When steel is the liner material, this ratio typically varies from 0–0.07 for geologic surroundings. The maximum static hoop stress magnitude in the surrounding medium is, in any case, bounded above by $(1/2)P_0$; the dynamic result may be derived from equations (3), (6), and (19) and is typically half

Downloaded 02 May 2010 to 171.66.16.250. Redistribution subject to ASME license or copyright; see http://www.asme.org/terms/Terms_Use.cfm

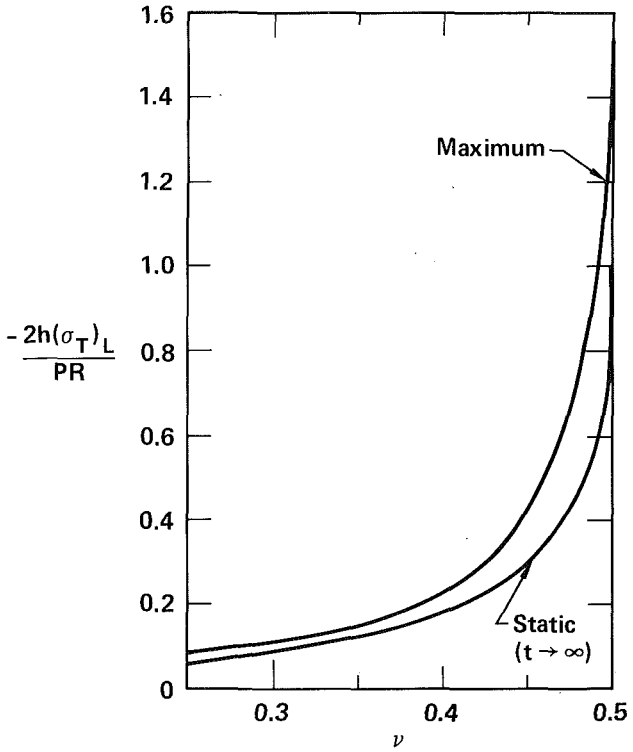


Fig. 2 Maximum and static liner hoop stress as a function of the Poisson's ratio of the surrounding medium for Heaviside loading. Same parameters as in Fig. 1.

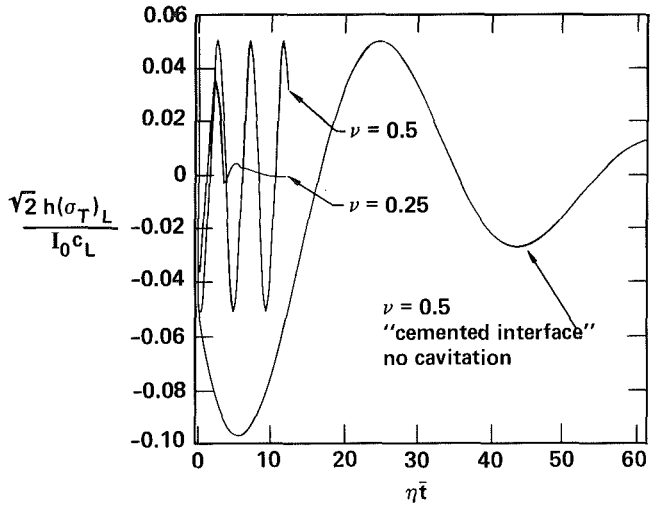


Fig. 3 Hoop stress in steel liner for impulsive loading (ρ/ρ_L = 0.35, R/h = 200, k_L/k = 9.7, ν_L = 0.29)

again as high. If the rock is unable to withstand these low values, it is still nevertheless possible to obtain satisfactory results by siting the container underground to take advantage of the lithostatic overburden.

3.2 Impulsive Loading. In Fig. 3 we depict the liner hoop stress as a function of time for impulsive loading. The stress is normalized to the peak undamped value, $I_0 c_L/\sqrt{2}h$ [3], rather than the static value, which in this case is zero. Three curves are shown. The curve marked $\nu = 0.5$, "cemented interface," no cavitation, corresponds to Duffey's solution for the same parameter set as in Figs. 1 and 2. It was obtained by setting $\nu = 0.5$ in equations (15), (20), and (23). The other two curves were obtained by a finite difference method with the impulsive loading condition (22) approximated by:

$$P = (I_0/t_*)[H(t) - H(t-t_*)], \quad t_*/T = 0.01 \tag{25}$$

where T is the natural period of the undamped spherical shell, i.e., $T = 2\pi/\omega_0$. The finite difference code, AFTON, is fully described in [4]; the full field equations can be solved in an arbitrary coordinate frame, with arbitrary boundary and initial conditions, and with arbitrary constitutive model specification. As a check on the accuracy of the code and the adequacy of the approximation (25), we first obtained the solution corresponding to the forementioned case of $\nu = 0.5$, "cemented interface," no cavitation. This was accomplished using a constitutive equation of the form

$$\sigma_R = \sigma_T = -k\Delta \tag{26}$$

(Δ is the elastic dilation) for the surrounding medium, and enforcing continuity of displacement at the liner interface, regardless of whether tensile stresses occurred at this juncture. The calculated solution was essentially congruent with that displayed in Fig. 3, except for the period $t_*/T \lesssim 0.01$, in which compressive hoop stresses appear in the linear; this early period is ignored in the derivation of equation (8).

The curve simply marked $\nu = 0.5$ was obtained with the surrounding medium described by

$$\sigma_R = \sigma_T = \begin{cases} -k\Delta, & \Delta \le 0 \\ 0 & \text{otherwise} \end{cases} \tag{27}$$

Equation (27) is consistent with the notion of a fluid possessing no tensile strength and ignores the vapor pressure of the liquid; both of these assumptions are realistic in the present circumstances. Moreover, and regardless of the constitutive model prescribed for the surrounding medium, separation of the medium from the liner was allowed whenever a radial tensile stress at this location would have been required to enforce continuity of displacement. The interfacial radial stress was thereafter set equal to zero until (unless) recompression occurred, which of course never obtained for $\nu = 0.5$. Without tensile hoop strength, there is no mechanism for flow reversal and the fluid continues to coast outward. Our model would subsequently predict large-scale cavitation as a result of the outward motion of a nearly incompressible fluid in a divergent field, however, in actuality gravity would eventually intervene.

In the calculation for $\nu = 0.5$ the radial stress at the interface vanished at $t_*/T = 0.053$ ($\eta\bar{t} = 0.23$) and separation occurred at this time. As seen in Fig. 3 the shell then subsequently continued to oscillate in undamped mode. The peak hoop stress, $\sqrt{2}\,h(\sigma)_{TL}/I_0 c_L = -0.051$, occurred at $\eta\bar{t} = 0.39$, the period after shell separation corresponding to inertial overshoot. We note that the magnitude of the peak, when separation is accounted for, is only about half that predicted with the Duffey model.

The third curve depicted in Fig. 3, is the result of a finite difference calculation similar to the one just described, with interfacial separation allowed, but with the Poisson's ratio of the surrounding medium set to 0.25, instead of 0.5. This curve is reproduced in Fig. 4 where it is compared with our model result, marked simply $\nu = 0.25$, obtained from equation (23). We also repeated the finite difference calculation, cementing the interface as described in the foregoing, with similar results, i.e., the computed result was congruent with our model result except for the early period of compression.

We have marked the uncemented (finite difference) calculation in Fig. 4 with vertical dashes, identified with an "S" for separation and a "C" for closure, to indicate when these two events occur. Initial separation of the liner from the surroundings appears at $\eta\bar{t} = 0.20$ with the peak hoop stress, $\sqrt{2}\,h(\sigma_T)_L/I_0 c_L = -0.035$, having previously been attained at $\eta\bar{t} = 0.14$. In this case the surrounding material was able to follow the liner inward for a brief period before the radial

Downloaded 02 May 2010 to 171.66.16.250. Redistribution subject to ASME license or copyright; see http://www.asme.org/terms/Terms_Use.cfm

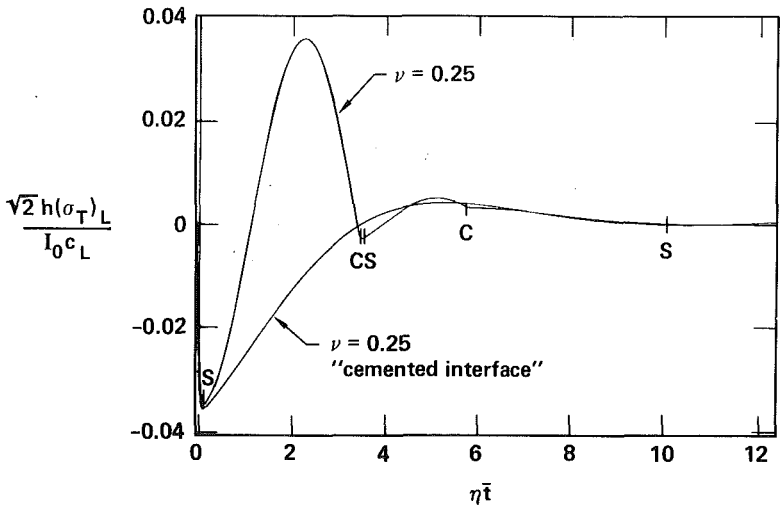


Fig. 4 Liner hoop stress with and without cemented interface for ν = 0.25 and impulsive loading. Same parameters as in Fig. 3.

interface stress vanished. At separation the liner begins to oscillate as a free body, but its outward motion is arrested at $\eta\bar{t} = 3.46$ when contact is again made with the outer region. Shortly thereafter, at $\eta\bar{t} = 3.60$, separation occurs again, followed by closure at $\eta\bar{t} = 5.74$ and separation at $\eta\bar{t} = 10.14$ – at which point the motion is essentially completely damped. Although it is possible in this case to accurately compute the peak stress with our simple model, the curve marked "cemented initerface," the subsequent motion is obviously in substantial error.

The magnitude of the peak liner hoop stress is reduced by about one-third when the Poisson's ratio of the surrounding material is varied from 0.5 to 0.25; the effect appears insignificant, however, in an overall sense, since the fluid medium in this case had already reduced the peak by a factor of 20 with respect to the undamped solution. This contrasts with the case of Heaviside loading, discussed earlier, in which the Poisson effect was much greater.

References

Forrestal, M. J., and Sagartz, M. J., "Radiated Pressure in an Acoustic Medium Produced by Pulsed Cylindrical and Spherical Shells," ASME JOURNAL OF APPLIED MECHANICS, Vol. 93, 1971, pp. 1057–1060.

2 Duffey, T. A., "Transient Response of Viscoplastic and Viscoelastic Shells Submerged in Fluid Media," ASME JOURNAL OF APPLIED MECHANICS, Vol. 98, 1976, pp. 137–143.

3 Karpp, R. R., Duffey, T. A., and Neal, T. R., "Response of Containment Vessels to Explosive Blast Loading," University of California, Los Alamos National Laboratory Report LA-8082, June 1980.

4 Glenn, L. A., "AFTON Revisited: An Improved Algorithm for Numerical Solution of Initial Value Problems in Continuum Mechanics; Part 1: The One-Dimensional Equations," University of California, Lawrence Livermore National Laboratory Report UCRL-52512, July 20, 1978.

Downloaded 02 May 2010 to 171.66.16.250. Redistribution subject to ASME license or copyright; see http://www.asme.org/terms/Terms_Use.cfm

On the Crushing Mechanics of Thin-Walled Structures

T. Wierzbicki
Professor of Mechanics,
Department of Ocean Engineering,
Massachusetts Institute of Technology,
Cambridge, Mass. 02139

W. Abramowicz
Assistant Professor,
Institute of Fundamental
Technological Research,
Swietokrzyska 21,
00-049 Warsaw, Poland

A self-consistent theory is presented which describes the crushing behavior of a class of thin-walled structures. Assuming a rigid-plastic material and using the condition of kinematic continuity on the boundaries between rigid and deformable zones, a basic folding mechanism is constructed. This mechanism closely reproduces all the main features of folds and wrinkles actually observed on typical crumpled sheet metal structures. Calculations based on the energy balance postulate show that two-thirds of the plastic energy is always dissipated through inextensional deformations at stationary and moving plastic hinge lines. The extensional deformations are confined to relatively small sections of the shell surface but they account for the remaining one-third of the dissipated energy. The theory is illustrated by application to the problem of progressive folding of thin-walled rectangular columns. A good correlation is obtained with existing experimental data as far as the mean crushing force and the geometry of the local collapse mode is concerned.

1 Introduction

Thin-walled structures are capable of carrying substantial loads for deflections far beyond those corresponding to ultimate or buckling loads. From the point of view of energy absorption characteristics of compressed members, one is mainly interested in deflections that exceed by two orders of magnitude the shell thickness and become comparable to the linear dimension of the structure. At the same time consideration of initial peak load is important only to the extent that the process of reaching this load may impose a certain mode of collapse.

Very large deflections can be accommodated by sheet metal structures through the formation of a complicated pattern of folds and wrinkles. A distinctive feature of such a deformation mechanism is that the strain energy (in the case of elastic shells) or the rate of energy dissipation (in the case of plastic shells) is concentrated over relatively narrow zones, while the remainder of the structure undergoes a rigid body motion. This is in sharp contrast with buckling or post-buckling behavior of plates or shells where small perturbations around a predominantly compressive state lead to a more or less uniform strain distribution.

Some further interesting observations can be made about the crumpling process. The fold lines, which actually form a double curvature surface, always lie in a certain plane. One radius of curvature of the "fold line" is small and comparable to the gauge thickness while the other is much larger. Once the local buckling wave is formed in the shell, its length stays essentially unchanged while the amplitude grows as the deformation progresses.

All these features of the structural response are local and thus, to a certain degree, are independent of the scale or type of the problem. This means that one should be able to describe the mechanics of the crushing process at this local level. Calculations of the crushing resistance of typical components of automobile, aircraft, or ship structures will then follow.

The progressive folding of box columns was studied among others by Johnson et al. [1], Ohokubo et al. [2], and one of the present author [3], under the assumption of purely inextensional deformation modes with stationary or moving hinge lines. On the other hand, for axially symmetric problems such as tube inversion [4], crumpling of cylindrical shells in the so-called crinkling deformation mode [5], and crushing of rotationally symmetric shells [6,7], a predominantly extensional type of deformation was assumed. In the present paper these two approaches are combined to develop a theory of the crushing behavior of a certain class of shells.

A kinematic method of plasticity will be used, suitably generalized to large deformation problems. The method consists of constructing a kinematically admissible solution, with at least three degrees of freedom (three free parameters) around a simple one-degree-of-freedom folding mechanism.

2 Assumptions

The shape of the plastic collapse mode with large local strains and curvatures can be assumed a priori on the basis of experimental observations. Alternatively, the folding mechanisms can be systematically developed from a set of basic assumptions in conjunction with the continuity conditions at the propagating hinge lines. Here, the latter ap-

Contributed by the Applied Mechanics Division and presented at the Winter Annual Meeting, Boston, Mass., November 13-18, 1983 of THE AMERICAN SOCIETY OF MECHANICAL ENGINEERS.

Discussion on this paper should be addressed to the Editorial Department, ASME, United Engineering Center, 345 East 47th Street, New York, N.Y. 10017, and will be accepted until two months after final publication of the paper itself in the JOURNAL OF APPLIED MECHANICS. Manuscript received by ASME Applied Mechanics Division, April, 1982; final revision, April, 1983. Paper No. 83-WA/APM-12.

Copies will be available until July, 1984.

Copyright © 1983 by ASME
Downloaded 02 May 2010 to 171.66.16.250. Redistribution subject to ASME license or copyright; see http://www.asme.org/terms/Terms_Use.cfm

proach is used since it will shed more light on the crushing process of thin-walled structures. The following assumptions are made:

(1) The structure consists initially of planar surface elements. This assumption restricts the class of the considered problem. For example, box beams and columns, plate intersections, cellular structures, stiffened panels etc., all fall within the considered class. The method may also be applied to curved shells that are approximated by a system of flat plates.

(2) The material is regarded as rigid-perfectly plastic with a constant value of the flow stress σ_0. Since large plastic strains are present in areas of high curvature, elastic effects can be neglected and σ_0 can be thought of as an average flow stress. Strain hardening and strain rate sensitivity can be accounted for in the present formalism at the expense of considerably more complicated calculations.

(3) The length of the local buckling wave $2H$ remains constant during the formation of each buckle or fold. This is true in many practical problems. Usually, the mode of collapse of a thin-walled structure is either imposed by initial imperfections or is dictated by initial elastic or plastic buckling modes. The fact that this wavelength is not subjected to any major changes later in the post-buckling process means that there must be a way of determining H from the energy consideration in the plastic range. We will explore this possibility further in the paper.

(4) The constraints imposed on the crushing process by the boundary and symmetry conditions are forcing the fold lines to move through the material. The consideration of folding about stationary (straight or curved) hinge lines is in general much easier. Such collapse mechanisms are possible to develop only if sufficient freedom is left for the boundaries to deform. This problem has been analyzed in the literature, cf. [1] and thus will not be considered here.

3 Analysis of Discontinuities

The conditions on the boundaries between rigid and deforming zones will now be examined. Consider a curved discontinuity line Γ moving down the middle surface of the shell χ with the velocity V_n. The hinge line is defined by the surface vector $\mathbf{n}$ normal to Γ. The line Γ is dividing the surface χ into two separable parts, the deformed part $(+)_\chi$ behind Γ, which is subjected to plastic deformations and the undeformed part $(-)_\chi$ in front of Γ. Denote by f any vector field defined over the surface χ. In particular $\mathbf{f}$ can be regarded as a displacement vector $f=\{u^\alpha,u^3\}$, in the local coordinate system (x^α,x^3).

The conditions of kinematic continuity of f across Γ take the form

$$[\dot{f}^i]+V_n[f^i|_\alpha]n^\alpha=0 \qquad i=\{1,2,3\} \qquad (3.1)$$

$$[f^i|_\alpha]+V_n\{[f^i|_{\beta\gamma}]n^\beta n^\gamma\}n_\alpha=0 \qquad \alpha,\beta,\gamma=\{1,2\} \qquad (3.2)$$

where the brackets denote discontinuities, if any of the enclosed quantities across Γ, i.e., $[\eta]={}^+\eta-{}^-\eta$, and V_n is the velocity of the hinge line in $\mathbf{n}$ direction. These equations can be obtained from general continuity conditions for a three-dimensional continuum formulated, for example, in [8] if the first and second gradient of the function f is replaced by the corresponding covariant differentiation.

In the case of rotationally symmetric shells the hinge line becomes a circle and each of the continuity conditions (3.1) and (3.2) yields only one scalar equation in the meridional plane

$$[\dot{f}]+V_n[f_{,\alpha}]=0 \qquad (3.3)$$

$$[\dot{f}_{,\alpha}]+V_n[f_{,\alpha\alpha}]=0 \qquad (3.4)$$

where $[\dot{f}_{,\alpha}]$ is a jump of the rate of rotation and $[f_{,\alpha\alpha}]$ is the corresponding jump in the principle (meridional curvature).

Assuming that f and $\dot{f}$ are continuous across Γ, equation (3.3) shows that the slope $f_{,\alpha}$ can be discontinuous only across stationary hinge lines, for which $V_n=0$. Similar results valid for beams and flat circular plates were obtained earlier by Hopkins [9] and Prager [10].

Two special cases of the general equations are of interest to us. Let a circular hinge Γ move down a cylindrical surface of the radius R. The curvature and rate of rotation vanish in front of Γ and behind Γ are denoted, respectively, by $f_{,\alpha\alpha}=\kappa=1/b$, $\dot{f}_{,\alpha}=\dot{\theta}$. Equation (3.4) says that such a line of discontinuity is leaving behind a curved surface, defined by

$$\dot{\theta}+V/b=0 \qquad (3.5)$$

In a small neighborhood of Γ this is the equation of a toroidal surface with the small radius b and large radius $a=R+b$, Fig. 1(*a*).

Consider now a straight hinge line moving down a plane surface. Equation (3.2) yields a condition analogous to (3.5) but its interpretation is different. A translating or rotating hinge lines is sweeping, respectively, a cylindrical or conical surface of the radius b, Fig. 1(*b*,*c*). Reversing the directions of motion, a converse statement is true. A toroidal surface is transformed into a cylinder while a cylindrical or conical surface becomes a plane.

4 Basic Folding Mechanism

Following assumption 1, consider a typical hinge line formed by an intersection of two plane surface elements which initially were of the height H. Referring to Fig. 2 we see that upon compression, the hinge line, originally positioned at

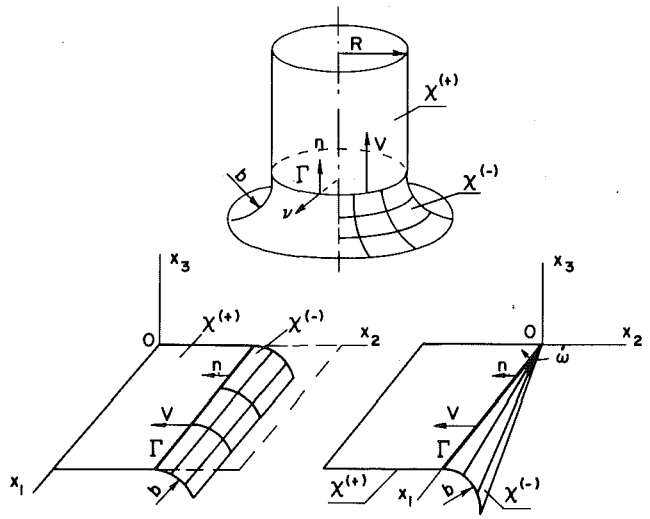


Fig. 1 Kinematic continuity at straight and curved propagating hinge lines

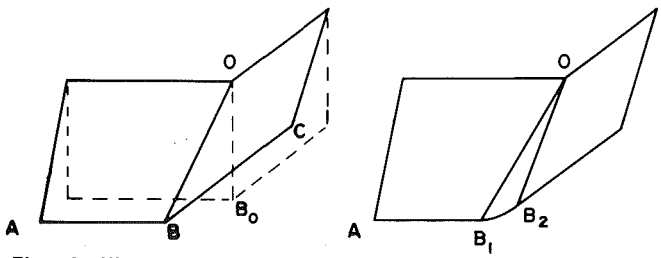


Fig. 2 Kinematically inadmissible and admissible folding mechanisms

Downloaded 02 May 2010 to 171.66.16.250. Redistribution subject to ASME license or copyright; see http://www.asme.org/terms/Terms_Use.cfm

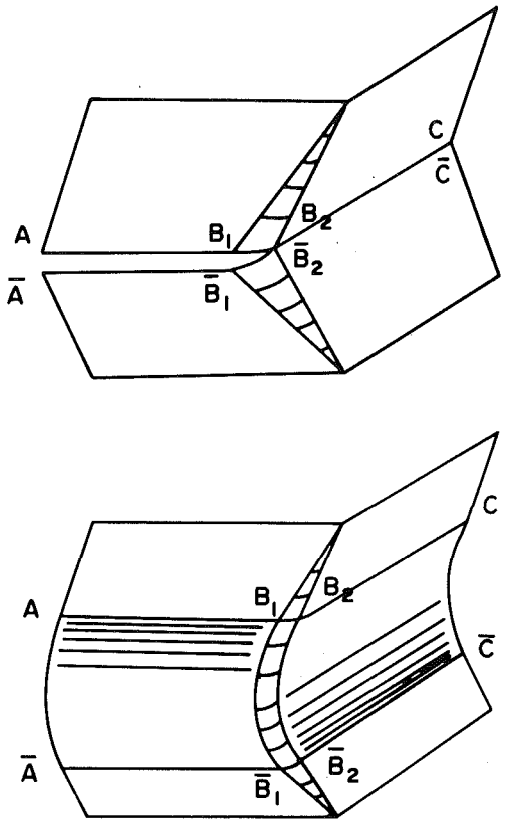


Fig. 3 (a)Assembling two asymmetric modes with material discontinuity; and (b) a fully consistant collapse mechanism

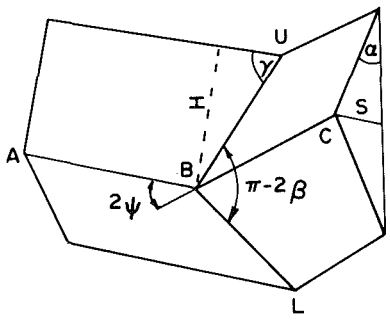


Fig. 4 Global geometry of the basic folding mechanism

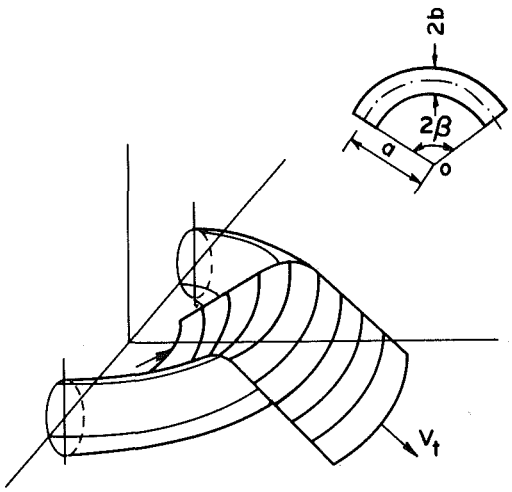


Fig. 5 Plastic flow of a metal sheet through a toroidal surface

OB_0, has moved to a new position OB. Such a mode of deformation is kinematically inadmissible since it incorporates a discontinuity in the slope across the moving hinge line. A consistent collapse mechanism is obtained by introducing two rotating hinge lines. The first line is imposing a curvature and this line is followed by another one that is removing the curvature back to zero. The resulting mode thus consists of two flat trapezoidal elements continuously joined by a section of a conical surface, Fig. 3. When two identical modes described in the foregoing are assembled, a stationary hingeline BC is formed across which the slope discontinuity is admissible. This however results in a material discontinuity over the remaining part of the joint line. The opening increases from B_2 to B_1 and then is held constant along BA, Fig. 3. The width of the gap indicates how much extension or compression would be required to ensure full geometric compatibility. This difficulty could be overcome by inserting a section of a cylindrical surface between the two deforming elements along the horizontal edge CAB, Fig. 3. As the deformation progresses, each of the horizontal lines split now into two hinges moving in opposite directions. According to the continuity condition (3.5) the central region bounded by four moving circular arcs must form a section of a toroidal surface. The deformation mode consisting of four trapezoidal elements, a section of two horizontal cylindrical surfaces, two inclined conical surfaces, and a section of a toroidal surface will be called a *basic folding mechanism*.

Velocity and Strain Rate Fields. The global geometry of four intersecting fold lines is shown in Fig. 4. The initial geometry of the compressed element is defined by the height $2H$, total width C, which is the length of the segments AB and BC, and the angle $2\psi_0$ between two adjacent plates. The current geometry is described either by the crushing distance δ or the angle of rotation of the side panels α or the horizontal displacements of the point B. These quantities are mutually related by

$$\delta = 2H(1-\cos\alpha) \tag{4.1}$$

$$S = H\sin\alpha \tag{4.2}$$

The other two angles γ (in the plane ABU) and 2β (in the plane UBL) are related to ψ_0 and α through

$$tg\gamma = \frac{tg\psi_0}{\sin\alpha}, \quad tg\beta = \frac{tg\gamma}{\sin\psi_0} \tag{4.3}$$

The motion of the element is described by the relative velocity of the upper and lower edges (Points U and L)

$$\dot{\delta} = 2H(\sin\alpha)\,\dot{\alpha} \tag{4.4}$$

and the horizontal velocity of the point C

$$V = \dot{S} = H(\cos\alpha)\dot{\alpha} \tag{4.5}$$

A central point in the present paper is the analysis of a continuous deformation field leading to extensional deformations in the localized zones. The velocity field in the section of a toroidal shell can be determined in the fixed coordinate system or more conveniently in the moving coordinate system referred to the global collapse mode.

On substracting the convective part of the velocity field it can be easily shown (cf. for example [19]), that the local motion of the shell middle-surface in the considered zone is nothing else but a radial flow of the material points over the toroidal surface with the tangential velocity V_t. This velocity is related to the horizontal velocity V by Fig. 5.

$$V_t = \dot{\omega}b = V/tg\psi_0 \tag{4.6}$$

Let us introduce a local coordinate system $\{\theta,\phi,x^3\}$ where θ and ϕ denote, respectively, meridional and circumferential coordinates of the toroidal surface. Assuming inextensibility of the shell in the meridional direction ($\lambda_\theta = 1$), the velocity

Downloaded 02 May 2010 to 171.66.16.250. Redistribution subject to ASME license or copyright; see http://www.asme.org/terms/Terms_Use.cfm

vector in this system of coordinates has the following components

$$\mathbf{v} = \{\dot{\omega} b, 0, 0\} \tag{4.7}$$

where $\dot{\omega}$ denotes the angular velocity of the flow.

It is natural to introduce a consistent Eulerian description of the plastic flow. The formulated problem is geometrically nonlinear in strains and displacements. However, the formula for the velocity strain is linear. The velocity field (4.7) gives rise to the following components of the rate of extension $\dot{\lambda}_{\alpha\beta}$ and rate of curvature $\dot{\kappa}_{\alpha\beta}$, in the continuous deformation field where $\alpha, \beta, = \theta, \phi$ (for details of derivation see, for example, reference [12])

$$\dot{\lambda}_{\alpha\beta} = \begin{bmatrix} 0 & 0 \\ 0 & \dot{\lambda}_{\phi\phi} \end{bmatrix}, \quad \dot{\kappa}_{\alpha\beta} = \begin{bmatrix} 0 & 0 \\ 0 & \dot{\kappa}_{\phi\phi} \end{bmatrix} \tag{4.8}$$

where

$$\dot{\lambda}_{\phi\phi} = -\frac{\dot{\omega} b \sin\theta}{r}, \quad \dot{\kappa}_{\phi\phi} - \frac{\dot{\omega} a \sin\theta}{r^2} \tag{4.9}$$

There is also a jump in the curvature rate across the two circular hinge lines

$$[\dot{\kappa}_{\theta\theta}] = \dot{\theta} = V_t / b \tag{4.9a}$$

In the preceding formulas a and b denote, respectively, larger and smaller radius of the toroidal surface and r is a current position of the point with θ coordinate with respect to the axis of symmetry $r = b \cos\theta + a$.

Incompressibility Condition. The general theory, on which the derivation of equations (4.8) and (4.9) was based, does not pose any restrictions as to the change of the shell thickness during the deformation process. Since the material is rigid-plastic, we can calculate the change of thickness from the incompressibility condition. In view of the property $\lambda_\theta = 1$, this conditions reads

$$\lambda_\phi \lambda_{x^3} = 1 \tag{4.10}$$

This condition can be written in an integral form which related local wall thickness to the current radius of the toroidal surface, $h_0 r_0 = hr$ where h_0 is the initial thickness of the shell and $r_0 = a + b \sin\psi$.

5 Energy Dissipation

The rate of energy dissipated in the crushing process results from the continuous and discontinuous velocity fields

$$\dot{E}_{int} = \int_S (M^{\alpha\beta}\dot{\kappa}_{\alpha\beta} + N^{\alpha\beta}\dot{\lambda}_{\alpha\beta})\, dS + \int_L M_0 \dot{\theta} d\ell \tag{5.1}$$

where $\dot{\alpha}_{\alpha\beta}$ and $\dot{\lambda}_{\alpha\beta}$ are given by (4.8) and (4.9) and the Cauchy stress tensor is used in the definition of stress resultants $N^{\alpha\beta}$ and stress couples $M^{\alpha\beta}$. Note that both the extent of continuous plastic deformations S and the length of hinge lines L increase as the deformation progresses. Consider now the first integral in (5.1).

Each element of the shell subjected to plastic flow undergoes a finite rotation from $\theta_1 = \pi/2 + \psi$ to $\theta_2 = \pi/2 - \psi$. It seems appropriate here to introduce the corotational definition of the yield condition discussed, for example, in [12]. The yield condition is described by the same function of the components of generalized stresses $F(M^{\alpha\beta}N^{\alpha\beta}) = 0$, independent of the actual configuration, i.e., the coordinates $\{\theta, \phi\}$. The form of the function F would then be formally analogous to that describing a similar problem with infinitesimal deformations. In the case of rotationally symmetric shells with only two nonvanishing components of the generalized strain rate tensor, the yield condition has the form

$$\left|\frac{M_{\phi\phi}}{M_0}\right| + \left(\frac{N_{\phi\phi}}{N_0}\right)^2 = 1 \tag{5.2}$$

where $M_0 = 1/4\ \sigma_0 h^2$, $N_0 = \sigma_0 h$ and h represents the current, variable shell thickness. The preceding equation in conjunction with the associated flow rule suffices to determine uniquely the continous rate of energy dissipation.

The surface element in (5.1) is expressed as

$$dS = r d\phi\ b d\theta \tag{5.3}$$

and the limits of integration are

$$\frac{\pi}{2} - \psi \le \theta \le \frac{\pi}{2} + \psi \tag{5.4}$$

$$-\beta < \phi < \beta$$

where 2β is a central angle of toroidal section, variable with the process, see Fig. 5, and the angle ψ is linearly increasing with ϕ from ψ_0 to $\pi/2$ according to

$$\psi = \psi_0 + \frac{\pi - 2\psi_0}{\pi}\phi \tag{5.4a}$$

In the most general case of variable thickness and nonlinear yield condition, the surface integral in (5.1) can be evaluated and expressed in terms of elementary functions as shown in [13]. However, the resulting expression is too complicated for our purposes.

The effect of variable thickness is small except for problems in which the ratio $\eta = b/a$ is relatively large, for example an outside-in tube inversion. We will restrict our analysis to small η and treat h as constant. We will also approximate (5.2) by a square yield locus, circumscribed on the parabola. The first integral in (5.1) is then reduced to

$$\dot{E}_1 = \int_{-\beta}^{\beta} b\left\{\int_{\pi/2-\psi}^{\pi/2+\psi}\left[M_0\frac{\dot{\omega}\, a \sin\theta}{r^2} + N_0\frac{\dot{\omega}\, b \sin\theta}{r}\right] r d\theta\right\} d\phi$$

The first integration can be easily performed to give

$$\dot{E}_1 = \int_{-\beta}^{\beta}\left\{2\dot{\omega} b^2 N_0 \sin\psi + \dot{\omega} b M_0\, 1/\eta\, \ell n\left(\frac{1+\eta\sin\psi}{1-\eta\sin\psi}\right)\right\} d\phi \tag{5.5}$$

For small η the second term in the integrand of (5.5) can be expanded in power series. Retaining only the linear term, this formula reduces to

$$\dot{E}_1 = \int_{-\beta}^{\beta}\{2\dot{\omega} b \sin\psi[N_0 b + M_0]\}\, d\phi \tag{5.6}$$

Note that the dependence of the solution on the larger radius **a** is weak and disappears altogether for small η. The first term in the integrand of (5.6) represents the contribution of circumferential extension while the second term the contribution of continuous bending (change of circumferential curvature). Since b is always greater than the thickness of the shells and in most cases is of the order of $b = 4h$, the continuous bending does not contribute much to the rate of energy dissipation in regions of continuous deformation and thus can be neglected in simplified calculations. Sawczuk and one of the present authors [13] studied the ratio $\dot{\kappa}\phi\phi/\dot{\lambda}_{\phi\phi}$ and found that for small η the stress profile is reduced to a single point on the yield condition $M = 0$, $N = N_0$. The second integration can be performed with the help of (4.5), (4.6), and (5.4a) and the result is

$$\dot{E}_1 = \frac{4N_0 bH\pi}{(\pi - 2\psi_0)tg\psi_0}\cos\alpha\left\{\sin\psi_0 \sin\left(\frac{\pi-2\psi_0}{\pi}\right)\beta + \cos\psi_0\left[1 - \cos\left(\frac{\pi-2\psi_0}{\pi}\right)\right]\beta\right\}\dot{\alpha} \tag{5.6a}$$

Integrating now (5.6a) over the whole deformation process, the work done on a complete folding of the element through the angle $\pi/2$ is

Downloaded 02 May 2010 to 171.66.16.250. Redistribution subject to ASME license or copyright; see http://www.asme.org/terms/Terms_Use.cfm

$$E_1 = 4Hb\, N_0\, I_1(\psi_0) = 16\, M_0\, Hb/h\, I_1(\psi_0) \tag{5.7}$$

where I_1 is defined by

$$I_1(\psi_0) = \frac{\pi}{(\pi - 2\psi_0) tg\psi_0} \int_0^{\pi/2} \cos\alpha \Big\{ \sin\psi_0 \sin \left(\frac{\pi - 2\psi_0}{\pi}\right)\beta + \cos\psi_0 \left[1 - \cos\left(\frac{\pi - 2\psi_0}{\pi}\right)\beta\right]\Big\} d\alpha \tag{5.7a}$$

Since, according to (4.3), the angle β is a function of α, the preceding integral is a known function of the angle ψ_0.

The second integral in the expression (5.1) represents the internal energy dissipation by the discontinuous velocity field on the horizontal and inclined hinge lines. Consider first the horizontal hinges. The length of each horizontal hinge line is constant and equal to C. Because the hinge line is split, there will be two such hinge lines in the basic folding mechanism. The contribution of this mechanism is

$$\dot{E}_2 = 2M_0 C\dot{\theta} = 2M_0 C\dot{\alpha}, \tag{5.8}$$

or after integration over the whole process

$$E_2 = 2\int_0^{\pi/2} M_0 C\, d\alpha = \pi M_0 C \tag{5.9}$$

Additional energy will be dissipated if the horizontal boundary condition of the basic folding mechanisms were of the clamped rather than simply supported type.

The length of the inclined hinge lines changes in the process and is equal approximately to

$$L = 2H/\sin\gamma \tag{5.10}$$

In more exact calculations, the large radius of the toroidal surface would enter the expression for L. The inclined hinge lines consist of two segments of straight lines and an arc of the circle defined by the radius r_0 and central angle 2β.

The discontinuity in the rate of rotation in the meridional direction is constant along L and equal to

$$\dot{\theta} = V_t/b \tag{5.11}$$

Since there are two inclined hinge lines (one imposing and one removing the curvature), the energy dissipation in this deformation mechanism becomes

$$\dot{E}_3 = 2M_0\, L\dot{\theta} = 4M_0 \frac{H^2}{b} \frac{1}{tg\psi_0} \frac{\cos\alpha}{\sin\gamma} \tag{5.12}$$

where the angle γ is related to α by means of (4.3). The corresponding work done upon complete folding, obtained from (5.12) is

$$E_3 = 4M_0\, I_3(\psi_0) H^2/b \tag{5.13}$$

where I_3 is defined by

$$I_3(\psi_0) = \frac{1}{tg\psi_0} \int_0^{\pi/2} \frac{\cos\alpha}{\sin\gamma}\, d\alpha$$

The rate of external work done on compressing the basic folding mechanisms is

$$\dot{E}_{ext} = P\dot{\delta} = P \cdot 2H(\sin\alpha)\dot{\alpha} \tag{5.14}$$

while the total plastic work required to crush the element through the distance $2H$ equals

$$E_{ext} = 2PH \tag{5.15}$$

6 Properties of the Solution

Having identified the basic mechanisms of plastic dissipation one can proceed now to the calculation of the crushing resistance of thin-walled structural members that can be assembled from the basic folding mechanism. Some interesting observations can be made at the general level without specifying any particular type of a structure.

The instantaneous crushing force P is defined by the requirement that the rate of internal and external energy dissipation be equal, $\dot{E}_{ext} = \dot{E}_1 + \dot{E}_2 + \dot{E}_3$. This is equivalent to assuming a global equilibrium in the shell. However, locally the equilibrium may be violated. The terms $\dot{\alpha}$ drops out from both sides of the equation and an expression is obtained for the force-shortening characteristics of the compressed member. This expression involves two unknown geometrical parameters H and b (the third parameter a disappeared in simplified calculations). To determine these parameters, consider the mean crushing force P_m, defined by the balance of total energies $E_{ext} = E_1 + E_2 + E_3$. It is easy to see from (5.7), (5.9), and (5.13) that the general form of the formula for P_m is

$$\frac{P_m}{M_0} = A_1 \frac{b}{h} + A_2 \frac{C}{H} + A_3 \frac{H}{b} \tag{6.1}$$

where numerical values of the parameters A_1, A_2, and A_3 are known and depend on the type of problem.

It seems reasonable to postulate that the collapse mechanism, which activates and persists in the course of the crushing process leads to the least possible amount of the mean crushing force. Indeed, the minimum of (6.1) does exist with respect to both H and b. The unknown parameters can thus be determined from the set of equations

$$\frac{\partial P_m}{\partial H} = 0, \quad \frac{\partial P_m}{\partial b} = 0 \tag{6.2}$$

Postulating a similar condition for the instantaneous rather than mean crushing force would be appropriate only if an additional dissipation mechanism, responsible for the change in the wavelength H was considered and if random or buckling-induced imperfections were accounted for. Without these measures, the optimality condition for the rate of energy dissipation would lead to the variable wavelength, which contradicts the assumption 3. This interesting problem is discussed at length in [14].

The solution to equation (6.2) is

$$b = \sqrt[3]{A_2 A_3/A_1^2}\ \sqrt[3]{Ch^2}, \quad H = \sqrt[3]{A_2^2/A_1 A_3}\ \sqrt[3]{C^2 h}, \tag{6.3}$$

Substituting (6.3) back into (6.1) we obtain

$$\frac{P_m}{M_0} = 3\sqrt[3]{A_1 A_2 A_3}\ \sqrt[3]{C/h} \tag{6.4}$$

This is an extremely interesting and important result. It shows that all three major mechanisms of energy dissipation discussed in the paper, contribute equally to the total energy dissipation, irrespective of the actual numerical values of the coefficient A_1, A_2, and A_3. This property follows directly from the coupling effect of the continuous deformations in the toroidal surface. In particular, we can see that two-thirds of the plastic energy is always dissipated through inextensional deformations at stationary and moving plastic hinge lines. The extensional deformations, confined to the small fraction of the total area of the shell, are responsible for the remaining one-third of the dissipated energy.

The expression (6.3) can be used in conjunction with the rate of energy balance equation to derive the load-deflection characteristics of the member. Its general form is

$$P(\delta) = P_m f(\delta) \tag{6.5}$$

and a detailed discussion of its validity is presented in [14].

7 Applications, Crushing of a Box Column

This problem received a great deal of attention in the literature in view of its obvious application in controlling the process of energy absorption by automobile bodies during a front or rear-end collision.

Downloaded 02 May 2010 to 171.66.16.250. Redistribution subject to ASME license or copyright; see http://www.asme.org/terms/Terms_Use.cfm

The experimentally observed collapse mechanism of a rectangular column can be modeled with a good accuracy by an assembly of four basic folding mechanisms, each of the length C. The crumpling process of a rectangular tube is progressive, each new fold is being formed after the previous one is completed, Fig. 6. The corresponding force-shortening characteritics exhibits fluctuations around a mean value with peaks and valleys positioned at regular intervals $2H$, Fig. 7. The energy absorption of the member is thus well characterized by the mean crushing for P_m. The dimensions of the rectangular cross section $c \times d$, the wall thickness h, the angle $2\psi_0 = 90$ deg between plates, and the flow stress σ_0 are all considered as known. The sought-off quantities are the mean crushing force P_m, the wavelength H, and the rolling radius b. The values of the integrals, corresponding to $\psi_0 = \pi/4$ are $I_1 = 0.58$, $I_3 = 1.11$.

Since a section of the rectangular tube is composed of four basic folding elements, all energies, calculated in Section 5 should be multiplied by four. Moreover, because of clamped boundary conditions at horizontal edges, the energy E_2 should be doubled. The energy balance equation yields

$$2H\,P_m = M_0\left\{64I_1\frac{bH}{h} + 8\pi C + 16\,I_3\frac{H^2}{b}\right\} \tag{7.1}$$

where $C = 1/2\ (c+d)$. By comparing (7.1) with (6.1), the values of the coefficients are found to be $A_1 = 32I_1 = 18.56$, $A_2 = 4\pi$, $A_3 = 8I_3 = 8.91$. The solution for H and b calculated from (6.3) is

$$H = 0.983\ \sqrt[3]{hC^2},\quad b = 0.687\ \sqrt[3]{h^2C} \tag{7.2}$$

while the expression (6.4) for the mean crushing force becomes

$$\frac{P_m}{M_0} = 38.27\ \sqrt[3]{\frac{C}{h}} \tag{7.3}$$

In particular, for a square tube, for which $c = d = C$, a simple and practical formula is obtained

$$P_m = 9.56\sigma_0 h^{5/3}\quad C^{1/3} \tag{7.4}$$

where in transforming of (7.3) into (7.4) a definition of the fully plastic moment was used.

Attention is drawn here to the term $h^{5/3}$. In all known solutions to this problem, based on inextensional collapse modes, the crushing force was proportional to h^2, [2, 3]. If pure extensions were present in sheet metal structures, the crushing force would be proportional to $N_0 = \sigma_0 h$. In the present analysis the ratio of bending and extension is 2:1 and this property is also reflected in the value of the exponent n. It is interesting to note that in crushing problems with axisymmetric deformation modes, the circumferential extension and bending are present in equal proportions, leading to the term $h^{1.5}$ in the expression for the crushing force, [4, 5,7].

Using a semiempirical approach coupled with the modified "effective width" theory, Aya and Takahashi, [15] obtained the same exponent as in the formula (7.4). A larger value $n = 1.86$ was suggested in [16] on purely empirical grounds while Magee and Thornton's fit of test result gave a smaller exponent $n = 1.60$, [17].

Introducing structural effectiveness $\eta = P_m/A\sigma_0$ (nondimensional crushing stress) and relative density $\phi = A/A_1$ (solidity ratio) the formula (7.4) can be rewritten as

$$\eta = 0.948\ \phi^{2/3} \tag{7.5}$$

where $A_1 = C^2$ and $A = 4hC$.

The prediction of the preceding formula is shown in Fig. 8 by a dotted line. The present solution correlates well with experimental points, reported in [17] and follows rather closely the Magee and Thorton's empirical fit of the test results. Note, that in converting the experimental points to the dimensionless coordinate $\eta - \phi$, the ultimate stress was used in reference [17].

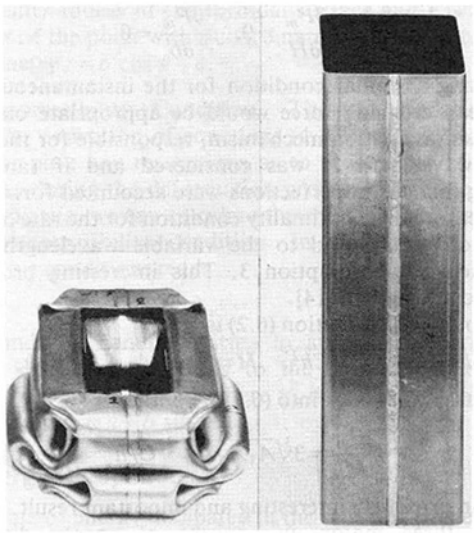


Fig. 6 Typical view of the fully crushed rectangular box column

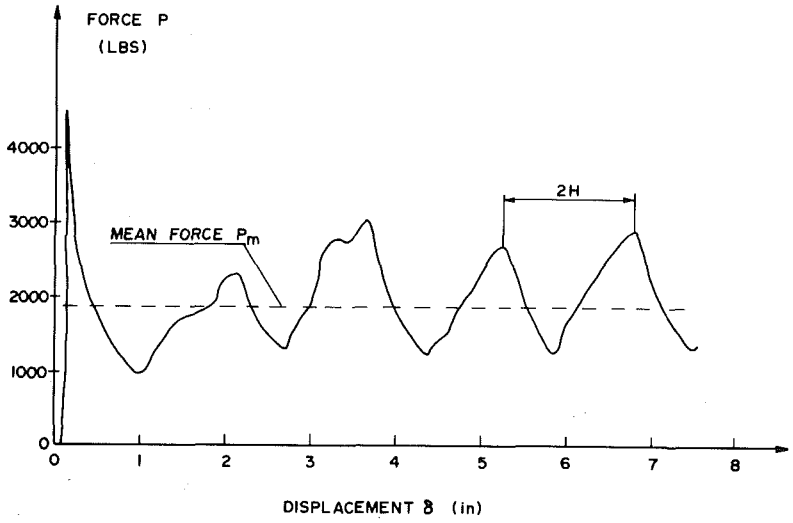


Fig. 7 Force-shortening characteristics of an axially compressed thin-walled column (courtesy of Ford Motor Co. Research Lab.)

Downloaded 02 May 2010 to 171.66.16.250. Redistribution subject to ASME license or copyright; see http://www.asme.org/terms/Terms_Use.cfm

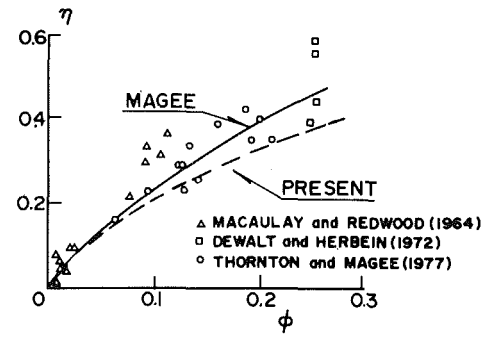


Fig. 8 Correlation between predicted and measured dimensionless crushing stress and relative thickness h/c

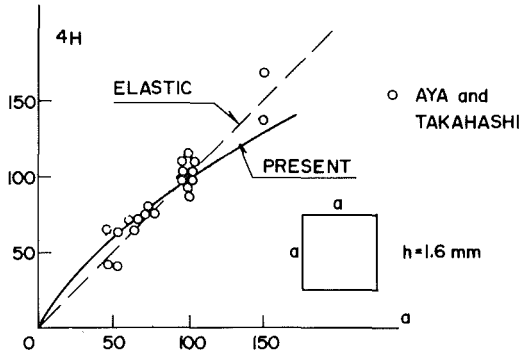


Fig. 9 Theoretical and experimental wavelength as a function of the column width

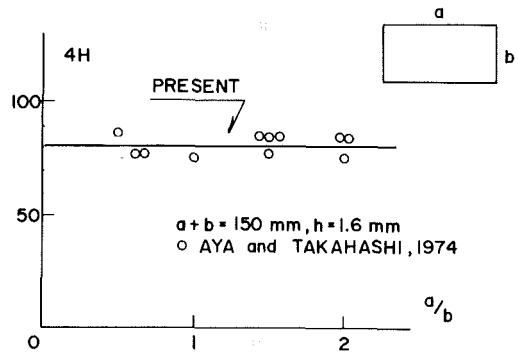


Fig. 10 Length of the folding mode versus the aspect ratio of rectangular cross section

Actually, for a work-hardening material, the plastic work should be related to an average flow stress σ_0. This average stress is much higher than the initial yield stress σ_y but is always below the ultimate stress σ_u. Taking in (7.5) as a reference stress a value that is smaller than σ_u would automatically raise all the experimental points.

At the same time the resulting discrepancies will be, to a large extent, offset by the fact that the actual distance over, while the force P_m exerts work, is $2H\text{-}a$ rather than $2H$. Also, inclusion of a variable (increasing) thickness in extensional zones and retension of a small but finite parameter b/a would bring the $\eta-\phi$ curve closer to experiments. As pointed out earlier, these effects were deliberately disregarded in the present analysis to offer a more clear interpretation of the crushing process and to derive a simple closed-form solution.

Perhaps an even more critical test for the validation of the present theory is to see how well it correlates with experimentally measured wavelength. This is shown in Fig. 9 and 10. The formula (7.2), which is now independent of σ_0, predicts correctly the height of the subsequent plastic folds in the entire range of h/C for which the folding process is progressive. The observation that for fixed $(c+d)$, both H and P_m do not depend on the aspect ratio c/d of the rectangular cross section is also featured by the present solution, Fig. 10.

8 Conclusions

The present analysis explains some important qualitative features of the crushing process of thin shells. It shows that plastic deformations of the magnitude exceeding by far those corresponding to the buckling or ultimate loads, are indeed confined to relatively small areas. The local curvature in these areas is relatively large, i.e., the radius of curvature b is small compared to a linear dimension C. The zones of extensional deformations are restricted to even smaller fraction of the total area of the shell but they always contribute to as much as one-third of the total energy dissipated in the structure. The remaining two-thirds of the energy results in equal proportions from inextensional deformations at stationary and moving hinge lines.

Calculations have shown that in all types of shells the mean crushing force depends markedly on the thickness of the shell ($h^{5/3}$). At the same time the dependence on the linear dimension C is much weaker ($C^{1/3}$). The present theory has also led to a good quantitative prediction of the mean crushing force and the associated collapse mechanism for axially compressed rectangular box columns.

The folding mode, developed in the paper has a potential of being used as a "special finite element" in numerical simulation of crash phenomena. This element could be used in the areas where sharp folds and wrinkles are formed to replace a necessarily dense and thus expansive finite element mesh.

The present methodology has been used in the calculation of the crushing strength of compressed and bent box columns with other cross-sectional shapes, for example closed hat-sections or channel sections. Some new results in this area can be found in reference [18]. Equally simple and accurate results were obtained for hexagonal cell structures and a relevant report will be released shortly, reference [19].

9 Acknowledgment

The work reported herein is a part of a research task No. J-F7F062P on "Structural Aspects of Vehicle Crashworthiness" jointly undertaken by the Department of Ocean Engineering of the Massachusetts Institute of Technology and the Institute of Fundamental Technological Research in Warsaw. The financial support of the Polish Academy of Sciences and National Science Foundation through the Maria Curie-Sklodowska fund and the Massachusetts Institute of Technology is gratefully acknowledged. The authors are indebted to Dr. Henryk Stolarski for his interesting discussions on the subject and to Mrs. Ellen Ray for typing this manuscript.

References

1 Johnson, W., Soden, P. D., and Al-Hassani, S. T. S., "Inextensional Collapse of Thin-Walled Tubes Under Axial Compression," *J. Strain Analysis*, Vol. 12, 1977, pp. 317-330.

2 Ohokubo, Y., Akamatsu, T., and Shirasawa, K., "Mean Crushing Strength of Closed-Hat Section Members," SAE Paper No. 740040.

3 Wierzbicki, T., and Akerstrom, T., "Dynamic Crushing of Strain Rate Sensitive Box Columns," SAE Paper No. 770592, *Proc. 2nd Int. Conf. Vehicle Struct. Mech.*, Southfield, Mich., Apr. 18-20, 1977.

4 Al-Hassani, S. T. S., Johnson, W., and Lowe, W. T., "Characteristics of Inversion Tubes Under Axial Loading," *J. Mechanical Engineering Sciences*, Vol. 14, 1972, pp. 370-381.

5 Alexander, J. M., "An Approximate Analysis of the Collapse of Thin Cylindrical Shells Under Axial Load," *Quart. J. Mechanics Applied Mathematics*, Vol. 13, 1969, pp. 10-15.

6 Morris, A. J., and Calladine, C. R., "The Local Strength of a Thin

Downloaded 02 May 2010 to 171.66.16.250. Redistribution subject to ASME license or copyright; see http://www.asme.org/terms/Terms_Use.cfm

Spherical Shell Loaded Radially Through a Rigid Boss," *Proc. 1st Int. Conf. on Pressure Vessel Technology*, ASEM, 1969.

7 de Oliveira, J. G., and Wierzbicki, T., "Crushing Characteristics of Rotationally Symmetric Plastic Shells," *J. Strain Analysis*, Vol. 17, 1982 (in print).

8 Kosinski, W., *Introduction to the Theory of Field Singularities and Wave Analysis*, (in Polish) Polish Scientific Publisher, Warsaw-Poznan, 1981.

9 Hopkins, H. G., "On the Plastic Theory of Plates," *Proceeding, Royal Society*, London, Series *A*, Vol. 241, 1957, pp. 153–179.

10 Hopkins, H. G., and Prager, W., "On the Dynamic of Plastic Circular Plates," *ZAMP*, Vol. 4, 1954, pp. 317–330.

11 Wierzbicki, T., "Crushing Analysis of Thin-Walled Structures," Structural Mechanics Series, Report No. 23, School of Engineering, Duke University, Feb. 1982.

12 Stolarski, H., "Dynamics of Strongly Deforming Rigid-Plastic Structures," Lecture notes prepared for the CISM Course on "Dynamics of Plastic Structures," Udine, Italy, Oct. 1979.

13 Abramowicz, W., and Sawczuk, A., "On Plastic Inversion of Cylinders," *Res. Mecanica Letters*, Nov. 1981.

14 Wierzbicki, T., "On the Formation and Growth of Folding Modes in Compressed Thin-Walled Structures," Paper offered for the IUTAM Symposium on Collapse: "The Buckling of Structures in Theory and Practice," University College London, Aug. 31–Sept. 3, 1982.

15 Aya, N., and Takahashi, K., "Energy Absorption Characteristics of Vehicle Body Structure," *Transactions of the Society of Automotive Engineers of Japan*, No. 7, May 1974.

16 Mahmood, H. F., and Paluszny, A., "Design of Thin Walled Columns for Crash Energy Management—Their Strength and Mode of Collapse," *Proc. 4th Instructural Conference on Vehicle Structural Mechanics*, Nov. 18–20, 1981, Detroit, pp. 7–18.

17 Magee, C. L., and Thornton, P. H., "Design Consideration in Energy Absorption by Structural Collapse," SAE Paper No. 780434, *Proc. Congress and Exposition*, Cobo Hall, Detroit, Mich., Feb. 27–Mar. 3, 1978.

18 Abramowicz, W., "Mechanics of the Crushing Process of Plastic Shells" (in Polish) Ph.D. Thesis, Institute of Fundamental Technological Research, Warsaw, Feb. 1981.

19 Wierzbicki, T., "Crushing Analysis of Metal Honeycombs," MIT Report #83-1, to appear in *Int. J. of Impact Engineering*, Vol. I, No. 2, 1983.

Downloaded 02 May 2010 to 171.66.16.250. Redistribution subject to ASME license or copyright; see http://www.asme.org/terms/Terms_Use.cfm

Small Deflections of Linear Elastic Circular Membranes Under Lateral Pressure

B. Storåkers
Department of Strength of Materials and Solid Mechanics, The Royal Institute of Technology, S-100 44 Stockholm, Sweden

The classical Föppl equations, governing the deflection of plane elastic membranes, are cast in a form convenient for numerical analysis in the case of a circular contour. A solution based on a standard computer method is given for uniform pressure load. Quantitative results within determined accuracy are reported in considerable detail together with a discussion of the physical range of validity.

Introduction

In the beginning of this century Föppl [1] laid down equations governing out-of-plane deflection of Hookean membranes subjected to lateral hydrostatic pressure. Except for degenerate contours the Föppl equations do not admit an analytical solution and as a consequence various methods of attack have been tried by several writers. In particular as regards a circular contour, Hencky [2], being an early investigator, reduced the governing equations to a single second-order nonlinear differential equation which was solved by aid of a series expansion method. After this pioneering effort there seems to have been no substantial progress until modern computer methods have rendered more accurate solutions possible.

In recent time, the mathematical structure of the equations governing circular membranes was discussed by Dickey [3], who converted Hencky's differential equation to a nonlinear integral equation. Despite the occurrence of a singularity, Dickey successfully solved some cases numerically by aid of a particularly devised iteration procedure. Koiter [4], in his discussion of complementary energy theorems in nonlinear elasticity, treated the circular membrane in a particular illustration and gave a solution based on direct numerical quadrature of the Hencky equation. Further specific numerical results have been provided by Kao and Perrone [5] through a nonlinear relaxation method having a more general range of applicability, [6], and employing finite difference approximations. In their attempt to provide extensive information on the behavior of circular inelastic membranes, Hill and Storåkers [7] cast the problem in the form of four coupled differential equations of lowest possible order, which were solved by a standard computer procedure. Linear incompressible material behavior then arose as a special case.

Despite these contributions there still seems to be a peculiar lack of detailed numerical results of high accuracy and associated physical interpretation for circular membranes exhibiting linear, isotropic, compressible material behavior. Apart from the interest per se, for one thing, such information is urgently needed when utilizing the circular membrane as a test case for approximate solution methods applicable also to other contours [6, 8]. In the sequel the Föppl equations are arranged in a form feasible for solution with a controlled accuracy by a standard computer method. Results of the solution are given in substantial detail and in particular the role of the material contraction ratio is displayed. As the Föppl formulation of the problem may be considered as the first consistent approximation to have any physical meaning, its range of validity is also estimated.

The Boundary Value Problem

The explicit problem to be dealt with concerns the mechanical behavior of an initially plane and stress-free membrane, of thickness t, rigidly constrained at a circular contour of radius a, and subjected to a lateral hydrostatic pressure, p.

By symmetry arguments it is then convenient to introduce a polar coordinate system (r, ϕ), as in case of material isotropy and uniform membrane thickness and pressure, the principal directions of stress and strain will then coincide with the coordinate directions. The deformed membrane shape then possesses an axis of symmetry and the principal stresses may be solved explicitly from equilibrium considerations as is shown in any textbook on shell theory.

Denoting the slope of the deformed membrane by

$$\theta = -\frac{dw}{dr} \tag{1}$$

$w(r)$ being lateral deflection, convenient expressions for the radial and circumferential stresses and associated strains are

$$\sigma_r = \frac{p}{2t}\frac{r}{\theta}, \quad \sigma_\phi = \frac{p}{2t}\frac{d}{dr}\left(\frac{r^2}{\theta}\right) \tag{2}$$

$$e_r = \frac{du}{dr} + \frac{1}{2}\theta^2, \quad e_\phi = \frac{u}{r} \tag{3}$$

Contributed by the Applied Mechanics Division for publication in the JOURNAL OF APPLIED MECHANICS.
Discussion on this paper should be addressed to the Editorial Department, ASME United Engineering Center, 345 East 47th Street, New York, N.Y. 10017, and will be accepted until two months after final publication of the paper itself in the JOURNAL OF APPLIED MECHANICS. Manuscript received by ASME Applied Mechanics Division, October, 1982.

Copyright © 1983 by ASME
Downloaded 02 May 2010 to 171.66.16.250. Redistribution subject to ASME license or copyright; see http://www.asme.org/terms/Terms_Use.cfm

where $u(r)$ is the radial displacement component.

The inherent assumptions and tacit simplifications already made have earlier been discussed in detail by Hill and Storåkers [7]. Suffice it to say that the membrane is assumed to be of vanishing thickness as compared to its radius and as a consequence is suffering under a state of plane stress only. The nonvanishing components of Cauchy stress, σ, acting in the deformed configuration, are labeled as in-plane components without any distinction between an embedded and a fixed coordinate system. Furthermore in (3) the in-plane displacement gradient has been neglected compared to the out-of-plane gradient of the same degree. The slope of the deformed membrane surface is assumed small in relation to unity. As a consequence of this approximation the distinction between unidirectional, lateral, and hydrostatic pressure loading vanishes.

For a Hookean material under plane stress the appropriate form of the constitutive equation is

$$\sigma_{\alpha\beta}=\frac{\mathrm{E}}{1+\nu}\left(\delta_{\alpha\gamma}\delta_{\beta\delta}+\frac{\nu}{1-\nu}\delta_{\alpha\beta}\delta_{\gamma\delta}\right)e_{\gamma\delta}\qquad \alpha=1,2 \tag{4}$$

in customary notation.

The setting of the problem is then completed by prescribing dynamic and/or kinematic conditions at the contour. At present attention is confined to rigid constraints, i.e., $(u, w) = \mathbf{0}$.

Already at this early stage is it possible to extract some explicit information regarding the membrane behavior as was indeed observed to a certain extent already by Föppl and subsequently by other writers. Presently it proves convenient, following Hill and Storåkers [7], to introduce dimensionless variables

$$\tilde{r}=r/a \tag{5}$$

$$\frac{u}{a\tilde{u}}=\left(\frac{w}{a\tilde{w}}\right)^2=\left(\frac{pa}{\mathrm{E}t}\right)^{2/3} \tag{6}$$

$$\frac{e_{\alpha\beta}}{\tilde{e}_{\alpha\beta}}=\frac{\sigma_{\alpha\beta}}{\mathrm{E}\tilde{\sigma}_{\alpha\beta}}=\left(\frac{pa}{\mathrm{E}t}\right)^{2/3} \tag{7}$$

It is then immediate that the governing equations (3) and (4), with E discarded, are valid also for the reduced variables. The equilibrium equations (2) reduce to

$$\tilde{\sigma}_r=\frac{\tilde{r}}{2\tilde{\theta}},\quad \tilde{\sigma}_\phi=\frac{d}{d\tilde{r}}\left(\frac{\tilde{r}^2}{2\tilde{\theta}}\right) \tag{8}$$

Furthermore, as the boundary conditions are homogeneous, the reduced variables do not depend on the magnitude of the external loading and as a consequence the pressure dependence of displacements, strains, and stresses is already determined by equations (6) and (7).

In their analysis of inelastic, incompressible membrane behavior, Wang and Shammany [9] and Hill and Storåkers [7] utilized equivalent stress and strain measures together with a parametric "stress angle" as dependent variables, a set that seems to originate from Nadai [10] in his treatment of various plasticity problems. As an alternative to solve one second-order differential equation and in analogy with the Nadai choice of variables, it proves advantageous for linear compressible material behavior to adopt the reduced stress and strain measures (in fact disguised measures of strain energy)

$$\tilde{\sigma}=(\tilde{\sigma}_r{}^2-2\nu\tilde{\sigma}_r\tilde{\sigma}_\phi+\tilde{\sigma}_\phi{}^2)^{1/2} \tag{9}$$

and

$$\tilde{e}=(1-\nu^2)^{-1/2}(\tilde{e}_r{}^2+2\nu\tilde{e}_r\tilde{e}_\phi+\tilde{e}_\phi{}^2)^{1/2} \tag{10}$$

Then upon introducing the parametric angle

$$\Psi=\tan^{-1}\left[\left(\frac{1+\nu}{1-\nu}\right)^{1/2}\frac{1-\tilde{\sigma}_\phi/\tilde{\sigma}_r}{1+\tilde{\sigma}_\phi/\tilde{\sigma}_r}\right] \tag{11}$$

the constitutive equation may be summarized in a form, convenient for the present purpose, as

$$\tilde{\sigma}=\tilde{e} \tag{12}$$

$$\left.\begin{matrix}\tilde{\sigma}_r\\ \tilde{\sigma}_\phi\end{matrix}\right\}=\frac{\tilde{\sigma}}{\sqrt{2(1-\nu)}}\left(\cos\Psi\pm\sqrt{\frac{1-\nu}{1+\nu}}\sin\Psi\right) \tag{13}$$

$$\left.\begin{matrix}\tilde{e}_r\\ \tilde{e}_\phi\end{matrix}\right\}=\sqrt{(1-\nu)/2}\tilde{e}\left(\cos\Psi\pm\sqrt{\frac{1+\nu}{1-\nu}}\sin\Psi\right) \tag{14}$$

Introduction of equations (13) and (14) into (3) and (8) yields via (12)

$$\left.\begin{aligned}&\frac{\tilde{e}}{\sqrt{2(1-\nu)}}(\cos\Psi+\sqrt{(1-\nu)/(1+\nu)}\sin\Psi)=\frac{\tilde{r}}{2\tilde{\theta}}\\ &\frac{\tilde{e}}{\sqrt{2(1-\nu)}}(\cos\Psi-\sqrt{(1-\nu)/(1+\nu)}\sin\Psi)=\frac{d}{d\tilde{r}}\left(\frac{\tilde{r}^2}{2\tilde{\theta}}\right)\\ &\sqrt{(1-\nu)/2}\tilde{e}(\cos\Psi+\sqrt{(1+\nu)/(1-\nu)}\sin\Psi)=\frac{d\tilde{u}}{d\tilde{r}}+\frac{1}{2}\tilde{\theta}^2\\ &\sqrt{(1-\nu)/2}\tilde{e}(\cos\Psi-\sqrt{(1+\nu)/(1-\nu)}\sin\Psi)=\frac{\tilde{u}}{\tilde{r}}\end{aligned}\right\} \tag{15}$$

This system is to be solved for the closed interval $0 \le \tilde{r} \le 1$. By symmetry arguments, initial conditions to be fulfilled are

$$\tilde{u}(0)=\tilde{\theta}(0)=\Psi(0)=0 \tag{16}$$

and the single kinematic boundary condition is

$$\tilde{u}(1)=0 \tag{17}$$

As was to be expected the only parameter entering the resulting equations is the contraction ratio ν.

Numerical Solution and Results

The governing system, equation (15), consists of two zero-order and two first-order ordinary coupled differential equations. To apply a library computer program (Numerical Algorithms Group), utilizing Merson's version of the Runge-Kutta integration procedure, all equations were solved for the first-order derivatives. A solution satisfying the boundary condition (17), within desired accuracy, was then readily obtained by aid of a simple "shooting-in" procedure choosing trial values of the reduced membrane center strain $\tilde{e}(0)$. Once the slope, θ, had been found the deflected shape is immediate from quadrature of (1). To render direct application possible, detailed and systematic numerical results are given in Table 1. All values exhibited are believed to be essentially accurate within three figures as in the numerical integration procedure, the relative truncation error in each step, out of 10, was chosen to be less than 0.0001. The variation of some representative variables is also depicted in Figs. 1–4 for lucidity reasons.

The deflected shape of the membrane may be well approximated by a paraboloid through the center and the boundary. The greatest deviation in the range $0 \le \nu \le 0.5$ occurs for $\nu = 0$ and this feature is illustrated in Fig. 1. The degree of sphericity is gradually lost toward the boundary and in Fig. 2 the ratio of the principal radii of curvature is depicted for three different contraction ratios. The influence

Downloaded 02 May 2010 to 171.66.16.250. Redistribution subject to ASME license or copyright; see http://www.asme.org/terms/Terms_Use.cfm

of the constrained boundary on the stress distribution is shown in Fig. 3. As may be seen, the stress state does not deviate appreciably from a balanced biaxial one in a substantial portion of the membrane. As regards the strain distribution, illustrated in Fig. 4, the circumferential strain component is virtually insensitive of the contraction ratio while one perhaps surprising feature is that, for higher contraction ratios, the radial strain increases toward the boundary. Except perhaps for the radial strain then, due to the fairly slow variation of all relevant variables with

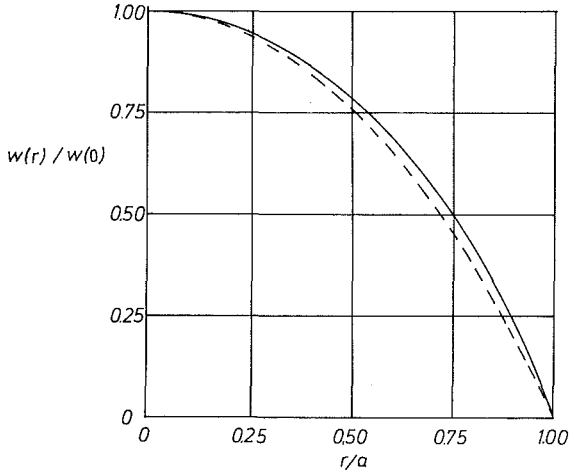


Fig. 1 Deflected membrane shape for zero contraction ratio (——) as compared to a parabola (– – –)

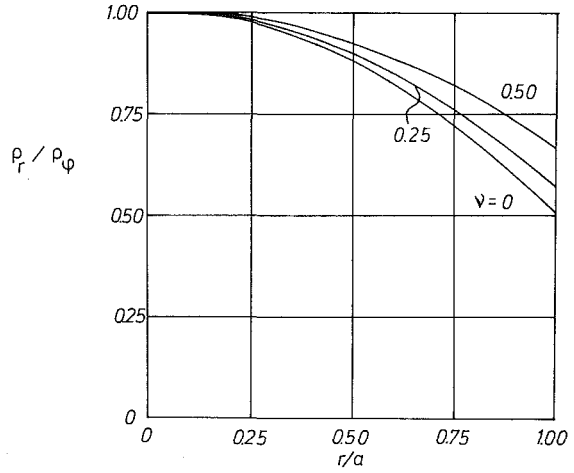


Fig. 2 Radial variation of the ratio of principal radii of curvature for contraction ratios 0, 0.25, 0.50

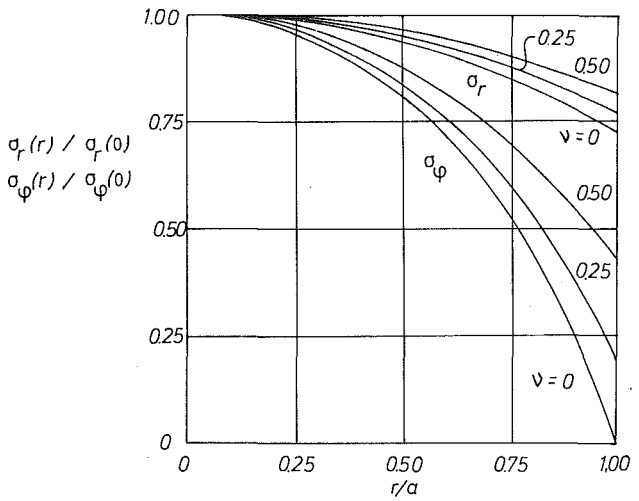


Fig. 3 Radial variation of normalized principal stresses for contraction ratios 0, 0.25, 0.50

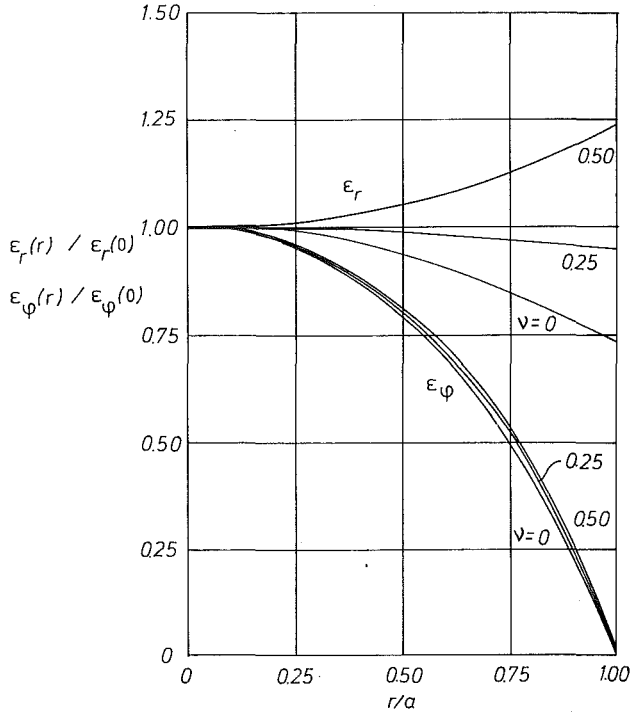


Fig. 4 Radial variation of normalized principal strains for contraction ratios 0, 0.25, 0.50

Table 1 Numerical values of reduced displacements $\tilde{u}$, $\tilde{w}$, strain $\tilde{e}$, and parametric angle Ψ (rad) as a function of reduced radius $\tilde{r}$ for various values of Poisson's ratio ν

ν	0				0.1				0.2			
$\tilde{r}$	$10\,\tilde{u}$	$\tilde{w}$	$\tilde{e}$	Ψ	$10\tilde{u}$	$\tilde{w}$	$\tilde{e}$	Ψ	$10\tilde{u}$	$\tilde{w}$	$\tilde{e}$	Ψ
0	0	0.718	0.573	0	0	0.699	0.553	0	0	0.677	0.532	0
0.1	0.402	0.712	0.570	0.0024	0.368	0.693	0.551	0.0025	0.334	0.672	0.530	0.0026
0.2	0.787	0.694	0.562	0.0097	0.720	0.675	0.543	0.0102	0.653	0.654	0.523	0.0106
0.3	1.136	0.662	0.548	0.0228	1.039	0.644	0.530	0.0238	0.942	0.623	0.512	0.0247
0.4	1.429	0.618	0.529	0.0430	1.306	0.600	0.513	0.0447	1.182	0.581	0.496	0.0463
0.5	1.643	0.559	0.503	0.0729	1.499	0.543	0.489	0.0755	1.354	0.525	0.475	0.0776
0.6	1.747	0.486	0.470	0.117	1.590	0.471	0.459	0.120	1.433	0.455	0.448	0.123
0.7	1.703	0.396	0.430	0.184	1.546	0.383	0.424	0.137	1.389	0.369	0.417	0.188
0.8	1.459	0.287	0.383	0.289	1.319	0.278	0.382	0.289	1.181	0.267	0.381	0.287
0.9	0.934	0.157	0.332	0.468	0.841	0.151	0.338	0.455	0.748	0.145	0.343	0.440
1.0	0.000	0	0.289	0.785	0.001	0	0.300	0.735	0.001	0	0.310	0.685

Downloaded 02 May 2010 to 171.66.16.250. Redistribution subject to ASME license or copyright; see http://www.asme.org/terms/Terms_Use.cfm

Table 1 Continued

ν	0.25				0.3				0.333			
$\tilde{r}$	$10\,\tilde{u}$	$\tilde{w}$	$\tilde{e}$	Ψ	$10\tilde{u}$	$\tilde{w}$	$\tilde{e}$	Ψ	$10\tilde{u}$	$\tilde{w}$	$\tilde{e}$	Ψ
0	0	0.666	0.521	0	0	0.653	0.510	0	0	0.645	0.503	0
0.1	0.317	0.660	0.519	0.0026	0.300	0.648	0.508	0.0027	0.288	0.639	0.501	0.0027
0.2	0.619	0.642	0.513	0.0108	0.585	0.630	0.502	0.0109	0.563	0.622	0.495	0.0110
0.3	0.892	0.612	0.502	0.0251	0.843	0.601	0.492	0.0254	0.810	0.593	0.485	0.0256
0.4	1.119	0.570	0.487	0.0469	1.056	0.559	0.478	0.0474	1.015	0.551	0.472	0.0477
0.5	1.281	0.515	0.467	0.0785	1.208	0.505	0.459	0.0791	1.159	0.498	0.454	0.0794
0.6	1.354	0.446	0.442	0.124	1.275	0.437	0.436	0.124	1.223	0.430	0.432	0.124
0.7	1.311	0.362	0.413	0.189	1.232	0.354	0.409	0.188	1.181	0.349	0.406	0.188
0.8	1.111	0.261	0.380	0.285	1.042	0.255	0.378	0.281	0.997	0.251	0.377	0.275
0.9	0.701	0.142	0.344	0.431	0.656	0.138	0.346	0.421	0.626	0.136	0.346	0.413
1.0	0.000	0	0.314	0.660	0.000	0	0.318	0.633	0.000	0	0.320	0.616

Table 1 continued

ν	0.4				0.5			
$\tilde{r}$	$10\tilde{u}$	$\tilde{w}$	$\tilde{e}$	Ψ	$10\tilde{u}$	$\tilde{w}$	$\tilde{e}$	Ψ
0	0	0.626	0.487	0	0	0.595	0.461	0
0.1	0.265	0.621	0.485	0.0027	0.229	0.590	0.460	0.0028
0.2	0.516	0.604	0.480	0.0112	0.447	0.573	0.455	0.0113
0.3	0.743	0.575	0.471	0.0259	0.642	0.546	0.448	0.0261
0.4	0.930	0.535	0.459	0.0481	0.801	0.507	0.438	0.0482
0.5	1.061	0.482	0.443	0.0797	0.912	0.457	0.424	0.0793
0.6	1.117	0.417	0.423	0.124	0.957	0.394	0.408	0.122
0.7	1.075	0.337	0.400	0.186	0.918	0.318	0.389	0.180
0.8	0.905	0.243	0.374	0.273	0.768	0.228	0.368	0.260
0.9	0.566	0.131	0.347	0.398	0.479	0.123	0.347	0.370
1.0	0.000	0	0.324	0.580	0.001	0	0.328	0.524

Poisson's ratio ν, values for ν other than those reported on in Table 1, should be readily obtainable within high accuracy through interpolation.

It should be emphasized in this context that Koiter [4], when solving the original Hencky equation, was able to suppress the ν-dependence to the utmost by an ingenious scaling of the independent variable. As a result, master curves were given from which reduced stresses and lateral deflection may be read off for arbitrary ν-values. For lucidity reasons this possibility was not drawn upon in Figs. 1–3.

Koiter's universal way of presenting results of generality through master curves may not be drawn upon directly when seeking numerical values of high accuracy. To obtain an independent check of the present results, some values given by Dickey [3] are, however, applicable. Thus a comparison of polar deflection and strain, expressed in current variables, is given in Table 2. As may be concluded, the agreement is quite satisfactory save for two values. It is believed, however, that this discrepancy is simply due to misprints, the figures 4 and 9 being mixed up in Dickey's original results.

It might be noted in passing that Dickey [3] also dealt with boundary conditions of stress. By a simple transformation of the load variable, however, also the solution to this case may, within the accuracy of a diagram, be extracted from Koiter's general results [4], although these apply formally only in the case of a constrained boundary. The same circumstances also prevail as regards the results given in the foregoing but as a condition of prescribed radial boundary stress seems less obvious from a physical point of view, this matter is not elaborated on further.

To bring out the accuracy of earlier approximate results it is appropriate to first note that Hencky [2] attacked the original Föppl equations by expanding relevant variables in Taylor series, assumed to be absolutely convergent, and for the case of $\nu = 0.3$ arrived at $\tilde{w}(0) = 0.662$ and $\tilde{e}(0) = 0.501$ in the present notation. These estimates were based on series truncated at seven terms. Subsequently Odqvist [11] applied the Hencky method to nonlinear material properties retaining four Taylor terms. In the degenerate linear case Odqvist found $\tilde{w}(0) = 0.60$ and $\tilde{e}(0) = 0.461$ in case of material incompressibility ($\nu = 0.5$). In Kao and Perrone's treatment of

Table 2 Numerical values of reduced polar deflection $\tilde{w}(0)$ and strain $\tilde{e}(0)$ obtained by Dickey [3] and by present method for various values of Poisson's ratio ν

ν	$\tilde{w}(0)$		$\tilde{e}(0)$	
	Dickey	Present	Dickey	Present
0	0.7183	0.7183	0.5729	0.5729
0.1	0.7052	0.6989	0.5530	0.5530
0.2	0.6775	0.6774	0.5321	0.5322
0.3	0.6534	0.6534	0.5101	0.5101
0.4	0.6262	0.6263	0.4845	0.4866
0.5	0.5948	0.5950	0.4613	0.4613

a circular membrane [5], the reduced polar deflection was given as 0.6541 for $\nu = 0.3$, which compares favorably with 0.6534 (abbreviated in Table 1), rendering additional confidence in the results obtained by these writers [6], for other contours.

An investigation of the physical range of validity of the results is prompted by the claim of several writers, utilizing the Föppl equations, that their results are valid at "large" deflections. From a mathematical point of view the denomination "large" is meaningless as referred to the membrane thickness as this dimension is assumed vanishingly small. The single membrane dimension relevant for reference is the contour radius. By the further basic assumption of a small deformed profile slope as compared to unity, the deflections must by necessity be small with respect to the contour radius. The remaining question is then: how small?

For the case of an annular circular membrane, with a free inner boundary at $r/a = 0.1$, Weinitschke [12] has investigated the accuracy of the Föppl theory as related to a finite deformation theory by Reissner. A general conclusion is that relative differences in stresses, and accordingly strains, are within 1 percent when $pa/(Et)$ is less than 0.0005. In the present case this corresponds roughly to a polar equivalent strain of 0.003 and a deflection relative to the membrane radius of 0.05. On the other hand it was demonstrated by Hill and Storåkers [7] in their investigation of inelastic membranes how the results may be modified, e.g., for the thinning of the membrane. Thus as a general finding it proved possible to

Downloaded 02 May 2010 to 171.66.16.250. Redistribution subject to ASME license or copyright; see http://www.asme.org/terms/Terms_Use.cfm

predict relevant variables within 2 percent for reduced deflections less than 0.2. It does not seem worthwhile to dwell on this matter further, however, as the concept of material linearity may not be uniquely defined in case of finite deformation but is related to the choice of stress and (conjugate) strain measures. Suffice it to state then that the Föppl equations seem quite safe to use for circular metal membranes below yield.

Concluding Remarks

The solution method devised may be labeled exact at least in the sense that any desirable accuracy may be determined in advance. As an alternative to integrate a higher order equation the method proved easy to apply and is believed to be capable of also handling cases such as annular membranes without any additional fundamental difficulties. The results given in the foregoing should be sufficient and accurate enough for most practical purposes and they readily carry over to viscoelastic material behavior via a correspondence principle recently given by Storåkers [13]. This principle is valid for arbitrary pressure histories and materials having relevant relaxation moduli of uniform time dependence.

References

1 Föppl, A., *Vorlesungen Über Technische Mechanik*, 1907, Teubner, Leipzig, pp. 132–144.

2 Hencky, H., "Über den Spannungszustand in kreisrunden Platten mit verschwindender Biegungssteifigkeit," *Zeitschrift für Mathematik und Physik*, Vol. 63, 1915, pp. 311–317.

3 Dickey, R. W., "The Plane Circular Elastic Surface Under Normal Pressure," *Archives for Rational Mechanics and Analysis*, Vol. 26, 1967, pp. 219–236.

4 Koiter, W. T., "On the Complementary Energy Theorem in Nonlinear Elasticity," *Trends in Applications of Pure Mathematics to Mechanics*, Fichera, G., ed., Pitman, 1976, pp. 207–232.

5 Kao, R., and Perrone, N., "Large Deflections of Axisymmetric Circular Membranes," *International Journal of Solids and Structures*, Vol. 7, 1971, pp. 1601–1612.

6 Kao, R., and Perrone, N., "Large Deflections of Flat Arbitrary Membranes," *Computers and Structures*, Vol. 2, 1972, pp. 535–546.

7 Hill, R., and Storåkers, B., "Plasticity and Creep of Pressurized Membranes: A New Look at the Small-Deflection Theory," *Journal of the Mechanics and Physics of Solids*, Vol. 28, 1980, pp. 27–48.

8 Storåkers, B., "Variation Principles and Bounds for the Approximate Analysis of Plane Membranes Under Lateral Pressure," ASME JOURNAL OF APPLIED MECHANICS , Vol. 50, 1983, pp. 743–749.

9 Wang, N. M., and Shammamy, M. R., "On the Plastic Bulging of a Circular Diaphragm by Hydrostatic Pressure," *Journal of the Mechanics and Physics of Solids*, Vol. 17, 1969, pp. 43–61.

10 Nadai, A., *Theory of Flow and Fracture of Solids*, McGraw-Hill, New York, 1950.

11 Odqvist, F. K. G., "Membrane Creep of Circular Plates," *Arkiv för Fysik*, Vol. 16, 1959, pp. 113–118.

12 Weiniitschke, H. J., "On Axisymmetric Deformations of Nonlinear Elastic Membranes," *Mechanics Today*, Vol. 5, Nemat-Nasser, S., ed., Pergamon Press, New York, 1980, pp. 523–542.

13 Storåkers, B., "A Viscoelastic Correspondence Principle for Plane Membranes Subjected to Lateral Prssure," ASME JOURNAL OF APPLIED MECHANICS, Vol. 50, 1983, pp. 740–742.

Downloaded 02 May 2010 to 171.66.16.250. Redistribution subject to ASME license or copyright; see http://www.asme.org/terms/Terms_Use.cfm

A Viscoelastic Correspondence Principle for Plane Membranes Subjected to Lateral Pressure

B. Storåkers
Department of Strength of Materials and Solid Mechanics,
The Royal Institute of Technology,
S-100 44 Stockholm, Sweden

The classical Föppl equations, governing the deflection of plane membranes, constitute the first-order consistent approximation in the case of linear elastic material behavior. It is shown that despite the static and kinematic nonlinearities present, for arbitrary load histories a correspondence principle for viscoelastic material behavior exists if all relevant relaxation moduli are of uniform time dependence. Application of the principle is illustrated by means of a popular material model.

Introduction

The common procedure to solve linear viscoelastic problems by application of integral transforms in order to arrive at a corresponding elastic problem, in general requires complete linearity in the setting of the boundary value problem. In the past, however, some kinds of nonlinearities have been mastered in this respect and a correspondence principle has been shown to exist. In particular nonlinearities due to moving boundaries have been treated in indentation and crack propagation problems, for a representative account; cf. [1]. Although not a necessary one, [2], a basic ingredient for a simple outcome proves to be that displacements and stresses appearing in the nonstationary boundary conditions must be separable with respect to constitutive parameters and spatial variables in the elastic problem. Thus geometric self-similarity is required to a certain extent. Even though fundamentally nonlinear, it is well known that Föppl's elastic membrane problem possesses geometric self-similarity for given material contraction ratios. As regards linear viscoelasticity of real materials, a restriction to time-independent but otherwise arbitrary contraction ratios does not seem too prohibitive in particular when remembering the mechancial behavior of common polymers. It is natural then to explore the possibility of deriving a correspondence principle also for viscoelastic membranes.

The idea of a correspondence principle for membranes having time-dependent material properties is, as it happens, not new. Evidently Bychawski, [3], was the first to point out that power-law creep of initially plane membranes under constant, uniform pressure may be dealt with as a nonlinear elasticity problem. Bychawski's finding was later given a simpler proof by Hill and Storåkers [4] and the principle was generalized to encompass time-dependent loading and viscoplastic material properties. For hereditary material behavior, Bychawski and Ledziński [5] have proposed a principle valid in case of incompressibility and time-independent loading. It is the present intention to alleviate these restrictions and provide a simple and straightforward proof which clearly displays the physics of the problem and elucidates some unwarranted claims made by Bychawski and Ledziński.

The Correspondence Principle

The explicit problem to be dealt with concerns the mechanical behavior of an initially plane and stress-free linear viscoelastic membrane, of thickness h, rigidly constrained at its contour and subjected to uniform lateral hydrostatic pressure, p, of arbitrary time variance.

Equilibrium considerations of a deformed configuration yields in customary notation

$$\left.\begin{aligned} &\frac{\partial \sigma_x}{\partial x}+\frac{\partial \sigma_{xy}}{\partial y}=0 \\ &\frac{\partial \sigma_{xy}}{\partial x}+\frac{\partial \sigma_y}{\partial y}=0 \\ &\sigma_x\frac{\partial^2 w}{\partial x^2}+2\sigma_{xy}\frac{\partial^2 w}{\partial x\partial y}+\sigma_y\frac{\partial^2 w}{\partial y^2}=-\frac{p}{h} \end{aligned}\right\} \tag{1}$$

referred to Cartesian coordinates and where $w(x,y)$ is the out-of-plane component of particle displacements.

Introducing the complete displacement vector (u,v,w), the relevant in-plane components of Green strain are

Contributed by the Applied Mechanics Division for publication in the JOURNAL OF APPLIED MECHANICS.

Discussion on this paper should be addressed to the Editorial Department, ASME United Engineering Center, 345 East 47th Street, New York, N.Y. 10017, and will be accepted until two months after final publication of the paper itself in the JOURNAL OF APPLIED MECHANICS. Manuscript received by ASME Applied Mechanics Division, October, 1982.

Copyright © 1983 by ASME
Downloaded 02 May 2010 to 171.66.16.250. Redistribution subject to ASME license or copyright; see http://www.asme.org/terms/Terms_Use.cfm

$$\left.\begin{aligned} e_x &= \frac{\partial u}{\partial x} + \frac{1}{2}\left(\frac{\partial w}{\partial x}\right)^2 \\ e_{xy} &= \frac{1}{2}\left(\frac{\partial u}{\partial y} + \frac{\partial v}{\partial x} + \frac{\partial w}{\partial x}\frac{\partial w}{\partial y}\right) \\ e_y &= \frac{\partial v}{\partial y} + \frac{1}{2}\left(\frac{\partial w}{\partial y}\right)^2 \end{aligned}\right\} \tag{2}$$

The systems (1) and (2) combined with Hooke's law constitute the classical Föppl equations [6], for which the inherent assumptions and tacit simplifications made have earlier been discussed in detail by Hill and Storåkers [4].

The mechanical membrane properties are taken to be linear viscoelastic, i.e., as represented in a general two-dimensional form for plane stress,

$$e_{\alpha\beta} = \int_0^t C_{\alpha\beta\gamma\delta}(t-\tau)\frac{\partial \sigma_{\gamma\delta}(\tau)}{\partial \tau}d\tau \quad \alpha = 1,2 \tag{3}$$

where the argument of the compliance tensor $\mathbf{C}$ is natural time t.

The setting of the problem is then completed by the prescription of rigid constraints, i.e., $(u,v,w) = \mathbf{0}$, at the contour.

To proceed it proves convenient, following Hill and Storåkers [4], to choose a typical in-plane dimension, l, and introduce dimensionless coordinates

$$\tilde{x} = x/l, \quad \tilde{y} = y/l \tag{4}$$

and a trial displacement field

$$\frac{u}{l\tilde{u}} = \frac{v}{l\tilde{v}} = \left(\frac{w}{l\tilde{w}}\right)^2 = f \tag{5}$$

where displacement components marked with a tilde are functions of $\tilde{x}$, $\tilde{y}$ and f is a so far arbitrary function of time.

Keeping dimensionless coordinates according to (4), the reduced strain field associated with (5) is then

$$\frac{e_{\alpha\beta}}{\tilde{e}_{\alpha\beta}} = f \tag{6}$$

The kinematical relations (2) are then preserved intact for the reduced variables as well.

Furthermore on introducing a dimensionless stress field

$$\frac{\sigma_x}{\tilde{\sigma}_x} = \frac{\sigma_{xy}}{\tilde{\sigma}_{xy}} = \frac{\sigma_y}{\tilde{\sigma}_y} = \frac{1}{\sqrt{f}}\frac{pl}{h} \tag{7}$$

the equilibrium equations (1) run as before except that the right-hand side of $(1)_3$ is replaced by -1.

Now in a situation where all components of the compliance tensor are of uniform time dependence, then $\mathbf{C}$ may be factorized as

$$C_{\alpha\beta\gamma\delta} = \frac{c}{E}c_{\alpha\beta\gamma\delta} \tag{8}$$

where the dimensionless function $c(t)$ depends on time solely, $\mathbf{c}$ is a dimensionless tensor, the components of which are constants, and E is a constant representative modulus.

Introducing stresses and strains into the constitutive equation (3) then yields via (8)

$$\tilde{e}_{\alpha\beta} f = \int_0^t c(t-\tau)c_{\alpha\beta\gamma\delta}\frac{\partial}{\partial \tau}\left(\frac{\tilde{\sigma}_{\gamma\delta}pl}{\sqrt{f}Eh}\right)d\tau \tag{9}$$

or when separating variables of space and time

$$\tilde{e}_{\alpha\beta}(x_\mu) = c_{\alpha\beta\gamma\delta}\tilde{\sigma}_{\gamma\delta}(x_\mu) \tag{10}$$

and

$$f(t) = \int_0^t c(t-\tau)\frac{d}{d\tau}\left(\frac{\tilde{p}}{\sqrt{f}}\right)d\tau \tag{11}$$

on introducing the dimensionless pressure $\tilde{p} = pl/(Eh)$.

Interpreting $\mathbf{c}/E$ in (8) as an elastic compliance tensor and as furthermore the boundary conditions are homogeneous, it is readily seen that the solution for all variables of space, marked with a tilde, is immediately available from the purely elastic context for which $f = \tilde{p}^{2/3}$. The effect of viscoelastic material properties manifests itself only through the ordinary integral equation (11). This outcome then establishes the principle and any elastic solutions, such as e.g. [7–10], are immediately applicable. It goes without saying that the same circumstances also prevail for the degenerate case of a string.

The existence of the principle hinges among other prerequisites on geometric self-similarity or more explicitly in the present case on the fact that any displacement component and its gradients must enter the strain tensor to the same degree such that equations (5) and (6) are compatible via (2). In general this is not so for membranes having initial curvature. In an attempt to derive a principle valid also for curved membranes, Bychawski and Ledziński [5], however, go one step too far. In their analysis spatial and time-dependent variables are separated in an unwarranted manner and the resulting claim of a general correspondence principle for curved membranes does not bear conviction.

To illustrate the application of the derived correspondence principle, as a representative choice of time-dependent material properties those of the so-called Standard Linear Solid are adopted. The corresponding one-dimensional rheological model is illustrated in Fig. 1 with obvious symbols.

By aid of the notation

$$\left.\begin{aligned} E &= E_K + E_M \\ \tau_M &= \eta/E_M \\ \tau_K &= \eta(E_K + E_M)/(E_K E_M) \end{aligned}\right\}$$

the dimensionless corresponding creep compliance (equation (8)) may be written

$$c = [1 - (1 - \tau_M/\tau_K)\exp(-t/\tau_K)]\tau_K/\tau_M \tag{12}$$

For these particular material properties the governing integral equation (11) is readily converted into a differential equation viz

$$\frac{df}{dt} + \frac{f}{\tau_K} = \frac{d}{dt}\left(\frac{\tilde{p}}{\sqrt{f}}\right) + \frac{\tilde{p}}{\sqrt{f}\tau_M} \tag{13}$$

with the associated initial condition $f(0) = [\tilde{p}(0)]^{2/3}$.

Choosing the simple loading case of a pressure step function

$$\tilde{p} = \tilde{p}_0 H(t)$$

$H(t)$ being the Heaviside function, and introducing the auxiliary variable

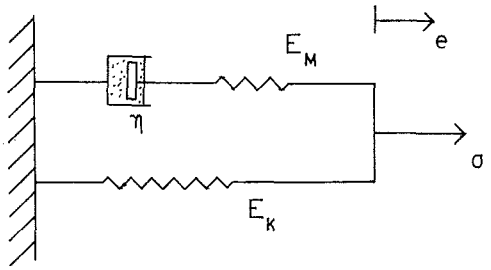


Fig. 1 Rheological model of a Standard Linear Solid

Downloaded 02 May 2010 to 171.66.16.250. Redistribution subject to ASME license or copyright; see http://www.asme.org/terms/Terms_Use.cfm

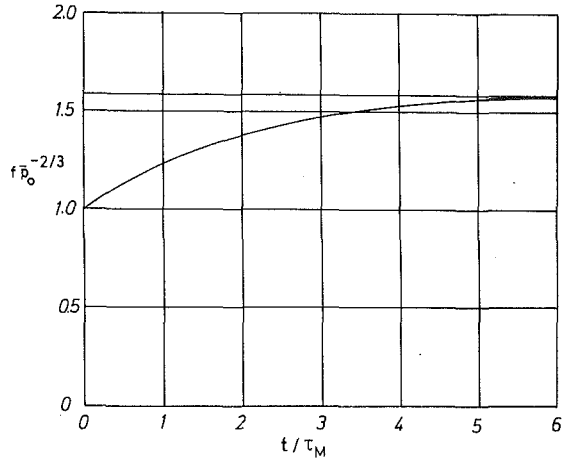


Fig. 2 Time dependence of normalized strain for pressure step function ($\tau_K = 2\tau_M$)

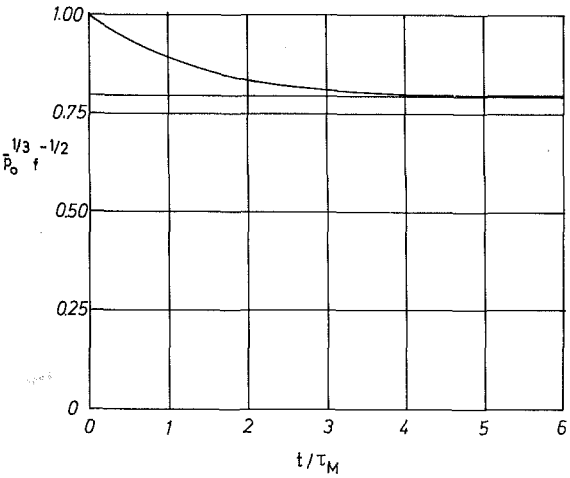


Fig. 3 Time dependence of normalized stress for pressure step function ($\tau_K = 2\tau_M$)

$$h = f^{1/2}\bar{p}_0^{\,-1/3} \tag{14}$$

the differential equation (13) reduces to

$$(2h^3+1)\frac{dh}{dt} + \left(\frac{h^3}{\tau_k} - \frac{1}{\tau_M}\right)h = 0 \tag{15}$$

with the initial condition $h(0) = 1$.

The solution is immediately

$$h\left(\frac{\kappa-1}{\kappa-h^3}\right)^{\frac{2\kappa+1}{3}} = \exp(t/\tau_M) \tag{16}$$

where $\kappa = \tau_K/\tau_M$.

To further illustrate the outcome, normalized strain and stress histories are depicted in Figs. 2 and 3, respectively, for the particular case $\kappa = 2$ ($E_K = E_M$).

As may be expected the solution for long times is

$$f(t\to\infty) = (\kappa\bar{p}_0)^{2/3} \tag{17}$$

The degenerate case of a pure Maxwell solid ($E_K = 0$) requires special attention though. In these circumstances the relevant differential equation reduces to

$$(2h^3+1)\frac{dh}{dt} - \frac{h}{\tau_M} = 0 \tag{18}$$

with the solution

$$h^3 + 1\mathrm{n}\, h^{3/2} = 3t/(2\tau_M) + 1 \tag{19}$$

Consequently for longer times

$$f(t\to\infty) = [3\bar{p}_0 t/2\tau_M]^{2/3} \tag{20}$$

References

1 Graham, G.A.C., "The Correspondence Principle of Linear Viscoelasticity Theory for Mixed Boundary Value Problems Involving Time-Dependent Boundary Regions," *Quarterly of Applied Mathematics*, Vol. 26, 1968, pp. 167-174.

2 Graham, G. A. C., and Sabin, G. C. W., "The Correspondence Principle of Linear Viscoelasticity for Problems That Involve Time-Dependent Regions," *International Journal of Engineering Sciences*, Vol. 11, 1973, pp. 123-140.

3 Bychawski, Z., "Elastic Analogue in the General Case of a Geometrically Nonlinear Membrane Subjected to Creep," *Archives for Mechanics*, Vol. 4, 1965, pp. 593-600.

4 Hill, R., and Storåkers, B., "Plasticity and Creep of Pressurized Membranes: A New Look at the Small-Deflection Theory," *Journal of the Mechanics and Physics of Solids*, Vol. 28, 1980, pp. 27-48.

5 Bychawski, Z., and Ledziński, J., "An Analogue for Non-linear Hereditary Viscoelastic Membranes," *Bulletin de l'Academie Polonaise des Sciences*, Sér. sci. tech., Vol. XXIII, 1975, pp. 255-260.

6 Föppl, A., *Vorlesungen uber Technische Mechanik*, 1907, Teubner, Leipzig, pp. 132-144.

7 Kao, R., and Perrone, N., "Large Deflections of Flat Arbitrary Membranes," *Computers and Structures*, Vol. 2, 1972, pp. 535-546.

8 Koiter, W. T., "On the Complementary Energy Theorem in Nonlinear Elasticity," *Trends in Applications of Pure Mathematics to Mechanics*, Fichera, G., ed., Pitman, 1976, pp. 207-232.

9 Storåkers, B., "Small Deflections of Linear Elastic Circular Membranes Under Lateral Pressure," ASME JOURNAL OF APPLIED MECHANICS, Vol. 50, 1983, pp. 735-739

10 Storåkers, B., "Variation Principles and Bounds for the Approximate Analysis of Plane Membranes Under Lateral Pressure," ASME JOURNAL OF APPLIED MECHANICS, Vol. 50, 1983, pp. 743-749.

Downloaded 02 May 2010 to 171.66.16.250. Redistribution subject to ASME license or copyright; see http://www.asme.org/terms/Terms_Use.cfm

Variation Principles and Bounds for the Approximate Analysis of Plane Membranes Under Lateral Pressure

B. Storåkers
Department of Strength of Materials and Solid Mechanics,
The Royal Institute of Technology,
S-100 44 Stockholm, Sweden

A first-order consistent approximation for the analysis of small deflections of membranes is given several variational formulations. Lower and upper bounds are derived for the volume enclosed by deformed and undeformed membranes. The power of the principles is discussed and their application is illustrated by some cases of practical interest. Explicit analytical results are given for linear elastic membranes having circular, elliptic, and rectangular contours.

Introduction

The equations governing small deflections of plane membranes subjected to lateral hydrostatic pressure, as laid down by Föppl [1] in the beginning of this century, do not in general admit an exact analytical solution. As a consequence several writers have attacked the problem by way of various approximate solution methods. Among early investigators of linear elastic membranes, Hencky applied a series expansion method to circular contours [2] and an iterative finite difference technique to square ones [3, 4]. More recently Kao and Perrone [5, 6] have dealt with various contours utilizing a nonlinear relaxation method employing finite difference approximations.

Variation methods seem to have been relied on only to an almost negligible extent in particular when it comes to employ a Rayleigh-Ritz procedure to obtain simple approximate results at applications. It is the present purpose to establish some variational formulations, investigate their power, and calculate explicit, analytical, though approximate results for especially Hookean membranes having contours of practical interest. Analytical results are of particular interest in this case because a correspondence principle for viscoelastic material behavior is available [7].

Variation Principles and Bounds

For arbitrary contours the present membrane problem may be given several variational formulations based on a Hellinger-Reissner-type functional

$$J=\int\!\!\int\Big\{U-\sigma_{\alpha\beta}\Big[e_{\alpha\beta}-\frac{1}{2}\left(u_{\alpha,\beta}+u_{\beta,\alpha}+u_{3,\alpha}u_{3,\beta}\right)\Big]-pu_3/t\Big\}\,t\,dS \tag{1}$$

where $\alpha,\beta = 1,2$ and a comma denotes partial differentiation with respect to in-plane Cartesian coordinates. Integration is to be carried out with regard to the undeformed surface S, the membrane being of thickness t, and subjected to lateral pressure p not necessarily uniform.

Furthermore (1) is based on the possibility to construct a constitutive potential U providing the necessary connection between Cauchy stress $\boldsymbol{\sigma}$ and Green strain $\mathbf{e}$. The displacement vector is (u_1, u_2, u_3).

Under the assumption of rigid constraints at the contour, i.e., $\delta(u_1, u_2, u_3) = \mathbf{0}$, the first variation of J is by use of the divergence theorem

$$\delta J=\int\!\!\int\Big\{\Big(\frac{\partial U}{\partial e_{\alpha\beta}}-\sigma_{\alpha\beta}\Big)\delta e_{\alpha\beta}-\Big[e_{\alpha\beta}-\frac{1}{2}\left(u_{\alpha,\beta}+u_{\beta,\alpha}+u_{3,\alpha}u_{3,\beta}\right)\Big]\cdot\delta\sigma_{\alpha\beta}-\sigma_{\alpha\beta,\alpha}\delta u_\beta-\left(\sigma_{\alpha\beta,\alpha}u_{3,\beta}+\sigma_{\alpha\beta}u_{3,\alpha\beta}+p/t\right)\delta u_3\Big\}\,t\,dS \tag{2}$$

Thus a sufficient condition to render J stationary, i.e.,

$$\delta J=0 \tag{3}$$

is the fulfillment of the equations

$$\sigma_{\alpha\beta}=\frac{\partial U}{\partial e_{\alpha\beta}} \tag{4}$$

$$\sigma_{\alpha\beta,\alpha}=0 \tag{5}$$

$$\sigma_{\alpha\beta}u_{3,\alpha\beta}=-p/t \tag{6}$$

Contributed by the Applied Mechanics Division and presented at the Winter Annual Meeting, Boston, Mass., November 13-18, 1983 of THE AMERICAN SOCIETY OF MECHANICAL ENGINEERS.

Discussion on this paper should be addressed to the Editorial Department, ASME, United Engineering Center, 345 East 47th Street, New York, N.Y. 10017, and will be accepted until two months after final publication of the paper itself in the JOURNAL OF APPLIED MECHANICS. Manuscript received by ASME Applied Mechanics Division, October, 1982. Paper No. 83-WA/APM-18.

Copies will be available until July, 1984.

Copyright © 1983 by ASME
Downloaded 02 May 2010 to 171.66.16.250. Redistribution subject to ASME license or copyright; see http://www.asme.org/terms/Terms_Use.cfm

$$e_{\alpha\beta}=\frac{1}{2}\,(u_{\alpha,\beta}+u_{\beta,\alpha}+u_{3,\alpha}u_{3,\beta}) \tag{7}$$

This set of equations, which in the particular case of isotropic linear material behavior constitute the Föppl equations, may be given an immediate physical interpretation. Equation (4) constitutes the constitutive equation, the material response not necessarily being linear. Equations (5) and (6) secure in-plane and out-of-plane equilibrium, respectively, and (7) is the strain definition.

The assumptions involved in this formulation of the problem have been recently discussed in detail by Hill and Storåkers [8] in their investigation of inelastic membranes. Suffice it to state in this context that displacement gradients are assumed to be of order $|\partial u_\alpha/\partial x_\beta| \approx |\partial u_3/\partial x_\beta|^2 << 1$, one consequence being that the distinction between the stress measure conjugate to **e**, the Piola-Kirchhoff-Trefftz stress, and Cauchy stress vanishes as has already been tacitly assumed.

Thus having established the physical relevance of the functional J, it is evident from an independent variation of all field variables in (2) that (3) generates an actual solution.

It is worth mentioning that to remove the restriction of kinematically admissible displacement fields at application of (3), a contour integral should be added to (1) in a standard manner. Presently, however, this possibility is not drawn upon as in the illustrations to follow; only kinematically admissible trial fields are adopted.

Some particular forms of (1) are immediately recoverable. By choosing compatible strain fields according to (7) and bearing (4) in mind, then by varying the displacement field solely, equation (3) reduces to the principle of stationary potential energy. An equivalent form of this principle was in fact derived already by Föppl and Föppl [9] from a virtual work principle and applied in an analysis of square membranes. Furthermore, if through a Legendre transformation a complementary constitutive potential

$$\bar{U}=\sigma_{\alpha\beta}e_{\alpha\beta}-U \tag{8}$$

generating

$$e_{\alpha\beta}=\frac{\partial\bar{U}}{\partial\sigma_{\alpha\beta}} \tag{9}$$

is introduced into (1) then a complementary functional

$$\bar{J}=\int\left[-\bar{U}+\frac{1}{2}\,\sigma_{\alpha\beta}\,(u_{\alpha,\beta}+u_{\beta,\alpha}+u_{3,\alpha}u_{3,\beta})-pu_3/t\right]t\,dS \tag{10}$$

with

$$\delta\bar{J}=\int\left\{\left[-\frac{\partial\bar{U}}{\partial\sigma_{\alpha\beta}}+\frac{1}{2}\,(u_{\alpha,\beta}+u_{\beta,\alpha}+u_{3,\alpha}u_{3,\beta})\right]\delta\sigma_{\alpha\beta}\right.$$

$$\left.-\sigma_{\alpha\beta,\alpha}\delta u_\beta-(\sigma_{\alpha\beta,\alpha}u_{3,\beta}+\sigma_{\alpha\beta}u_{3,\alpha\beta}+p/t)\,\delta u_3\right\}t\,dS \tag{11}$$

results.

Thus at an actual state the combination of (7) and (9) yields together with (5) and (6)

$$\delta\bar{J}=0 \tag{12}$$

By independently varying stress and displacement components in (11) it is seen that the converse is also true. The coupling of stress components and transverse displacement (u_3) in the equilibrium equation (6) does not admit a further reduction of $\bar{J}$ generating a principle relying on variation of Cauchy stress components solely.

The question whether the potential energy principle

$$\delta\int(U-pu_3/t)\,t\,dS=0 \tag{13}$$

is equivalent to a minimum principle hinges on the convexity properties of U and the composition of the prevailing stress state. This matter was also discussed at length by Hill and Storåkers [8] and, without repeating the arguments, these writers found that if U is strictly convex and the minor principle stress is non-negative, then a global minimum, i.e.,

$$\Delta\int(U-pu_3/t)\,t\,dS\geq 0 \tag{14}$$

prevails. There are no further restrictions for U and for instance in the case of a Hookean material, the explicit requirements for (13) to imply a minimum and also to guarantee uniqueness of solution, in the present case of plane stress, reduce to $E>0$, $-1<\nu<1$ in customary notation.

When U is a strictly convex, homogeneous function of the strain components, inequality (14) admits a possibility to derive an explicit global lower bound for the volume enclosed by the deformed and underformed membrane surfaces. In particular when the material behavior is linear, for an actual solution it is readily proved that

$$3\int Ut\,dS=\int pu_3\,dS \tag{15}$$

Introduction of (15) into (14) yields for a given uniform pressure

$$\int u_3\,dS\geq\frac{4}{3}\int(u_3^*-U^*t/p)\,dS \tag{16}$$

where the starred quantities have trial displacement fields as arguments solely. In contrast, the deformed volume may not be bounded from above by trail Cauchy stress fields soley due to the presence of coupling in the equilibrium equation (6) as referred to in the foregoing.

To obtain a variation principle and a bound relying on stress fields solely, it is necessary to introduce a stress measure related to the undeformed state. Thus the relevant choice of conjugate pair is the first Piola-Kirchhoff (nominal) stress and the displacement gradient which are connected through

$$s_{\alpha\beta}=\frac{\partial U(u_{\gamma,\delta},u_{3,\epsilon})}{\partial u_{\beta,\alpha}}\,,\quad s_{\alpha 3}=\frac{\partial U(u_{\gamma,\delta},u_{3,\epsilon})}{\partial u_{3,\alpha}} \tag{17}$$

As the displacement gradient is not a true deformation measure but rotation sensitive, generically constitutive equations such as (17) are not uniquely invertible. This issue has recently been the subject of a controversy in particular regarding the possibility to establish complementary energy principles; for an authoritative account cf. Koiter [10], who also showed generally that the problem does not arise in case of semilinear isotropic material and small squares of rotations as is presently assumed. As a particular illustration in this context, Koiter [10] derived and solved the Euler equation associated with a minimum of the complementary energy for a circular membrane.

Consequently a unique complementary constitutive potential may be introduced through an ordinary Legendre transformation

$$\bar{\bar{U}}(s_{\alpha\beta},s_{\gamma 3})=s_{\alpha\beta}u_{\beta,\alpha}+s_{\alpha 3}u_{3,\alpha}-U \tag{18}$$

For the particular reduced form of Green strain (7) and a Hookean material, an explicit inversion of (17) has been utilized by Stumpf in his variational treatments of von Karman plate theory [11] and Marguerre shell theory [12]. The resulting expression for the complementary constitutive potential $\bar{\bar{U}}$ may be put in a compact form as

$$\bar{\bar{U}}=\frac{1+\nu}{2E}\left(s_{\alpha\beta}s_{\alpha\beta}-\frac{\nu}{1+\nu}s_{\alpha\alpha}s_{\beta\beta}\right)+\frac{1}{2}\,\frac{\epsilon_{\alpha\beta}\epsilon_{\gamma\delta}s_{\alpha 3}s_{\beta\delta}s_{\gamma 3}}{\epsilon_{\alpha\beta}s_{\alpha 1}s_{\beta 2}} \tag{19}$$

$\epsilon_{\alpha\beta}$ denoting the two-dimensional permutation tensor.

With these preliminaries, application of the minimum potential energy principle (13) yields the equilibrium equations

$$s_{\alpha\beta,\alpha}=0,\quad s_{\alpha 3,\alpha}=-p/t \tag{20}$$

Downloaded 02 May 2010 to 171.66.16.250. Redistribution subject to ASME license or copyright; see http://www.asme.org/terms/Terms_Use.cfm

As regards a complementary principle, it is not difficult to prove that $\bar{\bar{U}}$ is strictly convex provided the potential energy is; the determinant of the Hessian matrix of the last term in (19) vanishes. As a consequence in view of the present boundary conditions

$$\Delta\int \bar{\bar{U}}t\, dS \geq 0 \tag{21}$$

globally, the minimum being analytic.

Introduction of $\bar{\bar{U}}$ by (18) and application of the divergence theorem yields by aid of (15) and (20) for an actual state

$$\int \bar{\bar{U}}t\, dS = \frac{3}{4}\int pu_3\, dS \tag{22}$$

and consequently, in case of uniform pressure, equation (21) generates an upper bound for the enclosed volume viz,

$$\int u_3\, dS \leq \frac{4}{3}\int \bar{\bar{U}}^* t/p\, dS \tag{23}$$

where by (19) $\bar{\bar{U}}^*$ has got equilibrated stress fields as arguments solely.

Illustrations for Isotropic Linear Elastic Membranes

1 Circular Contours. To investigate the power of the variation principles established, the case of a circular contour is immediate as an exact solution, at least within controlled accuracy, is available [13]. In case of the minimum potential-energy principle a natural choice for trial displacements is to adopt Taylor series expansions with respect to a radial coordinate r in a polar system (r, ϕ). Due to the prevailing symmetry the field containing the first nontrivial powers is

$$\left.\begin{aligned} u^*/a &= u^{(1)}(r/a) + u^{(3)}(r/a)^3 \\ w^*/a &= w^{(0)} + w^{(2)}(r/a)^2 \end{aligned}\right\} \tag{24}$$

where u^* and w^* are in-plane and transverse displacement components, respectively. Immediately the coefficients $u^{(3)} = -u^{(1)}$, $w^{(0)} = -w^{(2)}$ on account of the rigid constraints at the boundary $r = a$.

Introduction of this field into (13) and straightforward minimization, with the appropriate form of U expressed by means of Young's modulus E and Poisson's ratio ν, yields

$$\left.\begin{aligned} u^* &= \frac{3-\nu}{4}\bar{h}^2 r[1-(r/a)^2]/a^2 \\ w^* &= \bar{h}[1-(r/a)^2] \end{aligned}\right\} \tag{25}$$

where the polar height is

$$\bar{h} = a\left[\frac{3(1-\nu)}{7-\nu}\right]^{1/3}\left(\frac{pa}{Et}\right)^{1/3}$$

A comparison of reduced values at the pole of displacement

$$\tilde{w}(0) = \left(\frac{pa}{Et}\right)^{-1/3}\frac{\bar{h}}{a}$$

and a strain measure

$$\tilde{e} = (1-\nu^2)^{-1/2}(e_r{}^2 + 2\nu\, e_r\, e_\phi + e_\phi{}^2)^{1/2}\left(\frac{pa}{Et}\right)^{-2/3}$$

representative of the strain energy, is given in Table 1. The accuracy seems satisfactory for estimates but could still be improved by retaining more terms in the Taylor series expansions for displacements. The attractiveness of desk calculations is then lost, however, as the resulting equations for the determination of coefficients become nonlinear.

Table 1 Numerical values of reduced polar deflection $\tilde{w}(0)$ and strain $\tilde{e}(0)$ for circular contours obtained by variation and exact methods [13] for various values of Poisson's ratio ν

ν	$\tilde{w}(0)$		$\tilde{e}(0)$	
	Variation method	Exact	Variation method	Exact
0	0.754	0.718	0.603	0.573
0.1	0.731	0.699	0.578	0.553
0.2	0.707	0.677	0.552	0.532
0.3	0.679	0.653	0.526	0.510
0.4	0.648	0.626	0.499	0.487
0.5	0.613	0.595	0.470	0.461

It might be interesting in this context to note that Hencky [2] attacked the original Föppl equations by expanding relevant variables in Taylor series, assumed to be absolutely convergent, and for the case of $\nu = 0.3$ arrived at $\tilde{w}(0) = 0.662$ and $\tilde{e}(0) = 0.501$ in the present notation. These estimates were based on series truncated at seven terms. Subsequently Odqvist [14] applied the Hencky method to nonlinear material properties retaining four Taylor terms. In the degenerate linear case Odqvist found $\tilde{w}(0) = 0.60$ and $\tilde{e}(0) = 0.461$ in case of material incompressibility ($\nu = 0.5$).

Another route, which might possibly improve accuracy when still keeping computations simple, would be by appeal to one of the mixed principles. To this end by introducing general trial fields

$$\left.\begin{aligned} u^*/a &= \sum_{k=0}^{2n-1} u^{(2k+1)}(r/a)^{2k+1} \\ w^*/a &= \sum_{k=0}^{n} w^{(2k)}(r/a)^{2k} \\ e^*_{\alpha\beta} &= \sum_{k=0}^{2n-1} e_{\alpha\beta}{}^{(2k)}(r/a)^{2k} \\ \sigma^*_{\alpha\beta} &= \sum_{k=0}^{2n-1} \sigma_{\alpha\beta}{}^{(2k)}(r/a)^{2k} \end{aligned}\right\} \tag{26}$$

into (1), minimization with respect to the coefficients $\sigma_{\alpha\beta}{}^{(2k)}$ yields the $6n$ independent equations

$$\int\left[e^*_{\alpha\beta} - \frac{1}{2}(u^*_{\alpha,\beta} + u^*_{\beta,\alpha} + u^*_{3,\alpha}u^*_{3,\beta})\right](r/a)^{2k}t\, dS = 0$$

$$\alpha,\beta = 1,2, \quad k = 0,1,2,\ldots 2n-1 \tag{27}$$

In (27) the integrand should be evaluated in circular polars and for briefness the displacement notation is $u^*_1 = u^*$, $u^*_2 = 0$, $u^*_3 = w^*$ with respect to (26).

The general solution to (27) is then

$$e^*_{\alpha\beta} \equiv \frac{1}{2}(u^*_{\alpha,\beta} + u^*_{\beta,\alpha} + u^*_{3,\alpha}u^*_{3,\beta}) \tag{28}$$

Similarly

$$\sigma^*_{\alpha\beta} \equiv \frac{\partial U(e^*_{\gamma\delta})}{\partial e_{\alpha\beta}} \tag{29}$$

and thus nothing is gained.

Similar circumstances prevail when employing the complementary functional $\bar{J}$ according to (10). Thus via (26),

$$\frac{\partial \bar{J}}{\partial \sigma_{\alpha\beta}{}^{(2k)}} = 0 \tag{30}$$

generates

Downloaded 02 May 2010 to 171.66.16.250. Redistribution subject to ASME license or copyright; see http://www.asme.org/terms/Terms_Use.cfm

Table 2 Reduced polar stress s and polar deflection $\tilde{w}(0)$ for circular contours obtained by variation and exact methods [13] for various values of Poisson's ratio ν

ν	Variation method			Exact	Variation method		Exact
	$s^{(1)}$	c	$s^{(2)}$	s	$\tilde{w}^{(1)}(0)$	$\tilde{w}^{(2)}(0)$	$\tilde{w}(0)$
0	0.315	−0.305	0.417	0.405	0.794	0.758	0.718
0.1	0.326	−0.285	0.423	0.412	0.766	0.735	0.699
0.2	0.339	−0.264	0.430	0.421	0.737	0.709	0.677
0.3	0.355	−0.241	0.439	0.431	0.705	0.682	0.653
0.4	0.373	−0.216	0.451	0.445	0.669	0.650	0.626
0.5	0.397	−0.189	0.467	0.461	0.630	0.614	0.595

Table 3 Bounds for the reduced enclosed membrane volume V/V_0 together with exact results [13] for circular contours and various values of Poisson's ratio ν

ν	V/V_0			
	Lower bound	Exact	Upper bound $V^{(2)}/V_0$	Upper bound $V^{(1)}/V_0$
0	0.377	0.379	0.379	0.397
0.1	0.366	0.367	0.368	0.383
0.2	0.353	0.355	0.355	0.368
0.3	0.340	0.341	0.341	0.352
0.4	0.324	0.325	0.325	0.335
0.5	0.307	0.307	0.307	0.315

$$\frac{1}{2}\left(u^*_{\alpha,\beta}+u^*_{\beta,\alpha}+u^*_{3,\alpha}u^*_{3,\beta}\right)\equiv\frac{\partial\bar{U}(\sigma^*_{\gamma\delta})}{\partial\sigma_{\alpha\beta}} \tag{31}$$

It remains then to explore the utility of the complementary energy principle (21). As any trial stress field has to satisfy the equilibrium equations (20), the nonvanishing components of a suitable field, corresponding to the same order as the displacement field (24), are

$$\left.\begin{aligned} s_r &= \mathrm{E}\left(\frac{pa}{\mathrm{E}t}\right)^{2/3} s[1-c(r/a)^2] \\ s_\phi &= \mathrm{E}\left(\frac{pa}{\mathrm{E}t}\right)^{2/3} s[1-3c(r/a)^2] \\ s_{rz} &= -\frac{pr}{2t} \end{aligned}\right\} \tag{32}$$

where s,c are dimensionless parameters to be determined and z denotes the out-of-plane coordinate.

When applying the principle (21) via (19), it turns out that the two parameters may not be obtained in analytical form. Only in the reduced case of an assumed homogeneous in-plane stress state, i.e., for vanishing c, is it possible to solve explicitly for s viz,

$$s^{(1)}=[32(1-\nu)]^{-1/3} \tag{33}$$

More generally though, companion pairs $s^{(2)}$, c may readily be found by a simple numerical search technique. The result is given in Table 2 for a set of ν-values. The reduced central deflections, $\tilde{w}^{(1)}(0)$ and $\tilde{w}^{(2)}(0)$ corresponding to the two trial stress fields, respectively, are readily obtained by simple quadrature as by definition

$$u_{3,\alpha}=\frac{\partial\bar{\bar{U}}}{\partial s_{\alpha 3}} \tag{34}$$

or explicitly in the present case

$$\frac{dw}{dr}=\frac{s_{rz}}{s_r} \tag{35}$$

As may be seen in Table 2, the assumption of a homogeneous stress state yields a severe underestimation of the polar stress, which is no surprise. Still though this simple assumption provides a decent estimate of the polar deflection. The situation is substantially improved, however, when the complete trial field (32) is retained. The estimates of polar deflection are almost identical to those based on the potential energy principle (Table 1). As regards the polar stress, s, it is interesting to note that the maximum relative error in the ν-range exhibited does not exceed 3 percent. This is to be compared with the corresponding 5 percent accuracy obtained in Table 1 for polar strain.

The trial fields (24) and (32) may now be inserted into inequalities (16) and (23) to obtain bounds for the enclosed membrane volume V, say. Retaining only the first terms in (32), resulting in s according to (33), analytical bounds are arrived at viz,

$$\frac{1}{2}\left[\frac{3(1-\nu)}{7-\nu}\right]^{1/3} V_0<V<\frac{1}{2}\left(\frac{1-\nu}{2}\right)^{1/3} V_0 \tag{36}$$

where

$$V_0=\left(\frac{pa}{\mathrm{E}t}\right)^{1/3}\pi a^3$$

Numerical values based on (36) are given in Table 3 and supplemented by upper bounds $V^{(2)}/V_0$ computed by aid of the $s^{(2)}$, c-values given in Table 2. As may be concluded, the two term trial fields determine the enclosed volume essentially within three figures while the rather crude assumption of a homogeneous stress state generates a substantially larger relative error, which does not however exceed 5 percent for the upper bound.

2 Elliptic Contours. Having gained some confidence in the power of the variation principles as regards circular contours, attention is now directed toward elliptical ones. Proceeding in the same spirit as in the foregoing for circular contours, appropriate trial displacements satisfying the boundary conditions are in Cartesian coordinates

$$\left.\begin{aligned} u^*/a &= A\bar{h}xw^*/a^3 \\ v^*/a &= B\bar{h}yw^*/a^3 \\ w^*/a &= \bar{h}(1-x^2/a^2-y^2/b^2)/a \end{aligned}\right\} \tag{37}$$

a and b being the major and minor axes of the contour, respectively. A straightforward, though somewhat lengthy determination of the amplitudes A, B, $\bar{h}/a$ by (13) yields

$$\left.\begin{aligned} A &= 2\frac{2(3-\alpha)+(1-\nu)(4\alpha+1/\alpha-\nu)}{2(9-\nu)+3(1-\nu)\,(\alpha+1/\alpha)} \\ B &= \alpha A(1/\alpha)=2\frac{2(3\alpha-1)+(1-\nu)(4+\alpha^2-\alpha\nu)}{2(9-\nu)+3(1-\nu)\,(\alpha+1/\alpha)} \\ \frac{\bar{h}}{a} &= C\left(\frac{pa}{\mathrm{E}t}\right)^{1/3} \end{aligned}\right\} \tag{38}$$

where $\alpha=a^2/b^2$ and

$$\begin{aligned} C=\tilde{w}(0,0)=(3(1-\nu^2)/\{&[6+\alpha(1-\nu)]A^2 \\ &-4(\alpha-\nu+2)A+2(1+\nu)AB-4(1-\nu+2\alpha)B \\ &+[6+(1-\nu)/\alpha]B^2+2(3\alpha^2+2\alpha+3)\})^{1/3} \end{aligned} \tag{39}$$

For explicitness, amplitude computations have been carried out for some particular aspect and contraction ratios and the

Downloaded 02 May 2010 to 171.66.16.250. Redistribution subject to ASME license or copyright; see http://www.asme.org/terms/Terms_Use.cfm

results are given in Table 4. At present there seems to be no reliable way to investigate the accuracy of the complete set of computed values but hopefully the approximations involved are not much worse for moderate aspect ratios than those for a circular contour. It might be noted in passing that the displacement field (37) is wide enough to encompass the exact solution for elliptic membranes of perfectly plastic materials as first shown by Taylor [15].

To the best of the writer's knowledge, the only explicit results for elastic membranes having elliptic contours are those of Jones [16]. Starting from the reduced so-called Berger's equations, in which the second invariant is neglected in the strain energy expression as to decouple two partial differential equations, Jones was able to draw upon Prandtl's classical analogy for torsion of a bar having a cross section of the same contour as the membrane in question. By taking the membrane deflection proportional to the relevant Prandtl stress function, Jones arrived at the reduced polar deflection

$$C=\frac{(1-\nu^2)^{1/3}}{(1+\alpha)^{2/3}}$$

in the present notation (equation $(38)_3$). Jones' method generates strains only to their first invariant and no explicit results were given.

A comparison with the present polar deflections is given in Table 5 for different aspect and contraction ratios together with the exact results for a circular contour. As might be concluded the two methods bound the exact solution for the circular case but not necessarily so for other aspect ratios. For higher aspect ratios the agreement is, however, remarkably good but this is most probably due to the fact that within a proportionality factor the presently assumed deflection function $(37)_3$ coincides with the corresponding Prandtl stress function. It should be remembered, however, that a Prandtl function may correspond to an actual solution only in the fortuitous case of a stress state that is homogeneous and balanced biaxial. The equilibrium equations (5) are then trivially satisfied and (6) reduces to Poisson's equation.

Table 4 Displacement amplitudes for elliptic contours obtained by variation method for various aspect and contraction ratios

a/b	ν	0	0.25	0.50
1	A	0.750	0.688	0.556
	B	0.750	0.688	0.556
	C	0.754	0.693	0.613
2	A	0.927	0.739	0.503
	B	2.73	2.68	2.65
	C	0.373	0.358	0.324
4	A	1.150	0.815	0.281
	B	10.70	10.66	10.71
	C	0.152	0.150	0.135
6	A	1.238	0.848	0.162
	B	24.02	23.99	24.07
	C	0.089	0.086	0.080
8	A	1.276	0.864	0.102
	B	42.68	42.65	42.75
	C	0.060	0.059	0.055
10	A	1.296	0.873	0.0689
	B	66.67	66.65	66.76
	C	0.045	0.044	0.041

3 Rectangular Contours. As a final practical illustration, rectangular membranes may be of interest in particular since this case has been dealt with earlier to a certain extent. Having the procedure applied to elliptic contours in mind, it seems natural to try a particle displacement field

$$\left.\begin{aligned} u^*/a &= A\bar{h}xw^*/a^3 \\ v^*/a &= B\bar{h}yw^*/a^3 \\ w^*/a &= \bar{h}(1-x^2/a^2)(1-y^2/b^2)/a \end{aligned}\right\} \tag{40}$$

for rectangles of side lengths $2a$ and $2b$.

Minimization of the potential energy then yields

$$\left.\begin{aligned} A &= 8\frac{42(1-7\nu)\alpha^2+(507-26\nu+51\nu^2)\alpha+60(1-\nu)}{840(1-\nu)\alpha^2+(7107-298\nu+51\nu^2)\alpha+840(1-\nu)} \\ B &= \alpha A(1/\alpha) \\ &= 8\frac{42(1-7\nu)+(507-26\nu+51\nu^2)\alpha+60(1-\nu)\alpha^2}{840(1-\nu)\alpha^2+(7107-298\nu+51\nu^2)\alpha+840(1-\nu)} \\ \frac{\bar{h}}{a} &= C\left(\frac{pa}{Et}\right)^{1/3} \end{aligned}\right\} \tag{41}$$

where $\alpha=a^2/b^2$ and

$$C=\tilde{w}(0,0)=(175(1-\nu^2)/(8\{[42+5\alpha(1-\nu)]A^2 - 8[6+\alpha(1-3\nu)]A+7(1+\nu)AB-8(6\alpha+1-3\nu)B+[42 + 5(1-\nu)/\alpha]B^2+32(\alpha^2+\alpha/7+1)\}))^{1/3} \tag{42}$$

In this context it is interesting to note that the Föppl equations have been attacked earlier by Kao and Perrone [6] and by Seide [17] in case of rectangular contours. Seide in his iterative procedure based on Fourier series expansions chose to deal with mixed boundary conditions (zero in-plane shear

Table 5 Reduced polar deflection $\tilde{w}(0,0)$ for elliptic contours obtained by Jones [16] and by variation method for various aspect and contraction ratios

a/b		$\tilde{w}(0,0)$		
	ν	0	0.25	0.50
1	Jones	0.630	0.617	0.572
	Var. meth.	0.754	0.693	0.613
	Exact [13]	0.718	0.666	0.595
2	Jones	0.342	0.335	0.311
	Var. meth.	0.373	0.358	0.324
4	Jones	0.151	0.148	0.137
	Var. meth.	0.152	0.150	0.135
6	Jones	0.090	0.088	0.082
	Var. meth.	0.089	0.086	0.080
8	Jones	0.062	0.061	0.056
	Var. meth.	0.060	0.059	0.055
10	Jones	0.046	0.045	0.042
	Var. meth.	0.045	0.044	0.041

Downloaded 02 May 2010 to 171.66.16.250. Redistribution subject to ASME license or copyright; see http://www.asme.org/terms/Terms_Use.cfm

Table 6 Reduced polar deflection $\tilde{w}(0,0)$ and stress $\tilde{\sigma}_x(0,0)$ for rectangular contours obtained by Kao and Perrone [6] and by variation method for various aspect ratios and Poisson's ratio 0.3

	$\tilde{w}(0,0)$		$\sigma_x(0,0)$	
a/b	Kao and Perrone	Variation method	Kao and Perrone	Variation method
1	0.723	0.763	0.439	0.406
5/7	0.841	0.901	0.522	0.530
2/5	0.895	0.993	0.551	0.618

stress), however, which makes any comparison with the present results uncertain. Kao and Perrone's strategy was to introduce finite differences and solve the resulting nonlinear equations by a relaxation method. Some numerical results were given. A comparison of reduced central deflection and stress

$$\tilde{\sigma}_x(0,0) = \left(\frac{pa}{Et}\right)^{-2/3} \frac{\sigma_x(0,0)}{E}$$

with those derived from (41) and (42) is given in Table 6 for $\nu = 0.3$.

There are reasons to believe that Kao and Perrone's computer results come close to the exact ones. In a previous application to a circular membrane [5], these writers gave very accurate results for the polar deflection when $\nu = 0.3$. The accuracy of the present variation results could then only be considered as fair when contemplating the values given in Table 6. Föppl and Föppl [9] in their pioneering application of an energy method to a square membrane gave a still higher polar deflection ($\tilde{w}(0,0) = 0.802$) based on sinusoidally varying displacements. The corresponding result given by Jones [16] is $\tilde{w}(0,0) = 0.688$.

In case of narrow rectangles, the diminishing accuracy of central deflection is not surprising when contemplating the parabolic dependence on the length coordinate assumed in the trial field (40). To suppress this dependence, while still keeping the field kinematically admissible, more terms have to be added and the minimization procedure repeated. Although such a procedure would involve quite some labor, it has in fact been carried through by Way [18] for rectangular plates with membrane action taken into account. By determining 11 constants in a trial displacement field, being an enlarged version of (40), this early writer computed deflections of the same order as the plate thickness, when bending still dominates, for three aspect ratios assuming Poisson's ratio to be 0.3.

In the present case, however, it seems more attractive to turn attention to the complementary energy principle. In analogy with the circular contour dealt with in the foregoing, for narrow rectangles, the appropriate nonvanishing components of a statically admissible stress field are to first order

$$\left.\begin{aligned} s_x &= E\left(\frac{pa}{Et}\right)^{2/3} s_1 \\ s_y &= E\left(\frac{pa}{Et}\right)^{2/3} s_2 \\ s_{xz} &= -px/t \end{aligned}\right\} \tag{43}$$

where s_1, s_2 are dimensionless parameters to be determined.

The complementary energy then attains its minimum for

$$s_1 = s_2/\nu = [6(1-\nu^2)]^{-1/3} \tag{44}$$

The corresponding deflection is readily found as in this case application of (34) yields

$$\left.\begin{aligned} \frac{\partial w}{\partial x} &= \frac{s_{xz}}{s_x} \\ \frac{\partial w}{\partial y} &= 0 \end{aligned}\right\} \tag{45}$$

Introduction of (43) and (44) into (45) followed by simple integration yields the lateral deflection

$$w = \left[\frac{3(1-\nu^2)}{4}\right]^{1/3} \left(\frac{pa}{Et}\right)^{1/3} (1 - x^2/a^2)a \tag{46}$$

which satisfies the boundary condition $w(\pm a, y) = 0$.

Although one of the remaining boundary conditions, $w(x, \pm b) = 0$, may not be satisfied and as a consequence (46) is not fully kinematically admissible, in the limit $a/b \to 0$, equations (43), (44), and (46) converge to the exact solution [1]. In case of $\nu = 0.3$, equations (44) and (46) yield $\tilde{\sigma}_x(0,0) = 0.568$ and $\tilde{w}(0,0) = 0.880$, respectively, which also compares favorably with Kao and Perrone's results for a rectangle of side ratio 2:5 (Table 6). As emphasized by these writers, however, the maximum stress acts not at the center but at the boundary of rectangular membranes. It would be interesting to investigate this feature via a trial stress field more general than the present (43). No attempt is, however, made at present.

Concluding Remarks

Variation principles combined with a Rayleigh-Ritz procedure proved to be a useful and simple tool to analytically estimate variables of interest at small deflections of plane membranes. In particular it was noted that use of the principle of complementary energy in some situations proved to be more advantageous as compared to the ordinary principle of potential energy.

References

1 Föppl, A., "Vorlesungen uber Technische Mechanik," 1907, Teubner, Leipzig, pp. 132–144.

2 Hencky, H., "Über den Spannungszustand in kreisrunden Platten mit verschwindender Biegungssteifigkeit," *Zeitschrift für Mathematik und Physik*, Vol. 63, 1915, pp. 311–317.

3 Hencky, H., "Die Berechnung dünner Rechteckiger platten mit Verschwindender Biegungssteifigkeit," *Zeitschrift für Angewandte Mathematik und Mechanik*, Vol. 1, 1921, pp. 81–83.

4 Hencky, H., "Berechnung dünner platten mit Verschwindender Biegungssteifigkeit," *Zeitschrift für Angewandte Mathematik und Mechanik*, Vol. 1, 1921, pp. 423–424.

5 Kao, R., and Perrone, N., "Large Deflections of Axisymmetric Circular Membranes," *International Journal of Solids and Structures*, Vol. 7, 1971, pp. 1601–1612.

6 Kao, R., and Perrone, N., "Large Deflections of Flat Arbitrary Membranes," *Computers and Structures*, Vol. 2, 1972, pp. 535–546.

7 Storåkers, B., "A Viscoelastic Correspondence Principle for Plane Membranes Subjected to Lateral Pressure," ASME JOURNAL OF APPLIED MECHANICS, Vol. 50, 1983, pp. 740–742.

8 Hill, R., and Storåkers, B., "Plasticity and Creep of Pressurized Membranes: A New Look at the Small-Deflection Theory," *Journal of the Mechanics and Physics of Solids*, Vol. 28, 1980, pp. 27–48.

9 Föppl, A., and Föppl, F., "Drang und Zwang," Vol. 1, 1920, Oldenbourg, München und Berlin, pp. 216–230.

Downloaded 02 May 2010 to 171.66.16.250. Redistribution subject to ASME license or copyright; see http://www.asme.org/terms/Terms_Use.cfm

10 Koiter, W. T., "On the Complementary Energy Theorem in Nonlinear Elasticity," *Trends in Applications of Pure Mathematics to Mechanics*, Fichera, G., ed., Pitman, 1976, pp. 207–232.

11 Stumpf, H., "Die Extremalprinzipe der nichtlinearen Plattentheorie," *Zeitschrift für Angewandte Mathematik und Mechanik*, Vol. 55, 1975, pp. T110–112.

12 Stumpf, H., "Die dualen Variationsprinzipien mit Extremaleigenschaft in der nichtlinearen Theorie der flacher Schalen," *Zeitschrift für Angewandte Mathematik und Mechanik*, Vol. 56, 1976, pp. T153–155.

13 Storåkers, B., "Small Deflections of Linear Elastic Circular Membranes Under Lateral Pressure," ASME JOURNAL OF APPLIED MECHANICS, Vol. 50, 1983, pp. 735–739.

14 Odqvist, F. K. G., "Membrane Creep of Circular Plates," *Arkiv für Fysik*, Vol. 16, 1959, pp. 113–118.

15 Taylor, G. I., "The Distorsion Under Pressure of an Elliptic Diaphragm Which is Clamped Along its Edge," Unpublished report, Ministry of Home Security, U.K., 1942.

16 Jones, R., "A Simplified Approach to the Large Deflection of Membranes," *International Journal of Non-Linear Mechanics*, Vol. 9, 1974, pp. 141–145.

17 Seide, P., "Large Deflections of Rectangular Membranes Under Uniform Pressure," *International Journal of Non-Linear Mechanics*, Vol. 12, 1977, pp. 397–406.

18 Way, S., "Uniformly Loaded, Clamped, Rectangular Plates with Large Deflection," *Proceedings of the Fifth International Congress for Applied Mechanics*, den Hartog, J. P., and Peters, H., eds., Wiley, New York, 1939, pp. 123–128.

Downloaded 02 May 2010 to 171.66.16.250. Redistribution subject to ASME license or copyright; see http://www.asme.org/terms/Terms_Use.cfm

Effects of Geometric Imperfections on Vibrations of Biaxially Compressed Rectangular Flat Plates

David Hui
Assistant Professor.
Mem. ASME

A. W. Leissa
Professor.
Fellow ASME

Department of Engineering Mechanics,
The Ohio State University,
Columbus, Ohio 43210

This paper deals with the effects of geometric imperfections on the vibration frequencies of simply supported flat plates under in-plane uniaxial or biaxial compression. The analysis is based on a solution of the nonlinear von Kármán equations for finite deflections, incorporating the influence of an initial geometric imperfection. It is found that significant increase in the vibration frequencies may occur for imperfection amplitude of the order of a fraction of the plate thickness, even in the absence of in-plane forces.

1 Introduction

Vibrations of thin-walled structures is a topic that has received considerable attention over the past decades and continues to remain of major concern because of its importance as a critical design consideration in many mechanical, aerospace, and hydrospace structural applications. Extensive efforts have been devoted to the investigations of vibrations of flat plates and perfect shells of various types of shapes, loadings, boundary conditions, and initial preload [1–3]. Although it is well established that the main reason for the discrepancy between the theoretical and experimental buckling loads for shells is attributed to the presence of initial geometric imperfections, the effects of imperfections on the natural vibrational frequencies of shell structures has received relatively little attention. In fact, among hundreds of theoretical investigations on the vibrations of shells listed in [2], none of them deals with the influence of initial geometric imperfections. Since then, Rosen and Singer [4, 5], Watawala [6], Singer and Prucz [7], and Hui and Leissa [8] have shown that imperfections of the order of shell thickness may have a pronounced effect on the vibrations of isotropic cylindrical and spherical shells. Effects of geometric imperfections on large amplitude vibrations of circular [9] and rectangular plates [10], cylindrical panels [11], and shallow spherical shells [12] were also examined. Surprisingly, the effect of imperfections on the vibrations of flat plates under initial in-plane stress has not been previously investigated in the literature.

The present study deals with the effects of geometric imperfections on the small amplitute vibrations of simply supported rectangular flat plates with the possibility of in-plane uniaxial or biaxial preload. The imperfections are taken to be a sinusoidal wave in both the in-plane directions. The analysis is based on a solution of the von Kármán equations for finite deflections within the context of Koiter's special theory of elastic stability [13]. The previbration state of static equilibrium is solved by satisfying the nonlinear compatibility equation exactly. The nonlinear equilibrium equation is then satisfied approximately using the Galerkin procedure. The applied load is assumed to be fixed and the appropriate differential equations for the vibration state are obtained by perturbing the previbration state and linearizing the governing differential equations for the vibration state are obtained by perturbing the previbration state and linearizing the governing differential equations with respect to the perturbed quantities. Based on the assumed vibration mode shape, the exact solution for the compatibility equation is found while the Galerkin procedure is used to satisfy the dynamic equilibrium equation approximately. The frequencies are minimized for all possible discrete vibrational wave numbers and geometric imperfections of various wave numbers are considered in the analysis. Since both the previbration and vibration compatibility equations are identically satisfied, the present analysis will yield upper bound frequencies. It is found that the vibration frequencies may be significantly higher than those for perfect plates (the sensitivity to imperfections increase with the amount of preload) for imperfection amplitudes of the order of a fraction of the plate thickness.

2 Governing Differential Equations

The governing nonlinear dynamic analogue of von Kármán equilibrium and compatibility equations for an isotropic, homogeneous, flat plate [14] may be generalized to incorporate the possibility of an initial geometric imperfection W_0 written in terms of the normal displacement W and a stress function F as

Contributed by the Applied Mechanics Division and presented at the Winter Annual Meeting, Boston, Mass., November 13–18, 1983 of THE AMERICAN SOCIETY OF MECHANICAL ENGINEERS.

Discussion on this paper should be addressed to the Editorial Department, ASME, United Engineering Center, 345 East 47th Street, New York, N.Y. 10017, and will be accepted until two months after final publication of the paper itself in the JOURNAL OF APPLIED MECHANICS. Manuscript received by ASME Applied Mechanics Division, September, 1982; final revision, April, 1983. Paper No. 83-WA/APM-20.

Copies will be available until July, 1984.

Copyright © 1983 by ASME
Downloaded 02 May 2010 to 171.66.16.250. Redistribution subject to ASME license or copyright; see http://www.asme.org/terms/Terms_Use.cfm

$$D(W,_{XXXX}+W,_{YYYY}+2W,_{XXYY})+\rho\,\ddot{W}$$
$$=F,_{YY}(W+W_0),_{XX}+F,_{XX}(W+W_0),_{YY}$$
$$-2F,_{XY}(W+W_0),_{XY} \tag{1}$$

$$[1/(Eh)](F,_{XXXX}+F,_{YYYY}+2F,_{XXYY})$$
$$=[(W+W_0),_{XY}]^2-(W_{0,XY})^2$$
$$-(W+W_0),_{XX}(W+W_0),_{YY}+W_{0,XX}W_{0,YY} \tag{2}$$

In the foregoing, $(\ddot{\ })$ denotes differentiation twice with respect to time t, D is the flexural rigidity, E is Young's modulus, h is the plate thickness, ρ is the plate mass per unit area, and X and Y are the two in-plane coordinates. Introducing the nondimensional quantities w, w_0, f, x, and y defined by (ν is Poisson's ratio and b is the distance between the two edges parallel to the axial x coordinate),

$$(w,w_0)=(W,W_0)/h$$
$$f=2cF/(Eh^3)$$
$$c=[3(1-\nu^2)]^{1/2} \tag{3}$$
$$(x,y)=(1/b)(X,Y)$$

the governing nonlinear differential equations can be written in nondimensional form,

$$w,_{xxxx}+w,_{yyyy}+2w,_{xxyy}+[4\rho c^2b^4/(Eh^3)]\ddot{w}$$
$$=(2c)[f,_{yy}(w+w_0),_{xx}+f,_{xx}(w+w_0),_{yy}-2f,_{xy}(w+w_0),_{xy}] \tag{4}$$

$$f,_{xxxx}+f,_{yyyy}+2f,_{xxyy}$$
$$=(2c)\{[(w+w_0),_{xy}]^2-(w_{0,xy})^2$$
$$-(w+w_0),_{xx}(w+w_0),_{yy}+w_{0,xx}w_{0,yy}\} \tag{5}$$

The boundary conditions are taken to be simple support of the form (a is the length of the plate in the x direction),

$$w(y=0 \quad \text{or} \quad 1)=0$$
$$w,_{yy}(y=0 \quad \text{or} \quad 1)=0$$
$$w(x=0 \quad \text{or} \quad a/b)=0 \tag{6}$$
$$w,_{xx}(x=0 \quad \text{or} \quad a/b)=0$$

Furthermore, there is no in-plane shear along all the edges and the in-plane displacements normal to the edges are constant. The no shear boundary conditions imply,

$$f,_{xy}(y=0 \quad \text{or} \quad 1)=0$$
$$f,_{xy}(x=0 \quad \text{or} \quad a/b)=0 \tag{7a}$$

The in-plane displacements normal to the edges are constant, resulting in uniform normal stresses along the four edges. That is,

$$f,_{xx}(y=0 \quad \text{or} \quad 1)=\sigma_y=-N_y/h$$
$$f,_{yy}(x=0 \quad \text{or} \quad a/b)=\sigma_x=-N_x/h \tag{7b}$$

where N_x and N_y are the applied compressive stress resultants (force/unit length).

3 Previbration State

The previbration state of static equilibrium of a biaxially compressed plate is,

$$f_p(x,y)=(\bar{\sigma}_x)(-y^2/2)+(\bar{\sigma}_y)(-x^2/2)+f^*(x,y)$$
$$w_p(x,y)=w^*(x,y) \tag{8}$$

In the foregoing, the nondimensional compressive loads in the x and y directions are defined to be

$$(\bar{\sigma}_x,\bar{\sigma}_y)=[2cb^2/(Eh^3)](-N_x,-N_y) \tag{9}$$

Substituting $w=w_p(x,y)$ and $f=f_p(x,y)$ into equations (4) and (5), the appropriate nonlinear previbration equilibrium and compatibility equations are,

$$w^*,_{xxxx}+w^*,_{yyyy}+2w^*,_{xxyy}+(2c\bar{\sigma}_x)(w^*+w_0),_{xx}$$
$$+(2c\bar{\sigma}_y)(w^*+w_0),_{yy}$$
$$=(2c)[f^*,_{yy}(w^*+w_0),_{xx}+f^*,_{xx}(w^*+w_0),_{yy}$$
$$-2f^*,_{xy}(w^*+w_0),_{xy}] \tag{10}$$

$$f^*,_{xxxx}+f^*,_{yyyy}+2f^*,_{xxyy}$$
$$=(2c)\{[(w^*+w_0),_{xy}]^2-(w_{0,xy})^2$$
$$-(w^*+w_0),_{xx}(w^*+w_0),_{yy}+w_{0,xx}w_{0,yy}\} \tag{11}$$

The geometric imperfection is taken to be of the form

$$w_0(x,y)=\mu\sin(J\pi x)\sin(k\pi y) \tag{12}$$

where μ is the amplitude of the imperfection normalized with respect to the plate thickness, $J=jb/a$ and both j and k are positive integers. To avoid a discretized numerical solution, the preceding nonlinear previbration differential equations are solved in the following manner. From a physical point of view, it is reasonable to expect that the shape of the previbration displacement due to the in-plane preload is very similar to that of the initial geometric imperfection. Therefore, it is assumed that

$$w^*(x,y)=c_w\sin(J\pi x)\sin(k\pi y) \tag{13}$$

the nonlinear compatibility equation (11) becomes,

$$f^*,_{xxxx}+f^*,_{yyyy}+2f^*,_{xxyy}=(\pi^4cJ^2k^2)[(c_w+\mu)^2-\mu^2]$$
$$[\cos(2J\pi x)+\cos(2k\pi y)] \tag{14}$$

Thus, the stress function $f^*(x,y)$ which satisfies the compatibility equation exactly is

$$f^*(x,y)=[(c_w+\mu)^2-\mu^2][A_1\cos(2J\pi x)+A_2\cos(2k\pi y)] \tag{15}$$

where the constants A_1 and A_2 are found to be,

$$A_1=ck^2/(16J^2) \quad \text{and} \quad A_2=cJ^2/(16k^2) \tag{16}$$

Substituting $w^*(x,y)$, $f^*(x,y)$, and $w_0(x,y)$ into the nonlinear previbration equilibrium equation (10) and applying the Galerkin procedure (multiplying both sides by $\sin(J\pi x)\sin(k\pi y)$ and integrating from $x=0$ to a/b and $y=0$ to 1), one obtains a cubic equation in $c_w+\mu$ of the form,

$$[(4cJ^2k^2)(A_1+A_2)](c_w+\mu)$$
$$+[(J^2+k^2)^2-(J^2\bar{\sigma}_x+k^2\bar{\sigma}_y)(2c/\pi^2)$$
$$-(\mu^2)(4cJ^2k^2)(A_1+A_2)](c_w+\mu)^3 \tag{17}$$
$$-(\mu)(J^2+k^2)^2=0$$

Thus, for a given value of the axial or biaxial preload $\bar{\sigma}_x$ and $\bar{\sigma}_y$ and given values of the imperfection wave numbers and amplitude, one can find $c_w+\mu$ and hence $f^*(x,y)$. As a check, it can be seen that $\bar{\sigma}_x=\bar{\sigma}_y=0$ implies $c_w=0$. Care should be taken to ensure that prior to vibration, the preload does not cause excessive plate deformation.

4 Vibration of Imperfect Plates With Biaxial Preload

Using the perturbation procedure, the previbration state is added to the perturbed dynamic state $w_B(x,y,t)$ and $f_B(x,y,t)$ and the resulting differential equations are linearized with respect to the dynamic state. Doing so, the appropriate dynamic equilibrium and compatibility equations become,

Downloaded 02 May 2010 to 171.66.16.250. Redistribution subject to ASME license or copyright; see http://www.asme.org/terms/Terms_Use.cfm

$$w_{B,xxxx} + w_{B,yyyy} + 2w_{B,xxyy} + (4\rho c^2 b^4/(Eh^3))\ddot{w}_B$$
$$= (2c)\Big\{(-\bar{\sigma}_x + f^*,_{yy})(w_{B,xx}) + (-\bar{\sigma}_y + f^*,_{xx})(w_{B,yy})$$
$$+ (w^* + w_0),_{xx} f_{B,yy} + (w^* + w_0),_{yy} f_{B,xx}$$
$$- 2(w^* + w_0),_{xy} f_{B,xy}\Big\} \quad (18)$$

$$f_{B,xxxx} + f_{B,yyyy} + 2f_{B,xxyy}$$
$$= (2c)\Big\{(2)(w^* + w_0),_{xy} w_{B,xy} - (w^* + w_0),_{xx} w_{B,yy}$$
$$- (w^* + w_0),_{yy} w_{B,xx}\Big\} \quad (19)$$

The vibration mode that satisfies the boundary conditions is assumed to be

$$w_B(x,y,t) = \xi[\sin(M\pi x)\ \sin(n\pi y)]\ \exp(i\omega t) \quad (20)$$

where $i = (-1)^{1/2}$, ξ is the amplitude of the vibration mode normalized with respect to the plate thickness, ω is the frequency, $M = mb/a$, and both m and n are positive integers. Thus, the compatibility equation becomes,

$$f_{B,xxxx} + f_{B,yyyy} + 2f_{B,xxyy}$$
$$= \xi(c\pi^4/2)(c_w + \mu)$$
$$\Big\{-(Jn - kM)^2 \cos[(J-M)\pi x] \cos[(k-n)\pi y]$$
$$+ (Jn + kM)^2 \cos[(J-M)\pi x] \cos[(k+n)\pi y]$$
$$+ (Jn + kM)^2 \cos[(J+M)\pi x] \cos[(k-n)\pi y]$$
$$- (Jn - kM)^2 \cos[(J+M)\pi x] \cos[(k+n)\pi y]\Big\} \exp(i\omega t) \quad (21)$$

It follows that the solution for the stress function $f_B(x,y,t)$ which satisfies the compatibility equation exactly is,

$$f_B(x,y,t) = \Big\{c_1 \cos[(J-M)\pi x] \cos[k-n)\pi y]$$
$$+ c_2 \cos[(J-M)\pi x] \cos[(k+n)\pi y]$$
$$+ c_3 \cos[(J+M)\pi x] \cos[(k-n)\pi y]$$
$$+ c_4 \cos[(J+M)\pi x] \cos[(k+n)\pi y]\Big\}$$
$$\Big\{\xi(c_w + \mu) \exp(i\omega t)\Big\} \quad (22)$$

where the constants c_1, c_2, c_3, and c_4 are defined to be,

$$c_1 = \begin{cases} 0 & \text{if } Jn - kM = 0 \\ -(c/2)(Jn - kM)^2/[(J-M)^2 + (k-n)^2]^2 & \text{otherwise} \end{cases}$$
$$c_2 = (c/2)(Jn + kM)^2/[(J-M)^2 + (k+n)^2]^2$$
$$c_3 = (c/2)(Jn + kM)^2/[(J+M)^2 + (k-n)^2]^2 \quad (23)$$
$$c_4 = -(c/2)(Jn - kM)^2/[(J+M)^2 + (k+n)^2]^2$$

It may be observed that the stress function $f_B(x,y,t)$ satisfies the no shear boundary conditions.

The dynamic equilibrium equation is satisfied approximately using the Galerkin procedure by multiplying both sides by $\sin(M\pi x)\sin(n\pi y)$ and then integrating from $x = 0$ to a/b and $y = 0$ to 1. Doing so, one obtains an explicit expression for the frequency and the in-plane compressive loads in the form,

$$\Omega^2 + (\bar{\sigma}_x M^2 + \bar{\sigma}_y n^2)[c/2\pi^2)]$$
$$= -(2c)[(c_w + \mu)^2 - \mu^2][2M^2k^2A_2H_0 + 2J^2n^2A_1I_0]$$
$$+ (1/4)(M^2 + n^2)^2$$
$$-(2c)(c_w + \mu)^2\Big\{[J^2(k-n)^2 + k^2(J-M)^2]c_1I_1H_1$$
$$+ [J^2(k+n)^2 + k^2(J-M)^2]c_2I_1H_2$$
$$+ [J^2(k-n)^2 + k^2(J+M)^2]c_3I_2H_1$$
$$+ [J^2(k+n)^2 + k^2(J+M)^2]c_4I_2H_2$$
$$-(2Jk)[(J-M)(k-n)c_1I_3H_3 + (J-M)(k+n)c_2I_3H_4$$
$$+ (J+M)(k-n)c_3I_4H_3 + (J+M)(k+n)c_4I_4H_4]\Big\} \quad (24)$$

where

$$\Omega^2 = \rho\omega^2c^2b^4/(Eh^3\pi^4) \quad \text{or} \quad \Omega = [\omega cb^2/\pi^2][\rho/(Eh^3)]^{1/2}$$

and the definite integrals I_0, I_1, I_2, I_3, I_4, H_0, H_1, H_2, H_3, and H_4 are defined in Appendix A. In the important special case of no preload $\bar{\sigma}_x = \bar{\sigma}_y = 0$ and the geometric imperfection wave numbers $j = k = 1$, the fundamental frequency corresponds to $m = n = 1$ and the preceding frequency expression can be simplified to become ($c_w = 0$, $c_1 = c_4 = 0$),

$$\Omega_f = (1/2)\Big\{[(b/a)^2 + 1]^2 + [(b/a)^4 + 1](\mu^2c^2/2)\Big\}^{1/2} \quad (25)$$

5 Results and Discussion

To assess the effect of geometric imperfections on the vibration frequencies of flat rectangular plates, example problems are chosen from simply supported square ($a/b = 1$) and rectangular ($a/b = 5$) plates with Poisson's ratio of 0.3. Four types of geometric imperfections

$$\begin{aligned} &(1)\ J = k = 1 \\ &(2)\ J = 2,\quad k = 1 \\ &(3)\ J = 1,\quad k = 2 \\ &(4)\ J = k = 2 \end{aligned} \quad (26)$$

are considered and the uniaxial ($\bar{\sigma}_y = 0$) and equal biaxial ($\bar{\sigma}_x = \bar{\sigma}_y$) cases are examined. Due to symmetry consideration, a sign change in the imperfection amplitude will not affect the

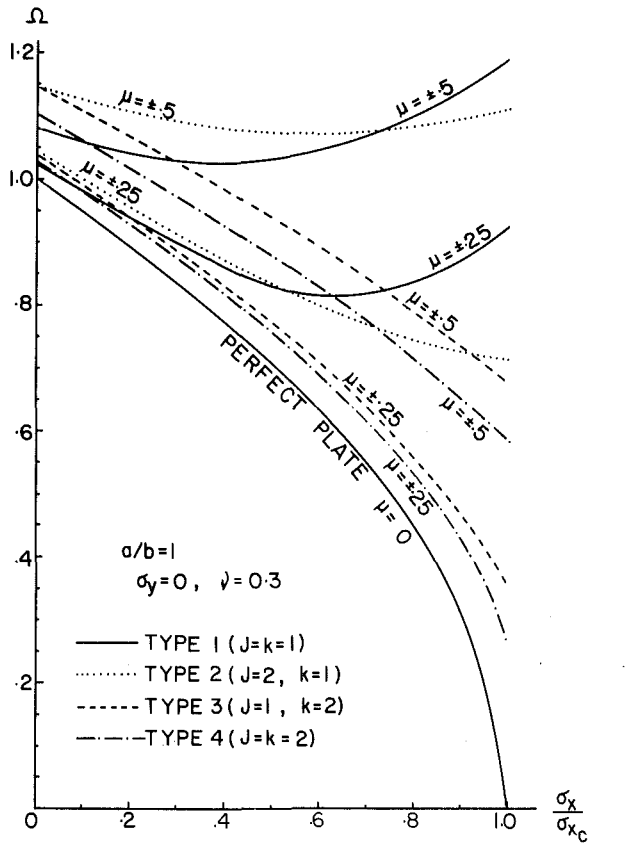


Fig. 1 Frequency versus uniaxial load interaction curves for simply supported square flat plates with imperfections

Downloaded 02 May 2010 to 171.66.16.250. Redistribution subject to ASME license or copyright; see http://www.asme.org/terms/Terms_Use.cfm

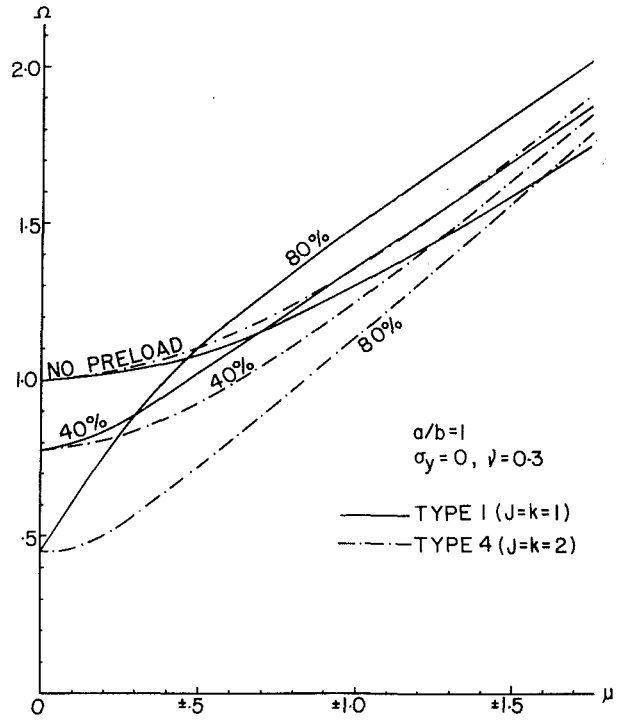


Fig. 2(a) Frequency versus imperfection amplitude for various values of uniaxial preload (imperfection types 1 and 4)

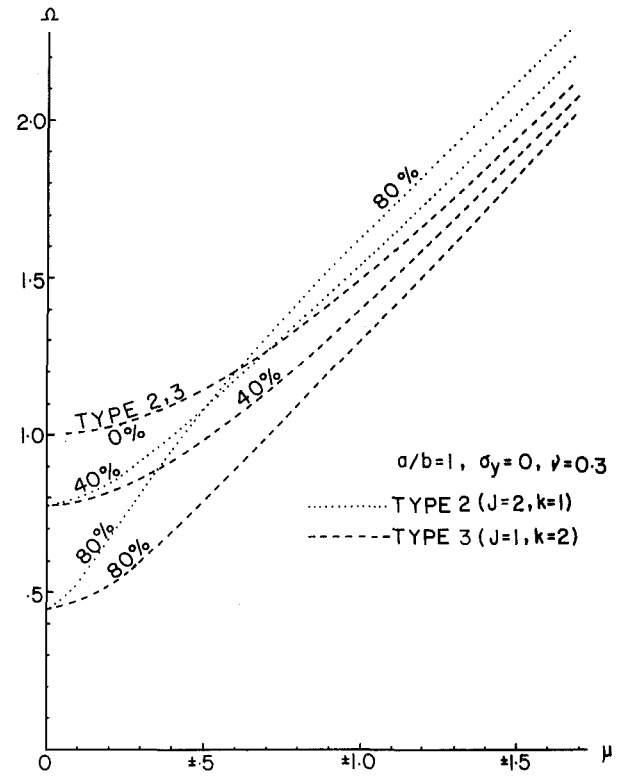


Fig. 2(b) Frequency versus imperfection amplitude for various values of uniaxial preload (imperfection types 2 and 3)

Fig. 2

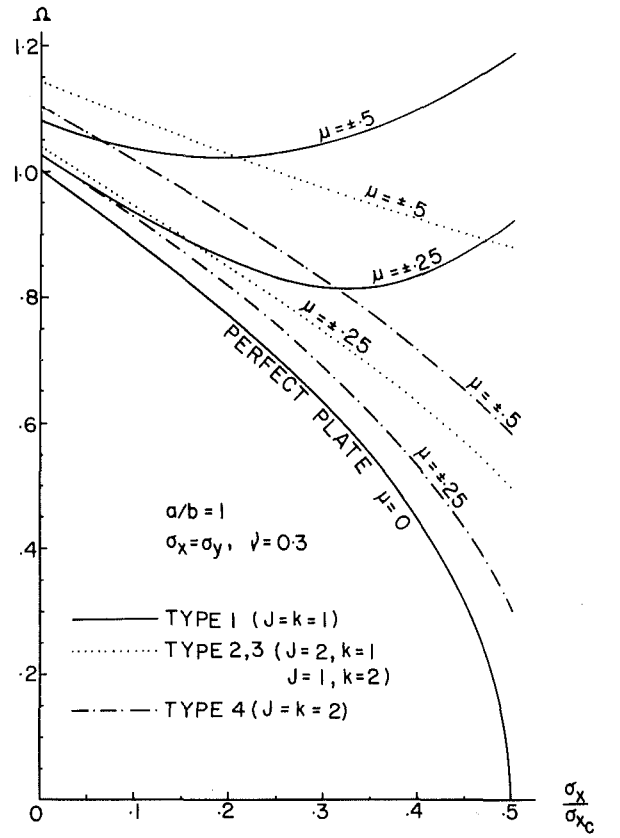


Fig. 3 Frequency versus equal biaxial load interaction curves for simply supported square flat plates with imperfections

problem. Unless otherwise specified, the optimum vibration discrete wave numbers M and n that render the frequency a minimum are $M=n=1$.

Figure 1 shows a graph of nondimensional frequency versus the uniaxial load ratio (σ_x/σ_{xc}), when σ_{xc} is the uniaxial, critical buckling load which would exist with no imperfection ($\mu=0$). Curves are shown for values of imperfection amplitudes $\mu=0$, 0.25, and 0.5. It can be seen that the vibration frequency of an imperfect plate may be significantly higher than that for the perfect plate. Furthermore, the sensitivity to imperfections increases with the amount of uniaxial preload. It appears that frequencies are generally more sensitive to imperfection types 1 and 2 than to types 3 and 4. Whereas all frequency curves initially decrease with increasing initial in-plane stress, certain ones eventually increase (e.g., $J = k = 1$) at larger in-plane initial stress values because of the increase of curvature as initial stress is increased.

Figures 2(a) and 2(b) show graphs of the vibration frequency versus imperfection ampltitude for σ_x/σ_{xc} = 0, 40, and 80 percent. The vibration frequency may increase significantly due to the presence of geometric imperfection with amplitude of the order of only a fraction of the plate thickness. The observation that the sensitivity to imperfections increases with the amount of uniaxial preload is again supported by these figures.

A plot of the load interaction curves for frequency versus equal biaxial load for various values of the imperfection amplitude is shown in Fig. 3. The uniaxial buckling stress is again used as a normalizing factor. It can be observed that results for the uniaxial and equal biaxial cases are qualitatively similar. In fact, the biaxial loading curves for the imperfection type 1 ($J=K=1$) and type 4 ($J=k=2$) are identical to those of the uniaxial cases. Of course, under biaxial loading the curves for imperfection types 2 and 3 coincide due to symmetry. Figure 4 shows a graph of frequency versus imperfection amplitude for values of equal biaxial preload of 0 and 80 percent. These results are qualitatively similar to that presented in Figs. 2(a, b).

Figure 5 shows a plot of interaction curves for vibration

Downloaded 02 May 2010 to 171.66.16.250. Redistribution subject to ASME license or copyright; see http://www.asme.org/terms/Terms_Use.cfm

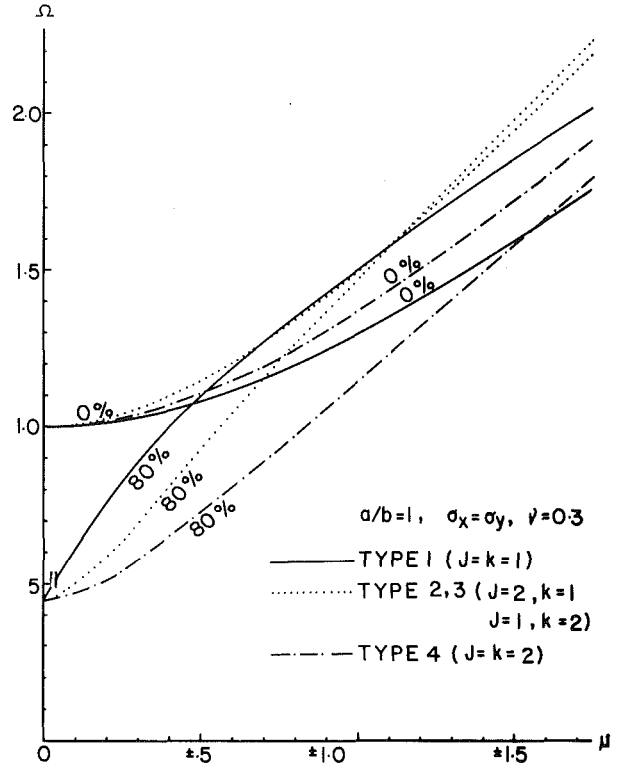


Fig. 4 Frequency versus imperfection amplitude for various values of equal biaxial preload

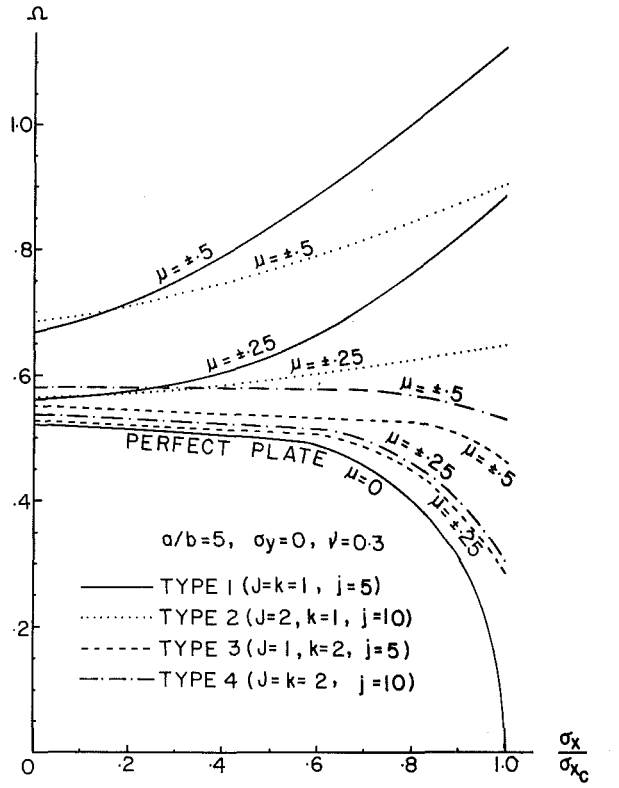


Fig. 5 Frequency versus uniaxial load interaction curves with various values of imperfection amplitudes for long rectangular plates ($a/b = 5$)

frequency versus uniaxial load with various values of imperfection amplitudes for long simply supported rectangular plates of aspect ratio $a/b = 5$ (so that $J = 1$ corresponds to $j = 5$ and $J = 2$ corresponds to $j = 10$). Again, it can be observed that imperfections may raise the frequencies significantly, especially in the case of large uniaxial preload. The vibration frequency is minimized for all possible discrete wave numbers m and n. The optimum value of n is always 1 whereas the optimum value of m varies from 1 (for sufficiently small values of uniaxial preload) to 5 (for sufficiently large preload). Furthermore, the presence of imperfections generally tends to reduce the optimum value of m. Since the optimum values of m change, the interaction curves should not be interpreted as perfectly smooth. They are the envelopes of separate curves obtained from each value of m. As the optimum value of m is 1 rather than 5 for sufficiently small amount of uniaxial preload, the nondimensional vibration frequencies for long plates ($a/b = 5$) are significantly smaller than those for square plates. It appears that the frequencies are more sensitive to imperfection types 1 and 2 than imperfection types 3 and 4.

Figures 6(a, b) show graphs of frequency versus imperfection amplitude with various values of uniaxial preload for long ($a/b = 5$) simply supported rectangular plates. The observations deduced from Fig. 5 are substantiated in these curves. The increase in frequency due to the amount of uniaxial preload is particularly more pronounced for imperfection types 1 and 2 than for imperfection types 3 and 4.

Figure 7 shows a graph of interaction curves for vibration frequency versus uniaxial load with values of imperfection amplitudes being 0, 0.25, 0.5, . . . , 1.5 for long simply supported rectangular plates of aspect ratio $a/b = 5$. The geometric imperfection assumes the shape of a half sine-wave in each of the two in-plane directions such that $J = 0.2$ (which corresponds to $j = 1$) and $k = 1$. For sufficiently large value of the imperfection amplitude, the optimum vibration frequency corresponds to $m = n = 1$. It is interesting to observe that the interaction curves tend to become more or less a horizontal straight line (i.e., independent of the in-plane preload) for the magnitude of the imperfection amplitudes greater than 0.75.

Finally, to provide an independent estimate of the effects of geometric imperfections on the vibration frequencies of simply supported flat plates, the frequencies of extremely shallow spherical shells of rectangular planform are studied. This permits direct comparison with the preceding imperfection type of analysis for type 1 imperfections ($J = k = 1$). The vibration frequency expression for spherical shells based on a solution of the linear Donnell type governing differential equation is (see Appendix B),

$$\Omega^2 + (2c/\pi^2)(M^2\bar{\sigma}_x + n^2\bar{\sigma}_y) = (M^2 + n^2)^2 + (Q^2/\pi^4) \qquad (27)$$

where $Q = 2cb^2/(Rh)$ and R is the shell radius.

The relevant results are tabulated in Table 1. It can be seen that significant increases in the vibration frequencies may occur for spherical shells with very small curvatures.

6 Concluding Remarks

The effects of various types of initial geometric imperfections on the small amplitude vibration frequencies of simply supported rectangular plates have been studied. It was found that the presence of small imperfections may significantly raise the frequencies, and the sensitivity to imperfections increases with the amount of uniaxial preload. The results for equal biaxial preloads are qualitatively similar to those for the case of uniaxial preload. The vibration frequencies for extremely shallow spherical shells of square planform supports qualitatively the increase in frequencies due to the presence of small amount of curvature. Further studies on the effects of geometric imperfections on the large amplitude vibrations of plates and shells were presented in separate papers [9–12].

7 Acknowledgments

The title problem was initiated and formulated by the first

Downloaded 02 May 2010 to 171.66.16.250. Redistribution subject to ASME license or copyright; see http://www.asme.org/terms/Terms_Use.cfm

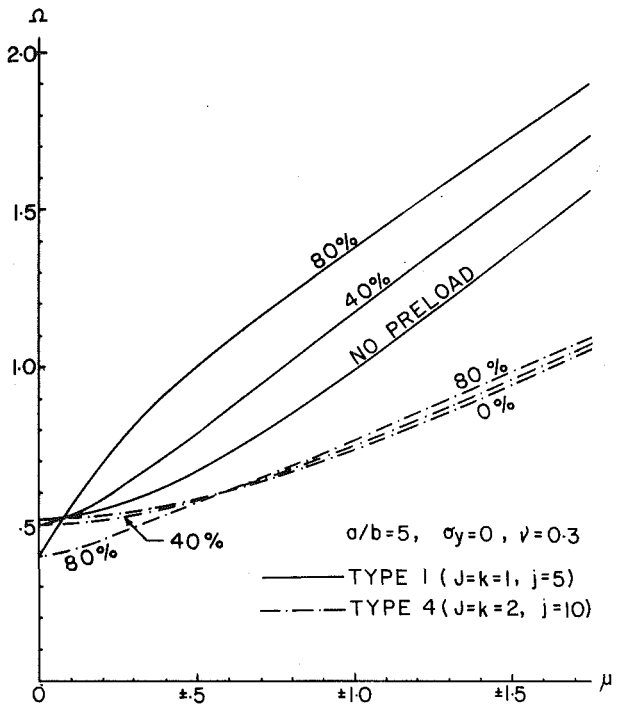


Fig. 6(*a*) Frequency versus imperfection amplitude with various values of uniaxial preload for long rectangular plates (imperfection types 1 and 4)

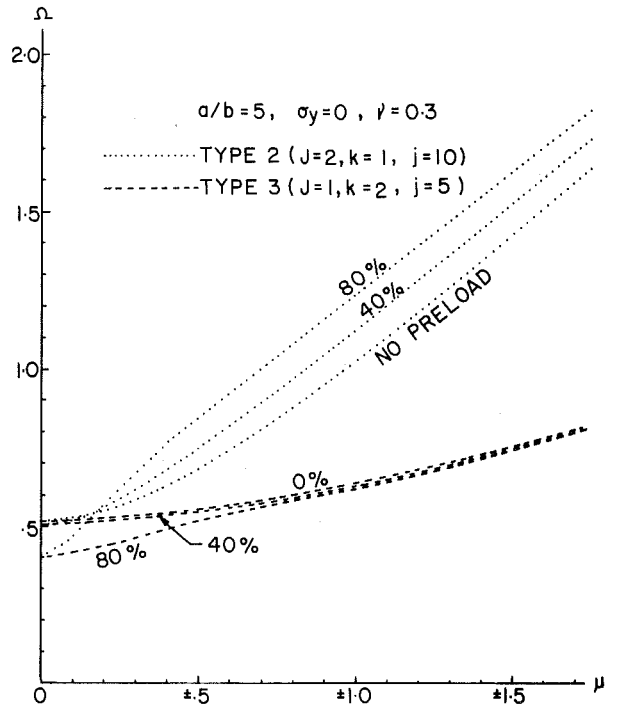


Fig. 6(*b*) Frequency versus imperfection amplitude with various values of uniaxial preload for long rectangular plates (imperfection types 2 and 3)

Fig. 6

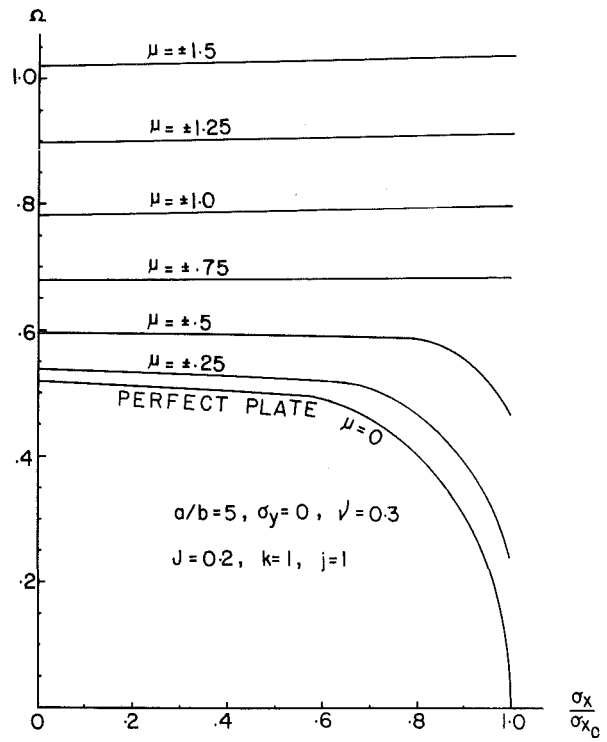


Fig. 7 Frequency versus uniaxial load interaction curves with various values of imperfection amplitudes for long rectangular plates ($a/b = 5$, $J = 0.2$, $k = 1$, $j = 1$)

author while he was a graduate student at the Department of Ocean Engineering, Massachusetts Institute of Technology. The second author wishes to thank Dr. I. H. Marshall of Paisley College, Scotland for an interesting discussion relevant to this topic in August, 1981.

References

1 Leissa, A. W., "Vibrations of Plates," NASA SP-160, 1969, 326 pp.

2 Leissa, A. W., "Vibration of Shells," NASA SP-288, 1973, 436 pp.

3 Gorman, D. J., *Free Vibration Analysis of Rectangular Plates*, Elsevier, North Holland, 1982.

4 Rosen, A., and Singer, J., "Effect of Axisymmetric Imperfections on the Vibrations of Cylindrical Shells Under Axial Compression," *AIAA Journal*, Vol. 12, 1974, pp. 995-997; also Technion Aeronautical Engineeirng, TAE Report No. 182, July 1973, 27 pp.

5 Rosen, A., and Singer, J., "Influence of Asymmetric Imperfections on the Vibrations of Axially Compressed Cylindrical Shells," *Israel J. of Technology*, Vol. 14, 1976, pp. 23-36; also Technion Aeronautical Engineering, TAE Report No. 212, March 1975, 76 pp.

6 Watawala, L., "Influence of Initial Geometric Imperfections on Vibrations of Thin Circular Cylindrical Shells," Ph.D. Dissertation, University of Massachusetts, Sept. 1981, 103 pp.; available from Univ. Microfilms Int., Order No. 8201413.

7 Singer, J., and Prucz, J., "Influence of Initial Geometrical Imperfections on Vibrations of Axially Compressed Stiffened Cylindrical Shells," *J. of Sound and Vibration*, Vol. 80, No. 1, 1982, pp. 117-143; also Technion Aeronautical Engineeirng TAE Report No. 369, Feb. 1980, 113 pp.

8 Hui, D., and Leissa, A. W., "Effects of Uni-Directional Geometric Imperfections on Vibrations of Pressurized Shallow Spherical Shells," *Intl. J. of Nonlinear Mechanics*, 1983, in press.

9 Hui, D., "Large Amplitude Axisymmetric Vibrations of Geometrically Imperfect Circular Plates," *J. of Sound and Vibration*, Vol. 91, 1983, in press

10 Hui, D., "Effects of Geometric Imperfections or Large Amplitude Vibrations of Rectangular Plates With Hysteresis Damping," ASME JOURNAL OF APPLIED MECHANICS, 1984, to appear.

11 Hui, D., "Influence of Geometric Imperfections and In-plane Constraints on Nonlinear Vibrations of Simply SUPPORTED Cylindrical Panels," ASME JOURNAL OF APPLIED MECHANICS, 1984, to appear.

12 Hui, D., "Large Amplitude Vibrations of Geometrically Imperfect Shallow Spherical Shells With Structural Damping," *AIAA Journal*, 1983, in press.

13 Koiter, W. T., "The Effect of Axisymmetric Imperfections on the Buckling of Cylindrical Shells Under Axial Compression," *Koninklijke Nederlandse Academie Wetenschappen*, Proc. Series *B*, Vol. 66, 1963, pp. 265-279.

14 Timoshenko, S., and Woinowsky-Krieger, S., *Theory of Plates and Shells*, 2nd. Ed., McGraw-Hill, New York, 1959.

15 Leissa, A. W., and Kadi, A. S., "Curvature Effects on Shallow Shell Vibrations," *Journal of Sound and Vibration*, Vol. 16, No. 2, 1971, pp. 173-187.

Downloaded 02 May 2010 to 171.66.16.250. Redistribution subject to ASME license or copyright; see http://www.asme.org/terms/Terms_Use.cfm

APPENDIX A

Definite Integrals

$$I_0 = (b/a)\int_0^{a/b} \sin^2(M\pi x) \quad \cos(2J\pi x)\ dx$$

$$= \begin{cases} -1/4 & \text{if } M=J \\ 0 & \text{otherwise} \end{cases}$$

$$I_1 = (b/a)\int_0^{a/b} (\sin(J\pi x)\ \cos[(J-M)\,\pi x])\sin(M\pi x)\ dx$$

$$= \begin{cases} 1/2 & \text{if } J=M \\ 1/4 & \text{otherwise} \end{cases}$$

$$I_2 = (b/a)\int_0^{a/b} (\sin(J\pi x)\ \cos[(J+M)\,\pi x])\sin(M\pi x)\ dx = -1/4$$

$$I_3 = (b/a)\int_0^{a/b} (\cos(J\pi x)\sin[(J-M)\,\pi x])\sin(M\pi x)\ dx$$

$$= \begin{cases} 0 & \text{if } J=M \\ -1/4 & \text{otherwise} \end{cases}$$

$$I_4 = (b/a)\int_0^{a/b} (\cos(J\pi x)\sin[(J+M)\,\pi x])\sin(M\pi x)\ dx = 1/4$$

Furthermore, $H_0 = I_0$, $H_1 = I_1$, $H_2 = I_2$, $H_3 = I_3$, and $H_4 = I_4$ provided J and M are replaced by k and n, respectively, the factor b/a is deleted and integration is carried from $y=0$ to $y=1$.

APPENDIX B

Vibration of Extremely Shallow Spherical Shells of Rectangular Planform

The governing dynamic equilibrium and compatibility equations for a spherical shell of radius R can be obtained from those for the flat plate by adding the terms $(1/R)\,(F_{,XX}+F_{,YY})$ and $(-1/R)\,(W_{,XX}+W_{,YY})$ to the left-hand sides of equations (1) and (2), respectively. Keeping only the linear terms, the differential equations can be written in the nondimensional form,

$$w_{,xxxx} + w_{,yyyy} + 2w_{,xxyy} + [4\rho c^2 b^4/(\mathrm{E}h^3)]\ddot{w} + (2c)\,(\bar{\sigma}_x w_{,xx} + \bar{\sigma}_y w_{,yy}) + (Q)\,(f_{,xx}+f_{,yy}) = 0 \qquad (B1)$$

$$(f_{,xxxx} + f_{,yyyy} + 2f_{,xxyy}) - (Q)\,(w_{,xx}+w_{,yy}) = 0 \qquad (B2)$$

where $Q = 2cb^2/(Rh)$. The vibrational mode is assumed to be,

$$w(x,y,t) = \xi_1[\sin(M\pi x)\sin(n\pi y)]\exp(i\omega t)$$

$$f(x,y,t) = \xi_2[\sin(M\pi x)\sin(n\pi y)]\exp(i\omega t) \qquad (B3)$$

so that the equilibrium and compatibility equations become,

$$[(M^2+n^2)^2 - \Omega^2 - (2c/\pi^2)(M^2\bar{\sigma}_x + n^2\bar{\sigma}_y)]\xi_1 - (Q/\pi^2)(M^2+n^2)\xi_2 = 0 \qquad (B4)$$

$$(M^2+n^2)\xi_2 + (Q/\pi^2)\xi_1 = 0 \qquad (B5)$$

Thus, the explicit expression for the vibration frequency squared is,

$$\Omega^2 + (2c/\pi^2)(M^2\bar{\sigma}_x + n^2\bar{\sigma}_y) = (M^2+n^2)^2 + (Q^2/\pi^4) \qquad (B6)$$

In the special case of $R/h = 1000$, $R/b = 2.5$, $\nu = 0.3$, and $a/b = 1$ one obtains $Q = 528.727$ and

$$\omega_{\text{sphere}}/\omega_{\text{flat plate}} = 26.8043 \qquad (B7)$$

which agrees with the tabulated results obtained by Leissa and Kadi [15].

Assuming that the spherical shell is resting on a flat planform such that the maximum distance between the spherical shell middle surface and the flat reference plane is ϵ, an approximate comparison between the spherical shell and the imperfect flat plate can be made by equating the nondimensional imperfection amplitude μ to ϵ/h. Furthermore, from the geometry, one obtains

$$b/R = 2\cos^{-1}[1-(\epsilon/h)\,(h/R)] \qquad (B8)$$

Thus, by fixing $R/h = 1000$ and $\nu = 0.3$, the value of Q can be found based on the inputed values of ϵ/h. The computed frequency can then be normalized with respect to that for the flat plate ($\omega_{\text{sphere}}/\omega_{\text{flat plate}}$). The relevant results are presented in Table 1 for the case of no initial in-plane stress.

Table 1 Frequency of a spherical shell normalized with respect to that for the flat plate for $a/b = 1$, $R/h = 1000$, $\nu = 0.3$ and $\Omega = [\omega c b^2/\pi^2][\rho/(\mathrm{E}h^3)]^{1/2}$

$\mu = \epsilon/h$	b/R	Q	Ω	$\omega/\omega_{\text{plate}}$
0.1	0.028285	2.6437	2.0179	1.0089
0.2	0.040001	5.2874	2.0705	1.0353
0.4	0.056570	10.575	2.2689	1.1345
0.5	0.063248	13.219	2.4071	1.2035
0.6	0.069286	15.863	2.5658	1.2829
0.8	0.080005	21.152	2.9314	1.4657
1.0	0.089450	26.441	3.3432	1.6716
1.5	0.10956	39.664	4.4890	2.2445
2.0	0.12651	52.890	5.7199	2.8599
3.0	0.15496	79.349	8.2848	4.1424
10.0	0.28308	264.81	26.905	13.452
20.0	0.40067	530.50	53.788	26.894

Downloaded 02 May 2010 to 171.66.16.250. Redistribution subject to ASME license or copyright; see http://www.asme.org/terms/Terms_Use.cfm

Vibrations of a Thick-Walled Pipe or a Ring of Arbitrary Shape in Its Plane

K. Nagaya
Department of Mechanical Engineering,
Gunma University,
Kiryu, Gunma 376, Japan

This paper is concerned with a method for solving in-plane vibration problems of thick-walled pipes and rings of arbitrary shape. The solution to the equation of motion based on the theory of elasticity under the plane-strain assumption is obtained exactly by using polar coordinates. The boundary conditions along both the outer and the inner surfaces of the ring of arbitrary shape are satisfied directly by means of the Fourier expansion collocation method which has been developed in the author's previous reports concerning vibration, dynamic response, and wave propagation problems of plates and rods with various shapes. Numerical calculations have been carried out for a thick elliptical ring, a rectangular ring with rounded corners, and a rectangular ring with a circular inner boundary. To discuss the accuracy of the present analysis, the results of a thick circular ring have also been calculated, and the present results are compared with the previously published ones.

1 Introduction

Rings are important elements of various machines and much research has been reported [1–10]. Most of these studies treated the flexural vibrations of thin circular rings [1–6]. The thick circular rings and cylinders have been discussed by Hermann and Mirsky [7], Gazis [8], and Morley [9]. Recently Brigham [10] and Sato [11] have also discussed the flexural vibrations of thin elliptical rings. These rings are treated by use of the cylindrical coordinates or the elliptical coordinates, and hence the method of general boundary value problems is applicable. However for the rings of irregular shape, it is difficult to obtain the solution that satisfies both the equation of motion and the boundary conditions. For the reason as just mentioned, vibrations of rings of irregular shape have not been thoroughly investigated. Especially the solution of thick rings with irregular shape has not been reported in the previous papers.

From this situation this paper gives a frequency equation that is applicable to rings of general shape. In the analysis the exact solutions have been derived from the equations of motion of elastic solids based on the plane-strain assumption. The boundary conditions along both the outer and the inner free surfaces have been satisfied by means of the Fourier expansion collocation method which has been developed in the author's previous reports concerning vibrations and dynamic response of plates with general shape [12] and wave propagations of rods with general cross section [13]. As demonstrations of this method, numerical calculations have been carried out for thick elliptical rings, thick rectangular rings with rounded corners, and thick rectangular rings with circular inner boundaries. To discuss the accuracy of the present analysis, the results for circular rings are compared with the previously published ones.

2 Derivation of the Frequency Equation

We choose the origin of cylindrical coordinates r, θ, and z in an arbitrary point inside the ring and denote the displacement u_r in the direction r and u_θ in the tangential direction θ. The equations of motion of elastic solids based on the plane-strain assumption are [1]

$$\left.\begin{aligned}\rho\frac{\partial^2 u_r}{\partial t^2} &= (\lambda+2\mu)\frac{\partial\Delta}{\partial r} - \frac{2\mu}{r}\frac{\partial\omega_z}{\partial\theta}\\ \rho\frac{\partial^2 u_\theta}{\partial t^2} &= (\lambda+2\mu)\frac{1}{r}\frac{\partial\Delta}{\partial\theta} + 2\mu\frac{\partial\omega_z}{\partial r}\end{aligned}\right\} \tag{1}$$

where

$$\left.\begin{aligned}\Delta &= \frac{1}{r}\frac{\partial}{\partial r}(ru_r) + \frac{1}{r}\frac{\partial u_\theta}{\partial\theta}\\ 2\omega_z &= \frac{1}{r}\left[\frac{\partial}{\partial r}(ru_\theta) - \frac{\partial u_r}{\partial\theta}\right]\end{aligned}\right\} \tag{2}$$

Contributed by the Applied Mechanics Division for publication in the JOURNAL OF APPLIED MECHANICS.
Discussion on this paper should be addressed to the Editorial Department, ASME, United Engineering Center, 345 East 47th Street, New York, N.Y., 10017, and will be accepted until two months after final publication of the paper itself in the JOURNAL OF APPLIED MECHANICS. Manuscript received by ASME Applied Mechanics Division, February, 1983; final revision, June, 1983.

Copyright © 1983 by ASME
Downloaded 02 May 2010 to 171.66.16.250. Redistribution subject to ASME license or copyright; see http://www.asme.org/terms/Terms_Use.cfm

and where ρ is the mass density, t is the time, λ and μ are Lame's constants, Δ is the dilatation, and ω_z is the rotation. For free vibrations, we may write

$$\left.\begin{aligned}\Delta &= \sum_{n=0}^{\infty} \epsilon_n (\Delta_n \cos n\theta + \bar{\Delta}_n \sin n\theta) \exp(jpt) \\ u_r &= \sum_{n=0}^{\infty} \epsilon_n (U_n \cos n\theta + \bar{U}_n \sin n\theta) \exp(jpt) \\ u_\theta &= \sum_{n=0}^{\infty} \epsilon_n (V_n \sin n\theta - \bar{V}_n \cos n\theta) \exp(jpt)\end{aligned}\right\} \quad (3)$$

where $\epsilon_n = 1/2$ for $n=0$, $\epsilon_n = 1$ for $n \geqq 1$, p is the circular frequency (rad/sec), and $j=\sqrt{-1}$. Substituting equations (3) into equations (1), the solution in the polar coordinates are shown to be

$$\left.\begin{aligned}\Delta_n &= -\alpha^2 A_n J_n(\alpha r) - \alpha^2 A_n' \, Y_n(\alpha r) \\ U_n &= A_n [\partial J_n(\alpha r)/\partial r] + B_n (n/r) J_n(\beta r) \\ &\quad + A_n' [\partial Y_n(\alpha r)/\partial r] + B_n' (n/r) Y_n(\beta r) \\ V_n &= -\{A_n (n/r) J_n(\alpha r) + B_n [\partial J_n(\beta r)/\partial r] \\ &\quad + A_n' (n/r) Y_n(\alpha r) + B_n' [\partial Y_n(\beta r)/\partial r]\}\end{aligned}\right\} \quad (4a)$$

$$\left.\begin{aligned}\bar{\Delta}_n &= -\alpha^2 \bar{A}_n J_n(\alpha r) - \alpha^2 \bar{A}_n' \, Y_n(\alpha r) \\ \bar{U}_n &= \bar{A}_n [\partial J_n(\alpha r)/\partial r] + \bar{B}_n (n/r) J_n(\beta r) \\ &\quad + \bar{A}_n' [\partial Y_n(\alpha r)/\partial r] + \bar{B}_n' (n/r) Y_n(\beta r) \\ \bar{V}_n &= -\{\bar{A}_n (n/r) J_n(\alpha r) + \bar{B}_n [\partial J_n(\beta r)/\partial r] \\ &\quad + \bar{A}_n' (n/r) Y_n(\alpha r) + \bar{B}_n' [\partial Y_n(\beta r)/\partial r]\}\end{aligned}\right\} \quad (4b)$$

where

$$\alpha^2 = \rho p^2/(\lambda+2\mu), \; \beta^2 = \rho p^2/\mu \quad (5)$$

and where A_n, A_n', B_n, B_n', $\bar{A}_n$, $\bar{A}_n'$, $\bar{B}_n$ and $\bar{B}_n'$ are the constants of integration, $J_n(\alpha r)$, $J_n(\beta r)$ are the Bessel functions of the first kind of order n, and $Y_n(\alpha r)$, $Y_n(\beta r)$ are the Bessel functions of the second kind.

The boundary conditions for the ring of stress-free surfaces are

$$(\sigma_{qq})_i = (\sigma_{qs})_i = 0 \quad (6)$$

where q is the coordinate normal to the boundary and s is the coordinate in the tangential direction, σ_{qq} is the normal stress, σ_{qs} is the shearing stress, and $(\;)_i$ is the value at ith boundary. To obtain the general transformed expressions that are applicable to the problem of rings of general shape, the curved boundary is divided into small segments as shown in Fig. 1 in reference [12], and the variations of the direction of the stresses along the segments are neglected. The direction of the coordinate normal to the segment is therefore assumed to be constant. By making use of this assumption, since the angle γ_i between the normal to the segment and the reference axis has a constant value, we can assume the curvilinear coordinate s as the orthogonal coordinate, y_i, and the coordinate q as the orthogonal coordinate x_i approximately (see Fig. 1 in reference [12]). The relations between the displacements $(u_x)_i$ in the direction x_i and $(u_y)_i$ in the direction y_i and u_r, u_θ have been shown in the author's previous report [13]. The relations between the coordinates r, θ and x_i and y_i are also given in reference [12]. Substituting these equations into the relations between the stresses and the displacements yield

$$\left.\begin{aligned}(\sigma_{xx})_i &= \lambda\Delta + 2\mu\{(\partial u_r/\partial r)\cos^2(\theta-\gamma_i) \\ &\quad + (1/r)(u_r + \partial u_\theta/\partial\theta)\sin^2(\theta-\gamma_i) \\ &\quad + 0.5[u_\theta/r - (1/r)(\partial u_r/\partial\theta) \\ &\quad - \partial u_\theta/\partial r]\sin 2(\theta-\gamma_i)\} \\ (\sigma_{xy})_i &= \mu\{[\partial u_r/\partial r - (1/r)(\partial u_\theta/\partial\theta) \\ &\quad - u_r/r]\sin 2(\theta-\gamma_i) + [(1/r)(\partial u_r/\partial\theta) \\ &\quad + \partial u_\theta/\partial r - u_\theta/r][\cos^2(\theta-\gamma_i) - \sin^2(\theta-\gamma_i)]\}\end{aligned}\right\} \quad (7)$$

Substituting equations (4) into (7), the transformed expressions of the normal and the shearing stresses with respect to the ith segment of the surface can be evaluated. Hence the transformed equations of equations (6) are written as follows:

$$\left.\begin{aligned}[(S_{xx})_i + (\bar{S}_{xx})_i]\exp(jpt) = 0 \\ [(S_{xy})_i - (\bar{S}_{xy})_i]\exp(jpt) = 0\end{aligned}\right\} \quad (8)$$

where

$$\left.\begin{aligned}S_{xx} &= 0.5\, e_0^{\,1} A_0 + 0.5\, e_0^{\,2} A_0' \\ &\quad + \sum_{n=1}^{\infty} (e_n^{\,1} A_n + e_n^{\,2} A_n' + e_n^{\,3} B_n + e_n^{\,4} B_n') \\ S_{xy} &= 0.5 f_0^{\,1} A_0 + 0.5 f_0^{\,2} A_0' \\ &\quad + \sum_{n=1}^{\infty} (f_n^{\,1} A_n + f_n^{\,2} A_n' + f_n^{\,3} B_n + f_n^{\,4} B_n') \\ \bar{S}_{xx} &= 0.5\, \bar{e}_0^{\,3} \bar{B}_0 + 0.5\, \bar{e}_0^{\,4} \bar{B}_0' \\ &\quad + \sum_{n=1}^{\infty} (\bar{e}_n^{\,1} \bar{A}_n + \bar{e}_n^{\,2} \bar{A}_n' + \bar{e}_n^{\,3} \bar{B}_n + \bar{e}_n^{\,4} \bar{B}_n') \\ \bar{S}_{xy} &= 0.5 \bar{f}_0^{\,3} \bar{B}_0 + 0.5 \bar{f}_0^{\,4} \bar{B}_0' \\ &\quad + \sum_{n=1}^{\infty} (\bar{f}_n^{\,1} \bar{A}_n + \bar{f}_n^{\,2} \bar{A}_n' + \bar{f}_n^{\,3} \bar{B}_n + \bar{f}_n^{\,4} \bar{B}_n')\end{aligned}\right\} \quad (9)$$

The equations for $e_n^{\,1} \sim f_n^{\,1}$ are given in the Appendix. The transformed equations for the straight line boundary are also the same as equations (8) and (9), but the angle γ_i has a constant value in one straight line boundary.

To satisfy the boundary conditions, the Fourier expansion is performed to the equations of the boundary conditions along the boundary line of the inner and the outer surfaces of the ring [12, 13]. For the present case, one straight line is considered to be one segment, while one curved line must be divided into many segments according to the convergence of the solution. Hence by adding the Fourier coefficients of each segment yields the Fourier coefficient of the expression along the whole range of the outer or the inner boundary line. When the ring is symmetric about more than an axis, the analysis can be separated into symmetric and antisymmetric cases. Hence when the variable θ is chosen from an axis of symmetry, the boundary conditions along the outer and the inner surfaces are expanded into the Fourier series, these gives the following matrix form:

Downloaded 02 May 2010 to 171.66.16.250. Redistribution subject to ASME license or copyright; see http://www.asme.org/terms/Terms_Use.cfm

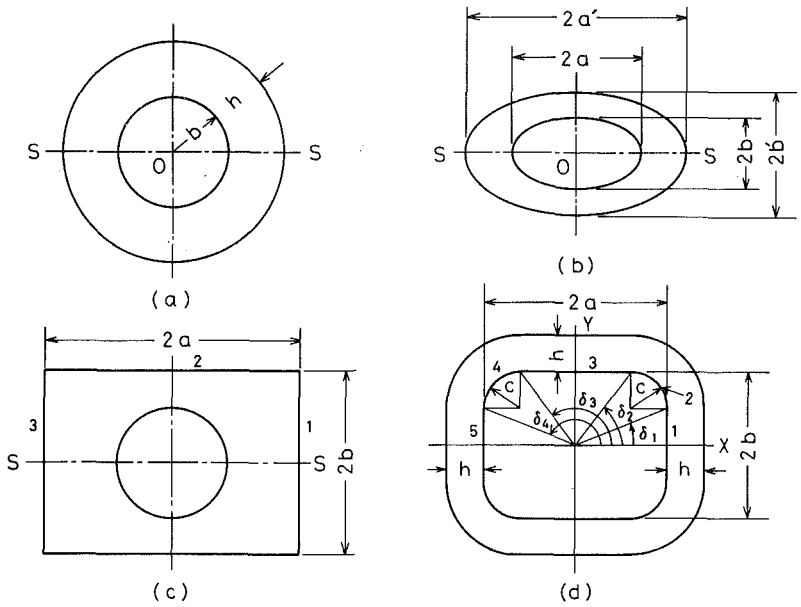


Fig. 1 Geometry of rings calculated in the numerical example

$$
\begin{bmatrix}
\hat{E}^1_{00} \cdots \hat{E}^1_{0N} & \hat{E}^2_{00} \cdots \hat{E}^2_{0N} & \hat{E}^3_{01} \cdots \hat{E}^3_{0N} & \hat{E}^4_{01} \cdots \hat{E}^4_{0N} \\
\hat{E}^1_{N0} \cdots \hat{E}^1_{NN} & \hat{E}^2_{N0} \cdots \hat{E}^2_{NN} & \hat{E}^3_{N1} \cdots \hat{E}^3_{NN} & \hat{E}^4_{N1} \cdots \hat{E}^4_{NN} \\
\hat{F}^1_{10} \cdots \hat{F}^1_{1N} & \hat{F}^2_{10} \cdots \hat{F}^2_{1N} & \hat{F}^3_{11} \cdots \hat{F}^3_{1N} & \hat{F}^4_{11} \cdots \hat{F}^4_{1N} \\
\hat{F}^1_{N0} \cdots \hat{F}^1_{NN} & \hat{F}^2_{N0} \cdots \hat{F}^2_{NN} & \hat{F}^3_{N1} \cdots \hat{F}^3_{NN} & \hat{F}^4_{N1} \cdots \hat{F}^4_{NN} \\
E^1_{00} \cdots E^1_{0N} & E^2_{00} \cdots E^2_{0N} & E^3_{01} \cdots E^3_{0N} & E^4_{01} \cdots E^4_{0N} \\
E^1_{N0} \cdots E^1_{NN} & E^2_{N0} \cdots E^2_{NN} & E^3_{N1} \cdots E^3_{NN} & E^4_{N1} \cdots E^4_{NN} \\
F^1_{10} \cdots F^1_{1N} & F^2_{10} \cdots F^2_{1N} & F^3_{11} \cdots F^3_{1N} & F^4_{11} \cdots F^4_{1N} \\
F^1_{N0} \cdots F^1_{NN} & F^2_{N0} \cdots F^2_{NN} & F^3_{N1} \cdots F^3_{NN} & F^4_{N1} \cdots F^4_{NN}
\end{bmatrix}
\begin{bmatrix}
A_0 \\ A_N \\ A_0' \\ A_N' \\ B_0 \\ B_N \\ B_0' \\ B_N'
\end{bmatrix}
= 0 \qquad (10)
$$

where

$$
\left.
\begin{aligned}
E^l_{mn} &= (2\epsilon_n/\pi) \sum_{i=1}^{I} \int_{\Theta_{i-1}}^{\Theta_i} e^l_n\,(R_i,\gamma_i,\theta)\,\cos m\theta\, d\theta \\
F^l_{mn} &= (2\epsilon_n/\pi) \sum_{i=1}^{I} \int_{\Theta_{i-1}}^{\Theta_i} f^l_n\,(R_i,\gamma_i,\theta)\,\sin m\theta\, d\theta \\
\hat{E}^l_{mn} &= (2\epsilon_n/\pi) \sum_{i=1}^{I'} \int_{\Theta_{i-1}}^{\Theta_i} e^l_n\,(\hat{R}_i,\hat{\gamma}_i,\theta)\,\cos m\theta\, d\theta \\
\hat{F}^l_{mn} &= (2\epsilon_n/\pi) \sum_{i=1}^{I'} \int_{\Theta_{i-1}}^{\Theta_i} f^l_n\,(\hat{R}_i,\hat{\gamma}_i,\theta)\,\sin m\theta\, d\theta
\end{aligned}
\right\} \quad l=1,2,3,4 \qquad (11)
$$

and where N is the number of trunction of the Fourier series, I is the number of the segments including the straight line segments of the outer surface in the range $\theta=0$ to $\theta=\pi$, and R_i is the coordinate r at the ith boundary of the outer surface which is expressed as a function of the angle θ in general. I' and $\hat{R}_i$ are those for the inner surface of the ring and $\hat{\gamma}_i$ is the

Downloaded 02 May 2010 to 171.66.16.250. Redistribution subject to ASME license or copyright; see http://www.asme.org/terms/Terms_Use.cfm

angle between the reference axis and the normal to the ith segment of the inner surface. Equation (10) determines the eigenfrequencies and the mode shapes of the rings of arbitrary shape.

The equation for the antisymmetric mode about the reference axis is obtained similarly as

$$\begin{bmatrix} \hat{E}^1_{11} \cdots \hat{E}^1_{1N} & \hat{E}^2_{11} \cdots \hat{E}^2_{1N} & \hat{E}^3_{10} \cdots \hat{E}^3_{1N} & \hat{E}^4_{10} \cdots \hat{E}^4_{1N} \\ \hat{E}^1_{N1} \cdots \hat{E}^1_{NN} & \hat{E}^2_{N1} \cdots \hat{E}^2_{NN} & \hat{E}^3_{N0} \cdots \hat{E}^3_{NN} & \hat{E}^4_{N0} \cdots \hat{E}^4_{NN} \\ \hat{F}^1_{01} \cdots \hat{F}^1_{0N} & \hat{F}^2_{01} \cdots \hat{F}^2_{0N} & \hat{F}^3_{00} \cdots \hat{F}^3_{0N} & \hat{F}^4_{00} \cdots \hat{F}^4_{0N} \\ \hat{F}^1_{N1} \cdots \hat{F}^1_{NN} & \hat{F}^2_{N1} \cdots \hat{F}^2_{NN} & \hat{F}^3_{N0} \cdots \hat{F}^3_{NN} & \hat{F}^4_{N0} \cdots \hat{F}^4_{NN} \\ \bar{E}^1_{11} \cdots \bar{E}^1_{1N} & \bar{E}^2_{11} \cdots \bar{E}^2_{1N} & \bar{E}^3_{10} \cdots \bar{E}^3_{1N} & \bar{E}^4_{10} \cdots \bar{E}^4_{1N} \\ \bar{E}^1_{N1} \cdots \bar{E}^1_{NN} & \bar{E}^2_{N1} \cdots \bar{E}^2_{NN} & \bar{E}^3_{N0} \cdots \bar{E}^3_{NN} & \bar{E}^4_{N0} \cdots \bar{E}^4_{NN} \\ \bar{F}^1_{01} \cdots \bar{F}^1_{0N} & \bar{F}^2_{01} \cdots \bar{F}^2_{0N} & \bar{F}^3_{00} \cdots \bar{F}^3_{0N} & \bar{F}^4_{00} \cdots \bar{F}^4_{0N} \\ \bar{F}^1_{N1} \cdots \bar{F}^1_{NN} & \bar{F}^2_{N1} \cdots \bar{F}^2_{NN} & \bar{F}^3_{N0} \cdots \bar{F}^3_{NN} & \bar{F}^4_{N0} \cdots \bar{F}^4_{NN} \end{bmatrix} \begin{bmatrix} \bar{A}_0 \\ \bar{A}_N \\ \bar{A}_0' \\ \bar{A}_N' \\ \bar{B}_0 \\ \bar{B}_N \\ \bar{B}_0' \\ \bar{B}_N' \end{bmatrix} = 0 \tag{12}$$

where

$$\begin{aligned} \bar{E}^l_{mn} &= (2\epsilon_n/\pi) \sum_{i=1}^{I} \int_{\text{Ⓗ}_{i-1}}^{\text{Ⓗ}_i} \bar{e}^l_n\,(R_i,\gamma_i,\theta)\,\sin m\theta\, d\theta \\ \bar{F}^l_{mn} &= -(2\epsilon_n/\pi) \sum_{i=1}^{I} \int_{\text{Ⓗ}_{i-1}}^{\text{Ⓗ}_i} \bar{f}^l_n\,(R_i,\gamma_i,\theta)\,\cos m\theta\, d\theta \\ \hat{E}^l_{mn} &= (2\epsilon_n/\pi) \sum_{i=1}^{I'} \int_{\text{Ⓗ}_{i-1}}^{\text{Ⓗ}_i} \bar{e}^l_n\,(\hat{R}_i,\hat{\gamma}_i,\theta)\,\sin m\theta\, d\theta \\ \hat{F}^l_{mn} &= -(2\epsilon_n/\pi) \sum_{i=1}^{I'} \int_{\text{Ⓗ}_{i-1}}^{\text{Ⓗ}_i} \bar{f}^l_n\,(\hat{R}_i,\hat{\gamma}_i,\theta)\,\cos m\theta\, d\theta \end{aligned} \tag{13}$$

The equations for a ring that has no symmetric axes can be obtained in the same way as previously. In such a case the Fourier expansion must be performed in the range $\theta=0$ to $\theta=2\pi$ with both sine and cosine terms included.

3 Numerical Examples

Numerical results for a thick circular ring have been obtained by Gazis [8] and Morler [9]. To investigate the accuracy of the present method, numerical calculations are carried out first for this problem. As applications, numerical calculations are demonstrated for thick elliptical rings, thick rectangular rings with rounded corners, and rectangular rings with circular inner boundaries as shown in Fig. 1. The number of Fourier series is taken up to five which gives reasonable results for calculating the eigenvalues. For the elliptical ring with $a/b=2$, the discrepancies between the results with $N=5$ and $N=8$ are limited to within 1.5 percent. We have the following relations under the plane-strain assumption:

$$\lambda=\nu E/[(1+\nu)(1-2\nu)], \quad \mu=E/[2(1+\nu)]$$

$$\zeta=(1-2\nu)/\nu, \quad \eta=[2(1-\nu)/(1-2\nu)]^{1/2} \tag{14}$$

where ν is Poisson's ratio and E is Young's modulus.

3.1 Thick Circular Rings. Geometrical relations used in the numerical calculation are as follows for a thick ring with the radius b and the thickness h:

$$\hat{R}_i/b=1, \quad R_i/b=1+h/b, \quad \gamma_i=\hat{\gamma}_i=(\text{Ⓗ}_{i-1}+\text{Ⓗ}_i)/2 \tag{15}$$

If we take the radius b as the reference length and substitute equations (15) into equations (A1) in the Appendix, the equations e_n and f_n at the boundaries are expressed as functions of the independent variable θ only. Hence the integration in equations (11) and (13) can be performed numerically.

Table 1 depicts the comparison between the present results and those given in the previous reports for the first dimensionless eigenfrequencies $\alpha'=\omega h[\rho(1-\nu^2)/E]^{1/2}$ with $\nu=0.25$. The present results are in good agreements with Gazis's and Morely's results.

Table 1 Comparison between the present results and Gazis's and Morley's ones of the circular rings as shown in Fig. 1(*a*) for dimensionless eigenfrequencies $\alpha'=\omega h[\rho(1-\nu^2)/E]^{1/2}$ with $\nu=0.25$

h/b	Author	Gazis[8]	Morley[9]
0.4	0.0845	0.081	0.084
0.6	0.1537	0.152	0.156
0.8	0.2255	0.223	0.232
1.0	0.2955	0.296	0.308

Downloaded 02 May 2010 to 171.66.16.250. Redistribution subject to ASME license or copyright; see http://www.asme.org/terms/Terms_Use.cfm

Table 2 Dimensionless eigenfrequencies α^* $(=\omega b\sqrt{\rho/E})$ for elliptical rings as shown in Fig. 1(b) for $a'/b'=a/b$ and $\nu=0.3$

a/b	b'/b	BS1	BS2	BS3	LS1
	1.2	0.1457	0.3785	0.6893	0.9558
	1.4	0.2213	0.5701	0.9967	0.8838
1.0	1.6	0.2673	0.6650	1.119	0.8256
	1.8	0.2939	0.7068	1.156	0.7763
	2.0	0.3080	0.7196		0.7343
	1.2	0.1257	0.5029	0.7868	0.7232
	1.4	0.1748	0.5853	0.9416	0.6647
1.5	1.6	0.2115	0.6305	1.002	0.6204
	1.8	0.2341	0.6466	0.9939	0.5804
	2.0	0.2467	0.6451	0.9791	0.5518
	1.2		0.2403	0.4221	0.5119
	1.4	0.1217	0.5845	0.9291	0.4853
2.0	1.6	0.1334	0.6236	0.9674	0.4705
	1.8	0.1584	0.6365	0.9591	0.4484
	2.0	0.1784	0.6330	0.9259	0.4272

3.2 Thick Elliptical Rings of Variable Cross Section. Figure 1(b) shows the geometry of a thick elliptical ring. For this example problem there are following geometrical relations:

$$\left.\begin{aligned} &R_i/b=(a'/b)/[\cos^2\theta+(a'/b')^2\sin^2\theta]^{1/2}\\ &\gamma_i=\pi/2-\tan^{-1}[(b'/a')^2/\tan \textcircled{H}_i^*] \quad \text{for } \textcircled{H}_i^*<\pi/2\\ &\gamma_i=\pi/2 \quad \text{for } \textcircled{H}_i^*=\pi/2\\ &\gamma_i=\pi/2+\tan^{-1}[(b'/a')^2/ABS(\tan \textcircled{H}_i^*)] \quad \text{for } \textcircled{H}_i^*>\pi/2 \end{aligned}\right\} \tag{16a}$$

for the outer surface and

$$\left.\begin{aligned} &R_i/b=(a/b)/[\cos^2\theta+(a/b)^2\sin^2\theta]^{1/2}\\ &\hat{\gamma}_i=\pi/2-\tan^{-1}[(b/a)^2/\tan \textcircled{H}_i^*] \quad \text{for } \textcircled{H}_i^*<\pi/2\\ &\hat{\gamma}_i=\pi/2 \quad \text{for } \textcircled{H}_i^*=\pi/2\\ &\hat{\gamma}_i=\pi/2+\tan^{-1}[(b/a)^2/ABS(\tan \textcircled{H}_i^*)] \quad \text{for } \textcircled{H}_i^*>\pi/2 \end{aligned}\right\} \tag{16b}$$

for the inner surface, where $\textcircled{H}_i^*=(\textcircled{H}_i+\textcircled{H}_{i-1})/2$ and ABS denotes the absolute values. Substituting equations (16) into equations (11) and (13), the eigenfrequencies and mode shapes are obtained directly by use of equations (10) and (12) in the same way as previously.

Table 2 depicts the dimensionless eigenfrequencies $\alpha^*(=\omega b/\sqrt{E/\rho})$ for various aspect ratios a/b and b'/b. For in-plane vibration problems there exists two types of vibrations one of which is governed mainly by flexural motions and the other by longitudinal motions. These are called hereafter the bending mode and the longitudinal mode, respectively. In the Tables $BS1$, $BS2$ and $BS3$ show first three symmetric bending modes about the axis of symmetry (the axis $S-S$ in Fig. 1(b)), and $LS1$ shows the first symmetric longitudinal mode. It can be seen that the eigenfrequencies of the longitudinal mode decreases with the thickness of the ring, while the frequency of the bending mode first increases then decreases and has a maximum value. Figure 2 shows the relations between α^* and b'/b for elliptical rings with $a/b=a'/b'=1.5$ and $\nu=0.3$. In the figures $BA1$, $BA2$, and $BA3$ denote the antisymmetric bending modes and $LA1$ the first antisymmetric longitudinal mode. In the papers concerning vibrations of elliptical rings given by Brigham [10] and Sato [11], they utilized the curved beam theory in which the thickness of the ring was constant. For such cases the eigenvalues of the symmetric mode are lower than the corresponding values of the antisymmetic mode. However in the present example, the thickness of the ring varies with the angle θ. For instance in case of $a/b=a'/b'=1.5$ and $b'/b=1.5$, we have $a'-a=0.75b$ and $b'-b=0.5b$. The rigidities of this variable thickness ring at the points $\theta=0$ and $\theta=\pi$ become large as compared with the one at the point $\theta=\pi/2$. For this reason the eigenvalues of the symmetric modes ($BS1$, $BS2$, and $BS3$) are lower than the corresponding values for the antisymmetric modes ($BA1$, $BA2$, and $BA3$) as shown in Fig. 2.

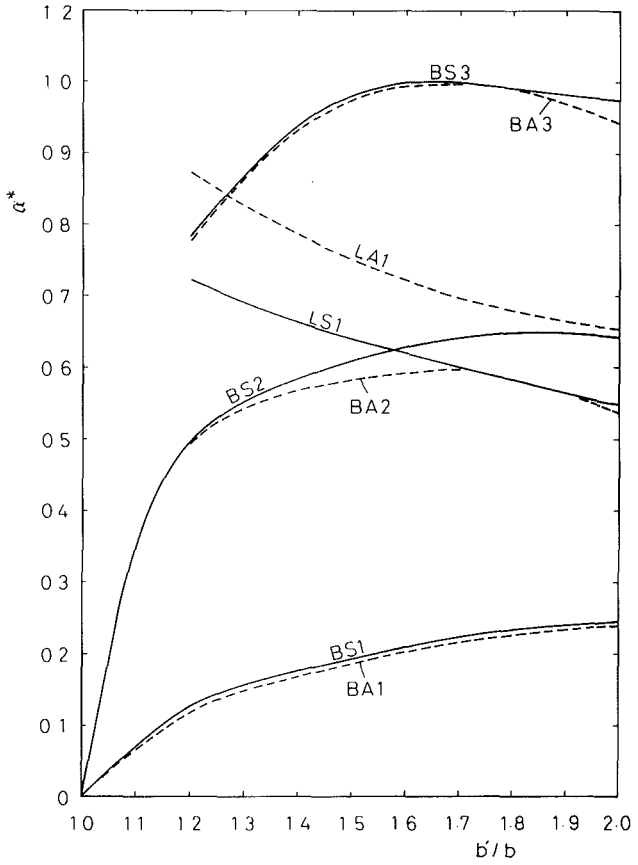


Fig. 2 Dimensionless eigenfrequencies $\alpha^*(=\omega b\sqrt{\rho/E})$ versus b'/b for elliptical rings with $a/b=a'/b'=1.5$ and $\nu=0.3$

3.3 Rectangular Rings With Circular Holes. Consider the ring as shown in Fig. 1(c). In this example we have

$$\begin{aligned} &R_1/b=(a/b)/\cos\theta, \quad \gamma_1=0 \quad \text{for the boundary 1}\\ &R_2/b=1/\sin\theta, \quad \gamma_2=\pi/2 \quad \text{for the boundary 2}\\ &R_3/b=-(a/b)/\cos\theta, \quad \gamma_3=\pi \quad \text{for the boundary 3} \end{aligned} \tag{17a}$$

for the outer rectangular surface, and

$$R_i/b=c/b,\ \hat{\gamma}_i=\textcircled{H}_i^* \tag{17b}$$

for the inner circular surface.

Downloaded 02 May 2010 to 171.66.16.250. Redistribution subject to ASME license or copyright; see http://www.asme.org/terms/Terms_Use.cfm

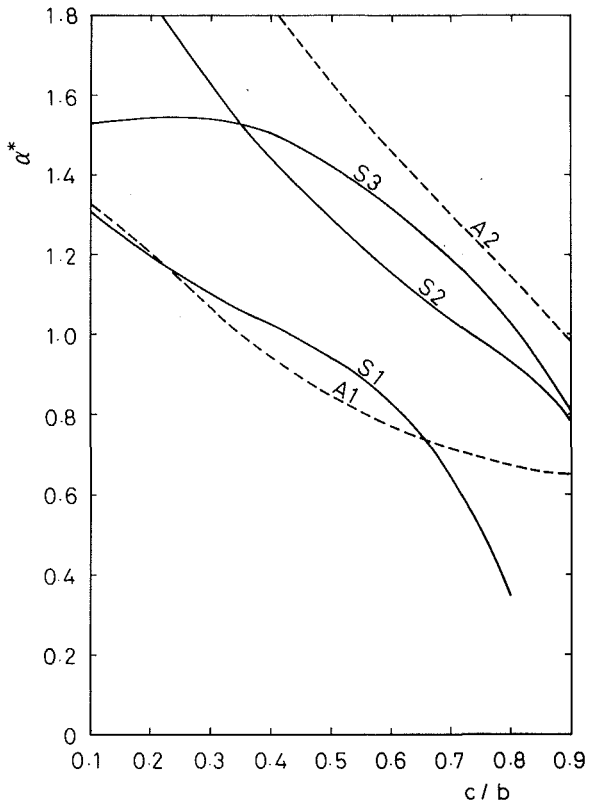


Fig. 3 Dimensionless eigenfrequencies α^* versus c/b for square rings with circular cavities as shown in Fig. 1(c) with $a/b=1$ and $\nu=0.3$

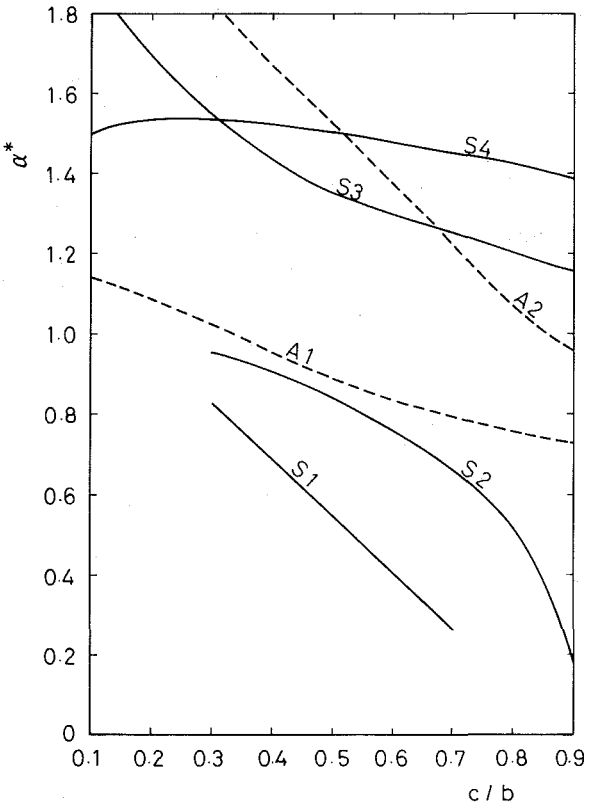


Fig. 4 Dimensionless eigenfrequencies α^* versus c/b for rectangular rings with circular cavities as shown in Fig. 1(c) with $a/b=1.5$ and $\nu=0.3$

Figures 3 and 4 depict the dimensionless eigenfrequencies α^* versus the ratio c/b between the radius of the inner circle and the length of the outer boundary. As seen in the figures, the eigenfrequencies decrease with the radius of the circular cavity. In this example both effects of the flexural and the longitudinal motions become moderately large on each curve, so that the flexural and the longitudinal modes are not separated. In the figures the solid lines denote the symmetric mode with respect to the axis of symmetry $S-S$ in Fig. 1(c), and dotted line the antisymmetric modes.

3.4 Thick Rectangular Rings With Rounded Corners. As an example of the ring with both curved and straight line boundaries, we consider a thick rectangular ring with rounded corners as shown in Fig. 1(d). The equations of the boundary curve are

$$\left.\begin{aligned}&[X-(a-c)]^2+[Y-(b-c)]^2=c^2 \quad \text{for the boundary 2}\\&[X+(a-c)]^2+[Y-(b-c)]^2=c^2 \quad \text{for the boundary 4}\end{aligned}\right\} \tag{18a}$$

$$\left.\begin{aligned}&\delta_1=\tan^{-1}(b/a-c/a)\\&\delta_2=\tan^{-1}[1/(a/b-c/b)]\\&\delta_3=\pi-\delta_2,\quad \delta_4=\pi-\delta_1\end{aligned}\right\} \tag{18b}$$

Then the expressions for R_i and γ_i are denoted, for the inner boundary 1, by

$$\hat{R}_i/b=(a/b)/\cos\theta,\ \hat{\gamma}_i=0 \tag{18c}$$

for the boundary 2, by

$$\left.\begin{aligned}\hat{R}_i/b&=(a/b-c/b)\cos\theta+(1-c/b)\sin\theta\\&+\{[(a/b-c/b)\cos\theta+(1-c/b)\sin\theta]^2\\&-(a/b-c/b)^2-(1-c/b)^2+c^2/b^2\}^{1/2}\\\hat{\gamma}_i&=\frac{\pi}{2}-\tan^{-1}\left[\frac{(R_i(\textcircled{H}_i^*)/b)\cos\textcircled{H}_i^*+c/b-a/b}{(R_i(\textcircled{H}_i^*)/b)\sin\textcircled{H}_i^*+c/b-1}\right]\end{aligned}\right\} \tag{18d}$$

for the boundary 3, by

$$\hat{R}_i/b=1/\sin\theta,\ \hat{\gamma}_i=\pi/2 \tag{18e}$$

for the boundary 4, by

$$\left.\begin{aligned}\hat{R}_i/b&=-(a/b-c/b)\cos\theta+(1-c/b)\sin\theta\\&+\{[(a/b-c/b)\cos\theta-(1-c/b)\sin\theta]^2\\&-(a/b-c/b)^2-(1-c/b)^2+c^2/b^2\}^{1/2}\\\hat{\gamma}_i&=\frac{\pi}{2}+\tan^{-1}\left\{\frac{-[(R_i(\textcircled{H}_i^*)/b)\cos\textcircled{H}_i^*+a/b-c/b]}{(R_i(\textcircled{H}_i^*)/b)\sin\textcircled{H}_i^*-1+c/b}\right\}\end{aligned}\right\} \tag{18f}$$

and for the boundary 5, by

$$\hat{R}_i/b=-(a/b)/\cos\theta,\ \hat{\gamma}_i=\pi \tag{18g}$$

The expressions for the outer boundaries become the same forms as equations (18) when we use the folllowing substitutions:

$$a/b\rightarrow(a/b+t/b)/(1+t/b),\ c/b\rightarrow(c/b+t/b)/(1+t/b),$$
$$\hat{R}_i/b\rightarrow R_i/(b+t) \tag{19}$$

Hence

$$R_i/b=[R_i/(b+t)](1+t/b),\ \gamma_i=\hat{\gamma}_i \tag{20}$$

for each outer boundary.

Downloaded 02 May 2010 to 171.66.16.250. Redistribution subject to ASME license or copyright; see http://www.asme.org/terms/Terms_Use.cfm

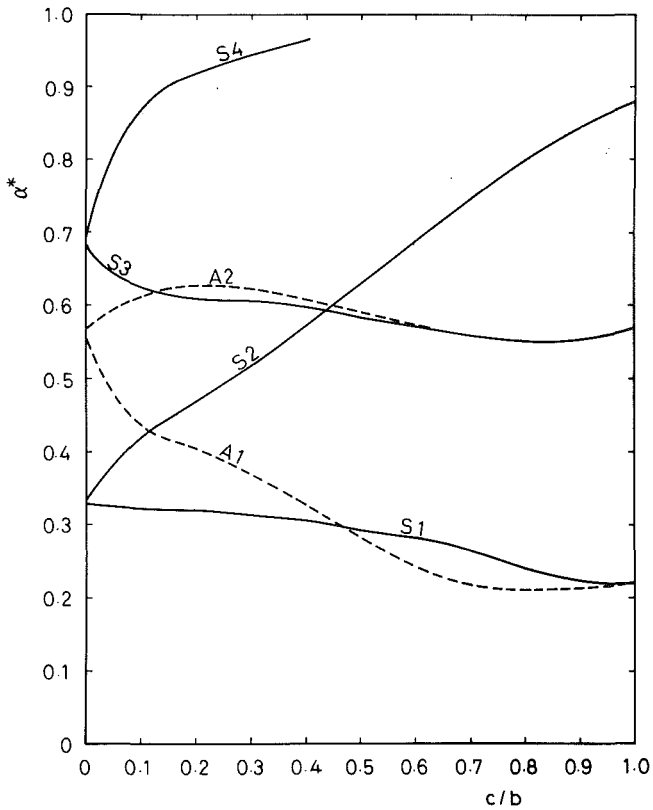


Fig. 5 Dimensionless eigenfrequencies α^* versus c/b for square rings with rounded corners as shown in Fig. 1(d) with $a/b = 1$, $h/b = 0.4$, and $\nu = 0.3$

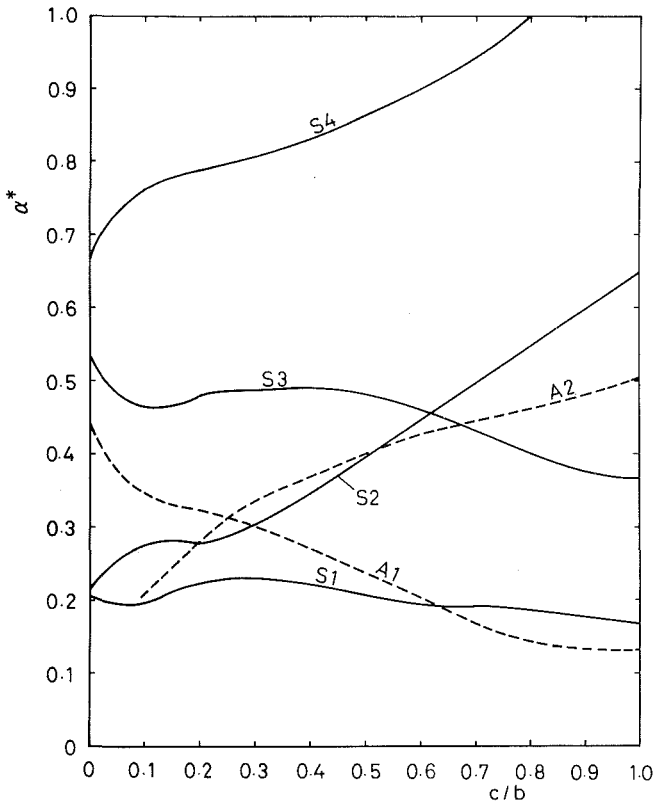


Fig. 6 Dimensionless eigenfrequencies α^* versus c/b for rectangular rings with rounded corners as shown in Fig. 1(d) with $a/b = 1.5$, $h/b = 0.4$, and $\nu = 0.3$

Figures 5–7 depict the dimensionless eigenfrequencies $\alpha^*(=\omega b/\sqrt{E/\rho})$ versus the ratio between the radius c of the circle and the reference length b. In the figures the solid lines represent the symmetric modes with respect to the axis of symmetry (the X-axis in Fig. 1(d)), and the dotted lines the antisymmetric modes. It is seen that since the ring has circular bends and the ring can be bent at the corners, there exists two curves that are generated from the same frequency of the rectangular ring. These curves reduce to the frequencies of the circular ring as the radius c of the circle increases and the result coincides with the one of the circular ring in the special case of $c = b$ of course.

4 Conclusion

This paper concerns the method for solving problems of vibrating thick rings of arbitrary shape. In the analysis the exact solutions for the equation of motion of elastic solids based on the plane-strain assumption is applied, and the boundary conditions along both the inner and outer surfaces of the ring are satisfied directly by making use of the Fourier expansion collocation method which has been developed in the author's previous reports concerning vibrations of plates and wave propagation of rods. The equation for finding the eigenfrequencies and mode shapes has been given for arbitrarily shaped rings.

Numerical calculations have been carried out for circular rings, elliptical rings, rectangular rings with circular holes, and rectangular rings with rounded corners. The present results for the typical example of circular rings are in very good agreements with the previously published ones. Since the numerical results for higher modes can be obtained easily by using a microcomputer with the same computer program and they possess sufficient accuracy, this method has advantages as compared with other general approximate methods. However it is important to point out that in the present method the convergence of the Fourier series becomes poor as the ring becomes thin and slender.

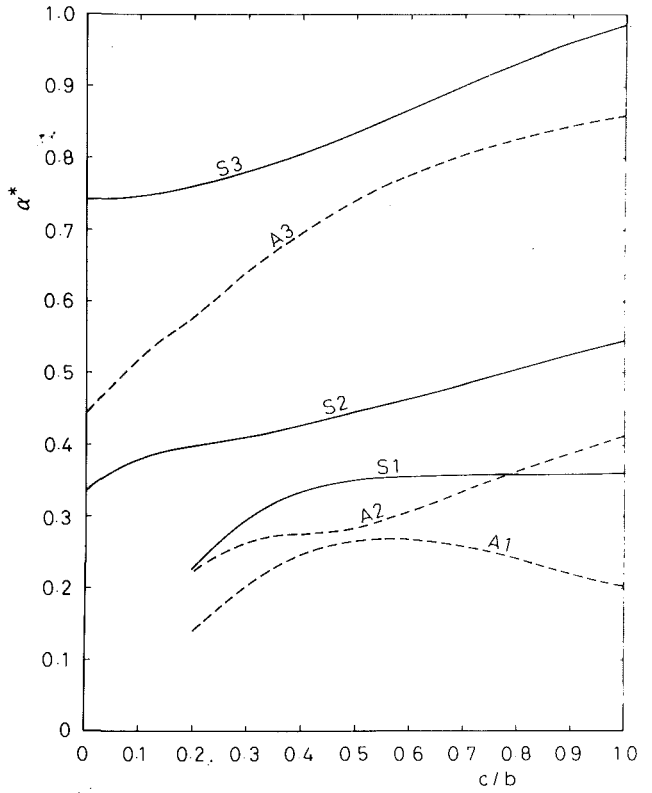


Fig. 7 Dimensionless eigenfrequencies α^* versus c/b for rectangular rings with rounded corners as shown in Fig. 1(d) with $a/b = 2$, $h/b = 0.4$, and $\nu = 0.3$

Downloaded 02 May 2010 to 171.66.16.250. Redistribution subject to ASME license or copyright; see http://www.asme.org/terms/Terms_Use.cfm

Acknowledgment

The author wishes to thank heartily Mr. S. Ikai, Gunma University, for his various contributions throughout the progress of the present investigation. The author is also indebted to the reviewers for their useful comments.

References

1 Love, A. E. H., *A Treatise on the Mathematical Theory of Elasticity*, 4th ed., Cambridge University Press, Chapter XXI.

2 Waltking, F. W., "Schwingungsformen von Kreisbogentragen," *Ingenieur-Archiv.*, Vol. 5, 1934, pp. 429–449.

3 Philipson, L. L., "On the Role of Extension in the Flexural Vibration of Rings," ASME JOURNAL OF APPLIED MECHANICS, Vol. 23, 1956, pp. 364–366.

4 Endo, M., and Taniguchi, M., "Flexural Vibration of a Ring," *Trans. Japan Society of Mechanical Engineers* (in Japanese), Vol. 36, 1970, pp. 2011–2019.

5 Endo, M., "'Flexural Vibration of a Ring With Arbitrary Cross Section," *Trans. Japan Society of Mechanical Engineers* (in Japanese), Vol. 37, 1971, pp. 1513–1521.

6 Sabir, A. B., and Ashwell, D. G., "A Comparison of Curved Beam Finite Elements When Used in Vibration Problem," *Journal of Sound and Vibration*, Vol. 18, 1971, pp. 555–563.

7 Herrmann, G., and Mirsky, I., "Three-Dimensional and Shell Theory Analysis of Axially Symmetric Motions of Cylinders," ASME JOURNAL OF APPLIED MECHANICS, Vol. 23, 1956, pp. 563–568.

8 Gazis, D. G., "Exact Analysis of the Plane-Strain Vibrations of Thick Walled Hollow Cylinders," *Journal of Acoustical Society of America*, Vol. 30, 1958, pp. 786–794.

9 Morley, L. S. D., "Elastic Waves in a Naturally Curved Rod," *Quarterly Journal of Mechanics and Applied Mathematics*, Vol. XIV, 1961, pp. 155–172.

10 Brighan, G. A., "In-Plane Free Vibrations of Tapered Oval Rings," *Journal of the Acoustical Society of America*, Vol. 54, 1973, pp. 451–460.

11 Sato, K., "Free Flexural Vibrations of an Elliptical Ring in Its Plane," *Journal of the Acoustical Society of America*, Vol. 57, 1975, pp. 113–115.

12 Nagaya, K., "Dynamic Response of a Plate With Arbitrary Shape," ASME JOURNAL OF APPLIED MECHANICS, Vol. 47, 1980, pp. 620–626.

13 Nagaya, K., "Stress Wave Propagation in a Bar of Arbitrary Cross Section," ASME JOURNAL OF APPLIED MECHANICS, Vol. 49, 1982, pp. 157–164.

APPENDIX

The expressions for $e_n{}^1 \sim f_n{}^2$ in equations (9) are as follows:

$$
\begin{aligned}
e_n{}^1 = e_n{}^1(r,\gamma_i,\theta) = \{ & -\cos n\theta - \zeta\cos^2(\theta-\gamma_i)\cos n\theta \\
& + [\zeta(n^2+n)/\alpha^2 r^2][\cos^2(\theta-\gamma_i)\cos h\theta \\
& - \sin^2(\theta-\gamma)\cos h\theta - \sin 2(\theta-\gamma_i)\sin n\theta]\} J_n(\alpha r) \\
& + (\zeta/\alpha r)[\sin^2(\theta-\gamma_i)\cos n\theta - \cos^2(\theta-\gamma_i)\cos n\theta \\
& + n\sin 2(\theta-\gamma_i)\sin n\theta] J_{n-1}(\alpha r) \\
e_n{}^2 = e_n{}^2(r,\gamma_i,\theta) = \{ & -\cos n\theta - \zeta\cos^2(\theta-\gamma_i)\cos n\theta \\
& + [\zeta(n^2+n)/\alpha^2 r^2][\cos^2(\theta-\gamma_i)\cos n\theta \\
& - \sin^2(\theta-\gamma_i)\cos n\theta - \sin 2(\theta-\gamma_i)\sin n\theta]\} Y_n(\alpha r) \\
& + (\zeta/\alpha r)[\sin^2(\theta-\gamma_i)\cos n\theta - \cos^2(\theta-\gamma_i)\cos n\theta \\
& + n\sin 2(\theta-\gamma_i)\sin n\theta] Y_{n-1}(\alpha r) \\
e_n{}^3 = e_n{}^3(r,\gamma_i,\theta) = (\eta^2\zeta/\beta^2 r^2)\{ & (n^2+n)[\sin^2(\theta-\gamma_i) \\
& - \cos^2(\theta-\gamma_i)]\cos n\theta \\
& + (n^2+n-0.5\beta^2 r^2)\sin 2(\theta-\gamma_i)\sin n\theta\} J_n(\beta r) \\
& + (\eta^2\zeta/\beta r)[n\cos^2(\theta-\gamma_i)\cos n\theta \\
& - n\sin^2(\theta-\gamma_i)\cos n\theta - \sin 2(\theta-\gamma_i)\sin n\theta] J_{n-1}(\beta r) \\
e_n{}^4 = e_n{}^4(r,\gamma_i,\theta) = (\eta^2\zeta/\beta^2 r^2)\{ & (n^2+n)[\sin^2(\theta-\gamma_i) \\
& - \cos^2(\theta-\gamma_i)]\cos n\theta \\
& + (n^2+n-0.5\beta^2 r^2)\sin 2(\theta-\gamma_i)\sin n\theta\} Y_n(\beta r) \\
& + (\eta^2\zeta/\beta r)[n\cos^2(\theta-\gamma_i)\cos n\theta \\
& - n\sin^2(\theta-\gamma_i)\cos n\theta - \sin 2(\theta-\gamma_i)\sin n\theta] Y_{n-1}(\beta r)
\end{aligned}
\tag{A1}
$$

$$
\begin{aligned}
f_n{}^1 = f_n{}^1(r,\gamma_i,\theta) = (\zeta/\alpha^2 r^2)\{ & (n^2+n \\
& - 0.5\alpha^2 r^2)\sin 2(\theta-\gamma_i)\cos n\theta \\
& + (n^2+n)[\cos^2(\theta-\gamma_i) - \sin^2(\theta-\gamma_i)]\sin n\theta\} J_n(\alpha r) \\
& - (\zeta/\alpha r)[\sin 2(\theta-\gamma_i)\cos n\theta \\
& + n\cos^2(\theta-\gamma_i)\sin n\theta - n\sin^2(\theta-\gamma_i)\sin n\theta] J_{n-1}(\alpha r) \\
f_n{}^2 = f_n{}^2(r,\gamma_i,\theta) = (\zeta/\alpha^2 r^2)\{ & (n^2+n \\
& - 0.5\alpha^2 r^2)\sin 2(\theta-\gamma_i)\cos n\theta \\
& + (n^2+n)[\cos^2(\theta-\gamma_i) - \sin^2(\theta-\gamma_i)]\sin n\theta\} Y_n(\alpha r) \\
& - (\zeta/\alpha r)[\sin 2(\theta-\gamma_i)\cos n\theta \\
& + n\cos^2(\theta-\gamma_i)\sin n\theta - n\sin^2(\theta-\gamma_i)\sin n\theta] Y_{n-1}(\alpha r) \\
f_n{}^3 = f_n{}^3(r,\gamma_i,\theta) = -(\zeta\eta^2/\beta^2 r^2)\{ & (n^2+n) \\
& \times \sin 2(\theta-\gamma_i)\cos n\theta + (n^2+n-0.5\beta^2 r^2)[\cos^2(\theta-\gamma_i) \\
& - \sin^2(\theta-\gamma_i)]\sin n\theta\} J_n(\beta r) \\
& + (\zeta\eta^2/\beta r)[n\sin 2(\theta-\gamma_i)\cos n\theta \\
& + \cos^2(\theta-\gamma_i)\sin n\theta - \sin^2(\theta-\gamma_i)\sin n\theta] J_{n-1}(\beta r) \\
f_n{}^4 = f_n{}^4(r,\gamma_i,\theta) = -(\zeta\eta^2/\beta^2 r^2)\{ & (n^2+n) \\
& \times \sin 2(\theta-\gamma_i)\cos n\theta + (n^2+n-0.5\beta^2 r^2)[\cos^2(\theta-\gamma_i) \\
& - \sin^2(\theta-\gamma_i)]\sin n\theta\} Y_n(\beta r) \\
& + (\zeta\eta^2/\beta r)\{n\sin 2(\theta-\gamma_i)\cos n\theta \\
& + \cos^2(\theta-\gamma_i)\sin n\theta - \sin^2(\theta-\gamma_i)\sin n\theta\} Y_{n-1}(\beta r)
\end{aligned}
$$

where

$$\eta = \beta/\alpha,\ \zeta = 2\mu/\lambda \tag{A2}$$

The expressions for $\bar{e}_n{}^1(r,\gamma_i,\theta) \sim \bar{e}_n{}^4(r,\gamma_i,\theta)$ and $\bar{f}_n{}^1(r,\gamma_i,\theta) \sim \bar{f}_n{}^4(r,\gamma_i,\theta)$ have the same forms as $e_n{}^1(r,\gamma_i,\theta) \sim e_n{}^4(r,\gamma_i,\theta)$ and $f_n{}^1(r,\gamma_i,\theta) \sim f_n{}^4(r,\gamma_i,\theta)$ in equations (A1), respectively, but in which $\cos n\theta$ is replaced by $\sin n\theta$ and $\sin n\theta$ is replaced by $-\cos n\theta$.

Downloaded 02 May 2010 to 171.66.16.250. Redistribution subject to ASME license or copyright; see http://www.asme.org/terms/Terms_Use.cfm

J. J. A. Rodal
Manager of Advanced Engineering,
Beloit Corp.,
Beloit, Wis. 53511

D. J. Steigmann
Graduate Student,
Division of Engineering,
Brown University,
Providence, R.I. 02912

E. A. Witmer
Professor,
Department of Aeronautics and Astronautics,
Massachusetts Institute of Technology,
Cambridge, Mass. 02139

Numerical Simulation of Transient Finite Deformations of Thin Beams

The formulation of the problem of finite elastic-viscoplastic deformation of thin beams is described. The finite element analysis of a representative problem is presented and various solution methods are surveyed.

The analysis employs convected coordinates ξ^i which maintain a one-one correspondence with material particles during the motion. The covariant basis vectors induced by the ξ^i are

$$\mathbf{G}_i(t) = \mathbf{R}_{,i}; \quad \mathbf{G}_i(0) = \mathbf{g}_i$$

where a comma denotes the partial derivative with respect to ξ^i and $\mathbf{R}$ is the position vector of a particle relative to a fixed origin. The associated metric components are

$$G_{ij} = \mathbf{G}_i \cdot \mathbf{G}_j; \quad g_{ij} = \mathbf{g}_i \cdot \mathbf{g}_j.$$

The following formulas are needed [1-4]:

$$\dot{\mathbf{G}}_i = L_{ji}\mathbf{G}^j, \quad \dot{\mathbf{G}}^i = -L^i{}_j\mathbf{G}^j \tag{1}$$

$$\mathbf{D} = L_{ij}\mathbf{G}^i\mathbf{G}^j - \mathbf{W} = \frac{1}{2}\dot{G}_{ij}\mathbf{G}^i\mathbf{G}^j \tag{2}$$

$$\boldsymbol{\gamma} = \frac{1}{2}(G_{ij} - g_{ij})\mathbf{g}^i\mathbf{g}^j; \quad \dot{\boldsymbol{\gamma}} = \frac{1}{2}\dot{G}_{ij}\mathbf{g}^i\mathbf{g}^j \tag{3}$$

$$d\mathbf{P} = \mathbf{T}dA = \mathbf{t}dA_0 = n_i\tau^{ij}\mathbf{G}_j dA_0 \tag{4}$$

$$\tau^{ij} = (G/g)^{1/2}\mathbf{G}^i \cdot \boldsymbol{\sigma} \cdot \mathbf{G}^j = \mathbf{g}^i \cdot \mathbf{S} \cdot \mathbf{g}^j \tag{5}$$

where a superposed dot denotes the material rate, L_{ji} are velocity gradient components, $\mathbf{D}$ is the rate of deformation, $\mathbf{W}$ is the spin, $\boldsymbol{\gamma}$ is the Green strain, $d\mathbf{P}$ is the force acting on surface element dA, $\mathbf{T}$ is the traction, $\mathbf{t}$ is the "nominal" traction associated with $dA_0 = dA(t=0)$, n_i are components of the unit normal to dA_0, τ^{ij} are the Kirchhoff stress components, $\boldsymbol{\sigma}$ is the Cauchy stress, $\mathbf{S}$ is the second Piola-Kirchhoff stress, $G = \det(G_{ij})$, and $g = \det(g_{ij})$.

Contributed by the Applied Mechanics Division and presented at the Winter Annual Meeting, Boston, Mass., November 13-18, 1983 of THE AMERICAN SOCIETY OF MECHANICAL ENGINEERS.

Discussion on this paper should be addressed to the Editorial Department, ASME, United Engineering Center, 345 East 47th Street, New York, N.Y. 10017, and will be accepted until two months after final publication of the paper itself in the JOURNAL OF APPLIED MECHANICS. Manuscript received by ASME Applied Mechanics Division, September, 1982; final revision, May, 1983. Paper No. 83-WA/APM-21.

Copies will be available until July, 1984.

From (2) and (3)

$$\dot{\gamma}^i_j = g^{il}D_{lj} = g^{il}G_{lk}D^k_j = (\delta^i_k + 2\gamma^i_k)D^k_j. \tag{6}$$

From (5),

$$\tau^i_k = G_{kj}S^{ji} = G_{kj}g^{jl}S^i_l = (\delta^l_k + 2\gamma^l_k)S^i_l. \tag{7}$$

We employ the linear hypoelastic constitutive relation [5]:

$$\mathbf{D} = \frac{1+\nu}{\mathrm{E}}\overset{\circ}{\boldsymbol{\tau}} - \frac{\nu}{\mathrm{E}}(\mathrm{tr}\overset{\circ}{\boldsymbol{\tau}})\mathbf{1} \tag{8}$$

where

$$\overset{\circ}{\boldsymbol{\tau}} = \dot{\boldsymbol{\tau}} - \mathbf{W}\cdot\boldsymbol{\tau} + \boldsymbol{\tau}\cdot\mathbf{W} \tag{9}$$

is the corotational rate of Kirchhoff stress, and E and ν are Young's and Poisson's moduli.

The material rate of $\boldsymbol{\tau}$ is

$$\dot{\boldsymbol{\tau}} = \dot{\tau}^i_j\mathbf{G}_i\mathbf{G}^j + \tau^i_j(\dot{\mathbf{G}}_i\mathbf{G}^j + \mathbf{G}_i\dot{\mathbf{G}}^j).$$

Substituting into (9) and employing (1) and (2) gives

$$\overset{\circ}{\boldsymbol{\tau}} = \dot{\tau}^i_j\mathbf{G}_i\mathbf{G}^j + \mathbf{D}\cdot\boldsymbol{\tau} - \boldsymbol{\tau}\cdot\mathbf{D}. \tag{10}$$

Bernoulli-Euler Beam Model

We consider deformations confined to the (x_2, x_3) plane (Fig. 1) with $\xi^2 = \eta$, $\xi^3 = \zeta$ such that $\zeta = 0$ defines the mid-surface. Then

$$\mathbf{r} = \mathbf{r}_0 + \zeta\mathbf{n}; \quad \mathbf{R} = \mathbf{R}_0 + \zeta(\lambda\mathbf{N})$$

where $\lambda(\eta, \zeta)$ is introduced to account for thickness changes. Expand λ in a Taylor series about $\zeta = 0$ and retain the lowest-order term: $\lambda(\eta, \zeta) = \lambda_0(\eta) + 0(\zeta)$. We assume that $\lambda_0(\eta)$ is a slowly varying function: $\lambda_0'(\eta) \simeq 0$.

The displacement vector is

$$\mathbf{u} = \mathbf{R} - \mathbf{r} = \mathbf{u}_0 + \zeta(\lambda\mathbf{N} - \mathbf{n});$$

$$\mathbf{u}_0 = \mathbf{R}_0 - \mathbf{r}_0 \equiv v(\eta)\mathbf{a} + w(\eta)\mathbf{n}$$

where $\mathbf{a} = \mathbf{r}_0'(\eta)$ is the unit tangent to the undeformed mid-surface. With $\mathbf{n}'(\eta) = \mathbf{a}/R$ [6] we have

$$\mathbf{g}_2 = (1 + \zeta/R)\mathbf{a}; \quad \mathbf{g}_3 = \mathbf{n}; \quad g = (1 + \zeta/R)^2$$

Copyright © 1983 by ASME
Downloaded 02 May 2010 to 171.66.16.250. Redistribution subject to ASME license or copyright; see http://www.asme.org/terms/Terms_Use.cfm

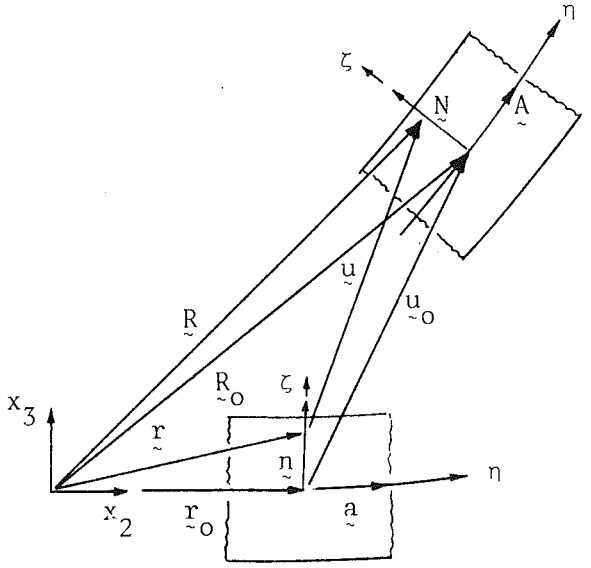


Fig. 1

Here R is the local radius of curvature (positive when the center of curvature lies in the $-\mathbf{n}$ direction). For slender beams $\zeta/R \ll 1$. Then $\mathbf{g}_2 \simeq \mathbf{a}$, $g_{22} \simeq g^{22} \simeq 1$, $g \simeq 1$. We also have

$$\mathbf{G}_2 \simeq \mathbf{A} + \zeta\lambda_0\mathbf{N}'; \quad \mathbf{G}_3 \simeq \lambda_0\mathbf{N} \tag{11}$$

with

$$\mathbf{A} = \mathbf{R}_o' = (\mathbf{r}_0 + \mathbf{u}_0)' = (1+\chi)\mathbf{a} + \psi\mathbf{n}$$

and

$$\chi = v' + w/R; \quad \psi = w' - v/R$$

where we have used the relation $\mathbf{a}'(\eta) = -\mathbf{n}/R$ [6]. The current unit normal is given by $\mathbf{N} = \mathbf{i}\times\mathbf{A}/|\mathbf{i}\times\mathbf{A}|$ where $\mathbf{i}\times\mathbf{A} = (1+\chi)\mathbf{n} - \psi\mathbf{a}$. Then

$$\mathbf{N} = (1+2\mathring{\gamma})^{-1/2}[(1+\chi)\mathbf{n} - \psi\mathbf{a}]$$

where

$$\mathring{\gamma} = \chi + \frac{1}{2}(\chi^2 + \psi^2).$$

From (11) we obtain

$$G_{33} = \lambda_0^2;$$
$$G_{23} = \lambda_0\mathbf{N}\cdot(\mathbf{A} + \zeta\lambda_0\mathbf{N}') = 0;$$
$$G_{22} = \mathbf{A}\cdot\mathbf{A} + 2\zeta\lambda_0\mathbf{A}\cdot\mathbf{N}' + 0(\zeta^2);$$
$$G = \lambda_0^2(\mathbf{A}\cdot\mathbf{A}) + 0(\zeta).$$

For finite straining dominated by plasticity it is reasonable to suppose that the deformation is approximately isochoric ($G = g$). Then

$$\lambda_0 = (\mathbf{A}\cdot\mathbf{A})^{-1/2} = (1+2\mathring{\gamma})^{-1/2}.$$

Thus

$$\mathbf{N} = \lambda_0[(1+\chi)\mathbf{n} - \psi\mathbf{a}] \text{ and } \mathbf{A}\cdot\mathbf{N}' = \lambda_0\left[\kappa + \frac{1}{R}(1+2\mathring{\gamma})\right] \text{ where}$$
$$\kappa \equiv \psi\chi' - (1+\chi)\psi'.$$

Neglecting the $0(\zeta/R)$ term gives

$$G_{22} = 1 + 2\left(\mathring{\gamma} + \frac{\zeta\kappa}{1+2\mathring{\gamma}}\right) + 0(\zeta^2).$$

Then

$$\gamma = \frac{1}{2}(g^{ik}G_{kj} - \delta^i_j)\mathbf{g}_i\mathbf{g}^j = \gamma_2^2\mathbf{g}_2\mathbf{g}^2 + \gamma_3^3\mathbf{g}_3\mathbf{g}^3$$

$$\gamma_2^2 = \mathring{\gamma} + \frac{\zeta\kappa}{1+2\mathring{\gamma}}, \quad \gamma_3^3 = \frac{1}{2}\left(\frac{1}{1+2\mathring{\gamma}} - 1\right) \tag{12}$$

Neglecting a term of order ζ/R leads to the displacement field

$$\mathbf{u} = \mathbf{u}_0 + \zeta(\lambda_0\mathbf{N} - \mathbf{n}) = u^2\mathbf{g}_2 + u^3\mathbf{g}_3;$$
$$u^2 = v - \zeta\psi/(1+2\gamma), \quad u^3 = w + \zeta(1+\chi)/(1+2\mathring{\gamma}) - \zeta. \tag{13}$$

Equations (12) and (13) are valid if $\lambda_0'(\eta)$ is negligible. This is evidently equivalent to the restrictions $|\mathring{\gamma}'(\eta)| \ll 1$ and $G_{23} = 0$. The latter condition implies zero shear deformation and the consequent reaction stress τ^{23} $(\mathbf{G}_2\mathbf{G}_3 + \mathbf{G}_3\mathbf{G}_2)$ [7]. This stress is not determined by the deformation and is assumed to have no influence on yielding. We retain the classical assumption that the only additional physical component of Kirchhoff stress is the membrane component τ_2^2:

$$\tau = \tau_2^2\mathbf{G}_2\mathbf{G}^2 + \tau^{23}(\mathbf{G}_2\mathbf{G}_3 + \mathbf{G}_3\mathbf{G}_2) \tag{14}$$

Then (7) gives

$$S_2^2 = \tau_2^2/(1+2\gamma_2^2), \quad S_3^3 = 0. \tag{15}$$

From (6),

$$\mathbf{D} = D_2^2\mathbf{G}_2\mathbf{G}^2 + \dot{\lambda}_0/\lambda_0\mathbf{G}_3\mathbf{G}^3; \quad D_2^2 = \dot{\gamma}_2^2/(1+2\gamma_2^2). \tag{16}$$

Then (10), (14), (16), and (8) give $\mathring{\tau}_2^2 = \dot{\tau}_2^2$, $\mathring{\tau}_3^3 = 0$,

$$\dot{\tau}_2^2 = \mathrm{E}D_2^2 \tag{17}$$

In the sequel we drop indices and write $\tau = \tau_2^2$, $D = D_2^2$, $S = S_2^2$, $\gamma = \gamma_2^2$.

The modeling of configuration-dependent loading is of interest in finite deformation analysis [8–10]. In the quasi-static case, pressure of prescribed magnitude may "follow" the deformation of the material surface. In the dynamic case it may be impossible to prescribe the pressure intensity independently of the structural response. However, this may serve as an approximation for loadings of interest (e.g., blast loading, pressure impulses).

For illustrative purposes we consider pressure of prescribed intensity $p(\eta,t)$,

$$\mathbf{T} = p\mathbf{N},$$

assumed to act at the midsurface ($\zeta = 0$). Then $d\mathbf{P} = p\mathbf{N}dA$ with

$$dA = |b\mathbf{i}\times d\mathbf{R}_0| = |\mathbf{i}\times\mathbf{A}|bd\eta = (1+2\mathring{\gamma})^{1/2}dA_0$$

where b is the width of the beam and $dA_0 = bd\eta$. Then the nominal traction is

$$\mathbf{t} = d\mathbf{P}/dA_0 = p[(1+\chi)\mathbf{n} - \psi\mathbf{a}] \tag{18}$$

In this study the subelement method is used to simulate strain-hardening behavior [5, 11–13]. Material elements are supposed to consist of equally strained "subelements" of elastic-perfectly plastic material with common modulus and varying yield stresses. The weighted sum of the subelement stresses at time t gives the actual stress at the material point in question:

$$\tau = \Sigma_1^n(A_k\tau_k) \tag{19}$$

where n is the number of subelements employed. The weights are given by

$$A_k = (\mathrm{E}_k^T - \mathrm{E}_{k+1}^T)/\mathrm{E}; \quad \Sigma A_k = 1$$

where

$$\mathrm{E}_1^T = \mathrm{E}, \ \mathrm{E}_k^T = (\tau_k - \tau_{k-1})/(e_k - e_{k-1}), \ \mathrm{E}_{n+1}^T = 0.$$

Here E_k^T is the slope of the kth segment of the piecewise linear representation of the actual Kirchhoff stress-logarithmic strain curve, defined by coordinates (τ_k, e_k). The accuracy of the representation is enhanced by increasing the number of subelements. The quasi-static yield stress of the kth subelement is $Y_k^0 = \mathrm{E}e_k$. Requiring each subelement to undergo the same deformation and noting (17) and (19) gives

Downloaded 02 May 2010 to 171.66.16.250. Redistribution subject to ASME license or copyright; see http://www.asme.org/terms/Terms_Use.cfm

$$\Sigma A_\rho \dot{\tau}_k = \dot{\tau} = E\dot{D} = \left(\Sigma A_\rho\right) E\dot{D}.$$

Thus for elastic increments

$$\dot{\tau}_k = E\dot{D}; \quad (\tau_k)^2 \le (Y_k)^2 \tag{20}$$

where Y_k is the instantaneous subelement yield stress. For inelastic increments the equality in (20*b*) holds. Rate dependence of the yield stress may be accounted for by the Cowper-Symonds relation [14]

$$Y_k = Y_k^0(1 + |D/d|^{1/p}) \tag{21}$$

with d and p material constants taken to be equal for all subelements. Since each subelement experiences the same strain (15*a*) gives $\tau_k = (1+2\gamma)S_k$ whence

$$(1+2\gamma)S = \tau = \Sigma A_k \tau_k = (1+2\gamma)\Sigma A_k S_k.$$

Then $S = \Sigma A_k S_k$. From (15)–(17),

$$\dot{S}_k(1+2\gamma) + 2S_k\dot{\gamma} = E\dot{\gamma}/(1+2\gamma)$$

whence

$$dS_k = \left[\frac{E - 2(1+2\gamma)S_k}{(1+2\gamma)^2}\right] d\gamma$$

during an elastic increment. This may be integrated from time t_{n-1} to t_n by the midpoint rule. With a view to subsequent calculations employing iteration and dropping subscript k,

$$S_{n,j} = S_{n-1} + \left\{\frac{E - 2S_{n-1}[(1+2\gamma_{n,j}) - \Delta\gamma]}{(1+2\gamma_{n,j})^2 - 2(1+2\gamma_{n,j})\Delta\gamma + (\Delta\gamma)^2}\right\}\Delta\gamma \tag{22}$$

where $\Delta\gamma = \gamma_{n,j} - \gamma_{n-1}$ and subscripts n,j refer to the time step and iteration cycle, respectively. To compute the subelement stress we assume the increment is elastic and use (22) to obtain the trial value $\hat{S}$. If $[\hat{S}(1+2\gamma_{n,j})]^2 \le (Y_k)^2$ with Y_k given by (21), then the assumption is correct and $S_k = \hat{S}$. If $\hat{S} \gtrless Y_k/(1+2\gamma_{n,j})$ then $S_k = \pm Y_k/(1+2\gamma_{n,j})$, respectively.

The subelement method outlined in the foregoing predicts Bauschinger and hysteretic effects which may be important for cyclic straining associated with dynamic response.

Numerical Method

With (12) and (15) the Principle of Virtual Displacements [15] becomes

$$\int_{V_0} S_2^2 \delta\gamma_2^2 dV_0 = \int_{A_0} \mathbf{t}\cdot\delta\mathbf{u} dA_0 - \int_{V_0} \rho_0 \ddot{\mathbf{u}}\cdot\delta\mathbf{u} dV_0 \tag{23}$$

where ρ_0 is the mass density in the initial configuration occupying volume V_0, δ denotes the variation with respect to $\mathbf{u}$, and the traction integral is evaluated at the midsurface ($\zeta = 0$). We restrict attention to the initially flat beam ($|R| \to \infty$). The basic variable is the midsurface displacement $\mathbf{u}_0$. Cubic Hermite polynomials are employed to represent the components v, w. Then

$$\mathbf{u}_0 \equiv \mathbf{U}\mathbf{q}; \quad \mathbf{q}^T = [v_1\, w_1\, \psi_1\, \chi_1\, v_2\, w_2\, \psi_2\, \chi_2]$$

for a two-node element and

$$\chi \equiv \mathbf{D}_1^T\mathbf{q}; \quad \psi \equiv \mathbf{D}_2^T\mathbf{q}; \quad -\psi' \equiv \mathbf{D}_3^T\mathbf{q}; \quad \chi' \equiv \mathbf{D}_4^T\mathbf{q}. \tag{24}$$

With (24) we compute $\mathring{\gamma}$, κ, and γ_2^2. Equation (23) gives the equations of motion:

$$\mathbf{R} \equiv \mathbf{M}\,\ddot{\mathbf{q}} + \mathbf{I} - \mathbf{F} = \mathbf{0}; \quad \mathbf{I} = \mathbf{P} + \mathbf{H}\,\mathbf{q} \tag{25}$$

where

$$\mathbf{P} = \int(\alpha\mathbf{D}_1 + \beta\mathbf{D}_3)d\eta;$$

$$\mathbf{H} = \int[\alpha(\mathbf{D}_1\mathbf{D}_1^T + \mathbf{D}_2\mathbf{D}_2^T) + \beta(\mathbf{D}_1\mathbf{D}_3^T + \mathbf{D}_3\mathbf{D}_1^T + \mathbf{D}_2\mathbf{D}_4^T + \mathbf{D}_4\mathbf{D}_2^T)]d\eta;$$

$$\alpha = L - 2M\kappa/(1+2\mathring{\gamma})^2; \quad \beta = M/(1+2\mathring{\gamma});$$

$$L = b\int S_2^2 d\zeta; \quad M = b\int S_2^2 \zeta d\zeta$$

and

$$\mathbf{F} = b\int p\mathbf{U}^T(1 + \mathbf{D}_1^T\mathbf{q} - \mathbf{D}_2^T\mathbf{q})d\eta$$

From (13) we note that $\mathring{\gamma}$ and $(\mathring{\gamma})\cdot$ contribute to the rotatory inertia. Retention of these terms results in a deformation-dependent mass matrix. Since rotatory inertia constitutes a smaller influence than shear deformation (at least in linear analysis [16]), which is presently neglected, we omit these terms. The mass matrix is then based on the approximations

$$\dot{u}^2 \simeq \dot{v} - \zeta\dot{\psi}; \quad \dot{u}^3 \simeq \dot{w} + \zeta\dot{\chi}.$$

Substituting the generalized implicit backward-difference expression [17, 18]

$$\ddot{\mathbf{q}}_n = \frac{1}{h^2}\Sigma_0^m(\gamma_i\mathbf{q}_{n-i}) + \Sigma_1^m\left(\frac{\epsilon_i}{h}\dot{\mathbf{q}}_{n-i} + \phi_i\ddot{\mathbf{q}}_{n-i}\right);$$

$$h \equiv t_n - t_{n-1}$$

into (25*a*) gives $\mathbf{R}$ as a function of $\mathbf{q}_n$. If we have an approximation $\mathbf{q}$ to the solution of (25*a*) which is sufficiently close to the true solution $\mathbf{q}_n$ then

$$\mathbf{0} = \mathbf{R}(\mathbf{q}_n) \simeq \mathbf{R}(\mathbf{q}) + \mathbf{B}(\mathbf{q})(\mathbf{q}_n - \mathbf{q})$$

where $\mathbf{B}(\mathbf{q})$ is the Jacobian of $\mathbf{R}$ evaluated at $\mathbf{q}$. We employ this relation repeatedly at time t_n:

$$\mathbf{B}_{n,j}\mathbf{d}_j = -\mathbf{R}_{n,j}; \quad \mathbf{d}_j \equiv \mathbf{q}_{n,j+1} - \mathbf{q}_{n,j}; \quad j = 0, \ldots, J \tag{26}$$

where J is the number of cycles required for convergence. The convergence criteria used in conjunction with (26) are based on those suggested in [18]:

$$|\mathbf{d}_j| / |\mathbf{q}_{n,j+1}| \le \epsilon_q; \quad |\mathbf{R}_{n,j}| / |\mathbf{R}_{n,0}| \le \epsilon_R \tag{27}$$

and

$$\mathbf{d}_j^T\mathbf{R}_{n,j} \le \mathbf{d}_0^T\mathbf{R}_{n,0} \quad \text{for all } j.$$

Presently quasi-Newton methods [18–21] are used to update the inverse Jacobian directly:

$$\mathbf{d}_j = -\mathbf{H}_j\mathbf{R}_{n,j}; \quad \mathbf{H}_j \equiv \mathbf{B}_{n,j}^{-1}.$$

Among the most popular and effective of these that preserve symmetry and positive-definiteness are the rank-two Davidon-Fletcher-Powell (DFP) update

$$\mathbf{H}_{j+1} = \mathbf{H}_j + \mathbf{d}_j\mathbf{d}_j^T/(\mathbf{d}_j^T\mathbf{y}_j) - \mathbf{H}_j\mathbf{y}_j\mathbf{y}_j^T\mathbf{H}_j/(\mathbf{y}_j^T\mathbf{H}_j\mathbf{y}_j),$$

$$\mathbf{y}_j \equiv \mathbf{R}_{j+1} - \mathbf{R}_j$$

and the Broyden-Fletcher-Goldfarb-Shanno (BFGS) update

$$\mathbf{H}_{j+1} = [\mathbf{I} - \mathbf{d}_j\mathbf{y}_j^T/(\mathbf{y}_j^T\mathbf{d}_j)]\mathbf{H}_j[\mathbf{I} - \mathbf{y}_j\mathbf{d}_j^T/(\mathbf{y}_j^T\mathbf{d}_j)] + \mathbf{d}_j\mathbf{d}_j^T/(\mathbf{y}_j^T\mathbf{d}_j)$$

where $\mathbf{I}$ is the unit matrix. A simple rank-one correction that preserves symmetry is the Davidon update

$$\mathbf{H}_{j+1} = \mathbf{H}_j + (\mathbf{d}_j - \mathbf{H}_j\mathbf{y}_j)(\mathbf{d}_j - \mathbf{H}_j\mathbf{y}_j)^T/[(\mathbf{d}_j - \mathbf{H}_j\mathbf{y}_j)^T\mathbf{y}_j].$$

For nonsymmetric equations (e.g., deformation-dependent loading), Engelman et al. [22] suggest the Broyden update

$$\mathbf{H}_{j+1} = \mathbf{H}_j + (\mathbf{d}_j - \mathbf{H}_j\mathbf{y}_j)\mathbf{d}_j^T\mathbf{H}_j/(\mathbf{d}_j^T\mathbf{H}_j\mathbf{y}_j).$$

Efficient schemes for utilizing the BFGS and Davidon updates for large systems have been presented in [20, 21], respectively. We take the initial trials as [18]:

$$\mathbf{q}_{n,0} = \mathbf{q}_{n-1}; \quad \mathbf{I}_{n,0} = \mathbf{I}_{n-1}; \quad \mathbf{P}_{n,0} = \mathbf{P}_{n-1}; \quad \mathbf{F}_{n,0} = \mathbf{F}_{n-1}$$

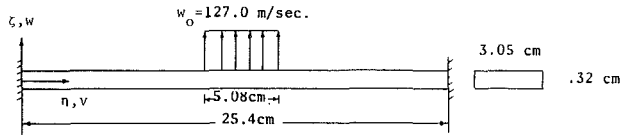
so that the only explicit matrix computation required is

$$\mathbf{B}_{0,0} = \frac{\gamma_0}{h^2}\mathbf{M} + \mathbf{K} - \mathbf{K}^F$$

where $\mathbf{K}$ is the linearly elastic stiffness matrix corresponding to the unstrained configuration at time zero and $\mathbf{K}^F$ is the constant asymmetric Jacobian of $\mathbf{F}$.

To compute the strain rate in (21) we may use the consistent approximation

Downloaded 02 May 2010 to 171.66.16.250. Redistribution subject to ASME license or copyright; see http://www.asme.org/terms/Terms_Use.cfm



$\rho_o = 2.67\times10^{-5}$ N-sec^2/cm^4

EL-PP: $E = 7.17\times10^{10}$ Pa

$Y^o = 2.85\times10^{8}$ Pa

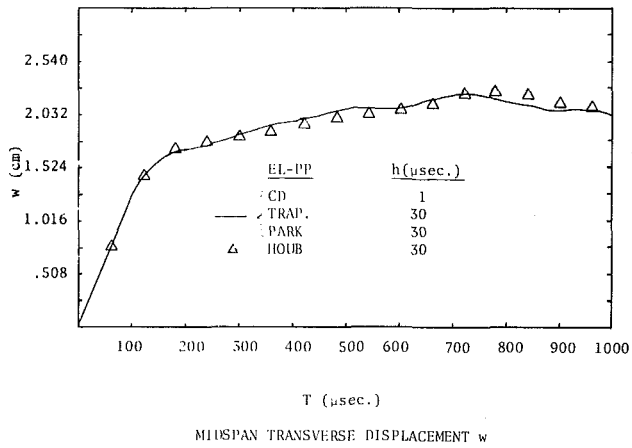
SR: d = 6500/sec, p = 4

EL-SH: $(\tau_1, e_1) = 2.85\times10^{8}$ Pa, .00398)

$(\tau_2, e_2) = 3.39\times10^{8}$ Pa, .07500)

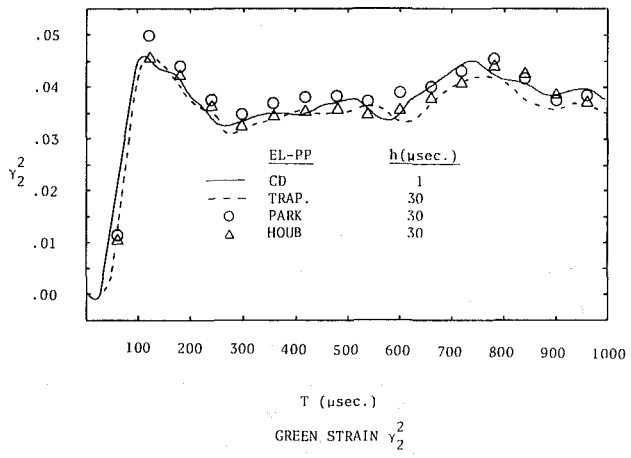
$(\tau_3, e_3) = 5.27\times10^{8}$ Pa, .61500)

Fig. 2 Example problem



MIDSPAN TRANSVERSE DISPLACEMENT w

Fig. 3(*a*)



GREEN STRAIN γ_2^2

Fig. 3(*b*)

Fig. 3 Transverse displacement w ($\eta = 12.7$ cm) and Green strain γ_2^2 ($\eta = 12.413$ cm, $\zeta = 0.137$ cm)

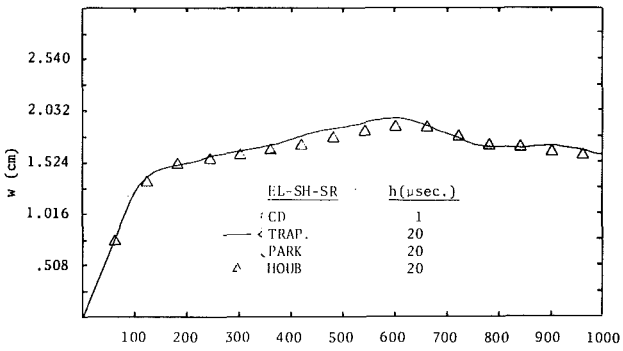
$$\dot{\gamma} = (\partial\gamma/\partial\mathbf{q})^T \dot{\mathbf{q}}_n \tag{28}$$

where [17, 18]

$$\dot{\mathbf{q}}_n = \frac{1}{h}\Sigma_0^m(\omega_i \mathbf{q}_{n-i}) + \Sigma_1^m(\rho_i \dot{\mathbf{q}}_{n-i} + h\sigma_i \ddot{\mathbf{q}}_{n-i}).$$

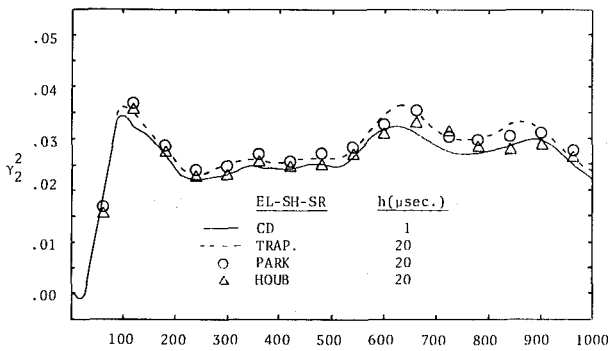
Applications

The preceding analysis has been applied to the problem shown in Fig. 2: a doubly clamped beam subjected to a large initial velocity distributed over the center span. Two cases are considered:



MIDSPAN TRANSVERSE DISPLACEMENT w

Fig. 4(*a*)



GREEN STRAIN γ_2^2

Fig. 4(*b*)

Fig. 4 Transverse displacement w ($\eta = 12.7$ cm) and Green strain γ_2^2 ($\eta = 12.413$ cm, $\zeta = 0.137$ cm)

(*i*) elastic-perfectly plastic (*EL-PP*) rate-insensitive material [$n = 1$ in (19) and $Y = Y^0$].

(*ii*) elastic strain-hardening, strain-rate sensitive (*EL-SH-SR*) material [$n = 3$ in (19) with Y_k given by (21) and $\dot{\gamma}$ given by (28)].

Owing to symmetry only the left half-span is modeled. In Figs. 3, 4 the midspan ($\eta = 12.7$ cm) transverse displacement w and Green strain γ ($\eta = 12.413$ cm, $\zeta = .137$ cm) (see Fig. 2) are plotted. Four depthwise Gauss points are used to evaluate the axial force, bending moment, and strain rate at each of three spanwise stations per element.

To facilitate a comparative study of various solution methods, a coarse mesh of five equal length elements is used. The integration methods employed here are the implicit Park and Houbolt (HOUB.) operators and the trapezoidal rule (TRAP.) [17, 18]. A converged baseline solution has been obtained for the preceding cases (*i*) and (*ii*) using the explicit central difference (CD) method applied directly to (25*a*). The critical CD step size [18] for the corresponding linear problem is 1.4 μsec. The converged solutions were obtained using $h = 1$ μsec. Each implicit integration method is combined with various quasi-Newton corrections using $\epsilon_q = \epsilon_R = 10^{-3}$ in (27).

For case (*i*) the DFP update proves to be marginally more efficient than the Davidon and BFGS methods, while the BFGS update is superior for (*ii*). Here the DFP and Davidon methods frequently exhaust the allowable number of iteration cycles without achieving convergence.

Downloaded 02 May 2010 to 171.66.16.250. Redistribution subject to ASME license or copyright; see http://www.asme.org/terms/Terms_Use.cfm

Table 1 Summary of examples ($\epsilon_q = \epsilon_R = 10^{-3}$)

method	h(μsec.)	material behavior	iteration method	mean # iter. per step	relative CPU
CD	1	EL-PP	--	--	1
TRAP.	30	EL-PP	DFP	5.80	.306
PARK	30	EL-PP	DFP	7.00	.344
HOUB.	30	EL-PP	DFP	7.46	.363
CD	1	EL-SH-SR	--	--	1.255
TRAP.	20	EL-SH-SR	BFGS	5.20	.701
PARK	20	EL-SH-SR	BFGS	5.32	.734
HOUB.	20	EL-SH-SR	BFGS	5.78	.780

Table 1 suggests greater efficiency for the trapezoidal rule and Park method. However, numerical experiments indicate that the Houbolt method is generally superior as step sizes become very large (50–100 μsec) [23].

In [24], Mikkola et al. report on applications of explicit and implicit methods (including those presently employed) to a problem very similar to that analyzed here. They conclude that explicit methods are more reliable and efficient than implicit methods combined with Picard iteration (successive substitution) and intermittent reformation of the coefficient matrix. The present study demonstrates that implicit integration schemes are more effective when used in conjunction with quasi-Newton methods. In particular, Picard iteration is known to be ineffective for highly nonlinear problems [20, 23].

Summary

The basic features of the transient finite strain elastic-viscoplastic analysis of thin structures have been presented for the simple case of bending-stretching of a beam undergoing planar deformations.

Numerical experiments indicate that quasi-Newton methods provide efficient and reliable solutions of the algebraic equations associated with implicit backward-difference operators, which appear to be unconditionally stable in the applications considered. The inclusion of a consistent representation of strain-rate dependence is seen to compromise the efficiency of implicit methods, however.

The development of improved iterative methods for solving nonlinear equations [25] is expected to lead to increasingly efficient implicit solutions.

Acknowledgment

The authors gratefully acknowledge the support of NASA Grant NGR 22-009-339 for the work reported in references [1, 23], on which this paper is based.

References

1 Rodal, J. J. A., and Witmer, E. A., "Finite Strain Large Deflection Elastic-Viscoplastic Finite Element Transient Response Analysis of Structures," MIT ASRL TR154-15, July 1979 (NASA CR-159874).

2 Sedov, L. I., *Foundations of the Non-Linear Mechanics of Continua*, translation edited by Adkins, J. E., and Spencer, A. J. M., Pergamon Press, 1966.

3 Green, A. E., and Zerna, W., *Theoretical Elasticity*, Oxford University Press, 2nd Ed., 1968.

4 Lodge, A. S., *Elastic Liquids*, Academic Press, New York, 1964.

5 Rodal, J. J. A., "Finite Strain Elastic-Viscoplastic Transient Response of Thin Structures," in *Plasticity of Metals at Finite Strain: Theory, Computation and Experiment*, Lee, E. H., and Mallett, R. L., eds., Stanford University, Stanford, Calif., and Rensselaer Polytechnic Inst., Troy, N.Y., 1981.

6 Spain, B., *Tensor Calculus*, Oliver and Boyd, Edinborough, 1956.

7 Chadwick, P., *Continuum Mechanics: Concise Theory and Problems*, Wiley, New York, 1976.

8 Sewell, M. J., "On Configuration Dependent Loading," *Arch. Rat. Mech.*, Vol. 23, 1966, pp. 327–351.

9 Needleman, A., "Finite Elements for Finite Strain Plasticity Problems," in *Plasticity of Metals at Finite Strain: Theory, Computation and Experiment*, Lee, E. H., and Mallett, R. L., eds., Stanford University, Stanford, Calif., and Rensselaer Polytechnic Inst., Troy, N.Y., 1981.

10 Oden, J. T., *Finite Elements of Nonlinear Continua*, McGraw-Hill, New York, 1972.

11 Besseling, J. F., "A Theory of Plastic Flow for Anisotropic Hardening in Plastic Deformation of an Initially Isotropic Material," Rep. S410, National Aeronautical Research Institute, Amsterdam, 1953.

12 Zienkiewicz, O. C., Nayak, G. C., and Owens, K. R. J., "Composite and Overlay Models in Numerical Analysis of Elastic-Plastic Continua," in *Foundations of Plasticity*, Sawczuk, A., ed., Noordhoff, Leyden, 1973.

13 Hunsaker, B. Jr., Vaughn, D. K., Stricklin, J. A., and Haisler, W. E., "A Comparison of Current Work-Hardening Models Used in the Analysis of Plastic Deformations," Texas A&M University, Department of Aerospace Engineering, TEES-RPT-2926-73-3, Oct. 1973.

14 Bodner, S. R., and Symonds, P. S., "Experimental and Theoretical Investigation of the Plastic Deformation of Cantilever Beams Subjected to Impulsive Loading," ASME JOURNAL OF APPLIED MECHANICS, Vol. 29, 1962, pp. 719–728.

15 Washizu, K., *Variational Methods in Elasticity and Plasticity*, 2nd ed., Pergamon Press, 1975.

16 Timoshenko, S., Young, D. H., and Weaver, W., *Vibration Problems in Engineering*, 4th ed., Wiley, New York, 1974.

17 Park, K. C., "An Improved Stiffly Stable Method for Direct Integration of Nonlinear Structural Dynamics Equations," ASME JOURNAL OF APPLIED MECHANICS, Vol. 42, 1975, pp. 464–470.

18 Bathe, K.-J., *Finite Element Procedures in Engineering Analysis*, Prentice-Hall, Englewood Cliffs, N.J., 1982.

19 Dennis, J. E., and Moré, J., "Quasi-Newton Methods: Motivation and Theory," *SIAM Rev.*, Vol. 19, 1977, pp. 46–89.

20 Matthies, H., and Strang, G., "The Solution of Nonlinear Finite Element Equations," *Int. J. Num. Meth. Eng.*, Vol. 14, 1979, pp. 1613–1626.

21 Geradin, M., Idelsohn, S., and Hogge, M. A., "Computational Strategies for the Solution of Large Nonlinear Problems via Quasi-Newton Methods," *Computers and Structures*, Vol. 13, 1981, pp. 73–81.

22 Engelman, M. S., Strang, G., and Bathe, K.-J., "The Application of Quasi-Newton Methods in Fluid Mechanics," *Int. J. Num. Meth. Eng.*, Vol. 17, 1981, pp. 707–718.

23 Steigmann, D. J., "Finite Strain Structural Response Predictions by Implicit Integration Methods," M.S. Thesis, M.I.T., Cambridge, Mass., 1981.

24 Mikkola, M. J., Tuomala, M., and Sinsalo, H., "Comparison of Numerical Integration Methods in the Analysis of Impulsively Loaded Elasto-Plastic and Viscoplastic Structures," *Computers and Structures*, Vol. 14, 1981, pp. 469–478.

25 Zhang, L., and Owen, D. R. J., "A Modified Secant-Newton Method for Nonlinear Problems," *Computers and Structures*, Vol. 15, 1982, pp. 543–547.

Downloaded 02 May 2010 to 171.66.16.250. Redistribution subject to ASME license or copyright; see http://www.asme.org/terms/Terms_Use.cfm

The Penny-Shaped Interface Crack With Heat Flow

Part 2: Imperfect Contact

J. R. Barber

Maria Comninou
Mem. ASME

Department of Mechanical Engineering
And Applied Mechanics,
University of Michigan,
Ann Arbor, Mich. 48109

The penny-shaped crack with heat flux is investigated for the case in which the heat flux is into the material with the lower distortivity. A harmonic potential function representation is used to reduce the problem to a boundary value problem which is solved by an integral equation method. If a sufficiently high tensile traction is applied, a solution is obtained involving a central circle of separation and surrounding annuli of imperfect and perfect thermal contact. For lower tractions, or higher heat fluxes, the crack closes completely and a closed-form solution is obtained in which the division of the crack face into imperfect and perfect contact regions is unaffected by further changes in heat flux or traction. Multiple solutions are obtained in an intermediate range.

Introductions

In a previous paper [1], a solution was given for the thermal stress field due to the obstruction of a uniform heat flux by a penny-shaped crack at the interface between two dissimilar half spaces. The half spaces were simultaneously subjected to tractions tending to open the crack. The treatment was restricted to the case where the heat flows into the material of higher distortivity, for which an annular contact region is developed at the crack tip surrounding a circular region of separation. The extent of the contact region depends on the relative magnitude of mechanical and thermal effects and the behavior is qualitatively affected by the sign of the product $\beta\gamma$ where β is a Dundurs constant and γ is a constant describing the mismatch of distortivities.

In this paper, we will consider the same system for the opposite direction of heat flow. The difficulties that arise when heat flows across a unilateral interface into the material of lower distortivity have been extensively discussed in previous publications [2–5]. Briefly, under certain conditions, all steady-state solutions with the conventional boundary conditions violate the unilateral inequalities (contact tractions nontensile and no interpenetration). The difficulty can be avoided by making the physically more realistic assumption of a pressure or gap-dependent interface thermal resistance and a limiting case of this is the state of "imperfect thermal contact" defined in [4]. The boundary conditions involving imperfect contact have been used to sovle a number of thermoelastic contact problems which are otherwise ill-posed [4, 6–8] and the reader is referred to these papers for further details.

Statement of the Problem

The geometry of the problem is illustrated in Fig. 1. The interface is the plane $z=0$ in cylindrical polar coordinates and the dissimilar half spaces $z>0$, $z<0$ are referred to by suffices, 1, 2, respectively. A uniform heat flux, $q_z=q_0$ and a uniform tenion, $\sigma_{zz}=\sigma_0$ are imposed distant from the crack, which extends over $0\le r\le c$, $z=0$. We assume provisionally that the arrangement of contact zones is the same as in [1] except that an annular region of imperfect contact is required between perfect contact and separation as shown in Fig. 1. The validity of this assumption can only be tested a posteriori by its ability to generate solutions satisfying the unilateral contact inequalities. It is also assumed that contact between the crack faces is frictionless.

As in [1] we denote coefficient of thermal epansion, thermal conductivity, modulus of rigidity, Poisson's ratio, and thermal distortivity by α, k, μ, ν, and δ, respectively, and we note that the direction of heat flux under consideration corresponds to

$$q_0(\delta_1-\delta_2)<0 \tag{1}$$

Mathematical Formulation

The initial stages of the solution are identical with [1] and will be omitted here in the interests of brevity. We note that the problem is formulated as a perturbation on the state of uniform traction σ_0 and uniform heat flux q_0. The displacement and temperature fields are represented in terms of three harmonic functions ω, ϕ, ψ and the problem is reduced to a mixed boundary value problem for the half space $z>0$ by using appropriate symmetry conditions.

Contributed by the Applied Mechanics Division and presented at the Winter Annual Meeting, Boston, Mass., November 13–18, 1983 of THE AMERICAN SOCIETY OF MECHANICAL ENGINEERS.

Discussion on this paper should be addressed to the Editorial Department, ASME, United Engineering Center, 345 East 47th Street, New York, N.Y. 10017, and will be accepted until two months after final publication of the paper itself in the JOURNAL OF APPLIED MECHANICS. Manuscript received by ASME Applied Mechanics Division, July, 1982; final revision, April, 1983. Paper No. 83-WA/APM-13.

Copies will be available until July, 1984.

Copyright © 1983 by ASME
Downloaded 02 May 2010 to 171.66.16.250. Redistribution subject to ASME license or copyright; see http://www.asme.org/terms/Terms_Use.cfm

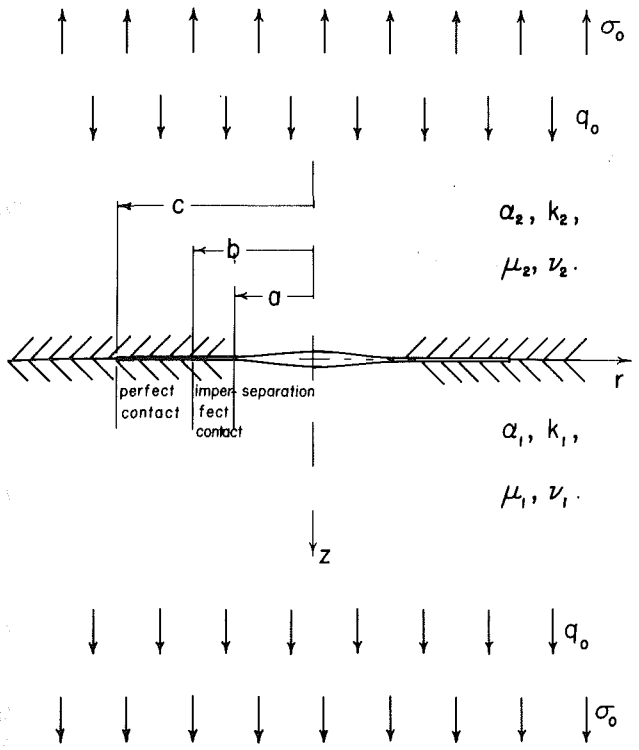


Fig. 1 Geometry of the problem

The boundary conditions for this problem—derived from the conditions at the crack plane—differ from those in [1] only through the inclusion of the region of imperfect contact, $a<r<b$, which can be defined as a region of contact in which the contact pressure is negligibly small permitting significant thermal contact resistance between the crack faces [4].

Using the formulation in [1] we obtain the following boundary conditions on the functions ω, ϕ, ψ at the plane $z=0$.

(*i*) The normal traction σ_{zz} is zero in the separation and imperfect contact regions:

$$\frac{\partial^2 \omega}{\partial z^2} = 0; \quad 0 \le r \le b \tag{2}$$

from [1], equation (8).

(*ii*) The shear traction σ_{rz} is zero throughout the crack face (all contact is frictionless):

$$\frac{\partial^2 \phi}{\partial r \partial z} = 0; \quad 0 \le r \le c \tag{3}$$

from [1] equation (10).

(*iii*) Normal displacement, u_z, is continuous everywhere *except* in the separation zone:

$$-B\frac{\partial \phi}{\partial z} - A\frac{\partial \omega}{\partial z} + (\delta_1 - \delta_2)\frac{\partial \psi}{\partial z} = 0; \quad r > a \tag{4}$$

from [1] equation (12).

(*iv*) Radial displacement, u_r, is continous in the bonded region:

$$A\frac{\partial \phi}{\partial r} + B\frac{\partial \omega}{\partial r} - (\delta_1 + \delta_2)\frac{\partial \psi}{\partial r} = 0; \quad r > c \tag{5}$$

from [1] equation (13).

(*v*) Temperature is continuous in the perfect contact region and in the bond:

$$\frac{\partial^2 \psi}{\partial z^2} = 0; \quad r > b \tag{6}$$

from [1] equation (16), and finally

(*vi*) The heat flux q_z is zero in the separation region

$$\frac{\partial^3 \psi}{\partial z^3} = q_0; \quad 0 \le r \le a \tag{7}$$

from [1] equation (9).

Note that these six conditions fall into the three pairs (2), (6); (3), (5); and (4), (7), each of which covers the entire plane $z=0$.

Isolation of Discontinuities

As in [1], it is convenient to isolate the discontinuities in the displacement field which arise at each of the transitions ($r=a$, b, c) in three separate functions. This can be done by defining linear combinations χ, θ of ω, ϕ, ψ through the equations

$$\omega = -\beta\phi + \theta \tag{8}$$

$$\psi = \chi + \frac{A}{(\delta_1 - \delta_2)}\theta \tag{9}$$

where $\beta = B/A$ is Dundurs constant.

This gives the modified boundary conditions

$$\frac{\partial^3 \chi}{\partial z^3} + \frac{A}{(\delta_1 - \delta_2)}\frac{\partial^3 \theta}{\partial z^3} = q_0; \quad 0 \le r \le a, z = 0, \tag{10}$$

$$\frac{\partial \chi}{\partial z} = 0; \quad r > a, z = 0 \tag{11}$$

$$\frac{\partial^2 \theta}{\partial z^2} - \beta\frac{\partial^2 \phi}{\partial z^2} = \sigma_0; \quad 0 \le r \le b, z = 0 \tag{12}$$

$$\frac{\partial^2 \chi}{\partial z^2} + \frac{A}{(\delta_1 - \delta_2)}\frac{\partial^2 \theta}{\partial z^2} = 0; \quad r > b, z = 0 \tag{13}$$

$$\frac{\partial^2 \phi}{\partial r \partial z} = 0; \quad 0 \le r \le c, z = 0 \tag{14}$$

$$(1-\beta^2)\frac{\partial \phi}{\partial r} + A(\beta - 1/\gamma)\frac{\partial \theta}{\partial r} - \frac{(\delta_1 - \delta_2)}{A\gamma}\frac{\partial \chi}{\partial r} = 0; \quad r > c, z = 0 \tag{15}$$

where

$$\gamma = \frac{\delta_1 - \delta_2}{\delta_1 + \delta_2} \tag{16}$$

We note that γ will lie in the range $-1 \le \gamma \le +1$ unless one of the materials has a negative coeffcient of thermal expansion.

Solution Strategy

As in previous papers [1, 4, 6, 9] we will satisfy certain of these conditions identically by the repesentation of Green [10] and Collins [11] and use the remaining conditions to develop a set of coupled Abel equations. The procedure is lengthy because of the complexity of the boundary conditions and can only be briefly outlined here. The reader is referred to the cited papers for more details and simpler illustrations of the method.

The relations to be satisfied identically by the representation are shown in Table 1 and appropriate representations are

$$\frac{\partial \theta_2}{\partial z} = Re\int_0^b \frac{g_1(t)\,dt}{\sqrt{r^2 + (z+it)^2}} \tag{17}$$

$$\frac{\partial \phi}{\partial z} = Re\int_c^b \frac{g_2(t)\,dt}{\sqrt{r^2 + (z+it)^2}} + \frac{2C_1}{\pi} Im[\log(\sqrt{r^2 + (z+ic)^2} + z + ic)] \tag{18}$$

Downloaded 02 May 2010 to 171.66.16.250. Redistribution subject to ASME license or copyright; see http://www.asme.org/terms/Terms_Use.cfm

$$\frac{\partial \chi}{\partial z} = Im\int_0^a \frac{g_3(t)\,dt}{\sqrt{r^2+(z+it)^2}} \tag{19}$$

$$\frac{\partial \theta_1}{\partial z} = Im\int_b^\infty \frac{g_4(t)\,dt}{\sqrt{r^2+(z+it)^2}} \tag{20}$$

where g_1, g_2, g_3, g_4 are four unknown functions to be determined. Two of these representations (18) and (19) are identical with those used in [1] (equations (26) and (27)). Note that the function θ is decomposed into two parts θ_1, θ_2 ($\theta_1+\theta_2=\theta$). The arbitrary constant C_1 in equation (18) is a constant of integration of (14). The four remaining boundary conditions (10), (12), (13), and (15) which are *not* satisfied identically by the representations (17)-(20) give a set of coupled Abel integral equations for the four unknown functions g_1, g_2, g_3, and g_4.

For example, substituting (17), (19), and (20) into (13) gives

$$d/dr\int_0^a \frac{tg_3(t)\,dt}{\sqrt{r^2-t^2}} = -\frac{A}{(\delta_1-\delta_2)}\,d/dr\int_b^r \frac{tg_4(t)\,dt}{\sqrt{r^2-t^2}} \tag{21}$$

and hence on integration

$$\int_b^r \frac{tg_4(t)\,dt}{\sqrt{r^2-t^2}} = C_2 - \frac{(\delta_1-\delta_2)}{A}\int_0^a \frac{tg_3(t)\,dt}{\sqrt{r^2-t^2}}; \quad r>b \tag{22}$$

where

$$C_2 = \lim_{r\to\infty}\int_b^r \frac{tg_4(t)\,dt}{\sqrt{r^2-t^2}} \tag{23}$$

Appying the same technique to equations (10), (12), and (15) we find, respectively,

$$\int_r^a \frac{g_3(t)\,dt}{\sqrt{r^2-r^2}} = \frac{A}{(\delta_1-\delta_2)}\left[\int_0^r \frac{g_1(t)\,dt}{\sqrt{r^2-t^2}} - \int_b^\infty \frac{g_4(t)\,dt}{\sqrt{t^2-r^2}}\right] + \frac{q_0 r^2}{4} - C_5; \quad 0\le r\le a, \tag{24}$$

$$\int_r^b \frac{tg_1(t)\,dt}{\sqrt{t^2-r^2}} = \beta\int_c^\infty \left[\frac{t}{\sqrt{t^2-r^2}} - 1\right]g_2(t) + \frac{\sigma_0 r^2}{2} - \frac{2C_1\beta}{\pi}(c-\sqrt{c^2-r^2}) + C_3; \quad 0\le r\le b, \tag{25}$$

and

$$(1-\beta^2)\int_r^\infty \frac{tg_2(t)\,dt}{\sqrt{t^2-r^2}} = \frac{\beta(\delta_1-\delta_2)}{A}\int_0^a \frac{tg_3(t)\,dt}{\sqrt{r^2-t^2}} + (1-\beta^2)\left(C_4+\frac{2C_1 c}{\pi}\right) + (\beta-1/\gamma)(C_3-C_2); \quad r>c \tag{26}$$

where

$$C_4 = \int_c^\infty g_2(t)\,dt \tag{27}$$

and C_3 and C_5 are constants of integration.

Equations (22) and (24)-(26) are Abel integral equations and they can be solved by standard methods giving, respectively,

$$g_4(x) = \frac{-2(\delta_1-\delta_2)}{\pi A\sqrt{x^2-b^2}}\int_0^a \frac{t\sqrt{b^2-t^2}\,g_3(t)\,dt}{(x^2-t^2)} + \frac{2C_2}{\pi\sqrt{x^2-b^2}}; \quad x>b \tag{28}$$

$$g_3(x) = \frac{-2Ax}{\pi(\delta_1-\delta_2)\sqrt{a^2-x^2}}\left[\int_0^a \frac{t\sqrt{a^2-t^2}\,g_1(t)\,dt}{(t^2-x^2)} + \int_b^\infty \frac{t\sqrt{t^2-a^2}\,g_4(t)\,dt}{(t^2-x^2)}\right] + \frac{q_0 x(2x^2-a^2)}{2\pi\sqrt{a^2-x^2}} - \frac{2C_5 x}{\pi\sqrt{a^2-x^2}}; \quad 0\le x\le a \tag{29}$$

$$g_1(x) = \frac{2\beta}{\pi\sqrt{b^2-x^2}}\int_c^\infty \left[1-\frac{\sqrt{t^2-b^2}}{(t^2-x^2)}\right]g_2(t)dt + \frac{\sigma_0(2x^2-b^2)}{\pi\sqrt{b^2-x^2}} + \frac{4C_1\beta}{\pi^2}\left[\frac{(\sqrt{c^2-b^2}-c)}{\sqrt{b^2-x^2}} + \arctan\sqrt{\frac{b^2-x^2}{c^2-b^2}}\right] + \frac{2C_3}{\pi\sqrt{b^2-x^2}}; \quad 0\le x\le b \tag{30}$$

and

$$g_2(x) = \frac{2\beta(\delta_1-\delta_2)}{\pi A(1-\beta^2)}\int_0^a \frac{tg_3(t)\,dt}{(x^2-t^2)}; \quad x>c. \tag{31}$$

Note that equation (26) is of the same form as (34) of [1] and the inversion is only possible if the right-hand side vanishes at infinity. This imposes the supplementary condition.

$$(1-\beta^2)\left[\int_c^\infty g_2(t)\,dt + \frac{2C_1 c}{\pi}\right] + (\beta-1/\gamma)(C_3-C_2) = 0. \tag{32}$$

Auxiliary Conditions

The arbitrary constants in these equations and the unknown radii of the contact zones a and b are determined by applying appropriate conditions to the asymptotic behavior of the stress and temperature fields at $r=a,b$; $z=0$. In particular, we demand continuity of temperature at both these points and continuity of normal traction (σ_{zz}) at $r=b$ (i.e., the normal traction in the perfect contact zone must tend to zero at the transition to imperfect contact [5]).

The representations used (17)-(20) and Table 1 will ensure suitably continuous fields throughout the half space except possibly at the ends of the integration ranges. Thus, at $r=a$, $z=0$, a discontinuity can occur in χ and its derivatives, but not in the other functions θ_1, θ_2, ϕ. From (6) and (9) it follows that continuity of temperature at $r=a$ is equivalent to continuity of the derivative $\partial^2\chi/\partial z^2$ which from (19) is given by

$$\frac{\partial^2 \chi}{\partial z^2} = \frac{1}{r}\frac{d}{dr}\int_0^{\min r,a} \frac{tg_3(t)\,dt}{\sqrt{r^2-t^2}} \quad \text{on} \quad z=0. \tag{33}$$

This expression is singular at $r=a^-$ unless

$$\lim_{t\to a}\,(a-t)^{1/2}\,g_3(t)\,dt = 0 \tag{34}$$

and on substituting from (29) we obtain two auxiliary conditions, one of which serves to determine C_5. Substituting for C_5 back into (29) gives

$$g_3(x) = \frac{2Ax\sqrt{a^2-x^2}}{\pi(\delta_1-\delta_2)}\int_0^a \frac{(g_1(t)-g_1(a))\,dt}{(x^2-t^2)\sqrt{a^2-t^2}} + \frac{2Ax\sqrt{a^2-x^2}}{\pi(\delta_1-\delta_2)}\int_b^\infty \frac{g_4(t)\,dt}{(t^2-x^2)\sqrt{t^2-a^2}} - \frac{q_0 x\sqrt{a^2-x^2}}{\pi}$$
$$0\le x\le a. \tag{35}$$

The second condition obtained from (34) is

Downloaded 02 May 2010 to 171.66.16.250. Redistribution subject to ASME license or copyright; see http://www.asme.org/terms/Terms_Use.cfm

Table 1

	θ_1	θ_2	ϕ	χ
$0 \le r \le a$	$\frac{\partial^2 \theta_1}{\partial z^2} = 0$	Eqn (12)	$\frac{\partial^2 \phi}{\partial r \partial z} = 0$	Eqn (10)
$a < r \le b$				$\frac{\partial \chi}{\partial z} = 0$
$b < r \le c$	Eqn (13)	$\frac{\partial^2 \theta_2}{\partial z^2} = 0$		
$r > c$			Eqn (15)	

$$\frac{2A}{(\delta_1-\delta_2)}\int_0^a \frac{(g_1(t)-g_1(a))\,dt}{(a^2-t^2)^{3/2}} + \frac{2A}{(\delta_1-\delta_2)}\int_b^\infty \frac{g_4(t)\,dt}{(t^2-a^2)^{3/2}} - q_0. \tag{36}$$

Conditions for determining the remaining constants are obtained from considerations of continuity in temperature ($\partial^2\psi/\partial z^2$) and contact pressure ($\partial^2\omega/\partial z^2$) at the transition from perfect to imperfect contact ($r=b$). From equations (8) and (9) and the representations (17)–(20) it follows that both conditions are satisfied if

$$\lim_{r\to b+} \frac{\partial^2\theta_1}{\partial z^2} = \lim_{r\to b-} \frac{\partial^2\theta_2}{\partial z^2} \quad \text{on} \quad z=0. \tag{37}$$

From (17) and (20) it can be shown that these limits exist if and only if

$$g_1(b)=0; \quad g_4(b)=0 \tag{38}$$

and hence

$$C_3 = \beta\int_c^\infty g_2(t)\left(1-\frac{t}{\sqrt{t^2-b^2}}\right)dt - \frac{\sigma_0 b^2}{2} - \frac{2C_1\beta}{\pi}(\sqrt{c^2-b^2}-c) \tag{39}$$

$$C_2 = \frac{(\delta_1-\delta_2)}{A}\int_0^a \frac{tg_3(t)\,dt}{\sqrt{b^2-t^2}} \tag{40}$$

from (30) and (28), respectively. In addition (37) imposes the condition

$$\lim_{r\to b+}\int_b^r \frac{g_4'(t)\,dt}{\sqrt{r^2-t^2}} = \lim_{r\to b}\int_b^r \frac{g_1'(t)\,dt}{\sqrt{t^2-r^2}} \tag{41}$$

which simplifies to

$$\frac{(\delta_1-\delta_2)}{A}\int_0^a \frac{tg_3(t)\,dt}{(b^2-t^2)^{3/2}} = \beta\int_c^\infty \frac{tg_2(t)\,dt}{(t^2-b^2)^{3/2}} + \sigma_0 - \frac{2C_1\beta}{\pi\sqrt{c^2-b^2}} \tag{42}$$

using (28), (30), (39), and (40).

We note at this stage that equations (32), (36), and (42) are sufficient to determine the remaining unknown constant C_1 and the contact radii a, b.

Reduction to a Single Fredholm Equation

The next stage in the solution is to reduce the four equations (28), (30), (31), and (35) to a single Fredholm equation by substitution. We substitute (31) into (30) to eliminate g_2 and the resulting equation and (28) into (35) to eliminate g_1, g_4. The procedure is lengthly but routine and gives the Fredholm equation

$$g_3(x) + \frac{8\beta^2 x\sqrt{a^2-x^2}}{\pi^3(1-\beta^2)}\int_0^a sg_3(s)\,ds\int_0^a\left[\frac{(f(s)-f(t))\sqrt{b^2-t^2}}{(s^2t^2)} - \frac{(f(s)-f(a))\sqrt{b^2-a^2}}{(s^2-a^2)}\right]\frac{dt}{(x^2-t^2)\sqrt{a^2-t^2}}$$
$$- \frac{4x\sqrt{a^2-x^2}}{\pi^2}\int_0^a \frac{sg_3(s)\,ds}{\sqrt{b^2-s^2}}\int_b^\infty\left(\frac{t^2-b^2}{t^2-a^2}\right)^{1/2}\frac{dt}{(t^2-s^2)(t^2-x^2)}$$
$$= -\frac{4A\sigma_0 x\sqrt{a^2-x^2}}{\pi^2(\delta^1-\delta^2)}\int_0^a \frac{(\sqrt{b^2-t^2})-\sqrt{b^2-a^2})}{(x^2-t^2)\sqrt{a^2-t^2}}\,dt$$
$$+ \frac{8C_1\beta A_x\sqrt{a^2-x^2}}{\pi^3(\delta^1-\delta^2)}\int_0^a \frac{[\sqrt{b^2-t^2}f(t)-\sqrt{b^2-a^2}f(a)]}{(x^2-t^2)\sqrt{a^2-t^2}}$$
$$- \frac{q_0 x\sqrt{a^2-x^2}}{\pi}; \quad 0\le x\le a, \tag{43}$$

where

$$f(x) = \frac{\arctan\sqrt{\dfrac{b^2-x^2}{c^2-b^2}}}{\sqrt{b^2-x^2}} \tag{44}$$

Note that in the derivation of equation (43), the constants C_2 and C_3 were eliminated using (39) and (40).

The three auxiliary conditions (32), (36), and (42) can also be expressed in terms of g_3 alone by similar substitutions giving

$$\frac{\beta(\delta_1-\delta_2)}{\pi A}\int_0^a g_3(s)\log\left(\frac{c+s}{c-s}\right)ds - \frac{(\beta-1/\gamma)(\delta_1-\delta_2)}{A}\int_0^a \frac{sg_3(s)\,ds}{\sqrt{b^2-s^2}} + \frac{(\beta-1/\gamma)\beta^2(\beta_1-\delta_2)}{\pi A(1-\beta^2)}\left[\int_0^a g_3(s)\log\left(\frac{c+s}{c-s}\right)ds - 2\int_0^a sf(s)g_3(s)\,ds\right] - \frac{(\beta-1/\gamma)\sigma_0 b^2}{2}$$
$$- \frac{2C_1\beta(\beta-1/\gamma)}{\pi}(\sqrt{c^2-b^2}-c) + \frac{2C_1 c(1-\beta^2)}{\pi} = 0 \tag{45}$$

from (32), using (31), (39), and (40);

$$\int_0^a \frac{sg_3(s)\,ds}{\sqrt{b^2-s^2}}\int_b^\infty \frac{\sqrt{t^2-b^2}\,dt}{(t^2-s^2)(t^2-a^2)^{3/2}} - \frac{2\beta^2}{\pi(1-\beta^2)}\int_0^a sg_3(s)\,ds\int_0^a\left[\frac{f(s)-f(t)}{(s^2-t^2)}\sqrt{b^2-t^2} - \frac{f(s)-f(a)}{(s^2-a^2)}\sqrt{b^2-a^2}\right]\frac{dt}{(a^2-t^2)^{3/2}}$$
$$- \frac{A\sigma_0}{(\delta_1-\delta_2)}\int_0^a \frac{\sqrt{b^2-t^2}-\sqrt{b^2-a^2}}{(a^2-t^2)^{3/2}}\,dt$$

Downloaded 02 May 2010 to 171.66.16.250. Redistribution subject to ASME license or copyright; see http://www.asme.org/terms/Terms_Use.cfm

$$+\frac{2C_1A\beta}{\pi(\delta_1-\delta_2)}\int_0^a \frac{\arctan\sqrt{\dfrac{b^2-t^2}{c^2-b^2}}-\arctan\sqrt{\dfrac{b^2-a^2}{c^2-b^2}}}{(a^2-t^2)^{3/2}}\,dt = \frac{\pi q_0}{4} \tag{46}$$

from (36) using (28), (30), (31), (39), and (40); and

$$\frac{(\delta_1-\delta_2)}{A}\int_0^a \frac{tg_3(t)\,dt}{(b^2-t^2)^{3/2}} = \frac{2\beta^2(\delta_1-\delta_2)}{\pi A(1-\beta^2)}\int_0^a sg_3(s)\,ds$$

$$\int_c^\infty \frac{t\,dt}{(t^2-s^2)(t^2-b^2)^{3/2}} + \sigma_0\frac{2C_1\beta}{\pi\sqrt{c^2-b^2}}, \tag{47}$$

from (42), using (31).

Dimensionless Presentation

The equations are all linear in the quantities σ_0, q_0, and C_1, any one of which could therefore be used as the basis for a dimensionless formulation. The procedure used here is to eliminate σ_0 and q_0 from (43) using (46) and (47), obtaining a Fredholm equation in the dimensionless function

$$g(x) = \frac{(\delta_1-\delta_2)g_3(x)}{AC_1\beta} \tag{48}$$

Some simplification can also be achieved at this stage and in the subsequent numerical solution by extending the range of the equation to $-a\le x\le +a$, making use of the fact that $g_3(x)$ and hence $g(x)$ is an odd function of x, as seen from equation (35). The resulting Fredholm equation is

$$g(x)+\frac{\sqrt{a^2-x^2}}{\pi^2}\int_{-a}^{+a}K(x,s)g(s)\,ds = h(x); \quad -a\le x\le +a \tag{49}$$

where

$$K(x,s) = \frac{2\beta^2}{\pi(1-\beta^2)}\int_{-a}^{+a}\left[\left(\frac{f(s)-f(t)}{(s-t)}\right)\sqrt{b^2-t^2} - \left(\frac{f(s)-f(a)}{s-a}\right)\sqrt{b^2-a^2} - \left(\frac{f(s)-f(b)}{s-b}\right)\left(\sqrt{b^2-t^2}-\sqrt{b^2-a^2}\right)\right]\left[\frac{1}{x-t}-\frac{x/a}{a-t}\right]\frac{dt}{\sqrt{a^2-t^2}}$$

$$-\frac{1}{\sqrt{b^2-s^2}}\left[\int_{-1/b}^{+1/b}\left(\frac{1-b^2r^2}{1-a^2r^2}\right)^{1/2}\left(\frac{1}{1-xr}-\frac{x/a}{1-ar}\right)\frac{dr}{(1-sr)}\right.$$

$$\left.-\frac{1}{(b-t)}\int_{-a}^{+a}\left[\frac{\sqrt{b^2-t^2}-\sqrt{b^2-a^2}}{\sqrt{a^2-t^2}}\right]\left[\frac{1}{x-t}-\frac{x/a}{a-t}\right]dt\right] \tag{50}$$

and

$$h(x) = \frac{4\sqrt{a^2-x^2}}{\pi^3}\int_{-a}^{+a}\left(\frac{1}{(x-t)}-\frac{x/a}{(a-t)}\right)\left[\sqrt{b^2-t^2}\left(f(t)-\frac{1}{\sqrt{c^2-b^2}}\right)-\sqrt{b^2-a^2}\left(f(a)-\frac{1}{\sqrt{c^2-b^2}}\right)\right]\frac{dt}{\sqrt{a^2-t^2}} \tag{51}$$

Notice that the integrals in the range $b<t<\infty$ have been converted to $0<r<1/b$ by the substitution $t=1/r$ to facilitate the numerical solution. The auxiliary conditions are expressed in the same terms by eliminating σ_0 and q_0 between (35)–(47), leaving the single condition

$$\int_{-a}^{+a}G(t)\,g(t)\,dt = -\frac{2(1-\beta^2)}{\pi(\beta-1/\gamma)}+\frac{\beta b^2/c^2}{\pi\sqrt{1-b^2/c^2}} + \frac{2\beta}{\pi}(\sqrt{1-b^2/c^2}-1) \tag{52}$$

where

$$G(t) = \frac{\beta^2\log(c+t)}{\pi(\beta-1/\gamma)c}+\frac{\beta^3}{\pi(1-\beta^2)c}\left[\log(c+t)-tf(t) - \frac{b^2(f(t)-f(b))}{2(b-t)}\right]-\frac{\beta}{2c\sqrt{b^2-t^2}}\left[t+\frac{b^2}{2(b-t)}\right] \tag{53}$$

Interface Tractions and Stress Intensity Factors

Once $g(x)$ is known, displacements and stresses throughout the bodies can be found by substituting (17)–(20) into [1] equation (3), making use of (28)–(31) where necessary. On the interface $z=0$, the expressions obtained are the same as those in [1] (equations (47)–(49)) except for minor differences of notation. Of particular interest are the stress intensity factors

$$K_1 = \lim_{r\to c^-}\frac{\sigma_{zz}\sqrt{1-r^2/c^2}}{\sigma_0} = -\frac{2\beta}{\pi}\left(\frac{C_1}{\sigma_0 c}\right) + \frac{\beta^3}{\pi(1-\beta^2)}\left(\frac{C_1}{\sigma_0 c}\right)\int_{-a}^{+a}\frac{g(s)\,ds}{(c-s)} \tag{54}$$

$$K_2 = \lim_{r\to c^+}\frac{\sigma_{rz}\sqrt{r^2/c^2-1}}{\sigma_0} = K_1/\beta. \tag{55}$$

The singularity in normal traction σ_{zz} occurs in a region of contact where $\sigma_{zz}<0$ and hence we must have $\sigma_0 K_1<0$ for a physically meaningful solution.

Numerical Procedure

In practice, the applied traction σ_0 and heat flux q_0 would be given and the contact radii a and b would be determined as part of the solution. The integral form of the kernel (50) would make the resulting iteration process computationally inefficient. A more practical procedure is to allow the constant γ and the ratio σ_0/q_0 to float while prescribing a and b. Equation (49) can then be solved for $g(x)$ and back substitution into (47) and (46) gives values for the dimensionless groups $\sigma_0 c/C_1$; $q_0(\delta_1-\delta_2)c^2/AC_1$, respectively, whose ratio is

$$SQ = \frac{\sigma_0 A}{q_0(\delta_1-\delta_2)c} \tag{56}$$

(see also [1] equation (42)).

Finally, the auxiliary condition (52) is used to determine γ.

Results

Results for $\beta=-0.5$ are shown in Fig. 2, where lines of constant a/c (fine lines), and b/c (heavy lines), are plotted against γ and $-SQ$. We note that all the results fall in the region $SQ<0$, which corresponds to tensile applied tractions in view of inequality (1).

The lines of constant a/c fall monotonically with increasing negative SQ and define an envelope to the left of which no solutions are obtained. (It is shown in the next section that the crack remains fully closed for values in this range.)

The curves of constant b/c originate at the line $a/c=0$ and extend to the left as a/c is increased until the envelope is reached after which they extend to the right and approach the corresponding a/c curves asymptotically. Solution for particular pairs of values of γ and SQ are represented in Fig. 2 by the intersections of (*i*) the upper portion of the b/c lines and

Downloaded 02 May 2010 to 171.66.16.250. Redistribution subject to ASME license or copyright; see http://www.asme.org/terms/Terms_Use.cfm

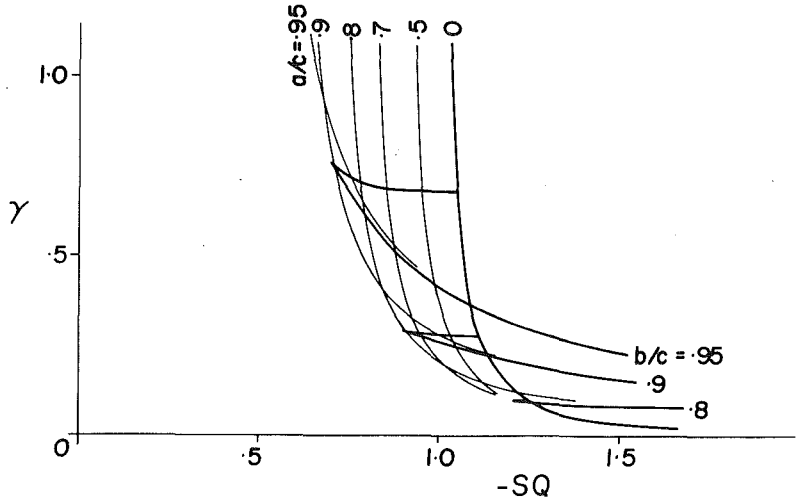


Fig. 2 Effect of γ, SQ on the radii a, b defining the regions of imperfect and perfect contact and separation

the a/c lines above their points of tangency with the envelope and (*ii*) the intersections of the lower portions of the two sets of curves.

There will be one intersection of each kind at any given point in the region between the envelope and the line $a/c=0$ and hence for pairs of values of γ and SQ in this range, there are two distinct solutions to the problem corresponding to different values of both a/c and b/c.

To the right of the line $a/c=0$, only a single solution is obtained, corresponding to intersections of type (*ii*), and a/c is very close to b/c. We note for example that the curves for $a/c=0.95$ and $b/c=0.95$ are already very close at $-SQ=1$ and cannot usefully be distinguished in Fig. 2 at larger values. In physical terms, this means that the extent of the imperfect contact regin ($a\le r\le b$) becomes very small when σ_0 is increased at constant γ, q_0 (i.e., when $-SQ$ is increased at constant γ).

Under these conditions, it is interesting to compare the results with the solution to reference [1] in which the extent of imperfect contact is exactly zero. We emphasize that this simple solution is strictly inapplicable for the physical constants corresponding to Fig. 2, since it predicts a small region of tensile contact traction and interpenetration near the contact/separation boundary, but the values of SQ and K_1 agree very closely with those obtained from the physically correct solution given here. In effect, when the imperfect contact region is small, it produces a purely local effect on the temperature and displacement fields.

Solution With No Separation

Figure 2 shows no solution to the problem in a range of small negative values of SQ. In this range, we will show that there is no separation region—the crack is completely closed, but contains a region of imperfect contact surrounded by an annulus of perfect contact.

No separate solution is required for this case since it can be treated by setting $a=0$ in the existing formulation.

It is easily verified that equations (11) and (13) are satisfied by taking g_3, g_4 identically zero. Equation (31) then gives $g_2(x)=0$ and hence $g_1(x)$ is obtained from (30), (39), and (42) as

$$g_1(x)=\frac{2\sigma_0}{\pi}\left[\sqrt{c^2-b^2}\,\arctan\sqrt{\frac{b^2-x^2}{c^2-b^2}}-\sqrt{b^2-x^2}\right] \tag{57}$$

The auxiliary condition (52) reduces to

$$\sigma_0[2(\gamma-\beta)\sqrt{1-b^2/c^2}-\beta(\beta\gamma-1)(2-b^2/c^2)]=0 \tag{58}$$

The traction on $z=0$ are easily obtained as

$$\sigma_{zz}=\sigma_0\left(1-\sqrt{\frac{c^2-b^2}{c^2-r^2}}\right);\quad b<r<c$$

$$=\sigma_0,\ r>c \tag{59}$$

$$\sigma_{rz}=-\frac{\sigma_0 c\sqrt{c^2-b^2}}{\beta r\sqrt{r^2-c^2}};\quad r>c \tag{60}$$

$$K_1=-\sqrt{1-b^2/c^2} \tag{61}$$

This simple solution is homogeneous in σ_0 and does not depend on q_0. The later result is of course predictable from the boundary conditions, since dependence on q_0 is eliminated along with the separation region $0\le r\le a$. Thus, in principle, equation (57) defines a solution for all values of SQ. Furthermore, the boundary between perfect and imperfect contact defined by the ratio b/c is independent of SQ—it depends only on the physical constants β and γ through equation (58). In these respects, the solution resembles "receding contact" problems of isothermal elasticity [12].

However, a restriction must be placed on the values of SQ because of the inequality

$$q_z(T_2(r,0)-T_1(r,0))\ge 0 \tag{62}$$

which must be satisfied in the imperfect contact region [4, 5]. This inequality follows from the requirement that only a positive thermal contact resistance is physically acceptable and in the present problem it leads to the condition

$$SQ>-c/b \tag{63}$$

which defines the region to the left of the line $a/c=0$ in Fig. 2.

Discussion

We are now in a position to define qualitatively the behavior of the crack as the thermal and mechanical conditions are slowly changed.

Suppose we first impose a tensile traction σ_0, with the isothermal condition $q_0=0$. This solution corresponds to $SQ\to-\infty$ for the appropriate value of γ in Fig. 2. It has already been discussed in [1, 13] and it gives a small annulus of contact surrounding a region of separation.

If we now apply a heat flux in the direction defined by (1), we move to the left along a horizontal line in Fig. 2. Initially the conditions corresponds to the intersections described as type (*ii*) in the preceding results section: An annulus of imperfect contact is developed and both contact regions grow at the expense of the separation region as q_0 is increased. This

Downloaded 02 May 2010 to 171.66.16.250. Redistribution subject to ASME license or copyright; see http://www.asme.org/terms/Terms_Use.cfm

state can persist until we reach the left boundary of the multiple solution region, but after we pass the line $a/c = 0$, it is also possible that a transition should occur to either the type (*i*) solution or to the state with no separation. Intuitively, it seems likely that the behavior will be continuous, i.e., the system will remain in the same qualitative state—as long as conditions permit, in which case a discontinuous transition to the solution with no separation must occur at the envelope of the a/c lines. Subsequently increase in heat flux then has no further effect on the perturbation in temperature or the stress field. By a similar argument, if we increase $(-SQ)$ slowly, we might expect a discontinuous transition from no separation to the type (*ii*) solution at the line $a/c = 0$.

However, a definitive statement of the conditions realized in the multiple solution region must wait on an analysis of the transient problem or a stability analysis of the three solutions.

Acknowledgments

The authors gratefully acknowledge support from the U.S. Army under contract DAAG 29-82-K-0001.

References

1 Martin-Moran, C . J., Barber, J. R., and Comninou, M., "The Penny-Shaped Interface Crack With Heat Flow. Part 1: Perfect Contact," ASME JOURNAL OF APPLIED MECHANICS, Vol. 50, 1983, pp. 29-36.

2 Barber, J. R., "The Effect of Thermal Distortion on Constriction Resistance," *Int. J. Heat Mass Transfer*, Vol. 14, 1971, pp. 751-766.

3 Barber, J. R., "Indentation of the Semi-Infinite Elastic Solid by a Hot Sphere," *Int. J. Mech. Sci.*, Vol. 15, 1973, pp. 813-819.

4 Barber, J. R., "Contact Problems Involving a Cooled Punch," *J. Elasticity*, Vol. 8, 1978, pp. 408-423.

5 Comninou, M., and Dundurs, J., "On the Barber Boundary Conditions for Thermoelastic Contact," ASME JOURNAL OF APPLIED MECHANICS, Vol. 46, 1979, pp. 849-853.

6 Barber, J. R., "Indentation of an Elastic Half-Space by a Cooled Flat Punch," *Q. P. Mech. Appl. Math.*, Vol. 35, 1982, pp. 141-154.

7 Comninou, M., Dundurs, J., and Barber, J. R., "Planar Hertz Contact With Heat Conduction," ASME JOURNAL OF APPLIED MECHANICS, Vol. 48, 1981, pp. 549-554.

8 Comninou, M., Barber, J. R., and Dundurs, J., "Heat Conduction Through a Flat Punch," ASME JOURNAL OF APPLIED MECHANICS, Vol. 48, 1981, pp. 871-875.

9 Barber, J. R., and Comninou, M., "The External Axisymmetric Interface Crack With Heat Flow," *Q. J. Mech. Appl. Math*, in press.

10 Green, A. E., and Zerna, W., *Theoretical Elasticity*, Clarendon Press, Oxford, 1954, pp. 174-178.

11 Collins, W. D., "On the Solution of Some Axisymmetic Boundary Value Problems by Means of Integral Equations. VIII: Potential Problems for a Circular Annulus," *Proc. Edin. Math. Soc.*, Vol. 13, 1963, pp. 235-246.

12 Dundurs, J., "Properties of Elastic Bodies in Contact," in *The Mechanics of the Contact Between Deformable Bodies*, de Pater, A., and Walker, J. J. eds., Delft Univ. Press.

13 Keer, L. M., Chen, S. H., and Comninou, M., "The Interface Penny-Shaped Crack Reconsidered," *Int. J. Eng. Sci.*, Vol. 16, 1978, pp. 765-772.

Downloaded 02 May 2010 to 171.66.16.250. Redistribution subject to ASME license or copyright; see http://www.asme.org/terms/Terms_Use.cfm

Analysis of the Optical Shadow Spot Method for a Tensile Crack in a Power-Law Hardening Material

A. J. Rosakis[1]
Research Assistant.

C. C. Ma
Research Assistant.

L. B. Freund
Professor and Chairman.
Fellow ASME

Divison of Engineering,
Brown University,
Providence, R.I. 02912

If the crack tip deformation field in a cracked ductile solid can be characterized by means of a single plastic intensity factor, then the shadow spot method has potential as a means for direct measurement of this intensity factor. The value of the J-integral is adopted as a plasticity intensity factor, and the lateral contraction of a planar specimen of elastic-plastic power-law hardening material is calculated in terms of J from the HRR asymptotic field of elastic-plastic fracture mechanics. The theoretical caustic curve which would be generated by geometrical reflection of normally incident light from points of the deformed specimen surface lying well within the plastic zone is determined, and it is shown that the value of J is proportional to the maximum transverse diameter of the shadow spot to the power $(3n + 2)/n$, where n is the power hardening exponent. Synthetic shadow spot patterns obtained by numerical simulation of the optical reflection process are also shown.

1 Introduction

The use of the optical shadow spot method for measuring the intensity of crack tip stress fields is now quite common in experimental work underlying the field of linear elastic fracture mechanics. The method, which is also known as the method of caustics, and some of its applications are reviewed in a recent article by Kalthoff and Beinert [1]. It was suggested in a recent paper by Rosakis and Freund [2] that the method may have potential for application in elastic-plastic fracture testing as well. This suggestion was based on the following observation. When a large plate that contains a long through-crack and which responds in a nominally manner is loaded so that crack opening occurs in the tensile mode, the stress and deformation fields very near to the crack tip assume the familiar universal spatial distributions. Only the magnitude of the near tip field varies with load and geometry, and this magnitude is customarily the mode I stress intensity factor. Within the framework of plane stress analysis, the deformed shape of the specimen surface near the crack tip is thus also known up to a scalar amplitude that is equivalent to the stress intensity factor. The success of the method of caustics is based on the fact that, with a suitable optical arrangement, the light pattern obtained by reflecting parallel incident light from the specimen surface near the crack tip provides a direct measure of the stress intensity factor.

Once the idea of the method is described in this way, it becomes clear that applicability of the method does not hinge on the material in the crack tip region responding in an elastic manner. Instead, the key feature is that the deformed shape of the specimen surface (that is, the reflecting surface) in the crack tip region is known up to a scalar amplitude. Although the mechanics of elastic-plastic fracture is not as fully developed as elastic fracture mechanics, the available asymptotic analyses of near-tip fields in power-law hardening materials suggest that this situation may prevail for these cases as well. Within the framework of plane stress analysis, with small strains and proportional stress histories for stationary cracks, the value of Rice's J-integral has been proposed as a plastic intensity factor. The viewpoint is adopted here that J provides a suitable scalar amplitude for the deformed shape of the surface of an elastic-plastic fracture specimen, and a means of directly measuring this amplitude is discussed. While there are methods available for measuring J values for ductile materials, they apply only for rate-independent materials subjected to quasi-static loading. While the direct optical method being discussed here has drawbacks of its own, its use is not subject to the same limitations on rate of loading or material response.

In the following sections, the use of the optical method of caustics in reflection is described in a way that is more general in some respects than previous descriptions. Then, the results of asymptotic elastic-plastic crack tip analysis which lead to

[1]Present Affiliation: Assistant Professor, Division of Engineering and Applied Science, California Institute of Technology, Pasadena, Calif. 91125.

Contributed by the Applied Mechanics Division for publication in the JOURNAL OF APPLIED MECHANICS.

Discussion on this paper should be addressed to the Editorial Department, ASME, United Engineering Center, 345 East 47th Street, New York, N.Y. 10017, and will be accepted until two months after final publication of the paper itself in the JOURNAL OF APPLIED MECHANICS. Manuscript received by ASME Applied Mechanics Division, January, 1983; final revision, June, 1983.

Copyright © 1983 by ASME
Downloaded 02 May 2010 to 171.66.16.250. Redistribution subject to ASME license or copyright; see http://www.asme.org/terms/Terms_Use.cfm

the so-called *HRR* field are summarized. The particular case of a power-law hardening material in a state of plane stress is examined in detail, and a relationship is derived between the value of J and the maximum transverse diameter D of the shadow spot obtained by reflection of parallel incident light from the crack tip region of the specimen surface for any value of the hardening parameter n. The complete reflected optical fields for several values of n have also been simulated for this situation, and these results show the influence of hardening on the shadow spot shapes.

2 Caustics in Reflection

Consider a highly polished planar specimen of uniform thickness d in the undeformed state occupying a region of the x_1, x_2 plane. When boundary loads that tend to open the crack are applied, the resulting change in thickness is nonuniform and the equation of the deformed specimen surface is assumed to be given by

$$x_3 + f(x_1, x_2) = 0 \tag{2.1}$$

Consider a family of light rays parallel to the x_3 axis incident on the reflecting surface (2.1). Upon reflection, the light rays will deviate from parallelism; see Fig. 1. If certain geometrical conditions are met by the reflecting surface, then the virtual extensions of the reflected rays will have an envelope in the form of a three-dimensional surface in space. This surface, which is called the *caustic surface*, is the locus of points of maximum luminosity (that is, highest density of rays) in the virtual extension of the reflected light field. The virtual extensions of the rays are tangent to the caustic surface. The reflected light field is recorded on a camera positioned in front of the specimen. The focal plane of the camera, which shall be called the "screen" for convenience, intersects the caustic surface at a distance z_0 behind the plane reflecting surface of the undeformed specimen. On the screen, a cross section of the caustic surface is observed as a bright curve (the *caustic curve*) bordering a relatively dark region (the *shadow spot*).

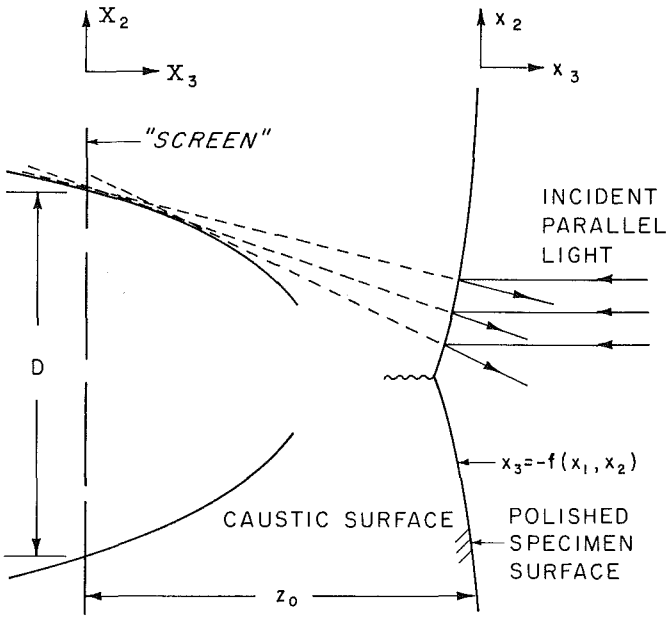


Fig. 1 Schematic diagram of the optical reflection process that results in the formation of a shadow spot pattern

If the shape of the reflecting surface and the distance z_0 are specified, then the size and shape of the shadow spot can be determined. Apparently, the prescription for doing so was first presented by Manogg [3] under the assumptions that the magnitude of the surface deflection f was much less than the distance z_0 and that the change in slope of the reflecting surface due to deformation was much less than unity. The analysis is only slightly more complicated if these assumptions are not invoked, it seems, and the essential steps are described in the following.

Consider that light ray that pierces the plane of the undeformed reflecting surface $x_3 = 0$ at position $\mathbf{x} = (x_1, x_2)$; see Fig. 2. This ray strikes the deformed reflecting surface at $x_3 = -f$, and the unit vector normal to the reflecting surface at this point, say ν, has components $(f_{,1}, f_{,2}, 1)/\sqrt{(1+f_{,j}f_{,j})}$ where the partial derivatives $f_{,j}$ are evaluated at $\mathbf{x}$ and the repeated index implies summation over $j = 1, 2$. Let $\mathbf{e}_3$ denote a unit vector in the x_3 direction. Then the plane that contains

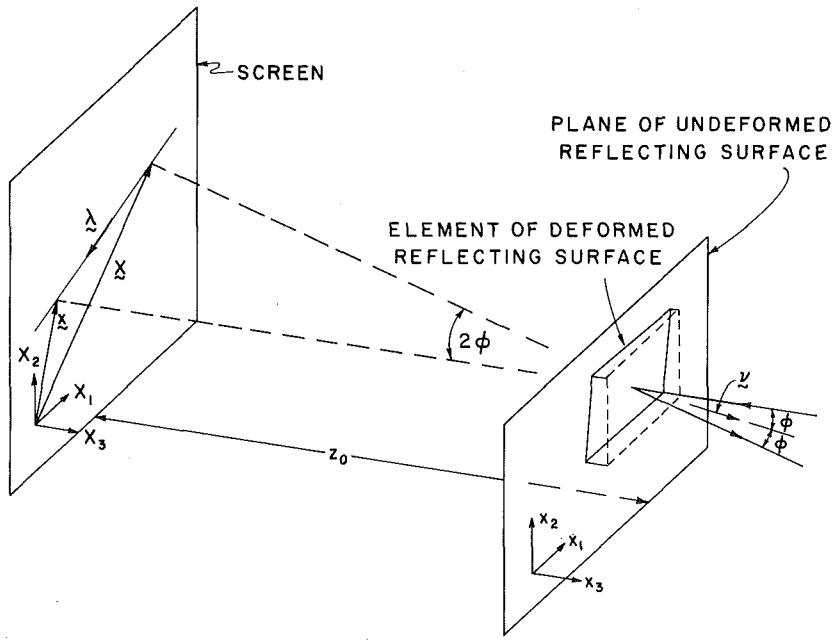


Fig. 2 Schematic diagram of the optical mapping represented by the mapping equation (2.3)

Downloaded 02 May 2010 to 171.66.16.250. Redistribution subject to ASME license or copyright; see http://www.asme.org/terms/Terms_Use.cfm

both the incident ray and the corresponding reflected ray is defined by the normal vector $\nu x \mathbf{e}_3$. The intersection of this plane with the plane of the screen is then that line that has direction specified by the unit vector

$$\lambda = \frac{\mathbf{e}_3 x\ (\nu\ x\ \mathbf{e}_3)}{|\mathbf{e}_3 x\ (\nu\ x\ \mathbf{e}_3)|} \tag{2.2}$$

With this direction specified, the position $\mathbf{X} = (X_1, X_2)$ in the screen at which the virtual extension of the reflected ray strikes the screen is

$$\mathbf{X} = \mathbf{x} - (z_0 - f) \tan 2\phi\ \lambda \tag{2.3}$$

where ϕ is the angle between the incident ray and the normal to the reflecting surface. With this definition,

$$\tan \phi = \frac{\sin \phi}{\cos \phi} = \frac{|\nu\ x\ \mathbf{e}_3|}{\nu \cdot \mathbf{e}_3} \tag{2.4}$$

Then, if the vector expressions are evaluated and the vector ν is expressed in terms of its components, the optical mapping may be written in component form as

$$X_i = x_i - 2(z_0 - f)\frac{f_{,i}}{1 - f_{,j} f_{,j}} \tag{2.5}$$

If it is now assumed that $|f| << z_0$ and that $f_{,j} f_{,j} << 1$ then the familiar form of the optical mapping proposed by Manogg results, viz,

$$X_i = x_i - 2z_0 f_{,i} \tag{2.6}$$

Equation (2.5) or its approximation (2.6) is a mapping of the points on the reflecting surface onto the points on the screen. If the screen intersects a caustic surface in the reflected light field, then the resulting caustic curve on the screen is a locus of points for which the mapping is not invertible. That is, for those points that map onto the caustic curve, the determinant of the Jacobian matrix of the mapping must vanish. The vanishing of the Jacobian determinant is a necessary and sufficient condition for the existence of a caustic curve. The points on the plane of the undeformed reflecting surface for which the Jacobian determinant vanishes are the points from which the rays forming the caustic curve are reflected. The locus of these points on the reflecting surface is the so-called *initial curve*.

That the caustic curve is the locus of points of maximum luminosity is clear from the following simple argument. Consider incident light of uniform intensity $q(x_1, x_2) = q_0$ measured per unit surface area on the plane of the undeformed reflecting surface. The light that passes through an arbitrary area α on this plane illuminates a corresponding area A on the screen with intensity $Q(X_1, X_2)$. Assuming perfect reflectivity, the conservation of light energy implies that the net intensity of light on α is equal to the net intensity of A, or

$$\int_\alpha q_0 dx_1 dx_2 = \int_A Q(\mathbf{X})\ dX_1 dX_2 \tag{2.7}$$

Using the mapping (2.5) to change variables on the right-hand side, equation (2.7) becomes

$$\int_\alpha q_0 dx_1 dx_2 = \int_\alpha Q[\mathbf{X}(\mathbf{x})]\ B(\mathbf{x})\ dx_1 dx_2 \tag{2.8}$$

where B is the determinant of the Jacobian matrix of (2.5). Because the area α is arbitrary, the integrands of (2.8) are equal,

$$Q[\mathbf{X}(\mathbf{x})] = q_0 / B(\mathbf{x}) \tag{2.9}$$

Thus, it is evident from (2.9) that points on the reflecting surface for which $B = 0$ are mapped into points of maximum luminosity on the screen.

3 Shape of the Reflecting Surface

Most structural materials that contain cracks undergo substantial plastic deformation under rising load prior to onset of crack growth. In many cases, including standard specimen configurations, a large plastic zone develops around the crack tip and there is no region of the body over which a stress intensity factor controlled elastic field prevails. The linear elastic fracture toughness approach to fracture resistance characterization is then not applicable and other criteria, such as the critical J criterion mentioned in the Introduction, must be adopted. Methods for measuring values of J for ductile fracture specimens are available but the methods are indirect, in general, in the sense that values of J are inferred from values of other measured quantities, typically load and deflection data. In this section, attention is focused on points deep within the crack tip plastic zone, and a means of inferring values of J from the local deformation field is suggested.

Consider a large plate of elastic-plastic material that exhibits power-law hardening behavior. Suppose the plate is initially of uniform thickness d and that it contains a long through-crack. The plate is subjected to edge loading which results in a plane stress opening mode of deformation. If the midplane of the plate undergoes no transverse displacement, then the normal displacement of the plate surface $u_3(x_1, x_2)$ is

$$u_3(x_1, x_2) = f(x_1, x_2) = \epsilon_{33} d/2 \tag{3.1}$$

where the orientation of Cartesian axes shown in Fig. 1 is assumed and ϵ_{33} is the total strain in the thickness direction.

Hutchinson [4] and Rice and Rosengren [5] showed that the strain components in the crack tip region scale with the value of J for a power-law hardening material. They considered a monotonically loaded stationary crack in an incompressible material described by a J_2-deformation theory of plasticity and a relationship between post-yield strain ϵ_{ij} and stress σ_{ij} of the form

$$\frac{\epsilon_{ij}}{\epsilon_0} = \frac{3}{2}\left(\frac{\sigma_e}{\sigma_0}\right)^{n-1}\frac{S_{ij}}{\sigma_0} \tag{3.2}$$

where

$$s_{ij} = \sigma_{ij} - \frac{1}{3}\delta_{ij}\sigma_{kk}, \quad \sigma_e^2 = \frac{3}{2} s_{ij} s_{ij} \tag{3.3}$$

and σ_0 is the tensile yield stress, ϵ_0 is the equivalent tensile yield strain, and n is the hardening exponent. By introducing the preceding assumptions, they observed that, within a small strain formulation, a possible asymptotic strain distribution in the crack tip region is

$$\epsilon_{ij} \to \epsilon_0 \left[\frac{J}{\sigma_0 \epsilon_0 I_n r}\right]^{\frac{n}{n+1}} E_{ij}(n, \theta) \tag{3.4}$$

as $r \to 0$ in a polar coordinate system with origin at the crack tip. The angular factors E_{ij} in (3.4) depend on the mode of loading and on the hardening exponent. The dimensionless quantity I_n, which is defined in [4], decreases from 5 for $n = 1$ to 2.57 for infinitely large values of n for cases of plane stress. The intensity factor J in (3.4) is the value of Rice's J-integral. The singular field (3.4) is customarily referred to as the *HRR* singularity. The asymptotic result (3.4) was derived under the further assumption that the dependence of the local field on the polar coordinates r and θ is indeed separable.

For plane deformation, the J-integral is defined for any path of integration C by [6]

$$J = \int_C \left[W n_1 - n_i \sigma_{ij} u_{j,1}\right] dC \tag{3.5}$$

where W is the local stress work density, n_i is a unit vector normal to C, and u_i is the particle displacement vector. The integral has the well-known property of path independence,

Downloaded 02 May 2010 to 171.66.16.250. Redistribution subject to ASME license or copyright; see http://www.asme.org/terms/Terms_Use.cfm

that is, $J=0$ for any simple closed path in the body in the absence of body forces. This implies that J has the same value for all paths that begin on one traction-free face of a crack in a plane with normal in the x_2 direction and that end on the opposite traction-free face of the crack. Because the path of integration can be chosen to be arbitrarily close to the crack tip, J has been interpreted as a measure of the strength of the crack tip singular field, a role that is obvious from the form of (3.4). Based on the observation that J is a characterizing parameter for the crack tip field, it has been suggested that a condition for onset of crack growth is the attainment of a critical value of J. This seems reasonable, provided that the one parameter characterization remains valid and that the one parameter field prevails over a region large in size compared to the fracture process zone. The interest in measuring values of J for ductile materials stems from the potential usefulness of this suggested criterion.

In view of the assumed incompressibility of material response, the strain in the thickness direction which appears in (3.1) is related to the in-plane strains by

$$\epsilon_{33} = -(\epsilon_{11} + \epsilon_{22}) = -(\epsilon_{rr} + \epsilon_{\theta\theta}) \tag{3.6}$$

For specified material parameters and a given value of J, the in-plane strains are known from (3.4), the out-of-plane strain is computed from (3.6), and the shape of the reflecting surface is then given by (3.1). Thus, for points near the crack tip, the shape of the reflecting surface is known up to a scalar amplitude, namely the plastic strain intensity J. In the next section, the relationship between the magnitude of J and the size of the shadow spot obtained by reflecting parallel incident light from this reflecting surface is established.

It should be noted that (3.6) will provide an overestimate of lateral contraction for given in-plane strains because, for most materials, the elastic part of the local deformation is not incompressible although the plastic part may be so. For points close enough to the crack tip for the plastic strain to dominate the elastic strain, however, the total strain is expected to satisfy (3.6) to an acceptable degree. An estimate of the ratio of total strain ϵ_{22} to tensile yield strain ϵ_0 as a function of distance ahead of a crack tip in a low hardening (large n) material may be obtained in the following way. For very large n, $E_{22}(n,0) \simeq 0.75$ and $I_n \simeq 2.6$. For contained plastic deformation in plane stress, the value of J is commonly related to the maximum extent of the plastic zone r_p by $J = \pi\sigma_0\epsilon_0 r_p$. Thus, from (3.4) for large values of n,

$$\epsilon_{22}/\epsilon_0 \simeq 0.9(r_p/r)$$

so that (3.6) is expected to provide a reasonably accurate relationship if the distance from the crack tip to the initial curve along $\theta = 0$ is less than one-half or one-third of the extent of the plastic zone along $\theta = 0$.

4 Shadow Patterns Associated With the HRR Field

In view of the discussion in the preceding section, the shape of the reflecting surface $f(x_1, x_2)$ in (2.1) is given by

$$f(x_1,x_2) = \tfrac{1}{2}\epsilon_0 d\left[\frac{J}{\sigma_0\epsilon_0 I_n r}\right]^{\frac{n}{n+1}} (E_{rr}+E_{\theta\theta}) \tag{4.1}$$

Numerical values of the angular variations E_{ij} are available for many values of hardening exponent n from the work of Shih [7]. Again, equation (4.1) represents the normal displacement of points on the initially plane specimen surface due to deformation. For an initial curve that is well within the crack tip plastic zone where the *HRR* field can be expected to dominate, the mapping (2.6) takes the form

$$X_i = x_i + G\frac{\partial}{\partial x_i}\left[\frac{\psi(\theta,n)}{r^{n/(n+1)}}\right] \tag{4.2}$$

where

Table 1 Values of the numerical coefficient S_n, which appears in (4.8), from evaluation (4.9)

n	S_n
1	0.0277
2	0.0513
3	0.0611
4	0.0660
5	0.0687
6	0.0701
7	0.0710
8	0.0715
9	0.0718
10	0.0719
15	0.0719
20	0.0717
25	0.0714

$$G = \epsilon_0 z_0 d\left[\frac{J}{\epsilon_0\sigma_0 I_n}\right]^{\frac{n}{n+1}}, \quad \psi = E_{rr}+E_{\theta\theta} \tag{4.3}$$

The mapping is written more conveniently in polar form as

$$\begin{aligned} X_1 &= r\cos\theta + G\,r^{-\frac{2n+1}{n+1}}\left[\frac{n}{n+1}\psi\cos\theta + \psi'\sin\theta\right] \\ X_2 &= r\sin\theta + G\,r^{-\frac{2n+1}{n+1}}\left[\frac{n}{n+1}\psi\sin\theta - \psi'\cos\theta\right] \end{aligned} \tag{4.4}$$

where the prime denotes the derivative with respect to θ.

If the determinant of the Jacobian matrix of the transformation (4.4) is set equal to zero, then the result is a quadratic equation for $r^{(3n+2)/(n+1)}$ in which the coefficients depend on ψ, ψ', and ψ'', as well as on the hardening exponent n. The root of the quadratic equation is

$$r(\theta,n)^{\frac{3n+2}{n+1}} = G\,R(\theta,n) \tag{4.5}$$

where

$$\begin{aligned} 2R(\theta,n) = &\left[\left(\frac{n}{n+1}\right)^2\psi+\psi''\right] + \left\{\left[\left(\frac{n}{n+1}\right)^2\psi+\psi''\right]^2\right. \\ &\left. +4\frac{2n+1}{n+1}\left[\left(\frac{n}{n+1}\right)^2\psi^2 - \frac{n}{n+1}\psi\psi'' + \frac{2n+1}{n+1}(\psi')^2\right]\right\}^{\frac{1}{2}} \end{aligned} \tag{4.6}$$

Equation (4.5) gives the initial curve on the specimen surface for a given intensity of local deformation field. Then, substitution of (4.5) into (4.2) yields the equation of the corresponding caustic curve in the X_1, X_2 plane, parametric in the angle θ,

$$\begin{aligned} X_1 &= G^{\frac{n+1}{3n+2}}R^{\frac{n+1}{3n+2}}\left[\cos\theta + R^{-1}\left(\frac{n}{n+1}\psi\cos\theta + \psi'\sin\theta\right)\right] \\ X_2 &= G^{\frac{n+1}{3n+2}}R^{\frac{n+1}{3n+2}}\left[\sin\theta + R^{-1}\left(\frac{n}{n+1}\psi\sin\theta = \psi'\cos\theta\right)\right] \end{aligned} \tag{4.7}$$

for values of θ in the range $-\pi < \theta < \pi$.

The shape of the caustic curve depends only on the distribution of plastic strain in the crack tip region. The absolute size of the caustic curve, on the other hand, depends on the strength of the plastic strain singularity, the bulk material properties, the geometrical parameters, and the optical parameters. In fact, equation (4.7) is a relationship among all of these parameters. Thus, if the values of the material, geometrical and optical parameters are known, then (4.7) provides a relationship between the size of the caustic curve D and the strength of the plastic singularity J. Adopting the maximum transverse diameter $D/2 = \max(X_2)$ as the characteristic dimension, the intensity of the strain singularity can be expressed as

Downloaded 02 May 2010 to 171.66.16.250. Redistribution subject to ASME license or copyright; see http://www.asme.org/terms/Terms_Use.cfm

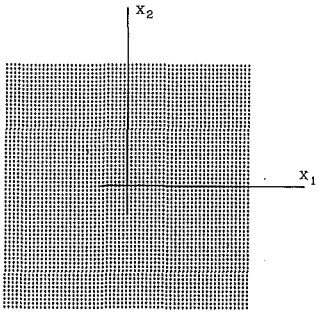


Fig. 3(*a*)

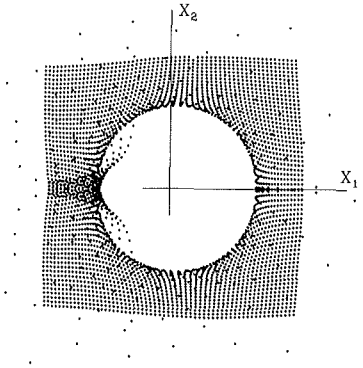


Fig. 3(*b*)

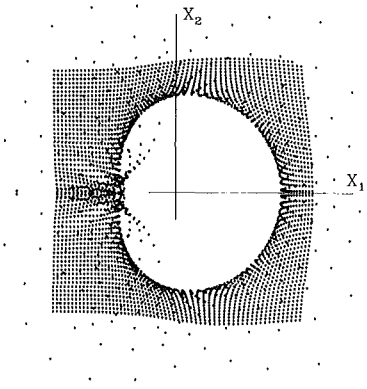


Fig. 3(*c*)

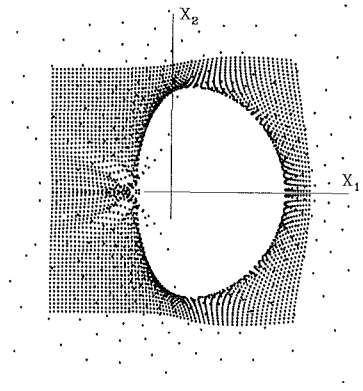


Fig. 3(*d*)

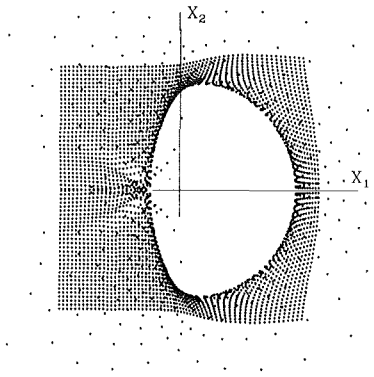


Fig. 3(*e*)

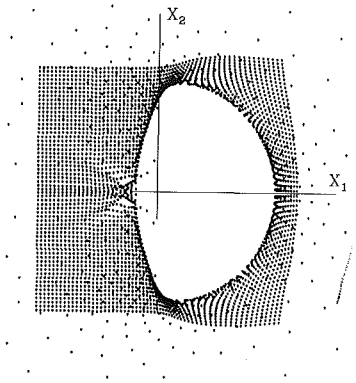


Fig. 3(*f*)

Fig. 3 (*a*) Regular array of incident light rays assumed in generating the synthetic shadow spot patterns in 3(*b–f*), based on the *HRR* asymptotic field. The numerical simulation of the reflection process is shown for the following hardening exponents: (*b*) $n = 1$, (*c*) $n = 3$, (*d*) $n = 9$, (*e*) $n = 13$, and (*f*) $n = 25$.

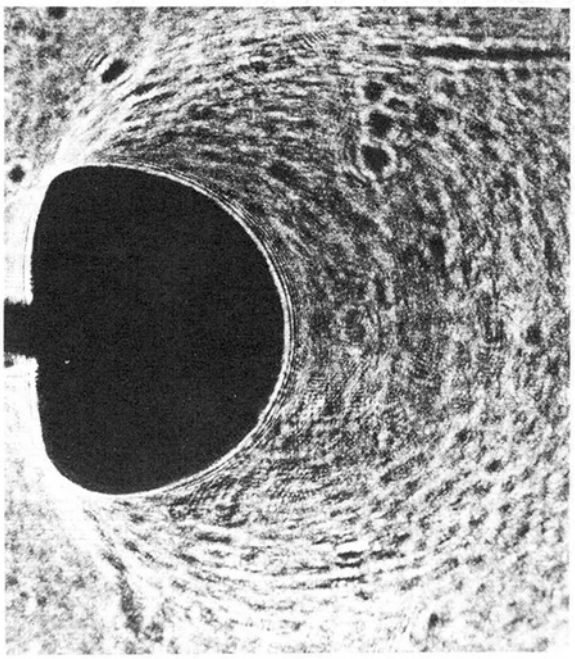


Fig. 4 Photograph of a shadow spot, surrounded by surface evidence of plastic deformation. The material is a tool steel with a low hardening rate [2].

$$J = S_n \epsilon_0 \sigma_0 \left[\frac{1}{\epsilon_0 z_0 d}\right]^{\frac{n+1}{n}} D^{\frac{3n+2}{n}} \tag{4.8}$$

Relation (4.8) is the main result of this section. It provides a simple relationship between the size of an observed shadow spot and the strength of the plastic singularity near the tip of the crack in an elastic-plastic power-law hardening material under conditions of plane stress.

All of the parameters that appear in (4.8) are determined

Downloaded 02 May 2010 to 171.66.16.250. Redistribution subject to ASME license or copyright; see http://www.asme.org/terms/Terms_Use.cfm

from prior knowledge of the material behavior or from the experimental set-up. The coefficient S_n is a function of n only and is given by

$$S_n = \frac{I_n}{\max_\theta \left\{ R^{\frac{n+1}{n}} \left[2\sin\theta + \frac{2}{R}\left(\frac{n}{n+1}\psi\sin\theta - \psi'\cos\theta \right) \right]^{\frac{3n+2}{n}} \right\}} \tag{4.9}$$

The expression in (4.9) has been evaluated numerically for a range of values of n from the data in [7], and the results are shown in Table 1. It is noted that for values of n greater than about 4 or 5, the value is almost indistinguishable from the asymptotic value 0.072 for large n. Further, it is noted that the limiting case of (4.8) for $n \to \infty$ is consistent with the corresponding result for nonhardening materials which was reported in [2]. Likewise, for an elastic material ($n = 1$), it is well-known that the stress intensity factor K is proportional to the shadow spot diameter raised to the power 5/2. That (4.8) is also consistent with this result is evident once the relationship $J = K^2/E$, which applies for elastic cracks under plane stress conditions, is recalled.

In order to more fully understand the phenomenon of shadow spot formation for a power-law hardening material, a companion study was carried out in which the full reflected optical field was simulated numerically. In this study, a square array of light rays was assumed to be normally incident on the surface of the specimen. The pattern in which these light rays pierce the plane reflecting surface of the undeformed specimen is shown in Fig. 3(*a*). These light rays were then "reflected" from a surface deformed according to (4.1), and the pattern in which the lines of the reflected rays pierce a screen positioned behind the reflecting surface was constructed. The patterns obtained for $n = 1$, 3, 9, 13, and 25 are shown in Fig. 3. The anticipated features, such as the shadow spot (zero density of rays) and the caustic curve (high density of rays), are evident in these constructions of the reflected optical fields. Further insight into the physical process of shadow spot formation can be gained by comparing a straight row or column of rays in Fig. 3(*a*) to the positions into which these points map in Fig. 3(*b–f*). These rows and columns map into curves that are tangent to the caustic curve at their common point, as is evident from the synthetic optical patterns.

Finally, the shadow spot photograph which appeared in [2] is reproduced here as Fig. 4 in order to illustrate the quality that might be expected in applying the ideas being proposed in laboratory testing. This photograph was produced by using light reflected from deep within the crack tip plastic zone of a tool steel with a low rate of strain hardening in the double cantilever beam configuration. It is clear from the photograph that surface evidence of plastic deformation extends far beyond the shadow spot. Some limited quantitative data are reported in [2].

Acknowledgments

This work has been supported by the Office of Naval Research, Contract N00014-78-C-0051, and by the NSF Materials Research Laboratory, Brown University.

The computations were performed on the VAX-11/780 Engineering Computer Facility at Brown University. This facility was made possible by grants from the National Science Foundation (Solid Mechanics Program), the General Electric Foundation, and the Digital Equipment Corporation.

References

1 Beinert, J., and Kalthoff, J. F., "Experimental Determination of Dynamic Stress Intensity Factors by the Method of Shadow Patterns," in *Mechanics of Fracture*, Sih, G. C., ed., Noordhoff, Leyden, 1979.

2 Rosakis, A. J., and Freund, L. B., "Optical Measurement of the Plastic Strain Concentration at a Crack Tip in a Ductile Steel Plate," ASME *Journal of Engineering Materials and Technology*, Vol. 104, 1982, pp. 115–120.

3 Manogg, P., "Anwendung der Schattenoptik zur Untersuchung des Zerreisvorganges von Platten," Doctoral Dissertation, University of Freiburg, 1964.

4 Hutchinson, J. W., "Singular Behavior at the End of a Tensile Crack," *Journal of the Mechanics and Physics of Solids*, Vol. 16, 1968, pp. 13–31.

5 Rice, J. R., and Rosengren, G. F., "Plane Strain Deformation Near a Crack Tip in Power Law Hardening Materials," *Journal of the Mechanics and Physics of Solids*, Vol. 16, 1968, pp. 1–12.

6 Rice, J. R., "Mathematical Analysis in the Mechanics of Fracture," in *Fracture: An Advanced Treatise II*, Liebowitz, H., ed., Academic Press, 1968, pp. 191–311.

7 Shih, C. F., "Elastic-Plastic Analysis of Combined Mode Crack Problems," Ph.D. Thesis, Harvard University, 1973.

Downloaded 02 May 2010 to 171.66.16.250. Redistribution subject to ASME license or copyright; see http://www.asme.org/terms/Terms_Use.cfm

On the Approach to Steady State for Frictional Contact Under Moving Loads

J. Dundurs
Department of Civil Engineering,
Northwestern University,
Evanston, Ill. 60201
Fellow ASME

A. K. Gautesen
Ames Laboratory and
Department of Mathematics,
Iowa State University,
Ames, Iowa 50011

There is a class of problems involving frictional contact for which a steady state of slip is possible under moving loads as, for instance, when a tire is press-fitted on a wheel, and loaded by forces that travel along its circumference and induce localized slip between the tire and the wheel. The steady state slip has been investigated before, but no estimates showing how quickly the steady state is approached are available. The present paper considers for this purpose a problem that can largely be reduced analytically. It involves two half spaces that are pressed together and sheared. The contact interface is locally pried apart by concentrated normal tractions which, after application, start to move. The moving normal forces induce localized separation and slip zones that travel along the interface. The analysis based on integral equations shows that the approach to steady state is relatively slow.

Introduction

Perhaps the most significant feature of frictional contact between bodies is that the deformations depend on the loading history. This has important physical consequences and, in analysis, requires that the loading process be generally followed in time. One of the exceptions is encountered for moving loads and suitable geometries when the deformations can be expected to approach a steady state, and become independent of time in a moving coordinate system. In fact, the few investigations of frictional contact under moving loads have hitherto been restricted to the steady state [1, 2]. There are no estimates, however, for how quickly the steady state is approached.

To probe this question, we devise a problem that can largely be reduced analytically and, although requiring a numerical solution of a nonlinear integral equation at the very end, does not necessitate an incremental treatment. The results show that the approach to steady state is much slower than might be anticipated intuitively.

The Problem and Mathematical Preliminaries

Consider two semi-infinite elastic solids that are first pressed together with the applied pressure p^∞ and subsequently sheared at infinity with the applied tractions q^∞. The restriction $q^\infty < fp^\infty$ is imposed to avoid catastrophic slip (f denotes the coefficient of friction). Next the contact interface is locally pried apart by applying some normal tractions to the surfaces of the semi-infinite bodies. For simplicity, the normal tractions are taken as a pair of concentrated forces. As the normal forces are increased from zero to the final magnitude P, a separation zone grows to cover the interval $(-a,a)$. At the same time, two slip zones develop at the ends of the separation zone, occupying the intervals $(-b,-a)$ and (a,b) when the concentrated forces reach their final magnitudes (see Fig. 1). Finally, the concentrated forces start to move to the right, taking the separation zone with them and causing further slip ahead of the separation zone. It is assumed that the loading rates are slow, so that inertia effects are insignificant and the equilibrium equations are satisfied.

It is convenient to formulate the problem using the well-known results for edge dislocations in an infinite solid [3], as most of the boundary conditions on $y = 0$ are then satisfied automatically, and the governing integral equations can be written at sight. We recall for this purpose that the distribution of a climb array with the density $B_y(x)$ on $y = 0$ is related to the gap $g(x)$ between the two surfaces by

$$g(x) = u_y(x,0^+) - u_y(x,0^-) = -\int_{-\infty}^{x} B_y(\xi)d\xi \tag{1}$$

$$B_y(x) = -\frac{dg(x)}{dx} \tag{2}$$

whereas a glide array of density $B_x(x)$ gives the tangential shift

$$h(x) = u_x(x,0^+) - u_x(x,0^-) = -\int_{-\infty}^{x} B_x(\xi)d\xi \tag{3}$$

Contributed by the Applied Mechanics Division for publication in the JOURNAL OF APPLIED MECHANICS.
Discussion on this paper should be addressed to the Editorial Department ASME, United Engineering Center, 345 East 47th Street, New York, N.Y. 10017, and will be accepted until two months after final publication of the paper itself in the JOURNAL OF APPLIED MECHANICS, Manuscript received by ASME Applied Mechanics Division, November, 1982; final revision, January 1983.

Copyright © 1983 by ASME
Downloaded 02 May 2010 to 171.66.16.250. Redistribution subject to ASME license or copyright; see http://www.asme.org/terms/Terms_Use.cfm

$$B_x(x) = -\frac{dh(x)}{dx} \tag{4}$$

It should be noted that most of the contact interface is in a condition of permanent stick and that, consequently, the dislocation arrays are restricted to finite intervals.

The total normal and shear tractions at the contact interface are

$$N(x) = \sigma_{yy}(x,0) = -p^\infty - \frac{2\mu}{\pi(\kappa+1)} \int_{-\infty}^{\infty} \frac{B_y(\xi)d\xi}{\xi - x} \tag{5}$$

$$S(x) = \sigma_{xy}(x,0) = -q^\infty - \frac{2\mu}{\pi(\kappa+1} \int_{-\infty}^{\infty} \frac{B_x(\xi)d\xi}{\xi - x} \tag{6}$$

The first terms in (5) and (6) are due to the applied tractions, and the integrals constitute the contributions of the dislocation arrays [3].

The boundary conditions in problems with friction involve also the slip velocity

$$V(x) = \frac{\partial}{\partial t} h(x) = -\int_{-\infty}^{\infty} \dot{B}_x(\xi)\, d\xi \tag{7}$$

To simplify the notation, the dependence on time is not indicated explicitly, unless there is a specific need to do so.

In the course of analyzing the problem, the singular Cauchy equation

$$\int_a^b \frac{\Phi(\xi)\, d\xi}{\xi - x} = F(x), \quad a < x < b \tag{8}$$

must be inverted repeatedly. The dislocation densities have to be bounded at the end points for finite contact tractions, and consequently the appropriate solution of (8) is [4]

$$\Phi(x) = -\frac{1}{\pi^2} w(x) \int_a^b \frac{F(\xi)d\xi}{(\xi - x)w(\xi)}, \quad a < x < b \tag{9}$$

where

$$w(x) = (x-a)^{1/2}(b-x)^{1/2} \tag{10}$$

For bounded solution, however, the right side of (8) must satisfy the consistency condition

$$\int_a^b \frac{F(x)dx}{w(x)} = 0 \tag{11}$$

The Phase of Load Application

As the applied pressure p^∞ and shear q^∞ are imposed at the very beginning and henceforth kept constant, only the pair of concentrated forces will be called loads for brevity.

It is seen from (5) and (6) that the localized separation and slip at the interface are not coupled. This is because the two semi-infinite solids are taken to have the same elastic constants. The extent of the separation zone and the distribution of the normal tractions are determined by enforcing the boundary conditions

$$N(x) = -P\delta(x), \quad g(x) > 0 \tag{12}$$

on the unknown interval $(-a,a)$ occupied by the separation zone. The first of these gives on the basis of (5) the integral equation

$$\int_{-a}^{a} \frac{B_y(\xi)\, d\xi}{\xi - x} = \frac{\pi(\kappa+1)}{2\mu} \{-p^\infty + P\delta(x)\}, \quad |x| < a \tag{13}$$

with the solution bounded at the end points

$$B_y(x) = \frac{p^\infty(\kappa+1)}{2\mu} \frac{(a^2 - x^2)^{1/2}}{x}, \quad |x| < a \tag{14}$$

The consistency condition (11) yields for the extent of the separation zone

$$a = \frac{P}{\pi p^\infty} \tag{15}$$

It can be confirmed using (1) that the computed dislocation density leads to a positive gap. Moreover, the condition

$$\int_{-a}^{a} B_y(x)\, dx = 0 \tag{16}$$

necessary for the gap to close outside the interval $(-a,a)$ is satisfied automatically. Finally, equation (14) substituted into (5) gives the following normal tractions in the contact zones:

$$N(x) = -p^\infty \frac{(x^2 - a^2)^{1/2}}{|x|}, \quad a < |x| < \infty \tag{17}$$

The boundary condition to be satisfied in the two slip zones indicated in Fig. 1 is

$$S(x) = -fN(x) \operatorname{sgn} V(x) \tag{18}$$

Anticipating that the slip velocity $V(x) > 0$ in both slip zones, equation (18) combined with (6) and (17) yields the integral equation

$$\int_{-b}^{b} \frac{B_x(\xi)\, d\xi}{\xi - x} = \frac{\pi(\kappa+1)}{2\mu} \{q^\infty - fp^\infty \frac{(x^2 - a^2)^{1/2}}{|x|} \times H(|x| - a)\}, \quad |x| < b \tag{19}$$

for the density of the glide array. Again, the unknown extent of the slip zones is determined by the consistency condition (11) and

$$b = a \frac{fp^\infty}{fp^\infty - q^\infty} \tag{20}$$

The bounded solution of the integral equation (19) is

$$B_x(x) = \frac{fp^\infty(\kappa+1)}{2\mu} \frac{a}{x} \left\{ -\frac{1}{a}(a^2 - x^2)^{1/2} H(a - |x|) + \frac{1}{b}(b^2 - x^2)^{1/2} \right\}, \quad |x| < b \tag{21}$$

and it is seen that the requirement

$$\int_{-b}^{b} B_x(x)\, dx = 0 \tag{22}$$

is identically satisfied. Viewing the magnitude of the loads as dependent on time, or $P = P(t)$, it can be shown using (7) and (21) that $V(x) > 0$ on $a < |x| < b$ for increasing loads or $\dot{P}(t) > 0$.

The shear tractions in the stick zones follow by substituting (21) into (6). Thus,

$$S(x) = fp^\infty \frac{a}{|x|} \left\{ \frac{1}{a}(x^2 - a^2)^{1/2} - \frac{1}{b}(x^2 - b^2)^{1/2} \right\}, \quad b < |x| < \infty \tag{23}$$

and it is clear that the stick condition

$$|S(x)| < f\,|N(x)| \tag{24}$$

is satisfied. Moreover,

$$S(\infty) = q^\infty \tag{25}$$

on the basis of (20). The distributions of the glide dislocations and the shear tractions are shown schematically in Fig. 1.

Steady Motion

It is instructive to solve the problem of steady motion directly. On the surface, one would expect slip zones at both ends of the moving separation zone. It stands to reason,

Downloaded 02 May 2010 to 171.66.16.250. Redistribution subject to ASME license or copyright; see http://www.asme.org/terms/Terms_Use.cfm

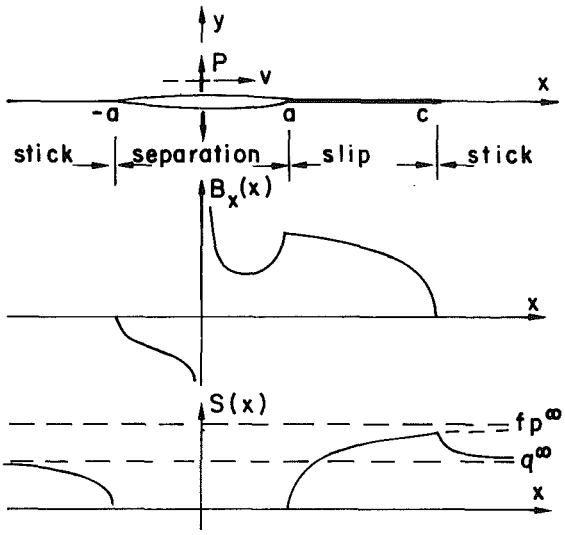


Fig. 1 The phase of load application

however, that the gap may close without an adjacent slip zone at the trailing end of the separation zone if the friction coefficient is sufficiently large. As this case is simpler to analyze, we start with the assumption that there is no trailing slip zone.

The geometry is shown in Fig. 2, where x denotes now a moving coordinates attached to the loads. Anticipating a positive slip velocity of $V(x) > 0$ in the slip zone $a < x < c$, the boundary condition on the separation and slip zones is

$$S(x) = -fN(x), \quad -a < x < c \tag{26}$$

It should be noted that, although some permanent tangential shift between the bodies is left on the interval $-\infty < x < -a$, the shift for steady motion is constant and, hence according to (4), the distribution of glide dislocations has nonzero values only on the interval $-a < x < c$. Using (5) and (6), the boundary condition yields the following integral equation

$$\int_{-a}^{c} \frac{B_x(\xi)d\xi}{\xi - x} = \frac{\pi(\kappa+1)}{2\mu}\left\{q^\infty - fp^\infty \frac{(x^2-a^2)^{1/2}}{x} H(x-a)\right\}, \quad -a < x < c \tag{27}$$

with the bounded solution

$$B_x(x) = \frac{fp^\infty(\kappa+1)}{2\mu} \frac{(a+x)^{1/2}}{x}\left\{-(a-x)^{1/2}H(a-x) + \left(\frac{a}{c}\right)^{1/2}(c-x)^{1/2}\right\}, \quad -a < x < c \tag{28}$$

The extent of the slip zone is determined by the consistency condition, and

$$c = a\left(\frac{fp^\infty}{fp^\infty - q^\infty}\right)^2 \tag{29}$$

Comparing (29) with (20) it follows that

$$c = \frac{b^2}{a} > b \tag{30}$$

which shows that the right slip zone grows in size when the loads start to move.

When a fixed configuration of dislocations moves with the velocity v, the slip velocity between the bodies is

$$V(x) = vB_x(x) \tag{31}$$

It is seen from (28) that $B_x(x) > 0$ and hence $V(x) > 0$ on $a < x < c$ as was assumed in writing the boundary condition (26).

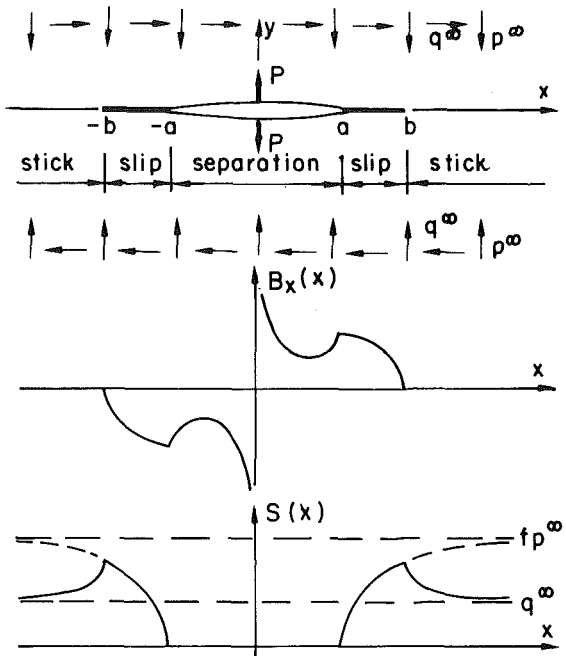


Fig. 2 Steady motion

Substituting (28) into (6), the shear tractions in the stick zones are found to be

$$S(x) = fp^\infty \frac{(x^2-a^2)^{1/2}}{|x|}\left\{1 - \left(\frac{a}{c}\right)^{1/2}\left|\frac{x-c}{x-a}\right|^{1/2}\right\}, \quad -\infty < x < -a \quad \text{or} \quad c < x < \infty \tag{32}$$

Comparing (32) with (17), it is clear that the stick condition

$$|S(x)| < f|N(x)| \tag{33}$$

is satisfied in the right stick zone $c < x < \infty$. The same is not immediately obvious for the left stick zone $-\infty < x < -a$, but it is not difficult to reason that the largest ratio $|S(x)|/|N(x)|$ is in the vicinity of $x = -a$, and that (33) is satisfied for all values of the friction coefficient. Hence there is no trailing slip zone in the present problem, and the initially assumed case is the only one possible. This result is quite suggestive, and a trailing slip zone for moving loads is more likely to be the exception than the rule in other problems.

The tangential shift left behind the moving slip and separation zones is

$$H = \int_{-a}^{c} B_x(x)dx = \frac{\pi a(\kappa+1)}{2\mu} \frac{q^\infty(2fp^\infty - q^\infty)}{fp^\infty - q^\infty} \tag{34}$$

The distribution of the dislocation density and the shear tractions are shown schematically in Fig. 2.

Transient Part of the Slip Process

Consider the moving loads in a general position specified by an increasing function $\eta(t)$ of time, and assume that there is no trailing slip zone, as indicated in Fig. 3. The slip zone ahead of the separation zone extends over the interval $(\eta + a, \eta + c)$, where c depends on η and $\eta + c(\eta)$ is an increasing function of η. The distribution of glide dislocations has nonzero values on the interval $(-b, \eta + c)$. On the interval $(-b, \eta - a)$ which at the instant considered is a stick zone, the dislocations are locked in and the density is constant in time, or independent of η. On the interval $(\eta - a, \eta + c)$ the density changes with time or, conversely, depends on η. In displaying formulas, it is convenient to introduce a coordinate x_m that moves with the separation zone and is defined by

Downloaded 02 May 2010 to 171.66.16.250. Redistribution subject to ASME license or copyright; see http://www.asme.org/terms/Terms_Use.cfm

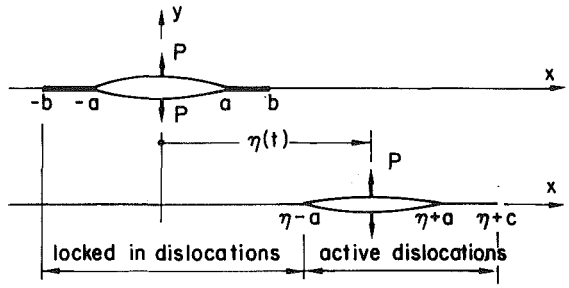


Fig. 3 Transient part of the slip process

$$x_m = x - \eta \tag{35}$$

Again anticipating a positive slip velocity, the boundary condition in the separation and slip zones is

$$S(x_m) = -f\,N(x_m), \quad -a < x_m < c \tag{36}$$

which with (6) and (17) yields the integral equation

$$\int_{-b}^{\eta+c} \frac{B_x(\xi,\eta)d\xi}{\xi - x} = \frac{\pi(\kappa+1)}{2\mu}\left\{q^\infty - fp^\infty \frac{(x_m^2 - a^2)^{1/2}}{x_m} H(x_m - a)\right\}, \quad -a < x_m < c \tag{37}$$

where the dependence of B_x on η, and thus time is now indicated explicitly. Note that the singular Cauchy integral equation (37) holds on an interval that is smaller than the range of integration and, hence, does not directly determine the unknown dislocation density $B_x(x,\eta)$.

Since $B_x(x,\eta)$ is continuous and does not depend on η in the interval $(-b,\ \eta-a)$, differentiation of (37) with respect to η gives the integral equation

$$\int_{\eta-a}^{\eta+c} \frac{B_x'(\xi,\eta)d\xi}{\xi - x} = \frac{\pi f p^\infty(\kappa+1)}{2\mu} \frac{a^2 H(x_m - a)}{x_m^2 (x_m^2 - a^2)^{1/2}}, \quad -a < x_m < c \tag{38}$$

where

$$B_x'(x,\eta) = \frac{\partial B_x(x,\eta)}{\partial \eta} \tag{39}$$

Note in particular that $B_x[\eta + c(\eta),\eta] = 0$. The singular solution is chosen for $B_x'(x,\eta)$, and from (38) then

$$B_x'(x,\eta) = Q(x,\eta)H[R(x,\eta)] \tag{40}$$

with H denoting the Heaviside step function,

$$Q(x,\eta) = \frac{fp^\infty(\kappa+1)}{2\mu} \frac{a^2}{[R(x,\eta)]^{1/2}} \left\{ -\frac{1}{x_m^2}\left[\frac{c(\eta) - x_m}{a - x_m}\right]^{1/2} \times H(a - x_m) + \frac{1}{x_m^2}\left[\frac{c(\eta)}{a}\right]^{1/2} + \frac{c(\eta) - a}{2a^{3/2} x_m [c(\eta)]^{1/2}} + A(\eta)\right\} \tag{41}$$

$$R(x,\eta) = [c(\eta) - x_m](x_m + a) \tag{42}$$

and $A(\eta)$ being an arbitrary function of η. Integrating (40)

$$B_x(x,\eta) = B_x(x,0) + \int_0^\eta Q(x,s)H[R(x,s)]\ ds \tag{43}$$

The initial dislocation density $B_x(x,0)$ is given by (21) and has nonzero values only on the interval $(-b,b)$.

Since there is no tangential shift between the solids outside the interval $(-b,\ \eta + c)$, the condition

$$\int_{-b}^{\eta + c(\eta)} B_x,(\eta)\ dx = 0 \tag{44}$$

must be enforced. Noting that $\eta + c(\eta)$ is an increasing function, i.e., $\eta + c(\eta) > s + c(s)$ if $\eta > s$, and that $c(0) = b$, equation (44) gives upon interchanging the order of integration

$$\int_{-b}^{b} B_x(x,0)dx + \int_0^\eta \int_{s-a}^{s+c(s)} Q(x,s)dx\ ds = 0 \tag{45}$$

Carrying out the integrations in (45) results in

$$\int_0^\eta A(s)\ ds = 0 \tag{46}$$

which must be satisfied for all η. Consequently,

$$A(\eta) = 0 \tag{47}$$

Next, equation (43) is substituted into (6), Interchanging the order of integration

$$S(x,\eta) = q^\infty - \frac{2\mu}{\pi(\kappa+1)}\left\{\int_{-b}^{b} \frac{B_x(\xi,0)d\xi}{\xi - x} + \int_0^\eta \int_{s-a}^{s+c(s)} \frac{Q(\xi,s)d\xi}{\xi - x} ds\right\} \tag{48}$$

where $B_x\ (x,0)$ is given by (21). For $\eta = 0$, equation (48) reduces to an identity on basis of (20) and (21). Finally, using (17) and (48) in the boundary condition (36), and performing the integration with respect to ξ yield the following integral equation for the determination of $c(\eta)$:

$$ab\int_0^\eta \frac{H[x - s - c(s)]}{(x-s)\{a\ c(s)[x - s + a][x - s - c(s)]\}^{1/2}} \left[\frac{c(s)}{x - s} + \frac{c(s) - a}{2a}\right] ds = \frac{(x^2 - b^2)^{1/2}}{x} H(x - b), \quad -a < x_m < c(\eta) \tag{49}$$

As the integral equation (49) is satisfied identically for $x < b$, we can restrict the subsequent analysis to $x > b$. We then introduce the new variable τ related implicitly to x by

$$x = \tau + c(\tau) \tag{50}$$

Since $\tau + c(\tau)$ is an increasing function, this transformation is one to one. Also, $x > b$ transforms to $\tau > 0$. With (50), the integral equation becomes

$$\int_0^\tau F(\tau,s)ds = \frac{\{[c(\tau) + \tau]^2 - b^2\}^{1/2}}{c(\tau) + \tau}, \quad \tau > 0 \tag{51}$$

where

$$F(\tau,s) = b_o \frac{2a\ c(s) + [c(\tau) + \tau - s][c(s) - a]}{2[c\ (\tau) + \tau - s]^2\{a\ c(s)[c(\tau) + \tau - s + a][c(\tau) - c(s) + \tau - s]\}^{1/2}} \tag{52}$$

Scaling as follows

$$r = b/a, \quad s = ar^2 s_0 \tag{53}$$

$$\tau = ar^2\tau_0, \quad c(\tau) = ar^2 c_0(\tau_0) \tag{54}$$

the integral equation (51) becomes

$$\int_0^{\tau_0} F_0(\tau_0,s_0)d\ s_0 = \frac{r\{r^2[c_0(\tau_0) + \tau_0]^2 - 1\}^{1/2}}{c_0(\tau_0) + \tau_0}, \tau_0 > 0 \tag{55}$$

with

$$F_0(\tau_0,s_0) = \frac{2c_0(s_0) + [c_0(\tau_0) + \tau_0 - s_0][r^2 c_0(s) - 1]}{2[c_0(\tau_0) + \tau_0 - s_0]^2\{c_0(s_0)[c_0(\tau_0) + \tau_0 - s_0 + r^{-2}][c_0(\tau_0) - c_0(s_0) + \tau_0 - s_0]\}^{1/2}} \tag{56}$$

Downloaded 02 May 2010 to 171.66.16.250. Redistribution subject to ASME license or copyright; see http://www.asme.org/terms/Terms_Use.cfm

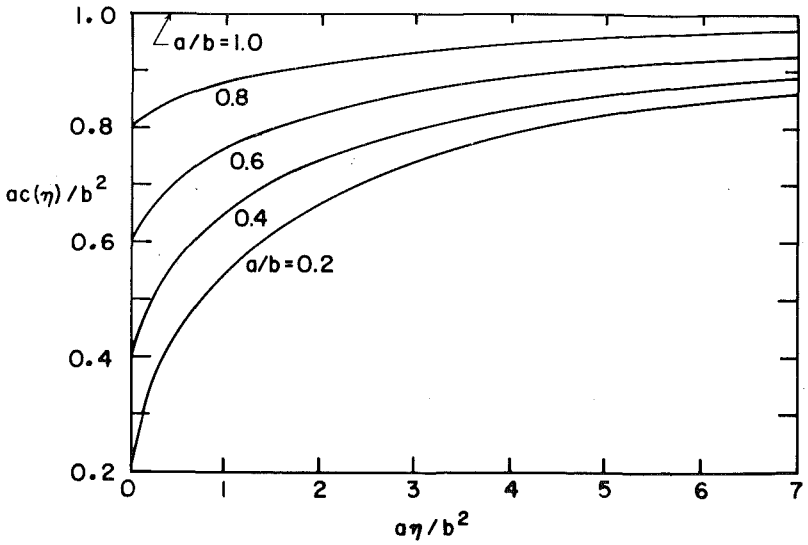


Fig. 4 Extent of the active slip zone during the transient part of the slip process

To solve (55) numerically, we note that

$$c_0(0) = 1/r \tag{57}$$

and assume that c_0 has the continuous piecewise linear form

$$c_0(\tau_0) = \frac{1}{\Delta\tau}\{A_k(\tau_{k+1} - \tau_0) + A_{k+1}(\tau_0 - \tau_k)\} \times H[(\tau_{k+1} - \tau_0)(\tau_0 - \tau_k)] \tag{58}$$

where

$$\tau_k = k\Delta\tau, \quad A_0 = 1/r \tag{59}$$

and $\Delta\tau$ is chosen as some small number. We note that

$$c_0(\tau_k) = A_k \tag{60}$$

Now (55) is approximated by

$$\sum_{k=1}^{N} G_0\left[\tau_N, \frac{1}{2}(\tau_k + \tau_{k-1})\right] \int_{\tau_{k-1}}^{\tau_k} \frac{ds_0}{[c_0(\tau_N) - c_0(s_0) + \tau_N - s_0]^{1/2}} = \frac{r[r^2 c_0^2(\tau_N) - 1]^{1/2}}{c_0(\tau_N)}, \quad N = 1,2, \ldots . \tag{61}$$

where

$$G_0(\tau_0, s_0) = [c_0(\tau_0) - c_0(s_0) + \tau_0 - s_0]^{1/2} F_0(\tau_0, s_0) \tag{62}$$

The integration in (61) is done exactly. For $N = m$, A_m is unknown, while $A_0, A_1, \ldots, A_{m-1}$ are known. Thus (61) can be solved for A_m by iteration using the secant method.

Discussion

Figure 4 shows the plot of $c_0(\tau_0)$ versus τ_0, or equivalently $ac(\eta)/b^2$ versus $a\eta/b^2$ for $a/b = 0.2, 0.4, 0.6, 0.8$ and 1.0. Note that $a/b = 1$ corresponds to no slip zone or $c(\eta) = a$. The curves in Fig. 4 suggest that $c_0(\infty) = 1$ and hence that

$$c(\infty) = c^\infty = b^2/a \tag{63}$$

which is in agreement with the value of c given by (30) for steady motion. To verify this, we assume that for large τ

$$c(\tau) = c^\infty + o(1) \tag{64}$$

make the change of integration variables $\eta_0 = \tau - s$ in (51) and take the limit $\tau \to \infty$ to achieve

$$\frac{b}{(ac^\infty)^{1/2}} \int_0^\infty \frac{d}{d\eta_0}\left\{\frac{[\eta_0(c^\infty + \eta_0 + a)]^{1/2}}{c^\infty + \eta_0}\right\} d\eta_0 = 1 \tag{65}$$

The solution to (65) for c^∞ is indeed given by (63).

For the purpose of illustration consider $q^\infty = 1/2\, fp^\infty$. Then $b = 2a$ from (20) and $c^\infty = 4a$ from (29). Taking $a\eta/b^2 = 7$ which corresponds to $\eta = 28a$, Fig. 4 gives approximately $ac(\eta)/b^2 = 0.87$ or $c(\eta) \doteq 3.5a$. This shows that the approach to steady state is rather slow. Note that the steady state is approached more quickly for smaller values of q^∞, but even more slowly for larger values of $q^\infty < fp^\infty$.

It is shown in the Appendix that just to the left of the trailing end of the separation zone

$$\left|\frac{S(x)}{fN(x_m)}\right| \sim 1 - \left[\frac{c(\eta) + a}{2c(\eta)}\right]^{1/2}, \quad -a - \epsilon < x_m < -a \tag{66}$$

with $x_m = x - \eta$. Thus the stick condition is satisfied near the trailing end of the separation zone for any coefficient of friction. Note that for $\eta \to \infty$, equation (66) is in agreement with the corresponding result for steady motion obtained from (32) near $x = -a$.

Acknowledgment

The work by one of the authors (A. K. G.) was supported by the U.S. Dept. of Energy under contract no. W-7405-ENG-82, Division of Engineering, Mathematical, and Geosciences, budget code AK-01-04-02.

References

1 Anscombe, H., and Johnson, K. L., "Slip of a Thin Solid Tyre Press-fitted on a Wheel," *International Journal of Mechanical Sciences*, Vol. 16, 1974, pp. 329-334.

2 Comninou, M., Barber, J. R., and Dundurs, J., "Interface Slip Caused by a Surface Load Moving at Constant Speed," *International Journal of Mechanical Sciences*, Vol. 25, 1983, pp. 41-46.

3 Mura, T., *Micromechanics of Defects in Solids*, Martinus Nijhoff, The Hague, 1982.

4 Muskhelishvili, N. I., *Singular Integral Equations*, P. Noordhoff, Groningen, 1953.

APPENDIX

To establish the asymptotic result (66) for the behavior of $S(x,\eta)$ near the trailing end of the separation zone, we consider values of x such that

Downloaded 02 May 2010 to 171.66.16.250. Redistribution subject to ASME license or copyright; see http://www.asme.org/terms/Terms_Use.cfm

$$0 < \frac{-x_m - a}{a} < \epsilon << 1 \tag{A.1}$$

where $x_m = x - \eta$. We begin by computing the singularity in the derivative of $S(x,\eta)$ with respect to η which from (48) is

$$S'(x,\eta) = I_1 + I_2 \tag{A.2}$$

where

$$I_1 = K(\eta)\int_{\eta-a}^{\eta+c(\eta)} \frac{d\xi}{(\xi - x)(\xi + a - \eta)^{1/2}}$$

$$\sim \frac{K(\eta)}{(-x_m - a)^{1/2}} \{\pi - 0[(-x_m - a)^{1/2}]\} \tag{A.3}$$

$$I_2 = \int_{\eta-a}^{\eta+c(\eta)} \left[-\frac{2\mu Q(\xi,\eta)}{\pi(\kappa+1)} - \frac{K(\eta)}{(\xi + a - \eta)^{1/2}} \right] \frac{d\xi}{\xi - x} \tag{A.4}$$

and

$$K(\eta) = -\frac{2\kappa}{\pi(\kappa+1)} \lim_{\xi \to (\eta-a)^+} + [Q(\xi,\eta)(\xi + a - \eta)^{1/2}]$$

$$= \frac{fp^\infty}{\pi(2a)^{1/2}} \left\{ 1 - \left[\frac{c(\eta) + a}{2c(\eta)} \right]^{1/2} \right\} \tag{A.5}$$

The integrand of I_2 is integrable at $x = \eta - a$. Thus I_2 is not singular near this point. Hence

$$S'(x,\eta) \sim \frac{\pi K(\eta)}{(-x_m - a)^{1/2}} \tag{A.6}$$

Integration of (A.6) with respect to η yields

$$S(x,\eta) \sim 2\pi \mathrm{K}(\eta)(-x_m - a)^{1/2} + 0(-x_m - a) \tag{A.7}$$

From (17) one obtains that

$$N(x_m) \sim -p^\infty (2/a)^{1/2}(-x_m - a)^{1/2} \tag{A.8}$$

and (66) follows immediately from (A.6), (A.8), and (A.5).

Downloaded 02 May 2010 to 171.66.16.250. Redistribution subject to ASME license or copyright; see http://www.asme.org/terms/Terms_Use.cfm

Endochronic Analysis of Cyclic Elastoplastic Strain Fields in a Notched Plate

K. C. Valanis
Mem. ASME

J. Fan

College of Engineering,
University of Cincinnati,
Cincinnati, Ohio 45221

In this paper we present an analytical cum-numerical scheme, based on endochronic plasticity and the finite element formalism. The scheme is used to calculate the stress and elastoplastic strain fields in a plate loaded cyclically in its own plane along its outer edges and bearing two symmetrically disposed edge notches. One most important result that stands out is that while the external loading conditions are symmetric and periodic, the histories of stress and strain at the notch tip are neither symmetric nor periodic in character. In cyclic tension ratcheting phenomena at the tip of the notches prevail and a progressive change of the residual stress field at the notch line is shown to occur.

1 Introduction

The problem of stress and elastoplastic strain distribution in a plate containing a notch or crack in the presence of plastic deformation is of vital importance as it relates to fracture and fatigue. This problem has been notoriously difficult to solve, even with finite element techniques, using classical plasticity theory, and we could find very few instances in the literature where the problem was tackled at all. Most of the work that we could find was limited to monotonic loading and quite frequently to the growth of the plastic zone, with scant attention to the detailed stress and strain distributions, as functions of the history of the loading [1].

A difficult element of the classical plasticity theory is the concept of the yield surface which leads to experimental and numerical difficulties when attempting to describe and analyze the two or three-dimensional response of a material. Valanis circumvented this difficulty by developing the *endochronic theory* which does not require the concept of yield for the description of plastic behavior of materials.

In a series of recent works, Valanis [2-4] demonstrated that the endochronic theory could apply more precisely to situations involving unloading the cyclic behavior of materials. Application to soils (Valanis and Read [3]) and metals (Valanis and Lee [4]) bore this out.

The applicability of the theory to these more complex situations became possible as a result of defining the intrinsic time in terms of the plastic strain tensor (Valanis [2]). In the foregoing papers it was demonstrated that cyclic behavior of materials can be described accurately over a large number of cycles (300 in the case of reference [3] and in the terminal steady state in the case of reference [4]). More importantly, this was achieved with ease of formulation and computation.

However, in the previous cited work the stress and strain fields were homogeneous. In this paper we apply the endochronic theory for the first time to the determination of inhomogeneous cyclic stress and plastic strain fields in more than one dimension and thereby demonstrate that such fields can be analyzed fairly routinely without the use of a yield surface.

To this end we first review the theory briefly and then introduce an incremental form of the elastoplastic constitutive equations which make it possible to determine the elastoplastic behavior in a unified manner. We then formulate a series of governing relations using the finite element method and proceed to analyze the cyclic stress and plastic strain distribution in a metal plate with two symmetrically disposed edge notches.

Specifically, a plate (both in plane stress and plane strain) with geometry shown in Fig. 1 was loaded cyclically in its own plane along its outer edges. See Fig. 1 where only one quarter of the plate is actually shown. Cases of symmetric and asymmetric loading histories were studied.

The results and conclusions are discussed in Section 5. However, one most important result of the analysis is that in the presence of externally symmetric periodic loading conditions the histories of stress and strain at the notch tip are neither symmetric nor periodic in character. Particularly in the case of cyclic tension, ratcheting takes place in regard to the strain near the tip of the crack (notch).

2 The Endochronic Theory

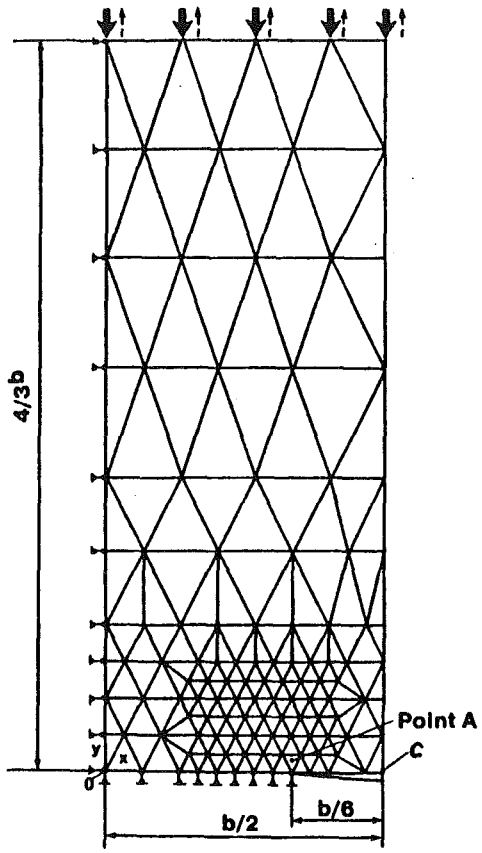
The greatest difficulty encountered in the application of the classical theory of plasticity is the lack of knowledge of the shape of the subsequent yield surface for the particular material at hand and the experimental difficulties encountered

Contributed by the Applied Mechanics Division and presented at the Winter Annual Meeting, Boston, Mass., November 13-18, 1983 of THE AMERICAN SOCIETY OF MECHANICAL ENGINEERS.

Discussion on this paper should be addressed to the Editorial Department, ASME, United Engineering Center, 345 East 47th Street, New York, N.Y. 10017, and will be accepted until two months after final publication of the paper itself in the JOURNAL OF APPLIED MECHANICS. Manuscript received by ASME Applied Mechanics Division, January, 1983; Final revision, April, 1983. Paper No. 83-WA/APM-14.

Copies will be available until July, 1984.

Copyright © 1983 by ASME
Downloaded 02 May 2010 to 171.66.16.250. Redistribution subject to ASME license or copyright; see http://www.asme.org/terms/Terms_Use.cfm



Symbol: ⊥ –v=o, u≠0; ⊢⊣ –u=0, v≠0

Fig. 1 Plate geometry and grid arrangement

in finding it in the fully three-dimensional case. More importantly, however, it has been found by many experimenters that the shape of the subsequent yield surface depends very strongly on the definition of the yield point, particularly in situations following initial deformation. For extensive discussion of the issue, the reader is referred to references [5–8].

To the extent that yield is strictly an idealization, one should be in a position to develop rate-independent theories, alternative to classical plasticity, which do not make use of this idealization a priori. This is the scope and purpose of the endochronic theory. It is a constitutive theory that describes the mechanical response of history-dependent materials without using the notion of a yield surface. However, this does not exclude the appearance of a yield surface in an a posteriori fashion.

The effects of history are introduced in the theory by defining a "memory path" in the plastic strain space such that the "distance" between two adjacent plastic strain states is given by $d\zeta$ where

$$d\zeta^2 = d\epsilon^p \cdot \underset{\sim}{\mathbf{P}} \cdot d\epsilon^p \tag{2.1}$$

where $\underset{\sim}{\mathbf{P}}$ is positive definite and symmetric and is a material property in the sense that it may vary from one material to another. Specifically, if $\underset{\sim}{\mathbf{P}}$ is isotropic and independent of ϵ^p then

$$P_{ijkl} = k_1\ \delta_{ij}\ \delta_{kl} + k_2\ \delta_{ik}\ \delta_{jl} \tag{2.2}$$

in which case

$$d\zeta^2 = k_1\ d\epsilon^p_{ii}\ d\epsilon^p_{jj} + k_2\ d\epsilon^p_{ij}\ d\epsilon^p_{ij} \tag{2.3}$$

In the specific case where the material is plastically incompressible then $d\epsilon^p_{ii} = 0$ and

$$d\zeta^2 = k_2\ de^p_{ij}\ de^p_{ij} \tag{2.4}$$

where de^p_{ij} is the deviatoric part of $d\epsilon^p_{ij}$ (however, in the case of plastic incompressibility they are equal).

Without loss of generality one may set $k_2 = 1$ since its value can be absorbed into the memory function of a material as will be discussed in the following. Hence one may set

$$d\zeta^2 = \|d\mathbf{e}^p\| \tag{2.5}$$

where double bars denote the euclidean norm. We remark that

$$d\epsilon^p = d\epsilon - d\epsilon^e \tag{2.6}$$

where $d\epsilon^e$ denotes the elastic part of the strain tensor given by relation (2.7)

$$d\epsilon^e = \underset{\sim}{\phi} \cdot d\sigma \tag{2.7}$$

where $\underset{\sim}{\phi}$ is the elastic compliance tensor and $d\sigma$ is the increment in stress.

Hardening properties associated with a strain history are introduced through a hardening function $f(z)$, which is a nondecreasing function of z, thereby defining a memory scale z such that

$$dz = \frac{d\zeta}{f(\zeta)} \tag{2.8}$$

This function accounts for the fact that the internal resistance to motion of a material increases with the history of deformation (reflecting the multiplication of dislocations in metals, for instance). It could be viewed as a measure of the increase of the rate of internal dissipation in a material as deformation progresses.

These points were discussed in papers on thermodynamics of internal variables, when the thermodynamic foundations of the theory were established by Valanis; see references [9–11].

If one then proceeds through the formalism of linear irreversible thermodynamics where the evolution of internal variables is with respect to z (rather than t, the Newtonian time scale), see reference [12], one finds that the stress is a linear hereditary functional of the plastic strain history in terms of the time scale z. In the case of an isotropic plastically incompressible material the hydrostatic response is elastic, i.e.,

$$\sigma_{kk} = 3K\epsilon_{kk} \tag{2.9}$$

where the deviatoric response is given by equation (2.10)

$$\mathbf{s} = \int_0^z \rho(z - z')\ \frac{\partial \mathbf{e}^p}{dz'}\ dz' \tag{2.10}$$

where $\rho(z)$ is weakly singular at the origin but integrable in the domain $0 \le z' \le \infty$.

The appearance of the singularity serves two main purposes. (*a*) It gives rise to closed hysteresis loops, however small these may be in the uniaxial or shear stress-strain space, (*b*) it ensures initially elastic unloading, i.e., initially zero rate of dissipation upon unloading, i.e., it implies an infinitesimally small elastic domain.

There are various explicit algebraic forms that have these properties of $\rho(z)$. Two of these were discussed at great length in reference [3]. They are

$$(i)\quad \rho(z) = z^{-\alpha} \sum_{r=1}^{n} R_r e^{-\beta_r z} \tag{2.11}$$

$$0 < \alpha < 1$$

$$(ii)\quad \rho(z) = \sum_{r-1}^{\infty} R_r e^{-\beta_r z} \tag{2.12}$$

with the conditions that β_r and R_r are positive for all r and

Downloaded 02 May 2010 to 171.66.16.250. Redistribution subject to ASME license or copyright; see http://www.asme.org/terms/Terms_Use.cfm

$$\sum_{r=1}^{\infty} R_r = \infty, \quad \sum_{r=1}^{\infty} \frac{R_r}{\beta_r} < \infty \qquad (2.13a,b)$$

Condition (2.13*a*) ensures that $\rho(z)$ is singular at the origin while equation (2.13*b*) ensures that $\rho(z)$ is integrable over a finite domain of z. In this paper we adopt the second form and approximate the infinite series (2.12) by means of three terms. We found three terms suffice to describe the tensile stress-strain response with good accuracy. See section under Application for further details.

The elastic deviatoric strain is related to the stress by the linear relation

$$2\mu_0 \mathbf{e}^e = \mathbf{s} \qquad (2.14)$$

where μ_0 is the elastic shear modulus.

3 The Material Functions $\rho(z)$ and $f(\zeta)$

Before the theory can be applied to a specific problem the form of the kernel $\rho(z)$ (equation (2.10)) and the form of the hardening function $f(\zeta)$ (equation (2.8)) must be known. Insofar as OFHC copper is concerned, the form of $f(\zeta)$ was determined by a strain-controlled cyclic test. The method of determination of this function from cyclic tests in shear was discussed in reference [13]. We do not wish to go into this method in great detail in this paper. Suffice it to say that the form of $f(\zeta)$ is determined from the reversal characteristics of the axial stress strain curve and is given in equation (3.1)

$$f(\zeta) = 1 + c_1 \zeta^{c_2} \qquad (3.1)$$

where $c_1 = 0.53$ and $c_2 = 0.72$. For the purposes of numerical analysis the form of $\rho(z)$ is given in approximation by three exponential terms. In effect

$$\rho(z) = \sum_{r=1}^{3} A_r e^{-\alpha_r z} \qquad (3.3)$$

where $A_1 = 5.9 \times 10^2$ GPA, $A_2 = 2.2 \times 10^2$ GPA, $A_3 = 46$ GPA, $\alpha_1 = 2.75 \times 10^4$, $\alpha_2 = 1.15 \times 10^4$, and $\alpha_3 = 7.67 \times 10^3$.

To illustrate the adequacy of this form a comparison between theory and experiment is made in Fig. 2 in the case of monotonic tensile response. It may be seen that the theoretical curve agrees well with experiment.

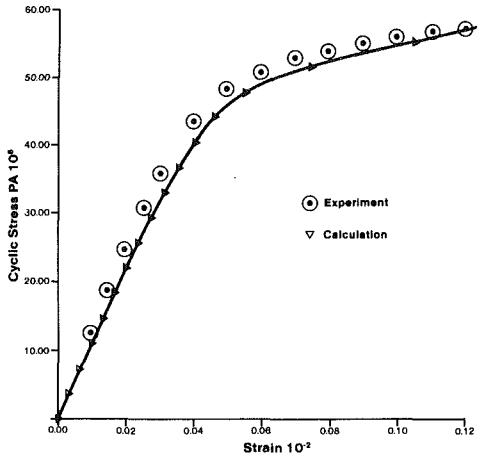


Fig. 2 Comparison between experimental and calculated stress-strain curve in tension

4 The Incremental Form of the Encochronic Elastoplastic Constitutive Equation and the Formulation of the Finite Element Method

In the present paper the form of $\rho(z)$ given by equation (2.12) was used in equation (2.10). This form of $\rho(z)$ is continuous and differentiable in (0, ∞) and therefore the incremental form of equation (2.10) specified in the following can be used in conjunction with a finite element code.

Specifically one may differentiate equation (2.10) with respect to z to obtain the following differential form of the endochronic constitutive equation:

$$d\mathbf{s} = \rho(0) d\mathbf{e}^p + \mathbf{h}(z)\, dz \qquad (4.1)$$

where

$$\mathbf{h}(z) = \int_0^z \hat{\rho}(z - z') \frac{\partial \mathbf{e}^p}{\partial z'} dz' \qquad (4.2)$$

and

$$\hat{\rho}(z) \equiv \frac{d\rho}{dz} \qquad (4.2a)$$

In view of equation (2.14), $d\mathbf{e}^p$ is given by equation (4.3), i.e.,

$$d\mathbf{e}^p = d\mathbf{e} - \frac{1}{2\mu} d\mathbf{s} \qquad (4.3)$$

The elastoplastic constitutive equation that combines equation (4.3) and (4.1) can then be expressed in the differential form

$$ds_{ij} = 2\mu_p \left\{ de_{ij} + \frac{1}{\rho(0)} h_{ij}(z)\, dz \right\} \qquad (4.4)$$

where

$$2\mu_p = \rho(0) \left\{ 1 + \frac{\rho(0)}{2\mu} \right\}^{-1} \qquad (4.4a)$$

Alternatively, for computational purposes the incremental form given by equation (4.5) may be used, i.e.,

$$\Delta s_{ij} = 2\mu_p \left\{ \Delta e_{ij} + \frac{1}{\rho(0)} h_{ij}(z)\, \Delta z \right\} \qquad (4.5)$$

By definition,

$$de_{ij} = d\epsilon_{ij} - 1/3\ d\epsilon_{\alpha\alpha}\delta_{ij} \qquad (4.6)$$

$$ds_{ij} = d\sigma_{ij} - 1/3\ d\sigma_{\alpha\alpha}\delta_{ij} \qquad (4.7)$$

Substituting (4.6) and (4.7) into (4.4) and using equation (2.9) we obtain the operational incremental form of the elastoplastic constitutive equation in terms of $d\sigma$, $d\epsilon$, and $d\mathbf{H}_p$ which in matrix notation is as follows:

$$\{d\sigma\} = [D]\{d\epsilon\} + \{dH_p\} \qquad (4.8)$$

where

$$[D] = \begin{bmatrix} c_1 & c_2 & 0 \\ c_2 & c_1 & 0 \\ 0 & 0 & \mu_p \end{bmatrix} \qquad (4.8a)$$

and

$$\{dH_p\} = \begin{Bmatrix} dH_{px} \\ dH_{py} \\ dH_{pxy} \end{Bmatrix} \qquad (4.8b)$$

In the plane stress condition

$$c_1 = \frac{12K\mu_p + 4\mu_p^2}{3K + 4\mu_p} \qquad (4.9)$$

$$c_2 = \frac{6K\mu_p - 4\mu p^2}{3K + 4\mu_p} \qquad (4.10)$$

Downloaded 02 May 2010 to 171.66.16.250. Redistribution subject to ASME license or copyright; see http://www.asme.org/terms/Terms_Use.cfm

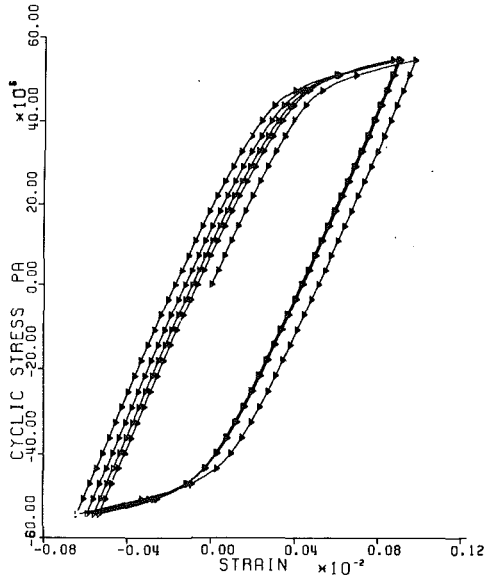


Fig. 3 Hysteresis loops of σ_y versus ϵ_y for cyclic loading with constant stress amplitude of 5.4 × 10^7 PA

$$dH_{px} = \{2\mu_p h_x(z) - D_1 h_z(z)\}\, dz/\rho(0) \tag{4.11}$$

$$dH_{py} = \{2\mu_p h_y(z) - D_1 h_z(z)\}\, dz/\rho(0) \tag{4.12}$$

$$dH_{pxy} = 2\mu_p h_{xy}(2)\, dz/\rho(0) \tag{4.13}$$

In the plane strain condition

$$c_1 = \frac{3K+4\mu_p}{3} \tag{4.14}$$

$$c_2 = \frac{3K-2\mu_p}{3} \tag{4.15}$$

$$dH_{px} = 2\mu_p h_x(z)\, dz/\rho(0) \tag{4.16}$$

$$dH_{py} = 2\mu_p h_y(z)\, dz/\rho(0) \tag{4.17}$$

$$dH_{xy} = 2\mu_p h_{xy}(z)\, dz/\rho(0) \tag{4.18}$$

We note that $\{D\}$ is an adequate approximation to the elastic matrix $\{E\}$. It is evident from equation (4.4*a*) that when $\rho(0)\to\infty$, $\{D\}$ becomes the elastic matrix $\{E\}$. Take plane stress as an example:

$$\lim_{\rho(0)\to\infty} \{D\} = \{E\} = \frac{E}{2(1+\nu)(1-\nu)} \begin{Bmatrix} 2 & 2\nu & 0 \\ 2\nu & 2 & 0 \\ 0 & 0 & (1-\nu) \end{Bmatrix} \tag{4.19}$$

Using (4.8) and the principle of virtual work, it is possible to formulate an initial stress finite element computational algorithm of the endochronic theory. The governing equation is:

$$\{K\}\{\Delta q\} = \{\Delta P_{ex}\} + \{\Delta P_p\} \tag{4.20}$$

where $\{K\}$ is the stiffness matrix of an individual element and is the same as the stiffness matrix of an element in the usual elastic analysis but the constants c_1 and c_2 are obtained from equations (4.9) and (4.10) or (4.14) and (4.15).

The quantities $\{\Delta q\}$ and $\{\Delta P_{ex}\}$ denote the matrices of the incremental node displacements and node external forces of the element, respectively.

The quantity $\{\Delta P_p\}$ is the incremental plastic pseudoforce matrix for a typical triangular element used in the analysis and has the form:

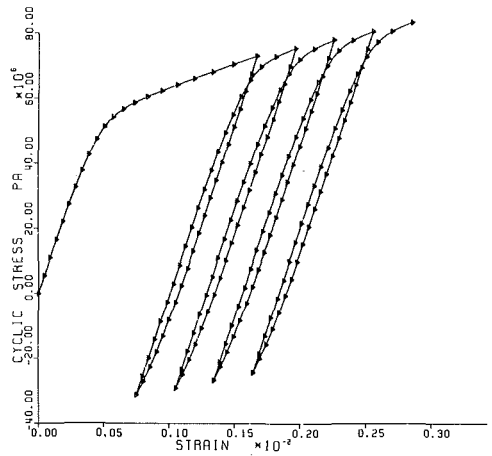


Fig. 4 Stress response σ_y to cyclic tension in the direction of loading at a point *A* near the notch top. See Fig. 1 (applied stress: 3.7 × 10^7 PA).

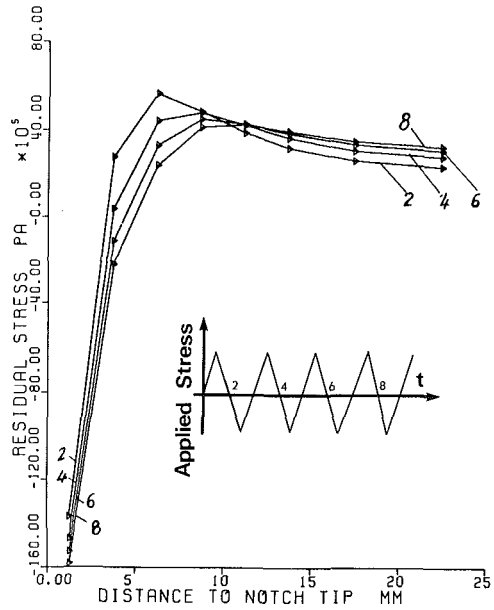


Fig. 5 Residual stress distribution $\sigma_y(x)$ along the notch line, as a function of number of reversals

$$\{\Delta P_p\} = -t/2 \begin{Bmatrix} \alpha_1 \Delta H_{px} + \beta_1 \Delta H_{pxy} \\ \alpha_2 \Delta H_{px} + \beta_2 \Delta H_{pxy} \\ \alpha_3 \Delta H_{px} + \beta_3 \Delta H_{pxy} \\ \beta_1 \Delta H_{py} + \alpha_1 \Delta H_{pxy} \\ \beta_2 \Delta H_{py} + \alpha_2 \Delta H_{pxy} \\ \beta_3 \Delta H_{py} + \alpha_3 \Delta H_{pxy} \end{Bmatrix} \tag{4.21}$$

where t is the thickness of the plate.

We note that ΔH_{px}, ΔH_{py}, and ΔH_{pxy} can be obtained from equations (4.11)–(4.13) or (4.16)–(4.18) by changing dz to Δz while α_i and β_i are related to the differences of the coordinates x_i, y_i, x_j, y_j, x_k, and y_k of the triangle, i.e.,

$$\alpha_i = 1/2 e_{ijk}\ \Delta y_{jk}, \quad \beta_i = 1/2 e_{ijk}\ \Delta x_{jk} \quad (i=1,2,3) \tag{4.22}$$

where $\Delta y_{jk} = y_j - y_k$, $\Delta x_{jk} = x_k - x_j$, and e_{ijk} is the permutation symbol.

The incremental elastoplastic solution is obtained by iteratively revising the right-hand side of the system of finite element equations by the addition of a vector of plastic

Downloaded 02 May 2010 to 171.66.16.250. Redistribution subject to ASME license or copyright; see http://www.asme.org/terms/Terms_Use.cfm

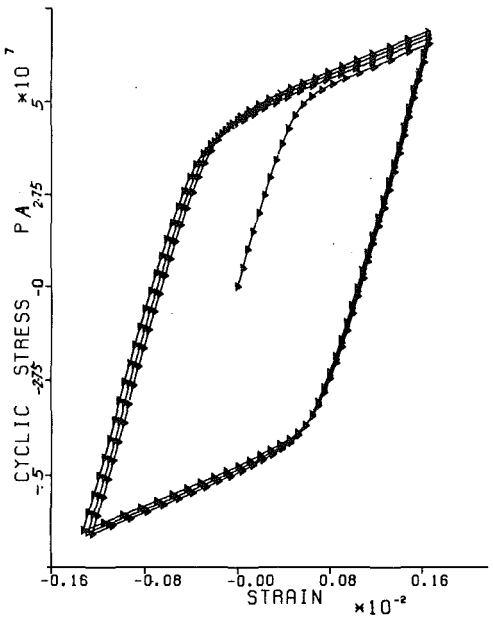


Fig. 6 Stress response σ_y at A to symmetric stress-controlled loading conditions (applied stress amplitude: 3.7 × 10^7 PA)

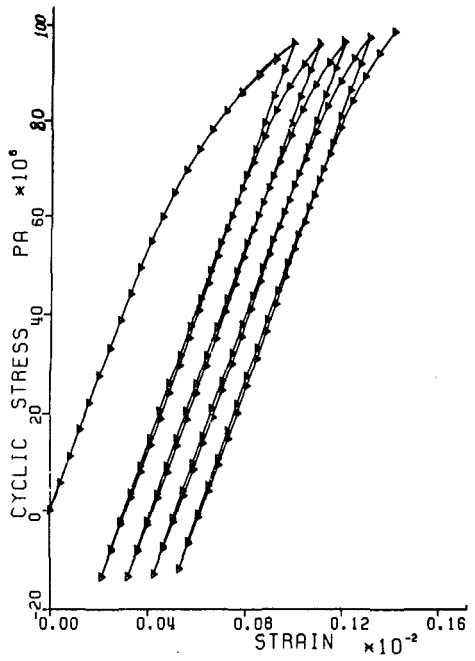


Fig. 7 Stress response σ_y to symmetric cyclic loading in plane strain at A

pseudoforces. The nonlinear solution is then obtained through solution of a series of linear equations and by variation of the pseudoplastic load terms until the maximum difference in the values of Δz between any two consecutive iterations is less than some defined tolerance. A new loading or unloading process is then initiated.

On the basis of the preceding formula, a computer program called Endo-2, was developed to analyze the material response to monotonic and cyclic loading.

5 Discussion of Results

Cyclic Stress Response of Unnotched Plate Under Stress-Controlled Conditions. The axial cyclic response of a uniformly loaded (unnotched) plate in plane stress was investigated under stress-controlled conditions, and the calculated hysteresis loops are shown in Fig. 3 for eight reversals, where the stress amplitude is 5.4 × 10^7 PA.

From the curve the following phenomena can be observed:

(*A*) During the cyclic process the material is hardening while ratcheting is basically absent.

(*B*) The strain response is asymmetric despite the symmetric loading conditions.

Stress Response of a Notched Plate Under Stress-Controlled Condition of Cyclic Tension. The response of a notched plate to a history of cyclic tension (stress: 3.7 × 10^7 PA) is shown in Figs. 4–5. Figure 4 shows the hysteresis loops ($\sigma_y - \epsilon_y^p$) at point A (see Fig. 2) (located at the top of the tip of the notch). On the basis of the stress response curves one can observe the following:

(*A*) Ratcheting takes place and plastic strains accumulate progressively in the tensile strain direction. At the tip of the crack (notch), there is a large tensile plastic strain field. It is easily seen that if the crack (notch) were propagating, a large permanent tensile plastic strain domain would remain in the wake of the propagating crack (notch). This point was discussed by W. Elber [14] who conjectured that "the crack closure phenomenon is a direct consequence of the permanent tensile plastic deformations left in the wake of the propagating crack."

(*B*) Figure 5 shows the distribution of the residual stress along the notch line for points 2, 4, 6, and 8. It is clear that the magnitude *and* the region of the compressive residual stress will both increase with increasing number of reversals. This is most likely due to a substantially elastic unloading process and the inherent ratcheting phenomena.

Stress Response of a Notched Plate Under Symmetric Stress-Controlled Conditions. Figure 6 shows the stress σ_y at point A of the notched plate as a function of the elastoplastic strain under symmetric cyclic loading (applied stress: ± 3.7 × 10^7 PA). From the curve we can see that hardening is dominant in symmetric cyclic loading. The response is substantially different in cyclic tension where ratcheting is very strong.

Cyclic Loading Under Plane Strain Conditions of Cyclic Tension. Figure 7 shows at point A a sequence of hysteresis loops that describe the cyclic relation between σ_y and ϵ_y^p, under plane strain conditions (applied stress as in Fig. 4). Qualitatively the stress response is the same as in plane stress except that the material appears to be harder in the sense that the plastic strain increment per cycle is smaller, while the stress amplitude is higher.

After eight reversals the maximum plastic strain ϵ_y^p in plane stress is 2.56 times greater than that in plane strain. It seems that the residual and peak plastic strain still accumulate in a tensile manner, but more slowly in plane strain than in plane stress.

Experiments to verify the theoretical predictions are now in progress. The results, however will be the basis of a future paper.

References

1 Lankford, J., Davidson, D. L., and Cook, T. S., "Fatigue Crack Tip Plasticity," *ASTM STP* 637, American Society for Testing and Materials, 1977, pp. 36–55.

2 Valanis, K. C., "Endochronic Theory With Proper Hysteresis Loop Closure Properties," Systems, Science and Software Report, SSS-R-80-4182, 1979.

3 Valanis, K. C., and Read, H., "New Endochronic Plasticity Model for

Downloaded 02 May 2010 to 171.66.16.250. Redistribution subject to ASME license or copyright; see http://www.asme.org/terms/Terms_Use.cfm

Soils," *Soil Mechanics—Transient and Cyclic Loads*, Pande, G. N., and Zienkiewicz, O. C., eds., Wiley, New York, 1982.

4 Valanis, K. C., and Lee, C. F., "Some Recent Developments of the Endochronic Theory With Applications," *Nuclear Eng. and Design*, Vol. 69, 1982, p. 327.

5 Michno, M. J., Jr., and Findley, W. N., "A Historical Perspective of Yield Surface Investigations for Metals," Report EMRL 47, Brown University, Providence, R.I., 1972.

6 Ikegami, K., "A Historical Perspective of Experimental Study on Subsequent Yield Surfaces of Metals (Part 1)," *J. Soc. Mats. Sci.*, Japan, Vol. 24, No. 261, 1975.

7 Liu, K. C., "Experimental Studies to Examine Elastic-plastic Behaviors of Metal Alloys Used in Nuclear Structures," The Winter Annual Meeting of the American Society of Mechanical Engineers, New York, Dec. 1976.

8 Hecker, S. S., "Experimental Studies of Yield Phenomena in Biaxially Loaded Metals," The Winter Annual Meeting of the American Society of Mechanical Engineers, New York, Dec. 1976.

9 Valanis, K. C., "The Viscoelastic Potential and its Thermodynamic Foundations," *J. of Math. and Phys.*, 1968, pp. 262–275.

10 Valanis, K. C., "Irreversibility and Existence of Entropy," *Int. J. Non-Linear Mech.*, 1971, p. 337.

11 Valanis, K. C., "Partial Integrability as the Basis for the Existence of Entropy in Irreversible Systems," *ZAMM*, Vol. 63, 1983, p. 73.

12 Valanis, K. C., "A Theory of Viscoplasticity Without a Yield Surface. Part II. Application to Mechanical Behavior of Metals," *Archives of Mechanics*, 1971, pp. 535–551.

13 Valanis, K. C., "Lectures on Endochronic Plasticity," Swiss Federal Institute of Technology, Zunich, Switzerland, 1983.

14 Elber, W., "Fatigue Crack Closure Under Cyclic Tension Loading," *Engineering Fracture Mechanics*, Vol. 2, No. 1, 1970.

Downloaded 02 May 2010 to 171.66.16.250. Redistribution subject to ASME license or copyright; see http://www.asme.org/terms/Terms_Use.cfm

J. Casey
Assistant Professor.
Assoc. Mem. ASME

H. H. Lin
Graduate Student.

Department of Mechanical Engineering,
University of Houston,
Houston, Texas 77004

Strain-Hardening Topography of Elastic-Plastic Materials

In the context of a purely mechanical rate-type theory of plasticity, a special set of constitutive equations is discussed. A method [1,2] of characterizing strain-hardening behavior is utilized to examine the different types of response that may be exhibited. Loci of constant strain-hardening behavior in stress space and regions of hardening, softening, and perfectly plastic behavior are determined.

1 Introduction

A significant feature of elastic-plastic behavior is that under a general stress history a material may exhibit a change in the character of its strain-hardening response. For example, it is possible for a material to exhibit a perfectly plastic response in certain states of stress, and for the same material to exhibit a hardening response in all other states of stress. Since the flow rules of plasticity, in their stress-space form, are not the same for perfectly plastic behavior as for hardening behavior, it is of importance both for theoretical analyses and numerical implementations to determine the stress systems for which changes in the type of strain-hardening response may occur. Associated with this problem is another, namely that of determining the stress systems for which not only the character but also the degree of strain-hardening is the same. In this connection, it is of interest to establish conditions for the existence of surfaces of constant strain-hardening behavior, and to determine the forms of those surfaces when they do exist.

In the present paper, we show that for a special set of constitutive equations, a complete solution to the two problems just mentioned can be given. The development is carried out within the framework of a purely mechanical theory of finitely deforming elastic-plastic materials which is based on the work of Green and Naghdi [3, 4], Naghdi and Trapp [5], and Casey and Naghdi [1, 2]. A detailed review of this theory is contained in [6]. For reasons discussed in [5, 1, 6], the loading criteria of the strain-space formulation are adopted as primary. The loading conditions in stress space are then determined through the constitutive equations of the theory. The different types of loading conditions that can exist in stress space in conjunction with a postulated condition of loading in strain space suggest a natural classification of strain-hardening behavior into three distinct types: hardening, softening, and perfectly plastic [1]. This classification involves a rate-independent dimensionless function Φ which is a measure of strain-hardening [1, 2, 6].

The special constitutive equations that are analyzed in the present paper were studied previously in [7, 1, 6]. For these equations, the measure Φ involves only material constants and the stress tensor: it does not depend explicitly on the plastic strain tensor nor on the work-hardening parameter. The two problems mentioned in the foregoing reduce to studying the manner in which Φ varies in stress space for any given values of the material constants. This variation in strain-hardening behavior is referred to as the "strain-hardening topography" of the material.

After recalling necessary background material from [1-7] in Section 2, we show in Section 3 that for the chosen constitutive equations, the yield surface in stress space may be represented by an ellipse in the plane of mean normal stress, $\bar{s}$, and $(\pm)$ the magnitude of the deviatoric stress, $\bar{\tau}$, as illustrated in Fig. 1.

In Section 4, conditions for the occurrence of perfectly plastic behavior are derived. These conditions involve only the material constants β and ϕ which appear in the constitutive equation (5) for the rate of the work-hardening parameter κ. Specifically, if a material is perfectly plastic under some stress system, then $\beta\,\phi \leqq 0$, whereas if it is never perfectly plastic, $\beta\,\phi > 0$. For a high-strength steel under uniaxial loading at constant pressure, Casey and Jahedmotlagh [8] found that the strain-hardening response is described by a positive value of β and a negative value of ϕ, so that at least the former condition is relevant for metals.

The loci of constant strain-hardening behavior are determined in Section 5. In the $\bar{s} - \bar{\tau}$ plane, these are straight lines through the origin, unless condition (24) is satisfied; if (24) is satisfied, Φ has the same value at all points of the $\bar{s} - \bar{\tau}$ plane through which the yield surface may pass. When (24) is not satisfied, there is in general a pair of lines of perfectly plastic behavior. As shown in Section 6, these lines divide the $\bar{s} - \bar{\tau}$ plane into adjoining regions, throughout each of which the strain-hardening behavior is of a fixed type, although not constant in value. This general situation is illustrated in Fig. 4. The various exceptional cases are also examined. The physical relevance of our results is discussed in Section 7.

It is appropriate to mention here a paper by Haythorn-

Contributed by the Applied Mechanics Division and presented at the Winter Annual Meeting; Boston, Mass., November 13-18, 1983 of THE AMERICAN SOCIETY OF MECHANICAL ENGINEERS.

Discussion on this paper should be addressed to the Editorial Department, ASME, United Engineering Center, 345 East 47th Street, New York, N.Y. 10017, and will be accepted until two months after final publication of the paper itself in the JOURNAL OF APPLIED MECHANICS. Manuscript received by ASME Applied Mechanics Division, September, 1982; final revision, February, 1983. Paper No. 83-WA/APM-8.

Copies will be available until July 1984.

Copyright © 1983 by ASME
Downloaded 02 May 2010 to 171.66.16.250. Redistribution subject to ASME license or copyright; see http://www.asme.org/terms/Terms_Use.cfm

thwaite [9], which was partly instrumental in motivating the present work. Utilizing a measure H of strain hardening, which is different from the function Φ, Haythornthwaite [9] suggested that surfaces of constant strain-hardening behavior may provide a useful alternative to yield surfaces. In [9], experiments on SAE 1045 steel are reported for which the surfaces of constant H are somewhat similar in form to yield surfaces. In the context of the constitutive equations of the present paper, yield surfaces and surfaces of constant strain-hardening behavior (whether measured by Φ or H) are not interchangeable: the former are ellipses in the $\bar{s} - \bar{\tau}$ plane, whereas the latter are straight lines intersecting these ellipses.

2 Constitutive Equations. Characterization of Strain-Hardening

Let the components of Lagrangian strain, plastic strain, and symmetric Piola-Kirchhoff stress be denoted as in [1, 2] by e_{KL}, e^p_{KL}, and s_{KL}, respectively. Further, let γ_{KL}, γ^p_{KL}, and τ_{KL} be the deviatoric parts of these three tensors, and $\bar{e}\,\delta_{KL}$, $\bar{e}^p\,\delta_{KL}$, and $\bar{s}\,\delta_{KL}$ their spherical parts, where δ_{KL} is the Kronecker symbol. Thus, for example,

$$s_{KL} = \tau_{KL} + \bar{s}\,\delta_{KL}, \quad \bar{s} = \frac{1}{3}\,s_{KK}, \tag{1}$$

summation being performed over repeated indices.

Consider a yield function that has a stress-space representation

$$f = \bar{\tau}^2 + 3\psi\,\bar{s}^2 - \kappa, \quad \bar{\tau} = \pm\sqrt{\tau_{KL}\,\tau_{KL}}, \tag{2}$$

where ψ is a material constant, the positive scalar function κ is a measure of work hardening, and $|\,\bar{\tau}\,|$ is the magnitude of the deviatoric stress tensor. We assume generalized Hooke's law in the form

$$\tau_{KL} = 2\,\mu(\gamma_{KL} - \gamma^p_{KL}), \quad \bar{s} = 3k(\bar{e} - \bar{e}^p), \tag{3}$$

where μ and k are, respectively, the shear modulus and bulk modulus of elasticity. The yield function then has a strain-space representation

$$g = 4\mu^2(\gamma_{KL} - \gamma^p_{KL})(\gamma_{KL} - \gamma^p_{KL}) + 27\,\psi k^2(\bar{e} - \bar{e}^p)^2 - \kappa. \tag{4}$$

At fixed values of e^p_{KL} and κ, the equations $f = g = 0$ represent the yield surfaces in stress space and in strain space [1]. These surfaces are assumed to be closed. The elastic region in strain space is given by $g < 0$, and that in stress space by $f < 0$. Corresponding to the values $e^p_{KL} = 0$, $\kappa = \kappa_0$, there is an initial elastic region and an initial yield surface in both strain space and stress space. We recall the notations $\hat{f} = (\partial f/\partial s_{KL})\,\dot{s}_{KL}$, $\hat{g} = (\partial g/\partial e_{KL})\,\dot{e}_{KL}$, where a superposed dot signifies material time differentiation. We suppose that

$$\dot{\kappa} = (\beta\tau_{KL} + \phi\,\bar{s}\,\delta_{KL})\,\dot{e}^p_{KL}, \tag{5}$$

where β and ϕ are material constants.

Constitutive equations of the type $(2)_1$ and (5) were previously utilized in [7; 1, Section 4] and are also discussed in [6]. The yield function in $(2)_1$ does not depend explicitly on plastic strain, but does depend on mean normal stress. Such a dependency is significant in the case of soils, but is less common for metals. However, certain metals do exhibit plastic volume expansion in association with a strength-differential (S-D) effect [10]. Casey and Jahedmotlagh [8] have shown that the S-D effect can be accounted for by allowing a suitable dependency of the yield function on mean normal stress.

The method proposed by Casey and Naghdi [1, 2, 6] for the characterization of strain-hardening behavior involves a measure of strain hardening Φ. At any point of stress space that the yield surface may traverse, Φ may be written for the preceding constitutive equations as

$$\Phi = \frac{\Gamma}{\Gamma + \Lambda} < 1, \quad \Gamma + \Lambda > 0, \tag{6}$$

where

$$\Gamma = 2\,(\beta\,\bar{\tau}^2 + 3\,\psi\,\phi\,\bar{s}^2), \quad \Lambda = 4(2\mu\,\bar{\tau}^2 + 9\,\psi^2\,k\,\bar{s}^2) > 0, \tag{7}$$

with $g = f = 0$. Adopting the definition given in [2], we say that an elastic-plastic material exhibits

$$\begin{cases} \text{hardening behavior if and only if } \Phi > 0, & (a) \\ \text{softening behavior if and only if } \Phi < 0, & (b) \\ \text{perfectly plastic behavior if an only if } \Phi = 0. & (c) \end{cases} \tag{8}$$

During loading from an elastic-plastic state, i.e., when $g = 0$ and $\hat{g} > 0$, the quotient $\hat{f}/\hat{g}$ and Φ have the same value [2, 6]. It then follows that while during loading the yield surface in strain space is always moving outward locally, the yield surface in stress space is concurrently moving outward in the case of hardening behavior, inward in the case of softening behavior, and is stationary in the case of perfectly plastic behavior [1]. The measure Φ may be written in terms of the ratio of the outward velocities of the yield surfaces in stress space and strain space [6]. This provides a method for determining Φ experimentally.

It should be noted that while $\hat{g}$ may have any positive value during loading, the value of $\hat{f}$ is then fixed by $\hat{f} = \Phi\,\hat{g}$. From (6) and (8), it is clear that hardening, softening, and perfectly plastic behavior are, respectively, characterized by the positivity, negativity, and vanishing of Γ. In connection with the expression $(7)_1$ for Γ, we observe that the type of strain-hardening being exhibited is not determined by the material coefficients alone but may vary in stress space (or strain space) for a given material.

During loading, the constitutive equation for plastic strain rate takes the form

$$\dot{e}^p_{KL} = \frac{\hat{f}}{\Gamma}\,\frac{\partial f}{\partial s_{KL}} \tag{9a}$$

if a material is exhibiting either hardening or softening behavior, and the form

$$\dot{e}^p_{KL} = \frac{\hat{g}}{\Lambda}\,\frac{\partial f}{\partial s_{KL}} \tag{9b}$$

if the material is exhibiting perfectly plastic behavior [1]. In both cases, not all components of $\dot{e}^p_{KL}$ vanish. If $g < 0$, or $g = 0$ and $\hat{g} \leqq 0$, all components of $\dot{e}^p_{KL}$ vanish.

For the yield function in $(2)_1$,

$$\frac{\partial f}{\partial s_{KL}} = 2(\tau_{KL} + \psi\bar{s}\delta_{KL}), \quad \frac{\partial g}{\partial e_{KL}} = 2(2\mu\tau_{KL} + 3\psi k\,\bar{s}\,\delta_{KL}),$$

$$\hat{f} = 2(\bar{\tau}\dot{\bar{\tau}} + 3\psi\,\bar{s}\,\dot{\bar{s}}), \tag{10}$$

$$\hat{g} = 2(2\mu\tau_{KL}\,\dot{\gamma}_{KL} + 9\psi k\bar{s}\,\dot{\bar{e}}) = \hat{f} + 2(2\mu\tau_{KL}\dot{\gamma}^p{}_{KL} + 9\,\psi\,k\,\bar{s}\,\dot{\bar{e}}^p).$$

Also, during loading $\dot{g} = \dot{f} = 0$ by the "consistency" condition, and hence

$$\hat{f} = \dot{\kappa}. \tag{11}$$

For certain purposes, it is useful to choose a special direction of loading. Thus, if

$$\dot{e}_{KL} = \sigma\frac{\partial f}{\partial s_{KL}}, \quad \sigma > 0, \tag{12}$$

it then follows with the use of $(10)_{1,2}$ and $(7)_2$ that

$$\hat{g} = \sigma\,\Lambda > 0. \tag{13}$$

Consequently, if the strain rate is chosen parallel to the normal to the yield surface in stress space, for the constitutive

Downloaded 02 May 2010 to 171.66.16.250. Redistribution subject to ASME license or copyright; see http://www.asme.org/terms/Terms_Use.cfm

equations being discussed, loading will result. Corresponding to (13),

$$\hat{f} = \sigma \, \Lambda \, \Phi. \tag{14}$$

We now discuss some other measures that have been used in connection with strain-hardening behavior.

Haythornthwaite [9] utilized a "hardening rate" H, which may be written as

$$H = \frac{\dot{e}^p_{KL} \dot{s}_{KL}}{\dot{e}^p_{MN} \dot{e}^p_{MN}}, \quad (g = 0, \hat{g} > 0). \tag{15}$$

H has the dimension of stress. For the present constitutive equations, it follows from (15), (9a), $(7)_1$, and $(10)_1$, that

$$H = \frac{\Gamma}{\dfrac{\partial f}{\partial s_{MN}} \dfrac{\partial f}{\partial s_{MN}}} = \frac{\beta \, \bar{\tau}^2 + 3 \, \psi \phi \, \bar{s}^2}{2(\bar{\tau}^2 + 3 \, \psi^2 \bar{s}^2)} \tag{16a}$$

if the material is exhibiting either hardening or softening behavior, while in view of (9b) and (8c),

$$H = 0 \tag{16b}$$

if the material is exhibiting perfectly plastic behavior. Consequently, H is positive for hardening behavior, and negative for softening behavior. Thus, for the constitutive equations of the present paper, H may be used to distinguish between the three types of strain-hardening behavior defined in (8). We observe, however, that if the normality condition (9a) does not hold, then (16a) does not follow from (15). Consequently, for more general constitutive equations, such as appear in [1, Section 2] for instance, H cannot be used to characterize hardening, softening, and perfectly plastic behavior. Moreover, H and Φ do not in general give the same measure of strain-hardening.

Shishmarev, in his experimental study [11], used a "modulus of the effective plastic strain increment," which may be written as $K = 1/H$, with H given by (15). For the present constitutive equations, K is positive for hardening behavior, and negative for softening behavior; for perfectly plastic behavior K becomes unbounded.

Palmer, Maier, and Drucker [12] made use of a "plastic work" criterion, based on the sign of the scalar $\dot{s}_{KL} \, \dot{e}^p_{KL}$. In view of (9) and (11), $\dot{s}_{KL} \, \dot{e}^p_{KL} = \dot{\hat{f}}^2/\Gamma = \dot{\kappa}^2/\Gamma$ if the material is exhibiting either hardening or softening behavior, and zero if the material is exhibiting perfectly plastic behavior. Clearly, $\dot{s}_{KL} \, \dot{e}^p_{KL}$ is positive for hardening behavior, and negative for softening behavior. However, $\dot{s}_{KL} \, \dot{e}^p_{KL} = 0$ for neutral loading, i.e., when $g = \hat{g} = 0$, so that the vanishing of this scalar measure is not a sufficient condition for perfectly plastic behavior unless a condition of loading be enforced.

We also note that the "rate of plastic work," $s_{KL} \, \dot{e}^p_{KL}$, is equal to $2\kappa \hat{f}/\Gamma$ for hardening and for softening behavior, and to $2 \, \kappa \hat{g}/\Lambda$ for perfectly plastic behavior. It is therefore positive for all three types of strain-hardening behavior and cannot be used to distinguish between them.

3 Form of the Yield Surface in the $\bar{s} - \bar{\tau}$ Plane

For the yield function f in $(2)_1$, the equation $f = 0$ (at fixed κ) describes a conic (or a degenerate form of a conic), in the $\bar{s} - \bar{\tau}$ plane. The curve is closed if and only if it is an ellipse, and hence if and only if $\psi > 0$. The equation $f = 0$, or

$$\bar{f} = 3 \, \psi \, \bar{s}^2 + \bar{\tau}^2 = \kappa, \tag{17}$$

therefore describes an ellipse with semimajor axis $a = \sqrt{\kappa/3\psi}$ and semiminor axis $b = \sqrt{\kappa}$, as shown in Fig. 1.[1] The eccentricity of the ellipse is $\sqrt{1 - 3\psi}$ —which may be approximated by $1 - 3/2 \, \psi$ for typical ductile metals. The initial elastic region ($\bar{f} < \kappa_0$) in the $\bar{s} - \bar{\tau}$ plane will be denoted by S_0 and its complement by S_0'. The initial yield surface in the plane will be denoted by ∂S_0.

The tangent vector to any trajectory in the $\bar{s} - \bar{\tau}$ plane, which may be parametrized by time, is $\mathbf{T} = (\dot{\bar{s}}, \dot{\bar{\tau}})$ and an outward normal vector to the ellipse described by (17) is $\mathbf{N} = 2(3\psi \bar{s}, \bar{\tau})$. The inner product of $\mathbf{T}$ and $\mathbf{N}$ therefore satisfies $\mathbf{T} \cdot \mathbf{N} = \dot{\hat{f}}$, where $(10)_3$ has been used. Thus, during loading, the vector $\mathbf{T}$ points outward from the elastic region in the case of hardening behavior (see Fig. 1), inward in the case of softening behavior, and is tangent to the ellipse in the case of perfectly plastic behavior. On account of the consistency condition (see its consequence (11)), for hardening behavior

[1] For metals, ψ is typically much less than unity, so that a is much greater than b, giving a flat elongated ellipse [8].

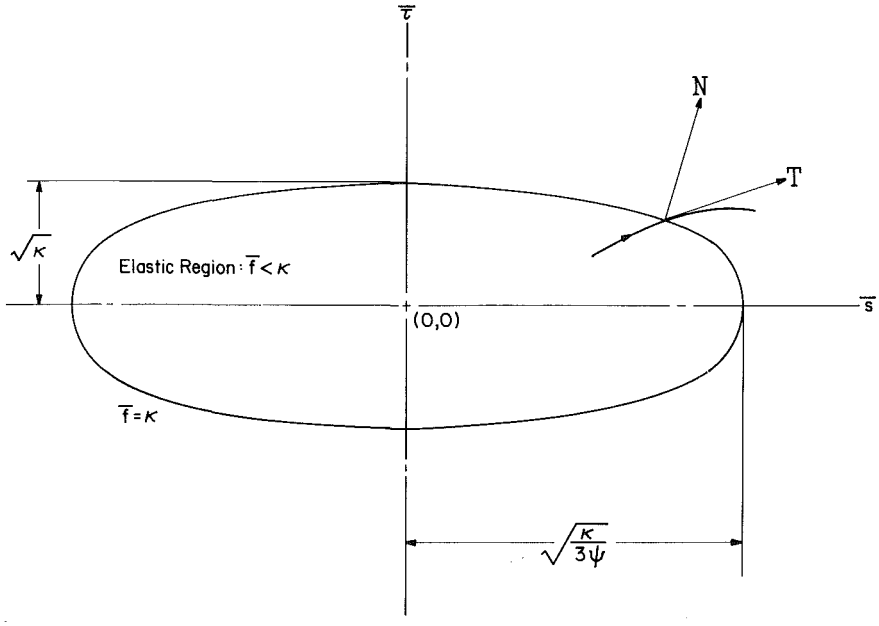


Fig. 1 A sketch of the yield surface ($\bar{f} = \kappa$) and the elastic region in the $\bar{s} - \bar{\tau}$ plane. Also shown is an $\bar{s} - \bar{\tau}$ trajectory as it appears for hardening behavior during loading, its tangent vector T, and the outward normal vector N to the yield surface.

Downloaded 02 May 2010 to 171.66.16.250. Redistribution subject to ASME license or copyright; see http://www.asme.org/terms/Terms_Use.cfm

the ellipse expands during loading, for softening behavior it shrinks, and for perfectly plastic behavior it is stationary. The strain-hardening behavior is of the isotropic type (see the discussion in [6]).

For later reference, we to discuss here another family of ellipses. Thus, considering $(6)_2$ and (7), and choosing first a purely deviatoric stress system and then a purely spherical stress system, we see that

$$\beta + 4\,\mu > 0, \quad \phi + 6\,\psi\,k > 0. \tag{18}$$

Therefore, the equation

$$\Gamma + \Lambda = \Pi, \tag{19}$$

where Π is an arbitrary positive constant, describes a family of ellipses whose principal axes coincide with the $\bar{s}$ and $\bar{\tau}$-axes.

4 Results Pertaining to Perfectly Plastic Behavior

For the class of materials described by the constitutive equations of Section 2, the following results hold:

(*i*) If a material exhibits perfectly plastic behavior under any (purely) deviatoric stress system, then it is perfectly plastic for all deviatoric stress systems. Similarly, if a material is perfectly plastic for any (purely) spherical stress system, it is perfectly plastic for all spherical stress systems. If a material is perfectly plastic for any deviatoric stress system, and also perfectly plastic for any spherical stress system, then it is perfectly plastic always.

(*ii*) If a material exhibits perfectly plastic behavior under any stress system for which neither the deviatoric nor the spherical part vanishes, then β and ϕ have opposite signs or are both zero.

(*iii*) If a material never exhibits perfectly plastic behavior, then both β and ϕ are nonzero, and they have the same sign.

To prove (*i*), first note that not both $\bar{\tau}$ and $\bar{s}$ can vanish, for otherwise the inequality in $(7)_2$ would be violated. Choose $\bar{\tau} \neq 0$, $\bar{s} = 0$. But $\Gamma = 0$ for perfectly plastic behavior. Hence, $\beta = 0$ in view of $(7)_1$. Consequently, $\Gamma = 0$ for all deviatoric stress systems. Similarly, choosing $\bar{\tau} = 0$, $\bar{s} \neq 0$ we deduce that $\phi = 0$. Hence $\Gamma = 0$ for all spherical stress systems. If $\beta = \phi = 0$, Γ is zero always; in this case, the yield surface never moves from its initial location ($\bar{f} = \kappa_0$). The result (*ii*) follows at once from $(7)_1$ with any choice of $\bar{\tau} \neq 0$, $\bar{s} \neq 0$. With regard to (*iii*), we first note that for any $\bar{\tau} = 0$, $\Gamma = 6\psi\phi\bar{s}^2$. Hence, if the material never exhibits perfectly plastic behavior, ϕ cannot vanish. Likewise choosing $\bar{s} = 0$, we find that β cannot vanish. Next, let the ellipse that represents the yield surface be parametrized by θ ($0 \leqq \theta < 2\pi$), with $\bar{s} = a \cos\theta$, $\bar{\tau} = b \sin\theta$. Then, from $(7)_1$

$$\Gamma(\theta) = 2\kappa\,(\beta \sin^2\theta + \phi \cos^2\theta). \tag{20}$$

Now $\Gamma(0) = 2\kappa\phi$, which has the same sign as ϕ, while $\Gamma(\pi/2) = 2\kappa\beta$, which has the same sign as β. By hypothesis, the material is not perfectly plastic at any value of θ, so that Γ does not vanish in the interval $0 \leqq \theta \leqq \pi/2$. Hence, by continuity, Γ cannot change sign in this interval. Consequently, β and ϕ have the same sign. The preceding results are summarized in Table 1.

Table 1 Conditions for perfectly plastic behavior

Stress system under which material exhibits perfectly plastic behavior	Condition
$\bar{\tau} \neq 0$, $\bar{s} = 0$	$\beta = 0$
$\bar{\tau} = 0$, $\bar{s} \neq 0$	$\phi = 0$
$\bar{\tau} \neq 0$, $\bar{s} \neq 0$	$\beta\,\phi < 0$ or $\beta = \phi = 0$
None	$\beta\,\phi > 0$

5 Loci of Constant Strain-Hardening Behavior

We now wish to determine which stress systems correspond to $\Phi = c$, a constant. To begin, it is obvious that if $\phi = \beta = 0$, then $\Phi = 0$. The material can then exhibit only perfectly plastic behavior. Also, the yield surface remains in its initial location, so that the portion S_0' of the $\bar{s} - \bar{\tau}$ plane is, with the exception of the initial yield surface ∂S_0, inaccessible.

Consider now any straight line $\bar{\tau} = m\,\bar{s}$, of slope m ($-\infty < m < \infty$) which passes through the origin in the $\bar{s} - \bar{\tau}$ plane.[2]

[2] The case of uniaxial tension, for which $m = \sqrt{6}$, $\bar{s} \geqq 0$, was analyzed in detail in [1, Section 4].

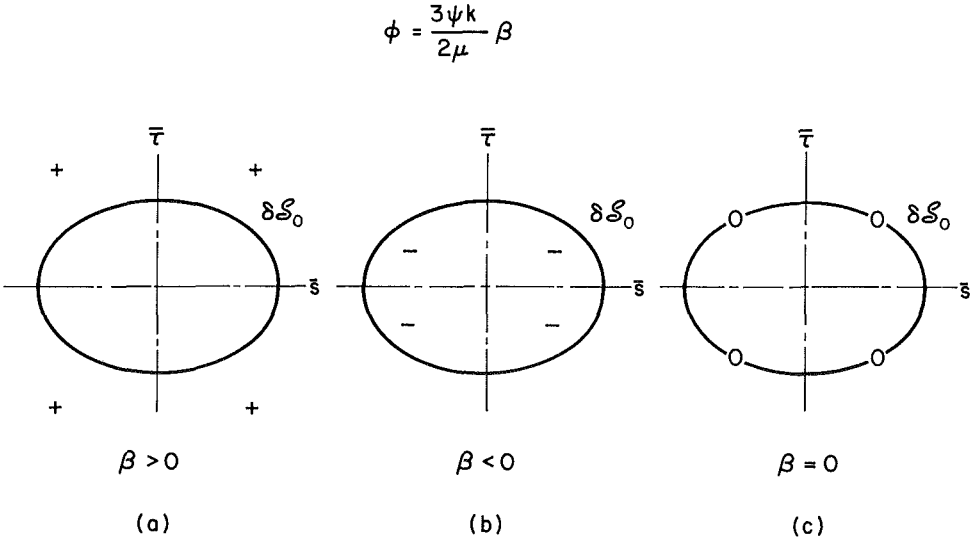


Fig. 2 Constant strain-hardening behavior occurs when (24) is satisfied. (*a*) If $\beta > 0$, the yield surface (during loading) expands arbitrarily from its initial location into a region of constant hardening ("+") behavior; (*b*) if $\beta < 0$, the yield surface shrinks into a region of constant softening ("−") behavior; (c) if $\beta = 0$, the yield surface remains in its initial location; only perfectly plastic ("0") behavior is possible.

Downloaded 02 May 2010 to 171.66.16.250. Redistribution subject to ASME license or copyright; see http://www.asme.org/terms/Terms_Use.cfm

For such a line

$$\Phi(m)=\frac{\beta m^2+3\psi\phi}{(\beta+4\mu)m^2+3\psi(\phi+6\psi k)}, \tag{21}$$

where use has been made of (6) and (7). For the vertical line $\bar{s}=0$, we write $\Phi(\infty)=\beta/(\beta+4\mu)$. Therefore, on each straight line through the origin, Φ is a constant. To investigate whether these straight lines are the only loci of constant Φ, it is preferable to express Φ in terms of an angular variable rather than the slope m, because of difficulties associated with m becoming unbounded. To this end, let each point in the $\bar{s}-\bar{\tau}$ plane be identified by the value of the parameter Π corresponding to that ellipse in the family described by (19) which passes through the point, and by the angle α ($0 \leqq \alpha < 2\pi$), so that

$$\bar{s}=\sqrt{\frac{\Pi}{6\psi(\phi+6\psi k)}}\cos\alpha, \quad \bar{\tau}=\sqrt{\frac{\Pi}{2(\beta+4\mu)}}\sin\alpha. \tag{22}$$

We may parametrize the family of straight lines through the origin by α.

Substituting (22) in $(6)_1$, we obtain

$$2\,\Phi(\alpha)=\frac{\phi}{\phi+6\psi k}+\frac{\beta}{\beta+4\mu}+\left\{\frac{\phi}{\phi+6\psi k}-\frac{\beta}{\beta+4\mu}\right\}\cos 2\alpha. \tag{23}$$

If

$$\phi=\frac{3\psi k}{2\mu}\beta, \tag{24}$$

then

$$\Phi(\alpha)=\frac{\beta}{\beta+4\,\mu} \tag{25}$$

for all α. Materials for which (24) holds with $\beta>0$ exhibit constant hardening behavior, while those with $\beta<0$ exhibit constant softening behavior. In the former case, the yield surface can expand arbitrarily, and all of S_0' is accessible. To see this, it suffices to consider the special choice (12) of loading direction, for which in view of (11), (14), and (25), $\dot{\kappa}=\hat{f}>0$. In the case $\beta<0$, $\dot{\kappa}=\hat{f}<0$ for any choice of loading, so that the yield surface shrinks into a smaller and smaller ellipse during loading and, with the exception of ∂S_0, the region S_0' is inaccessible. The case $\phi=\beta=0$ has already been discussed. These three cases are illustrated schematically in Fig. 2, in which, as in later figures, "+" signifies hardening, "−" signifies softening, and "0" signifies perfectly plastic behavior. There is, of course, symmetry about both the $\bar{s}$ and the $\bar{\tau}$-axis.

Suppose next that (24) does not hold. If

$$\phi>\frac{3\psi k}{2\mu}\beta, \tag{26a}$$

then $\Phi(\alpha)$ is monotonically increasing on the intervals $\pi/2 \leqq \alpha \leqq \pi$ and $3\pi/2 \leqq \alpha < 2\pi$, and is monotonically decreasing on the intervals $0 \leqq \alpha \leqq \pi/2$ and $\pi \leqq \alpha \leqq 3\pi/2$. If

$$\phi<\frac{3\psi k}{2\mu}\beta, \tag{26b}$$

then $\Phi(\alpha)$ is monotonically decreasing for $\pi/2 \leqq \alpha \leqq \pi$ and $3\pi/2 \leqq \alpha < 2\pi$, and monotonically increasing for $0 \leqq \alpha \leqq \pi/2$ and $\pi \leqq \alpha \leqq 3\pi/2$. Thus, $\Phi(\alpha)$ changes as α varies. Consequently, when (24) is not satisfied, Φ is constant only on straight lines through the origin.[3]

In the case of materials for which (24) is not satisfied, it is of interest to consider lines of perfectly plastic behavior. These are given by solutions to

$$\frac{\beta}{\beta+4\mu}\sin^2\alpha+\frac{\phi}{\phi+6\psi k}\cos^2\alpha=0, \tag{27}$$

where $(7)_1$ and (22) have been used. Since we are supposing that (24) does not hold, it is clear from the results of Section 4 that lines of perfectly plastic behavior will exist only if $\phi\beta \leqq 0$, with not both ϕ and β vanishing. It then follows from (27) and $(22)_1$ that if $\beta=0$, the only perfectly plastic line is

$$\bar{s}=0, \tag{28}$$

whereas if $\beta\neq 0$, the perfectly plastic lines are given by

$$\tan\alpha=\pm\sqrt{-\frac{\beta+4\mu}{\phi+6\psi k}\,\frac{\phi}{\beta}}. \tag{29a}$$

With the help of (22), (29*a*) can also be written as

$$m=\pm\sqrt{-3\psi\frac{\phi}{\beta}}, \tag{29b}$$

where the identity

$$\tan\alpha=\sqrt{\frac{\beta+4\mu}{3\psi(\phi+6\psi k)}}\;m, \tag{30}$$

which follows from elementary geometry, has been used.

In closing this section, we would like to comment briefly on the measure H defined at the end of Section 2. It is obvious that H is constant on straight lines through the origin. Moreover, introducing the parametrization $\sqrt{3}\psi\bar{s}=\cos\gamma$, $\bar{\tau}=\sin\gamma$, ($0 \leqq \gamma < 2\pi$), we deduce from (16*a*) that

$$4\psi H(\gamma)=\phi+\psi\beta+(\phi-\psi\beta)\cos 2\gamma, \tag{31}$$

so that unless $\phi=\psi\beta$, H is constant only on straight lines. If $\phi=\psi\beta$, H is constant at all points through which the yield surface may pass. Even in this case, it is clear from (23) that Φ is not necessarily constant. The lines of perfectly plastic behavior may of course be obtained by setting $H=0$.

6 Regions of Hardening and Softening Behavior

In Section 5, we saw that any material for which (24) holds will exhibit constant strain-hardening behavior at all points of the $\bar{s}-\bar{\tau}$ plane through which the yield surface may pass. For materials for which (24) does not hold, we will now demonstrate that the $\bar{s}-\bar{\tau}$ plane consists, in general, of regions[4] throughout each of which the strain-hardening behavior is of a fixed type, although not constant in value. Four cases can occur, viz.

$$\begin{array}{lll} I. & \beta=0,\ \phi\neq 0, & (a) \\ II. & \beta\neq 0,\ \phi=0, & (b) \\ III. & \beta\phi<0, & (c) \\ IV. & \beta\phi>0, & (d) \end{array} \tag{32}$$

(with (24) not satisfied).

Case *I*. The only perfectly plastic line is given by (28). In view of $(7)_1$, $\Gamma=6\psi\phi\bar{s}^2$, and hence if $\phi>0$ the material exhibits hardening behavior at all other points through which the yield surface may pass, and softening behavior if $\phi<0$. In the former case, the yield surface may expand arbitrarily,

[3] To prove this, suppose that Φ is constant on a curve that is not a straight line through the origin. Let the curve intersect any two distinct straight lines through the origin at points A and B. Then Φ has the same value at A and B, which leads to a contradiction.

[4] Or, exceptionally, a single region.

Downloaded 02 May 2010 to 171.66.16.250. Redistribution subject to ASME license or copyright; see http://www.asme.org/terms/Terms_Use.cfm

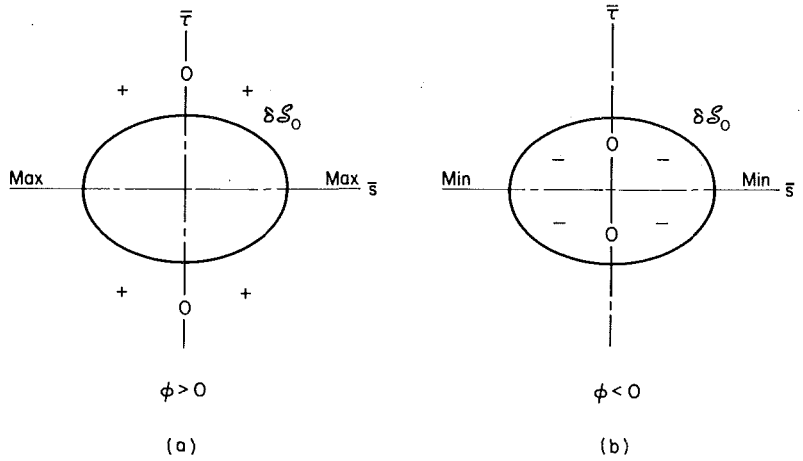


Fig. 3 Strain-hardening topography, Case I. The $\bar{\tau}$-axis is a line of perfectly plastic behavior dividing the plane into two regions of hardening behavior in (*a*), and two regions of softening behavior in (*b*). In (*a*), the yield surface expands, in (*b*) it contracts. Extremal values of the measure of strain-hardening Φ are also indicated.

whereas in the latter case the yield surface can only shrink from its initial location into smaller and smaller ellipses within the initial elastic region. Parametrizing the family of lines through the origin by the variable α, we deduce from (23) that $\Phi(\alpha) = (\phi \cos^2 \alpha)/(\phi + 6\psi k)$. Thus, as noted in the foregoing, the material is perfectly plastic for deviatoric stress systems ($\alpha = \pi/2, 3\pi/2$). If $\phi > 0$, maximum hardening occurs for spherical stress systems ($\alpha = 0, \pi$), whereas if $\phi < 0$, maximum softening (i.e., Φ attains a minimum which is negative) occurs there. In betweeen these four values of α, $\Phi(\alpha)$ is monotonic. See Fig. 3.

Case *II*. It follows from (32*b*) and (29) that the only perfectly plastic line is

$$\bar{\tau} = 0. \tag{33}$$

In view of $(7)_1$, $\Gamma = 2\beta\bar{\tau}^2$, and hence if $\beta > 0$ the material exhibits hardening behavior at all other points through which the yield surface may pass, and softening behavior if $\beta < 0$. By (23) and (32*b*), $\Phi(\alpha) = (\beta \sin^2 \alpha)/(\beta + 4\mu)$. For $\alpha = 0$ and $\alpha = \pi$, the material is perfectly plastic. If $\beta > 0$, maximum hardening occurs for deviatoric stress systems ($\alpha = \pi/2, 3\pi/2$), whereas, if $\beta < 0$, maximum softening occurs there. In between these four values, $\Phi(\alpha)$ is monotonic. For $\beta > 0$ and $\beta < 0$, respectively, figures similar to Figs. 3 (*a*) and (*b*) may be drawn, but with the $\bar{s}$-axis a perfectly plastic line and the $\bar{\tau}$-axis a line of maximum Φ if $\beta > 0$ and minimum Φ is $\beta < 0$.

Case *III*. There are two perfectly plastic lines, given by (29). In view of (23),

$$\Phi(0) = \frac{\phi}{\phi + 6\psi k}, \quad \Phi\left(\frac{\pi}{2}\right) = \frac{\beta}{\beta + 4\mu}. \tag{34}$$

Thus, by continuity and symmetry, if $\phi > 0$ (and $\beta < 0$), hardening occurs on all lines whose slopes satisfy

$$-\sqrt{-3\psi\frac{\phi}{\beta}} < m < \sqrt{-3\psi\frac{\phi}{\beta}}, \tag{35}$$

and softening occurs on all other lines, with the exception of the pair of perfectly plastic lines. The inequality (26*a*) is satisfied, and hence maximum hardening occurs for spherical stress systems and maximum softening occurs for deviatoric stress systems. All points in $\mathcal{S}_0'$ are accessible, but in addition the yield surface may shrink within the initial elastic region $\mathcal{S}_0$. To see this, first specialize (12) to spherical stress systems, so that

$$\dot{\kappa} = \hat{f} = 12\frac{\phi\psi k}{\phi + 6\psi k}\sigma\kappa > 0, \tag{36a}$$

where (11), $(12)_2$, (14), $(7)_2$, (17), and $(34)_1$ have been used. This choice of loading direction causes the yield surface to expand into larger and larger ellipses. Similarly, specializing (12) to deviatoric stress systems, we see that

$$\dot{\kappa} = \hat{f} = 8\frac{\beta\mu}{\beta + 4\mu}\sigma\kappa < 0, \tag{36b}$$

so that the yield surface shrinks. See Fig. 4(*a*).

On the other hand, if $\phi < 0$ (and $\beta > 0$), softening occurs on the lines (35), and hardening occurs on all other lines except the perfectly plastic pair. Inequality (26*b*) is satisfied and hence maximum hardening occurs for deviatoric stress systems, and maximum softening for spherical stress systems. Again, the yield surface may expand or shrink, with the relations (36) now holding with the inequality signs reversed. See Fig. 4(*b*).

Case *IV*. It is clear from the results of Section 4 that in this case perfectly plastic behavior never occurs. Indeed, if $\phi > 0$ (and $\beta > 0$), $\Gamma(\theta)$ in (20) is positive for all θ, so that hardening occurs at all points through which the yield surface may pass, which in this case is all of $\mathcal{S}_0'$; a figure similar to Fig. 3(*a*) results. If $\phi < 0$ (and $\beta < 0$), $\Gamma(\theta) < 0$ for all θ, and softening occurs; a figure similar to Fig. 3(*b*) may be drawn.

The values of Φ for spherical and deviatoric stress systems are given by (34). If inequality (26*a*) holds with $\beta > 0$, then maximum hardening occurs for spherical stress systems ($\alpha = 0, \pi$), and minimum hardening for deviatoric stress systems ($\alpha = \pi/2, 3\pi/2$), with Φ monotonic in between. If (26*a*) holds with $\beta < 0$, then $\Phi(\alpha)$ has minima at $\alpha = \pi/2$ and $\alpha = 3\pi/2$, and maxima at $\alpha = 0$ and $\alpha = \pi$. Therefore, maximum softening occurs for deviatoric stress systems, and minimum softening for spherical stress systems. If (26*b*) holds with $\beta > 0$, maximum hardening occurs for deviatoric stress systems, and minimum hardening for spherical stress systems. If (26*b*)

Downloaded 02 May 2010 to 171.66.16.250. Redistribution subject to ASME license or copyright; see http://www.asme.org/terms/Terms_Use.cfm

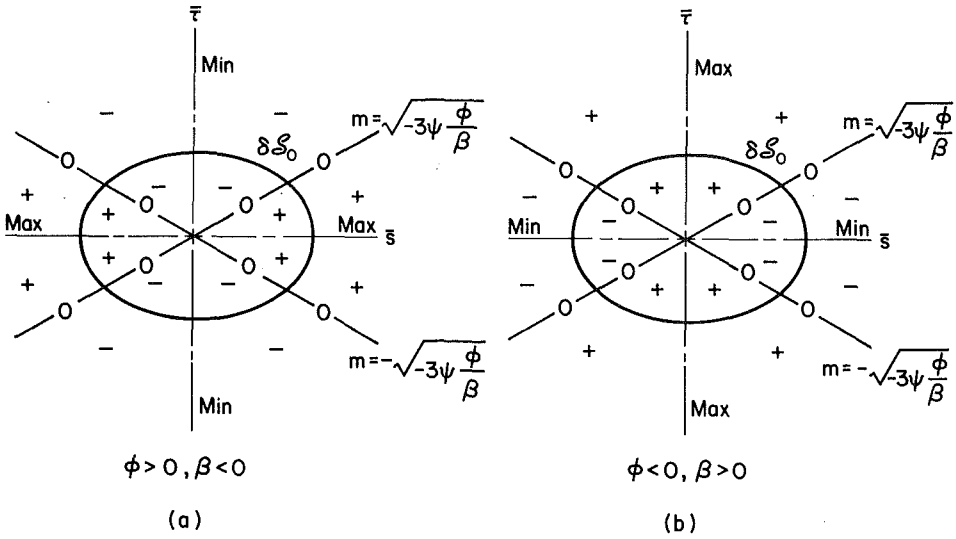


Fig. 4 Strain-hardening topography, Case III. There are two perfectly plastic lines, which divide the plane into regions of hardening and softening behavior, as indicated.

holds with $\beta < 0$, maximum softening occurs for spherical stress systems, and minimum softening for deviatoric stress systems.

7 Discussion

All of the cases examined in Sections 5 and 6 are possible in theory. Not enough experimental data are available to state conclusively that all have physical relevance. For metals, there is evidence to suggest that evolution from hardening to perfectly plastic and softening bahavior occurs only well into the plastic strain range. For AISI 4330 steel, the data of Spitzig et al. [10] yield a positive value for β and a negative value for ϕ [8], so that a situation of the type illustrated in Fig. 4(*b*) occurs. The situation illustrated in Fig. 4(*a*) may or may not be relevant for metals but it does appear to be typical of rocks (see e.q. [14, Fig. 1]).

Additional evidence of relevance is contained in the paper [13] of Tanaka and Spretnak. These authors subjected cylindrical specimens of AISI 4340 steel to torsional loading in which very large shear strains were attained. It was found that after an initial period of rapid strain-hardening followed by a very brief period of strain-softening, a state of perfectly plastic behavior was reached at strains of about 10 percent and endured up to strains of at least 50 percent. We may conjecture that the initial elastic region in stress space is surrounded by a hardening region that is bordered by a perfectly plastic surface, and that this in turn is enclosed by a region of softening behavior.

The results of the present paper have been derived under the assumption of special constitutive equations. Corresponding, but more complicated results will exist for constitutive equations that are more realistic.

The possibility of the existence of regions of radically different strain-hardening response has obvious practical implications both for metal-forming processes and for structural design. The results of experimental and further theoretical investigations of this question should be of much interest.

Acknowledgement

The support of the Engineering Foundation under Grant RC-A-79-1C is gratefully acknowledged.

References

1 Casey, J., and Naghdi, P. M., "On the Characterization of Strain-Hardening in Plasticity," ASME JOURNAL OF APPLIED MECHANICS, Vol. 48, 1981, pp. 285-296.

2 Casey, J., and Naghdi, P. M., "A Remark on the Definition of Hardening, Softening and Perfectly Plastic Behavior," *Acta Mechanica*, to appear.

3 Green, A. E., and Naghdi, P. M., " A General Theory of an Elastic-Plastic Continuum," *Archive for Rational Mechanics and Analysis*, Vol. 18, 1965, pp. 251-281.

4 Green, A. E., and Naghdi, P. M., "A Thermodynamic Development of Elastic-Plastic Continua," *Proceedings of the IUTAM Symposium on Irreversible Aspects of Continuum Mechanics and Transfer of Physical Characteristics in Moving Fluids*, Parkus, H., and Sedov, L. I., eds., Springer-Verlag, 1966, pp. 117-131.

5 Naghdi, P. M., and Trapp, J. A., "The Significance of Formulating Plasticity Theory With Reference to Loading Surfaces in Strain Space," *International Journal of Engineering Science*, Vol. 13, 1975, pp. 785-797.

6 Casey, J., and Naghdi, P. M., "Strain-Hardening Response of Elastic-Plastic Materials," *International Conference on Constitutive Laws for Engineering Materials: Theory and Application*, Tucson, Ariz., Jan. 10-14, 1983. To appear in *Mechanics of Engineering Materials*, Wiley, U. K.

7 Green, A. E., and Naghdi, P. M., "A Comment on Drucker's Postulate in the Theory of Plasticity," *Acta Mechanica*, Vol. 1, 1965, pp. 334-338.

8 Casey, J., and Jahedmotlagh, H., "The Strength-Differential Effect in Plasticity," *International Journal of Solids and Structures*, to appear.

9 Haythornthwaite, R. M., "A More Rational Approach to Strain-Hardening Data," in *Engineering Plasticity*, Heyman, J., and Leckie, F. A., eds., Cambridge, 1968, pp. 201-218.

10 Spitzig, W. A., Sober, R. J., and Richmond, O., "Pressure Dependence of Yielding and Associated Volume Expansion in Tempered Martensite," *Acta Metallurgica*, Vol. 23, 1975, pp. 885-893.

11 Shishmarev, O. A., "Experimental Study on One Type of Plastic Anisotropy Not Considered In Simplified Flow Theories," in *Foundations of Plasticity*, A. Sawczuk, ed., Noordhoff, 1973, pp. 491-505.

12 Palmer, A. C., Maier, G., and Drucker, D. C., "Normality Relations and Convexity of Yield Surfaces for Unstable Materials or Structural Elements," ASME JOURNAL OF APPLIED MECHANICS, Vol. 30, 1967, pp. 464-470.

13 Tanaka, K., and Spretnak, J. W., "An Analysis of Plastic Instability in Pure Shear in High Strength AISI 4340 Steel," *Metallurgical Transactions*, Vol. 4, 1973, pp. 443-454.

14 Maier, G., and Hueckel, T., "Nonassociated and Coupled Flow Rules of Elastroplasticity for Rock-Like Materials," *International Journal of Rock Mechanics and Mining Sciences of Geomechanic Abstracts*, Vol. 16, 1979, pp. 77-92.

Downloaded 02 May 2010 to 171.66.16.250. Redistribution subject to ASME license or copyright; see http://www.asme.org/terms/Terms_Use.cfm

V. V. Varadan[1]
Associate Professor.

T. A. K. Pillai
Post-Doctoral Researcher.

V. K. Varadan[1]
Associate Professor.
Mem. ASME

Wave Propagation Group,
Department of Engineering Mechanics,
The Ohio State University,
Columbus, Ohio 43210

Ultrasonic Wave Scattering by a Subsurface Flaw in Joined Fluid-Solid Half Spaces

The scattering of waves by a flaw (cavity or inclusion) that is embedded in an elastic half space at a finite depth below the interface with a fluid half space is studied using the T-matrix approach. Expressions are derived for the scattered fields generated in the fluid and solid half spaces as well as the asymptotic form of the field in the fluid at a large distance from the interface. Numerical results are presented for spherical voids and steel inclusions embedded in epoxy as well as oblate spheroidal voids in a metal for various flaw depths, scattering geometries, and frequency of the incident wave. The results obtained by keeping different orders of multiple scattering between the flaw and the interface are critically discussed.

Introduction

The study of wave scattering by a subsurface flaw in an elastic half space finds several practical applications. Often the elastic half space interfaces with a fluid half space and it is of interest to study the field produced in the fluid. A typical application is the ultrasonic NDE (Nondestructive Evaluation) of a structural part containing a near-surface flaw. The part is usually immersed in a water tank and the receiving and transmitting transducers are both located in water. There are also applications to scattering by objects in the ocean bottom for both geophysical and sonar applications.

The mathematical problem involves taking into account multiple reflections between the flaw and the fluid-solid interface as well as transmission in and out through the interface. Very often the measurements are made at distances far from the interface. In this paper expressions are derived for the scattered fields produced in the solid and liquid half space for a plane harmonic-wave incident on a subsurface flaw. These expressions, which include all multiple scattering processes, can be rewritten as an expansion in different orders of scattering. The asymptotic form of the scattered field in the fluid at distances far from the interface are evaluated by the method of steepest descent. The formulation is a self-consistent one using the T-matrix to characterize the response of the flaw.

The problem of a buried inhomogeneity in a free elastic half space for Rayleigh wave incidence was studied by Bostrom and Kristensson [1]. Their derivation is a more formal one starting with an integral representation for the displacement field in the half space. At the present time no results are available for the problem considered in this paper, especially a study of the far field as a function of frequency. If the fluid half space is absent, the expressions presented here will agree with those of reference [1]. Previously Varadan and Varadan [2] have given a self-consistent formulation for problems involving scatterers in the presence of nearby boundaries. The present paper is an extension of this approach to joined half spaces. The corresponding scalar problem of a scatterer in a fluid half space can be treated by the method of images.

In the second section the multiple scattering formulation is presented. In the third section the numerical procedure is explained and results are presented for spherical cavities and steel inclusions embedded in epoxy and an oblate spheroidal

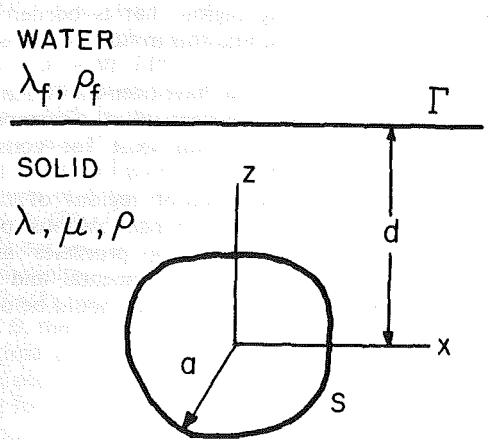


Fig. 1 Scattering geometry

[1] As of August, 1983, affiliation is: Department of Engineering Science and Mechanics, Hammond Building, The Pennsylvania State University, University Park, Pa. 16802.

Contributed by the Applied Mechanics Division and presented at the Winter Annual Meeting, Boston, Mass., November 13-18, 1983 of THE AMERICAN SOCIETY OF MECHANICAL ENGINEERS.

Discussion on this paper should be addressed to the Editorial Department, ASME, United Engineering Center, 345 East 47th Street, New York, N.Y. 10017, and will be accepted until two months after final publication of the paper itself in the JOURNAL OF APPLIED MECHANICS. Manuscript received by ASME Applied Mechanics Division, December, 1982; final revision, May, 1983. Paper No. 83-WA/APM-22.

Copies will be available until July, 1984.

Copyright © 1983 by ASME
Downloaded 02 May 2010 to 171.66.16.250. Redistribution subject to ASME license or copyright; see http://www.asme.org/terms/Terms_Use.cfm

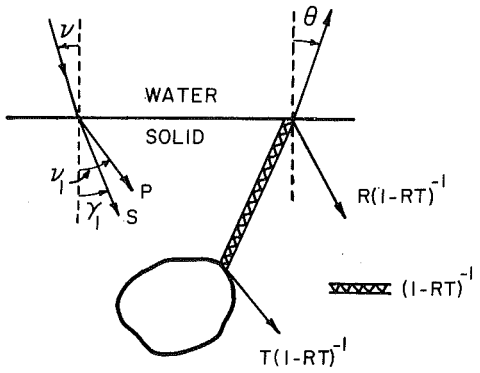


Fig. 2 Multiple scattering processes

cavity embedded in titanium. If a is the radius of the flaw and d the depth below the fluid-solid interface, various values of d/a are considered. The scattered far field pressure in the fluid is plotted as a function of frequency for several different angles of incidence and observation. The full multiple scattering series as well as partial series are considered and compared. It was found that retaining first-order multiple scattering was enough for the case of normal incidence and that for oblique incidence mode conversion at the fluid-solid interface seems to play a major role.

Self-Consistent Multiple Scattering Formulation

Consider fluid-solid half spaces that interface along the planar boundary Γ. The z-axis is normal to the interface Γ as shown in Fig. 1. The fluid is assumed to be linear and isotropic, described by the mass density ρ_f and compressibility λ_f which results in a sound wave speed $c_f = \sqrt{\lambda_f/\rho_f}$. The solid is also assumed to be linear and isotropic and hence characterized by the Lame constants λ and μ and mass density ρ. The longitudinal or P-wave speed in the solid is thus $c_p = \sqrt{(\lambda+2\mu)/\rho}$ and the transverse or shear wave speed $c_s = \sqrt{\mu/\rho}$. An obstacle bounded by the surface S and enclosing a volume V is embedded in the elastic half space; see Fig. 1. A coordinate system with origin 0 in V is such that the interface Γ is at a distance d above 0. Let a be some typical radius characterizing the scatterer.

Plane harmonic waves of frequency ω are generated in the fluid half space and are incident in a direction $\hat{k}_0(\alpha, \beta)$ where α is measured with respect to the positive z-axis and β is measured in the x-y plane counterclockwise from the x-axis. The total displacement field $\mathbf{U}_f$ in the fluid half space is given by

$$\mathbf{U}_f(\mathbf{r}) = \mathbf{U}_f^0(\mathbf{r}) + \mathbf{U}_f^r(\mathbf{r}) + \mathbf{U}_f^s(\mathbf{r}); \quad \hat{z}\cdot\mathbf{r} > d \tag{1}$$

where

$$\mathbf{U}_f^0(\mathbf{r}) = \hat{k}_0 \exp\left(i\frac{\omega}{c_f}\hat{k}_0\cdot\mathbf{r}\right) \tag{2}$$

is the incident field and $\mathbf{U}_f^s$ is the field due to waves scattered by the obstacle, which are transmitted through Γ, and $\mathbf{U}_f^r$ is the reflection of the incident field at the interface Γ. The first two terms of equation (1) are known and we wish to derive an expression for the field scattered by the subsurface flaw. The time dependence $\exp(-i\omega t)$ of all fields will not be written explicitly in what follows.

The field $\mathbf{U}_{sol}$ in the elastic half space may be written as follows,

$$\mathbf{U}_{sol}(\mathbf{r}) = \mathbf{U}_{sol}^0(\mathbf{r}) + \mathbf{U}_{sol}^r(\mathbf{r}) + \mathbf{U}_{sol}^s(\mathbf{r}); \quad \hat{z}\cdot\mathbf{r} < d \tag{3}$$

where $\mathbf{U}_{sol}^0$ is the field arising from the incident wave in the fluid transmitting through Γ, $\mathbf{U}_{sol}^r$ is a multiply scattered field that reaches the field point $\mathbf{r}$ with the final reflection from Γ, and $\mathbf{U}_{sol}^s$ is a multiply scattered field that undergoes final scattering from S. These fields are schematically represented in Fig. 2.

We now introduce the concept of exciting fields, i.e., what are the fields incident on S and Γ that give rise to $\mathbf{U}_{sol}^s$ and $\mathbf{U}_{sol}^r$, respectively,

$$\mathbf{U}_S^{ex} \equiv \mathbf{U}_{sol} - \mathbf{U}_{sol}^s \tag{4}$$

and

$$\mathbf{U}_\Gamma^{ex} \equiv \mathbf{U}_{sol} - \mathbf{U}_{sol}^r - \mathbf{U}_{sol}^0 \tag{5}$$

Thus from equation (3), we have

$$\mathbf{U}_S^{ex} = \mathbf{U}_{sol}^0 + \mathbf{U}_{sol}^r \tag{6}$$

and

$$\mathbf{U}_\Gamma^{ex} = \mathbf{U}_{sol}^s. \tag{7}$$

To relate the field exciting a surface to the field that it scatters via a T-matrix or an R-(Reflection) matrix, as appropriate, it is necessary to express these fields in a suitable set of basis functions. To expand fields associated with the finite scatterer S, it is appropriate to use vector spherical functions. For the fields associated with the infinite planar surface Γ, it is more convenient to use a set of vector plane waves. But we see that the two types of fields are coupled by equations (6) and (7). Thus it is necessary to introduce transformation formulas between vector spherical functions and vector plane waves and vice versa. An excellent treatment of this has been recently given by Bostrom et al. [3] and we only cite the final results here.

The vector spherical functions are denoted as

$\psi_{\tau lm\sigma} \rightarrow \psi_{\tau n}; \quad \tau \equiv 1,2,3; \quad l \epsilon [0,\infty]; \quad m \epsilon [0,l]; \quad \sigma = e,0$

and the vector plane waves by

$\phi_j(\hat{\gamma};\mathbf{r}); \quad j = 1,2,3; \quad \hat{\gamma} = (\sin\alpha\cos\beta, \sin\alpha\sin\beta, \cos\alpha)$

The symbols τ and j denote the polarization of the wave, $\tau = j = 1$ represent P-waves and $\tau, j = 2, 3$ represent the two components of the S- wave. For a detailed definition of these functions see reference [1]. The transformation between the two sets of functions is given by

$$\phi_j(\hat{\gamma};\mathbf{r}) = \sum_{\tau lm\sigma} B^{\dagger}_{\tau lm\sigma,j}(\hat{\gamma})\ Re\ \psi_{\tau lm\sigma}(\mathbf{r}); \tag{8}$$

$$Re\ \psi_{\tau lm\sigma}(\mathbf{r}) = \sum_j \int d\hat{\gamma}\ B_{\tau lm\sigma,j}(\hat{\gamma})\,\phi_j(\hat{\gamma};\mathbf{r}) \tag{9}$$

and

$$Ou\ \psi_{\tau lm\sigma}(\mathbf{r}) = 2\sum_j \int_{C_\pm} d\hat{\gamma}\ B_{\tau lm\sigma,j}(\hat{\gamma})\,\phi_j(\hat{\gamma};\mathbf{r}); \quad \hat{z}\cdot\mathbf{r} \gtrless 0 \tag{10}$$

where the matrices $B_{\tau lm\sigma,j}$ are related to the vector spherical harmonics. The complex integration contours $C_\pm$ for $\hat{z}\cdot\mathbf{r} \gtrless 0$ assure that for the left-hand side to be an outgoing wave, part of the plane wave spectrum on the right-hand side should be evanescent.

The fields exciting the obstacle and the resulting scattered field are expanded as follows

$$\mathbf{U}_S^{ex}(\mathbf{r}) = \sum_{\tau n} \alpha_{\tau n} Re\ \psi_{\tau n}(\mathbf{r}), \tag{11}$$

$$\mathbf{U}_{sol}^s(\mathbf{r}) = \sum_{\tau n} f_{\tau n} Ou\ \psi_{\tau n}(\mathbf{r}), \tag{12}$$

and

$$\mathbf{U}_{sol}^0(\mathbf{r}) = \sum_{\tau n} a_{\tau n} Re\ \psi_{\tau n}(\mathbf{r}) \tag{13}$$

where the coefficients $\{\alpha\}$ and $\{f\}$ are both unknown.

Downloaded 02 May 2010 to 171.66.16.250. Redistribution subject to ASME license or copyright; see http://www.asme.org/terms/Terms_Use.cfm

Similarly the fields exciting and reflected by the interface Γ are given by

$$\mathbf{U}_{\Gamma}^{ex}(\mathbf{r}) = \sum_{j} \int_{C_+} d\hat{\gamma}\, \alpha_j(\hat{\gamma})\, \boldsymbol{\phi}_j(\hat{\gamma};\mathbf{r}) \tag{14}$$

and

$$\mathbf{U}_{sol}^{r}(\mathbf{r}) = \sum_{j} \int_{C_-} d\hat{\gamma}\, f_j(\hat{\gamma})\, \boldsymbol{\phi}_j(\hat{\gamma};\mathbf{r}) \tag{15}$$

We further define the T-matrix of the obstacle S as follows

$$f_{\tau n} = \sum_{\tau' n'} T_{\tau n,\tau' n'}\, \alpha_{\tau' n'} \tag{16}$$

and the reflection matrix R of the planar interface Γ as

$$f_j(\hat{\gamma}) = \sum_{j'} R_{jj'}(\hat{\gamma},\hat{\gamma}^*)\alpha_{j'}(\hat{\gamma}^*) \tag{17}$$

In equation (17), the incident and reflected wave vectors $\hat{\gamma}^*$ and $\hat{\gamma}$ are related by Snell's law. The detailed form of the reflection matrix for different types of interfaces may be obtained from Brekhovskikh [4]. The projection of the reflaction matrix for vector plane waves into a spherical vector basis may be written as

$$R_{\tau n,\tau' n'} = 2 \sum_{jj'} \int_{C_-} d\hat{\gamma}\, B^{\dagger}_{\tau n,j}(\hat{\gamma}) R_{jj'}(\hat{\gamma},\hat{\gamma}^*) B_{\tau' n' j'}(\hat{\gamma}^*) \tag{18}$$

Equations (6) and (7) may now be solved in a self-consistent manner to yield in matrix notation

$$f_{\tau n} = \sum_{\tau' n'} [T(1-RT)^{-1}]_{\tau n,\tau' n'}\, a_{\tau' n'} \tag{19}$$

where $a_{\tau' n'}$ are the coefficients of expansion of the plane wave in the fluid that has been transmitted through the solid-fluid interface. Thus this field consists in general of both P and S- waves that are polarized in the plane of incidence. We observe that the expansion of the matrix inverse in equation (19) yields a multiple scattering series, each term of which represents different orders of scattering between the obstacle and the interface Γ, with the final scattering from the obstacle denoted by a T-matrix.

The field $\mathbf{U}_{sol}^{s}$ that can now be computed by substituting equation (19) into equation (12) must now be transmitted through the interface Γ to give rise to $\mathbf{U}_{f}^{s}(r)$ in the fluid. We can use the transmission matrix (τ_{fj}) for plane waves incident from the solid side of Γ to accomplish this. Thus,

$$\mathbf{U}_{f}^{s}(\mathbf{r}) = 2i \sum_{\tau,n} \sum_{j} \int_{C_+} d\hat{\gamma}\, B_{\tau n,j}(\hat{\gamma}^*)\tau_{fj}(\hat{\gamma},\hat{\gamma}^*)\boldsymbol{\phi}_f(\hat{\gamma};\mathbf{r})\, f_{\tau n} \tag{20}$$

where again $\hat{\gamma}$ and $\hat{\gamma}^*$ the transmitted and incident wave angles are related by Snell's law and $\boldsymbol{\phi}_f$ is the plane wave in the fluid.

In practice the field scattered by the flaw is usually observed at distances $|\mathbf{r}|$ that are much larger than the flaw depth d or its radius a. Thus we only need the asymptotic value of the integral in equation (20) as $k_f r \to \infty$. This can be conveniently done by the method of steepest descent. The integration on the azimuthal angle β of $\hat{\gamma}$ is first performed analytically by resolving $\boldsymbol{\phi}_f$ into cylindrical polar components, measuring the angle β from $\hat{\rho}$ where $\mathbf{r} = \hat{z}z + \hat{\rho}\rho$. Again the field is written in spherical coordinates and it is apparent that the ϕ-component of $\mathbf{U}_f^s$ is zero due to the properties of τ_{fj}. In the resulting integral on α over the complex contour C_+, the contour is deformed so as to allow us to use the asymptotic form of the Hankel functions as $k_f r \to \infty$. The point of stationary phase is obtained from the roots of the equations $\sin(\theta - \alpha) = 0$ which is obviously $\theta = \alpha$. Physically this means that in the far field, from the spectrum of plane waves scattered by the obstacle and reaching Γ, only one particular wave incident at an angle, such that $\alpha = \theta$ will propagate in the direction $\mathbf{r}$.

Table 1 Material properties used in calculations

Material	Density ρ (g/cc)	Longitudinal wave speed m/s	Transverse wave speed m/s
Water	1.0	1480	0
Epoxy	1.18	2720	1340
Steel	8.0	5800	3100
Titanium	4.42	6340	3030

The final expression for the far field in the fluid is

$$\mathbf{U}_{f}^{s}(\mathbf{r}) \underset{k_f r \to \infty}{=} \hat{r} \exp(ik_f r/k_f r) \sum_{lm\sigma} i^{-l}\gamma_{lm}$$

$$\left\{ P_l^m(\hat{\gamma}^*)\tau_{f1}(\hat{\gamma}) f_{1lm\sigma} \begin{pmatrix} \cos m\phi \\ \sin m\phi \end{pmatrix} \right.$$

$$- \frac{1}{\sqrt{l(l+1)}} \frac{mP_l^m(\hat{\gamma}^*)}{\sin\gamma} \tau_{f3}(\hat{\gamma})\, f_{2lm\sigma} \begin{pmatrix} -\sin m\phi \\ \cos m\phi \end{pmatrix}$$

$$\left. - \frac{i}{\sqrt{l(l+1)}} \frac{d}{d\gamma} P_l^m(\gamma)\Big|_{\gamma=\gamma^*} \tau_{f3}(\hat{\gamma}) f_{3lm\sigma} \begin{pmatrix} \cos m\phi \\ \sin m\phi \end{pmatrix} \right\} \tag{21}$$

As $|r| \to \infty$, the field in the fluid is an outgoing spherical wave whose amplitude is given by equation (21). Both P and S-waves scattered by the flaw contribute to the field in the fluid.

Numerical Procedure and Results

To compute the amplitude of the far scattered field, the R and T-matrices must be computed first. For cavities and inclusions embedded in elastic solids, the procedure for calculating the T-matrix has been described by Varadan and Varadan [5]. In the present calculations, only rotationally symmetric obstacles like spheroids with the rotational axis of symmetry parallel to the z-axis are considered. This renders all matrices block diagonal in the azimuthal indices, m,m' and thus the calculation can be done separately for each index and the results added.

The reflection and transmission factors for plane waves incident on a solid-fluid interface are given by Brekhovskikh [4]. However, those expressions must be rewritten measuring all angles with respect to the positive z-axis and including the proper phase factors because the interface Γ is at $z = d$. Further the Dirac delta functions arising from Snell's law must be included as part of the reflection and transmission factors. In evaluating the integral on the complex contour $C-$ in equation (18), attention must be paid to the denominator of the reflection factors. All elements of $R_{jj'}$ have a common denominator, which has the form

$$R_{jj'}(\hat{\gamma},\hat{\gamma}^*) = N_{jj'}/D \tag{22}$$

with

$$D = \frac{Z_f}{4Z_l} + \frac{c_s}{c_p}\sin^2\gamma_1 \cos\nu_1 \cos\gamma_1 + \left(\frac{\cos 2\gamma_1}{2}\right)^2 \tag{23}$$

where

$$Z_f = \rho_f c_f/\cos\nu; \quad Z_l = \rho c_p/\cos\nu_1$$

and ν, ν_1, and γ_1 are the angles that the acoustic wave, P-wave, and S-wave, respectively, make with the z-axis.

The denominator has two roots one of which is complex. These roots correspond to the propagation of surface waves at the interface Γ. One zero of D has a complex value for γ_1. This wave is called the leaky Rayleigh wave and has a speed

Downloaded 02 May 2010 to 171.66.16.250. Redistribution subject to ASME license or copyright; see http://www.asme.org/terms/Terms_Use.cfm

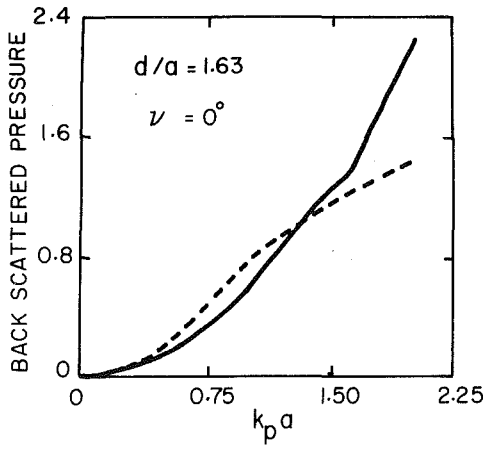


Fig. 3 Spherical cavity - - - single scattering (T), —— multiple scattering ($T(1-RT)^{-1}$ and $T(1+RT)$)

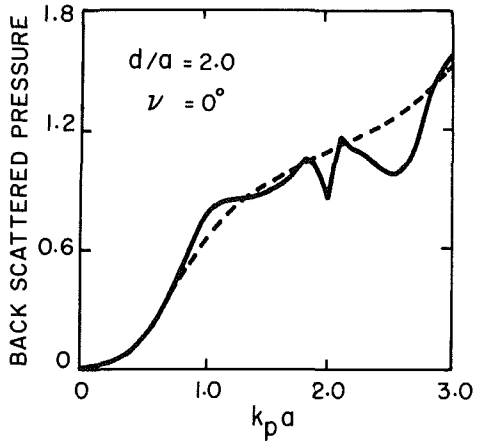


Fig. 4 2:1 Oblate spheroidal cavity, - - - single scattering (T), —— multiple scattering ($T(1-RT)^{-1}$ and $T(1+RT)$)

nearly equal to the Rayleigh wave speed at a metal-air interface. This is not a true surface wave since the energy leaks from the solid to the fluid. The other root of equation (23) is real, and this gives rise to a Scholte wave. The speed of the Scholte wave is less than the lowest bulk wave speed, which for a metal-water interface would be the acoustic wave speed in water. It is a true surface wave. For a more complete description of these zeros we refer to Cagniard [6].

In our calculations, we deform the contour $C-$ to avoid these poles. This is achieved by changing the variable of integratio to sin γ and integrating along a circular arc in the fourth quadrant and then out along the real axis. The upper limit of the integral depends on the parameter $k_s d$ and must be adjusted to achieve convergence. The arc must swing wide enough to avoid both zeros of the reflection factors. In performing the integral in equation (20) asymptotically, these poles will not give any contributions at distances far from Γ since the energy is concentrated near the interface.

In calculating the scattered field coefficients f_m from equation (19), three possible cases were considered

$$f = T(1-RT)^{-1}\, a \qquad (24a)$$

$$f \approx T(1+RT)\, a \qquad (24b)$$

$$f \approx Ta \qquad (24c)$$

Equation (24a) includes all multiple scattering effects between the flaw and the interface. Equation (24b) is a correction to the single scattering term by including one additional reflection from Γ and final scattering from the flaw, and finally equation (24c) is the single scattering approximation

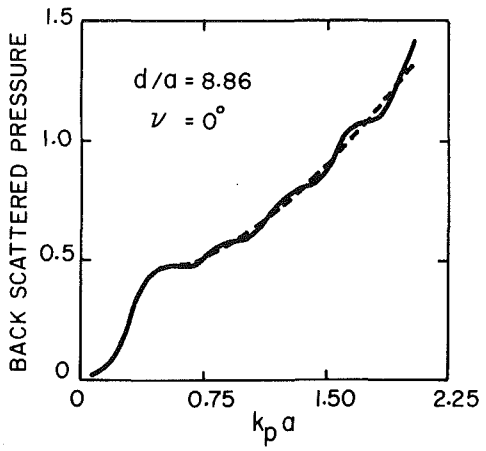


Fig. 5 Spherical inclusion (steel) - - - single scattering (T), —— multiple scattering ($T(1-RT)^{-1}$ and $T(1+RT)$)

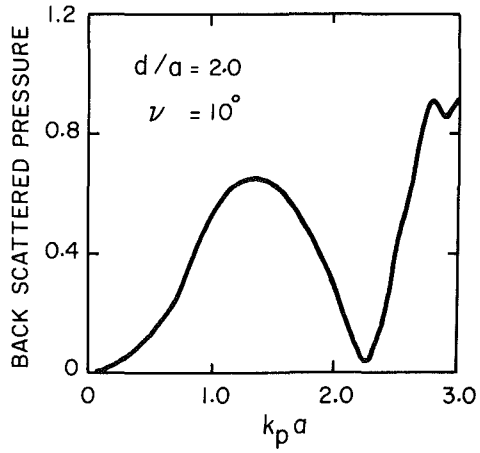


Fig. 6 2:1 Oblate spheroidal cavity

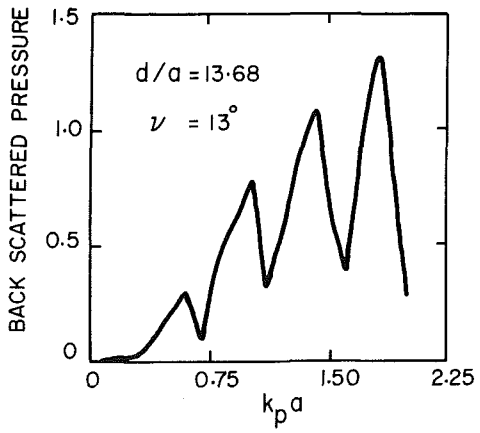
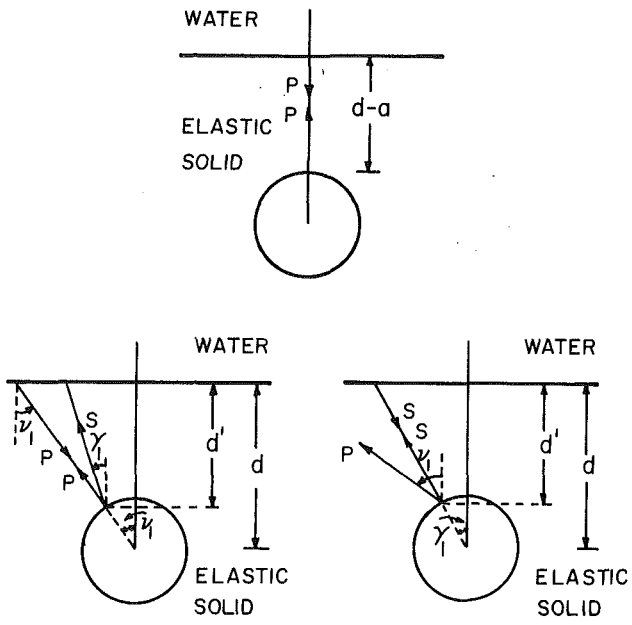


Fig. 7 Spherical cavity

that neglects any reflection from Γ. Equations (24b) and (24c) are expected to approach equation (24a) as the flaw depth d increases. In the numerical results that are presented, all three forms of f_m are used in equation (21) to calculate the scattered field.

In the following calculations the spherical void or stainless steel inclusion is embedded in epoxy. The oblate shperoidal void is embedded in Titanium. Its aspect ratio is 2:1 and its rotational axes of symmetry is normal to the in interface. The depth of the center of the flaw from the interface is d and the maximum flaw radius is a. All results are presented as a function of the P-wave number in the solid. Table 1 summarizes the material properties used.

Downloaded 02 May 2010 to 171.66.16.250. Redistribution subject to ASME license or copyright; see http://www.asme.org/terms/Terms_Use.cfm



Δka - Spacing of minima
for ν=13°, ν_1=24.42°, γ_1=11.75°

d/a	P→P,S→S	P→P, P→S	P→P, S→P	S→S,P→S	S→S,S→P
13.68	0.255	0.505	0.513	0.516	0.508

Fig. 8 Approximate ray paths and arrival times for normal and oblique incidence

In Fig. 3, the back-scattered far field pressure is plotted as a function of $k_p a$ (longitudinal wave number in the solid) for the case of waves incident normally on a spherical cavity buried at a depth $d/a = 1.63$. The solid line is the single scattering approximation and the other is an exact calculation. In Fig. 4 similar results are plotted for an oblate spheroidal void buried at a depth of $d/a = 2.0$ where a is the semimajor axis of the void. The rotational axis of symmetry coincides with the normal to the interface. In both cases we observe that the exact calculation deviates from the approximate calculation indicating that the effect of the interface is quite strong. In Fig. 5 corresponding results are presented for a spherical steel inclusion at a depth $d/a = 8.86$. We see that the exact calculation is a high-frequency modulation of the single scattered result. The spacing of the minima of the modulation is $ka = 2\pi/(2d'/a)$, indicating that the modulation is due to the interference between the specularly reflected wave from the top of the flaw and the wave that specularly reflects from the same point after one additional scattering at the interface ($d' = d - a$). In Fig. 6, the back-scattered pressure for waves incidents at an angle of 10 deg to the normal to an oblate spheroidal cavity is presented. In this case although not plotted explicitly, all three expressions for the scattered field coefficient in equation (24) give the same result. This indicates that the interference of the mode converted P and S- waves from the interface, which then specularly reflect from the void, makes the major contribution to the scattering. This is better illustrated in Fig. 7, for waves incident at 13 deg to the normal on a spherical cavity at a depth $d/a = 13.68$. In Fig. 8, all possible ray paths that undergo specular reflection are shown and the accompanying table summarizes the approximate spacing of the minima due to interference. It can be seen from the table that four different interference processes (*PP,PS*), (*PP,SP*), (*SS,PS*), and (*SS,SP*) produce approximately the same spacing $ka = 0.51$. (The exact spacing due to these four processes must in fact be the same due to time reversal invariance or reciprocity but for our purpose the approximate calculation is sufficient.) This predicted value compares quite well with the value of $ka = 0.45$ from Fig. 7.

Conclusions

We have provided a scheme to study the scattering of ultrasonic waves by subsurface flaws in joined fluid-solid half spaces. The formulation predicted that the far scattered field in the fluid is comprised of different orders of multiple scattering between the flaw and the interface Γ. The scattered field was computed exactly and by two different approximations, including no reflection from Γ and one reflection from Γ. These results are discussed in relation to flaw depth and angle of incidence for several types of scatterers. It is concluded that for normal incidence, for $d/a \geq 2.0$, the first-order multiple reflection produces a small modulation of the single scattered result. For oblique incidence again for $d/a > 2.0$, the major contribution is due to interference of the P and S-waves scattered by the flaw and not due to multiple reflections from Γ.

The calculation is not limited by the depth of the flaw. But with increasing frequency, the higher-order reflection matrix elements have very large values and hence it becomes difficult to invert $1\text{-}RT$ accurately. Further the numerical integration in the complex plane to generate the R-matrix is more time-consuming than the integrations for the T-matrix. Due to machine limitations, the present calculations were limited to $ka < 3.5$.

Acknowledgment

This work was sponsored in part by the Center for Advanced NDE operated by the Ames Laboratory, USDOE, for DARPA and AFWAL/ML under Contract No. W-7405-ENG-82 with Iowa State University. Computer time provided by the Instructional and Research Computer Center is gratefully acknowledged. The authors gratefully acknowledge interactions with Drs. Bruce Thompson, David Hsu, and Tim Grey of the Ames Laboratory, Iowa State University.

References

1 Bostrom, A., and Kristensson, G., "Elastic Wave Scattering by a Three-Dimensional Inhomogeneity in an Elastic Half Space," *Wave Motion*, Vol. 2, 1980, p. 335.

2 Varadan, V. V., and Varadan, V. K., "Scattering of Waves by Obstacles in the Presence of Nearby Boundaries—A Self-Consistent *T*-Matrix Approach," in: *Elastic Wave Scattering and Propagation*, Varadan, V. K., and Varadan, V. V., eds., Ann Arbor Science Publishers, Ann Arbor, Mich., 1982.

3 Bostrom, A., Kristensson, G., and Strom, S., "Transformation Properties of Plane, Spherical and Cylindrical Scalar and Vector Wave Functions—A Review," to be published.

4 Brekhovskikh, L. M., *Waves in Layered Media*, Academic Press, New York, 1960.

5 Varadan, V. V., and Varadan, V. K., "Scattering Matrix for Elastic Waves, III. Application to Spheroids," *J. Acoust. Soc. Am.*, Vol. 65, 1979, p. 396.

6 Cagniard, L., *Reflection and Refraction of Progressive Seismic Waves*, McGraw-Hill, New York, 1962.

Downloaded 02 May 2010 to 171.66.16.250. Redistribution subject to ASME license or copyright; see http://www.asme.org/terms/Terms_Use.cfm

E. Tsuchida[1]

T. Mura
Mem. ASME

Department of Civil Engineering
and Materials Research Center,
The Technological Institute,
Northwestern University,
Evanston, Ill. 60201

The Stress Field in an Elastic Half Space Having a Spheroidal Inhomogeneity Under All-Around Tension Parallel to the Plane Boundary

Stress distributions are evaluated for a semi-infinite elastic body having a spheroidal inhomogeneity under an all-around tension (axisymmetric uniform tension) at infinity. Boussinesq's potential functions are used for the analysis. A special technique is employed for the traction-free condition on the free surface, where the ordinary Legendre functions are expressed in terms of the Bessel functions in cylindrical coordinates. A closed-form expression for the stress concentration factor is found for a special case of a needlelike inhomogeneity.

1 Introduction

When inhomogeneous inclusons exist in an elastic material, the intensification of applied stress in their vicinity plays a dominant role in controlling the mechanical behavior of the material [1].

The degree of this stress concentration depends on the inhomogeneity of the elastic moduli, shapes, sizes, and locations of the inclusions and loading conditions, etc. Evaluation of the effect of inclusions is especially important in fatigue and fracture mechanics.

Most of the existing analyses [2–11] on inclusions have dealt with an infinite medium. Therefore, their solutions do not satisfactorily clarify the mechanics of inclusions near or at the free surface of the material.

In 1973, Tsutsui and Saito [12] solved the problem of a semi-infinite body containing a spherical inhomogeneity under axisymmetric tension, and made clear the effect of free surface on the stress field. Later on, one of the authors studied problems of a circular cylinder [13–15] and a thick plate [16, 17] containing a spherical inclusion under various loading conditions.

Mindlin and Cheng [18], Seo and Mura [19], and Aderogba [20, 21] gave the solutions for a half space when uniform dilatational eigenstrains are given inside a spherical or an ellipsoidal subdomain. Their solutions however, have a limitation to apply into the problem of inhomogeneous inclusions under loads, since they are based on uniform eigenstrains.

In this paper, an axisymmetric solution is given for the stresses in an elastic half space when uniform dilatational eigenstrains are given inside a spherical or an ellipsoidal subdomain. Their solutions however, have a limitation to apply into the problem of inhomogeneous inclusions under loads, since they are based on uniform eigenstrains.

In this paper, an axisymmetric solution is given for the stresses in an elastic half space having a spheroidal inclusion when it is subjected to all-around tension. The analysis is developed on the basis of Boussinesq's harmonic function approach. The solution is represented in terms of simple forms of cylindrical and spheroidal harmonics in an infinite integral form and in infinite series. The boundary conditions on the surface of a half space and the inclusion interface conditions for perfect bonding are satisfied with the aid of the relations between the cylindrical and spheroidal harmonics. Numerical examples of this stress analysis are given for a prolate spheroidal inclusion.

2 Method of Solution

Consider a semi-infinite elastic body having a spheroidal inclusion that has elastic moduli different from those of the remainder (matrix), as shown in Fig. 1. The present problem is to solve the stress field around the inclusion when an all-around tension parallel to the plane boundary is applied at infinity.

Let the origin of coordinates be at the center of the inclusion and the z-axis be directed into the interior of the semi-infinite body. Denote the cylindrical and prolate spheroidal coordinates by (r, θ, z) and (α, β, γ), respectively. The two coordinate systems are associated with each other by

[1] On leave from Faculty of Engineering, Saitama University, 255 Shimo-Okubo, Urawa, Japan.

Contributed by the Applied Mechanics Division for publication in the JOURNAL OF APPLIED MECHANICS.

Discussion on this paper should be addressed to the Editorial Department, ASME, United Engineering Center, 345 East 47th Street, New York, N.Y. 10017 and will be accepted until two months after final publication of the paper itself in the JOURNAL OF APPLIED MECHANICS. Manuscript received by ASME Applied Mechanics Division, March, 1983; final revision, June, 1983.

Copyright © 1983 by ASME
Downloaded 02 May 2010 to 171.66.16.250. Redistribution subject to ASME license or copyright; see http://www.asme.org/terms/Terms_Use.cfm

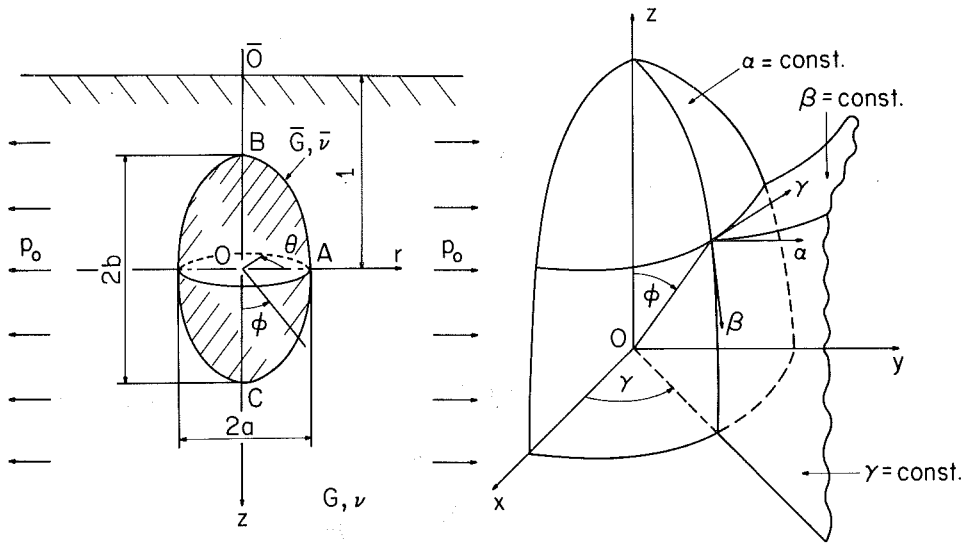


Fig. 1 Coordinate system

$$r=c\tilde{q}\tilde{p}, \quad \theta=\gamma, \quad z=cqp \tag{1}$$

in which $q = \cosh\alpha$, $\tilde{q} = \sinh\alpha$, $p = \cos\beta$, and $\tilde{p} = \sin\beta$. The surface of the inclusion is given by $\alpha=\alpha_0$ and $b=c\cosh\alpha_0$ and $a=c\sinh\alpha_0$, where b and a are the major and minor semiaxes of the inclusion.

The coordinate surfaces $\alpha=$const., $\beta=$const., and $\gamma=$const. form a triply orthogonal family of surfaces consisting of prolate spheroids, hyperboloids of two sheets, and meridional half planes, respectively.

Although the stress analysis will be performed for a prolate spheroidal inclusion, the solution for an oblate spheroidal inclusion can be obtained from the result of the prolate case by changing c to $-ic$, α to $i\pi/2+\alpha$, $\cosh\alpha$ to $i\sinh\alpha$ and $\sinh\alpha$ to $i\cosh\alpha$ (see Sadowsky and Sternberg [10]). Without loss of generality, the distance between the center of the inclusion and the plane boundary is taken as a unit. The surface of the semi-infinite body is thus represented by $z=-1$.

Following Boussinesq, a general solution of the displacement equations of equilibrium for rotational symmetry is given by

$$\left.\begin{aligned} 2Gu_r &= \frac{\partial\phi_0}{\partial r}+z\frac{\partial\phi_3}{\partial r}, \quad u_\theta=0 \\ 2Gu_z &= \frac{\partial\phi_0}{\partial z}+z\frac{\partial\phi_3}{\partial z}-(3-4\nu)\phi_3 \end{aligned}\right\} \tag{2}$$

where

$$\nabla^2\phi_0=\nabla^2\phi_3=0, \quad \nabla^2\equiv\frac{\partial^2}{\partial r^2}+\frac{1}{r}\frac{\partial}{\partial r}+\frac{\partial^2}{\partial z^2}.$$

Here (u_r, u_θ, u_z) are the cylindrical components of the displacement, and G and ν are the shear modulus and Poisson's ratio, respectively.

Transforming equations (2) into prolate spheroidal coordinates by use of equation (1), we obtain

$$\left.\begin{aligned} 2Gu_\alpha &= h\tilde{q}\frac{\partial\phi_0}{\partial q}+ch\tilde{q}p\left\{q\frac{\partial\phi_3}{\partial q}-(3-4\nu)\phi_3\right\} \\ 2Gu_\beta &= -h\tilde{p}\frac{\partial\phi_0}{\partial p}-ch q\tilde{p}\left\{p\frac{\partial\phi_3}{\partial p}-(3-4\nu)\phi_3\right\} \\ u_\gamma &= 0 \end{aligned}\right\} \tag{3}$$

where

$$\nabla^2\phi_0=\nabla^2\phi_3=0, \quad \nabla^2\equiv h^2\left\{\tilde{q}^2\frac{\partial^2}{\partial q^2}+2q\frac{\partial}{\partial q}+\tilde{p}^2\frac{\partial^2}{\partial p^2}-2p\frac{\partial}{\partial p}\right\},$$

$$h^2 = 1/\{c^2(q^2-p^2)\}$$

and $(u_\alpha, u_\beta, u_\gamma)$ are the components of the displacement in the prolate spheroidal coordinates (α, β, γ).

The corresponding components of stress $(\sigma_\alpha, \ldots, \tau_{\alpha\beta} \ldots)$ are derived from equation (3) by use of Hooke's law.

$$\begin{aligned} \sigma_\alpha &= h^2\left\{\tilde{q}^2\frac{\partial^2\phi_0}{\partial q^2}+c^2h^2\tilde{p}^2\left(q\frac{\partial\phi_0}{\partial q}-p\frac{\partial\phi_0}{\partial p}\right)\right\} \\ &\quad +ch^2\left[q\tilde{q}^2p\frac{\partial^2\phi_3}{\partial q^2}+\{c^2h^2q^2\tilde{p}^2\right. \\ &\quad \left.-2(1-\nu)\tilde{q}^2\}p\frac{\partial\phi_3}{\partial q}-(c^2h^2p^2+2\nu)q\tilde{p}^2\frac{\partial\phi_3}{\partial p}\right], \\ \sigma_\beta &= h^2\left\{\tilde{p}^2\frac{\partial^2\phi_0}{\partial p^2}+c^2h^2\tilde{q}^2\left(q\frac{\partial\phi_0}{\partial q}-p\frac{\partial\phi_0}{\partial p}\right)\right\} \\ &\quad +ch^2\left[qp\tilde{p}^2\frac{\partial^2\phi_3}{\partial p^2}-\{c^2h^2\tilde{q}^2p^2\right. \\ &\quad \left.+2(1-\nu)\tilde{p}^2\}q\frac{\partial\phi_3}{\partial p}+(c^2h^2q^2-2\nu)\tilde{q}^2p\frac{\partial\phi_3}{\partial q}\right], \\ \sigma_\gamma &= h^2\left(q\frac{\partial\phi_0}{\partial q}-p\frac{\partial\phi_0}{\partial p}\right)+ch^2\left\{(q^2-2\nu\tilde{q}^2)p\frac{\partial\phi_3}{\partial q}\right. \\ &\quad \left.-(p^2+2\nu\tilde{p}^2)q\frac{\partial\phi_3}{\partial p}\right\}, \\ \tau_{\alpha\beta} &= h^2\tilde{q}\tilde{p}\left\{-\frac{\partial^2\phi_0}{\partial q\partial p}+c^2h^2\left(q\frac{\partial\phi_0}{\partial p}-p\frac{\partial\phi_0}{\partial q}\right)\right\} \\ &\quad -ch^2\tilde{q}\tilde{p}\left[qp\frac{\partial^2\phi_3}{\partial q\partial p}+\left\{c^2h^2p^2\right.\right. \\ &\quad \left.\left.-(1-2\nu)q\frac{\partial\phi_3}{\partial q}\right\}q\frac{\partial\phi_3}{\partial q}-\{c^2h^2q^2\right. \\ &\quad \left.+(1-2\nu)\}p\frac{\partial\phi_3}{\partial p}\right]. \end{aligned} \tag{4}$$

Downloaded 02 May 2010 to 171.66.16.250. Redistribution subject to ASME license or copyright; see http://www.asme.org/terms/Terms_Use.cfm

The expressions (3) and (4) are used for the matrix and the inclusion. However, the shear modulus and Poisson's ratio are taken as $\bar{G}$ and $\bar{\nu}$ for the inclusion.

The following boundary conditions are used. The traction-free conditions on the surface of the half space are

$$(\sigma_z)_{z=-1} = (\tau_{zr})_{z=-1} = 0. \tag{5}$$

The perfect bonding conditions and the continuity of tractions at the interface of the inclusion are

$$(u_\alpha)_{\alpha=\alpha_0} = (\bar{u}_\alpha)_{\alpha=\alpha_0}, \quad (u_\beta)_{\alpha=\alpha_0} = (\bar{u}_\beta)_{\alpha=\alpha_0}$$
$$(\sigma_\alpha)_{\alpha=\alpha_0} = (\bar{\sigma}_\alpha)_{\alpha=\alpha_0}, \quad (\tau_{\alpha\beta})_{\alpha=\alpha_0} = (\bar{\tau}_{\alpha\beta})_{\alpha=\alpha_0}. \tag{6}$$

The stress state at infinity is all-around tension.

$$(\sigma_r)_{r\to\infty} = (\sigma_\theta)_{r\to\infty} = p_0 \tag{7}$$

In the preceding expressions the quantities defined in the inclusion are denoted by a superior bar.

To satisfy these boundary conditions, we choose ϕ_0 and ϕ_3 as follows. For the matrix ($\alpha > \alpha_0$), ϕ_0 and ϕ_3 are the sum of [*I*], [*II*], and [*III*].

$$[I] \begin{cases} \phi_0 = \dfrac{1-\nu}{2(1+\nu)} p_0 (r^2 - 2z^2) \\ \quad = -\dfrac{1-\nu}{2(1+\nu)} c^2 p_0 [2q^2 p^2 - (q^2-1)(1-p^2)] \\ \phi_3 = -\dfrac{p_0 z}{1+\nu} = -\dfrac{p_0 c}{1+\nu}\, qp, \end{cases} \tag{8}$$

$$[II] \begin{cases} \phi_0 = p_0 \sum_{m=0}^{\infty} A_m Q_m(q) P_m(p) \\ \phi_3 = p_0 \sum_{m=0}^{\infty} B_m Q_m(q) P_m(p), \end{cases} \tag{9}$$

$$[III] \begin{cases} \phi_0 = p_0 \int_0^\infty \psi_1(\lambda) J_0(\lambda r) e^{-\lambda z} d\lambda \\ \phi_3 = p_0 \int_0^\infty \lambda \psi_2(\lambda) J_0(\lambda r) e^{-\lambda z} d\lambda. \end{cases} \tag{10}$$

For the inclusion ($\alpha < \alpha_0$), ϕ_0 and ϕ_3 are

$$[IV] \begin{cases} \phi_0 = p_0 \sum_{n=0}^{\infty} \bar{A}_n P_n(q) P_n(p), \\ \phi_3 = p_0 \sum_{n=0}^{\infty} \bar{B}_n P_n(q) P_n(p). \end{cases} \tag{11}$$

Here, A_m, B_m, $\bar{A}_n$, $\bar{B}_n$, and $\psi_1(\lambda)$, $\psi_2(\lambda)$ are unknown constants and unknown functions of λ which are determined from the boundary conditions. $J_n(\lambda r)$ is the Bessel function of the first kind. $P_n(p)$ and $Q_n(q)$ are the ordinary Legendre functions of the first and second kinds, respectively, defined as

$$P_n(p) = (2^n n!)^{-1} \frac{d^n}{dp^n}(p^2-1)^n$$
$$Q_n(q) = (1/2) P_n(q) \log\{(q+1)/(q-1)\} - W_{n-1}(q),$$

where $W_{n-1}(q)$ is the regular part of the expansion.

The stresses and displacements derived from [*I*] in (8) are expressed as

$$u_r = \{(1-\nu)/\mathrm{E}\} p_0 r, \quad u_\theta = 0, \quad u_z = -(2\nu/\mathrm{E}) p_0 z$$
$$\sigma_r = \sigma_\theta = p_0, \quad \sigma_z = \tau_{r\theta} = \tau_{\theta z} = \tau_{zr} = 0, \tag{12}$$

where E is Young's modulus.

In the prolate spheroidal coordinate system they are expressed as

$$\frac{2Gu_\alpha}{p_0} = \{c^2 h q \bar{q}/(1+\nu)\}\{(1-\nu)-(1+\nu)p^2\}$$
$$= h\bar{q}\left\{\frac{2(1-2\nu)}{3(1+\nu)} c^2 q P_0(p) - \frac{2}{3} c^2 q P_2(p)\right\}$$
$$\frac{2Gu_\beta}{P_0} = -c^2 h p \bar{p}/(1+\nu)$$
$$= h\bar{p}\left[\frac{c^2}{3(1+\nu)}\{(1+\nu)q^2 - (1-\nu)\}\right] P_2'(p)$$
$$u_\gamma = 0$$
$$\frac{\sigma_\alpha}{p_0} = -(c^2 h^2 \bar{q}^2 - 1) q^2$$
$$= c^2 h^4 \left[c^2 q^2 \left\{\left(\frac{2}{3} q^2 - \frac{2}{15}\right) P_0(p) - \left(\frac{2}{21} + \frac{2}{3} q^2\right) P_2(p) + \frac{8}{35} P_4(p)\right\}\right]$$
$$\frac{\sigma_\beta}{p_0} = (c^2 h^2 q^2 - 1)\bar{q}^2, \quad \frac{\sigma_\gamma}{p_0} = 1$$
$$\frac{\tau_{\alpha\beta}}{p_0} = c^2 h^2 q \bar{q} p \bar{p}$$
$$= c^2 h^4 \bar{q}\bar{p}\left[c^2 q \left\{\left(\frac{1}{3} q^2 - \frac{1}{7}\right) P_2'(p) - \frac{2}{35} P_4'(p)\right\}\right]. \tag{13}$$

Thus, ϕ_0 and ϕ_3 given by [*I*] yield all-around tension of p_0. Therefore, the boundary condition (7) is automatically satisfied since the stress components derived from [*II*] and [*III*] vanish at infinity.

Before considering the boundary condition (5), the expressions (9) are written in terms of the cylindrical coordinates by using the following relation [22-24],

$$Q_n(q) P_n(p) = (-1)^n c \int_0^\infty e^{\lambda z} J_0(\lambda r) i_n(\lambda c) d\lambda, \quad (z<0) \tag{14}$$

where

$$i_n(\lambda c) \equiv i^{-n} j_n(i\lambda c) = (\pi/2\lambda c)^{1/2} I_{n+1/2}(\lambda c), i = (-1)^{1/2}.$$

$j_n(x)$ is the spherical Bessel function of the first kind and $I_{n+1/2}(\lambda c)$ is the modified Bessel function of the first kind.

With this relation the functions in [*II*] are transformed into the following forms,

$$[II]' \begin{cases} \phi_0 = p_0 \sum_{m=0}^{\infty} (-1)^m c\, A_m \int_0^\infty e^{\lambda z} J_0(\lambda r) i_m(\lambda c) d\lambda \\ \phi_3 = p_0 \sum_{m=0}^{\infty} (-1)^m c\, B_m \int_0^\infty e^{\lambda z} J_0(\lambda r) i_m(\lambda c) d\lambda \end{cases} \tag{15}$$

By using [*I*], [*II*]', and [*III*], the boundary condition (5) is written as

$$(\sigma_z/p_0)_{z=-1} = \int_0^\infty \lambda^2 \left[\psi_1(\lambda) + (2-2\nu-\lambda)\psi_2(\lambda)\right.$$

Downloaded 02 May 2010 to 171.66.16.250. Redistribution subject to ASME license or copyright; see http://www.asme.org/terms/Terms_Use.cfm

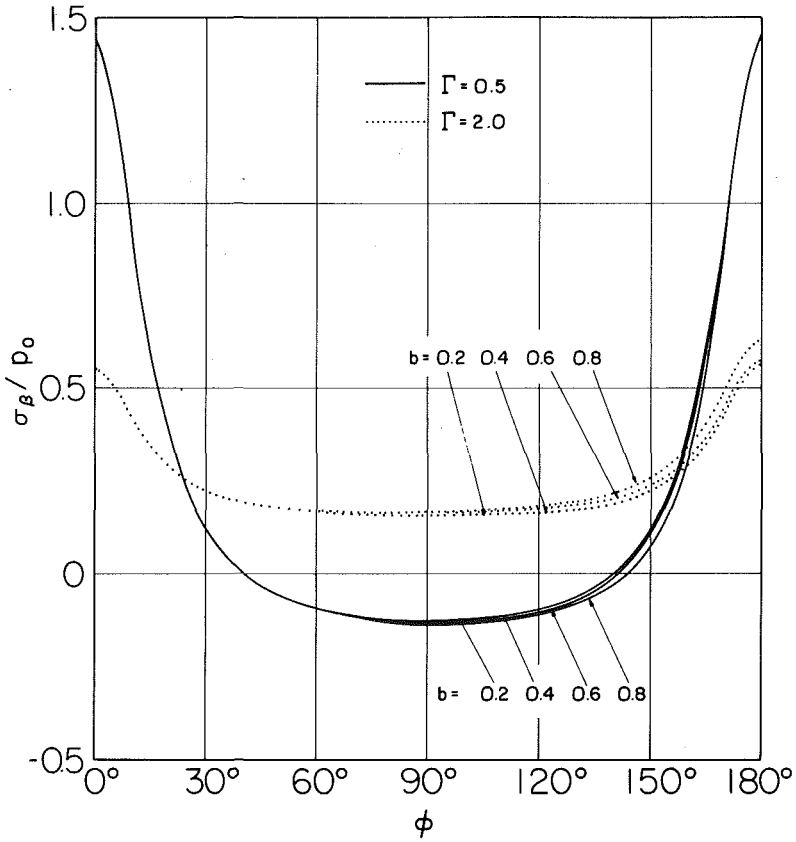


Fig. 2 Variation of σ_β (in matrix) on the spheroidal interface with ϕ for $s = a/b = 0.5$, $\Gamma = \hat{G}/G$, $\nu = \bar{\nu} = 0.3$

$$+\sum_{m=0}^{\infty}(-1)^m c\Big\{A_m - \frac{(2-2\nu+\lambda)}{\lambda}B_m\Big\}i_m(\lambda c)e^{-2\lambda}\Big]e^{\lambda}J_0(\lambda r)\,d\lambda = 0, \tag{16}$$

$$(\tau_{zr}/p_0)_{z=-1} = \int_0^{\infty}\lambda^2\Big[\psi_1(\lambda)+(1-2\nu-\lambda)\psi_2(\lambda) + \sum_{m=0}^{\infty}(-1)^m c\Big\{-A_m + \frac{(1-2\nu+\lambda)}{\lambda}B_m\Big\}i_m(\lambda c)e^{-2\lambda}\Big]e^{\lambda}J_1(\lambda r)\,d\lambda = 0 \tag{17}$$

The precedings expressions are the Hankel transforms. The vanishing of the transforms leads to the vanishing of the coefficients of $J_0(\lambda r)$ and $J_1(\lambda r)$. Thus, we have

$$\begin{aligned}\psi_1(\lambda) &= \sum_{m=0}^{\infty}\Big[(3-4\nu-\lambda)A_m - \frac{1}{\lambda}\{4(1-\nu)(1-2\nu) - 2\lambda\}B_m\Big](-1)^m c\, i_m(\lambda c)e^{-2\lambda},\\ \psi_2(\lambda) &= \sum_{m=0}^{\infty}\Big\{-2A_m + \frac{1}{\lambda}(3 - 4\nu + 2\lambda)B_m\Big\}(-1)^m c\, i_m(\lambda c)e^{-2\lambda}.\end{aligned} \tag{18}$$

Before considering the boundary conditions (6), expressions (10) are written in terms of the prolate spheroidal coordinates, by using the relation [22–24]

$$e^{-\lambda z}J_0(\lambda r) = \sum_{n=0}^{\infty}(-1)^n(2n+1)i_n(\lambda c)P_n(q)P_n(p) \tag{19}$$

Then, we have

$$[III]'\begin{cases}\phi_0 = p_0\sum_{n=0}^{\infty}\alpha_n P_n(q)P_n(p)\\ \phi_3 = p_0\sum_{n=0}^{\infty}\beta_n P_n(q)P_n(p)\end{cases} \tag{20}$$

where

$$\begin{aligned}\alpha_n &= \sum_{m=0}^{\infty}(-1)^{m+n}(2n+1)\,c\int_0^{\infty}\Big[(3-4\nu-2\lambda)A_m - \Big\{\frac{4(1-\nu)(1-2\nu)}{\lambda} - 2\lambda\Big\}B_m\Big]i_m(\lambda c)\,i_n(\lambda c)\,e^{-2\lambda}d\lambda\\ \beta_n &= \sum_{m=0}^{\infty}(-1)^{m+n}(2n+1)\,c\int_0^{\infty}\lambda\Big[(-2A_m + \frac{(3-4\nu+2\lambda)}{\lambda}B_m\Big]i_m(\lambda c)\,i_n(\lambda c)\,e^{-2\lambda}d\lambda\end{aligned} \tag{21}$$

Downloaded 02 May 2010 to 171.66.16.250. Redistribution subject to ASME license or copyright; see http://www.asme.org/terms/Terms_Use.cfm

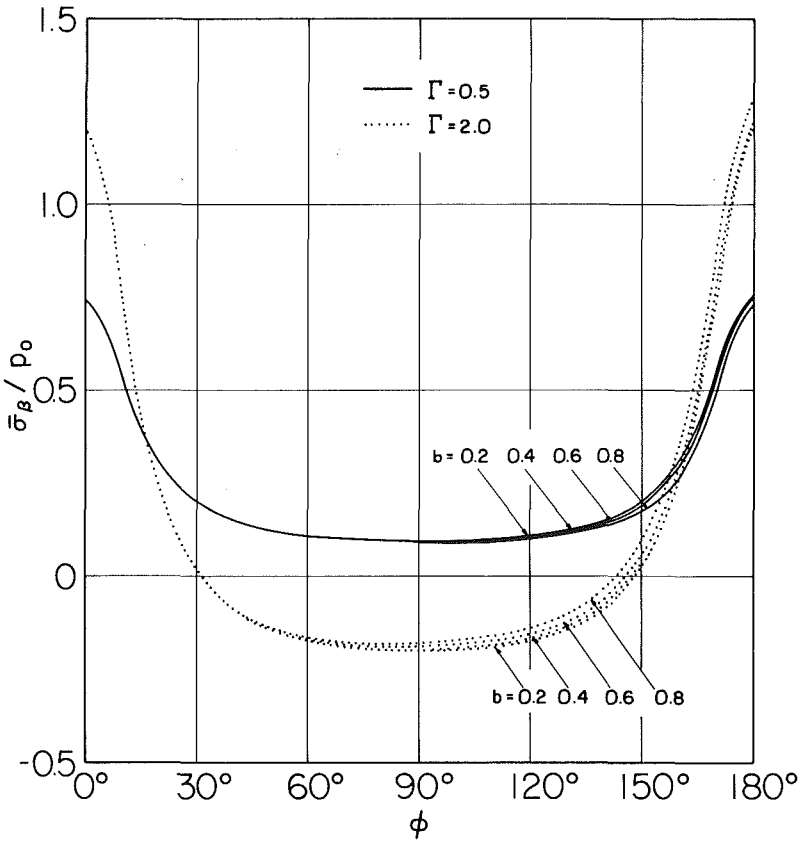


Fig. 3 Variation of $\bar{\sigma}_\beta$ (in inclusion) on the spheroidal interface with ϕ for $s = a/b = 0.5$

Deriving the stresses from the potential functions given by [*II*], [*III*]′, and [*IV*], the boundary conditions $(u_\alpha)_{\alpha=\alpha_0} = (\bar{u}_\alpha)_{\alpha=\alpha_0}$ can be written as

$$\sum_{n=0}^{\infty} \Big[\{k_{A1}A_n + k_{B1}B_{n-1} + k_{B2}B_{n+1} + k_{\alpha 1}\alpha_n + k_{\beta 1}\beta_{n-1} + k_{\beta 2}\beta_{n+1}\} - \frac{1}{\Gamma}\{\bar{k}_{A1}\bar{A}_n + \bar{k}_{B1}\bar{B}_{n-1} + \bar{k}_{B2}\bar{B}_{n+1}\}\Big]P_n(p) = -\frac{2(1-2\nu)}{3(1+\nu)}c^2 q_0 P_0(p) + \frac{2}{3}c^2 q_o P_2(p) \tag{22}$$

The condition $(u_\beta)_{\alpha=\alpha_0} = (\bar{u}_\beta)_{\alpha=\alpha_0}$ is written as

$$\sum_{n=1}^{\infty} \Big[\{l_{A1}A_n + l_{B1}B_{n-1} + l_{B2}B_{n+1} + l_{\alpha 1}\alpha_n + l_{\beta 1}\beta_{n-1} + l_{\beta 2}\beta_{n+1}\} - \frac{1}{\Gamma}\{\bar{l}_{A1}\bar{A}_n + \bar{l}_{B1}\bar{B}_{n-1} + \bar{l}_{B2}\bar{B}_{n+1}\}\Big]P_n'(p) = -\frac{c^2}{3(1+\nu)}[(1+\nu)q_0^2 - (1-\nu)]P_2'(p) \tag{23}$$

The condition $(\sigma_\alpha)_{\alpha=\alpha_0} = (\bar{\sigma}_\alpha)_{\alpha=\alpha_0}$, is written as

$$\sum_{n=0}^{\infty} [\{s_{A1}A_{n-2} + s_{A2}A_n + s_{A3}A_{n+2} + s_{B1}B_{n-3} + s_{B2}B_{n-1} + s_{B3}B_{n+1} + s_{B4}B_{n+3} + s_{\alpha 1}\alpha_{n-2} + s_{\alpha 2}\alpha_n + s_{\alpha 3}\alpha_{n+2} + s_{\beta 1}\beta_{n-3} + s_{\beta 2}\beta_{n-1} + s_{\beta 3}\beta_{n+1} + s_{\beta 4}\beta_{n+3}\} - \{\bar{s}_{A1}\bar{A}_{n-2} + \bar{s}_{A2}\bar{A}_n + \bar{s}_{A3}\bar{A}_{n+2} + \bar{s}_{B1}\bar{B}_{n-3} + \bar{s}_{B2}\bar{B}_{n-1} + \bar{s}_{B3}\bar{B}_{n+1} + \bar{s}_{B4}\bar{B}_{n+3}]P_n(p) = -c^2 q_0^2\Big[\Big(\frac{2}{3}q_0^2 - \frac{2}{15}\Big)P_0(p) - \Big(\frac{2}{21} + \frac{2}{3}q_0^2\Big)P_2(p) + \frac{8}{35}P_4(p)\Big] \tag{24}$$

The condition $(\tau_{\alpha\beta})_{\alpha=\alpha_0} = (\bar{\tau}_{\alpha\beta})_{\alpha=\alpha_0}$ is

$$\sum_{n=1}^{\infty} [\{t_{A1}A_{n-2} + t_{A2}A_n + t_{A3}A_{n+2} + t_{B1}B_{n-3} + t_{B2}B_{n-1} + t_{B3}B_{n+1} + t_{B4}B_{n+3} + t_{\alpha 1}\alpha_{n-2} + t_{\alpha 2}\alpha_n + t_{\alpha 3}\alpha_{n+2} + t_{\beta 1}\beta_{n-3} + t_{\beta 2}\beta_{n-1} + t_{\beta 3}\beta_{n+1} + t_{\beta 4}\beta_{n+3}\} - \{\bar{t}_{A1}\bar{A}_{n-2} + \bar{t}_{A2}\bar{A}_n + \bar{t}_{A3}\bar{A}_{n+2} + \bar{t}_{B1}\bar{B}_{n-3} + \bar{t}_{B2}\bar{B}_{n-1} + \bar{t}_{B3}\bar{B}_{n+1} + \bar{t}_{B4}\bar{B}_{n+3}\}]P_n'(p) = -c^2 q_0\Big[\Big(\frac{1}{3}q_0^2 - \frac{1}{7}\Big)P_2'(p) - \frac{2}{35}P_4'(p)\Big] \tag{25}$$

where

$$q_0 = \cosh\alpha_0, \quad \tilde{q}_0 = \sinh\alpha_0, \quad \Gamma = \bar{G}/G,$$

$$k_{A1} = Q_n'(q_0)$$

$$k_{B1} = -\frac{nc}{2n-1}[q_0 Q_{n-1}'(q_0) - (3-4\nu)Q_{n-1}(q_0)]$$

$$k_{B2} = -\frac{(n+1)c}{2n+3}[q_0 Q_{n+1}'(q_0) - (3-4\nu)Q_{n+1}(q_0)] \tag{26}$$

Downloaded 02 May 2010 to 171.66.16.250. Redistribution subject to ASME license or copyright; see http://www.asme.org/terms/Terms_Use.cfm

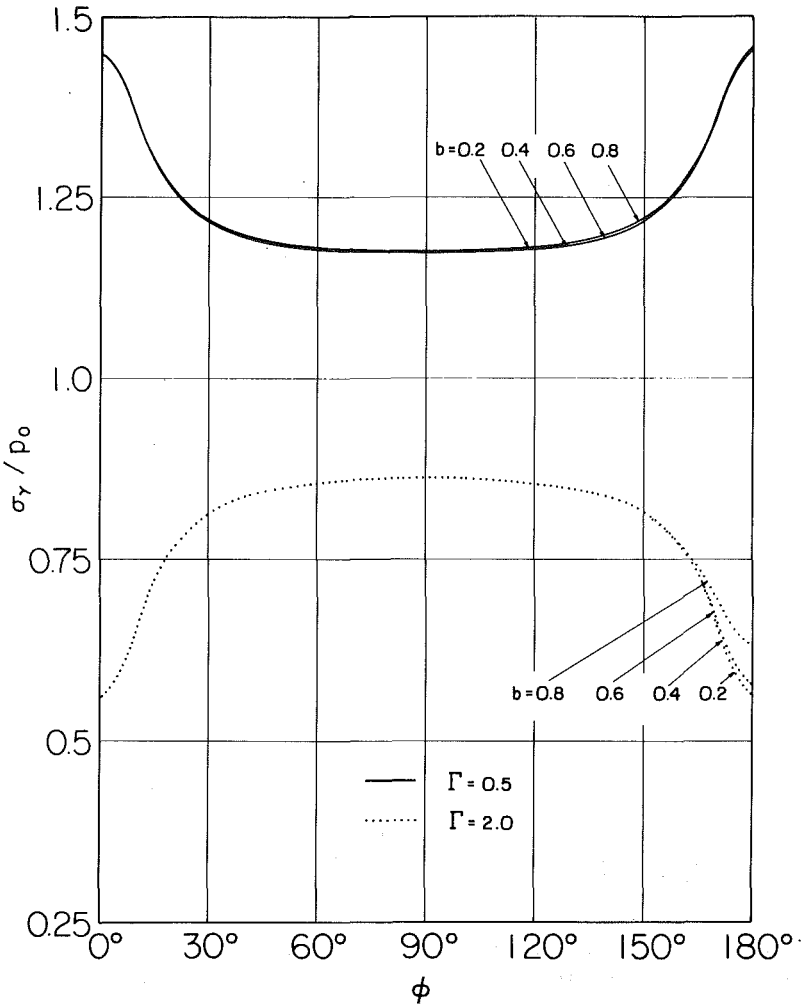


Fig. 4 Variation of σ_γ on the spheroidal interface with ϕ for $s = a/b = 0.5$

$$l_{A1} = -Q_n(q_0)$$

$$l_{B1} = \frac{-c}{2n-1}(n-4+4\nu)q_0 Q_{n-1}(q_0) \tag{27}$$

$$l_{B2} = -\frac{c}{2n+3}(n+5-4\nu)q_0 Q_{n+1}(q_0)$$

$$s_{A1} = \frac{(n-1)n}{(2n-3)(2n-1)}\{-\tilde{q}_0^2 Q''_{n-2}(q_0) - q_0 Q'_{n-2}(q_0) + (n-2)Q_{n-2}(q_0)\}$$

$$s_{A2} = \frac{1}{(2n-1)(2n+3)}[\{-(2n^2+2n-1)+(2n-1)(2n+3)q_0^2\}\tilde{q}_0^2 Q''_n(q_0) + 2(n^2+n-1)q_0 Q'_n(q_0) - n(n+1)Q_n(q_0)]$$

$$s_{A3} = \frac{(n+1)(n+2)}{(2n+3)(2n+5)}[-\tilde{q}_0^2 Q''_{n+2}(q_0) - q_0 Q'_{n+2}(q_0) - (n+3)Q_{n+2}(q_0)]$$

$$s_{B1} = \frac{(n-2)(n-1)nc}{(2n-5)(2n-3)(2n-1)}[-q_0\tilde{q}_0^2 Q''_{n-3}(q_0) + \{2(1-\nu)\tilde{q}_0^2 - q_0^2\}Q'_{n-3}(q_0) + (1-2\nu)(n-3)q_0 Q_{n-3}(q_0)] \tag{28}$$

$$s_{B2} = \frac{nc}{(2n-3)(2n-1)(2n+3)}[\{-3(n^2-2)+(4n^2-9)q_0^2\}q_0\tilde{q}_0^2 Q''_{n-1}(q_0) + \{2(1-\nu)\tilde{q}_0^2\{3n^2-6-[4n^2-9]q_0^2\} + (n^2-3)q_0^2\}Q'_{n-1}(q_0) + (n-1)\{2\nu(4n^2-9)q_0^2 + (1-2\nu)(n^2-n-3)\}q_0 Q_{n-2}(q_0)]$$

$$s_{B3} = \frac{(n+1)c}{(2n-1)(2n+3)(2n+5)}[\{(2n-1)(2n+5)q_0^2 - 3(n^2-2n+1)\}q_0\tilde{q}_0^2 Q''_{n+1}(q_0) + (2(1-\nu)\tilde{q}_0^2\{3(n^2+2n-1) - q_0^2[2n-1][2n+5]\} + (n^2+2n-2)q_0^2)Q'_{n+1}(q_0) - (n+2)\{2\nu(2n-1)(2n+5)q_0^2 + (1-2\nu)(n^2+3n-1\}q_0 Q_{n+1}(q_0)]$$

$$s_{B4} = -\frac{(n+1)(n+2)(n+3)c}{(2n+3)(2n+5)(2n+7)}[q_0\tilde{q}_0^2 Q''_{n+3}(q_0) - \{2(1-\nu)\tilde{q}_0^2 - q_0^2\}Q'_{n+3}(q_0) + (1-2\nu)(n+4)q_0 Q_{n+3}(q_0)]$$

$$t_{A1} = \frac{(n-3)(n-1)}{(2n-3)(2n-1)}Q'_{n-2}(q_0)$$

$$t_{A2} = \frac{1}{(2n-1)(2n+3)}[\{2n^2+2n-4-(2n-1)(2n+3)q_0^2\}Q'_n(q_0) + (2n-1)(2n+3)\times q_0 Q_n(q_0)]$$

Downloaded 02 May 2010 to 171.66.16.250. Redistribution subject to ASME license or copyright; see http://www.asme.org/terms/Terms_Use.cfm

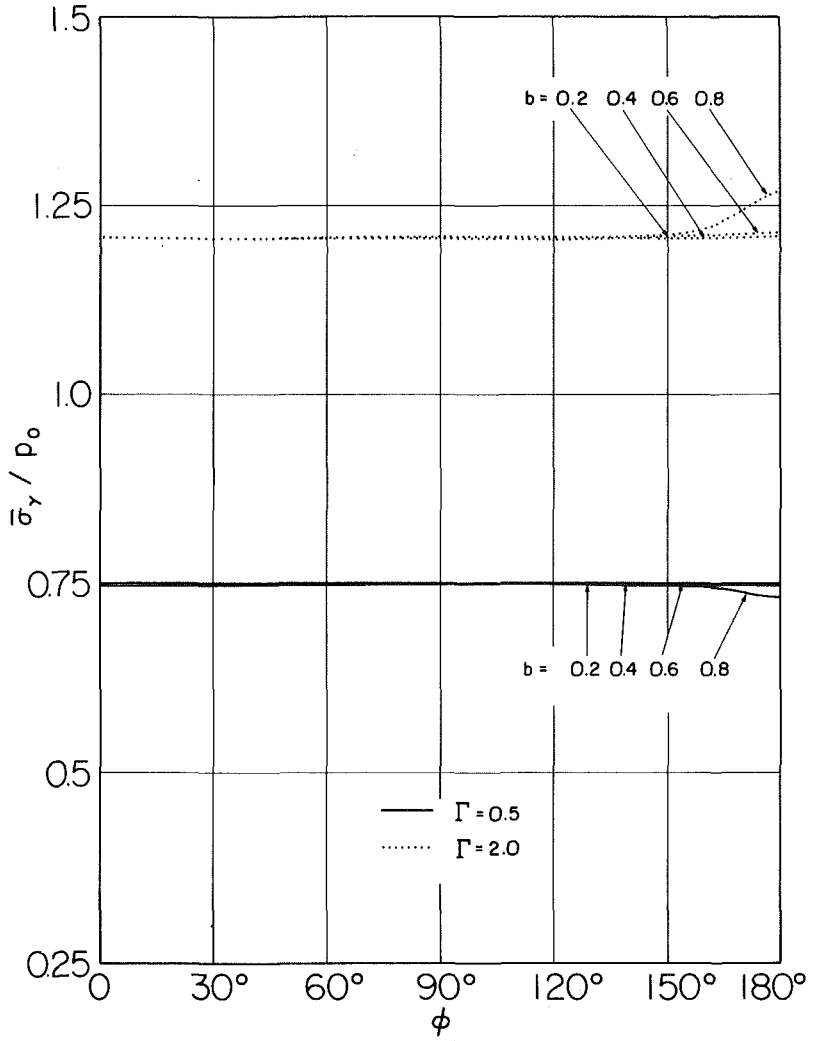


Fig. 5 Variation of $\bar{\sigma}_\gamma$ on the spheroidal interface with ϕ for $s = 0.5$

$$t_{A3} = \frac{(n+2)(n+4)}{(2n+3)(2n+5)} Q'_{n+2}(q_0)$$

$$t_{B1} = \frac{(n-2)(n-1)c}{(2n-5)(2n-3)(2n-1)} [(n-5+2\nu)q_0 Q'_{n-3}(q_0) - (1-2\nu)(n-3)Q_{n-3}(q_0)]$$

$$t_{B2} = \frac{c}{(2n-3)(2n-1)(2n+3)} [\{-(4n^2-9)(n-2+2\nu)q_0^2 + 3(n-1)(n^2-3) - 2(1-\nu)(n^2+n-3)\} q_0 Q'_{n-1}(q_0) + (n-1)\{2(1-\nu)(4n^2-9)q_0^2 - 3(1-2\nu)\times(n^2-3)\}Q_{n-1}(q_0)]$$

$$t_{B3} = \frac{c}{(2n-1)(2n+3)(2n+5)} [\{-(2n-1)(2n+5)(n+3-2\nu)q_0^2 + 3(n+2)(n^2+2n-2) + 2(1-\nu)(n^2+n-3)\} q_0 Q'_{n+1}(q_0) + (n+2)\{2(1-\nu)(2n-1)(2n+5)q_0^2 - 3(1-2\nu)(n^2+2n-2)\} Q_{n+1}(q_0)]$$

$$t_{B4} = \frac{(n+2)(n+3)c}{(2n+3)(2n+5)(2n+7)} [(n+6-2\nu)q_0 Q'_{n+3}(q_0) - (1-2\nu)(n+4)Q_{n+3}(q_0)] \quad (29)$$

in which $Q'_n(q_0)$ denotes a derivative of $Q_n(q_0)$ with regard to q_0.

The coefficients $k_{\alpha i}, k_{\beta i}, l_{\alpha i}, l_{\beta i}, s_{\alpha i}, s_{\beta i}, t_{\alpha i}$, and $t_{\beta i}$ are obtained from the coefficients $k_{Ai}, k_{Bi}, l_{Ai}, l_{Bi}, s_{Ai}, s_{Bi}, t_{Ai}$, and t_{Bi} by replacing $Q_n(q_0)$ by $P_n(q_0)$, respectively. Also the coefficients $\bar{k}_{Ai}, \bar{k}_{Bi}, \bar{l}_{Ai}, \bar{l}_{Bi}, \bar{s}_{Ai}, \bar{s}_{Bi}, \bar{t}_{Ai}$, and $\bar{t}_{Bi}$ are obtained from the coefficients $k_{Ai}, k_{Bi}, l_{Ai}, l_{Bi}, s_{Ai}, s_{Bi}, t_{Ai}$, and t_{Bi} by replacing $Q_n(q_0)$ and ν by $P_n(q_0)$ and $\bar{\nu}$, respectively.

The displacement containing the coefficients α_1 and β_0 corresponds to the rigid body motion of the matrix. Therefore, we put $\alpha_1 = \beta_0 = 0$.

The displacement containing $\bar{A}_1$, $\bar{B}_0$ represents the rigid body motion of the inclusion in the direction of the z-axis. Since both of the terms containing $\bar{A}_1$ and $\bar{B}_0$ show the same rigid body motion of the inclusion, one of the two constants can be chosen at zero. We put $\bar{B}_0 = 0$, $\bar{A}_1 \neq 0$ ($\bar{B}_0 \neq 0$, $\bar{A}_1 = 0$ give the same result).

Equating the coefficients of $P_n(p)$ and $P'_n(p)$ ($n = 0, 1, 2, \ldots$) in the left and right sides of equations (22)–(24), we obtain an infinite system of algebraic equations for A_n, B_n, $\bar{A}_n$, and $\bar{B}_n$.

3 Numerical Results

Numerical examples of the stress fields are given for $b = 0.2$, 0.4, 0.6, and 0.8 with various $s = a/b$ and different values of $\Gamma = \bar{G}/G$, $\Gamma = 0$, 0.1, 0.5, 2, 10, and ∞. All examples are carried out for $\nu = \bar{\nu} = 0.3$. According to Tsutsui and Saito [12], the influence of Poisson's ratio difference is very small compared with that of the shear modulus

Downloaded 02 May 2010 to 171.66.16.250. Redistribution subject to ASME license or copyright; see http://www.asme.org/terms/Terms_Use.cfm

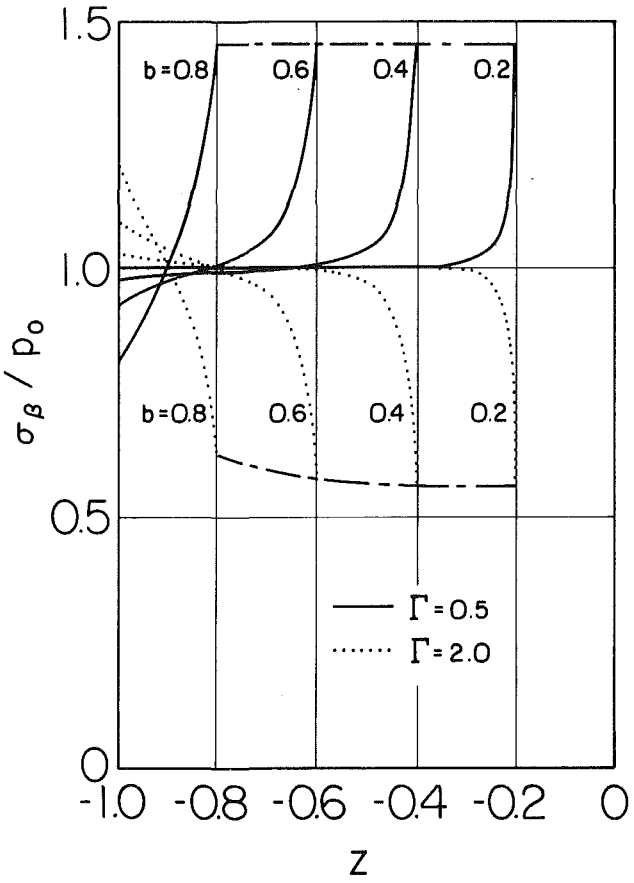


Fig. 6 Variation of σ_β along the z-axis with z for s = 0.5 (z < 0)

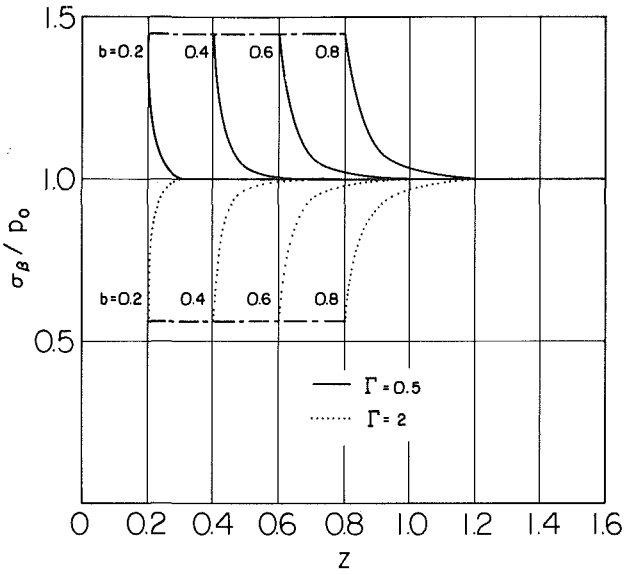


Fig. 7 Variation of σ_β along the z-axis with z for s = 0.5 (z > 0)

difference. The infinite system of algebraic equations for A_n, B_n, ,$\bar{A}_n$, and $\bar{B}_n$ is truncated by $n = 7 \sim 20$. This approximation is accurate enough to show three significant figures for the largest value of b. Once the coefficients are determined, we can compute the stresses and displacements at any point in the half space and the inclusion.

Figures 2–5 present the variations of σ_β, $\bar{\sigma}_\beta$, σ_γ, $\bar{\sigma}_\gamma$ with ϕ (see Fig. 1) at the interface between the matrix and the inclusion for $s = a/b = 0.5$. The value of ϕ is evaluated from β by using the relation $\tan \phi = (a/b) \tan \beta$.

Comparing Fig. 2 and Fig. 3, it is seen that the curves of σ_β for the soft inclusion have forms similar to the curves of $\bar{\sigma}_\beta$ for the hard inclusion. Also, the curves of σ_β for the hard inclusion have forms similar to those of $\bar{\sigma}_\beta$ for the soft inclusion.

The maximum tensile stress occurs at $\phi = 180$ deg in the matrix if the inclusion is soft. On the other hand, the maximum tensile stress occurs at $\phi = 180$ deg in the inclusion if the inclusion is hard.

In Figs. 4 and 5 the variations of σ_γ and $\bar{\sigma}_\gamma$ with ϕ at the interface are shown. It is seen that the curves are little influenced by the inclusion size and $\bar{\sigma}_\gamma$ is almost constant.

Figures 6 and 7 show the variations of σ_β for $s = 0.5$ along the z-axis, corresponding to $z < 0$ and $z > 0$, respectively. It should be noted that $\sigma_\beta = \sigma_\gamma$ along the z-axis.

From the foregoing results it is concluded that the maximum tensile stress occurs at $\alpha = \alpha_0$, $\phi = \beta = 180$ deg in the matrix or in the inclusion, depending on the hardness of the inclusion.

Denoting

$$\sigma_B = (\sigma_\beta)_{\alpha=\alpha_0,\phi=180\,\text{deg}} = (\sigma_\gamma)_{\alpha=\alpha_0,\phi=180\,\text{deg}}$$
$$\bar{\sigma}_B = (\bar{\sigma}_\beta)_{\alpha=\alpha_0,\phi=180\,\text{deg}} = (\bar{\sigma}_\gamma)_{\alpha=\alpha_0,\phi=180\,\text{deg}}$$

the variations of those stresses with b are plotted in Fig. 8 under various values of Γ and s.

For comparison, the result for the infinitely extended solid containing an inclusion under the all-around tensoin is shown in Fig. 9. The associated analysis is obtained as a special case of the present analysis where the constants that appeared in [*I*], [*II*], and [*IV*] are chosen as

$$B_1 = \frac{cq_0\tilde{q}_0^2\left(1-\frac{1}{\Gamma}\right)}{D}\left[-2\left(1-\frac{1}{\Gamma}\right)(1-2\bar{\nu})(1-\tilde{q}_0^2Q_1) - 6\,\frac{(\nu-\bar{\nu})}{1+\nu}\,\tilde{q}_0^2Q_1 + \frac{2(1-2\bar{\nu})+2\nu(2-\bar{\nu})}{1+\nu}\right]$$

$$\bar{A}_2 = \frac{2}{3}\,\frac{c^2q_0\tilde{q}_0^2}{D}\left[\left(1-\frac{1}{\Gamma}\right)^2\{2(1-\nu)(1-2\bar{\nu})\tilde{q}_0^2Q_1 + 2(1-2\bar{\nu})\tilde{q}_0^2 + 2\nu(1-2\bar{\nu})\} + \left(1-\frac{1}{\Gamma}\right)\left\{-\frac{6(1-\nu)(\nu-\bar{\nu})}{1+\nu}\,\tilde{q}_0^2Q_1 - 3(1-\bar{\nu})\tilde{q}_0^2 - \frac{4\bar{\nu}(1-\nu^2)+6\nu(\nu-\bar{\nu})}{1+\nu} - \frac{4(1-\nu)(\nu-\bar{\nu})}{1+\nu}\right]$$

$$A_0 = -A_2 - cq_0^2B_1$$

$$A_2 = \frac{\Gamma}{3q_0\tilde{q}_0^2}\left[2A_0 - (1-3\tilde{q}_0^2Q_1)A_2 - \frac{2(1-\nu)}{1+\nu}\,c^2q_0\tilde{q}_0^2\right] \quad (30)$$

$$\bar{B}_1 = \frac{1}{4c(1-2\bar{\nu})q_0\tilde{q}_0^2}[3(1-3\tilde{q}_0^2Q_1)A_2 - 2c(1-2\nu)(1-2\tilde{q}_0^2Q_1)B_1 + 9q_0\tilde{q}_0^2\bar{A}_2 + 2c^2q_0\tilde{q}_0^2]$$

$$A_1 = 0, \quad A_m = 0 (m \geq 3), \quad B_0 = 0, \quad B_m = 0 (m \geq 2)$$

$$\bar{A}_0 = \bar{A}_1 = 0, \quad \bar{A}_m = 0 (m \geq 3), \quad \bar{B}_0 = 0, \quad \bar{B}_m = 0 (m \geq 2)$$

where

$$Q_1 \equiv Q_1(q_0) = \frac{q_0}{2}\log\frac{q_0+1}{q_0-1} - 1$$

$$D = \left(1-\frac{1}{\Gamma}\right)^2(1-2\bar{\nu})[2(1+\nu)\tilde{q}_0^4\{Q_1\}^2 + 2\{2(1-\nu)\tilde{q}_0^2 + 3\tilde{q}_0^4\}Q_1 - 2(1-\nu+\tilde{q}_0^2)] + \left(1-\frac{1}{\Gamma}\right)[-6(\nu$$

Downloaded 02 May 2010 to 171.66.16.250. Redistribution subject to ASME license or copyright; see http://www.asme.org/terms/Terms_Use.cfm

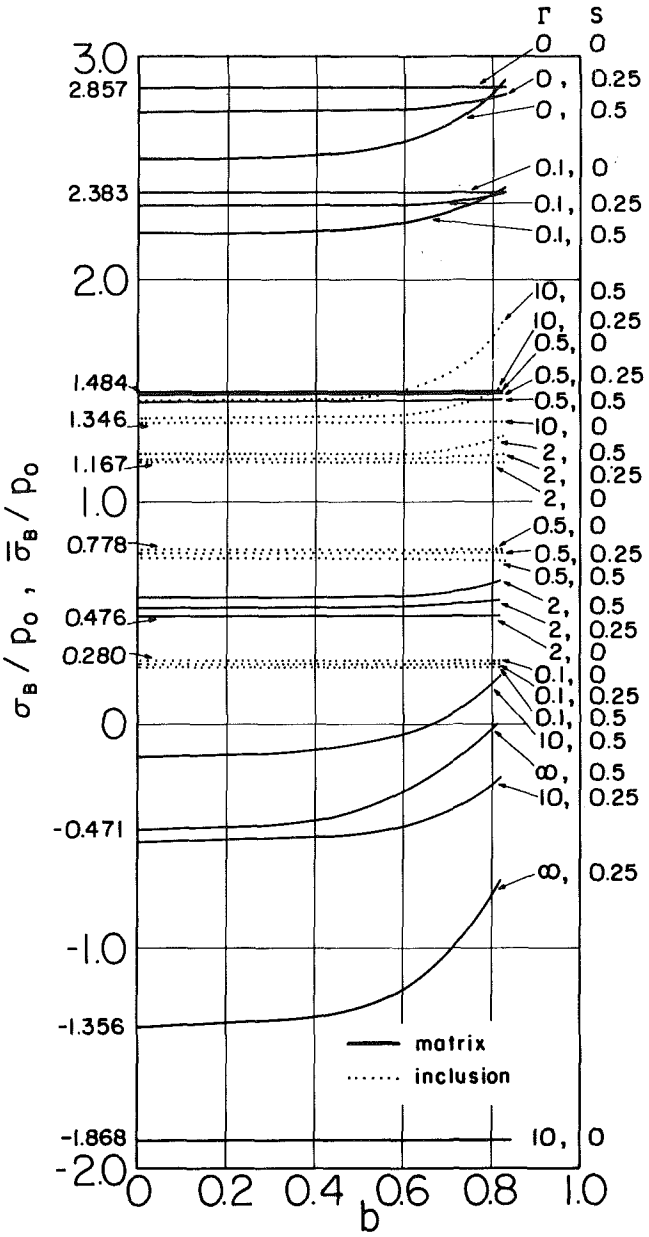


Fig. 8 Variations of σ_B and $\bar{\sigma}_B$ with the major semiaxis of the inclusion

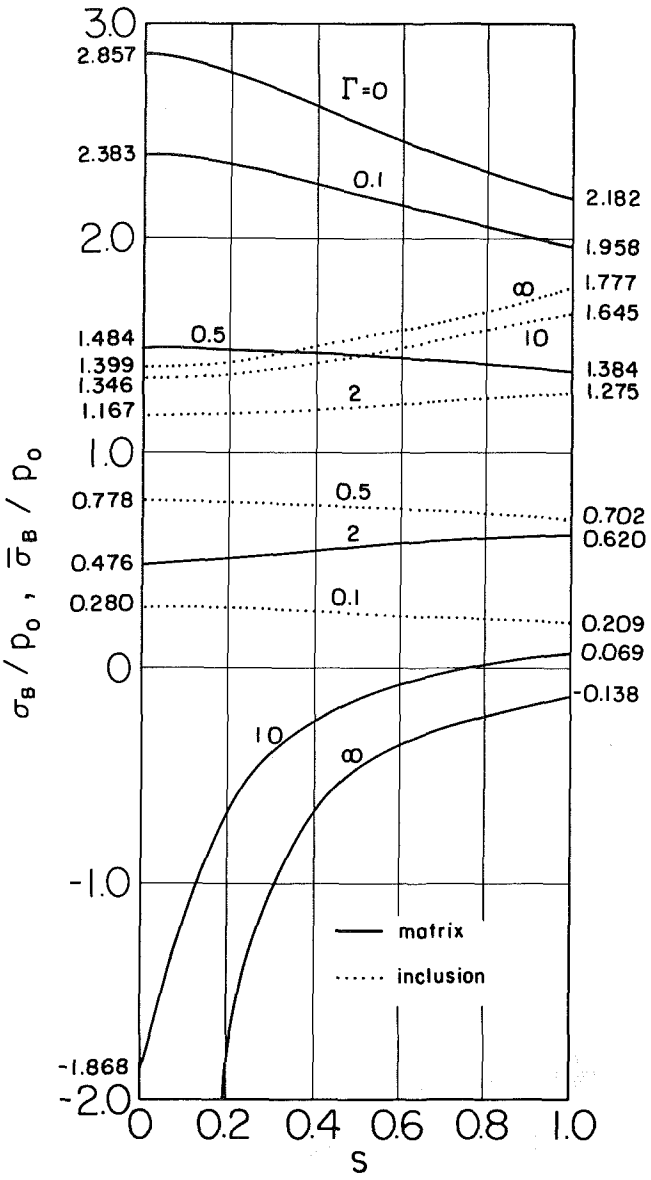


Fig. 9 Variations of σ_B and $\bar{\sigma}_B$ with shape ratio (infinite body with a spheroidal inclusion)

$$-\bar{\nu})\tilde{q}_0^4\{Q_1\}^2 - Q_1\{4\tilde{q}_0^2(1-\nu)(2-\bar{\nu}) + 9(1-\bar{\nu})\tilde{q}_0^4\}$$
$$+3(1-\bar{\nu})\tilde{q}_0^2 + 2(1-\nu)(3-4\bar{\nu})] - 4(1-\nu)(1-\bar{\nu})$$

The maximum stress in the matrix at the tip of a needle inclusion ($s=0$, the spheroid degenerates into a straight-line segment) is explicitly obtained as

$$\left(\frac{\sigma_\beta}{p_0}\right)_{\substack{\alpha=\alpha_0\to 0\\ p=1}} = 1 + \frac{1}{D^*}\left[\left(1-\frac{1}{\Gamma}\right)^2 2\nu(1-2\bar{\nu}) + \left(1\right.\right.$$
$$\left.-\frac{1}{\Gamma}\right)\frac{(-4\bar{\nu}+6\nu\bar{\nu}+4\nu^2\bar{\nu}-6\nu^2)}{1+\nu}$$
$$\left.-\frac{4(1-\nu)((\nu-\bar{\nu})}{1+\nu}\right] + \frac{(1+2\nu)}{D^*}\left(1-\frac{1}{\Gamma}\right)\left[-\left(1\right.\right.$$
$$\left.-\frac{1}{\Gamma}\right)2(1-2\bar{\nu}) + \frac{(2-4\bar{\nu}+4\nu-2\nu\bar{\nu})}{1+\nu}\right]$$

$$D^* = 2(1-\nu)\left[-\left(1-\frac{1}{\Gamma}\right)^2(1-2\bar{\nu}) + \left(1-\frac{1}{\Gamma}\right)(3-4\bar{\nu})\right.$$
$$\left.-2(1-\bar{\nu})\right]$$

4 Conclusion

In this paper, we presented a method of solution to the axisymmetric problem of a half space having a spheroidal inclusion, when the body is subjected to all-around tension. Following the analysis, we carried out some numerical calculations for a prolate spheroidal inclusion, showing the stress distributions around the inclusion, the effects of the free surface, the shape ratio of the inclusion, and the stiffness ratio. It is concluded that the maximum tensile stress occurs at point B at the interface near the free boundary. When the shape ratio s is small, the maximum tensile stress is scarcely affected by the free surface. When the inclusion is hard ($\Gamma > 1$), the maximum stress concentration is found in the inclusion. $\bar{\sigma}_\beta$ becomes larger when the inclusion is located nearer to the free surface and when the shape ratio becomes larger. On the other hand, when the inclusion is soft ($\Gamma < 1$), the maximum stress concentration is found in the matrix.

Downloaded 02 May 2010 to 171.66.16.250. Redistribution subject to ASME license or copyright; see http://www.asme.org/terms/Terms_Use.cfm

Acknowledgment

The authors wish to thank Mr. H. Yamada and Mr. T. Uchiyama for their help in the numerical calculations. This research was supported by NSF-MRL-07923573 and partially by U.S. Army Research Grant DAAG 29-81-k-0090.

References

1 Yokobori, T., *An Interdisciplinary Approach to Fracture and Strength of Solids*, Walters-Noordhoff, 1966, pp. 239–247.

2 Goodier, J. N., "Concentration of Stress Around Spherical and Cylindrical Inclusions and Flaws," ASME JOURNAL OF APPLIED MECHANICS, Vol. 57, 1933, pp. 39–44.

3 Miyamoto, H., "Stress Concentration Around a Heterogeneous Insertion of Ellipsoid in an Infinite Body I.," *J. Japan Soc. Appl. Mech.*, Vol. 3, 1950, pp. 15–19.

4 Miyamoto, H., "Stress Concentration Around a Heterogeneous Insertion of Spheroid in an Elastic Body III. (Torsion)," *Proc. 1st Japan Nat. Congr. Appl. Mech.*, 1951, pp. 43–46.

5 Edwards, R. H., "Stress Concentration Around Spheroidal Inclusions and Cavities," ASME JOURNAL OF APPLIED MECHANICS, Vol. 18, 1951, pp. 19–30.

6 Robinson, K., "Elastic Energy of an Ellipsoidal Inclusion in an Infinite Solid," *J. Appl. Phys.*, Vol. 22, 1951, pp. 1045–1054.

7 Chen, W. T., "On a Spherical Elastic Inclusion in a Transversely Isotropic Material Under an Axisymmetric Torsion Field," ASME JOURNAL OF APPLIED MECHANICS, Vol. 33, 1966, pp. 944–945.

8 Chen, W. T., "Axisymmetric Stress Field Around Spheroidal Inclusions and Cavities in a Transversely Isotropic Material," ASME JOURNAL OF APPLIED MECHANICS, Vol. 35, 1968, pp. 770–773.

9 Bose, S. C., "On the Torsion of a Transversely Isotropic Circular Cylinder Having a Small Elastic Inclusion of an Isotropic Material," *Z. Angew. Math. Mech.*, Vol. 45, 1965, pp. 133–135.

10 Sadowsky, M. A., and Sternberg, E., "Stress Concentration Around an Ellipsoidal Cavity in an Infinite Body Under Arbitrary Plane Stress Perpendicular to the Axis of Revolution of Cavity," ASME JOURNAL OF APPLIED MECHANICS, Vol. 69, 1947, pp. *A*191–*A*201.

11 Eshelby, J. D., "The Determination of the Elastic Field of an Ellipsoidal Inclusion, and Related Problems," *Proc. Royal Soc. London*, Ser. *A*, Vol. 241, 1957, pp. 376–396.

12 Tsutsui, S., and Saito, K., "On the Effect of a Free Surface and a Spherical Inhomogeneity on Stress Fields of a Semi-Infinite Medium Under Axisymmetric Tension," *Proc. 23rd Japan Nat. Congr. Appl. Mech.*, Vol. 23, 1973, pp. 547–560.

13 Kawashima, K., Tsuchida, E., and Nakahara, I., "Stresses in a Circular Cylinder Having a Spherical Inclusion Under Torsion," Proc. *24th Japan Nat. Congr. Appl. Mech.*, Vol. 24, 1974, pp. 357–363.

14 Kawashima, K., Tsuchida, E., and Nakahara, I., "Stresses in an Elastic Cylinder Having a Spherical Inclusion under Tension," *Proc. 27th Japan Nat. Congr. Appl. Mech.*, Vol. 27, 1977, pp. 79–89.

15 Kawashima, K., Tsuchida, E., and Nakahara, I., "Stresses in a Circular Cylinder Having a Spherical Inclusion, Under Transverse Bending," *Bulletin of the JSME*, Vol. 22, 1979, pp. 1719–1726.

16 Tsuchida, E., et al., "Stresses in an Elastic Thick Plate Having a Spherical Inclusion Under Transverse Bending," *Proc. 26th Japan Nat. Congr. Appl. Mech.*, Vol. 26, 1976, pp. 137–155.

17 Nakahara, I., et al., "Stresses in an Elastic Thick Plate Having a Spherical Inclusion Under Uniaxial Tension," *Recent Research on Mechanical Behaviour of Solids*, University of Tokyo Press, 1979, pp. 119–138.

18 Mindlin, R. D., and Cheng, D. H., "Thermoelastic Stress in the Semi-Infinite Solid," *J. Appl. Phys.*, Vol. 21, 1950, pp. .373–376.

19 Seo, K., and Mura, T., "The Elastic Field in a Half Space Due to Ellipsoidal Inclusions With Uniform Dilatational Eigenstrains," ASME JOURNAL OF APPLIED MECHANICS, Vol. 46, 1979, pp. 568–572.

20 Aderogba, K., "On Eigenstresses in a Semi-Infinite Solid," *Math. Proc. Camb. Phil. Soc.*, Vol. 80, 1976, pp. 555–562.

21 Aderogba, K., "The Determination of Thermal Stresses in Dissimilar Media," *Math. Proc. Camb. Phil. Soc.*, Vol. 89, 1980, pp. 533–542.

22 Tsuchida, E., Saito, Y., Nakahara, I., and Kodama, M., "Stress Concentration Around a Prolate Spheroidal Cavity in a Semi-Infinite Elastic Body Under All-Round Tension," *Bulletin of the JSME*, Vol. 25, 1982, pp. 493–500.

23 Nicholson, J. W., "Oblate Spheroidal Harmonics and Their Applications," *Phil. Trans. Roy. Soc.* Ser. *A*, Vol. 224, 1924, pp. 49–93, 303–369.

24 Cooke, J. C., "Some Relations Between Bessel and Legendre Functions," *Monatschefte für Math.*, Vol. 60, 1956, pp. 322–328.

Downloaded 02 May 2010 to 171.66.16.250. Redistribution subject to ASME license or copyright; see http://www.asme.org/terms/Terms_Use.cfm

Finite Element Analysis of Dynamic Coupled Thermoelasticity Problems With Relaxation Times

J. H. Prevost
Associate Professor of Civil Engineering.

D. Tao
Graduate Student.

Princeton Univesity,
Princeton, N.J. 08544

A general finite element model is proposed to analyze transient phenomena in thermoelastic solids. Green and Lindsay's dynamic thermoelasticity model is selected for that purpose since it allows for "second sound" effects and reduces to the classical model by appropriate choice of the parameters. Time integration of the semidiscrete finite element equations is achieved by using an implicit-explicit scheme proposed by Hughes, et al. The procedure proves to be most effective and versatile in thermal and stress wave propagation analysis. A number of examples are presented which demonstrate the accuracy and versatility of the proposed model, and the importance of finite thermal propagation speed effects.

Introduction

The dynamic propagation of mechanical and thermal disturbances in solids has been the subject of many recent investigations. The first attempt to include inertia effects in a transient thermoelasticity problem was reported early in 1950 by Danilovskaya [5]. Although one-dimensional and strictly speaking "uncoupled," the solution enlightened the process of transmission of thermal stresses through the propagation of elastic waves. Further refinements to that analytical solution have been reported by Danilovskaya [6], Sternberg and Chakrovorty [22], Boley and Tolins [4], and Nowacki [18]. The class of problems that admits closed-form solutions in dynamic thermoelasticity is evidently very small, and numerical techniques have to be resorted to for more complex geometries and/or more sophisticated coupled field theories. Numerical solutions have been reported by Nickell and Sackman [17], Oden [20], and Ting and Chen [24]. However, all these investigations have been based on "classical" thermoelasticity theory (see e.g., Eringen [7]), which allows thermal disturbances to propagate with infinite velocity. To remedy this physically unacceptable situation, modified dynamic thermoelasticity theories have been proposed to allow for so-called "second sound" effects, even though such effects in elastic solids may well be small and short-lived. In 1967, Lord and Shulman [15] proposed a new theory based on a modified Fourier's Law of heat conduction with one relaxation time, t_0. The resulting heat equation becomes hyperbolic, and thus implies a finite wave speed propagation for the temperature. In 1972, Green and Lindsay [8] proposed a generalized theory of dynamic thermoelasticity based on a rigorous treatment of thermodynamics. The new theory introduces two relaxation times t_1 and t_2 for the thermoelastic process. As opposed to Lord and Shulman's theory, Green and Lindsay's theory does not violate Fourier's Law when the solid has a center of symmetry. Potential applications for these new theories have been reported in the survey article by Ignaczak [14] and the references therein. Increased interest has recently been directed toward these theories mainly due to the advent of pulsed lasers, fast burst nuclear reactors, and particle accelerators which can supply heat pulses with very fast time rises [1, 3]. It is the purpose of this paper to propose a general and efficient numerical procedure for analyzing dynamic thermoelasticity problems, and to investigate the effects of finite propagation speeds for thermal disturbances.

For completeness, a brief review of the various linearized coupled field equations is first presented. Attention is thereafter concentrated on Green and Lindsay's theory. The finite element spatial discretization of the field equations is next described. Time integration of the resulting coupled semidiscrete equations for the displacement and the temperature, is considered next. The Newmark [16] family of methods is selected for that purpose, and an implicit-explicit predictor-corrector scheme developed by Hughes and coworkers [11, 12] is used. The procedure allows for a convenient selection of implicit and explicit elements. Solutions for the coupled displacement and temperature fields are obtained simulataneously. It is shown that the numerical procedure allows solutions to be obtained for both quasi-static and dynamic coupled thermoelasticity problems with or without finite wave speeds for thermal disturbances. Numerical results that demonstrate the versatility and accuracy of the method are presented, and the effect of finite propagation speeds for thermal disturbances is investigated.

Contributed by the Applied Mechanics Division and presented at the Winter Annual Meeting, Boston, Mass., November 13-18, 1983 of THE AMERICAN SOCIETY OF MECHANICAL ENGINEERS.

Discussion on this paper should be addressed to the Editorial Department, ASME, United Engineering Center, 345 East 47th Street, New York, N.Y. 10017, and will be accepted until two months after final publication of the paper itself in the JOURNAL OF APPLIED MECHANICS. Manuscript received by ASME Applied Mechanics Division, July, 1982; final revision, April, 1983. Paper No. 83-WA/APM-9.

Copies will be available until July, 1984.

Copyright © 1983 by ASME
Downloaded 02 May 2010 to 171.66.16.250. Redistribution subject to ASME license or copyright; see http://www.asme.org/terms/Terms_Use.cfm

Linearized Basic Equations of Thermoelasticity

The basic equations of linearized thermoelasticity are summarized herein. For convenience and comparison, the equations pertaining to the three theories mentioned previously are listed. Cartesian tensors are used throughout.

Balance Equations

(*a*) Mass

$$\frac{\rho_0}{\rho} = 1 + u_{k,k} \tag{1}$$

(*b*) Momentum

$$\sigma_{ji,j} + \rho\, b_i = \rho\, \ddot{u}_i \tag{2a}$$

$$\sigma_{ij} = \sigma_{ji} \tag{2b}$$

(*c*) Energy (Heat Conduction)

$$\rho\, T\, \dot{\eta} = -q_{k,k} + \rho\, h \tag{3}$$

in which

ρ = mass density in current configuration
ρ_0 = mass density in reference configuration
σ_{ij} = (Cauchy) stress tensor
u_i = displacement vector
b_i = body force vector
q_i = heat flux vector
η = entropy density
T = absolute temperature
h = heat source
c = specific heat

A superposed dot ($\dot{}$) is used to denote material time differentiation and a comma ($,_j$) to denote partial differentiation with respect to x_j ($j = 1,2,3$).

Constitutive Equations. In the following

$$T = T_0 + \theta \tag{4}$$

where T_0 is the reference temperature of the natural (stress-free) state of the solid body:

$$\sigma_{ij} = C_{ijkl} u_{(k,l)} - \beta_{ij}(\theta + t_1\, \dot{\theta}) \tag{5a}$$

$$q_i + t_0 \dot{q}_i = -k_{ij}\, \theta_{,j} \tag{5b}$$

$$\eta = \eta_0 + \frac{c}{T_0}\theta + \frac{\mathrm{ct}_2}{T_0}\dot{\theta} + \frac{1}{\rho_0}\beta_{ij}\quad u_{(i,j)} \tag{5c}$$

in which

C_{ijkl} = tensor of elastic moduli ($C_{ijkl} = C_{jikl} = C_{ijlk} = C_{klij}$)
β_{ij} = tensor of thermal moduli ($\beta_{ij} = \beta_{ji}$)
k_{ij} = thermal conductivity tensor ($k_{ij} = k_{ji}$)

$$u_{(k,l)} = \frac{1}{2}(u_{k,l} + u_{l,k}) \;=\; \text{strain tensor.}$$

When t_0, t_1, and t_2 vanish, equations (5*a–c*) reduce to the classical theory [7]. In Lord and Shulman's theory, [15], $t_1 = t_2 = 0$ and Fourier's Law of heat conduction (equation (5*b*)) is modified by the introduction of the relaxation time t_0, which is the time needed to establish steady-state heat conduction in a unit volume element subject to sudden temperature gradient. When $t_0 = 0$, Lord and Shulman's theory reduces to the classical theory. In Green and Lindsay's theory [8], $t_0 = 0$ and both the Duhamel-Neuman relations (equation (5*a*)) and entropy density function (equation (5*c*)), are modified by the introduction of the two relaxation times t_1 and t_2. When t_1 and t_2 vanish, Green and Lindsay's theory reduces to the classical theory.

Field Equations. In terms of displacements u_i and temperature θ, the resulting field equations are:

$$\rho\ \ddot{u}_i + (t_1 \beta_{ij}\dot{\theta})_{,j} - (C_{ijkl}u_{k,l} - \beta_{ij}\theta)_{,j} = \rho\, b_i \tag{6a}$$

$$\rho c(t_0 + t_2)\ddot{\theta} + t_0 T_0 \beta_{ij}\ddot{u}_{i,j} + \rho c\dot{\theta} + T_0\beta_{ij}\dot{u}_{i,j} - (k_{ij}\theta_{,j})_{,i} = \rho(h + t_0\dot{h}) \tag{6b}$$

Weak Form: Semidiscrete Equations

The weak formulation associated wit the initial-boundary-value problem of coupled thermoelasticity is obtained by proceeding along standard lines (see e.g. references [2, 19, 25]). The associated matrix problem is obtained by discretizing the domain Ω occupied by the solid body into nonoverlapping finite elements. Associated with this discretization are nodal points at which shape functions N are defined. Two sets of shape functions in general, will be required for the displacement and temperature fields. The shape functions for the displacment and temperature associated with node A are denoted N^A and N'^A, respectively, in the following. They satisfy the relations $N^A(\mathbf{x}^B) = N'^A(\mathbf{x}^B) = \delta_{AB}$, in which $\mathbf{x}^B$ denotes the position vector of node B, δ_{AB} = Kronecker delta. The solution of the Galerkin counterpart of the weak formulation is then expressed in terms of the shape functions and gives rise to the following system of equations for Green and Lindsay's theory (equation (6) in which $t_0 = 0$):

$$\begin{bmatrix} \mathbf{M}^{SS} & \mathbf{0} \\ \mathbf{0} & \mathbf{M}^{\theta\theta} \end{bmatrix} \begin{bmatrix} \ddot{\mathbf{d}}^S \\ \ddot{\theta} \end{bmatrix} + \begin{bmatrix} \mathbf{0} & \mathbf{C}^{S\theta} \\ \mathbf{C}^{\theta S} & \mathbf{C}^{\theta\theta} \end{bmatrix} \begin{bmatrix} \dot{\mathbf{d}}^S \\ \dot{\theta} \end{bmatrix} + \begin{bmatrix} \mathbf{K}^{SS} & \mathbf{K}^{S\theta} \\ \mathbf{0} & \mathbf{K}^{\theta\theta} \end{bmatrix} \begin{bmatrix} \mathbf{d}^S \\ \theta \end{bmatrix} = \begin{bmatrix} \mathbf{F}_S^{\text{ext}} \\ \mathbf{F}_\theta^{\text{ext}} \end{bmatrix}, \tag{7}$$

where $\mathbf{d}^S$ and θ represent the nodal displacement and temperature vectors. The elemental contributions to node A from node B, for directions a and b, to the various matrices appearing in equation (7) are given by the following equations:

$$(M_{ab}^{AB})^{SS} = \delta_{ab}\int_{\Omega^e} \rho\, N^A N^B\, d\Omega \tag{8}$$

$$(M^{AB})^{\theta\theta} = \int_{\Omega^e} \rho\, c\, t_2\, N'^A N'^B\, d\Omega \tag{9}$$

$$(C_b^{AB})^{S\theta} = -\int_{\Omega^e} t_1 \beta_{ab}\, N'^A N_{,a}^B\, d\Omega \tag{10}$$

$$(C_a^{AB})^{\theta S} = \int_{\Omega^e} T_0\, \beta_{ab}\, N_{,b}^A\, N'^B\, d\Omega \tag{11}$$

$$(C^{AB})^{\theta\theta} = \int_{\Omega^e} \rho\, c\, N'^A N'^B\, d\Omega \tag{12}$$

$$(K_{ab}^{AB})SS = \int_{\Omega^e} C_{abcd}\, N_{,d}^A\, N_{,c}^B\, d\Omega \tag{13}$$

$$(K_b^{AB})^{S\theta} = -\int_{\Omega^e} \beta_{ab}\, N'^A\, N_{,a}^B\, d\Omega \tag{14}$$

$$(K^{AB})^{\theta\theta} = \int_{\Omega^e} k_{ab}\, N'^A_{,b} N'^B_{,a} d\Omega \tag{15}$$

where Ω^e = domain of the finite element. Several computational simplifications result in using a diagonal mass matrix, and in the following, a "lumped" mass matrix is used throughout. For the two-dimensional (three-dimensional) four (eight) node bilinear isoparametric element

$$(M_{ab}^{AB})^{SS} = \delta^{AB}\delta_{ab}\int_{\Omega^e} \rho\, N^A\, d\Omega \quad \text{(no sum on } A\text{)} \tag{16}$$

and

Downloaded 02 May 2010 to 171.66.16.250. Redistribution subject to ASME license or copyright; see http://www.asme.org/terms/Terms_Use.cfm

$$(M^{AB})^{\theta\theta} = \delta^{AB} \int_{\Omega^e} \rho\, c\, t_2\, N'^A\, d\Omega \quad \text{(no sum on } A\text{)} \tag{17}$$

Lumping schemes for other elements may be found in [13].

Symbollically, the discretized equations of motion of equation (7) can be written as

$$\mathbf{M}\,\mathbf{a} + \mathbf{C}\,\mathbf{v} + \mathbf{K}\,\mathbf{d} = \mathbf{F}^{\text{ext}} \tag{18}$$

where $\mathbf{M}$, $\mathbf{C}$, and $\mathbf{K}$ represent the (generalized) mass, damping, and stiffness matrices, respectively; $\mathbf{a}$, $\mathbf{v}$, $\mathbf{d}$, and $\mathbf{F}^{\text{ext}}$ represent the (generalized) acceleration, velocity, displacement, and external force vectors, respectively. Thus, $\mathbf{v} = \dot{\mathbf{d}}$ and $\mathbf{a} = \dot{\mathbf{v}} = \ddot{\mathbf{d}}$. Note that the global damping and stiffness matrices are nonsymmetric. The initial value problem consists of finding the function $\mathbf{d} = \mathbf{d}(t)$ satisfying equation (18) and the initial conditions $\mathbf{d}(0) = \mathbf{d}_0$, $\dot{\mathbf{d}}(0) = \mathbf{v}_0$ where $\mathbf{d}_0$ and $\mathbf{v}_0$ are given vectors of initial data.

Time Integration

Time integration is performed by using the implicit-explicit algorithm of Hughes et al. [11, 12], which consists of satisfying the following equations

$$\mathbf{M}\,\mathbf{a}_{n+1} + \mathbf{C}^I\mathbf{v}_{n+1} + C^E\tilde{\mathbf{v}}_{n+1} + \mathbf{K}^I\mathbf{d}_{n+1} + \mathbf{K}^E\tilde{\mathbf{d}}_{n+1} = \mathbf{F}^{\text{ext}}_{n+1} \tag{19}$$

$$\begin{aligned} \mathbf{d}_{n+1} &= \tilde{\mathbf{d}}_{n+1} + \gamma\Delta t^2\mathbf{a}_{n+1} \\ \mathbf{v}_{n+1} &= \tilde{\mathbf{v}}_{n+1} + \alpha\Delta t\,\mathbf{a}_{n+1} \end{aligned} \tag{20}$$

where

$$\begin{aligned} \tilde{\mathbf{d}}_{n+1} &= \mathbf{d}_n + \Delta t\mathbf{v}_n + (1-2\gamma)\frac{\Delta t^2}{2}\mathbf{a}_n \\ \tilde{\mathbf{v}}_{n+1} &= \mathbf{v}_n + (1-\alpha)\,\Delta t\,\mathbf{a}_n \end{aligned} \tag{21}$$

and the superscript I and E refer to the implicit and explicit groups, respectively. The notation is as follows: Δt is the time step; $\mathbf{F}^{\text{ext}}_n = \mathbf{F}^{\text{ext}}(t_n)$; $\mathbf{d}_n$, $\mathbf{v}_n$, and $\mathbf{a}_n$ are the approximations to $\mathbf{d}(t_n)$, $\mathbf{v}(t_n)$, and $\mathbf{a}(t_n)$; α and γ are parameters that control the accurcy and stability of the method [10, 16]. By appropriate choice of the values of the parameters α and γ, various well-known integration methods are obtained as summarized in Table 1. The quantities $\tilde{\mathbf{d}}_{n+1}$ and $\tilde{\mathbf{v}}_{n+1}$ are referred to as "predictor" values, and $\mathbf{d}_{n+1}$ and $\mathbf{v}_{n+1}$ are referred to as "corrector" values [11, 12]. It may be recognized that equations (20) and (21) correspond to the Newmark formulas [16].

Calculations commence with the given initial data (i.e., $\mathbf{d}_0$ and $\mathbf{v}_0$) and $\mathbf{a}_0$ which is defined by

$$\mathbf{M}\,\mathbf{a}_0 = \mathbf{F}^{\text{ext}}_0 - \mathbf{C}\,\mathbf{v}_0 - \mathbf{K}\,\mathbf{d}_0 \tag{22}$$

Since $\mathbf{M}$ is diagonal, the solution to equation (22) is rendered trivial.

Implementation. At each time step, equations (19)–(21), constitute an algebraic problem. The most useful and versatile implementation is to form an "effective static problem" from equations (19)–(21) in terms of the unknown $\mathbf{a}_{n+1}$. Within each time step the calculations are performed as summarized in Table 2. As long as Δt is kept constant, it is only necesary to form and factorize $\mathbf{M}^*$ once. Each time Δt is changed, step 1 must be repeated. Note that in the implicit group, $\mathbf{M}^*$ is always nonsymmetric. However, $\mathbf{M}^*$ still possesses the usual "band-profile" structure associated with the connectivity of the finite element mesh, and has a symmetric profile. A Crout elimination algorithm [23] is used in step 3 which fully exploits that structure in that zeroes outside the profile are neither stored nor operated on.

Stability Conditions. Stability analysis of the algorithm for symmetric operators have been reported in [11]. As mentioned previously, the damping and stiffness matrix (equation (7)), are always nonsymmetric, and the stability conditions reported in [11] therefore do not strictly apply to the problem at hand. However, extensive numerical testing has shown that these stability conditions have always resulted in stable calculations in our uses.

Numerical Examples

In the following, a number of examples are presented that demonstrate the versatility and accuracy of the model. Equations (7)–(17) have been incorporated into the computer code DYNA-FLOW [21] and implemented for both two and three-dimensional applications. In the calculations reported herein, the four-node (plane-strain) bilinear isoparametric element (see e.g., reference [2] for detailed description) was used with the standard integration scheme (see e.g., references [2, 13, 25]).

1. Half-Space Subject to Surface Heating. The problem geometry is depicted in Fig. 1(*a*). A half space ($x > 0$) is subjected to surface heating on its traction-free boundary $x = 0$, by sudden exposure to a temperature θ_0 at time $t = 0^+$, which remains constant thereafter (i.e., step surface heating).

The problem is essentially one-dimensional and has been solved analytically [5, 22] within the context of classical uncoupled thermoelasticity (i.e., $t_0 = t_1 = t_2 = 0$ and $T_0 = 0$ in equation 6). Analytical [4] and numerical [17] solutions to this problem have also been reported for a classical coupled thermoelastic model (i.e., $t_0 = t_1 = t_2 = 0$ and $T_0 \neq 0$ in equation 6). The solution is conveniently interpreted in terms of the following dimensionless variables:

$$\bar{x} = \frac{x}{a} \quad \bar{\theta} = \frac{\theta}{\theta_0} \quad \tau = \frac{k}{\rho c}\frac{t}{a^2} \quad \bar{\sigma} = \frac{\sigma}{\beta\,\theta_0} \quad \bar{u} = \frac{(\lambda+2\mu)\,u}{a\,\beta\,\theta_0}$$

where $\sigma = \sigma_x$ = axial stress; $u = u_x$ = axial displacement;

$$a = \frac{1}{c_s}\frac{k}{\rho c}$$

and

$$c_s = \sqrt{\frac{\lambda+2\mu}{\rho}}$$

is the elastic stress wave speed, and λ and μ = Lamé's constant. As proposed in [4] the thermomechanical coupling is conveniently interpreted in terms of the following parameter δ,

$$\delta = \frac{\beta^2\, T_0}{\rho c(\lambda+2\mu)}$$

Table 1

Integration Method	α	γ
Central Difference	1/2	0
Linear Acceleration	1/2	1/6
Trapezoidal	1/2	1/4
Backward Difference	3/2	1

Table 2 Flowchart

1. Form Effective Mass: (reform and factorize only if required)

$$\mathbf{M}^* = \mathbf{M} + \gamma\Delta t\mathbf{C}^I + \gamma\Delta t^2\mathbf{K}^I$$

2. Form Residual Force:

$$\mathbf{F}^*_{n+1} = \mathbf{F}^{\text{ext}}_{n+1} - \mathbf{C}^I\tilde{\mathbf{v}}_{n+1} - \mathbf{C}^E\tilde{\mathbf{v}}_{n+1} - \mathbf{K}^I\tilde{\mathbf{d}}_{n+1} - \mathbf{K}^E\tilde{\mathbf{d}}_{n+1}$$

3. Solution Phase:

$$\mathbf{M}^*\mathbf{a}_{n+1} = \mathbf{F}^*_{n+1}$$

4. Corrector Phase:

$$\begin{aligned} \mathbf{d}_{n+1} &= \tilde{\mathbf{d}}_{n+1} + \gamma\,\Delta t^2\,\mathbf{a}_{n+1} \\ \mathbf{v}_{n+1} &= \tilde{\mathbf{v}}_{n+1} + \alpha\,\Delta t\,\mathbf{a}_{n+1} \end{aligned}$$

Downloaded 02 May 2010 to 171.66.16.250. Redistribution subject to ASME license or copyright; see http://www.asme.org/terms/Terms_Use.cfm

For $\delta=0$, the problem is uncoupled. In that case, the temperature wave speed may be computed as

$$c_\theta=\sqrt{\frac{k}{\rho c\, t_2}}$$

Figure 1(*b*) shows the finite element representation of the problem geometry. The half space is modeled by a row of two-dimensional finite elements constrained to undergo axial displacements only. The mesh consists of two groups of elements. Group *I*, $0\le\bar{x}\le3.$, consists of 75 equally spaced elements, and group *II*, $3.\le\bar{x}\le20.$, consists of 20 equally spaced elements. The total length of the mesh was selected such that within the time window of interest, negligible temperature changes would take place at the end of the bar to insure proper simulation of an infinite domain. For the case of the classical thermoelastic model, $c_\theta=\infty$, both group *I* and group *II* were treated *implicitly*. For the case of Green and Lindsay's thermoelastic model, c_θ is finite and group *I* was treated *explicitly*. All calculations reported hereafter were performed with $\alpha=0.65$ and $\gamma=0.33$. The material properties were selected as follows:

$$\beta=3.34\times10^4\ \text{kg/°K/cm/sec}^2$$
$$\lambda+2\mu=1.99\times10^9\ \text{kg/cm/sec}^2$$
$$\rho=7.82\times10^{-3}\ \text{kg/cm}^3$$
$$c=4.61\times10^6\ \text{cm}^2/\text{°K/sec}^2$$
$$k=1.70\times10^3\ \text{kg}\times\text{cm/°K/sec}^3$$

to correspond to stainless steel. Experimental values for the two relaxation times of Green and Lindsay's model are not available. However, an estimate for the value of the second relaxation time t_2, can be obtained by restricting the propagation velocity of thermal disturbances c_θ to be less than or equal to the speed of sound c_s (see e.g. [1]), from which

$$t_2\approx\frac{K}{c_s^2}$$

where $K=k/\rho c=$ diffusivity. Hence, for stainless steel, t_2 is approximately 0.18×10^{-12} sec. Based on thermodynamical arguments, Green [9] showed that the first relaxation time t_1 is restricted by

$$t_1\ge t_2\ge0$$

and in the following, $t_1=t_2$.

Figure 2 shows the dimensionless temperature (Fig. 2(*a*)), axial displacement (Fig. 2(*b*)), and axial stress (Fig. 2(*c*)) time histories recorded at $\bar{x}=1.0$ ($\bar{x}=1.0$ is the location of the elastic wave front at the dimensionless time $\tau=1.0$) for the case of a classical thermoelastic model. The uncoupled results presented in Fig. 2 show good agreement with the analytical solution [22]. The slight smearing of the wave fronts is due to the introduction of artificial numerical damping ($\alpha>0.5$). The use of artificial numerical damping was required to damp out the stress oscillations (Fig. 2(*c*)) which take place after the passage of the elastic stress wave. These oscillations do not represent a physical phenomenon and could, in principle, be eliminated by using a finer special zoning. However, such refinements are usually limited in practice by computer time considerations, and it is better practice to resort to numerical damping to wipe out such oscillations. The coupled results presented in Fig. 2 were obtained for $\delta=1.0$ which, physically, is an unrealistically high value for the material of interest (for which $\delta\approx10^{-2}$). However, for realistic values of the coupling coefficient, the coupled results do not differ appreciably from the uncoupled results and the coupling effects have therefore been exaggerated here for illustration purposes only.

Figure 3 shows the dimensionless temperature (Fig. 3(*a*)), axial displacement (Fig. 3(*b*)), and axial stress (Fig. 3(*c*)) time histories recorded at $\bar{x}=1.0$ for the case of the Green and Lindsay's thermoelastic model. Also shown in Fig. 3 are for comparsion, the results corresponding to the classical (uncoupled) thermoelastic model. The effects of different temperature wave speeds are also illustrated in Fig. 3 where $c_\theta=c_s$ and $c_\theta=2c_s/3$. Note that the incorporation of the first and second relaxation times drastically affects the responses. The drastic differences observed between the predictions of Green and Lindsay's model and those of the classical model are due mainly to the incorporation of the first relaxation time. The results presented here clearly demonstrate that, although restricted to very short time durations, the effect of finite thermal propagation speeds is important.

2. One-Dimensional Heat Conduction. As shown in Table 1, by appropriate choice of the algorithmic parameters α and β, the integration scheme may reduce to a backward difference scheme. The high dissipative properties of the algorithm then kill all dynamic transient phenomena and allow purely diffusive solutions to be obtained "dynamically." The accuracy of the procedure is demonstrated in Fig. 4 which shows the time-dependent heating of a bar, free at one end, clamped at the other, and whose free end is heated to θ_0 at time $t=0^+$. Figure 4 shows the resulting displacement time history at the free end of the bar, for the case of a classical (uncoupled) thermoelastic model.

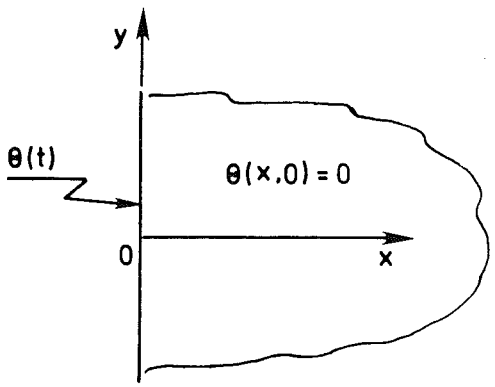


Fig. 1(*a*) Problem geometry

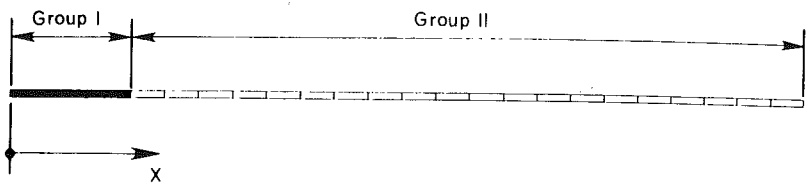


Fig. 1(*b*) Finite element mesh

Fig. 1 Half space subject to surface heating

Downloaded 02 May 2010 to 171.66.16.250. Redistribution subject to ASME license or copyright; see http://www.asme.org/terms/Terms_Use.cfm

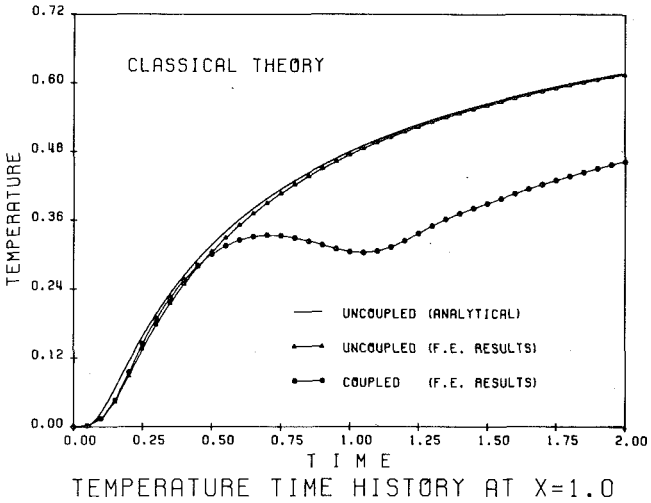


Fig. 2(*a*) Temperature time history

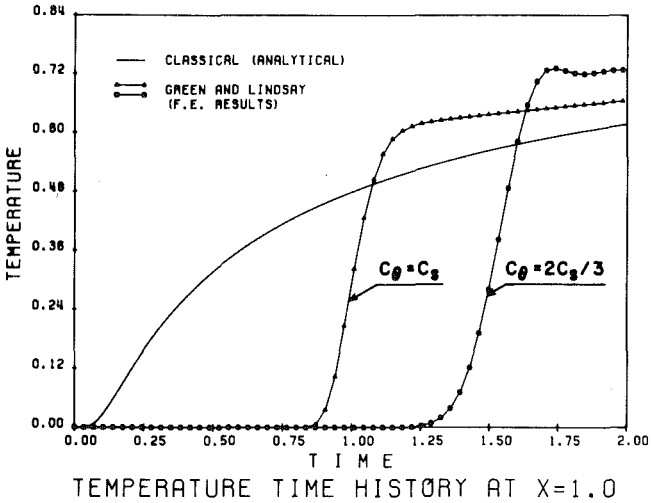


Fig. 3(*a*) Temperature time history

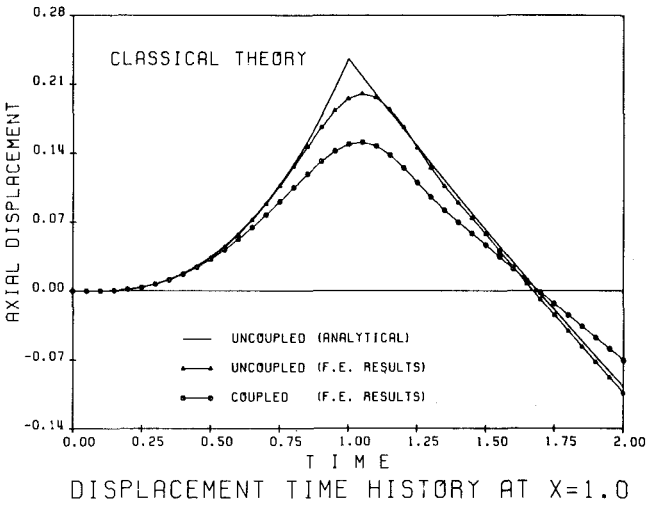


Fig. 2(*b*) Axial displacement time history

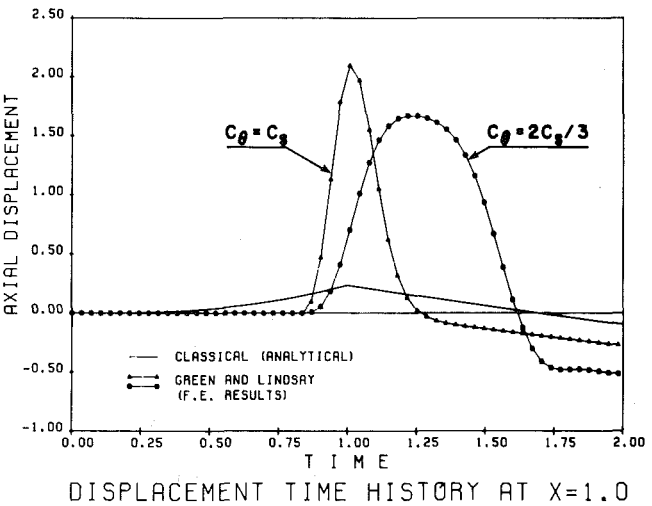


Fig. 3(*b*) Axial displacement time history

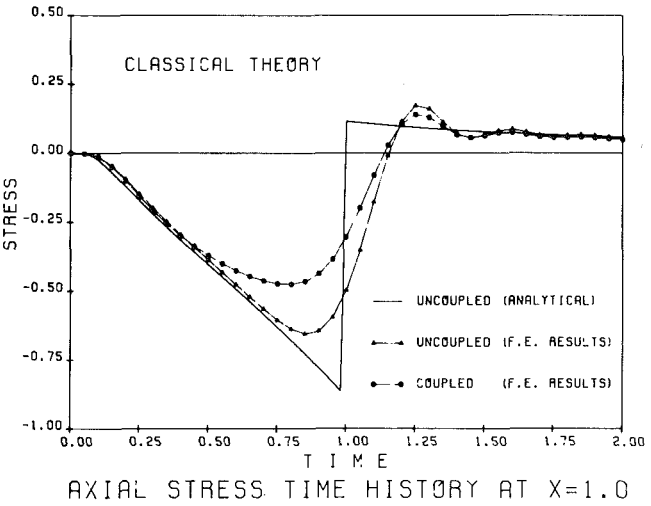


Fig. 2(*c*) Axial stress time history

Fig. 2 Components time histories at $\bar{x} = 1.0$; classical thermoelastic model

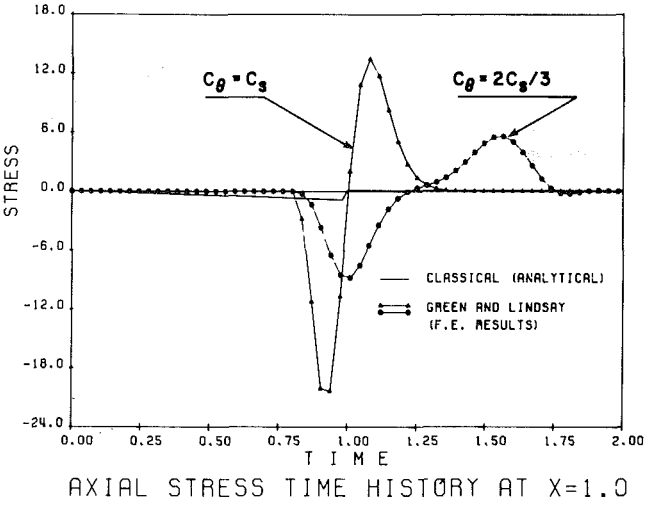


Fig. 3(*c*) Axial stress time history

Fig. 3 Components time histories at $\bar{x} = 1.0$; Green and Lindsay's thermoelastic model

Downloaded 02 May 2010 to 171.66.16.250. Redistribution subject to ASME license or copyright; see http://www.asme.org/terms/Terms_Use.cfm

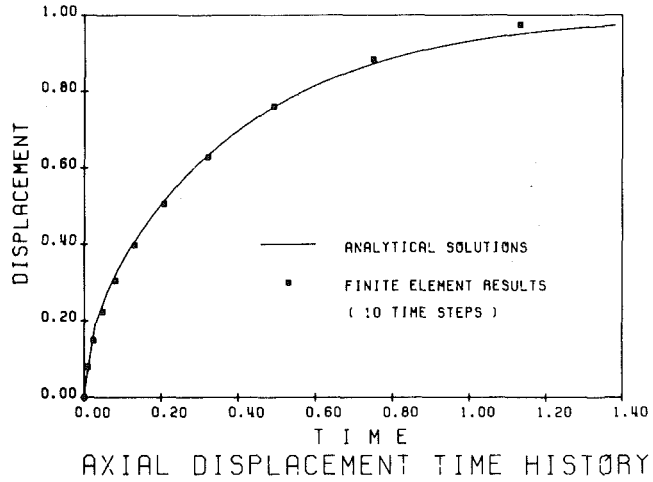


Fig. 4 One-dimensional heat conduction: displacement time history

Numerical agreement with the analytical solution for this problem is shown in Fig. 4.

Summary and Conclusions

In this paper, a general finite element model is proposed to analyze transient phenomena in thermoelastic solids. Green and Lindsay's dynamic thermoelastic equations are selected for that purpose since they reduce to the classical equations by appropriate choice of the parameters, and allow for so-called "second sound" effects. Time integration of the semidiscrete finite element equations is achieved by using an implicit-explicit scheme proposed by Hughes et al. It is shown that the algorithm can be simply and concisely implemented. The procedure allows for a convenient selection of implicit and explicit elements, and proves to be most effective and versatile in thermal and stress wave propagation analysis. Accuracy and versatility of the proposed model are demonstrated by applying it to obtain solutions to a heat surface loading problem. The results obtained with Green and Lindsay's model clearly indicate that, although restricted to very short time durations, the effect of finite thermal propagation speeds is important. Whether such effects have any physical meaning can only be determined through further experiments.

Acknowledgments

This work was supported by a grant from the Department of Energy, via the Plasma Physics Laboratory, Princeton University, Princeton, New Jersey. This support is gratefully acknowledged.

References

1 Bargmann, H., "Recent Develoments in the Field of Thermally Induced Waves and Vibrations," *Nuclear Engineering and Design*, Vol. 27, 1974, pp. 372–385.

2 Bathe, K. J., and Wilson, E. L., *Numerical Methods in Finite Element Analysis*, Prentice-Hall, Englewood Cliffs, N.J., 1976.

3 Boley, B. A., "Thermal Stresses: a Survey," in *Thermal Stresses in Severe Environments*, Hasselman, D. P. H., and Heller, R. A., eds., Plenum Press, 1980, pp. 1–11.

4 Boley, B. A., and Tolins, I. S., "Transient Coupled Thermoelastic Boundary-Value Problems in the Half-Space," ASME JOURNAL OF APPLIED MECHANICS, Vol. 29, 1962, pp. 637–646.

5 Danilovskaya, V. I., "Thermal Stresses in an Elastic Half-Space due to a Sudden Heating of its Boundary," (in Russian), *Prikladnaya Matematika i Mekhanika*, Vol. 14, 1950, pp. 316–318.

6 Danilovskaya, V. I., "On a Dynamic Problem of Thermoelasticity," (in Russian), *Prikladnaya Matematika i Mekhanika*, Vol. 16, 1952, pp. 341–344.

7 Eringen, A. C., *Mechanics of Continua*, R. E. Krieger, Huntington, N.Y. 1980.

8 Green, A. E., and Lindsay, K. E., "Thermoelasticity," *J. Elasticity*, Vol. 2, 1972, pp. 1–7.

9 Green, A. E., "A Note on Linear Thermoelasticity," *Mathematika*, Vol. 19, 1972, pp. 69–75.

10 Hilber, H. M., "Analysis and Design of Numerical Integration Methods in Structural Dynamics," Report No. EERC 76-29, Earthquake Engineering Research Center, Univ. of California, Berkeley, Calif., 1976.

11 Hughes, T. J. R., and Liu, W. K., "Implicit-Explicit Finite Element in Transient Analysis: Stability Theory," ASME JOURNAL OF APPLIED MECHANICS, Vol. 45, 1978, pp. 371–374.

12 Hughes, T. J. R., and Liu, W. K., "Implicit-Explicit Finite Element in Transient Analysis: Implementation and Numerical Examples," ASME JOURNAL OF APPLIED MECHANICS, Vol. 45, 1978, pp. 375–378.

13 Hughes, T. J. R., Liu, W. K., and Brooks, A., "Finite Element Analysis of Incompressible Viscous Flow by the Penalty Function Formulation," *Journal of Computational Physics*, Vol. 30, No. 1, 1979, pp. 1–60.

14 Ignaczak, J., "Linear Dynamic Thermoelasticity–A Survey," *The Shock and Vibration Digest*, Vol. 13, No. 9, 1981, pp. 3–8.

15 Lord, H. W., and Shulman, Y., "A Generalized Dynamical Theory of Thermoelasticity," *J. Mech. Phys. Solids*, Vol. 15, 1967, pp. 299–309.

16 Newmark, N. M., "A Method of Computation for Structural Dynamics," ASCE *Journal of the Engineering Mechanics Division*, Vol. 85, No. EM3, 1959, pp. 67–94.

17 Nickell, R. E., and Sackman, J. L., "Approximate Solutions in Linear Coupled Thermoelasticity," ASME JOURNAL OF APPLIED MECHANICS, Vol. 35, 1968, pp. 255–266.

18 Nowacki, W., "A Dynamic Problem of Thermoelasticity," *Arch. Mech.*, Vol. 9, 1957, p. 3.

19 Oden, J. T., and Reddy, J. N., *An Introduction to the Mathematical Theory of Finite Elements*, Wiley, New York, 1976, p. 429.

20 Oden, J. T., "Finite Element Analysis of Nonlinear Problems in the Dynamic Theory of Coupled Thermoelasticity," *Nuclear Engineering Design*, Vol. 10, 1969, pp. 465–475.

21 Prevost, J. H., "DYNA-FLOW: A Nonlinear Transient Finite Element Analysis Program," Department of Civil Engineering, Princeton Univesity, Princeton, N.J., 1981.

22 Sternberg, E., and Chakravorty, J. G., "On Inertia Effects in a Transient Thermoelastic Problem," ASME JOURNAL OF APPLIED MECHANICS, Vol. 26, 1959, pp. 503–509.

23 Taylor, R. L., "Computer Procedures for Finite Element Analysis," in *The Finite Element Method*, Zienckiewicz, O. C., ed., 3rd Ed., McGraw Hill, London, 1977, Chapter 24.

24 Ting, E. C., and Chen, H. C., "A Unified Numerical Approach for Thermal Stress Waves," *Computers and Structures*, Vol. 15, No. 2, 1982, pp. 165–175.

25 Zienckiewicz, O. C., *The Finite Element Method*, 3rd Ed., McGraw-Hill, London, 1977.

Downloaded 02 May 2010 to 171.66.16.250. Redistribution subject to ASME license or copyright; see http://www.asme.org/terms/Terms_Use.cfm

Y. Lee[1]
Research Associate,
Davey Laboratory,
Physics Department,
The Pennsylvania State University,
State College, Pa. 16801

J. F. Hamilton
Professor,
Ray W. Herrick Laboratories,
School of Mechanical Engineering,
Purdue University,
W. Lafayette, Ind. 47907
Mem. ASME

J. W. Sullivan
Associate Professor,
School of Mechanical Engineering,
Purdue University,
W. Lafayette, Ind. 47907

The Lumped Parameter Method for Elastic Impact Problems

Transverse impact problems have recently been solved by several different methods including Timoshenko's integral equation method, the energy method, and the finite element method. This paper presents a lumped parameter method (LMP) for impact analysis, which is attractive for the solutions of impact of complex bodies. The advantages are in its simplification of mathematical formulation, computational efficiency, and improved understanding of the coupling effect of excited modes on the occurrence of multiple impacts. Experimentally obtained information of the dynamic characteristics of these impacting bodies permit easy extension to nonsimple body shapes.

1 Introduction

Classical elastic impact theories may be separated into two types: (1) Saint-Venant's theory [1] and (2) Hertz's theory [2]. Saint-Venant's theory neglects the local deformation, and is therefore seldom useful in local point contact analysis. Hertz's theory neglects the effect of elastic vibration to consider only local deformation and is therefore only accurate for the impact of very compact bodies.

In the more general case of localized impact problems of extended bodies, i.e., rods, beams, and plates, vibrations of the impacting bodies are excited during the impact and interact with the local deformation. Timoshenko [3] proposed a combined method by combining the local deformation using the Hertz's contact law and the vibrational effects using the Euler beam theory for the case of the central impact of a sphere on a beam. The resulting equation of motion for impact force was a nonlinear integral equation which he solved by stepwise numerical integration.

Due to the tedious work of formulating and solving the integral equation, there have been several attempts to simplify the integral equation for the impact force. These methods mainly consist of Lennertz's simplification [4], the Galerkin method and the Collocation method by Eringen [5], and the energy method [6, 7, 13]. These methods are based on an assumed contact force function which is evaluated as an approximation of the real contact force function. In many cases, the impact force can have irregular multiple peaks making it very difficult to select an appropriate force function.

For these reasons classical impact problems have been generally restricted to simplified cases of balls, beams, and plates. More generally, impact occurs between components of complex geometries. Impact analysis of general-shaped mechanical bodies has usually been avoided due to the complexities of the bodies themselves. This paper presents a lumped parameter method (LPM) for impact analysis which is effective in the solution of multiple impacts as well as impact between complex bodies.

The equivalent lumped parameter model will only predict the dynamic response at the contact point, i.e., impact force and motion; however, only the drive-point mobility information is necessary for the lumped parameter model definition. Many times it is difficult to measure the transfer mobility at the required number of points using a spacing sufficient for accurate modal evaluation. If the drive-point mobility is determined analytically rather than experimentally, then either method is generally acceptable as in Part 2 of this paper. The distinct advantage of the presented method occurs when experimental evaluation of the drive-point mobility is utilized.

In this paper, several impact problems, including beams and plates, are solved to present the lumped parameter method and are compared with existing solutions for establishing the accuracy of the method. The drive-point mobility will be evaluated analytically for the simple shapes of the colliding bodies. A later paper will treat the use of experimentally determined mobilities.

[1] From a thesis submitted in partial fulfillment of the requirements for the degree of Doctor of Philosophy in the Faculty of Mechanical Engineering, Purdue University, W. Lafayette, Ind., 1982.

Contributed by the Applied Mechanics Division and presented at the Winter Annual Meeting, Boston, Mass., November 13-18, 1983 of THE AMERICAN SOCIETY OF MECHANICAL ENGINEERS.

Discussion on this paper should be addressed to the Editorial Department, ASME, United Engineering Center, 345 East 47th Street, New York, N. Y. 10017, and will be accepted until two months after final publication of the paper itself in the JOURNAL OF APPLIED MECHANICS. Manuscript received by ASME Applied Mechanics Division September, 1982, final revision, February, 1983. Paper No. 83-WA/APM-10.

Copies will be available until July, 1984.

Copyright © 1983 by ASME
Downloaded 02 May 2010 to 171.66.16.250. Redistribution subject to ASME license or copyright; see http://www.asme.org/terms/Terms_Use.cfm

2 Formulation of Drive-Point Mobility

The analytical development of the drive-point mobility for a simple shape-simple boundary condition body is based on a modal expansion description of the response of the body to a harmonic force applied at a single point. Linear vibrational Euler's theory is assumed [8].

The following expressions for the drive-point mobilities at the center point of related continuous bodies were derived from natural frequencies and mode shapes taken from reference [9].

(*a*) Simply supported beam:

$$Y_{11} = \sum_{m=1,3,5,\ldots}^{\infty} \frac{i2\omega}{\rho AL(\omega_m{}^2 - \omega^2)}. \tag{1}$$

(*b*) Simply supported rectangular plate:

$$Y_{11} = \frac{4\pi\omega}{\rho hab} \sum_{m=1}^{\infty} \sum_{n=1}^{\infty} \frac{i}{(\omega_{mn}{}^2 - \omega^2)} \quad n,m = 1,3,5,\ldots \tag{2}$$

(*c*) Clamped circular plate:

$$Y_{11} = i\omega \sum_{m=0}^{\infty} \frac{\left[J_0(0) - \dfrac{J_0(\lambda_m a)}{I_0(\lambda_m a)} I_0(0)\right]^2}{M_{m0}[\omega_{m0}{}^2 - \omega^2]}, \tag{3}$$

where

$$M_{m0} = 2\pi \int_0^{a_c} \left[J_0(\lambda_m r) - \frac{J_0(\lambda_m a)}{I_0(\lambda_m a)} I_0(\lambda_m r)\right] r dr \tag{4}$$

where:

a, b = length, width of rectangular plate
r = radial position from center of clamped circular plate
a_c = outside radius of clamped circular plate
h = thickness of plate
L = length of beam
A = cross section of beam
ρ = density of material
J_0 = zero-order Bessel function
I_0 = modified zero-order Bessel function
Y_{11} = drive-point mobility
ω = angular frequency
ω_{mn}, ω_{m0} = angular resonance frequency
λ_m = mth root of circular plate characteristic equation

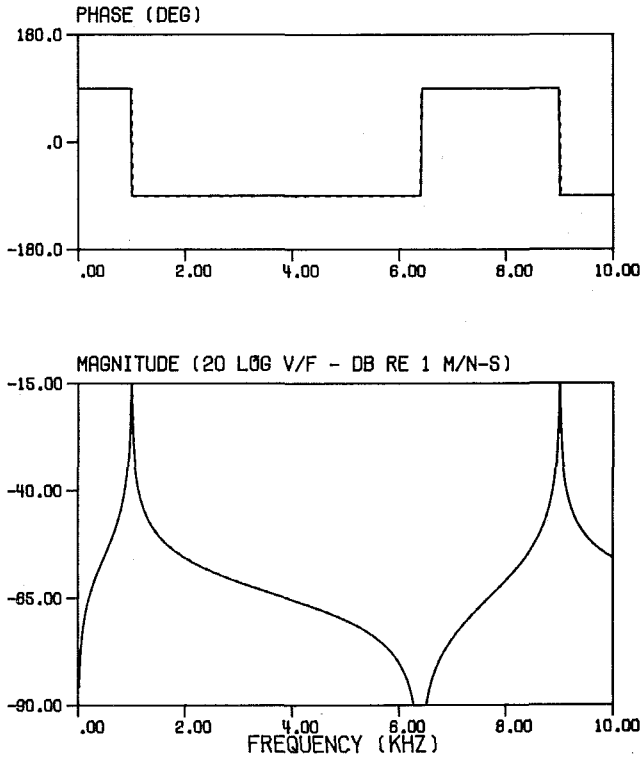


Fig. 1 The drive-point mobility of an s-s beam ($1^{cm} \times 1^{cm} \times 15.34^{cm}$) at the center point

The natural frequencies and mode shapes in the preceding mobility expressions are from reference [9].

3 Lumped Parameter Models

Based on a direct analogy between electrical systems and mechanical systems, the electric network synthesis method of a passive system [10] is capable of converting a drive-point mobility into an one-dimensional lumped parameter model which represents the same drive-point characteristics as the original body. Its application to modeling an elastic impact body is illustrated in the following example.

Consider the resulting drive-point mobility of a simply supported beam shown in Fig. 1. The mobility plot indicates that there are two resonance frequencies below 10 KHz. A lumped parameter model to match this mobility will require at least two masses and two springs. With one end of the lumped parameter model fixed, the magnitude of the drive-point mobility can be written as

$$\lfloor Y_{11} \rfloor = \cfrac{1}{\omega M_1 - \cfrac{1}{\cfrac{\omega}{k_1} - \cfrac{1}{\omega M_2 - \cfrac{1}{\cfrac{\omega}{k_2}}}}} \tag{5}$$

The magnitude of the drive-point mobility of Fig. 1 can also be represented as a ratio of two polynomial factors as

$$\lfloor Y_{11} \rfloor = \frac{c_0 \omega[\omega^2 - (2\pi 6250)^2]}{[\omega^2 - (2\pi 1000)^2][\omega^2 - (2\pi 9000)^2]}, \tag{6}$$

where $f = 1000$ and 9000 (Hz) are the resonance frequencies, and $f = 6250$ (Hz) is the antiresonance frequency in the mobility plot of Fig. 1. The weighting constant c_0 is evaluated at low frequency. Expanding equation (6) into a continued fraction form yields

$$\lfloor Y_{11} \rfloor = \cfrac{1}{0.0291\omega - \cfrac{1}{\cfrac{\omega}{4.918 \times 10^7} - \cfrac{1}{0.0335\omega - \cfrac{\omega}{2.496 \times 10^6}}}} \tag{7}$$

Comparing equations (5) and (7), the mass and spring parameter values of the model can be identified as

$$\begin{aligned} M_1 &= 0.0291\ (\text{kg}) & k_1 &= 4.918 \times 10^7\ (\text{N/m}) \\ M_2 &= 0.0335 & k_2 &= 2.496 \times 10^6. \end{aligned} \tag{8}$$

It can be seen in Fig. 1 that the drive-point mobility of this model matches exactly with the original drive-point mobility.

4 Impact Analysis

Consider two continuous bodies, A and B, colliding with

Downloaded 02 May 2010 to 171.66.16.250. Redistribution subject to ASME license or copyright; see http://www.asme.org/terms/Terms_Use.cfm

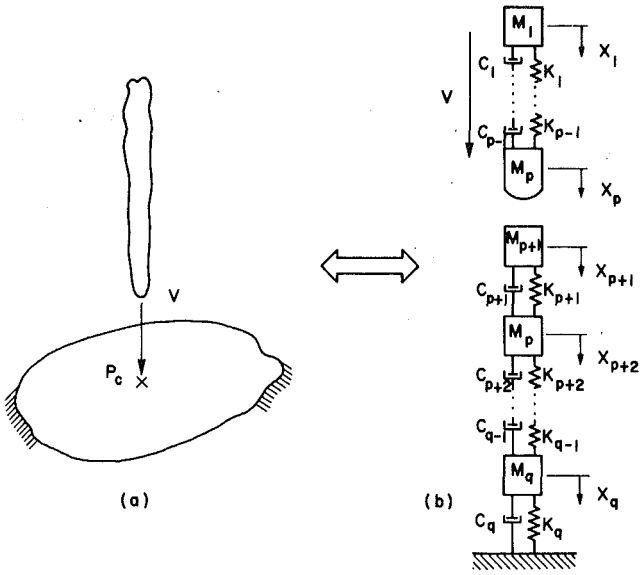


Fig. 2 Impact between two arbitrary bodies

each other as shown in Fig. 2(*a*). Body A moving with the velocity V impacts on body B at point P_c. By applying the previous modeling steps, and assuming that the drive-point mobilities of two colliding bodies at the contact point are given, a lumped parameter impact model is obtained. This model is shown in Fig. 2(*b*).

At $t=0$, the two lumped parameter models enter into collision. By the force balance, the equation of motion during impact can be written in matrix form as

$$[M]\{\ddot{x}\}+[C]\{\dot{x}\}+[K]\{x\}=\{F\}, \tag{9}$$

where

$$\{F\}=\begin{Bmatrix}0\\0\\\vdots\\-F(x_p-x_{p+1})\\F(x_p-x_{p+1})\\\vdots\\0\\0\end{Bmatrix}. \tag{10}$$

Here:

$[M],[C],[K]$ = characteristic matrices of the LPM's
$(\ddot{x}),(\dot{x}),(x)$ = acceleration, velocity and displacement vectors of the LPM's
x_p, x_{p+1} = contact displacements of the contacting LPM's

The term $F(x_p-x_{p+1})$ indicates the functional dependence of the contact force on the relative elastic deformation, i.e., local flexibility. For a quadratic contact surface, the static Hertzian contact indentation in which $F(x_p-x_{p+1})=K_H(x_p-x_{p+1})^{1.5}$ can be used [12]. For nonquadratic contacting surfaces or if a cushioning pad is located at the point of contact, an equivalent contact model will be necessary to replace the Hertzian contact model.

The solution to equation (9) is achieved numerically as a time propagation solution. All initial conditions are zero except $X_i = V, i = 1,2, \ldots P$.

5 Criteria of Convergence

The conversion of a continuous system to the lumped parameter model is not unique because the selected degree of freedom of the lumped parameter model is related to the frequency range of interest.

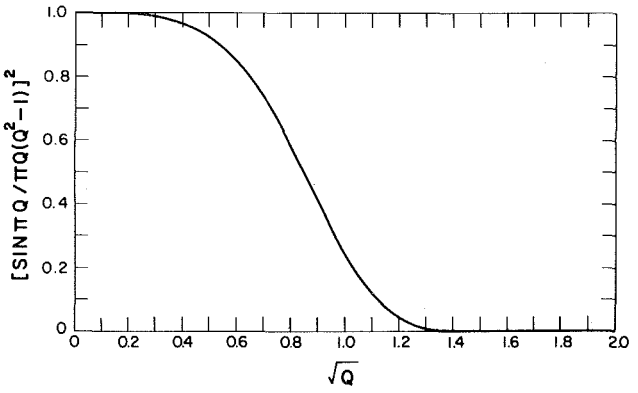


Fig. 3 Energy distribution curve

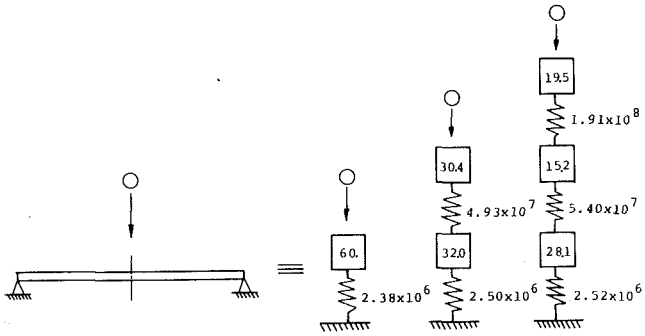


Fig. 4 Lumped parameter models of an s-s beam ($1^{cm} \times 1^{cm} \times 15.34^{cm}$) subjected to impact of a steel ball ($R = 1^{cm}$)

A criterion devised by H. Lee [7] for calculating the energy distribution between the normal modes of vibration was used to determine the required number of masses and springs for obtaining accurate impact predictions. The required quantities to calculate the energy distribution from Fig. 3 are the resonance frequencies of the impact bodies f_n and the contact times T_c. The resonance frequencies can be found from the mobility curve, which the contact time was estimated, from a simple one degree-of-freedom impact model. From the calculation of the energy distribution among normal modes, the number of modes primarily involved in impact can be determined. This number of modes is then considered as the minimum degree of freedom of the model to be used in the force prediction.

6 Numerical Examples

To gain insight into the accuracy of the lumped parameter method for the prediction of impact force, several impact problems for beams and plates were solved and compared with existing solutions from other methods.

(*A*) Simply Supported Beam. The dimensions and material properties of this example are from Timoshenko's paper [3]. Making use of equation (1) to model the beam yields the three different lumped parameter models shown in Fig. 5, which are associated with three different frequency ranges of interest. To examine the model for convergence, the simple impact model of Fig. 4(*a*) is used to predict the contact time T_c = 145 (μs). Applying this value, and the resonance frequencies of the beam to Fig. 3, results in the proportion of the energy distribution among modes ΔE_i; ΔE_2; ΔE_3; . . . = 0.956; 0.012; 0.0; . . . . This distribution indicates that only the first two odd modes of the beam affect the impact, and means that a two degree-of-freedom lumped parameter model (two LPM) is required to obtain convergence.

Downloaded 02 May 2010 to 171.66.16.250. Redistribution subject to ASME license or copyright; see http://www.asme.org/terms/Terms_Use.cfm

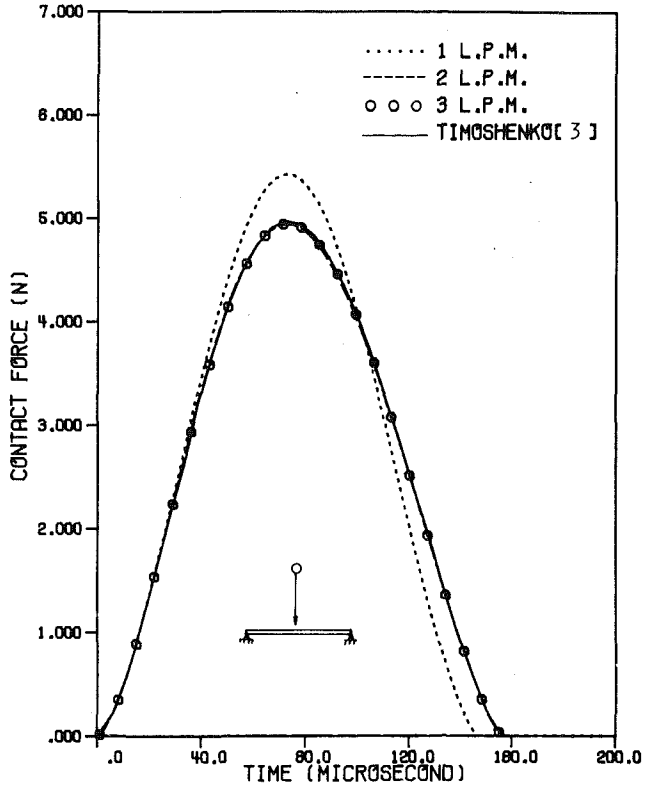


Fig. 5 Comparison of contact force history using the Timoshenko's solution and the LPM with $V = 1$ cm/s

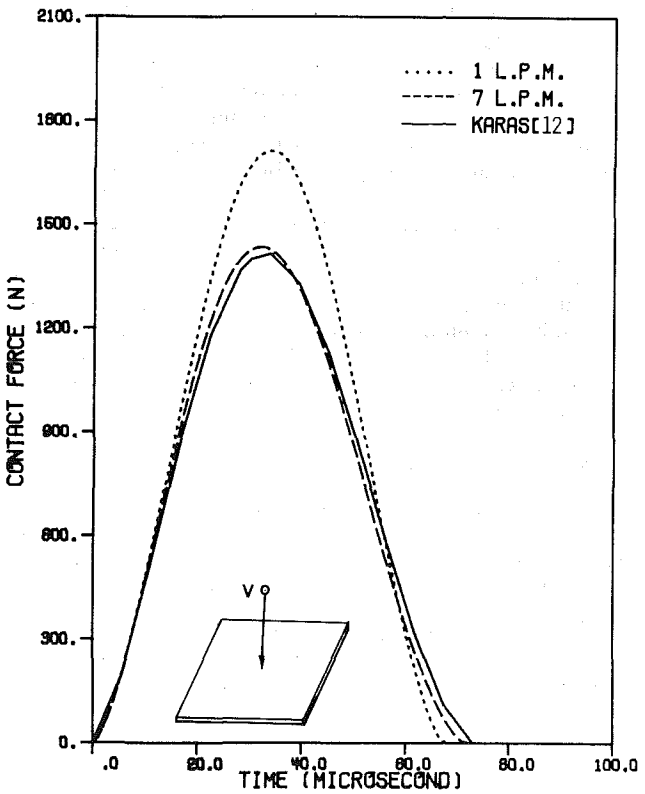


Fig. 6 Comparison of contact force history using the Karas' solution and the LPM with $V = 100$ cm/s

Figure 5 shows a comparison of contact force histories. The predictions by using two LPM and three LPM match well with Timoshenko's result [3], and prove the validity of convergent test with the use of two LPM.

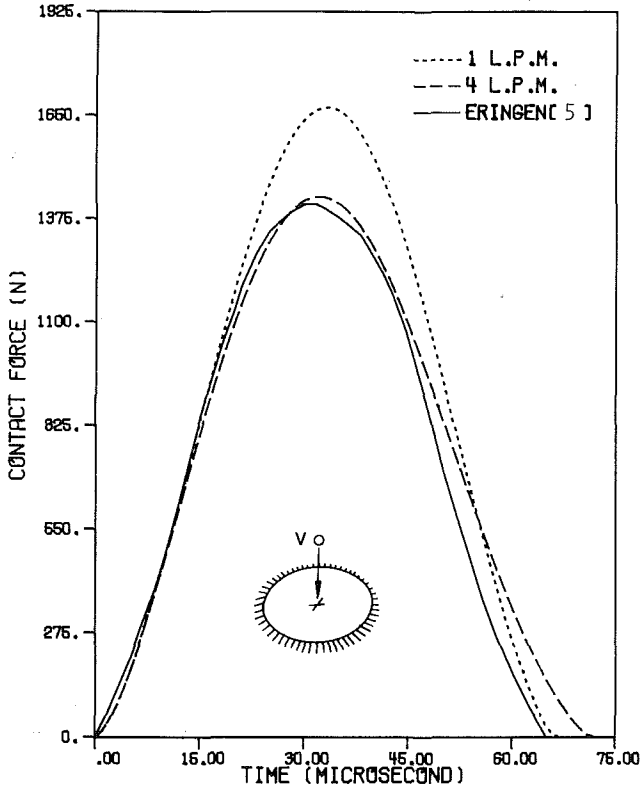


Fig. 7 Comparison of contact force history using the Eringen's solution and the LPM with $V = 100$ cm/s

(*B*) **Simply Supported Rectangular Plate.** The center impact of a simply supported rectangular plate was studied using equation (2). Following the same procedures as in the foregoing, the lumped parameter method was used to solve the problem. The solution of impact by using a nine LPM is in excellent agreement with the result by Karas [12] as shown in Fig. 6.

(*C*) **Clampled Circular Plate.** Figure 7 shows the contact force histories according to the Galerkin method by Eringen [5] and the lumped parameter method using equation (3). The prediction using four LPM is satisfactory.

(*D*) **Multiple Impact.** The previous case studies were limited to the striking mass being small in comparison with the beam or plate mass. As a result, the contact history is a single pulse. However, when the striking mass is no longer "small" it is found that the complete impact consists of a succession of separate rapid impacts. In the next example, the lumped parameter method was used to predict the occurrence of multiple impacts.

Timoshenko [3] had investigated the study of a simply supported beam subjected to impact of a heavy sphere. The same beam and sphere are taken in this example.

For multiple impact, the criterion of Fig. 3 is no longer valid because of the complexity of the contact force function. Hence a convergent test for the impact solution is necessary. Figure 8 shows the result of the convergent test by using four kinds of lumped parameter impact models compared to the results of Timoshenko [3].

The result of using one LPM exhibits two separately repeated sinusoidal-like blows. Making use of two LPM leads to an additional smaller pulse occurring right at the end of the first contact. In addition, the second contact comes earlier than the prediction of one LPM. Hence, the occurrence of the additional small pulse has resulted from the coupled effect of the second symmetric mode of the vibrating beam during the impact process. Both the predictions of four LPM and

Downloaded 02 May 2010 to 171.66.16.250. Redistribution subject to ASME license or copyright; see http://www.asme.org/terms/Terms_Use.cfm

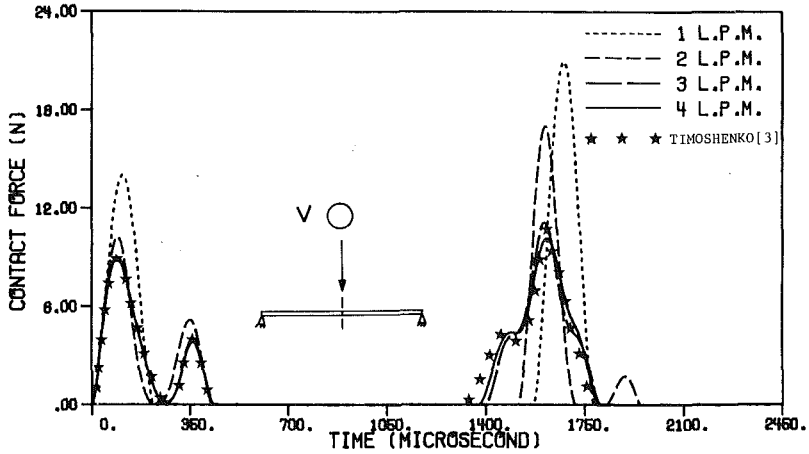


Fig. 8 A convergent test of contact force history for a heavy sphere impacting on an s-s beam

Timoshenko converge to a similar contact force function with satisfactory agreement.

7 Conclusion

From the results of the previous examples, it is argued that the lumped parameter method is an effective method for predicting the contact force of elastic colliding bodies. The advantages of this method are in its simplification of mathematical formulation, computational efficiency, and better understanding of the coupling effect of the excited modes on the occurrence of multiple impact. In addition, the impact of existing bodies of complex geometries can be described with considerable ease by this method utilizing an experimental method to find the drive-point mobilities at the contact point.

References

1 Saint-Venant, Barre de, "Theorie de Pelasticite de Corps Solide de Clebsch," Paris, 1883, note finale due paragraphe 61, pp. 490–497.

2 Hertz, H., "Uber die Beruhrung Fester Elasticher Korper," *Journal fur Mathematik*, Vol. 92, 1882a, pp. 156–171.

3 Timoshenko, S., "Zur Frage der Wirkung eines Stosses auf Einer Balken," *Zaitschrift fur Mathematik and Physik*, Vol. 62, 1913, pp.198–209.

4 Lennertz, L., "Beitrag zur Frage nach der Wirkung eines Querstosses auf einer Stab," *Ingenieur-Archiv*, Vol. 8, 1937, pp. 37–45.

5 Eringen, A. C., "Transverse Impact on Beams and Plates," ASME JOURNAL OF APPLIED MECHANICS, Vol. 72, 1950, pp. 461–468.

6 Zener, C., and Feshbach, H., "A Method of Calculating Energy Losses During Impact," ASME JOURNAL OF APPLIED MECHANICS, Vol. 61, 1939, pp. A67–A70.

7 Lee, E. H., "The Impact of a Mass Striking a Beam," ASME JOURNAL OF APPLIED MECHANICS, Vol. 62, 1940, pp. A129–A138.

8 Meirovitch, L., *Analytical Methods in Vibrations*, Macmillan, New York, 1967.

9 Soedel, Werner, *Vibrations of Shells and Plates*, Marcel Dekker, New York and Basel, 1981.

10 Guillemin, E. A., *Synthesis of Passive Network*, Wiley, New York, 1957.

11 Goldsmith, W., *Impact*, Edward Arnold, London, 1960.

12 Karas, K., "Platten unter Seitlichem Stob," *Ingenieur-Archiv*, Vol. 10, 1939, pp. 237–250.

13 Sun, C. T., and Yang, S. H., "Contact Law and Impact Responses of Laminated Composites," NASA CR 159884, Feb. 1980.

Downloaded 02 May 2010 to 171.66.16.250. Redistribution subject to ASME license or copyright; see http://www.asme.org/terms/Terms_Use.cfm

U. Tzadka
Head,
Building Construction Unit,
Practical Engineering College,
Beer Sheva, Israel

K. Schulgasser
Senior Lecturer,
Department of Mechanical Engineering,
Ben Gurion University of the Negev,
Beer Sheva, Israel
Mem. ASME

Effective Properties of Fiber-Reinforced Materials

A material consisting of a matrix in which aligned fibers of uniform circular cross section are embedded is considered. A method is developed for computing the effective axial shear modulus and transverse thermal conductivity (which are mathematically analogous) for such materials. The method, an approximate technique based on pairwise interactions, introduces a new consistency concept uniquely appropriate for this problem, and is universal in the sense that it is readily and quickly applicable to any fiber arrangement. It overcomes an apparent inconsistency in other interaction methods.

Introduction

The problem of predicting the effective thermal and elastic properties of fiber-reinforced materials (FRM) has engaged investigators for many years. Here we consider materials consisting of a matrix in which aligned fibers of uniform solid circular cross section are embedded. The present work concerns itself specifically with finding effective thermal conductivity (and axial shear modulus) transverse to the fiber direction. It is assumed that the conductivity properties of the materials constituting fiber and matrix are known and are each individually homogeneous and isotropic, and that there is perfect contact between fiber and matrix. The fibers are arranged in a known, ordered array in the cross section. Approaches used in the prediction of effective properties of this material are usually parallel to those used for materials with embedded *spherical* inclusions. Techniques for predicting *elastic* properties of both FRM's and for embedded spherical inclusions are also similar, although usually more complex by virtue of the increased complexity of the governing equations. In one instance, transverse thermal conductivity on the one hand and axial shear modulus on the other hand, the computation of effective properties is identical by virtue of the complete mathematical analogy between the two problems [1]. The language of thermal conductivity will be used here, but the translation to axial shear modulus is trivial. In fact, many of the references to both analytical and experimental works cited hereafter deal with the latter problem.

Rayleigh [2] was apparently the first to seriously consider the present problem. He investigated square and rectangular arrays of fibers. More recently numerical and approximate methods utilizing computers (finite differences, point-matching, least squares, etc.) have been employed, in each case for a single specific fiber arrangement [3-9]. Peterson and Hermans [10] were apparently the first to consider pairwise interactions. They considered the case of random parallel fibers and took into consideration the effects of all other fibers on one typical fiber. This approach was also taken by Jeffrey [11] for the case of random arrangement of spheres, following the lead of Batchelor [12] who applied this approach in considering sedimentation of suspensions. Both Peterson and Hermans and Jeffrey seek solutions only to the order of quadratic terms in c, the volume concentration of inclusions (fibers or spheres). Both must contend with the problem of convergence of the procedure, since although the influence of a far inclusion falls off rapidly, the number of such influences rises infinitely and unless care is taken the process is only conditionally convergent. Additionally, it is tacitly assumed that the effect of a "far" inclusion is the same whether or not a closer inclusion intervenes. But since solutions only to the extent of improving on the linear term in c are sought, such an approach can perhaps be justified based on the unlikelihood of "intervention" for volume fractions for which the series expansion to the quadratic term in c is applicable. McCoy and Beran [13] in considering conduction through a random suspension of spheres avoid both the convergence and intervention difficulties by considering only the inclusion closest to the typical sphere. Since they also seek effective conductivity to the quadratic order in c this seems a reasonable approach, since influence of a neighboring inclusion falls off rapidly as its distance increases, and if also the results are to be valid only for moderate volume fractions. McCoy and Beran do raise a new and crucial question in applying the pairwise interaction approach: What is the proper average temperature gradient in which the pair of inclusions is to be considered located when performing an analysis to find the approximate field inside the typical inclusion? Mal and Chatterjee [14] apply the approach of pairwise interaction to the problem of determining the three truly independent elastic constants of a FRM with fibers arranged in a hexagonal array. (That the five independent

Contributed by the Applied Mechanics Division and presented at the Winter Annual Meeting, Boston, Mass., November 13-18, 1983 of THE AMERICAN SOCIETY OF MECHANICAL ENGINEERS.

Discussion on this paper should be addressed to the Editorial Department, ASME, United Engineering Center, 345 East 47th Street, New York, N.Y. 10017, and will be accepted until two months after final publication of the paper itself in the JOURNAL OF APPLIED MECHANICS. Manuscript received by ASME Applied Mechanics Division, April, 1982; final revision, April, 1983. Paper No. 83-WA/APM-16.

Copies will be available until July, 1984.

Copyright © 1983 by ASME
Downloaded 02 May 2010 to 171.66.16.250. Redistribution subject to ASME license or copyright; see http://www.asme.org/terms/Terms_Use.cfm

elastic constants of a material with transverse isotropy can be reduced to three for a FRM was shown by Hill [15].) They consider individually the influences of all six fibers surrounding a typical fiber. That the validity of their computation at high volume fractions is questionable is due to their not considering the question raised by McCoy and Beran, and due to apparently cutting off their power series solutions for the strain fields (analogous to temperature gradient for the conductivity problem) too soon. This will be more fully discussed in the final section of this paper.

FRM's in practice usually contain relatively high volume fractions of fibers. it is worthwhile noting just what this implies about closeness of fibers. For a square array of fibers, a 50 percent volume implies a fiber separation of only one-fourth of a fiber diameter; at 60 percent the separation is only 0.14 diameters. This should imply appreciable interaction between fibers. However, in terms of overall composite properties the influence of the fibers on bulk transverse conductivity is less than one might expect. We learn this as follows: Hashin [1] sought bounds for transverse conductivity for a two-phase FRM with arbitrary transverse phase geometry, i.e., a generalized FRM in which matrix and fiber are not even necessarily distinguishable, only requiring that phase boundaries all be parallel to the longitudinal axis. The bounds he found for the effective conductivity λ^*, are

$$\lambda_1\left(1+\frac{2\beta v_2}{1-\beta v_2}\right)\leq\lambda^*\leq\lambda_2\left(1-\frac{2\beta v_1}{1+\beta v_1}\right). \tag{1}$$

Here λ_1 and λ_2 are the conductivities of the two phases, v_1 and v_2 are the respective volume fractions ($v_1 + v_2 = 1$), and

$$\beta=\frac{\lambda_2-\lambda_1}{\lambda_2+\lambda_1}. \tag{2}$$

Here we have taken $\lambda_2 > \lambda_1$. For the opposite case the bounds are reversed. Hashin was able to show that these are the best bounds determinable in the absence of any further geometric information about phase geometry by actually constructing models that realize these bounds. The lower bound is realized by a material consisting of a space completely filled by composite cylinders of varying sizes, each consisting of a core of material "2" and outer sheath of material "1." The ratio between the diameters is maintained constant such that the proper volume fractions are achieved. This model represents the case of minimum influence of the fibers (material 2) on the overall properties of the composite, and we see that it is achieved only for a material containing fibers of different diameters. (If $\lambda_1 > \lambda_2$ and the "2" material is still identified with the fibers then the upper bound, the left-hand side of equation (1), represents minimum fiber influence on overall thermal conductivity.) Both experimental and analytical experience have shown that for composites of uniform fiber size, even at fairly high volume fractions, effective transverse conductivities are not too far from those of the composite cylinder model. This apparent contradiction between expected great interaction when fibers are close and the fact that effective conductivities are yet reasonably close to those of the composite cylinder model (minimum fiber influence) is explained by the fact that the interaction between close fibers is localized to a certain extent to the region of closest approach of the fibers, and because the influence of a pair of fibers whose centers fall on a line parallel to the direction of the temperature gradient largely cancels the influence of a pair of fibers whose centers fall on a line perpendicular to the direction of the temperature gradient, as will be seen in the following section. It is precisely for these reasons that one would expect a pairwise interaction scheme, properly formulated, to be a promising approach for predicting the conductivities of FRM's with high fiber content. These underlying reasons for the validity will become apparent in the next section. Additionally, it will be seen that mutual interaction between fibers falls off rapidly as separation increases.

In the present work a pairwise interaction scheme will be presented which utilizes interactions with nearest inclusions and which shows how a proper average temperature gradient in the material surrounding the two interacting inclusions can be rationally chosen. Application of the scheme to any special case is then quite direct and simple. The method is applied to square, rectangular, and hexagonal arrays. The results are compared to previous computations and to available experimental data. In some senses our scheme is an inversion of the self-consistent (SC) approach. (See for instance Kerner [16] and Hashin [17].) There, the inclusion and part of the matrix that is taken to surround the inclusion, are considered to exist in a "sea" of material having the sought-after effective conductivity. The average temperature gradient imposed on the sample is imposed at the edges of this sea. As stated, McCoy and Beran point out that in any interaction scheme it is necessary that the temperature gradient in that portion of the matrix in which the interacting inclusions are located be so chosen that the overall temperature gradient (including inclusions) is the average gradient imposed on the sample. For a single inclusion the necessary average gradient in the surrounding material is easily calculated. For an interaction scheme it is "difficult to explicitly calculate" [13] this average gradient, to understate the situation. In fact McCoy and Beran leave the average gradient in the surrounding material undetermined and show that for certain inclusion arrangements its exact determination is not necessary *for a c^2 approximation*. In the present case a c^2 approximation cannot be expected to give useful results since for the composite materials being considered here (relatively high fiber content) the overall effective conductivities may be several times higher (or lower) than those of the matrix material alone. For the two-dimensional case considered in the present investigation we show that a direct calculation of the proper average gradient in the surrounding material can be avoided by appealing to a certain phase interchange theorem first proposed by Keller [18] and later generalized by Mendelson [19], which enables us to choose a *consistent matrix field* for a known average gradient imposed on the sample, as opposed to the self-consistent in which a *consistent effective conductivity* is chosen for material far from the isolated inclusions on which attention is focused. The present scheme will be referred to as field consistent (FC).

Derivation of Basic Equations

We consider a material consisting of a matrix of conductivity λ_1, containing fibers each of radius a and conductivity λ_2. There are a large number of fibers, all oriented in the z direction, either in an ordered array or randomly. The $x - z$ and $y - z$ planes are taken to be planes of symmetry of the geometry (in a statistical sense for random arrays). Then the x and y directions are principal directions of conductivity transverse to the fibers. An average temperature gradient **G** is imposed on the sample. It is easily shown (see [11] for the isotropic case for instance) that

$$\frac{\lambda_\alpha^*-\lambda_1}{\lambda_2-\lambda_1}=\frac{<G_{2\alpha}>}{<G_\alpha>}\,c. \tag{3}$$

Here λ_α^* is the effective thermal conductivity in the α direction, $\alpha = x, y$; $<G_{2\alpha}>$ is the average of the α component of temperature gradient in the volume occupied by the fibers, and $<G_\alpha>$ is the average α component of the temperature gradient in a large sample of the material. Hence it is only necessary to know the *average* temperature gradient within the fibers resulting from an imposed temperature gradient

Downloaded 02 May 2010 to 171.66.16.250. Redistribution subject to ASME license or copyright; see http://www.asme.org/terms/Terms_Use.cfm

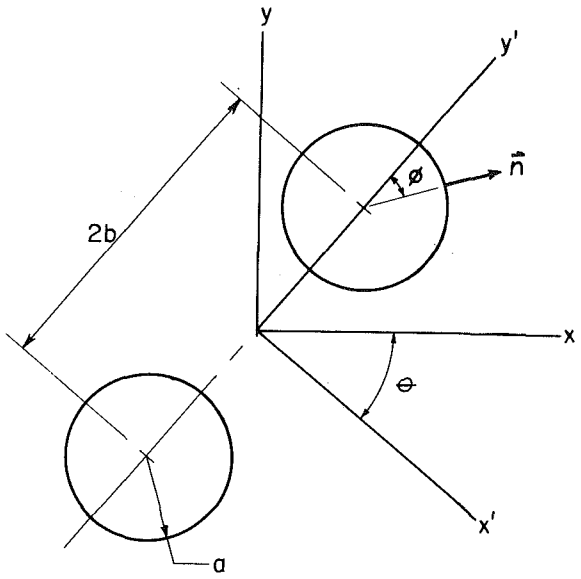


Fig. 1 Fiber pair geometry

over the whole sample in order to determine effective conductivity.

To apply the method to be proposed it is first necessary to determine the average gradient within a fiber in a matrix of infinite extent when it is influenced by only a single neighboring fiber. Consider the geometry shown in Fig. 1; $2b$ is the center-to-center fiber separation; $2a$ is the fiber diameter. Impose a temperature gradient that approaches a constant vector having only an x component H_{x0} at a great distance from the fiber pair. The average temperature gradient inside either of the fibers can be found to be (see Appendix 1)

$$\frac{<H_{2x}>}{H_{x0}} = \frac{2\lambda_1}{\lambda_1+\lambda_2} K_x(f,\beta,\theta) \tag{4}$$

where

$$K_x(f,\beta,\theta) = \frac{(f-1)^2}{f}\left(\sin^2\theta \sum_{n=1}^{\infty} \frac{n}{f^n-\beta} + \cos^2\theta \sum_{n=1}^{\infty} \frac{n}{f^n+\beta}\right) \tag{5}$$

and

$$\sqrt{f} = \frac{b}{a} + \sqrt{\left(\frac{b}{a}\right)^2 - 1}. \tag{6}$$

K_x can be written

$$K_x(\theta) = K_x(90 \text{ deg}) \sin^2\theta + K_x(0 \text{ deg}) \cos^2\theta \tag{7}$$

and we note that the average of K for all orientations is

$$\frac{1}{2\pi}\int_0^{2\pi} K_x(\theta)\, d(\theta) = \frac{1}{2}[K_x(90 \text{ deg}) + K_x(0 \text{ deg})]$$

$$= K_x(45 \text{ deg}). \tag{8}$$

It is easily seen that for large fiber separations, i.e., no mutual influence, K_x approaches 1. As the fiber separation gets smaller the rate of convergence is slower. For example to get the last considered term as small as 10^{-5} one needs 16 terms for $b/a = 1.1$, 130 terms for $b/a = 1.001$, and 1006 terms for $b/a = 1.00001$.

If a fiber is influenced independently by several other fibers the cumulative effect, under the assumption of pairwise influence, would be

$$K_x = 1 + \sum_i (K_{xi} - 1) \tag{9}$$

where K_{xi} is calculated for each of the influencing fibers. If

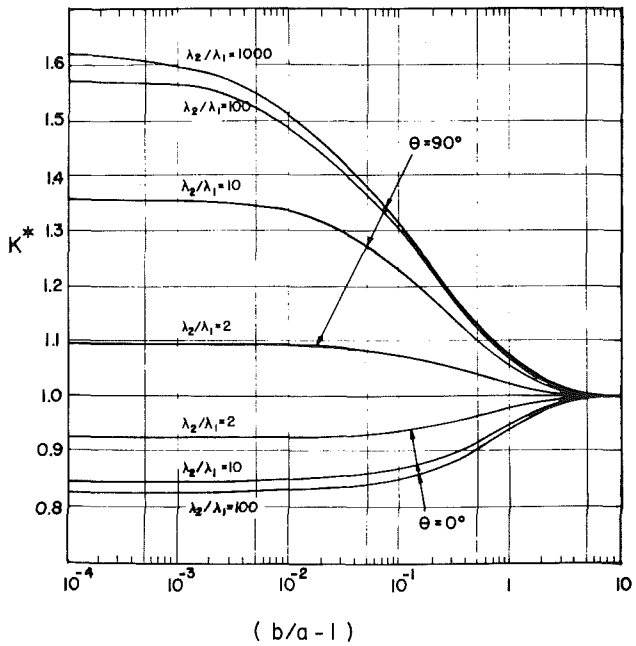


Fig. 2 Behavior of the mutual influence coefficient K_x

the average $<H_{2x}>$ is being calculated for all the fibers in a sample wherein fibers may be subjected to different neighboring geometry then K_x in equation (4) would be obtained by taking an average over a large number of fibers.

Now for low-fiber volume fractions we expect the average temperature gradient in the matrix material surrounding the fibers to be very nearly equal to the average gradient imposed on a large sample of the composite material. Thus we can write

$$\frac{<H_{2x}>}{H_{x0}} \approx \frac{<G_{2x}>}{<G_x>} \tag{10}$$

and use equation (3) directly to compute effective conductivity, obtaining

$$\lambda_x^* = \lambda_1[1 + 2c\beta K_x] \tag{11}$$

For complete noninfluence of the fibers on each other, i.e., well-separated fibers, $K_x = 1$ and

$$\lambda^* = \lambda_1[1 + 2c\beta] \tag{12}$$

which is the known dilute solution [1, 10]. It is worthwhile investigating the behavior of the factor K_x as it depends on fiber separation, the ratio of fiber to matrix conductivity, and fiber orientation. This is shown in Fig. 2. It is seen that fiber separation of 1/100 or less of fiber diameter is tantamount to fiber contact and that when the separation is more than one diameter K_x rapidly approaches 1. One can see that for the angular average of K_x ($=K_x$ (45 deg)) the influence of K_x(0 deg) and K_x(90 deg) will tend to cancel each other so that K_x(45 deg) never deviates from 1 by more than 25 percent.

From the expression for K_x we see that

$$K_x(\beta,\theta) = K_x(-\beta,\theta + 90 \text{ deg}) = K_y(-\beta,\theta) \tag{13}$$

and we note that a sign change in β implies an interchange of the conductivities of fibers and matrix. That the relationship (13) holds could have been deduced even without knowing the expression for K_x. Keller [18] and Mendelson [19] proved a phase interchange theorem, valid for any phase boundary geometry, which relates effective transverse conductivities to those for a material with identical phase boundary geometry but with phase conductivities interchanged, as follows

$$[\lambda_x^*(\lambda_1,\lambda_2)][\lambda_y^*(\lambda_2,\lambda_1)] = \lambda_1\lambda_2. \tag{14}$$

This theorem is valid only in the two-dimensional case

Downloaded 02 May 2010 to 171.66.16.250. Redistribution subject to ASME license or copyright; see http://www.asme.org/terms/Terms_Use.cfm

considered here. For three-dimensional composite materials only the inequality

$$[\lambda_x^*(\lambda_1,\lambda_2)][\lambda_y^*(\lambda_2,\lambda_1)] \geq \lambda_1\lambda_2 \tag{15}$$

holds [20]. Now requiring the relationship (14) to hold when applied to equation (11) leads to

$$\lambda_1\lambda_2[1+2c\beta K_x(\beta,\theta)][1-2c\beta K_x(-\beta,\theta+90 \text{ deg})] = \lambda_1\lambda_2 \tag{16}$$

which to first order in c (all that can be expected for the dilute case wherein the assumption of equation (10) is made) implies (13).

In handling the nondilute case we can no longer assume the identicalness of the average field imposed on the sample with the field in which the fiber group is considered to be isolated. But the relationship (14) must remain valid and we can use it to determine a consistent field to be used in computing the average temperature gradient in the fiber $<G_{2\alpha}>$ needed in equation (3). This sought-after consistent surrounding field would be expected to fall between the imposed macroscopic temperature gradient $<G_\alpha>$ and the average gradient in the matrix $<G_{1\alpha}>$. Hence we can write it as

$$H_{\alpha 0} = \gamma_\alpha <G_{1\alpha}> + (1-\gamma_\alpha)<G_\alpha> \tag{17}$$

where γ_α is some weighting factor between 0 and 1 and may depend on geometry and material properties. Now if $H_{\alpha 0}$ is the proper consistent field, $<H_{2\alpha}>$ in equation (4) can be identified with $<G_{2\alpha}>$, thus

$$<G_{2\alpha}> = \frac{2\lambda_1}{\lambda_1+\lambda_2} K_\alpha[\gamma_\alpha <G_{1\alpha}> + (1-\gamma_\alpha)<G_{2\alpha}>], \tag{18}$$

and we know how to calculate K_α for any fiber configuration. Further the average matrix gradient $<G_{1\alpha}>$ in the right-hand side can be related to the average fiber gradient through

$$<G_\alpha> = <G_{1\alpha}>(1-c) + <G_{2\alpha}>c. \tag{19}$$

Thus equation (18) becomes

$$\frac{<G_{2\alpha}>}{<G_\alpha>} = \frac{2\lambda_1}{\lambda_1+\lambda_2} K_\alpha\left(\gamma_\alpha \frac{1-\dfrac{<G_{2\alpha}>}{<G_\alpha>}c}{1-c} + (1-\gamma_\alpha)\right), \tag{20}$$

and using equation (3)

$$\frac{\lambda_\alpha^*-\lambda_1}{\lambda_2-\lambda_1} = \frac{2\lambda_1}{\lambda_1+\lambda_2} K_\alpha\left(\gamma_\alpha \frac{1-\dfrac{\lambda_\alpha-\lambda_1}{\lambda_2-\lambda_1}}{1-c} + (1-\gamma_\alpha)\right) \tag{21}$$

or

$$\lambda_\alpha^* = \lambda_1\left(1+\frac{2K_\alpha(\lambda_2-\lambda_1)(1-c+\gamma_\alpha c)c}{(\lambda_2+\lambda_1)(1-c)+2\gamma_\alpha K_\alpha\lambda_1 c}\right). \tag{22}$$

The only assumption contained in equation (22) is that a proper surrounding field $H_{\alpha 0}$ does indeed exist. To find that proper field we must find γ_α and we do this by turning to the phase interchange theorem expressed in equation (14), first using its special form (13) to find the relationship for any fiber configuration

$$K_x(\lambda_1,\lambda_2) = K_y(\lambda_2,\lambda_1). \tag{23}$$

Thus

$$\lambda_x^*(\lambda_1,\lambda_2) = \lambda_1\left(1+\frac{2K_x(\lambda_2-\lambda_1)(1-c+\gamma_x c)c}{(\lambda_2+\lambda_1)(1-c)+2\gamma_x K_x\lambda_1 c}\right) \tag{24}$$

$$\lambda_y^*(\lambda_2,\lambda_1) = \lambda_2\left(1+\frac{2K_x(\lambda_1-\lambda_2)(1-c+\gamma_y c)c}{(\lambda_2+\lambda_1)(1-c)+2\gamma_y K_x\lambda_2 c}\right). \tag{25}$$

It is easily shown that the required relationship (14), with the expressions for effective conductivities in the foregoing, is identically satisifed for

$$\gamma_x = \gamma_y = 1. \tag{26}$$

We can further show that no other pair for which both γ's are less than or equal to one can satisfy the relationship. (The easiest way is by examining $d\lambda_\alpha^*/d\gamma_\alpha$. These derivatives are positive for both $\alpha = x$ and $\alpha = y$ for $\lambda_2 > \lambda_1$ and are negative for both $\alpha = x$ and $\alpha = y$ for $\lambda_2 < \lambda_1$ for all possible values of K_x. Coupled with the fact that (26) is a solution one concludes as in the foregoing.) Then we obtain

$$\lambda_x^* = \lambda_1\left(1+\frac{2c\beta K_x}{1-c\left(1-\dfrac{2K_x\lambda_1}{\lambda_1+\lambda_2}\right)}\right). \tag{27}$$

Equation (27) can now be used to compute the effective transverse conductivity for any fiber arrangement. It is interesting to examine the preceding expression for noninteraction of fibers, i.e., $K_x = 1$. Then

$$\lambda^* = \lambda_1\left(1+\frac{2\beta c}{1-\beta c}\right). \tag{28}$$

The three-dimensional analog of (28) ($3\beta c$ instead of $2\beta c$) was found by McCoy and Beran [13] to be the effective conductivity of spheres in a matrix for the dilute case. For that case they showed by direct calculation that the required temperature gradient in the surrounding medium should be $H_{\alpha 0} = <G_{1\alpha}>$, i.e., $\gamma = 1$. For the two-dimensional case considered here we have shown this conclusions to be valid for all fiber volume fractions when using a pairwise interaction scheme. Equation (28) is also the effective conductivity for the cylinder assemblage and the Hashin lower (upper) bound when $\lambda_1 < \lambda_2$ ($\lambda_1 > \lambda_2$).

Results and Conclusions

Effective conductivity for any particular fiber configuration is now easily found from equation (27) with the

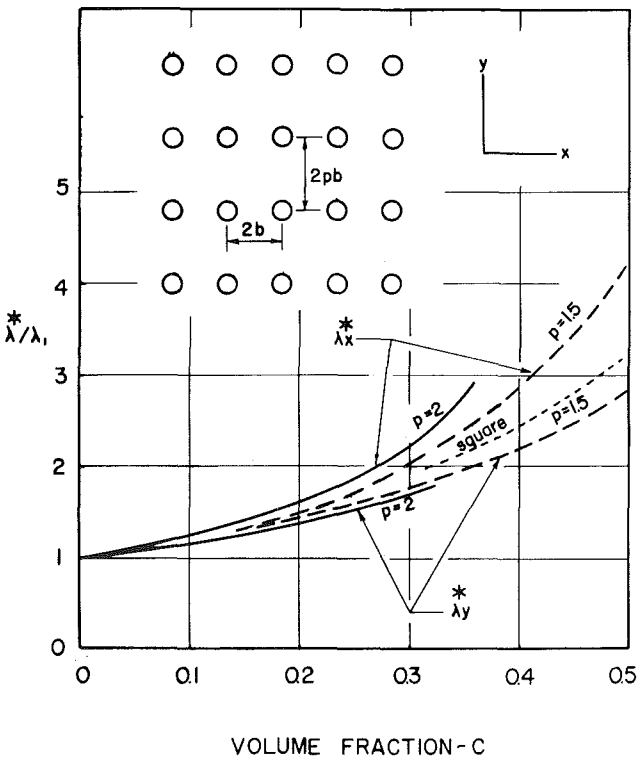


Fig. 3 Computed effective transverse conductivity for rectangular arrays of fibers. $\lambda_2/\lambda_1 = 120$.

Downloaded 02 May 2010 to 171.66.16.250. Redistribution subject to ASME license or copyright; see http://www.asme.org/terms/Terms_Use.cfm

factor K_x computed from equations (5) and (9). For square and hexagonal arrays, results for $\lambda_2/\lambda_1 = 1000$ are shown in Table 1. In computing K_x's only the contribution of K_x from the first ring of fibers around a typical fiber were taken into consideration. This was done first because of the rapid falloff of contributions to K_x with increased fiber center-to-center distance. and secondly, because computations using equation (9) would not be expected to be very reliable anyway when applied to a fiber pair if another fiber intervenes. For rectangular arrays with $\lambda_2/\lambda_1 = 1000$ results are shown in Table 2 and for $\lambda_2/\lambda_1 = 120$ in Fig. 3. When the ratio of fiber spacing p as defined in the figure is greater than $\sqrt{3}$ a "second ring" fiber in the horizontal direction from the typical fiber is closer than a "first ring" fiber in the vertical direction. Taking such a "second ring" fiber into account would probably be a correction in the right direction, but at even moderate volume fractions the fibers are so close when $p > \sqrt{3}$ that second ring corrections using equation (9) are negligibly small and their inclusion or noninclusion does not appreciably affect the results.

For the hexagonal case, the results of Pickett [8] and apparently of Ishikawa and Kobayashi [5] are below the lower bounds of Hashin in some instances and are therefore impossible. The results of Mal and Chatterjee [14] are only very slightly above the Hashin bound, e.g. about 5 percent for $\lambda_2/\lambda_1 = \infty$ and a fiber volume fraction of 0.8 which represents a fiber separation of only about one-sixteenth of a fiber diameter. This is probably due to their solution being based on a power series expansion in the parameter a/b (= fiber diameter/center-to-center fiber distance) with terms of order $(a/b)^{10}$ and higher neglected. For close packing, tenth-order terms are not negligible. Additionally, the average field in which the interacting fibers are taken is that imposed on a large material sample, an inconsistent choice.

For the square array the present results generally agree quite well with the numerical results of Keller and Sachs [6], Kobayashi and Ishikawa [7], and Heaton [4] for fiber volume fractions up to about 60 to 70 percent, although even at these volume fractions significant disparities between the numerical results reported in these sources are evident. Beyond 70 percent all numerical results diverge from each other. A more detailed comparison can be found in [21]. It is interesting that for rectangular arrays even when the fiber spacing in the x and y directions is significantly different, the effective conductivities in these two directions are reasonably close.

Han and Cosner [9] have recently performed extensive calculations of apparently high accuracy for square, hexagonal, and rectangular arrays. They used a point-matching technique. Comparison of their results with those obtained by the present technique are given in Tables 1 and 2. (The precise numerical results obtained by Han and Cosner are taken from [22]). The agreement is good even for high volume fractions. For example, in the square array the disagreement is only 6 percent and 16 percent for volume fractions of 0.7 and 0.75, respectively. For hexagonal arrays it becomes 23 percent and 27 percent for volume fractions of 0.8 and 0.85, respectively. For a rectangular array ($p = 1.732$) it becomes 8 percent and 10 percent for volume fractions of 0.3 and 0.4 (where the maximum volume fraction is 0.45). It must be kept in mind that the scheme used takes into account pairwise interactions only. At very high concentrations, such a scheme must break down. Indeed we see that in the hexagonal case at 80 and 85 percent fiber volume fraction (maximum packing ratio is 0.91) the error is not negligible. But for arrangements where the maximum packing ratio is lower (0.79 for a square array, 0.45 for the rectangular array) the accuracy remains remarkably good even close to the maximum packing ratio.

Table 1 Comparison of numerical results of effective conductivity for $\lambda_1:\lambda_2 = 1:1000$

Fiber volume fraction	Present work		Han and Cosner [9]	
	Square array	Hexagonal array	Square array	Hexagonal array
0.1	1.2229	1.2228	1.2217	1.2217
0.3	1.9017	1.8973	1.8577	1.8548
0.5	3.3534	3.3136	3.0714	2.9967
0.7	7.8476	7.4506	7.3653	5.7780
0.75	10.7573	-	12.4660	-
0.8	-	13.7545	-	9.8569
0.85	-	21.0216	-	15.4060

Table 2 Comparison of numerical results of effective conductivity for rectangular array ($p = 1.732$ as shown in Fig. 3) for $\lambda_1:\lambda_2 = 1:1000$

Fiber volume fraction	Present work		Han and Cosner [9]	
	λ_x^*	λ_y^*	λ_x^*	λ_y^*
0.1	1.2135	1.1819	1.2165	1.1841
0.2	1.51416	1.39672	1.5402	1.3752
0.3	1.95589	1.64992	2.0947	1.5770
0.4	-	1.98043	-	1.7966

Table 3 Comparison of experimental with calculated values of effective axial shear modulus for a glass epoxy compoiste. $\lambda_2 = 4.34 \times 10^6$ psi, $\lambda_1 = 0.196 \times 10^6$ psi. Data from [23].

Volume fraction	Experimental value	Present work	Composite cylinder model and lower bound
0.2	0.30	0.285	0.284
0.3	0.35	0.351	0.350
0.4	0.45	0.441	0.422
0.45	0.50	0.499	0.470
0.6	0.75	0.771	0.672
0.7	1.25	1.102	0.891

Downloaded 02 May 2010 to 171.66.16.250. Redistribution subject to ASME license or copyright; see http://www.asme.org/terms/Terms_Use.cfm

As pointed out in the Introduction real fiber-reinforced composites usually do not have a precisely ordered structure. However, often the fiber arrangement is more or less square and such is the case for the glass-epoxy composite reported on in [23]. Table 3 shows a comparison of experimental results with computations by the present method for a square array (the material properties are actually shear moduli). The agreement is quite good.

The present method can easily be applied to the case of random fiber arrangements. As a first correction to a dilute theory it is only necessary to introduce a probability distribution for the distance to the nearest neighbor of a typical fiber. Some possible distributions are suggested in [13]; the Poisson distribution is given in [24]. The usefulness of such calculations is questionable for two reasons. First, in a nondilute suspension it is hard to assess what probability distributions might reasonably be expected; second, as soon as the arrangement is not dilute it might be necessary to also consider the second nearest neighbor, the third, etc., and it is not clear when to cut off the process.

An interesting conclusion of the present work is that a consistent temperature gradient for the matrix medium in which isolated interacting inclusions are taken to interact is the average gradient in the matrix (and not the average gradient in the composite). This result is for the two-dimensional case for "diffusion-type" material constants considered here. This agrees with the conclusions of McCoy and Beran for the three-dimensional dilute case. One is lead to suspect that the conclusion might be valid (or at least better than using the composite average) for the nondilute three-dimensional case, and perhaps even that an analogous result is valid for the stress (or strain) fields in the medium surrounding inclusions when interaction schemes are applied to the three-dimensional elastic problem.

It is unfortunate that no obvious way presents itself for applying the current approach to the three-dimensional problem. This is so since, as pointed out, no equality equivalent to equation (14) exists, or can exist [20], in the three-dimensional case. But the present two-dimensional result does emphasize the importance of considering the proper average gradient to be taken surrounding an inclusion. It is hoped that other criteria, more universally applicable than (14), will be found.

We note in closing that the solution in the Appendix could apparently be used to find a self-consistent solution taking into account pairwise interactions. One need only apply equation (4) with the left-hand side given by equation (10) and K_x evaluated using λ_x^* as the matrix conductivity instead of λ_1. One would not expect reliable results since such a scheme smears out the properties *between* the typical fiber pair as well as around it, and central to the pairwise approach is that the material between close fibers is the *matrix* material. Indeed the self-consistent scheme has been carried out [21] and as expected the calculated effective conductivity consistently varies from expected results.

References

1 Hashin, Z., "Theory of Fiber Reinforced Materials," NASA Report, Contract NASI-8818, Nov. 1970.

2 Lord Rayleigh, "On the Influence of Obstacles Arranged in Rectangular Order Upon Properties of the Medium," *Philosophical Magazine*, Vol. 34, 1894, pp. 481-502.

3 Adams, D. F., and Doner, D. L., "Longitudinal Shear Loading of a Unidirectional Composite," *Journal of Composite Materials*, Vol. 1, 1967, pp. 4-17.

4 Heaton, M. D., "A Calculation of the Elastic Constants of a Unidirectional Fiber-Reinforced Composite," *British Journal of Applied Physics*, Series 2, Vol. 1, 1968, pp. 1039-1048.

5 Ishikawa, T., and Kobayashi, S., "Elastic Properties of Unidirectional Fiber-Reinforced Composites," *Composite Materials and Structures*, Vol. 3, 1974, pp. 23-31.

6 Keller, H. B., and Sachs, D., "Calculation of the Conductivity of a Medium Containing Cylindrical Inclusions," *Journal of Applied Physics*, Vol. 35, 1964, p. 537-538.

7 Kobayashi, S., and Ishikawa, T., "Elastic Properties of Unidirectional Fiber-Reinforced Composites," *Composite Materials and Structures*, Vol. 3, 1974, pp. 12-20.

8 Pickett, G., "Elastic Moduli of Fiber-Reinforced Plastic Composites," in *Fundamental Aspects of Fiber-Reinforced Composites*, Schwartz, R. T., and Schwartz, H. S., eds., Interscience, New York, 1968.

9 Han, L. S., and Cosner, A. A., "Effective Thermal Conductivity of Fibrous Composites," ASME *Journal of Heat Transfer*, Vol. 103, 1981, pp. 387-392.

10 Peterson, J. M., and Hermans, J. J., "The Dielectric Constants of Non-Conducting Suspensions," *Journal of Composite Materials*, Vol. 3, 1969, pp. 338-354.

11 Jeffrey, D. J., "Conduction Through a Random Suspension of Spheres," *Proceedings of the Royal Society London*, Series *A*, Vol. 335, 1973, pp. 355-367.

12 Batchelor, G. K., "Sedimentation in a Dilute Suspension of Spheres," *Journal of Fluid Mechanics*, Vol. 52, 1972, pp. 245-268.

13 McCoy, J. J., and Beran, M. J., "On the Effective Thermal Conductivity of a Random Suspension of Spheres," *International Journal of Engineering Science*, Vol. 14, 1976, pp. 7-18.

14 Mal, A. K., and Chatterjee, A. K., "The Elastic Moduli of a Fiber-Reinforced Composite," ASME JOURNAL OF APPLIED MECHANICS, Vol. 44, 1977, pp. 61-67.

15 Hill, R., "Theory of Mechanical Properties of Fiber-Strengthened Materials, I. Elastic Behaviour," *Journal of the Mechanics and Physics of Solids*, Vol. 12, 1964, pp. 199-212.

16 Kerner, E. H., "The Electrical Conductivity of Composite Media," *Proceedings of the Physical Society*, Vol. 69*B*, 1956, pp. 802-813.

17 Hashin, Z., "Assessment of the Self Consistent Scheme Approximation: Conductivity of Particulate Composites," *Journal of Composite Materials*, Vol. 2, 1968, pp. 284-300.

18 Keller, J. B., "A Theorem on the Conductivity of a Composite Medium," *Journal of Mathematical Physics*, Vol. 5, 1964, pp. 548-549.

19 Mendelson, K. S., "Effective Conductivity of a Two-Phase Material with Cylindrical Phase Boundaries," *Journal of Applied Physics*, Vol. 46, 1975, pp. 917-918.

20 Schulgasser, K., "On a Phase Interchange Relationship for Composite Materials," *Journal of Mathematical Physics*, Vol. 17, 1976, pp. 378-381.

21 Tzadka, U., "Approximate Calculation of the Longitudinal Shear Modulus in Composite Materials," M.Sc. Thesis (in Hebrew), Ben-Gurion Univeristy of the Negev, Beer Sheva, Israel, 1979.

22 Zimmerman, R. H., "Predicting the Transverse Conductivity of Unidirectional and Bidirectional Filamentary Composites," Interim Technical Report AFWAL-TR-80-3155, Ohio State University Research Foundation, Oct. 1980.

23 Adams, R. D., Fox, M. A. O., Friend, R. J., and Hewitt, R. L., "The Dynamic Properties of Unidirectional Carbon and Glass Fiber Reinforced Plastics in Torsion and Flexure," *Journal of Composite Materials*, Vol. 3, 1969, pp. 594-603.

24 Kendall, M. G., and Moran, P. A. P., *Geometrical Probability*, Charles Griffin, London, 1963, p. 47.

APPENDIX 1

Calculation of Average Gradient for Pairwise Interacting Fibers

The average temperature gradient inside the fiber can be written as

$$<\mathbf{H}_2> = \frac{1}{A}\int_A (-\text{grad } T)\, dA \tag{30}$$

where A is the fiber cross-sectional area and T is the temperature. Using the extended Gauss theorem, equation (30) becomes

$$<\mathbf{H}_2> = \frac{1}{A}\int_S (-T)\,\mathbf{n}\, dS \tag{31}$$

where $\mathbf{n}$ is a unit vector normal (as shown in Fig. 1), and S is the arc length along the fiber circumference. Because we are interested only in the x component, we need only the x component of the unit vector.

$$n_x = \sin(\phi + \theta). \tag{32}$$

Substituting n_x instead of $\mathbf{n}$, and using the bipolar coordinates defined by

Downloaded 02 May 2010 to 171.66.16.250. Redistribution subject to ASME license or copyright; see http://www.asme.org/terms/Terms_Use.cfm

$$x' = \frac{\sqrt{b^2 - a^2}\sin\eta}{\cosh\xi - \cos\eta} \tag{33a}$$

$$y' = \frac{\sqrt{b^2 - a^2}\sinh\xi}{\cosh\xi - \cos\eta} \tag{33b}$$

with

$$\sin\phi = \frac{\sinh\xi_0 - \sin\eta}{\cosh\xi_0 - \cos\eta} \tag{34a}$$

$$\cos\phi = \frac{\cosh\xi_0 - 1}{\cosh\xi_0 - \cos\eta} \tag{34b}$$

$$\xi_0 = \cosh^{-1}(b/a) \tag{35}$$

we find the x component of $<\mathbf{H}_2>$.

$$<H_{2x}> = \frac{\sqrt{b^2 - a^2}\sin\theta}{A}\int_\eta (-T)\frac{\cosh\xi_0\cos\eta - 1}{(\cosh\xi_0 - \cos\eta)^2}d\eta + \frac{\sqrt{b^2 - a^2}\cos\theta}{A}\int_\eta (-T)\frac{\sinh\xi_0 \sin\eta}{(\cosh\xi_0 - \cos\eta)^2}d\eta. \tag{36}$$

Using the technique of separation of variables the solution to Laplace's equation which governs the thermal conductivity can be written in bipolar coordinates. Applying the appropriate conditions at the fiber-matrix interface, i.e., continuity of temperature and of heat flux perpendicular to the interface, the solution for the temperature field inside the fibers is found to be (see [10] for instance),

$$T = -\sqrt{b^2 - a^2}H_{x0}\sin\theta - H_{x0}\sin\theta\sum_{n=1}^{\infty} B_{ny}\cos(n\eta) - H_{x0}\cos\theta\sum_{n=1}^{\infty} B_{nx}\sin(n\eta), \tag{37}$$

where

$$B_{nx} = \frac{2\sqrt{b^2 - a^2}\lambda_1}{\lambda_2\cosh(n\xi_0) + \lambda_1\sinh(n\xi_0)} \tag{38a}$$

$$B_{ny} = \frac{2\sqrt{b^2 - a^2}\lambda_1}{\lambda_1\cosh(n\xi_0) + \lambda_2\sinh(n\xi_0)}. \tag{38b}$$

Substituting equation (37) into (36) we find, after executing all the integrations and after much algebraic manipulation (see [21] for details)

$$\frac{<H_{2x}>}{H_{x0}} = \frac{2\lambda_1}{\lambda_1 + \lambda_2}K_x(f,\beta,\theta) \tag{4}$$

where

$$K_x(f,\beta,\theta) = \frac{(f-1)^2}{f}\left(\sin^2\theta\sum_{n=1}^{\infty}\frac{n}{f^n - \beta} + \cos^2\theta\sum_{n=1}^{\infty}\frac{n}{f^n + \beta}\right) \tag{5}$$

$$\beta = \frac{\lambda_2 - \lambda_1}{\lambda_2 + \lambda_1} \tag{2}$$

$$f = \frac{b}{a} + \sqrt{\left(\frac{b}{a}\right)^2 - 1}. \tag{6}$$

We note that $|\beta| < 1$. $|\beta| = 1$ would imply that the ratio of fiber to matrix conductivity is either 0 or ∞. $f \geq 1$; $f = 1$ implies that the fibers touch. It can easily be shown that the series in equation (5) are convergent for all f greater than 1 (including when $|\beta| = 1$), and further that as f approaches 1 the series approach a limit for all $|\beta| < 1$. Indeed it can be shown that

$$\lim_{f\to 1} K_x(f,\beta,\theta) = \sin^2\theta\sum_{n=1}^{\infty}\frac{(+\beta)^{n-1}}{n^2} + \cos^2\theta\sum_{n=1}^{\infty}\frac{(-\beta)^{n-1}}{n^2} \tag{39}$$

For $\beta = +1$ the first series approaches $\pi^2/6$ and the second approaches $\pi^2/12$; for $\beta = -1$ the reverse is true.

Downloaded 02 May 2010 to 171.66.16.250. Redistribution subject to ASME license or copyright; see http://www.asme.org/terms/Terms_Use.cfm

A Hybrid Finite Element Approach to Composite Laminate Elasticity Problems With Singularities

S. S. Wang
Associate Professor.
Assoc. Mem. ASME

F. G. Yuan
Graduate Assistant.

Department of Theoretical and Applied Mechanics,
University of Illinois,
Urbana, Ill. 61801

A hybrid finite element method is presented for studying composite laminate elasticity problems with singularities. The basic equations of laminate anisotropic elasticity and stress singularities in composite laminates are discussed briefly. Formulation of a singular, hybrid composite-wedge element for this class of problems is given in detail. Two numerical examples are shown to illustrate the accuracy and efficiency of the present method of approach. The first example is the well-known laminate free-edge problem, which has a rather weak stress singularity; the second one is the important composite problem, which is shown to have a strong stress singularity. Results are compared with existing analytical elasticity solutions for these problems. Excellent solution accuracy, convergence, and computational efficiency are demonstrated.

1 Introduction

Due to attractive thermal and mechanical properties, lightweight, high-strength, fiber-reinforced composite laminates have been widely used in advanced engineering structures. It is well known that stress singularities arise at geometric discontinuities such as cutouts, free edges, delaminations, and reentrant corners, which are prevalent in many laminated composite materials and structures. The problem is further complicated by the strong material anisotropy, nonhomogeneity (or property discontinuity between layers), and the almost unlimited number of combinations of lamination variables, leading to a class of singular elasticity problems which have recently attracted much attention due to their technical importance. To the authors' knowledge, only very few cases have been solved in closed form, and orders (or strengths) of stress singularity in the composites are determined explicitly [1-9]. For the composites with complicated lamination, geometric, and loading variables, laminate elasticity solutions for these problems are not available in general. Numerical methods such as finite element methods are considered most attractive due to their versatility in handling mechanics problems with a variety of complexities. Based on the recently developed laminate anisotropic elasticity theory [6-9], a singular, hybrid finite element method is introduced in this paper for studying this important class of composite mechanics problems.

In the finite element approach to singular elasticity problems, it is well recognized that the rate of solution convergence is generally independent of the order of polynomials used for interpolation functions in element formulation [10]. That is, the use of higher-order elements does not necessarily improve the rate of convergence of the numerical solution. This phenomenon has been indeed observed in many singular computational mechanics problems. For example, in a linear elastic fracture mechanics problem in which a $1/\sqrt{r}$ stress singularity is involved, using conventional (nonsingular) elements of different orders results in similarly slow rates of solution convergence and, hence, a very fine mesh with a large number of degrees of freedom is required to achieve numerical results of acceptable accuracy [11-13]. In fact, it has been shown [10] that for a singular elasticity problem, the rate of convergence of the finite element solution is governed by the order of the singularity rather than the order of the polynomial for interpolation functions. For the present composite laminate elasticity problems with various kinds of stress singularities, the convergence of finite element solutions is also anticipated to be dominated by the order of laminate stress singularity in each individual problem. Thus, to expedite the rate of solution convergence and to insure better accuracy, inclusion of proper singular terms in the formulation of improved finite elements to account for the stress singularity is essential in solving this class of problems. Among various models that incorporate local stress singularities in the recent development of finite element methods [14-20], the hybrid element approach pioneered by Pian, et al. [19] and later refined by Tong, et al. [20] is one of the most attractive methods and, therefore, is used here, because of its greater flexibility in element formulation and demonstrated solution accuracy and convergence.

In the next section, basic equations in laminate anisotropic elasticity for composite laminates with stress singularities are

Contributed by the Applied Mechanics Division and presented at the Winter Annual Meeting, Boston, Mass., November 13-18, 1983 of THE AMERICAN SOCIETY OF MECHANICAL ENGINEERS.

Discussion on this paper should be addressed to the Editorial Department, ASME, United Engineering Center, 345 East 47th Street, New York, N.Y. 10017, and will be accepted until two months after final publication of the paper itself in the JOURNAL OF APPLIED MECHANICS. Manuscript received by ASME Applied Mechanics Division, March, 1982; final revision, April, 1983. Paper No. 83-WA/APM-15.

Copies will be available until July, 1984.

Copyright © 1983 by ASME
Downloaded 02 May 2010 to 171.66.16.250. Redistribution subject to ASME license or copyright; see http://www.asme.org/terms/Terms_Use.cfm

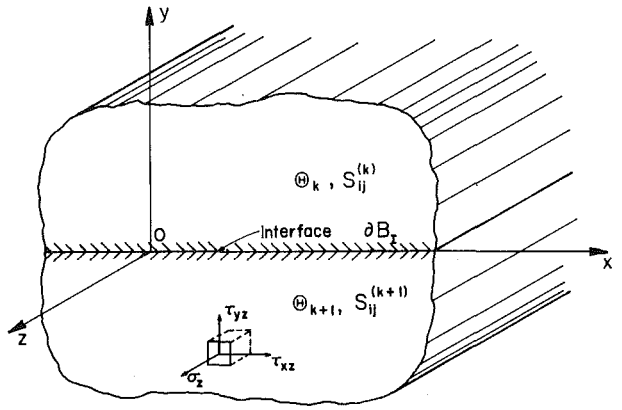


Fig. 1 Fiber composite with ply orientations Θ_k and Θ_{k+1} and material constants, $S_{ij}^{(k)}$ and $S_{ij}^{(k+1)}$. Note that Θ_k and Θ_{k+1} are angles measured counterclockwise from the positive z-axis to the fiber directions in the x-z plane.

briefly introduced. Formulation of a singular, hybrid composite-wedge finite element for this class of problems based on a modified hybrid functional is presented in Section 3. In the special hybrid element formulation, the assumed stress and displacement within the element contain the complete eigenfunction series, including both the singular and high-order terms, derived from eigenfunction expansion of Lekhnitskii's complex-variable stress potentials in the laminate elasticity solution. The interelement compatibility between the singular hybrid composite-wedge element and adjacent nonsingular elements is achieved by proper selection of interpolation functions to match element boundary displacements. Numerical examples on two very important problems in the composite laminate mechanics, i.e., the boundary-layer problem and the delamination fracture problem, are given in Section 4. Comparisons of current numerical results with recently obtained elasticity solutions are made. Solution accuracy, convergence, and computational efficiency are studied to demonstrate unique features of the present approach.

2 Basic Equations and Stress Singularities in Laminate Anisotropic Elasticity

Formulation of composite laminate elasticity problems with stress singularities has been given in detail in references [6–9] for finite-dimensional composite laminates with general lamination and geometric variables. For the convenience of later development in this paper, basic equations in laminate anisotropic elasticity are briefly introduced in this section; detailed derivation is omitted. Some of the fundamental relationships are discussed for later use in the singular hybrid finite element formulation in Section 3.

2.1 Governing Partial Differential Equations and General Solutions. Consider a composite laminate subjected to surface tractions acting in planes normal to the generator of the lateral surface, i.e., the z-axis, without variation (Fig. 1). For a composite body of finite length and finite cross section, equivalent axial force and moments acting on the ends are considered. The composite is assumed to be sufficiently long that in the region away from the ends, end effects are neglected by virtue of Saint Venant's principle. Consequently, stresses in the laminate are independent of the z-axis. The cases of finite-width composite laminates with edges, reentrant corners, and delamination cracks subjected to a uniform axial strain, $\epsilon_z = \epsilon_0$, along the z-axis have recently received much attention [6–9] in the investigation of the fundamental failure behavior in composite laminates. This class of problems may be formulated on the basis of theory of laminate anisotropic elasticity [6–9] using Lekhnitskii's complex-variable stress potentials, F and Ψ [21].

Following the procedure given in [6–9, 21], one can establish a system of coupled governing partial differential equations in F and Ψ for a composite lamina as

$$\begin{cases} L_3 F + L_2 \Psi = -2A_4 + A_1 S_{34} - A_2 S_{35}, & (1a) \\ L_4 F + L_3 \Psi = 0, & (1b) \end{cases}$$

where L_2, L_3, and L_4 are linear differential operators of the second, third, and fourth orders with constant coefficients related to lamina elastic constants S_{ij}, and A_1, A_2, A_4 are constants defined in references [6, 7, 21].

Introduce the complex variables $Z_k = x + \mu_k y$ $(k = 1,2,3)$ and $Z_{k+3} = \bar{Z}_k$, where μ_k and $\bar{\mu}_k$ with $\bar{\mu}_k = \mu_{k+3}$ are complex conjugate roots of the characteristic algebraic equation given in [21]. General expressions for the stress functions F and Ψ can be shown to have the forms

$$F = \sum_{k=1}^{6} F_k(Z_k) \quad \text{and} \quad \Psi = \sum_{k=1}^{6} \eta_k F_k'(Z_k),$$

where η_k are complex constants defined in [7, 21] and the prime $(')$ denotes differentiation of the functions F_k with respect to their arguments. Choosing the following form for the stress functions $F_k(Z_k)$:

$$F_k(Z_k) = C_k Z_k^{\delta+2}/[(\delta+1)(\delta+2)], \quad (2)$$

where C_k and δ are complex constants to be determined later, one can show that complete solutions for the stress and displacement fields have the following forms [6, 7, 9]:

$$\sigma_x = \sum_{k=1}^{3} (C_k \mu_k^2 Z_k^\delta + C_{k+3} \bar{\mu}_k^2 \bar{Z}_k^\delta) + \sigma_{ox}, \quad (3a)$$

$$\sigma_y = \sum_{k=1}^{3} (C_k Z_k^\delta + C_{k+3} \bar{Z}_k^\delta) + \sigma_{oy}, \quad (3b)$$

$$\tau_{yz} = -\sum_{k=1}^{3} (C_k \eta_k Z_k^\delta + C_{k+3} \bar{\eta}_k \bar{Z}_k^\delta) + \tau_{oyz}, \quad (3c)$$

$$\tau_{xz} = \sum_{k=1}^{3} (C_k \eta_k \mu_k Z_k^\delta + C_{k+3} \bar{\eta}_k \bar{\mu}_k \bar{Z}_k^\delta) + \tau_{oxz}, \quad (3d)$$

$$\tau_{xy} = -\sum_{k=1}^{3} (C_k \mu_k Z_k^\delta + C_{k+3} \bar{\mu}_k \bar{Z}_k^\delta) + \tau_{oxz}, \quad (3e)$$

$$u = \sum_{k=1}^{3} (C_k p_k Z_k^{\delta+1} + C_{k+3} \bar{p}_k \bar{Z}_k^{\delta+1})/(\delta+1) + u_o, \quad (3f)$$

$$v = \sum_{k=1}^{3} (C_k q_k Z_k^{\delta+1} + C_{k+3} \bar{q}_k \bar{Z}_k^{\delta+1})/(\delta+1) + v_o, \quad (3g)$$

$$w = \sum_{k=1}^{3} (C_k t_k Z_k^{\delta+1} + C_{k+3} \bar{t}_k \bar{Z}_k^{\delta+1})/(\delta+1) + w_o, \quad (3h)$$

where the first part in equations $(3a\text{–}h)$ represents homogeneous solutions for the stress and displacement; σ_{ox}, σ_{oy}, . . . τ_{oxy} and u_o, v_o, and w_o are particular solutions associated with the loading condition of each individual problem; η_k, μ_k and p_k, q_k, t_k are complex constants related to S_{ij}, and their expressions can be found in references [6, 7].

2.2 Stress Singularity at a Composite Laminate Wedge. The homogeneous solutions for stress and displacement in equations $(3a\text{–}h)$ are required to satisfy traction boundary conditions on the composite-wedge surface and continuity conditions along the ply interface as shown in Fig. 2, leading to a standard eigenvalue problem.

For the convenience of further developments, the stress and displacement components are transformed into a polar coordinate system (r,θ,z) with the complex variables Z_k having the following expressions:

Downloaded 02 May 2010 to 171.66.16.250. Redistribution subject to ASME license or copyright; see http://www.asme.org/terms/Terms_Use.cfm

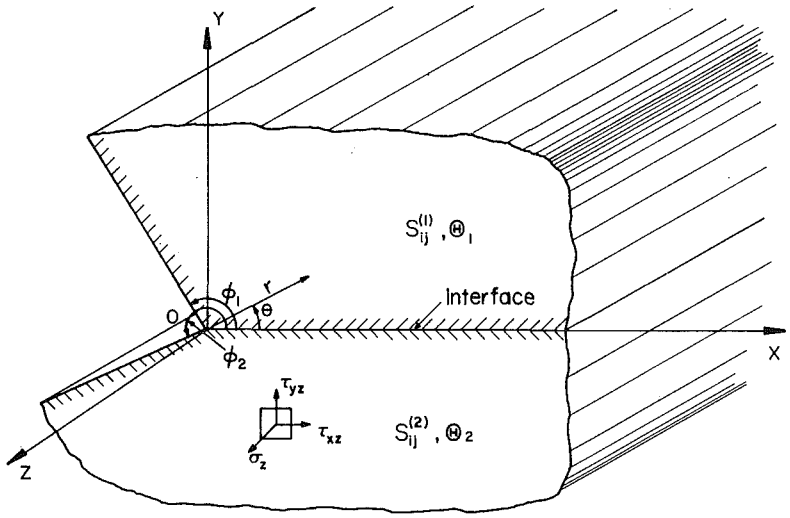


Fig. 2 Coordinates and geometry of the Θ_1/Θ_2 composite wedge

$$Z_k = r(e^{i\theta} + \lambda_k\, e^{-i\theta})/(1+\lambda_k), \quad Z_{k+3} = \bar{Z}_k \quad (k=1,2,3), \tag{4a}$$

where

$$\lambda_k = (1+i\mu_k)/(1-i\mu_k), \quad \lambda_{k+3} = \bar{\lambda}_k = (1-i\bar{\mu}_k)/(1+i\bar{\mu}_k). \tag{4b}$$

The traction boundary conditions along surfaces of the composite wedge in Fig. 2 are

$$\sigma_{\theta\theta}^{(\alpha)} = \tau_{r\theta}^{(\alpha)} = \tau_{\theta z}^{(\alpha)} = 0 \quad \text{on } \theta=\phi_1,\ \alpha=1; \quad \text{and on } \theta=\phi_2,\ \alpha=2, \tag{5a}$$

where the superscript, $\alpha = 1$ or 2, denotes the upper or lower composite lamina, respectively. The stress and displacement continuity conditions along the composite interface require

$$[\sigma_{\theta\theta},\ \tau_{r\theta},\ \tau_{\theta z},\ u_r,\ u_\theta,\ u_z] = 0 \quad \text{along } \theta = 0, \tag{5b}$$

where the bracket in equation (5*b*) represents the jump of the associated quantities across the interface, e.g., $[\sigma_{\theta\theta}] = \sigma_{\theta\theta}^{(1)}(r,0^+) - \sigma_{\theta\theta}^{(2)}(r,0^-)$.

Substituting the stresses and displacements in polar coordinates into equations (5*a*) and (5*b*), one obtains the following system of homogeneous equations:

$$\sum_{k=1}^{3} \{ C_k^{(1)} H_{jk}^{(1)}(\phi_1)[\Omega_k^{(1)}(\phi_1)]^\delta + C_{k+3}^{(1)}\, \overline{H_{jk}^{(1)}(\phi_1)}\ \overline{[\Omega_k^{(1)}(\phi_1)]^\delta} \} = 0, \tag{6a}$$

$$\sum_{k=1}^{3} \{ C_k^{(2)} H_{jk}^{(2)}(\phi_2)[\Omega_k^{(2)}(\phi_2)]^\delta + C_{k+3}^{(2)}\, \overline{H_{jk}^{(2)}(\phi_2)}\ \overline{[\Omega_k^{(2)}(\phi_2)]^\delta} \} = 0, \tag{6b}$$

$$\sum_{k=1}^{3} \{ [C_k^{(1)}\Gamma_{mk}^{(1)} + C_{k+3}^{(1)}\bar{\Gamma}_{mk}^{(1)}] - [C_k^{(2)}\Gamma_{mk}^{(2)} + C_{k+3}^{(2)}\bar{\Gamma}_{mk}^{(2)}] \} = 0, \quad (j=1,2,3;\ m=1,2,3,\ \ldots\ 6), \tag{6c}$$

where H_{ik} and Ω_i are functions of ϕ_i, μ_k, and η_k, and their explicit forms can be determined in a manner similar to those shown in [7, 9]. The Γ_{mk} are known complex constants related to μ_k, η_k, p_k, q_k, and t_k defined in Appendix 1 and reference [7]. Equations (6*a–c*) consist of a system of 12 linear equations in $C_k^{(1)}$, $C_{k+3}^{(1)}$, and $C_k^{(2)}$, $C_{k+3}^{(2)}$. The existence of a nontrival solution for the unknowns requires vanishing of the coefficient determinant, i.e.,

$$|\Delta(\delta)| = 0, \tag{7}$$

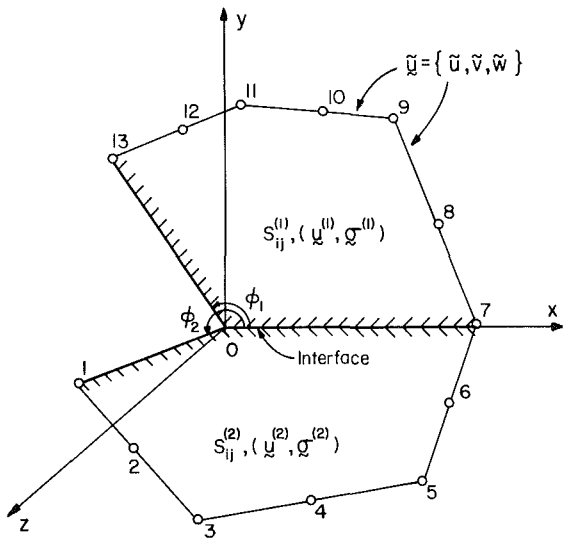


Fig. 3 Thirteen-node, singular hybrid composite-wedge element

where $\Delta(\delta)$ is a 12×12 matrix involving δ in a transcendental form. The $\Delta(\delta)$, as can be seen from equations 6(*a–c*), has a very complex structure. One can solve for the eigenvalues δ_n from the transcendental equation, equation (7), using a standard numerical scheme such as Muller's method [22] with the aid of a digital computer. Numerical values of δ_n for various composite laminate systems of interest have been given in references [6–9, 23].

The eigenvalues δ_n obtained from equation (7) provide important information on the fundamental structure of laminate elasticity solutions for this class of problems. Owing to positive-definiteness of strain energy of an elastic body and the arguments given in [7], the eigenvalues δ_n bounded by

$$-1 < Re[\delta_n] < 0 \tag{8}$$

characterize the order of stress singularity at the composite wedge.

3 Singular Hybrid Finite Element Formulation

3.1 Formulation of Singular Hybrid Composite-Wedge Element. To illustrate the general characteristics of hybrid element formulation for the singular composite-wedge element (Fig. 3), the well-known problem of a composite laminate subjected to traction on the lateral surface and a

Downloaded 02 May 2010 to 171.66.16.250. Redistribution subject to ASME license or copyright; see http://www.asme.org/terms/Terms_Use.cfm

uniform axial strain $\epsilon_z = \epsilon_0$ along the z-axis (Fig. 1) is considered. The element stiffness matrix and loading vector are formulated on the basis of the modified hybrid variational functional $\pi_{mh}(\sigma,\mathbf{u},\tilde{\mathbf{u}})$ [18, 20]:

$$\pi_{mh}(\sigma,\mathbf{u},\tilde{\mathbf{u}}) = \iint_{A_m} (\sigma^T\epsilon - \frac{1}{2}\sigma^T\mathbf{S}\,\sigma)dA - \int_{\partial A_m} \mathbf{T}^T(\mathbf{u}-\tilde{\mathbf{u}})ds - \int_{s_{\sigma_m}} \mathbf{T}^{*T}\tilde{\mathbf{u}}\,ds, \tag{9a}$$

where A_m is the area of the mth element; ∂A_m is the boundary of A_m; S_{σ_m} is the portion of element boundary ∂A_m where traction $\mathbf{T}^*$ is prescribed; and $\tilde{\mathbf{u}}$ is the displacement vector defined over the element boundary. Standard matrix notations, $\mathbf{S}$, σ, ϵ, $\mathbf{u}$, and $\mathbf{T}$, in the finite element analysis are used here for convenience to represent the compliance matrix, stresses, strains, and displacements in the interior of the element, and tractions along the element boundary, respectively. For the present problem under consideration, the hybrid functional π_{mh} can be shown to have a slightly modified form as follows:

$$\pi_{mh}(\bar{\sigma},\mathbf{u},\tilde{\mathbf{u}}) = \iint_{A_m} (\bar{\sigma}^T\bar{\epsilon} - \frac{1}{2}\bar{\sigma}^T\,\bar{\mathbf{S}}\,\bar{\sigma})dA - \int_{\partial A_m} \mathbf{T}^T(\mathbf{u}-\tilde{\mathbf{u}})ds - \int_{s_{\sigma_m}} \mathbf{T}^{*T}\,\tilde{\mathbf{u}}\,ds - \iint_{A_m} \bar{\sigma}^T\,\bar{\epsilon}_o\,dA + C_o, \tag{9b}$$

where

$$\bar{\sigma}^T = \{\sigma_x,\sigma_y,\tau_{yz},\tau_{zx},\tau_{xy}\}, \tag{10a}$$

$$\bar{\epsilon}^T = \{\epsilon_x,\epsilon_y,\gamma_{yz},\gamma_{zx},\gamma_{xy}\}, \tag{10b}$$

$$\bar{\epsilon}_o^T = \{\epsilon_{oi}\} = \{\epsilon_{ox},\epsilon_{oy},\gamma_{oyz},\gamma_{ozx},\gamma_{oxy}\}, \tag{10c}$$

with

$$\epsilon_{oi} = \frac{S_{i3}}{S_{33}}\epsilon_o, \quad C_o = \frac{1}{2}\iint_{A_m} \frac{\epsilon_o^2}{S_{33}}dA, \tag{11}$$

and $\bar{\mathbf{S}} = \{\bar{S}_{ij}\}$ is the reduced compliance matrix defined in references [6–9].

The hybrid finite element approach requires that the stress and displacement, $\bar{\sigma}$ and $\mathbf{u}$, within the element and the boundary displacement, $\tilde{\mathbf{u}}$, be independently assumed. Since the general structure of the solution for the laminate elasticity problem has been explicitly determined by the eigenfunction expansion in the preceding section, the stress and displacement expressions given by equations (3*a–h*) can be used directly in the hybrid element stiffness matrix formulation. Thus, the following relationships for $\bar{\sigma}$ and $\mathbf{u}$ used in the singular, hybrid composite-wedge element (Fig. 3) can be immediately established[1]:

$$\sigma_i = \sum_{n=1}^{N_1} \beta_n \Big(\sum_{k=1}^{3} \{Re[b_{kn}\Lambda_{ik}Z_k^{\delta_n}] + Im[b_{(k+3)n}\bar{\Lambda}_{ik}\bar{Z}_k^{\delta_n}]\}\Big) + \sum_{k=1}^{3} [\beta_{N_1+1}\,b_{k(N_1+1)} + \beta_{N_1+2}\,b_{k(N_1+2)}]Im(\Lambda_{ik}), \tag{12a}$$

$$u_j = \sum_{n=1}^{N_1} \beta_n \Big(\sum_{k=1}^{3} \{Re[b_{kn}\Gamma_{(j+3)k}Z_k^{\delta_n+1}] + Im[b_{(k+3)n}\bar{\Gamma}_{(j+3)k}\bar{Z}_k^{\delta_n+1}]\}/(\delta_n+1)\Big) + \sum_{k=1}^{3} [\beta_{N_1+1}\,b_{k(N_1+1)} + \beta_{N_1+2}\,b_{k(N_1+2)}]Im(\Gamma_{(j+3)k}Z_k), \tag{12b}$$

if δ_n are real, where N_1 is the number of distinct, nonzero real δ_n selected; b_{kn} are known eigenvectors, and Λ_{ik} and Γ_{jk} are constants defined in Appendix 1; and

$$\sigma_i = \sum_{n=N_1+3}^{N-1} \Big\{\beta_n Re\Big[\sum_{k=1}^{6} b_{kn}\Lambda_{ik}Z_k^{\delta_n}\Big] + \beta_{n+1}Im\Big[\sum_{k=1}^{6} b_{kn}\Lambda_{ik}Z_k^{\delta_n}\Big]\Big\} + \sigma_{oi}, \tag{13a}$$

$$u_j = \sum_{n=N_1+3}^{N-1} \Big\{\beta_n Re\Big[\sum_{k=1}^{6} b_{kn}\,\Gamma_{(j+3)k}Z_k^{\delta_n+1}/(\delta_n+1)\Big] + \beta_{n+1}Im\Big[\sum_{k=1}^{6} b_{kn}\Gamma_{(j+3)k}Z_k^{\delta_n+1}/(\delta_n+1)\Big]\Big\} + u_{oj}, \quad (i=1,2,4,5,6;\ j=1,2,3) \tag{13b}$$

if δ_n are complex conjugates, where N denotes the total number of terms in the truncated eigenfunction series, and β_i are real unknown stress parameters to be determined in the hybrid finite element analysis.

Expressed in matrix forms, the element stress, boundary traction, and interior displacement can be written as

$$\bar{\sigma} = \bar{\mathbf{P}}\beta + \bar{\sigma}_o, \quad \mathbf{T} = \mathbf{R}\beta + \mathbf{T}_o, \quad \mathbf{u} = \mathbf{U}\beta + \mathbf{u}_o, \tag{14a–c}$$

where $\beta^T = \{\beta_1,\beta_2,\beta_3,\ldots\}$ are unknown stress parameters, and $\bar{\sigma}_o$, $\mathbf{T}_o$ and $\mathbf{u}_o$ are known quantities resulting from particular solutions for stress and displacement in each individual problem.

The problem of matching the singular hybrid composite-wedge element with adjacent nonsingular elements is resolved by expressing the boundary displacements $\tilde{\mathbf{u}}$ in terms of element nodal displacements $\mathbf{q}$ by

$$\tilde{\mathbf{u}} = \mathbf{L}\mathbf{q}, \tag{15}$$

where $\mathbf{L}$ is a matrix of properly selected shape functions defined along the element boundary. The $\mathbf{L}$ is chosen such that when the corresponding nodal displacements of the adjacent elements are matched, $\tilde{\mathbf{u}}$ is the same for the two different kinds of elements over their common boundaries.

In the present finite element study, a 13-node, general hybrid composite-wedge element (Fig. 3) with 39 degrees of freedom (3 DOF per node) is constructed. Standard quadratic interpolation functions are used for the $\mathbf{L}$ to ensure proper matching with boundary displacements of adjacent eight-node, isoparametric nonsingular elements whose formulation is given in [24, 25].

Following the similar procedure of derivation for hybrid finite elements [18–20, 24], the variational functional may now be expressed in terms of β and $\mathbf{q}$ as

$$\pi_{mh} = -\frac{1}{2}\beta^T\,\mathbf{H}\,\beta + \beta^T\,\mathbf{G}\,\mathbf{q} - \beta^T\,\mathbf{I} + \mathbf{J}\,\mathbf{q} + C_o^*, \tag{16}$$

where

$$\mathbf{H} = \frac{1}{2}\int_{\partial A_m} (\mathbf{R}^T\,\mathbf{U} + \mathbf{U}^T\,\mathbf{R})\,ds, \tag{17a}$$

$$\mathbf{G} = \int_{\partial A_m} \mathbf{R}^T\,\mathbf{L}\,ds, \tag{17b}$$

[1] Equations (12*a*,*b*) are for a composite wedge shown in Fig. 3 (including a special case of the well-known free-edge problem to be discussed in Section 4.1) which has a double root $\delta = 0$ in general. In other cases, different numbers of algebraic multiplicity of the roots δ_n may exist, and equations (12*a*,*b*) need to be modified. For example, for the important composite delamination problem in Section 4.2, slightly different expressions for $\bar{\sigma}$ and $\mathbf{u}$ are given in Appendix 1 for illustration.

Downloaded 02 May 2010 to 171.66.16.250. Redistribution subject to ASME license or copyright; see http://www.asme.org/terms/Terms_Use.cfm

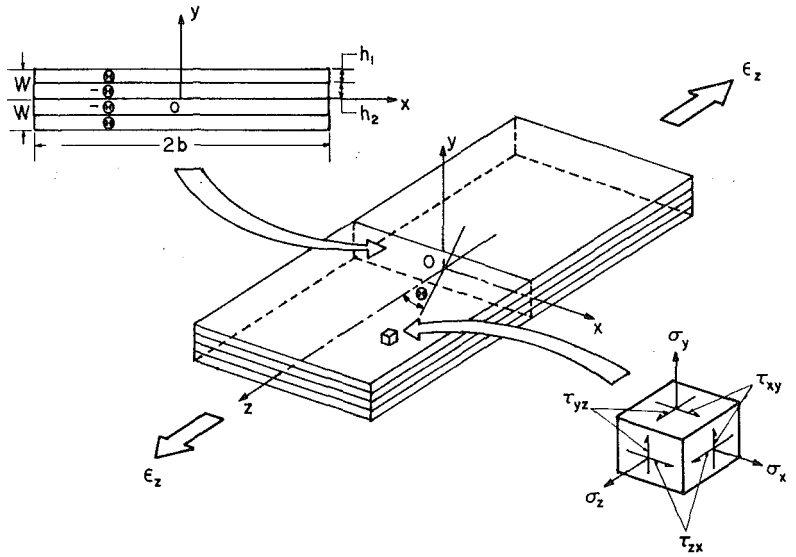


Fig. 4 Geometry and coordinates of a $[\theta/-\theta/-\theta/\theta]$ composite laminate under uniform axial extension $\epsilon_z = \epsilon_0$

$$\mathbf{I} = \frac{1}{2}\int_{\partial A_m} \mathbf{R}^T \mathbf{u}_o \, ds + \frac{1}{2}\int_{\partial A_m} \mathbf{U}^T \mathbf{T}_o \, ds + \frac{1}{2}\iint_{A_m} \bar{\mathbf{P}}^T \bar{\epsilon}_o \, dA, \tag{17c}$$

$$\mathbf{J} = \int_{\partial A_m} \mathbf{T}_o^T \mathbf{L} \, ds, \tag{17d}$$

$$C_o^* = C_o - \frac{1}{2}\int_{\partial A_m} \mathbf{T}_o^T \mathbf{u}_o \, ds - \frac{1}{2}\iint_{A_m} \bar{\sigma}_o^T \bar{\epsilon}_o \, dA. \tag{17e}$$

Taking variation of the functional π_{mh} with respect to β, one obtains

$$\beta = \mathbf{H}^{-1}(\mathbf{G}\,\mathbf{q} - \mathbf{I}). \tag{18}$$

Eliminating β from equation (16) leads to

$$\pi_{mh} = \frac{1}{2}\mathbf{q}^T \mathbf{k}_s \mathbf{q} - \mathbf{q}^T \mathbf{G}^T \mathbf{H}^{-1} \mathbf{I} + \frac{1}{2}\mathbf{I}^T \mathbf{H}^{-1} \mathbf{I} + \mathbf{J}\,\mathbf{q} + C_o^*, \tag{19}$$

where $\mathbf{k}_s$ is the stiffness matrix of the singular hybrid composite-wedge element, defined as

$$\mathbf{k}_s = \mathbf{G}^T \mathbf{H}^{-1} \mathbf{G}. \tag{20}$$

The final displacement-force equations for the singular hybrid element can be obtained by taking variation of π_{mh} in equation (19) with respect to $\mathbf{q}$, yielding

$$\mathbf{k}_s \mathbf{q} = \mathbf{Q}_s, \tag{21}$$

where

$$\mathbf{Q}_s = \mathbf{G}^T \mathbf{H}^{-1} \mathbf{I} - \mathbf{J}^T. \tag{22}$$

3.2 Solution Procedure. Since quadratic interpolation functions are used for displacements along the hybrid element boundaries, the singular hybrid composite element can match exactly with adjacent eight-node, isoparametric regular elements. The matrices, $\mathbf{k}_s$ for the singular hybrid element and $\mathbf{k}_r$ for surrounding nonsingular elements, are true stiffness matrices relating unknown nodal displacements to nodal force vectors. The standard procedure of the matrix-displacement method [26] can be used to assemble the global stiffness matrix and the loading vector, $\mathbf{K}$ and $\mathbf{Q}$, as

$$\mathbf{K}\,\mathbf{q} = \mathbf{Q}, \tag{23}$$

where the assemblage process may be expressed symbolically by

$$\mathbf{K} = \sum_m \mathbf{k}_r^{(m)} + \mathbf{k}_s, \tag{24a}$$

$$\mathbf{Q} = \sum_m \mathbf{Q}_r^{(m)} + \mathbf{Q}_s. \tag{24b}$$

A formal theoretical basis has been discussed in reference [27] for the use of a combination of different variational principles, each for a given subregion of the underlying region of space, in the hybrid finite element method.

After the displacement solution $\mathbf{q}$ is determined, stresses at any point (x_o, y_o) in the singular hybrid element can be calculated by

$$\bar{\sigma} = [\bar{\mathbf{P}}\,\mathbf{H}^{-1}(\mathbf{G}\,\mathbf{q} - \mathbf{I}) + \bar{\sigma}_o]_{(x_o, y_o)}, \tag{25a}$$

and in the surrounding elements by

$$\bar{\sigma} = \bar{\mathbf{C}}(\bar{\mathbf{B}}\,\mathbf{q} - \bar{\epsilon}_o). \tag{25b}$$

4 Numerical Examples

The aforementioned method of approach has been programmed for studying general singular laminate elasticity problems of fiber-reinforced composite materials. The singular, hybrid composite-wedge element is used in conjunction with eight-node, quasi three-dimensional, nonsingular isoparametric elements. Two examples are given in this section for illustration. The first example is the well-known Pipes-Pagano problem [28], i.e., the so-called boundary-layer or free-edge problem in composite laminates, which has been shown [6, 7, 9] to possess a very weak stress singularity in general. The second example is the important delamination problem, i.e., the interlaminar crack problem in composite laminates, which has been shown to have a strong crack-tip stress singularity [8, 9, 23]. Both examples are subjects of significant current interest and technical importance in the areas of fracture and fatigue failure of advanced fiber-reinforced composites. Laminate elasticity solutions for these problems have recently been obtained by using theory of laminate anisotropic elasticity and an eigenfunction expansion method [6–9, 23]. The independently determined elasticity solutions are used here as references for comparative purposes. Solution accuracy and computational efficiency of the present approach for this class of problems are demonstrated and discussed in this section.

For the illustrative purpose, the study of a four-layer symmetric composite laminate with [45 deg/−45 deg/−45 deg/45 deg] fiber orientation and equal and uniform ply

Downloaded 02 May 2010 to 171.66.16.250. Redistribution subject to ASME license or copyright; see http://www.asme.org/terms/Terms_Use.cfm

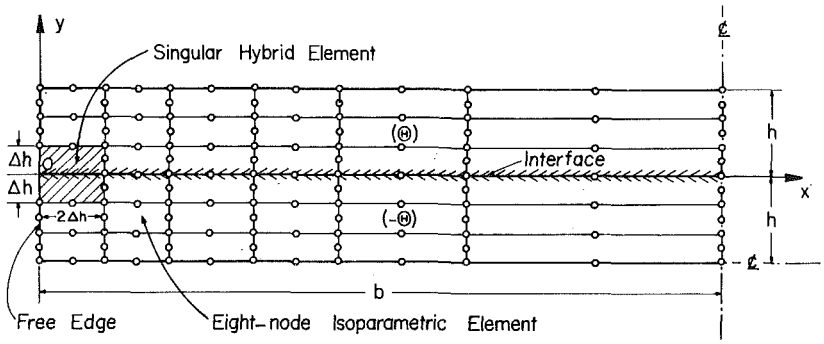


Fig. 5 Finite-element discretization of one quadrant of a cross section of a symmetric [Θ/ − Θ/ − Θ/Θ] composite laminate

Table 1 Dominant stress singularity in the boundary-layer region of [Θ/ − Θ/ − Θ/Θ] graphite-epoxy composite

Θ	δ_1
0 deg	0.00 *E* 0
15 deg	−0.64322 *E*-3
30 deg	−0.11658 *E*-1
45 deg	−0.02575 *E*-1
60 deg	−0.23346 *E*-1
75 deg	−0.89444 *E*-2
90 deg	0.00 *E* 00

thickness, $h_i = h (i = 1,2,3,4)$, is presented. The composite laminate has a finite width of $b = 8h$ subjected to a nominal uniform axial strain $\epsilon_z = \epsilon_0$ as shown in Fig. 4. Each individual ply is assumed to have the following elastic constants typical of high-modulus graphite-epoxy composite lamina:

$$E_L = 20 \times 10^6 \text{ (psi)}, \quad E_T = E_z = 2.1 \times 10^6 \text{ (psi)},$$
$$G_{LT} = G_{Lz} = G_{Tz} = 0.85 \times 10^6 \text{ (psi)}, \tag{26}$$
$$\nu_{LT} = \nu_{Lz} = \nu_{Tz} = 0.21,$$

where L, T, and z refer to principal material axes along fiber, transverse, and thickness directions, respectively. These particular elastic constants have been used in previous studies [6-9, 23-25, 28] for this class of problems and, therefore, are selected in the present numerical study for comparison.

4.1 Example 1 – The Boundary-Layer Stress Problem in Composite Laminates. The boundary-layer stress problem in composite laminates is selected first, because it is one of the very few cases in laminate elasticity known to possess very weak stress singularity and because the exact laminate elasticity solution is available for comparison. In general, the strength of boundary-layer stress singularity between two laminae with Θ_k and Θ_{k+1} fiber orientations has a value of the order of 10^{-2}, which is considered to be very small as compared with those in other singular laminate elasticity problems such as the interlaminar crack case [8, 23]. More specifically, the exact boundary-layer stress singularities at several angle-ply Θ/ − Θ graphite-epoxy composite edges (determined from equations (7) and (8) on the basis of ply elastic constants in equation (26) are illustrated in Table 1. The corresponding boundary-layer stress intensity factors, K_i ($i = 1,2, \ldots, 6$) [6, 7], which are quantities of physical significance and practical interest, can be easily obtained by using the stress parameters β_i determined from equation (18) and by the following relationships in the current hybrid finite element formulation:

$$K_1 = \beta_1 \left\{ \sum_{k=1}^{3} [Re(b_{k1} \mu_k^2) + Im(b_{(k+3)1} \bar{\mu}_k^2)] \right\}, \tag{27a}$$

$$K_2 = \beta_1 \left\{ \sum_{k=1}^{3} [Re(b_{k1}) + Im(b_{(k+3)1})] \right\}, \tag{27b}$$

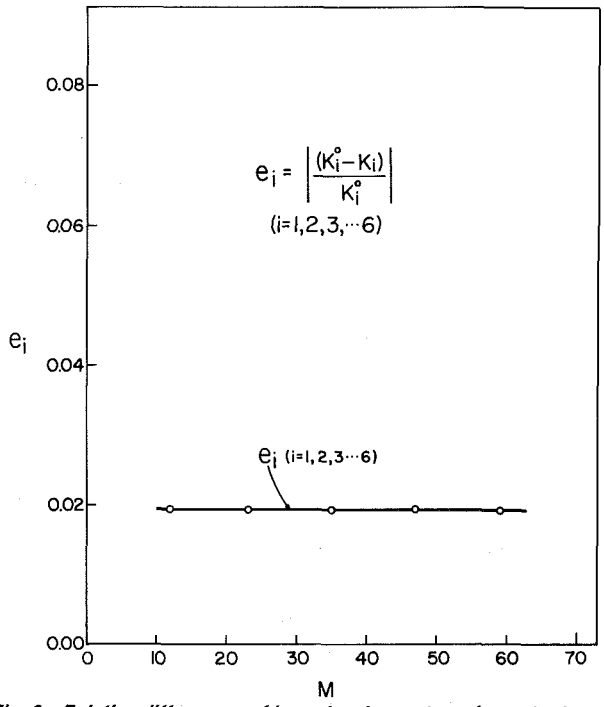


Fig. 6 Relative differences of boundary-layer stress intensity factors, e_i ($i = 1,2, \ldots, 6$), versus total number of elements, *M*, for [45 deg/ − 45 deg/ − 45 deg/45 deg] graphite-epoxy composite

$$K_4 = -\beta_1 \left\{ \sum_{k=1}^{3} [Re(b_{k1} \eta_k) + Im(b_{(k+3)1} \bar{\eta}_k)] \right\}, \tag{27c}$$

$$K_5 = \beta_1 \left\{ \sum_{k=1}^{3} [Re(b_{k1} \eta_k \mu_k) + Im(b_{(k+3)1} \bar{\eta}_k \bar{\mu}_k)] \right\}, \tag{27d}$$

$$K_6 = -\beta_1 \left\{ \sum_{k=1}^{3} [Re(b_{k1} \mu_k) + Im(b_{(k+3)1} \bar{\mu}_k)] \right\}, \tag{27e}$$

$$K_3 = -\sum_{j=1}^{6} S_{3j} K_j / S_{33}, \quad (j = 1, 2, 4, 5, 6). \tag{27f}$$

For the [45 deg/ − 45 deg/ − 45 deg/45 deg] graphite-epoxy composite under a nominal loading $\epsilon_o = 10^{-6}$ with material and geometric variables aforementioned, detailed laminate elasticity solutions for edge stress and deformation were reported in [7]. The analytical solution for boundary-layer stress intensity factors, K_i^o, calculated by using a boundary-collocation method has the following values for reference:

$$K_1^o = 0.5730\ E\ 0, \qquad K_2^o = -0.7534\ E\ 1,$$
$$K_3^o = -0.2952\ E - 1, \qquad K_4^o = 0.1644\ E\ 2, \tag{28}$$
$$K_5^o = 0.1444\ E\ 1, \qquad K_6^o = 0.00\ E\ 0,$$

where the K_i^o carry the dimension of [psi-in.$^{-\delta_1}$] with $\delta_1 = -0.02558$.

Downloaded 02 May 2010 to 171.66.16.250. Redistribution subject to ASME license or copyright; see http://www.asme.org/terms/Terms_Use.cfm

Table 2 Influence of the number of elements, M, and size * of the singular hybrid element ($\Delta h/h$), on relative differences, e_i†, of boundary-layer stress stress intensity factors in [45 deg/ − 45 deg/ − 45 deg/45 deg] graphite-epoxy

M	(Δh/h)	e_1	e_2	e_3	e_4	e_5	e_6
23	0.5	0.01904	0.01905	0.01904	0.01904	0.01904	0.0
35	0.33	0.01902	0.01902	0.01902	0.01902	0.01902	0.0
47	0.25	0.01900	0.01902	0.01902	0.01902	0.01902	0.0
59	0.2	0.01900	0.01902	0.01902	0.01902	0.01902	0.0

* The singular hybrid element has a square shape, $(2\Delta h \times 2\Delta h)$.

† $e_i = \left| \frac{K_i^\circ - K_i}{K_i^\circ} \right|$ $(i = 1, 2, 3, \ldots 6)$; K_i° are from Ref. [7]

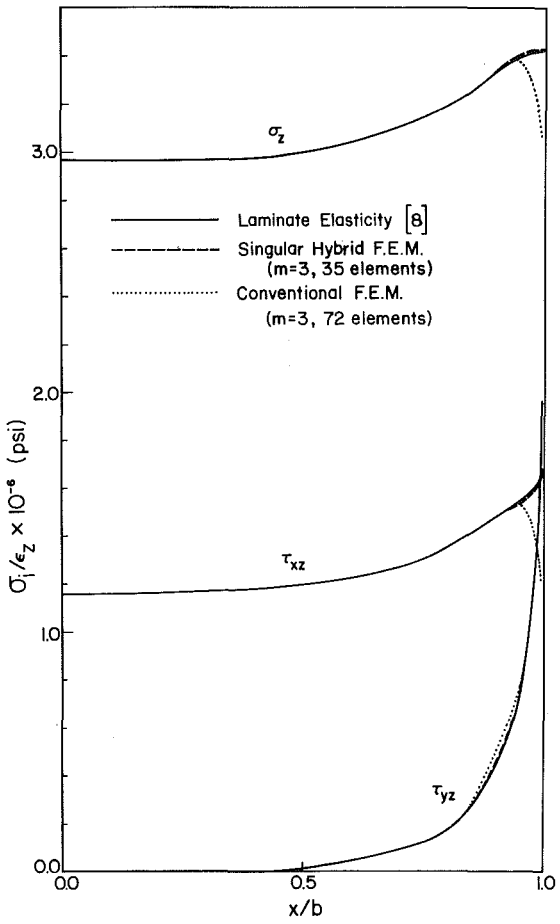


Fig. 7 Comparison of in-plane and interlaminar stresses along the 45 deg − 45 deg ply interface in [45 deg/ − 45 deg/ − 45 deg/45 deg] graphite-epoxy composite obtained by various methods of approach

Numerical results for the problem are obtained by using the present singular hybrid finite element approach. Owing to geometric and material symmetry conditions, only one quadrant of a cross section in the composite laminate needs to be modeled, and a typical finite element mesh configuration used in the analysis is shown in Fig. 5. The singular composite-wedge element in Fig. 3 is degenerated into a composite-edge element by setting $\phi_1 = \pi/2$ and $\phi_2 = -\pi/2$ and by collapsing nodes 1, 2, and 3 into one node and 11, 12, and 13 into another one. This special nine-node, hybrid composite-edge element has 27 degrees of freedom and contains a laminate edge with dissimilar materials and a ply interface. The optimum configuration for the hybrid singular element is found [24] to be in a square shape (Fig. 5), $(2\Delta h) \times (2\Delta h)$, although rectangular geometry can be used to give slightly less accurate results. Assessment of solution accuracy and convergence is carried out by evaluating relative differences, e_i $(i = 1,2, \ldots, 6)$, between the reference solution K_i^o and current numerical results K_i for the composite laminate with different degrees of discretization (i.e., numbers of elements, M) and sizes of the special element (i.e., $\Delta h/h$). In Fig. 6, values of e_i are shown for the cases with different numbers of elements used in the numerical analysis. It is observed that differences from the reference solution, e_i, remain almost unchanged when different meshes with various numbers of elements are used. That is, all the K_i $(i = 1, 2, \ldots, 6)$ obtained from the analysis seem to be insensitive to the number of elements and the mesh configuration. Thus only few elements are actually needed to give accurate results; e.g., fewer than 35 elements provide a solution within 2 percent difference from the reference one for the boundary-layer stress problem. This nature is particularly advantageous in analyzing a composite laminate containing a large number of layers with different fiber orientations. Detailed information on the influence of element size on solution accuracy is of interest too and is reported in Table 2. The results show that the size of the special hybrid edge element does not affect the solution accuracy. For example, changing the linear dimension Δh of the composite-edge element from $0.2h$ to $0.5h$ gives approximately constant e_i in all cases studied. Moreover, comparisons of in-plane and interlaminar stresses along the 45 deg/ − 45 deg ply interface obtained by the current approach and by other methods are given in Fig. 7. One can clearly see from the figure that the results obtained by the present singular hybrid finite element analysis are in excellent agreement with the reference solution [7] and that the conventional numerical method (i.e., the nonsingular finite element analysis) errs very badly in the boundary-layer region due to the fact that the singular terms are not included.

4.2 Example 2 − The Edge Delamination Problem in Composite Laminates. The edge delamination problem in composite laminates is selected here as another example to be solved by the present approach because of its technical importance and the unusual stress singularity associated with the delamination crack tip. Consider the symmetric $[\Theta/-\Theta/-\Theta/\Theta]$ graphite-epoxy composite with delamination cracks of length $a = h = 1.0$ in. emanating from the edges (Fig. 8) due to the high stresses developed in the boundary-layer region as discussed in the preceding section. The composite laminate is again subjected to a nominal uniform axial strain

Downloaded 02 May 2010 to 171.66.16.250. Redistribution subject to ASME license or copyright; see http://www.asme.org/terms/Terms_Use.cfm

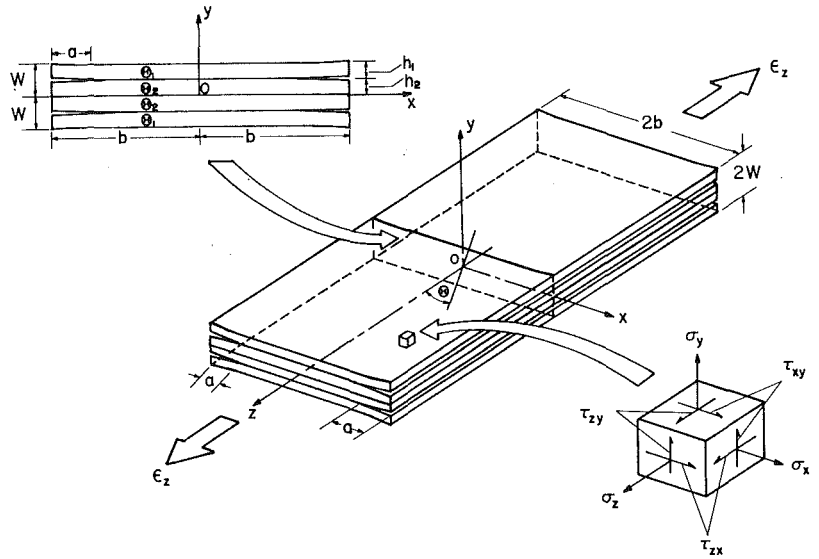


Fig. 8 Coordinates and geometry of delamination cracks in a symmetric $[\Theta/-\Theta/-\Theta/\Theta]$ composite laminate under uniform axial extension $\epsilon_z = \epsilon_0$

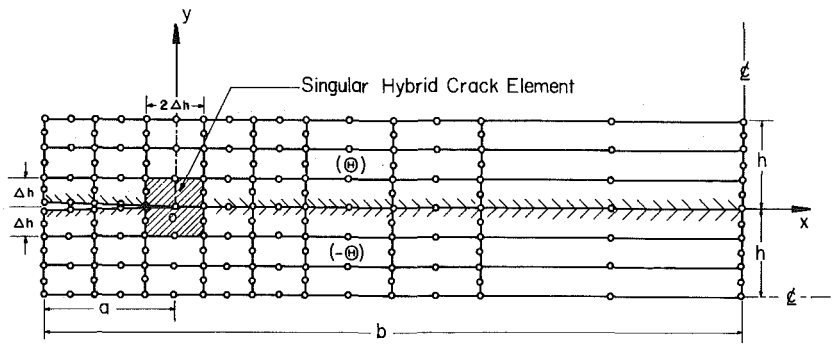


Fig. 9 Finite-element discretization of one quadrant of a cross section of delaminated $[\Theta_1/\Theta_2/\Theta_2/\Theta_1]$ composite laminate

Table 3 Dominant stress singularities for a delamination crack in $[\Theta/-|/-\Theta/\Theta]$ graphite-epoxy composite

Θ	δ_1	$\delta_{2,3}$
0 deg	−0.5	−0.5
15 deg	−0.5	$-0.5\pm0.00642i$
30 deg	−0.5	$-0.5\pm0.02399i$
45 deg	−0.5	$-0.5\pm0.03434i$
60 deg	−0.5	$-0.5\pm0.02942i$
75 deg	−0.5	$-0.5\pm0.01579i$
90 deg	−0.5	−0.5

$\epsilon_z = \epsilon_o = 10^{-6}$ and has a geometry and ply elastic constants as previously stated. Using the eigenfunction expansion method aforementioned in Section 2, one can immediately determine the stress singularity of the delamination, i.e., the interlaminar crack, between Θ and $-\Theta$ plies. Exact values of the stress singularity determined by the eigenfunction expansion [23] for the delamination in $[\Theta/-\Theta/-\Theta/\Theta]$ graphite-epoxy composites are illustrated in Table 3. The stress singularities for composite delamination crack between two highly anisotropic laminae are seen to contain a constant, $\delta_1 = -0.5$, and a pair of complex conjugates, $\delta_{2,3} = -0.5 \pm i\gamma$. The oscillatory stress singularities $\delta_{2,3}$ in a delaminated fiber-reinforced composite laminate are also observed to occur in the problem of an interface crack between dissimilar isotropic or orthotropic media [1-4, 29, 30]. The physical significance of the oscillatory singularity and associated problems are discussed in detail in related papers [8, 23]. Based on the definition of delamination stress intensity factors in [23], values of K_i $(i=I, II, III)$ in the edge-delaminated composite laminate (Fig. 8) can be found easily in the present study. In the hybrid finite element formulation, the K_i can be conveniently determined from the stress parameters β_i of the singular crack element as follows:

$$K_I = \sqrt{2\pi}\Big\{\beta_1\Big[Re\Big(\sum_{k=1}^{3} b_{k1}\Big) + Im\Big(\sum_{k=1}^{3} b_{(k+3)1}\Big)\Big] + \beta_{4N_1+1} Re\Big(\sum_{k=1}^{6} b_{k(4N_1+1)}\Big) + \beta_{4N_1+2} Im\Big(\sum_{k=1}^{6} b_{k(4N_1+2)}\Big)\Big\}, \tag{29a}$$

$$K_{II} = -\sqrt{2\pi}\Big\{\beta_1\Big[Re\Big(\sum_{k=1}^{3} b_{k1}\mu_k\Big) + Im\Big(\sum_{k=1}^{3} b_{(k+3)1}\mu_{k+3}\Big)\Big] + \beta_{4N_1+1} Re\Big(\sum_{k=1}^{6} b_{k(4N_1+1)}\mu_k\Big) + \beta_{4N_1+2} Im\Big(\sum_{k=1}^{6} b_{k(4N_1+2)}\mu_k\Big)\Big\}, \tag{29b}$$

Downloaded 02 May 2010 to 171.66.16.250. Redistribution subject to ASME license or copyright; see http://www.asme.org/terms/Terms_Use.cfm

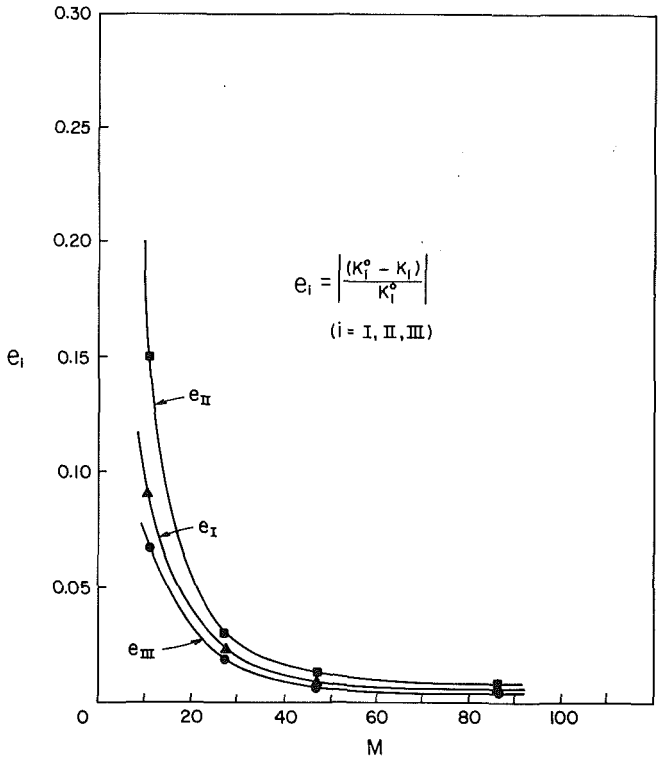


Fig. 10 Relative differences of delamination stress intensity factors, $e_i (i = I, II, III)$, versus total number of elements, M, in the delaminated [45 deg/ – 45 deg/ – 45 deg/45 deg] graphite-epoxy composite

$$K_{III} = -\sqrt{2\pi}\Big\{\beta_1\Big[Re\Big(\sum_{k=1}^{3} b_{k1}\eta_k\Big) + Im\Big(\sum_{k=1}^{3} b_{(k+3)1}\eta_{k+3}\Big)\Big] + \beta_{4N_1+1} Re\Big(\sum_{k=1}^{6} b_{k(4N_1+1)}\eta_k\Big) + \beta_{4N_1+2} Im\Big(\sum_{k=1}^{6} b_{k(4N_1+2)}\eta_k\Big)\Big\}, \quad (29c)$$

where b_{kn}, μ_k, and η_k are known constants defined in [6, 7].

For a 45 deg/ – 45 deg/ – 45 deg/45 deg] graphite-epoxy composite with delamination shown in Fig. 8, the analytical solution for delamination crack-tip stress intensity factors, K_i $(i = I, II, III)$, in the problem determined by a boundary collocation method [23] provides the following numerical values as a reference for comparison:

$$K_I^\circ = 0.1347\, E\,0\ (\text{psi} - \sqrt{\text{in.}}),$$
$$K_{II}^\circ = 0.1381\, E - 1\ (\text{psi} - \sqrt{\text{in.}}),$$
$$K_{III}^\circ = -0.1297\, E\,1\ (\text{psi} - \sqrt{\text{in.}}). \quad (30)$$

Numerical solutions for the problem are obtained using the currently developed singular hybrid finite element approach. The singular hybrid element contains a delamination crack and a ply interface as shown in Fig. 9. This element is also a special case of the general composite-wedge element shown in Fig. 3 by setting $\phi_1 = \pi$ and $\phi_2 = -\pi$. The special crack-tip element for delamination has 13 nodes with 39 degrees of freedom with an optimum configuration also being found in a square shape. The singular hybrid element incorporates the first 23 terms of the eigenfunction series and can be be matched compatibly with surrounding nonsingular elements. A typical finite element mesh for the delaminated composite is also shown in Fig. 9. Numerical results for delamination stress intensity factors determined by the present method of approach are compared with the reference solution (Fig. 10). The current solutions are observed to approach the reference one very rapidly by employing rather coarse meshes. For instance, with 47 elements (three elements per ply in the thickness direction) being used, the relative differences in K_i between the reference solution and the finite element results are within 2 percent. When finer meshes are introduced, the solutions become more accurate and stable, and are relatively insensitive to the grid arrangement

5 Concluding Remarks

The excellent solution accuracy and convergence obtained in the hybrid singular finite element solutions for this class of laminate anisotropic elasticity problems with stress singularities are thought to be attributed to several unusual features of the method of approach. First, the exact stress singularity and the high-order terms in the eigenfunction series solutions for stress and displacement are included in the assumed stress and displacement functions in the hygrid element stiffness formulation. Second, the stress singularity is known to be very localized in the composite and the singular hybrid element has a size generally large enough to enclose the entire singular domain for the problem. Third, stress equilibrium equations, strain compatibility, wedge-surface traction boundary conditions, and ply interface continuity conditions are all satisfied exactly in the formulation. These actually lead to numerically exact solutions for this class of composite laminate elasticity problems.

6 Acknowledgments

The research work described in this paper was supported in part by the Office of Naval Research (ONR), Arlington, Va., under Grant N000-14-79-C-0579 to the University of Illinois, Urbana, Ill. The authors are grateful to Drs. N. Perrone and Y. Rajapakse of ONR for their constant support and encouragement. The authors are also indebted to Professor T. H. H. Pian of the Massachusetts Institute of Technology and Dr. C. C. Chamis of NASA-Lewis Research Center for fruitful discussion during the course of this study.

7 References

1 Gotoh, M., "Some Problems of Bonded Anisotropic Plates With Cracks Along the Bond," *International Journal of Fracture Mechanics*, Vol. 3, No. 5, 1967, pp. 253–265.

2 Bogy, D. B., "Edge-Bonded Dissimilar Orthogonal Elastic Wedges Under Normal and Shear Loading," ASME JOURNAL OF APPLIED MECHANICS, Vol. 35, 1968, pp. 460–466.

3 Hein, V. L., and Erdogan, F., "Stress Singularities in a Two-Material Wedge," *International Journal of Fracture Mechanics*, Vol. 7, 1971, pp. 317–330.

4 Clements, D. L., "A Crack Between Dissimilar Anisotropic Media," *International Journal of Engineering Science*, Vol. 9, 1971, pp. 257–265.

5 Kuo, M. C., and Bogy, D. B., "Plane Solutions for Traction Problems on Orthotropic Unsymmetrical Wedges and Symmetrically Twinned Wedges," ASME JOURNAL OF APPLIED MECHANICS, Vol. 41, 1974, pp. 203–208.

6 Wang, S. S., and Choi, I., "Boundary-Layer Thermal Stresses in Angle-Ply Composite Laminates," in *Modern Developments in Composite Materials and Structures*, Vinson, J. R., ed., ASME, New York, Dec. 1979, pp. 315–342.

7 Wang, S. S., and Choi, I., "Boundary-Layer Effects in Composite Laminates: Part 1—Free-Edge Stress Singularities; Part 2—Free-Edge Stress Solutions and Characteristics," ASME JOURNAL OF APPLIED MECHANICS, Vol. 49, 1982, pp. 541–559.

8 Wang, S. S., and Choi, I., "The Interface Crack Between Dissimilar Anisotropic Composites," ASME JOURNAL OF APPLIED MECHANICS, Vol. 50, 1983, pp. 169–178.

9 Wang, S. S., "Elasticity Solutions for a Class of Composite Laminate Problems With Stress Singularities," in *Mechanics of Composite Materials: Recent Advances*, Hashin, Z., and Herakovich, C. T., eds., Pergamon Press, New York, 1983, pp. 259–281.

10 Tong, P., and Pian, T. H. H., "On the Convergence of the Finite Element Methods for Problems With Singularity," *International Journal of Solids and Structures*, Vol. 9, 1973, pp. 313–321.

11 Chan, S. K., Tuba, I. S., and Wilson, W. K., "On the Finite Element Method in Linear Elastic Fracture Mechanics," *Engineering Fracture Mechanics*, Vol. 2, 1970, pp. 1–17.

Downloaded 02 May 2010 to 171.66.16.250. Redistribution subject to ASME license or copyright; see http://www.asme.org/terms/Terms_Use.cfm

12 Anderson, G. P., Ruggles, V. L., and Stibor, G. S., "Use of Finite Element Computer Programs in Fracture Mechanics," *International Journal of Fracture Mechanics*, Vol. 7, 1971, pp. 63–76.

13 Rice, J. R., and Tracey, D. M., "Computational Fracture Mechanics," *Numerical and Computer Methods in Structural Mechanics*, Fenvas, S., et al., eds., Academic Press, New York, 1973, pp. 585–623.

14 Hilton, P., and Hutchinson, J. W., "Plastic Stress Intensity Factors for Cracked Plate," *Journal of Engineering Fracture Mechanics*, Vol. 3, 1971, pp. 435–451.

15 Atluri, S. N., Kobayashi, A. S., and Nakagaki, M., "An Assumed Displacement Hybrid Finite Element Method for Fracture Mechanics," *International Journal of Fracture Mechanics*, Vol. 11, 1975, pp. 257–271.

16 Akin, J. E., "The Generation of Elements With Singularities," *International Journal for Numerical Methods in Engineering*, Vol. 11, 1976, pp. 1249–1259.

17 Tracey, D. M., and Cook, S. T., "Analysis of Power Type Singularities Using Finite Elements," *International Journal for Numerical Methods in Engineering*, Vol. 11, 1977, pp. 1225–1233.

18 Lin, K. Y., and Mar, J. W., "Finite Element Analysis of Stress Intensity Factors for Cracks at a Bi-Material Interface," *International Journal of Fracture*, Vol. 12, 1976, pp. 521–531.

19 Pian, T. H. H., Tong, P., and Luk, C. H., "Elastic Crack Analysis by a Finite Element Method," in *Proceedings of the Third Conference on Matrix Methods in Structural Mechanics*, Wright-Patterson AFB, Oct. 1971, pp. 19–21.

20 Tong, P., Pian, T. H. H., and Lasry, S. J., "A Hybrid-Element Approach to Crack Problems in Plane Elasticity," *International Journal for Numerical Methods in Engineering*, Vol. 7, 1973, pp. 297–308.

21 Lekhnitskii, S. G., *Theory of Elasticity of an Anisotropic Body*, Holden-Day, San Francisco, 1963.

22 Muller, D. E., "A Method for Solving Algebraic Equations Using an Automatic Computer," *Mathematical Tables and Computations*, Vol. 10, 1956, pp. 208–215.

23 Wang, S. S., "Edge Delamination in Angle-Ply Composite Laminates," *American Institute of Aeronautics and Astronautics Journal*, Vol. 21, No. 11, Nov. 1983.

24 Wang, S. S., and Yuan, F. G., "A Singular Hybrid Finite Element Analysis of Boundary-Layer Stresses in Composite Laminates," *International Journal of Solids and Structures*, Vol. 19, No. 9, 1983, pp. 825–837.

25 Wang, S. S., and Stango, R. J., "Optimally Discretized Finite Elements for Boundary-Layer Stresses in Composite Laminates," *Proceedings of the 23rd AIAA/ASME/ASCE/AHS Structures, Structural Dynamics and Materials Conference*, Paper No. 82-0748-CP, New Orleans, La., May 10–12, 1982, pp. 328–337; also *AIAA Journal*, Vol. 21, No. 4, 1983, pp. 614–620.

26 Zienkiewicz, O. C., *The Finite Element Method*, 3rd Ed., McGraw-Hill, New York, 1977.

27 Gurtin, M. E., "On Patched Variational Principles in Elasticity," *Journal of Elasticity*, Vol. 10, July 1980, pp. 329–332.

28 Pipes, R. B., and Pagano, N. J., "Interlaminar Stresses in Composite Laminates Under Uniform Axial Extension," *Journal of Composite Materials*, Vol. 4, Oct. 1970, pp. 538–548.

29 Comninou, M., "The Interface Crack," ASME JOURNAL OF APPLIED MECHANICS, Vol. 44, 1977, pp. 631–636.

30 Comninou, M., "The Interface Crack In a Shear Field," ASME JOURNAL OF APPLIED MECHANICS, Vol. 45, 1978, pp. 287–290.

APPENDIX 1

For a delamination crack with the homogeneous boundary conditions, equation (5*a*), the algebraic multiplicity of all integer eigenvalues δ_n including zero is 3, in addition to the single roots $\delta_n = (-1/2+n)$ and $(-1/2+n) \pm i\,\gamma$. The modified forms of equations (12*a*,*b*) for this problem are as follows:

$$\sigma_i \sum_{n=1}^{N_1} \beta_n \Bigg(\sum_{k=1}^{3} \{ \mathrm{Re}[b_{kn} \Lambda_{ik} Z_k^{\delta n}] + Im[b_{(k+3)n} \bar{\Lambda}_{ik} \bar{Z}_k^{\delta n}] \} \Bigg) + \sum_{n=N_1+1}^{2N_1} \sum_{k=1}^{3} \{ [\beta_n b_{kn} + \beta_{N_1+n} b_{k(N_1+n)}] Re(\Lambda_{ik} Z_k^m) + [\beta_{2N_1+n} b_{k(2N_1+n)}] Im(\Lambda_{ik} Z_k^m) \}, \quad (i = 1,2,4,5,6) \tag{12a'}$$

$$u_j = \sum_{n=1}^{N_1} \beta_n \Bigg(\sum_{k=1}^{3} \{ Re[b_{kn} \Gamma_{(j+3)k} Z_k^{\delta n+1}] + Im[b_{(k+3)n} \bar{\Gamma}_{(j+3)k} \bar{Z}_k^{\delta n+1}] \} / (\delta_n + 1) \Bigg) + \sum_{n=N_1+1}^{2N_1} \sum_{k=1}^{3} \{ [\beta_n b_{kn} + \beta_{N_1+n} b_{k(N_1+n)}] Re[\Gamma_{(j+3)k} Z_k^{m+1}/(m+1)] + [\beta_{2N_1+n} b_{k(2N_1+n)}] Im[\Gamma_{(j+3)k} Z_k^{m+1}/(m+1)] \}, \quad (j = 1,2,3) \tag{12b'}$$

where $m = n - (N_1 + 1)$; b_{kn} are known eigenvectors, and

$$\Lambda_{1k} = \mu_k^2, \Lambda_{2k} = 1, \Lambda_{4k} = -\eta_k, \Lambda_{5k} = \mu_k \eta_k, \Lambda_{6k} = -\mu_k;$$

$$\Gamma_{1k} = 1, \Gamma_{2k} = \eta_k, \Gamma_{3k} = \mu_k, \Gamma_{4k} = p_k, \Gamma_{5k} = q_k, \Gamma_{6k} = t_k.$$

The expressions equations (13*a*,*b*) corresponding to the complex conjugates δ_n remain the same except that the lower and upper limits of summation need to be changed to $(4N_1 + 1)$ and $6N_1$, respectively.

Downloaded 02 May 2010 to 171.66.16.250. Redistribution subject to ASME license or copyright; see http://www.asme.org/terms/Terms_Use.cfm

Stress Concentrations in a Hybrid Composite Sheet

H. Fukuda
Institute of Interdisciplinary Research,
University of Tokyo,
4-6-1, Komaba, Meguro-ku,
Tokyo 153, Japan

T. W. Chou
Mechanical and Aerospace
Engineering Department,
University of Delaware,
Newark, Del. 19711

This paper examines the load redistribution in a hybrid composite sheet due to fiber breakage. The hybrid composite contains both high modulus and low modulus fibers arranged in alternating positions. Stress concentration factors for both types of fibers immediately adjacent to a group of fractured fibers have been evaluated. The method of influence function and Fourier series representation are adopted. Results of stress concentration factors are presented in terms of the number of fractured fibers and their geometric arrangements. Reduction of the stress concentration factor of the high modulus fibers when dispersed among the low modulus fibers provides a theoretical explanation of the observed "hybrid effect." The present analysis can be readily incorporated into a failure model taking into account the statistical nature of fiber strength.

1 Introduction

The term hybrid is used to describe composites containing more than one type of fiber material in a common matrix. Hybrid composites have several advantages as compared with conventional composites. For example, the freedom in tailoring material properties increases; the cost of fiber can be reduced by using less amount of expensive fibers such as graphite and boron; crack-arresting properties and fracture toughness of composites can be improved due to the "hybrid effect" in fiber fracture strain. Research on hybrid composites has grown rapidly in recent years as reviewed by Chou and Kelly [1], and Renton [2].

To predict the mechanical properties of hybrid composites, such as ultimate strength, ultimate strain, and hybrid effect, it is first necessary to know the stress redistributions near the sites of fiber breakages. In the following, the work of stress concentration in unidirectional continuous fiber composites is first reviewed, beginning with composites containing a single type of fiber.

The work of Hedgepeth [3] first reported the stress redistributions around discontinuous fibers in a unidirectionally stiffened sheet. The stress concentration factor (SCF) in a continuous fiber immediately adjacent to an array of discontinuous fibers was derived using a shear-lag theory. Hedgepeth and Van Dyke [4] later expanded the idea of [3] to consider three-dimensional models. The works of Fichter [5, 6] are the advancements of Hedgepeth's theory [4]. Zweben [7] reported an approximate method for the calculation of stress concentration at the tip of a notch in a unidirectional composite. Fukuda and Kawata [8] examined the stress concentration in a laminate that contains several discontinuous layers. They concluded that the stress concentration factor approaches that of Hedgepeth's result [3] as the number of layer increases. The work of Reddy [9] also investigates stress concentration of this type. The knowledge of stress concentration at fiber breakages is basic to the understanding of the strength of fiber composites. The works in references [10–16], for instance, are concerned with stress redistributions at fiber fracture and their effects on composite strength.

In the case of a hybrid composite where more than one type of fibers is used in a common matrix material, the problem of stress redistribution is more complex than single fiber composites. According to the geometric pattern of fiber arrangements, hybrid composites can be conveniently categorized as interlaminated (interply) and intermingled (intraply) [1, 2]. Zweben [18] predicted the strength of hybrid composites in which the stress concentration factor was calculated by modifying his approximate method for conventional composites [7]. Chou and Fukuda [19] also calculated the stress concentration by applying the method of [8], although details of the calculations were not shown in [19]. More recently, Ji, Hsiao, and Chou [20] examined the dynamic aspect of stress concentration in an interlaminated hybrid, and Fukuda and Chou [21], on the other hand, studied the stress concentration in an intermingled hybrid sheet containing only one discontinuous fiber.

The purpose of this paper is to examine load redistribution in an intermingled hybrid sheet in a comprehensive manner. Results of this analysis can be incorporated into a statistical strength theory of hybrid composites.

2 Analysis

The analytical model is shown in Fig. 1 where the two kinds of fibers assume alternating positions in an intermingled arrangement. Applied tensile load is along the fiber direction.

Contributed by the Applied Mechanics Division and presented at the Winter Annual Meeting, Boston, Mass., November 13–18, 1983 of THE AMERICAN SOCIETY OF MECHANICAL ENGINEERS.

Discussion on this paper should be addressed to the Editorial Department, ASME, United Engineering Center, 345 East 47th Street, New York, N.Y. 10017 and will be accepted until two months after final publication of the paper itself in the JOURNAL OF APPLIED MECHANICS. Manuscript received by ASME Applied Mechanics Division, September, 1981; final revision, February, 1983. Paper No. 83-WA/APM-11.

Copies will be available until July, 1984.

Copyright © 1983 by ASME
Downloaded 02 May 2010 to 171.66.16.250. Redistribution subject to ASME license or copyright; see http://www.asme.org/terms/Terms_Use.cfm

We use the terminologies of low modulus (LM) and high modulus (HM) to distinguish the two kinds of fibers. It should be noted that the terminologies of low elongation (LE) and high elongation (HE) fibers are often used in the literature of hybrid composites [1]. This is because the difference in elongations of the component fibers plays an important role in affecting the ductility of the hybrid. For hybrid composites such as glass/carbon and Kevlar/carbon, HE and LE fibers correspond to LM and HM fibers, respectively. The character of fiber elongation does not directly enter into the present mathematical derivations. Fibers in this hybrid sheet are numbered in series and for analytical reasons, each number m designates one HM fiber and one LM fiber. Asterisks (*) are used to denote quantities related to LM fibers.

Three types of combinations of fiber discontinuity are investigated here. Let r_1 and r_2 be the number of broken HM and LM fibers, respectively. Thus, in Fig. 1: (*a*) $r_1 = r, r_2 = 0$; (*b*) $r_1 = r, r_2 = r - 1$; and (*c*) $r_1 = r_2 = r$. The counting of discontinuous fibers starts at $m = 0$.

The axial load and displacement of the mth fiber are denoted by $p_m(x)$ and $u_m(x)$ where $x = 0$ denotes the plane of fiber fracture. The axial coordinate, x, will sometimes be omitted hereafter. Based on the well-known shear-lag assumptions [3, 20], the force equilibrium equations of the mth HM and LM fibers are, respectively,

$$EA\frac{d^2u_m}{dx^2}+\frac{Gh}{d}(u_m^*+u_{m-1}^*-2u_m)=0$$

$$E^*A^*\frac{d^2u_m^*}{dx^2}+\frac{Gh}{d}(u_{m+1}+u_m-2u_m^*)=0 \tag{1}$$

where EA and G denote the fiber extensional stiffness and the shear modulus of the matrix, respectively.

Under linear elasticity condition, the force-displacement relations become

$$p_m=EA\frac{du_m}{dx},\quad p_m^*=E^*A^*\frac{du_m^*}{dx} \tag{2}$$

The boundary conditions are

$$\begin{aligned}&p_m(\infty)=p\\&p_m^*(\infty)=\frac{E^*A^*}{EA}p\\&p_m(0)=0,\quad p_m^*(0)=0\quad\text{for broken fibers}\\&u_m(0)=0,\quad u_m^*(0)=0\quad\text{for unbroken fibers}\end{aligned} \tag{3}$$

To simplify equations (1)–(3) the following dimensionless parameters are introduced:

$$\begin{aligned}&p_m=p\cdot P_m && p_m^*=p\cdot P_m^*\\&u_m=p\sqrt{d/EAGh}\;U_m && u_m^*=p\sqrt{d/EAGh}\;U_m^*\\&x=\sqrt{EAd/Gh}\;\xi && E^*A^*/EA=R\end{aligned} \tag{4}$$

Thus equations (1) and (2) become

$$\frac{d^2U_m}{d\xi^2}+U_m^*+U_{m-1}^*-2U_m=0$$

$$R\frac{d^2U_m^*}{d\xi^2}+U_{m+1}+U_m-2U_m^*=0 \tag{5}$$

$$P_m=\frac{dU_m}{d\xi}\qquad P_m^*=R\frac{dU_m^*}{d\xi} \tag{6}$$

The concept of influence functions proposed by Hedgepeth [3] are adopted here, and the dimensionless displacements, U_m and U_m^*, are expressed as follows:

$$\begin{aligned}U_m(\xi)&=\xi+\sum_{k=-\infty}^{\infty}V_{m-k}(\xi)U_k(0)+\sum_{k=-\infty}^{\infty}W_{m-k}(\xi)U_k^*(0)\\U_m^*(\xi)&=\xi+\sum_{k=-\infty}^{\infty}V_{m-k}^*(\xi)U_k(0)+\sum_{k=-\infty}^{\infty}W_{m-k}^*(\xi)U_k^*(0)\end{aligned} \tag{7}$$

where V, V^*, W, and W^* are the influence functions. The third condition of equation (3) provides the necessary equations for deriving $U_k(0)$ and $U_k^*(0)$.

Then from equations (5), the following two sets of equations in terms of the influence functions are obtained

(*I*)

$$\frac{d^2V_m}{d\xi^2}-2V_m+V_m^*+V_{m-1}^*=0$$

$$R\frac{d^2V_m^*}{d\xi^2}-2V_m^*+V_{m+1}+V_m=0 \tag{8}$$

with the boundary conditions of

$$\begin{aligned}&V_m(0)=1\quad(m=0),\quad V_m(0)=0\quad(m\neq0)\\&V_m^*(0)=0\\&\frac{dV_m(\infty)}{d\xi}=0\qquad\frac{dV_m^*(\infty)}{d\xi}=0\end{aligned} \tag{9}$$

(*II*)

$$\frac{d^2W_m}{d\xi^2}-2W_m+W_m^*+W_{m-1}^*=0$$

$$R\frac{d^2W_m^*}{d\xi^2}-2W_m^*+W_{m+1}+W_m=0 \tag{10}$$

with the boundary conditions of

$$\begin{aligned}&W_m(0)=0\\&W_m^*(0)=1\quad(m=0)\qquad W_m^*(0)=0\quad(m\neq0)\\&\frac{dW_m(\infty)}{d\xi}=0\qquad\frac{dW_m^*(\infty)}{d\xi}=0\end{aligned} \tag{11}$$

Since equations (10) are identical to equations (8) except the boundary conditions, only the procedure of solution to equation (8) is described in the following. To solve equations (8) and (9) the following Fourier series expressions are introduced here:

$$\bar{V}=\sum_{m=-\infty}^{\infty}V_me^{-im\theta},\quad\bar{V}^*=\sum_{m=-\infty}^{\infty}V_m^*e^{-im\theta} \tag{12}$$

or inversely,

$$V_m=\frac{1}{2\pi}\int_{-\pi}^{\pi}\bar{V}\,e^{im\theta}d\theta,\quad V_m^*=\frac{1}{2\pi}\int_{-\pi}^{\pi}\bar{V}^*\,e^{im\theta}d\theta \tag{13}$$

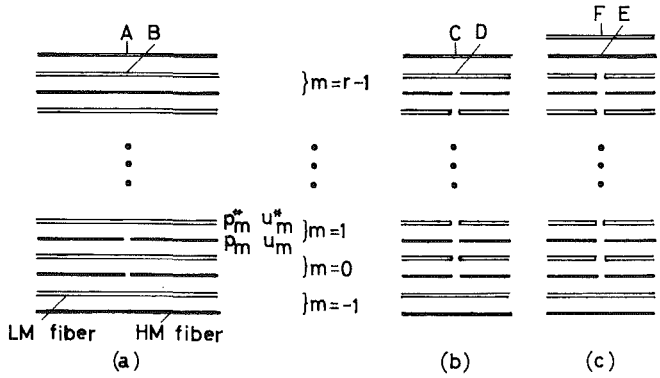


Fig. 1 Array of discontinuous fibers; (*a*) $r_1 = r, r_2 = 0$; (*b*) $r_1 = r, r_2 = r - 1$; (*c*) $r_1 = r_2 = r$; and (*d*) general case. r_1 and r_2 are, respectively, number of discontinuous fibers of LE and HE fibers.

Downloaded 02 May 2010 to 171.66.16.250. Redistribution subject to ASME license or copyright; see http://www.asme.org/terms/Terms_Use.cfm

Then, multiplying equations (8) by $e^{-im\theta}$ and summing over all m give

$$\frac{d^2\bar{V}}{d\xi^2} - 2\bar{V} + D\bar{V}^* = 0$$

$$R\frac{d^2\bar{V}^*}{d\xi^2} - 2\bar{V}^* + E\bar{V} = 0 \tag{14}$$

where

$$D = 1 + e^{-i\theta}, \quad E = 1 + e^{i\theta} \tag{15}$$

From equations (9)

$$\bar{V}(0,\theta) = 1, \qquad \bar{V}^*(0,\theta) = 0$$
$$\frac{d\bar{V}(\infty,\theta)}{d\xi} = 0, \quad \frac{d\bar{V}^*(\infty,\theta)}{d\xi} = 0 \tag{16}$$

are obtained.

The solutions to equations (14) under boundary conditions (16) are

$$\bar{V} = C_1 e^{-\lambda_1\xi} + C_2 e^{-\lambda_2\xi}$$
$$\bar{V}^* = C_3 e^{-\lambda_1\xi} + C_4 e^{-\lambda_2\xi} \tag{17}$$

where

$$\lambda_1 = \sqrt{a + \sqrt{a^2 - b}} \qquad \lambda_2 = \sqrt{a - \sqrt{a^2 - b}}$$
$$a = 1 + \frac{1}{R} \qquad b = \frac{2}{R}(1 - \cos\theta) \tag{18}$$
$$C_1 = \frac{2 - \lambda_2^2}{\lambda_1^2 - \lambda_2^2} \qquad C_2 = -\frac{2 - \lambda_1^2}{\lambda_1^2 - \lambda_2^2}$$
$$C_3 = \frac{(2 - \lambda_1^2)(2 - \lambda_2^2)}{D(\lambda_1^2 - \lambda_2^2)} \qquad C_4 = -C_3$$

Substituting equations (17) into equations (13) and considering a, b, λ_1, λ_2, C_1, C_2, and $C_3 D$ being even functions with respect to θ, the following results are obtained

$$V_m = \frac{1}{\pi}\int_0^\pi (C_1 e^{-\lambda_1\xi} + C_2 e^{-\lambda_2\xi})\cos m\theta\, d\theta$$
$$V_m^* = \frac{1}{\pi}\int_0^\pi C_3 D(e^{-\lambda_1\xi} - e^{-\lambda_2\xi})\frac{\cos m\theta + \cos(m+1)\theta}{2(1+\cos\theta)}\, d\theta \tag{19}$$

Differentiating equations (19) and substituting the result for $\xi = 0$ into equations (7) and the third condition of equations (3), the unknown values $U_k(0)$ $(0 \leqq k \leqq r_1 - 1)$ and $U_k^*(0)$ $(0 \leqq k \leqq r_2 - 1)$ can be obtained.

The dimensionless axial loads, P_m and P_m^* are calculated by substituting equations (7) into (6). The SCF of the mth group of fibers is defined as $P_m(0)/P_m(\infty)$ or $P_m^*(0)/P_m^*(\infty)$, that is,

$$P_m(0)/P_m(\infty) = 1 + \sum_{k=0}^{r_1-1}\frac{dV_{m-k}(0)}{d\xi}U_k(0) + \sum_{k=0}^{r_2-1}\frac{dW_{m-k}(0)}{d\xi}U_k^*(0) \tag{20}$$

$$P_m^*(0)/P_m^*(\infty) = 1 + \sum_{k=0}^{r_1-1}\frac{dV_{m-k}^*(0)}{d\xi}U_k(0) + \sum_{k=0}^{r_2-1}\frac{dW_{m-k}^*(0)}{d\xi}U_k(0)$$

For a HM or LM fiber adjacent to the discontinuous fibers, the SCF can be calculated by substituting the corresponding value of m into equation (20). For example, the SCF's at points B and A of Fig. 1 are, respectively, $P_{r_1-1}^*(0)/P_{r_1-1}^*(\infty)$ and $P_{r_1}(0)/P_{r_1}(\infty)$. The primary objection of this paper is to evaluate equations (20).

3 Results and Discussions

3.1. Comparison With Hedgepeth's Theory. The present analysis should include Hedgepeth's theory as a special case of $R = 1$, which means one type of fiber. We compare the present analysis with those of Hedgepeth for the following limiting cases:

(*a*) $r_1 = 1, r_2 = 0$

Consider, for instance, Fig. 1(*a*), and $r = 1$. The fiber nearest to the broken fibers is a LM fiber of $m = 0$ and therefore the SCF of the fiber immediately adjacent to the breakage is

$$P_0(0)/P_0^*(\infty) = 1 + \frac{dV_0^*(0)}{d\xi}U_0(0) = \frac{4}{3} \tag{21}$$

This result coincides with Hedgepeth's solutions [3]. The same conclusion can be reached by considering the case $r_1 = 0$ and $r_2 = 1$ in Fig. 1(*a*).

(*b*) $r_1 = r_2 = 1$

Again consider Fig. 1(*a*), the SCF is obtained from

$$P_1(0)/P_1(\infty) = 1 + \frac{dV_1(0)}{d\xi}U_0(0) + \frac{dW_1(0)}{d\xi}U_0^*(0) \tag{22}$$
$$= \frac{4}{3}\cdot\frac{6}{5}$$

and it is the same as predicted by Hedgepeth [3].

3.2. Hybrid Composites. When $R \neq 1$, equations (20) are difficult to solve analytically and therefore, numerical integrations have been carried out using a trapezoidal rule. The limiting case of the fracture of one HM fiber ($r_1 = 1$, $r_2 = 0$) has been discussed in reference [21]. The implication of the relative magnitude of SCF's on the "hybrid effect" was also examined.

Figure 2 depicts the relations between SCF's and the total number of discontinuous fibers, $r_1 + r_2$, in the case of $R = 1$. The alphabetical letters ($A - F$) corresponds to $A - F$ in Fig. 1. The curve (D,E) shows the SCF of the nearest fiber (Figs. 1(*b*) and (*c*)) which coincides exactly with Hedgepeth's result [3]. The curve (C,F) gives the SCF of the second nearest fiber to the cracked region.

Figure 3 shows the SCF's at $R = 1/3$, which approximately corresponds to carbon /glass hybrid composites. We assume that the HM fibers have lower ultimate strain and we focus on the SCF of the HM fibers nearest to the discontinuous fibers, i.e., at locations C and E in Figs. 1(*b*) and (*c*). The SCF value of C or E in Fig. 3 is smaller than that of D in Fig. 2 for a fixed number of broken fibers. This means that, as far as the HM fibers are concerned, the SCF is reduced in a hybrid composite.

The SCF's of LM fibers are shown by curves D and F of Fig. 3. Comparing the curves D of Figs. 2 and 3, we observe that the SCF of the LM fiber increases with decreasing R. This means that LM fibers are more susceptible to fracture in a hybrid composite than in a single fiber composite. If the reduction of the SCF of the HM fiber has a dominant effect on the strength compared with the effect due to the increase of SCF of the HE fiber, a "hybrid effect" [1] can be realized. However, the magnitude of the hybrid effect depends on the ratio of the ultimate tensile strains of the two kinds of fibers as was discussed in [21].

It would be a rare case that the failure pattern of Fig. 1(*a*) appears in a single fiber composite. However, this failure pattern is possible in a hybrid composite. The SCF's in the model of Fig. 1(*a*) are also shown in Figs. 2 and 3 by curves A and B. In both figures the SCF appears to be insensitive to the number of broken fibers. This may be considered as a beneficial effect of hybrid composites.

Downloaded 02 May 2010 to 171.66.16.250. Redistribution subject to ASME license or copyright; see http://www.asme.org/terms/Terms_Use.cfm

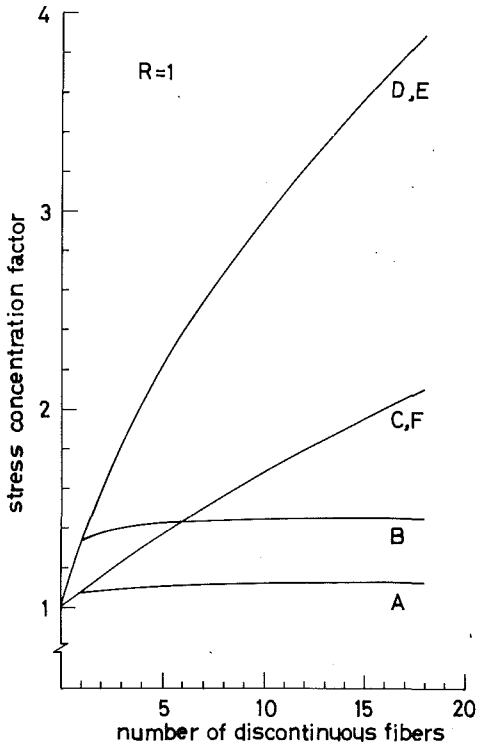


Fig. 2 Stress concentration factors versus total number of discontinuous fibers (R = 1, single fiber composite)

4 Conclusions

The static stress concentration factors of a unidirectional hybrid composite with discontinuous fibers have been calculated using a shear-lag analysis. The present work reproduces the results of the limiting cases of references [3] and [21].

The result of the analysis indicates that in a hybrid composite containing both high modulus and low modulus fibers, the stress concentration factor on the high modulus fibers adjacent to a crack is lower than that in an all-high modulus fiber composite for the same number of fractured fibers. Thus it is possible for the high modulus fibers in a hybrid composite to sustain higher loading and elongation than in the all-high modulus fiber composite, and a "hybrid effect" could be realized.

The present approach can be extended to consider more general fiber fracture configurations in hybrid composites, and the results can be incorporated into failure models considering the statistical aspect of hybrid composite strength.

Acknowledgment

This work was supported by the U.S. Army Research Office. We also thank C. Zweben for helpful discussions.

References

1 Chou, T. W., and Kelly, A., "Mechanical Properties of Composites," *Ann. Rev. Mater. Sci.*, 1980, pp. 229–259.

2 Renton, W. J., "An Overview of Hybrid Composite Applications to Advanced Structures," *Composite Materials: Mechanics, Mechanical Properties and Fabrication*, Kawata, K., and Akasaka, T., eds., Japan Society for Composite Matertials, 1981, pp. 362–382.

3 Hedgepeth, J. M., "Stress Concentrations in Filamentary Structures," NASA TN D-882, 1961.

4 Hedgepeth, J. M., and Van Dyke, P., "Local Stress Concentrations in Imperfect Filamentary Composite Materials," *J. Composite Mater.*, Vol. 1, 1967, pp. 294–309.

5 Fichter, W. B., "Stress Concentration Around Broken Filaments in a Filament-Stiffened Sheet," NASA TN D-5453, 1969.

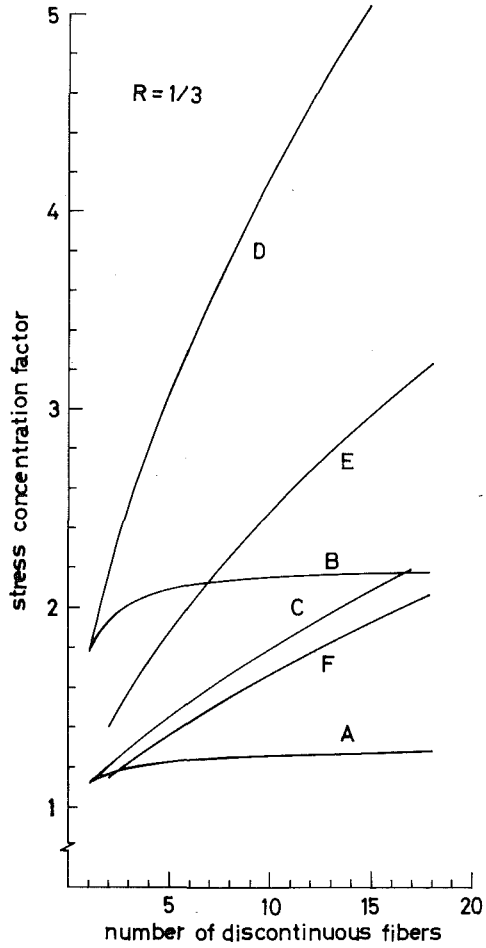


Fig. 3 Stress concentration factor versus total number of discontinuous fibers (R = 1/3, glass/graphite hybrid)

6 Fichter, W. B., "Stress Concentration Factors in Filament-Stiffened Sheets of Finite Length," NASA TN D-5947, 1970.

7 Zweben, C., "An Approximate Method of Analysis for Notched Unidirectional Composites," *Eng. Frac. Mech.*, Vol. 6, 1974, pp. 1–10.

8 Fukuda, H., and Kawata, K., "Stress Distribution of Laminates Including Discontinuous Layers," *Fibre Sci. Tech.*, Vol. 13, 1980, pp. 255–267.

9 Reddy, E. D., Jr., "Analysis of Center-Notched Monolayers With Application to Boron/Aluminum Composites," *J. Mech. Phys. Solids*, Vol. 28, 1980, pp. 265–286.

10 Zweben, C., "Tensile Failure of Fiber Composites," *AIAA J.*, Vol. 6, 1968, pp. 2325–2331.

11 Rosen, B. W., "Tensile Failure of Fibrous Composites," *AIAA J.*, Vol. 2, 1964, pp. 1985–1991.

12 Harlow, D. G., and Phoenix, S. L., "The Chain-of-Bundles Probability Model for the Strength of Fibrous Materials, I. Analysis and Conjection," *J. Composite Mater.*, Vol. 12, 1978, pp. 195–214.

13 Fukuda, H., and Kawata, K., "Strength Estimation of Unidirectional Composites," *Trans. Japan Soc. Composite Mater.*, Vol. 2, 1976, pp. 59–62.

14 Kimpara, I., Watanabe, I., Ohkatsu, T., and Ueda, N., "A Simulation of Failure Process of Fiber-Reinforced Materials," *The Seventh Symp. of Composite Mater.*, JUSE, Japan, Oct. 1974, (in Japanese), pp. 169–174.

15 Fukuda, H., and Kawata, K., "On the Strength Distribution of Unidirectional Fibre Composites," *Fibre Sci. Tech.*, Vol. 10, 1977, pp. 53–63.

16 Okuno, O., and Miura, I., "Analysis of Fracture Process and Strength in Fiber Reinforced Alloys by Monte Carlo Simulation," *J. Japan Soc. Metals*, Vol. 42, 1978, (in Japanese), pp. 736–742.

17 Oh, K. P., "A Monte Carlo Study of the Strength of Unidirectional Fiber-Reinforced Composites," *J. Composite Mater.*, Vol. 13, 1979, pp. 311–328.

18 Zweben, C., "Tensile Strength of Hybrid Composites," *J. Mater. Sci.*, Vol. 12, 1977, pp. 1325–1337.

19 Chou, T. W., and Fukuda, H., "Stiffness and Strength of Hybrid Composites," *Composite Materials: Mechanics, Mechanical Properties and Fabrication*, Kawata, K., and Akasaka, T., eds., Japan Society for Composite Mater., 1981, pp. 78–88.

20 Xing, Ji, Hsiao, G. C., and Chou, T. W., "A Dynamic Explanation of the Hybrid Effect," *J. Comp. Mater.*, Vol. 15, 1981, pp. 443–461.

21 Fukuda, H., and Chou, T. W., "Stress Concentrations Around a Discontinuous Fiber in a Hybrid Composite Sheet," *Trans. Japan Soc. Comp. Mater.*, Vol. 7, 1981, pp. 37–42.

Downloaded 02 May 2010 to 171.66.16.250. Redistribution subject to ASME license or copyright; see http://www.asme.org/terms/Terms_Use.cfm

S. W. Shaw[1]
Department of Theoretical and Applied Mechanics, Assoc. Mem. ASME

P. J. Holmes
Department of Theoretical and Applied Mechanics and Center for Applied Mathematics.

Cornell University, Ithaca, New York 14853

A Periodically Forced Impact Oscillator With Large Dissipation

We consider the simple harmonic oscillator with harmonic excitation and a constraint that restricts motions to one side of the equilibrium position. Thus, on the achievement of a specified displacement, the direction of motion is reversed using the simple impact rule. The coefficient of restitution for this impact, r, is taken to be small. For $r=0$ the motions of the system can be studied using a one-dimensional mapping. Analysis of this map shows that stable periodic orbits exist at almost all forcing frequencies but that transient nonperiodic or chaotic motions can also occur. Moreover, over certain (narrow) frequency windows arbitrarily long stable periodic motions exist. These results are then extended to the case $r \neq 0$, small.

1 Introduction and Model

The oscillator considered here is a limiting case of a system with a piecewise linear restoring force. Such models play an important role in the studies of motion of mechanical oscillators and linkages with amplitude constraining stops. Thompson [1, 2] has done extensive numerical work on a system similar to the one discussed here. Robinson [3] has done experiments on several systems with piecewise linear components using electrical circuits. Shaw and Holmes [4] studied bilinear systems using analytical methods. In all these investigations complicated periodic and chaotic motions were found to occur.

The motion of the mass, m, of the mechanical oscillator shown in Fig. 1 is restricted to one side of its equilibrium position and the system is excited by a sinusoidal base motion of frequency ω. Letting $v(t)$ denote the base displacement, $w(t)$ the inertial displacement of m, and $x(t)$ the displacement of m relative to the base, we have

$$x(t) = w(t) - v(t). \tag{1}$$

Impacts occur whenever $x(t) = 0$ and the following simple impact rule is then used, cf. [5]:

$$\dot{w}(t^+) - \dot{v}(t^+) = -r(\dot{w}(t^-) - \dot{v}(t^-)) \tag{2a}$$

or

$$\dot{x}(t^+) = -r\dot{x}(t^-), \tag{2b}$$

where r is the coefficient of restitution and has a value between zero and unity. In this paper we consider the case when r is small, including the limiting case $r=0$.

This paper is arranged as follows. In Section 2 we derive the one-dimensional mapping for the limiting case and show that it is a $2\pi/\omega$ periodic discontinuous map defined on the circle. In Sections 3 and 4 we study single-impact periodic orbits analytically and show that period doubling bifurcations occur, followed by sequences of "transitions," due to the discontinuous nature of the map, in which the period is reduced. As the driving frequency is increased, a period n orbit bifurcates to period $2n$ and then transits, via a complex succession of long period orbits, to period $n+1$, before period doubling (to $2(n+1)$) once more.

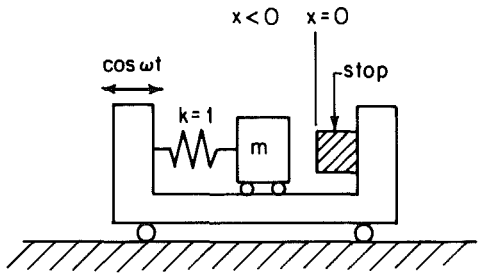


Fig. 1 The physical system

In Section 5 we describe an analogue of earlier results on impact systems [6, 4] in which we find a complicated invariant set containing infinitely many unstable periodic orbits and bounded nonperiodic orbits: a Smale horseshoe [7, 8], and in Section 6 we extend these results to the case of large, but finite dissipation ($0 < r \ll 1$). We summarize and comment on the practical implications of our work in Section 7.

2 Derivation of a One-Dimensional Mapping

Impacting systems are conveniently studied by use of a mapping derived from the equations of motion. Each iterate of this map corresponds to the mass striking the stop once (see Shaw and Holmes [4]).

The dimensionless equation of motion is

$$\ddot{x} + x = \cos\omega t; \quad x < 0, \tag{3}$$

and the solution based at $(x, \dot{x} \equiv y, t) = (0, y_0, t_0)$, i.e., at the stop, is

[1] Present address: School of Engineering, Oakland University, Rochester, Mich. 48063.

Contributed by the Applied Mechanics Division and presented at the Winter Annual Meeting, Boston, Mass., November 13-18, 1983 of THE AMERICAN SOCIETY OF MECHANICAL ENGINEERS.

Discussion on this paper should be addressed to the Editorial Department, ASME, United Engineering Center, 345 East 47th Street, New York, N.Y. 10017, and will be accepted until two months after final publication of the paper itself in the JOURNAL OF APPLIED MECHANICS. Manuscript received by ASME Applied Mechanics Division, March, 1983. Paper No. 83-WA/APM-23.

Copies will be available until July, 1984.

Copyright © 1983 by ASME
Downloaded 02 May 2010 to 171.66.16.250. Redistribution subject to ASME license or copyright; see http://www.asme.org/terms/Terms_Use.cfm

$$x(t;t_0,y_0)=\frac{1}{1-\omega^2}\left[-\cos\omega t_0\cos(t-t_0)\right.$$
$$\left.+(\omega\sin\omega t_0+(1-\omega^2)y_0)\sin(t-t_0)+\cos\omega t\right]. \quad (4)$$

This system cannot be solved in closed form, since the impact times are roots of the transcendental equation

$$x(t_1;t_0,y_0)=0, \quad t_1>t_0. \quad (5)$$

At these impact times we incorporate the impact rule (2*b*), which serves to set new initial conditions. The motion then continues according to (4).

For the "inelastic" case, $r=0$, the velocity just after impact is $\dot{x}(t^+)=0$ so that $y_0=0$ is used in equations (4) and (5). Thus the mass leaves the stop at time t_0 with zero velocity and strikes the stop again at time t_1, given by equation (5). The forcing phase at departure, given by $\phi_0 = t_0 \bmod 2\pi/\omega$, uniquely determines the forcing phase at the next arrival $\phi_1 = t_1 \bmod 2\pi/\omega$. In this way we construct a one-dimensional mapping, each iterate taking the phase at one impact, ϕ_i, to the phase at the next impact, ϕ_{i+1}. We denote this mapping by

$$f_\omega:\phi_i\to\phi_{i+1};\phi_j\in S^1, \quad (6)$$

where the subscript ω indicates that this is a one parameter family of mappings, the parameter being the driving frequency ω. Owing to the periodicity of the forcing function, the phase space for the mapping is the circle, S^1.

The function f_ω cannot be obtained in closed form because of the transcendental nature of equation (5). However, it may be easily constructed by numerical means for a given ω by solving equation (5) using a root solver for a discrete set of values of t_0 between 0 and $2\pi/\omega$. In this way we can generate the mapping for various values of ω and then use analytical tools to study the associated dynamics.

3 Single-Impact Periodic Orbits

Although the zero crossing times are in general unknown quantities, it is possible to determine them analytically for single-impact periodic orbits. This is done by taking the time of flight between successive impacts to be $t_1-t_0 = 2\pi n/\omega$. This simple condition, along with equations (4) and (5) with $y_0=0$, may be immediately solved for the impact phase on the periodic orbit to give:

$$\bar{\phi}=\frac{1}{\omega}\arctan\left(\frac{1-\cos\left(\frac{2\pi n}{\omega}\right)}{-\omega\sin\left(\frac{2\pi n}{\omega}\right)}\right). \quad (7)$$

It is important to note that this condition insures only that the motion based at $x=0$ with phase $\bar{\phi}$ returns to $x=0$ at the same phase (i.e., an integer number of forcing periods later). It does not insure that $x<0$ during the entire time of flight. In fact there are ranges of values of n and ω which give $\bar{\phi}$ which correspond to nonphysical, penetrating orbits (c.f. Senator [9] and Shaw and Holmes [4]). Based on the studies of these maps in the next section it is found that for any value of ω, values of n may be taken only up to the integer part of $(\omega+1)/2$ for physically possible orbits.

The stability of these periodic orbits is determined by computing the slope of $f_\omega(\bar{\phi})$. If $|\partial f_\omega/\partial\phi\ (\bar{\phi})|<1$ then $\bar{\phi}$ corresponds to a stable periodic orbit (a stable fixed point of f_ω). If $|\partial f_\omega/\partial\phi\ (\bar{\phi})|>1$ the corresponding orbit and fixed point are unstable. The condition $|\partial f_\omega/\partial\phi\ (\bar{\phi})|=1$ gives the bifurcation points. This derivative is computed by using implicit differentiation on equation (5) with $y_0=0$. The quantity $\partial t_1/\partial t_0$ is easily obtained. Since $\phi = t \bmod 2\pi/\omega$ and $\phi_1 = f_\omega(\phi_0)$, we have $\partial t_1/\partial t_0 = \partial f_\omega(\phi)/\partial\phi$. Performing the calculation we obtain

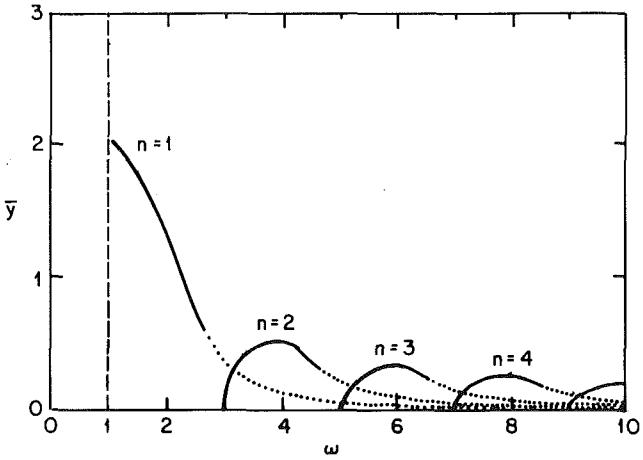


Fig. 2 $r=0$ resonance curve for period n single-impact orbits

$$\frac{\partial f_\omega(\phi)}{\partial\phi}=\frac{\partial t_1}{\partial t_0}=\frac{\cos\omega t_0\sin(t_1-t_0)}{\dot{x}(t_1)}. \quad (8)$$

On a periodic orbit we have the following conditions:

$$\bar{t}_1-\bar{t}_0=\frac{2\pi n}{\omega}$$
$$\bar{t}_0=\bar{\phi}$$
$$\bar{c}_0=\cos\omega\bar{t}_0=-\frac{\omega\sin\left(\frac{2\pi n}{\omega}\right)}{\Delta}$$
$$\bar{s}_0=\sin\omega\bar{t}_0=\frac{1-\cos\left(\frac{2\pi n}{\omega}\right)}{\Delta},$$

where

$$\Delta^2=\omega^2\sin^2\left(\frac{2\pi n}{\omega}\right)+\left(1-\cos\left(\frac{2\pi n}{\omega}\right)\right)^2,$$

and

$$\dot{x}(\bar{t}_1)=\frac{1}{1-\omega^2}\left[\bar{c}_0\sin\left(\frac{2\pi n}{\omega}\right)+\omega\bar{s}_0\left(\cos\left(\frac{2\pi n}{\omega}\right)-1\right)\right]. \quad (9)$$

Using these conditions in equation (8) we obtain

$$\frac{\partial f_\omega(\bar{\phi})}{\partial\phi}=\frac{\sin^2\left(\frac{2\pi n}{\omega}\right)(1-\omega^2)}{\sin^2\left(\frac{2\pi n}{\omega}\right)+\left(1-\cos\left(\frac{2\pi n}{\omega}\right)\right)^2}. \quad (10)$$

The bifurcation condition is found by setting $\partial f_\omega(\bar{\phi})/\partial\phi = \pm 1$ and can be written as

$$\sin^2\left(\frac{2\pi n}{\omega}\right)[\omega^2-1\pm1]\pm\left(1-\cos\left(\frac{2\pi n}{\omega}\right)\right)^2=0. \quad (11)$$

The $+1$ case occurs only at parameter values for which points on the orbit lie at the boundaries of the region S, defined in equation (13). It does not correspond to a bifurcation point in which orbits are created or destroyed, but may, however, occur when double-impact orbits transit to single-impact orbits of the same period (see the following). The -1 case reduces to

$$2\left(1-\cos\left(\frac{2\pi n}{\omega}\right)\right)+\sin^2\left(\frac{2\pi n}{\omega}\right)(1-\omega^2)=0. \quad (12)$$

Downloaded 02 May 2010 to 171.66.16.250. Redistribution subject to ASME license or copyright; see http://www.asme.org/terms/Terms_Use.cfm

This equation was solved numerically; results are given in Table 1 for $n=1$ to 5, and asymptotically for $n\to\infty$.

The period n single-impact orbit changes its stability as ω is varied through the corresponding bifurcation value. Local nonlinear analysis shows that, as the slope of the period n fixed point $\bar{\phi}$ passes through -1 and $\bar{\phi}$ becomes unstable, a period $2n$ *double impact* orbit is thrown off [8]. It can also be shown in this case that this new periodic orbit is stable. In many physical systems these period doublings continue to occur until the motion becomes nonperiodic [10]. In contrast, for this mapping, as we will see, *period doubling cascades do not occur.*

4 Analysis of the Mapping: Periodic Orbits

Each iterate of the mapping f_ω corresponds to an impact. When $r=0$ all of the mechanical energy is dissipated on impact and the mass essentially sticks to the stop. There is no elastic rebound. However, the forcing may drive the mass off again, as in the case of the periodic orbits previously discussed. In those cases the phase of the forcing is such that $\cos\omega\phi<0$, i.e., the forcing pushes the mass into the permissible region $x<0$. In contrast, when $\cos\omega\phi\geq 0$, i.e., when ϕ is in the range S defined by

$$S=\left\{\phi\,\middle|\,0\leq\phi\leq\frac{\pi}{2\omega}\quad\text{or}\quad\frac{3\pi}{2\omega}\leq\phi\leq\frac{2\pi}{\omega}\right\},\qquad(13)$$

the force simply pushes the mass m against the stop, with which it remains in contact until the force changes sign. The force begins to push m away from the stop at $\phi=\pi/2\omega$; this implies that any orbit of f_ω which lands in S is degenerate in the sense that m simply follows the stop until $\phi=\pi/2\omega$. If ϕ lands outside S, that is, in $\pi/2\omega<\phi<3\pi/2\omega$, then the force immediately pushes m away from the stop. This observation is important in the construction of the map, since it implies that $f_\omega(\phi)$ over the range S has zero slope and the value of $f_\omega\ (\pi/2\omega)$. This fact will allow us to iterate the map directly in our analysis of physical orbits.

We may compute a type of resonance curve for this system by plotting the velocity immediately *before* impact on the periodic orbits against the driving frequency ω. The equation for the period n curve for those y corresponding to $\bar{\phi}$ not in S is obtained directly from equation (9):

$$\dot{x}(\bar{t}_1)\equiv\bar{y}=\frac{-\omega\left[\sin^2\left(\frac{2\pi n}{\omega}\right)+\left(1-\cos\left(\frac{2\pi n}{\omega}\right)\right)^2\right]}{(1-\omega^2)\left[\left(\omega\sin\left(\frac{2\pi n}{\omega}\right)\right)^2+\left(1-\cos\left(\frac{2\pi n}{\omega}\right)\right)^2\right]^{1/2}}.\qquad(14)$$

This equation is valid for $\omega>2n$ only since $\bar{\phi}$ is in S for $2n-1<\omega<2n$, as we demonstrate in the following. We will also indicate how these single-impact orbits appear at $\omega=2n-1$. In Fig. 2 stable orbits are shown as a solid curve and unstable orbits as a dotted curve. The loss of stability shown for each n corresponds to the period doubling just described. When $\bar{\phi}$ is in S the $x<0$ excursion time on a single-impact periodic orbit is not $2\pi n/\omega$ but is $t_e=2\pi n/\omega-t_s$, where t_s is the time during which the mass is in contact with the stop. One can show, using the one-dimensional map constructed as previously described, that t_e and t_s are given by the following expressions for the parameter values indicated. For $f_\omega\ (\pi/2\omega)<\pi/2\omega$ we have

$$t_s=\frac{\pi}{2\omega}-f_\omega\left(\frac{\pi}{2\omega}\right)$$

and

$$t_e=\frac{\pi}{2\omega}(4n-1)+f_\omega\left(\frac{\pi}{2\omega}\right).$$

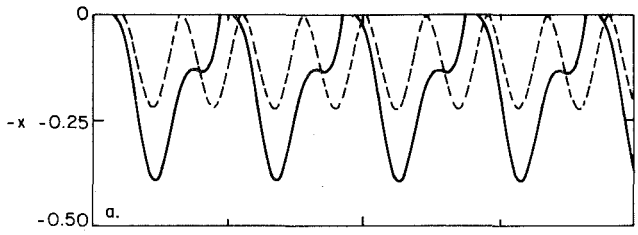


Fig. 3(*a*) $\omega=3.5$ unstable period one, single-impact orbit and *super* stable period two, single-impact orbits

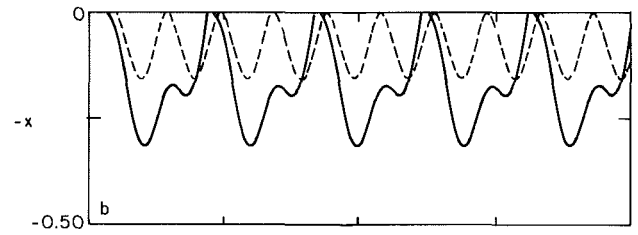


Fig. 3(*b*) $\omega=4.0$ unstable period one, single-impact orbit and stable period two, single-impact orbits

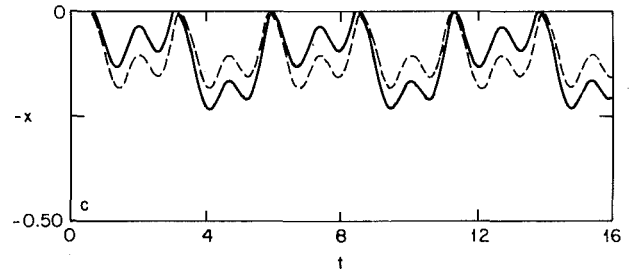


Fig. 3(*c*) $\omega=4.7$ unstable period two, single-impact orbits and stable period four, double-impact orbits (unstable period one, single-impact orbit not shown here or in the following two cases)

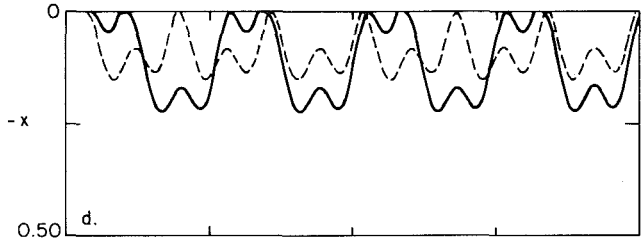


Fig. 3(*d*) $\omega=4.9$ unstable period two, single-impact orbits and *super* stable period three, double-impact orbits

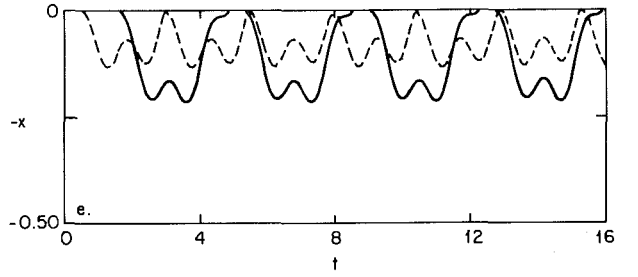


Fig. 3(*e*) $\omega=5.1$ unstable period two, single-impact orbits and *super* stable period three, single-impact orbits

Fig. 3 Periodic orbits: solid curves are stable orbits, dashed curves are unstable orbits

Similarly, for $f_\omega\ (\pi/2\omega)>3\pi/2\omega$ we have

$$t_s=\frac{5\pi}{2\omega}-f_\omega\left(\frac{\pi}{2\omega}\right)$$

and

Downloaded 02 May 2010 to 171.66.16.250. Redistribution subject to ASME license or copyright; see http://www.asme.org/terms/Terms_Use.cfm

$$t_e = \frac{\pi}{2\omega}(4n-5) + f_\omega\left(\frac{\pi}{2\omega}\right).$$

In both cases $t_s + t_e = 2\pi n/\omega$ as required. Note that $f_\omega(\pi/2\omega)$ must be determined numerically since it is the root of a transcendental equation. Thus, for $\bar{\phi}$ in S (i.e., $2n-1 < \omega < 2n$) we replace $2\pi n/\omega$ with t_e and t_0 with $\pi/2\omega$ in evaluating $\bar{y}$ using $\dot{x}(t;t_0)$ from (4). (The orbits for $\bar{\phi}$ in S are stable since $f_\omega(\phi)$ has zero slope in S.) Using this procedure for $2n-1 < \omega < 2n$ and equation (14) for $\omega > 2n$ we obtain the resonance curve shown in Fig. 2.

We now analyze the map for $\omega > 1$. We will show that new stable periodic orbits are created as ω is increased and that the development of each of these orbits follows a definite pattern. It will also be shown that unstable orbits of all periods and unstable nonperiodic orbits coexist over certain ranges of the parameter ω. For most $\omega > 1$, however, the stable periodic orbits attract almost all initial conditions. First we follow the evolution of a stable periodic orbit as ω is increased from $\omega = 2n-1$ to $\omega = 2n+1$ ($n = 1, 2, \ldots$).

A definition is required: we define a *superstable* periodic orbit as one that contains a point at which $\partial f_\omega(\phi)/\partial\phi = 0$. In this problem several superstable orbits will arise due to the flatness of $f_\omega(\phi)$ over S.

For $2n-1 < \omega < 2n$ there exists a superstable single-impact period n orbit. In this orbit, the mass is stuck to the stop for duration t_s less than π/ω, is released at $\phi = \pi/2\omega$ to make an excursion of length $2\pi n/\omega - t_s$ and hits the stop at the value of ϕ corresponding to the fixed point $\bar{\phi}$ (which is in S). Figure 3(a) shows such an orbit for $\omega = 3.5$. Figure 4(a) shows $f_\omega(\phi)$ versus ϕ at the same value of ω. At $\omega = 2n$, $\bar{\phi} = \pi/2\omega = f_\omega(\pi/2\omega)$ and the periodic orbit now spends no time stuck to the stop; its excursion (of length $2\pi n/\omega$) ends exactly as the forcing begins to push m away from the stop. The orbit for $\omega = 4$ is shown in Fig. 3(b) and the corresponding $f_\omega(\phi)$ is shown in Fig. 4(b).

For $2n < \omega < \omega_n$, where the ω_n are the period doubling bifurcation values, the fixed point is outside of S, its value being given by equation (7) in this region. The orbit is qualitatively the same as that for $\omega = 2n$ except it is merely stable, not superstable. At $\omega = \omega_n$ this fixed point becomes unstable and a stable period $2n$ double-impact orbit is thrown off. Such a case is shown for $\omega = 4.7$ in Fig. 3(c) and $f_\omega(\phi)$ is shown in Fig. 4(c) (note the two impact orbit). The unstable single-impact orbit moves nearer to π/ω but remains essentially unchanged as ω is increased further. We now follow the development of the double-impact orbit in detail.

As ω increases in $\omega_n < \omega < 2n+1$ the points on the orbit move away from the unstable fixed point. The left point of the orbit finally lies in S and thus we have a superstable double-impact orbit. The mass is stuck to the wall for a finite time after one impact, corresponding to the point in S. As ω is increased further this two-impact orbit undergoes a sequence of transitions that change it from a period $2n$ orbit to a period $n+1$ orbit. These transitions are not regular bifurcations but arise from the discontinuities of $f_\omega(\phi)$, which we now consider in detail.

The graphs of $f_\omega(\phi)$ for $3 < \omega < 5$ show that it is a discontinuous function. In general, for $2n-1 < \omega < 2n+1$ the map has $n-1$ discontinuities.[2] As ω increases and the period $2n$ orbit grows, the right point in the orbit crosses these discontinuities while the left point remains in S.

In Fig. 5(a) we show $f_\omega(t)$ versus ϕ for $\omega = 5$. Here we do *not* take t mod $2\pi/\omega$, thus showing the actual excursion times, not just the phase upon subsequent impacts. Note that the discontinuities correspond to differences in times of flight of roughly one period. These jumps in excursion times arise at points at which the orbit in the $(x,\dot{x})$ phase plane is tangent to the stop at $x=0$: i.e., at degenerate zero velocity impacts. Figure 5(b) shows $x(t,t_0)$ versus t for values of t_0 near the discontinuities at $\omega = 9$. It clearly shows how discontinuities arise in $f_\omega(\phi)$. As t_0 is increased through a value causing a tangency, the time of flight suddenly decreases. These tangencies occur, as t_0 is increased, from right to left in $x(t,t_0)$ versus t and the time of flight is reduced by a finite amount at each one. These tangencies affect the double-impact stable orbit in the following way. As ω is increased the two points on the orbit of $f_\omega(\phi)$ move away from each other. The left point remains in S or on the leftmost branch of $f_\omega(\phi)$. The other point moves rightward and crosses the discontinuities. Ultimately we have a two-impact orbit containing a point in S and a point on the rightmost branch of $f_\omega(\phi)$ (excluding the flat portion for $\phi > 3\pi/2\omega$). In the general case, therefore, $n-1$ discontinuities have been crossed and the period thereby reduced from $2n$ to $2n-(n-1) = n+1$. The precise manner in which this occurs depends delicately on the structure of the $n-2$ "short" branches of $f_\omega(\phi)$, and we have only studied it in detail for the first transition ($n=2$), in which orbits of period 4 with two impacts transit to orbits of period 3 with two impacts: Figs. 4(c) and 4(d) show the map for this case, the two points on the orbit corresponding to impacts also being indicated. The details of the complex sequence of transitions occurring in the range between $\omega = 4.7$ and $\omega = 4.9$ is discussed in another paper [15]. The main point is that, for certain frequencies in this range, some iterate $f_\omega^n(S)$ of the flat portion S lands directly on one of the unstable fixed points of f_ω (marked L and R in Fig. 4(c)). For such values of ω no stable periodic orbit exists, but for nearby and very narrow frequency ranges, superstable orbits of arbitrarily long period occur. On figures like Figs. 4(c) and 4(d), an iterate of S would land near a fixed point and slowly spiral away before returning to S and repeating the process. The physical orbit therefore contains a long sequence of impacts that, while similar to the periodic impacts associated with L and R, gradually diverge before ultimately repeating. For example, numerical simulations in this range (at $\omega = 4.796$) give orbits of period 15 containing eight impacts: seven on the left (period 2) branch of f_ω and one on the right (period 1) branch. See [15] for more details.

We now return to the "simple" superstable period $n+1$ orbit that exists after the transition region is passed. This orbit persists until $\omega = 2n+1$, at which point there are two critical events. First a new discontinuity in $f_\omega(\phi)$ appears at this value. This discontinuity will play a similar role to the previous ones, reducing the period of the periodic orbits as ω is increased. Second, at this value the shorter excursion of the double-impact superstable period $n+1$ orbit has shrunk to zero so that the orbit has become a degenerate single-impact orbit. The orbit spends exactly one-half of a period stuck to the stop and time $(2n+1)\pi/\omega$ time in its excursion. Note that, at these values of ω, $f_\omega(\pi/2\omega) = 3\pi/2\omega$, which makes the map continuous at $3\pi/2\omega$, this point is the new fixed point corresponding to the single-impact superstable orbit.

As ω is increased above $2n+1$, $f_\omega(\pi/2\omega)$ (i.e., the value of $f_\omega(\phi)$ over S) rises and the fixed point moves rightward, still in S. This is shown in Figs. 3(e) and 4(e) for $\omega = 5.1$. Note that now there are two discontinuities. The fixed point continues to move to the right as ω is increased until it exceeds $2\pi/\omega$, and therefore reappears at 0 (recall that $\phi = t$ mod $2\pi/\omega$). At that point the situation is analogous to that for $2n-1 < \omega < 2n$, n having been increased by one.

In this manner period $2n$ orbits are created through period doublings, have their periods reduced to $n+1$ and eventually period double again. A bifurcation diagram summarizing this

[2] Note that additional fictitious discontinuities appear on our plots of $f_\omega(\phi)$ since $\phi = t$ mod $2\pi/\omega$. Also any discontinuities in the boundaries of S are not included in our count of $n-1$.

Downloaded 02 May 2010 to 171.66.16.250. Redistribution subject to ASME license or copyright; see http://www.asme.org/terms/Terms_Use.cfm

behavior is given in Fig. 6. The single-impact orbits, after period doubling, remain unstable as ω increases and are the fixed points given by equation (7). Analysis of that equation for large ω shows that these fixed points accumulate near π/ω with the asymptotic values

$$\bar{\phi} = \frac{\pi}{\omega}\left(1 - \frac{n}{\omega^2}\right) + 0(\omega^{-4}). \tag{15}$$

The slopes of the map $f_\omega(\phi)$ at these fixed points approach $-\infty$ as $\omega \to \infty$. The discontinuities created at each $\omega = 2n+1$ allows each of these fixed points its own continuous piece of $f_\omega(\phi)$. These pieces, separated by discontinuities, have a dramatic effect on the dynamics of the system, as we will now show.

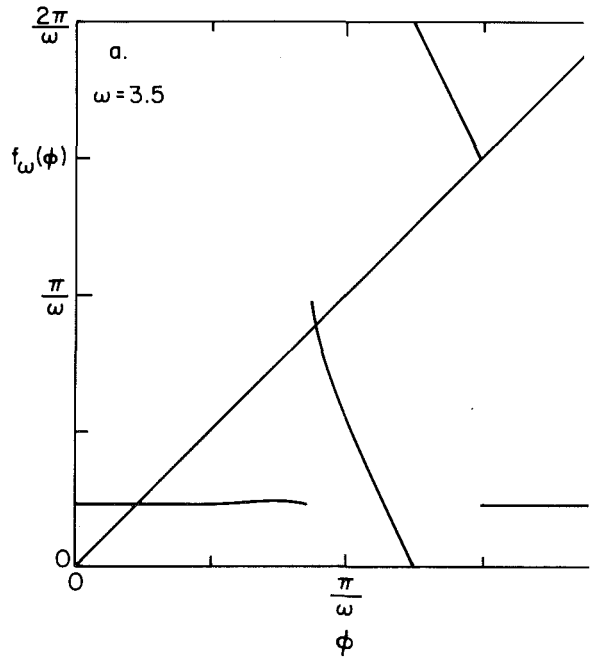


Fig. 4(*a*) $\omega = 3.5$

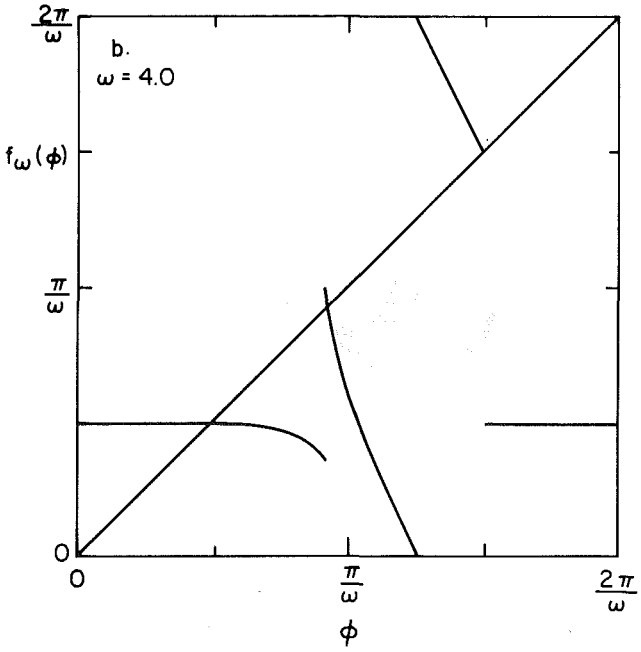


Fig. 4(*b*) $\omega = 4.0$

5 Transient Chaos and Sensitive Dependence on Initial Conditions

The preceding analysis demonstrates that there exists a unique stable periodic orbit at most values of ω. In fact at such ω almost all initial conditions are in the domain of attraction of that orbit, and thus almost all orbits are asymptotically periodic. However, as we will now show, there exist many orbits of arbitrarily long periods for certain ranges of parameter values, and although these orbits are not stable, they can have a great effect on the nature of the transient motions.

Figure 7(*a*) shows $f_\omega(\phi)$ for $\omega = 5.0$ and in Fig. 7(*b*) we show the interval I bounded by $\phi = 0.37\ (2\pi/\omega)$ and $\phi = 0.495\ (2\pi/\omega)$. We have divided I into four subintervals $I_j, j = 0, 1, 2, 3$ and we note that

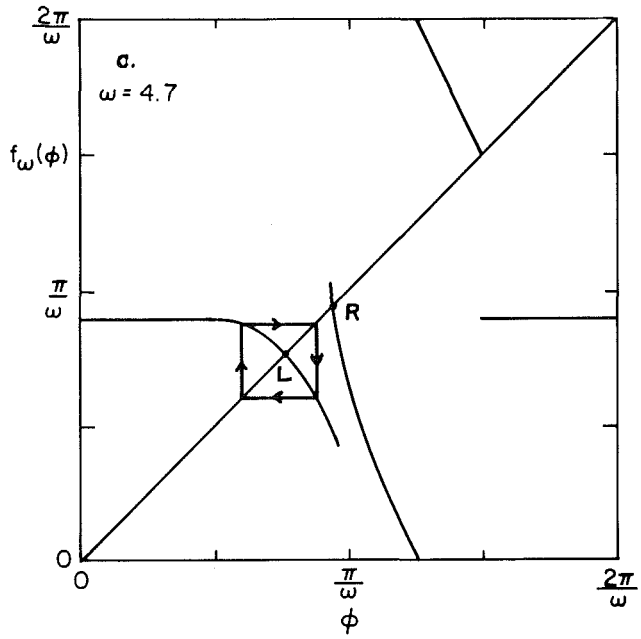


Fig. 4(*c*) $\omega = 4.7$

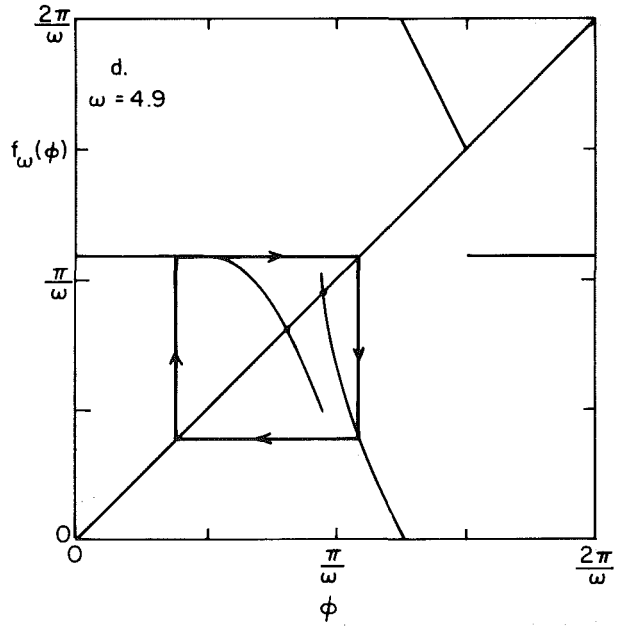


Fig. 4(*d*) $\omega = 4.9$

Downloaded 02 May 2010 to 171.66.16.250. Redistribution subject to ASME license or copyright; see http://www.asme.org/terms/Terms_Use.cfm

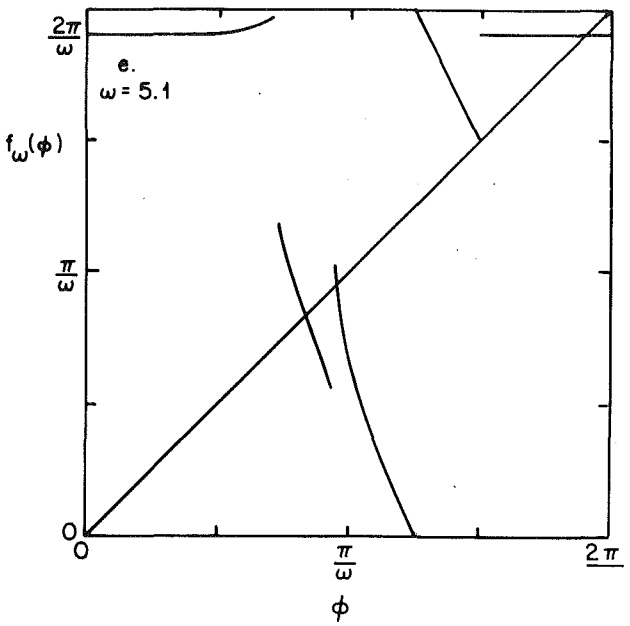


Fig. 4(e) $\omega = 5.1$

Fig. 4 $f_\omega(\phi)$ versus ϕ

$$f_\omega(I_0) \supset I$$
$$f_\omega(I_2) \supset I; \tag{16}$$

i.e., the images of I_0 and I_2 cover I. (I_0 and I_2 are closed, I_1 and I_3 open.) We can write the corresponding *transition matrix* (see Guckenheimer and Holmes [8]) as

$$\mathbf{A} = [a_{ij}] = \begin{bmatrix} 1 & 1 \\ 1 & 1 \end{bmatrix}, \tag{17}$$

where $a_{ij} = 1$ if $f(I_i) \supset I_j$ and $a_{ij} = 0$ otherwise ($i,j = 0$ or 2). Since that matrix is full, there exist orbits that visit I_0 and I_2 in *any* specified order. It should be noted that points in I_1 and I_3 are mapped out of I, and by considering the preimages of I_1 and I_3 we see that almost all points are eventually mapped out of I (and hence are asymptotic to the stable periodic orbits discussed in the foregoing). Those points that are never mapped out of I under forward iterates of f_ω form part of the *invariant set* of f_ω, $\Lambda_1 \subset I$, defined by

$$\Lambda_1 = \bigcap_{n=0}^{\infty} f_\omega^{-n}(I). \tag{18}$$

Λ_1 contains a countable infinity of unstable periodic orbits and an uncountable infinity of nonperiodic orbits. The points in Λ_1 may be characterized by representing an orbit of f_ω by a semi-infinite sequence of 0's and 2's, $\{a_k\}_{k=0}^{\infty}$, where

$$a_k = 0 \quad \text{if} \quad f_\omega^k(\phi_0) \in I_0,$$
and
$$a_k = 2 \quad \text{if} \quad f_\omega^k(\phi_0) \in I_2, \tag{19}$$

and ϕ_0 is a point in Λ_1. Such a symbol sequence may be used to study the iterates of f_ω in the following way. It can be shown [8] that the map f_ω, restricted to Λ_1, is topologically equivalent (homeomorphic) to the shift operation

$$(\sigma\{a_k\})_j = a_{j+1}.$$

defined by (20)

$$\sigma\{a_0, a_1, a_2 \ldots\} = \{a_1, a_2, \ldots\},$$

defined on the sets of two symbol sequences. In this case, $\omega = 5.0$, one can verify that $|\partial f_\omega(\phi)/\partial\phi| > 1$ everywhere in I_0

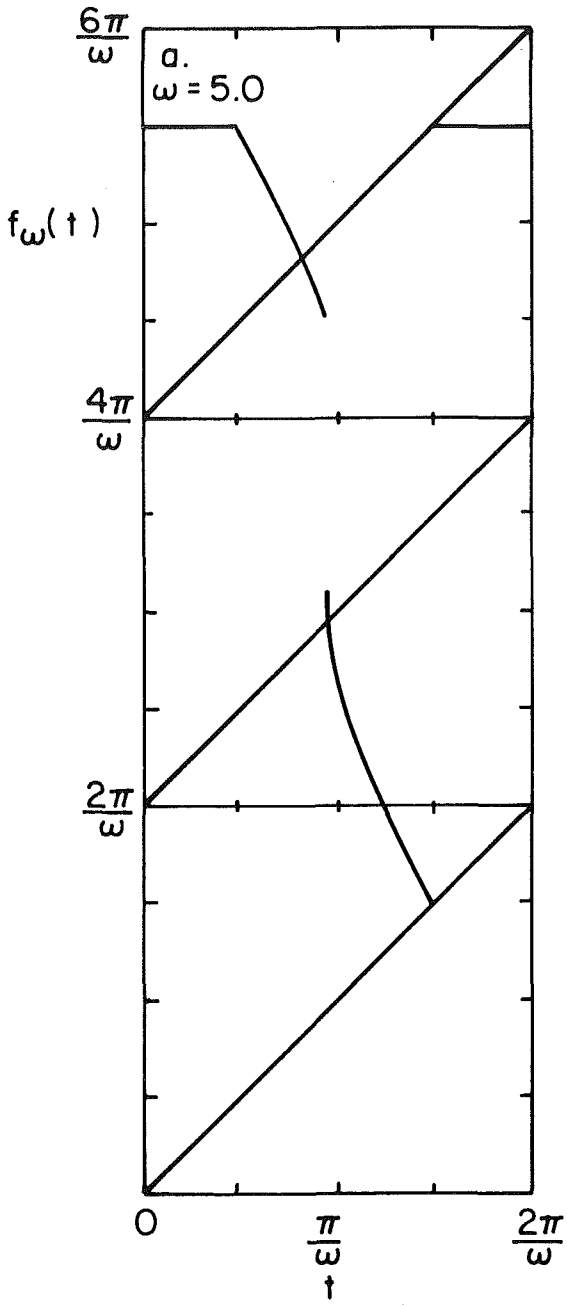


Fig. 5(a) $f_\omega(t)$ versus t, $\omega = 5.0$

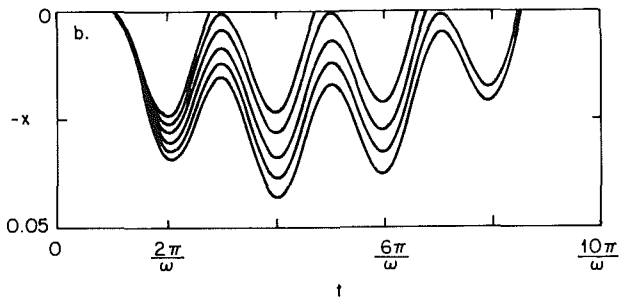


Fig. 5(b) x versus t, $\omega = 9.0$; $t_0\left(\frac{\omega}{\pi}\right)$ = 0.92, 0.935, 0.95, 0.969, 0.985, 1.00

Fig. 5

Downloaded 02 May 2010 to 171.66.16.250. Redistribution subject to ASME license or copyright; see http://www.asme.org/terms/Terms_Use.cfm

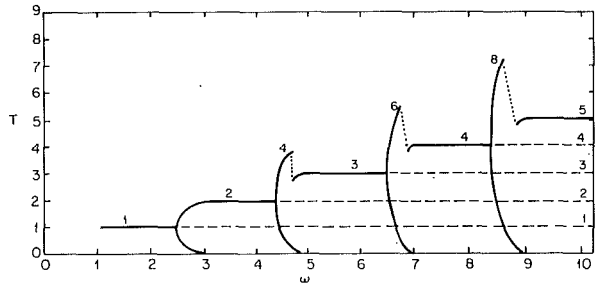


Fig. 6 Bifurcation diagram showing T, the normalized time (fraction of period) between successive impacts on a periodic orbit, versus ω. Solid lines are stable (or superstable) orbits, dashed lines are unstable orbits and dotted regions indicate transitions. The period of the orbit is labeled. Note the period doublings followed by the transitions.

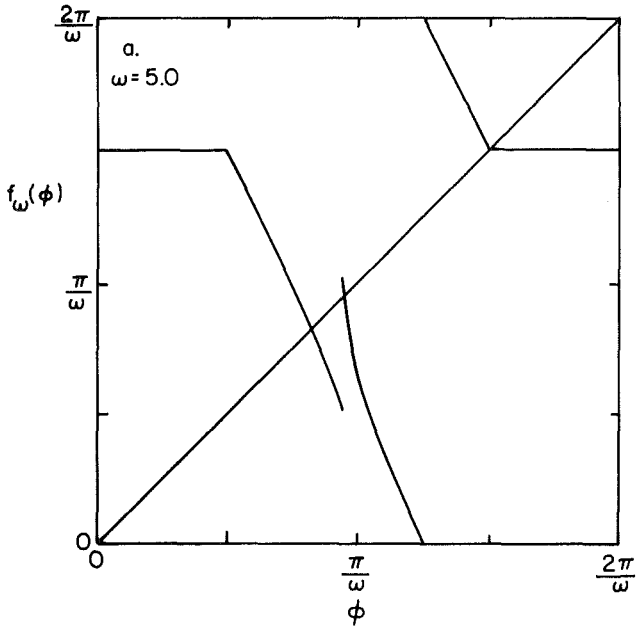


Fig. 7(*a*) $f_\omega(\phi)$ versus ϕ, $\omega = 5.0$

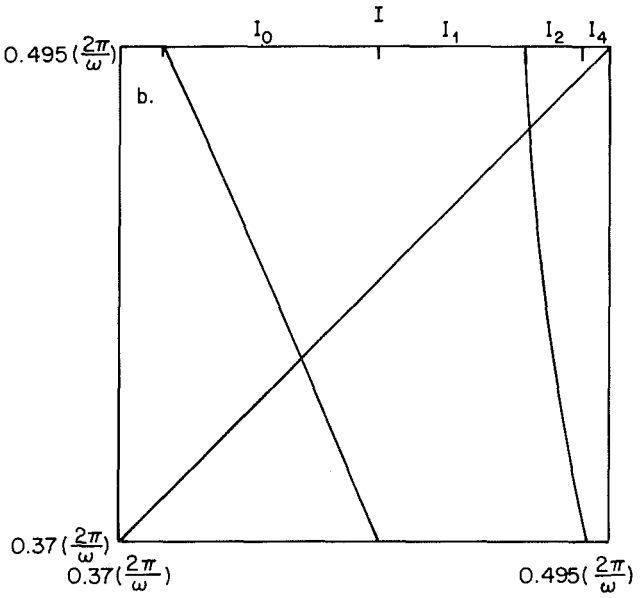


Fig. 7(*b*) Region between 0.37 $\left(\frac{2\pi}{\omega}\right)$ and 0.495 $\left(\frac{2\pi}{\omega}\right)$ shown in detail

Fig. 7

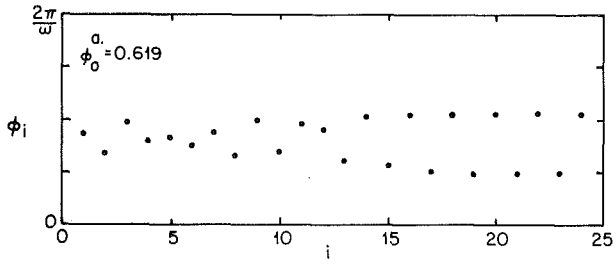


Fig. 8(*a*) $\phi_0 = 0.619001$

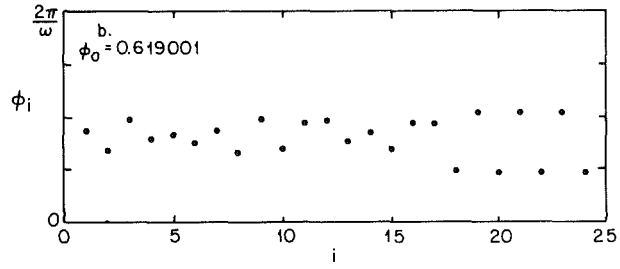


Fig. 8(*b*) $\phi_0 = 0.619$

Fig. 8 ϕ_i versus *i* for $\omega = 4.88$

and I_2, this together with (16) and (17), is sufficient to establish topological equivalence. Note that all of these orbits are unstable, for, by the chain rule, the derivative $|\partial(f_\omega^n)/\partial\phi|$ along any n-periodic orbits exceeds 1. Table 2 gives examples of symbol sequences of orbits of up to period 4. Precisely one orbit exists for each symbol sequence, via the topological equivalence.

These unstable orbits can have a great effect on transient motions of the system. All initial conditions except those on the unstable orbits in I and their preimages, eventually are asymptotic to a stable periodic orbit. However, the route to that orbit can differ greatly with very small perturbations in the initial condition. The duration of the transient chaos varies with the parameter ω (Grebogi, Ott, and Yorke [11]). We take $\omega = 4.88$ in the following example since it exhibits typically longer chaos than the system at $\omega = 5.0$. Figure 8 shows two orbits with initial conditions that vary by only 10^{-6}, yet the orbits appear very different. This *sensitive dependence on initial conditions* exists in other one-dimensional maps that do not possess stable periodic orbits. Such cases are the only ones where the existence of a *strange attractor* has rigorously been proved [12]. For more information on such sensitive dependence, see Guckenheimer and Holmes [8] and the literature cited therein.

6 Extension to Finite Dissipation

When r is small but finite the mapping used to describe the motion is one that takes the forcing phase, ϕ, and velocity, y, from one impact to the next

$$F_{\omega,r}:(\phi,y) \to (\phi,y);\ (\phi,y) \in S^1 \times \mathbb{R}^+. \tag{21}$$

This two-dimensional map can be viewed as a singular perturbation of the one-dimensional map analyzed in the foregoing. The velocity immediately after impact is small since r is small, but is nonzero almost everywhere. (The map is not defined at points which are mapped to $y = 0$.) Iterating this map involves successively solving the transcendental equation (5) with $y_0 \neq 0$, as in [4].

With an inelastic rebound, even when $0 < r \ll 1$, the motion is qualitatively different. Each rebound provides a velocity component away from the stop, thus no sticking occurs. However, the departure velocity is small for small r, and, for ϕ in the range S, the force simply pushes the mass

Downloaded 02 May 2010 to 171.66.16.250. Redistribution subject to ASME license or copyright; see http://www.asme.org/terms/Terms_Use.cfm

Table 1 Period doubling bifurcation values

n	ω_n
1	2.70467
2	4.65719
3	6.64646
4	8.64238
5	10.64040
as $\omega \to \infty$	$\omega_n \to 2n + \frac{2}{\pi}$

Table 2 Orbits of periods ≤ 4.

Period	No. of orbits	Symbol sequence
1	2	000 . . . ,222 . . .
2	1	020202 . . ,
3	2	022022 . . ,0020020 . . . , 022202202 . . .

back toward the stop. This results in small, brief excursions which continue until the force pushes the mass away from the stop, i.e., until $\phi > \pi/2\omega$. This makes the extension of $F_{\omega,r}$ from f_ω in the region S complicated, and it will not be dealt with in detail here. It is sufficient to note that points mapped into S with y_0 sufficiently small will behave essentially as if they were sticking to the wall up to $\phi = \pi/2\omega$. Also, highly stable periodic orbits exist for values of ω at which the superstable periodic orbits exist in the $r=0$, case. These orbits contain a large number of these "small" impacts.

The region of interest here is outside S. We will show that a complex two-dimensional invariant set Λ_2 corresponding to Λ_1 in the one-dimensional system exists when $r \neq 0$ is sufficiently small. This is done by considering the map at $\omega = 5.0$, $r = 0.01$. The analysis in Shaw and Holmes [4] provides an expression by which the following single-impact periodic points can be computed

$$(\bar{\phi},\bar{y})_1 = (0.60002,\ 0.059347)\ \ (n=1)$$

and (22)

$$(\bar{\phi},\bar{y})_2 = (0.51974,\ 0.21743)\quad (n=2).$$

These are both unstable fixed points of $F_{r,\omega}$, and are continuations of the $n=1$ and 2 fixed points of f_ω for $r=0$. These two unstable fixed points are part of the aforementioned set Λ_2.

In Fig. 9 we show the image of the set of points $\bar{S} = \{(\phi,y) \mid \pi/2\omega < \phi < 3\pi/2\omega,\ y=0\}$ under $F_{r,\omega}$ with $r=0$ and $\omega = 5.0$. The primed points are the images of the corresponding unprimed points under $F_{r,\omega}$. In this limiting case the impact rule collapses everything into $y=0$ and thus the curve shown is the image of $\bar{S}$ under $F_{0,\omega} = f_\omega$. The discontinuity is at point $B \cong 0.476\ (2\pi/\omega)$. (This jump replaces the bending found in horseshoes for continuous maps, cf. [6].) We note that the arrival velocity (just prior to the impact) is bounded above by 0.3. We now consider r small and nonzero.

Our aim is to show that the map $F_{r,\omega}$ is "almost linear" on a certain subset Q of the phase space and that on the invariant set $\Lambda_2 \subset Q$, it behaves much as does the one-dimensional map f_ω on the two subintervals I_0, I_2. The second (y) dimension adds a (vertical) contracting direction to the (horizontal) expansion in ϕ already present in f_ω. Moreover, the introduction of a second dimension implies that $F_{r,\omega}$, $r>0$, can have chaotic orbits while remaining an invertible map. In one dimension, only noninvertible maps can exhibit chaos. The fact that such maps, which expand in one direction, contract in another, and cut, could lead to chaotic motions was first clearly demonstrated by Smale [7]. See Holmes [6] or Guckenheimer and Holmes [8] for more information.

To check that $F_{r,\omega}$ is a bounded perturbation of a linear map we examine $DF_{r,\omega}$. The determinant of $DF_{r,\omega}$ over the

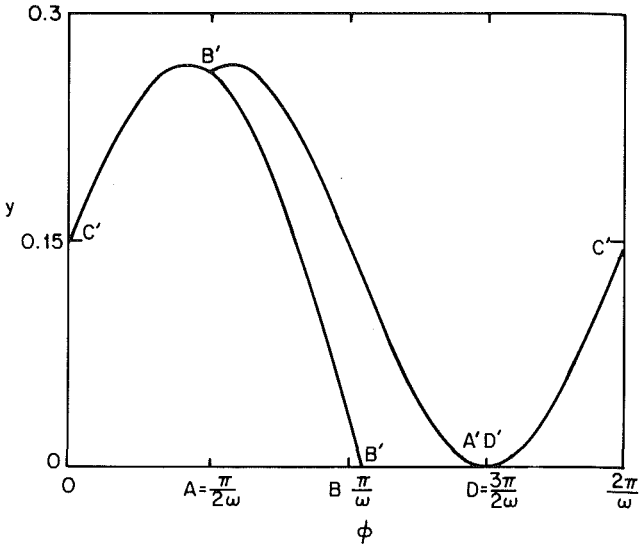


Fig. 9 Image of $y=0, \frac{\pi}{2\omega} \leq \phi \leq \frac{3\pi}{2\omega}$ under $F_{r,\omega}$ with $r=0$ and $\omega = 5.0$

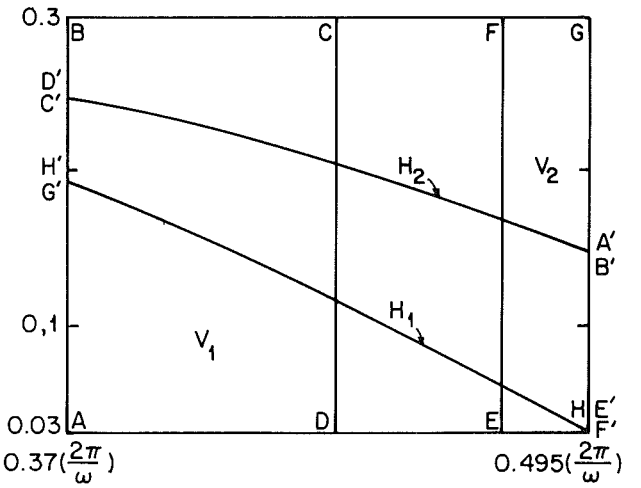


Fig. 10 Region of interest from Fig. 9; $0.03 < y < 0.3$ and $0.37\left(\frac{2\pi}{\omega}\right) < \phi < 0.495\left(\frac{2\pi}{\omega}\right)$

region of interest is proportional to r^2. Thus when $r=0$ the images of open regions in (ϕ,y) space are simply curves (of zero area), as shown in Fig. 9. For $0 < r \ll 1$ their images look essentially the same as for $r=0$ but now have finite area. We consider the image of the rectangle $Q = ABGH$ under $F_{r,\omega}$

$$Q = ABGH = \{(\phi,y) \mid 0.37P < \phi < 0.495P,$$

$$0.03 < y < 0.3\}, \quad \text{where} \quad P = \frac{2\pi}{\omega}. \tag{23}$$

Again the unprimed points are mapped into the primed points under $F_{r,\omega}$. (See Fig. 10.) Note that vertical (y) distances are greatly contracted so that intervals are *almost* shrunk to points. In particular we define "vertical" strips $V_1 = ABCD$ and $V_2 = EFGH$. By considering their images, the "horizontal" strips $H_1 = (ABCD)'$ and $H_2 = (EFGH)'$, we see that

$$F_{r,\omega}(V_i) = H_i, \quad i = 1,2 \tag{24}$$

and thus we have a *topological horseshoe* [13]. In fact, it can be shown that this horseshoe is *hyperbolic* [14]. For a more detailed description of the hyperbolic horseshoe, see Holmes [6]. Here we state only the implications of its existence. We define the invariant set of $F_{r,\omega}$ over Q as

Downloaded 02 May 2010 to 171.66.16.250. Redistribution subject to ASME license or copyright; see http://www.asme.org/terms/Terms_Use.cfm

$$\Lambda_2 = \bigcap_{n=-\infty}^{\infty} F_{r,\omega}^n(Q). \tag{25}$$

(This is the analogue of equation (18).) $F_{r,\omega}$ having a horseshoe implies that Λ_2 contains

(*i*) a countable infinity of unstable periodic orbits, including orbits of arbitrarily long periods;

(*ii*) an uncountable infinity of bounded, nonperiodic orbits;

(*iii*) and a dense orbit.

Doubly infinite symbol sequences are used to identify these orbits [8, 13] since the map is now invertible and we can follow orbits backward. The fact that the horseshoe is hyperbolic implies that each such sequence $\{a_n\}_{n=-\infty}^{\infty}$ corresponds to a single orbit of the map and that the map is stable to small perturbations. Here

$$a_j = 1 \quad \text{if} \quad F_{r,\omega}^j(\phi_0, y_0) \in V_1,$$

and

$$a_j = 2 \quad \text{if} \quad F_{r,\omega}^j(\phi_0, y_0) \in V_2,$$

where $(\phi_0, y_0) \in \Lambda_2$. We do not include the hyperbolicity proof here.

In this section we have extended the $r = 0$ case to $r \neq 0$ small. A complex invariant set for the map has been shown to exist at $r = 0.01$, $\omega = 5$. The existence of this set implies that complicated dynamics can occur and that transient chaos can be expected. However, the asymptotic (steady state) behavior will be dominated by the high impact number, low-period orbits previously described.

7 Discussion

We have shown for inelastic impacts that, while stable periodic orbits exist at almost all forcing frequencies, there also exist more complex dynamics. In fact for some (open sets of) parameter values, infinitely many unstable periodic and nonperiodic orbits coexist with the stable orbit. These unstable orbits can have a dramatic effect on the transient motion of the system, and cause sensitive dependence on initial conditions. The low-period stable periodic orbits are well understood and are found to develop in a regular manner as ω is increased, being created via period doubling followed by successive transitions that reduce that period, and then becoming unstable once more through a period doubling bifurcation that creates the next stable orbit. These stable orbits attract almost all initial conditions. When r is made nonzero, but small, similar results are obtained. However, in the "transitions regions" stable periodic orbits of arbitrarily long period occur, so that the dynamical behavior might appear irregular if observed for only limited times.

This system is a limiting case of the more general system studied by the authors in a previous paper [4]. The analysis in [4] was performed for general r and finite constraint stiffness. In that paper, as in [6], it was shown that sustained chaotic "strange attractor" motions could occur in impacting systems with weak dissipation. Such problems arise in the study of the motions of mechanical systems that have "play" or amplitude constraints. Such systems arise, for example, in impact printer technology [16] and their study is important in the understanding of machinery noise [17, 18]. Piecewise linear equations are also used in the study of nonlinear feedback control systems [19]. The analysis in the present paper demonstrates that very long and irregular transients, as well as arbitrarily long stable periodic motions, may occur in such systems even when the dissipation is very large. Thus, although the addition of energy absorbing dampers may prevent the occurrence of strange attractors, it does not necessarily rule out transient chaos. However, the relatively simple forms of the frequency response curve of Fig. 2 and bifurcation diagram of Fig. 6 enable the practicing engineer to select excitation frequency ranges in which stable low-period responses can be expected to occur, and to predict the peak velocities (and hence amplitudes) of such responses. As the numerical simulations of Fig. 8 show, while unstable chaotic solutions can coexist with stable motions, they generally lead only to brief periods of irregular behavior, provided that the excitation frequency is selected to lie outside a transition region, so as to avoid long period motions.

References

1 Thompson, J. M. T., and Ghaffari, R., "Chaos After Period-Doubling Bifurcations in the Resonance of an Impact Oscillator," *Physics Letters*, Vol. 91*A*, No. 1, 1982, pp. 5–8.

2 Thompson, J. M. T., "Complex Dynamics of Compliant Off-Shore Structures," *Proc. Roy. Soc. Lund.*, Series *A*, Vol. 387, 1983, pp. 407–427.

3 Robinson, F. N. H., "An Experimental Study of the Catastrophic Behavior of a Nonlinear Differential Equation," preprint, Clarendon Laboratory, Oxford, U.K., 1982.

4 Shaw, S. W., and Holmes, P. J., "A Periodically Forced Piecewise Linear Oscillator," to appear in *Journal of Sound and Vibration.*

5 Meriam, J. P., *Dynamics*, Wiley, New York, 1975.

6 Holmes, P. J., "The Dynamics of Repeated Impacts With a Sinusoidally Vibrating Table," *Journal of Sound and Vibration*, Vol. 84, 1982, pp. 173–189.

7 Smale, S., "Diffeomorphisms With Many Periodic Points," in *Differentiable and Combinatorial Topology*, Cairns, S. S., ed., Princeton University Press, 1963, pp. 63–80.

8 Guckenheimer, J., and Holmes, P., *Nonlinear Oscillations, Dynamical Systems, and Bifurcations of Vector Fields*, Springer Verlag, New York, 1983.

9 Senator, M., "Existence and Stability of Periodic Motions of a Harmonically Forced Impacting System," *Journal of Acoustical Society of America*, Vol. 47, 1970, pp. 1390–1397.

10 Feigenbaum, M., "Quantitative Universality for a Class of Nonlinear Transformations," *Journal of Statistical Physics*, Vol. 19, 1978, pp. 25–52.

11 Grebogi, C., Ott, E., and Yorke, J., "Crises, Sudden Changes in Chaotic Attractors and Transient Chaos," Publication 83-037, Laboratory for Plasma and Fusion Energy Studies, College Park, Md., Aug. 1982.

12 Collet, P., and Eckmann, J. P., *Iterated Maps on the Interval as Dynamical Systems*, Progress in Physics, No. 1, Birkhauser, Boston, 1980.

13 Moser, J., *Stable and Random Motions in Dynamical Systems*, Princeton University Press, 1973.

14 Shaw, S. W., Ph.D. Thesis, Dept. of Theoretical and Applied Mechanics, Cornell University, 1983.

15 Shaw, S. W., and Holmes, P. J., "Periodically Forced Linear Oscillator With Impacts: Chaos and Long Period Motions," *Physical Review Letters*, Vol. 51, 1983, pp. 623–626.

16 Hendriks, F., "Bounce and Chaotic Motion in Impact Print Hammers," *IBM Journal*, Vol. 27, 1983, pp. 273–280.

17 Wood, L. A., and Byrne, K. P., "Analysis of a Random Repeated Impact Process," *Journal of Sound and Vibration*, Vol. 78, 1981, pp. 329–345.

18 Wood, L. A., and Byrne, K. P., "Experimental Investigation of a Random Repeated Impact Process," *Journal of Sound and Vibration*, Vol. 85, 1982, pp. 53–69.

19 Sparrow, C. T., "Chaos in a Three-Dimensional Single Loop Feedback System With a Piecewise Linear Feedback Function," *Journal of Mathematical Analysis and Applications*, Vol. 83, 1981, pp. 275–291.

Downloaded 02 May 2010 to 171.66.16.250. Redistribution subject to ASME license or copyright; see http://www.asme.org/terms/Terms_Use.cfm

C. S. Hsu
Professor of Applied Mechanics.
Fellow ASME

R. S. Guttalu
Research Associate.
Mem. ASME

Department of Mechanical Engineering,
University of California,
Berkeley, Calif. 94720

Index Evaluation for Dynamical Systems and Its Application to Locating All the Zeros of a Vector Function

An index evaluation method is discussed in this paper. It can also serve as the basis of a procedure to locate all the zeros of a vector function. An application of the procedure is made to a strongly nonlinear point-mapping dynamical system in order to locate all the periodic solutions of period one and period two, 41 in total number.

1 Introduction

In the analysis of nonlinear dynamics problems, the determination of the global behavior of the systems is probably one of the most difficult. General tools available to us for that purpose are very few. One of them, the Poincaré index theory for a vector field $\mathbf{F}(\mathbf{x})$, [1], is however a remarkable one because it is simple and yet truly global in nature. In the past this theory, although discussed in most of the nonlinear vibration books [2,3], has not seen much utilization in application. It is our belief that as a tool of global analysis the potential of this theory probably has not been fully explored and developed. This paper is a follow-up to [4,5] in which Poincaré's index theory is extended to systems of order higher than two by using a well-known concept in topology, the degree of a map. One sees in [6] that this extended index theory is quite useful since it can be used to establish other interesting analytical results for higher order systems.

In the paper we first describe the basic idea of the index evaluation procedure to be discussed here and the procedure itself. An example of application will be given in Section 4. Next, we show how this index evaluation procedure can be employed to locate *all* the equilibrium and periodic points of a point-mapping dynamical system. Locating these points is usually a necessary step toward a complete understanding of the global behavior of the system. An application of this kind to a highly nonlinear two degree-of-freedom mechanical system will then be given.

With regard to both locating the zeros of vector function and degree evaluation of a map, we wish to mention here many of the recent developments in this area. The classical methods of locating a zero of a function are Newton's method and its many variations. However, unless the zero being searched happens to be a "dominating" one, for a method of this kind to work it is usually necessary to have some prior knowledge of the approximate location of the zero. Often such a prior knowledge is not available and the search process could become a hit and miss proposition. This is particularly true when one wishes to locate *all* the zeros of a function. To alleviate this difficulty many new methods and numerical procedures have been developed in recent years. Most of them are based on the idea of homotopy. Roughly speaking, the idea is as follows. The dimension of the space is increased by one by introducing a parameter t such that at $t=1$ the homotopy reduces to the given function and at $t=0$ it takes on the form of an artificially created function whose zeros are known. Properly devised numerical procedures then allow us to follow a path in the augmented space leading from a known zero at $t=0$ to a zero of the given function at $t=1$. In generating the path, there are two basic approaches: the differential approach and the discrete approach utilizing simplexes. These methods have been called homotopic methods, simplicial methods, continuation methods, complementary pivot methods, and so forth. The references are too numerous to be given here. We will merely cite an excellent review article [7] and also [8–10] which contain several articles on this general topic.

The homotopic methods are quite powerful. However, if one is interested in locating all the zeros in a domain of interest and if the given function is transcendental, instead of having a polynomial form [11], so that even the number of zeros in the domain is unknown, then it is difficult to apply the homotopic method. In those circumstances it seems very unlikely that an exhaustive search can be avoided. Consequently, there is a need of a viable exhaustive search procedure. The method described in Section 3 is aimed to be a procedure of this kind.

With regard to the global task of degree evaluation of a mapping relative to a domain, Stenger [12] and Prüfer and Sieberg [13] have discussed evaluation procedures based on examining the simplexes making up the boundary of the

Contributed by the Applied Mechanics Division and presented at the Winer Annual Meeting, Boston, Mass., November 13–18, 1983 of THE AMERICAN SOCIETY OF MECHANICAL ENGINEERS.

Discussion on this paper should be addressed to the Editorial Department, ASME, United Engineering Center, 345 East 47th Street, New York, N.Y. 10017, and will be accepted until two months after final publication of the paper itself in the JOURNAL OF APPLIED MECHANICS. Manuscript received by ASME Applied Mechanics Division, January, 1983; final revision, May 1983. Paper No. 83-WA/APM-19.

Copies will be available until July, 1984.

Copyright © 1983 by ASME
Downloaded 02 May 2010 to 171.66.16.250. Redistribution subject to ASME license or copyright; see http://www.asme.org/terms/Terms_Use.cfm

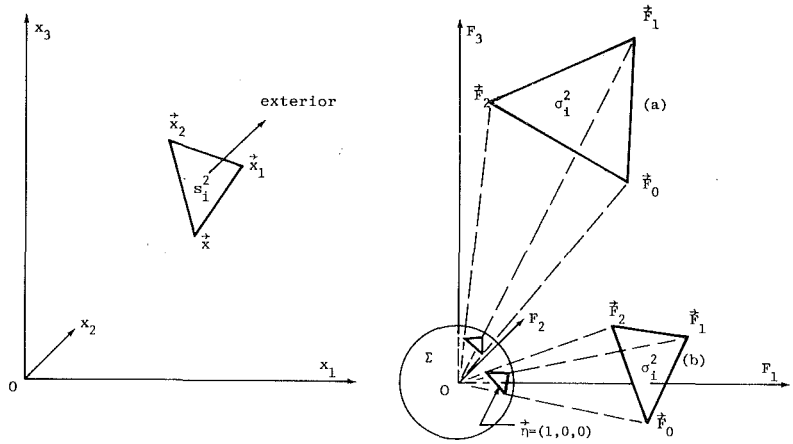


Fig. 1 Covering or not covering of $\vec{\eta}$ by σ_i^{n-1}. Here n is taken to be 3.

domain. The method discussed in Section 2 is in the same category. It differs from that of [13] in not using Sperner simplexes and it differs from [12] in the manner by which the contribution by each boundary simplex to the total degree (or index) value is evaluated.

2 Index Evaluation for an Hypersurface S

Let X^n and F^n be two euclidean n-spaces. Let $\mathbf{F}(\mathbf{x})$ be a function defined over X^n, $\mathbf{F}(\mathbf{x})$: $X^n \rightarrow F^n$. Consider now a collection of small oriented $(n-1)$-simplexes which form a closed oriented hypersurface S and which divides X^n into two parts, the interior and the exterior of S. We write, [14, 15],

$$S = \sum_{i=1}^{N_s} b_i \, s_i^{n-1} \tag{2.1}$$

where s_i^{n-1} is the ith $(n-1)$-simplex in the collection, N_s is the total number of these simplexes, and b_i is the orientation coefficient with value $+1$ or -1. In this paper a simplex will always be an oriented one with its vertices ordered according to a given order.

Let the interior of S be triangulated into N_I number of n-simplexes consistent with the $(n-1)$-simplexes of S. Over each n-simplex the function values of $\mathbf{F}(\mathbf{x})$ at the $(n+1)$ vertices define an affine vector function, [16]. In aggregate, the function values at all the vertices of the n-simplexes define a continuous and piecewise affine function $\mathbf{F}^L(\mathbf{x})$ over S and the interior of S. Assuming that S does not contain any singular points of $\mathbf{F}(\mathbf{x})$, we may ask for the index of S with respect to the given function $\mathbf{F}(\mathbf{x})$, [4]. Having the piecewise affine function $\mathbf{F}^L(\mathbf{x})$ at hand, we can first evaluate the index of S with respect to $\mathbf{F}^L(\mathbf{x})$. If all the s_i^{n-1} are sufficiently small and if S is not extremely near to a singular point of $\mathbf{F}(\mathbf{x})$, we can expect, in general, the index of S with respect to $\mathbf{F}(\mathbf{x})$ to be the same as the index of S with respect to $\mathbf{F}^L(\mathbf{x})$.

Each member s_i^{n-1} of S is mapped by $\mathbf{F}^L(\mathbf{x})$ into an $(n-1)$-simplex σ_i^{n-1} in F^n. Let us denote by $F^L(S)$ the total image of S under $\mathbf{F}^L(\mathbf{x})$. $F^L(S)$ is a collection of N_s number of $(n-1)$-simplexes and is a hypersurface in F^n. To evaluate $I(S,\mathbf{F}^L(\mathbf{x}))$, the index of S with respect to $\mathbf{F}^L(\mathbf{x})$, we use the preimage formula for the degree of a map, [4, 17, 18]:

$$\deg(f) = \sum_{\xi = f^{-1}(\eta)} \deg_\xi(f) \tag{2.2}$$

where f is the map from M^m to N^m, η is any regular value of f in N^m, ξ in M^m is a preimage of η, $\deg_\xi(f)$ is the degree of f at ξ which is $+1$ or -1 depending on whether f is locally orientation preserving or orientation reversing. The summation is over all the preimages of η. For our problem M^m is S, N^m is a unit spherical surface Σ in F^n with its center at the origin, and $m = n-1$.

Now we take the positive F_1-axis of F^n. This ray intersects Σ at $(1,0,\ldots,0)$. We take this to be point η in (2.2). In the most unlikely event that this point is not a suitable one because the map is degenerate at one of its preimages, we only need to replace η by another convenient point. Having η, we proceed to determine (1) how many times a small neighborhood of η on Σ is covered by the map f, and (2) whether the coverage is orientation preserving or reversing each time. We accomplish the first task by examining, one by one, all σ_i^{n-1} in relation to the positive F_1-axis. If σ_i^{n-1} does not intersect with this half axis, it means that η on Σ lies outside the projected spherical triangle of σ_i^{n-1} on Σ, as shown in Fig. 1(a). Hence η is not covered by this simplex. If σ_i^{n-1} does intersect with the positive F_1-axis, then as shown in Fig. 1(b) η is covered by the projected spherical triangle of σ_i^{n-1}. In that case we examine whether the covering is orientation preserving or reversing. If after we search through all the $(n-1)$-simplexes we find a_1 orientation reversing coverings and a_2 orientation preserving coverings, then the degree of the map f, hence the index of S, is given by

$$\deg(f) = I(S,\mathbf{F}^L(\mathbf{x})) = a_2 - a_1. \tag{2.3}$$

Our next task is to implement the preceding idea by devising a simple operational procedure to test whether a simplex σ_i^{n-1} and the positive F_1-axis intersect. Here we make use of the properties of barycentric coordinates of an arbitrary point relative to the vertices of an n-simplex, [14]. Let the vertices of σ_i^{n-1} be $\mathbf{F}_1, \mathbf{F}_2, \ldots, \mathbf{F}_n$. Consider an n-simplex with vertices $\mathbf{O}, \mathbf{F}_1, \mathbf{F}_2, \ldots, \mathbf{F}_n$ where $\mathbf{O}$ is the origin of F^n. Then any point $\mathbf{F}$ in F^n can be expressed as

$$\begin{bmatrix} 1 \\ \mathbf{F} \end{bmatrix} = \begin{bmatrix} 1 & 1 & 1 & . & . & 1 \\ \mathbf{O} & \mathbf{F}_1 & \mathbf{F}_2 & . & . & \mathbf{F}_n \end{bmatrix} \mathbf{t} \tag{2.4}$$

where $\mathbf{t}$ is a column vector with the $(n+1)$ barycentric coordinates $t_j, j = 0,1, \ldots, n$, as it components. Now we take $\mathbf{F}$ to be on the positive F_1-axis so that $F = [f_1, 0, 0, \ldots, 0]^T$, where $f_1 > 0$ and T denotes the transpose. Using this $\mathbf{F}$ in (2.4), we obtain

$$\Psi[t_1, t_2, \ldots, t_n]^T = \mathbf{F} \tag{2.5}$$

where

$$\Psi = [\mathbf{F}_1, \mathbf{F}_2, \ldots, \mathbf{F}_n] \tag{2.6}$$

is an $n \times n$ matrix. Solving (2.5) for t_j, $j = 1,2, \ldots, n$, we obtain

Downloaded 02 May 2010 to 171.66.16.250. Redistribution subject to ASME license or copyright; see http://www.asme.org/terms/Terms_Use.cfm

$$t_j = \frac{f_1\, C_{1j}}{\det \Psi}, \quad j = 1,2, \ldots, n. \tag{2.7}$$

where C_{1j} are the first row cofactors of Ψ. The properties of the barycentric coordinates, [14, 15], then imply the following important result.

Result 2.1. The positive F_1-axis of F^n intersects with σ_i^{n-1} if and only if t_j, $j = 1,2, \ldots, n$, are all positive. Since f_1 and (det Ψ) are common to all t_j, the condition means all C_{1j}, $j = 1,2, \ldots, n$, to be of the same sign.

This result gives us a very simple testing procedure. For each σ_i^{n-1} the matrix Ψ is known. Using any efficient numerical scheme, we compute the cofactors C_{1j} sequentially, one by one, by taking $j = 1,2, \ldots, n$, and compare the sign of the newly computed one against that of C_{11}. Whenever a cofactor with a different sign is found we can immediately conclude that the point η is not covered by the projected spherical triangle of σ_i^{n-1} and we can proceed to test the next simplex σ_{i+1}^{n-1}. When all the cofactors C_{1j}, $j = 1,2, \ldots, n$, are of the same sign, then we compute (det Ψ)

$$\det \Psi = \sum_{i=1}^{n} F_{1j}\, C_{1j} \tag{2.8}$$

where F_{1j} is the first component of $\mathbf{F}_j$. If (det Ψ) has a sign opposite to that of the cofactors, then t_j, $j = 1,2, \ldots, n$, are all negative and again there is no coverage of η so far as σ_i^{n-1} is concerned. We can proceed to the next simplex σ_{i+1}^{n-1}. If (det Ψ) and the cofactors do have the same sign, we have found a covering of η. In that case we proceed to determine the positive or negative sense of the covering, [14, 15].

As mentioned in the Introduction, the present method differs from those of [12, 13]. The difference with [14] may now be explained further. For an n-dimensional mapping the formula given in [12] requires the evaluation of an $n \times n$ determinant (although only with $+1$, 0, -1 entries) for every $(n-1)$-simplex of the boundary. By the present method only cofactors of order $(n-1) \times (n-1)$ are needed. Moreover, for most of the $(n-1)$-simplexes only two or a few of the cofactors need be computed to disqualify them as a contributor to the index value.

3 An Index Method of Locating the Zeros of a Vector Function

In analyzing nonlinear systems it is often necessary to find all the singular points of a vector field. It is interesting that the present method of index evaluation provides us with a viable procedure to search through a domain of interest and to locate approximately all the zeros of a function in the domain under only very minor restrictions. Let the vector field be $\mathbf{F}(\mathbf{x})$ and let the domain of interest D be given by $x_i' \leqq x_i \leqq x_i''$, $i = 1,2, \ldots, n$. Let us adopt a set of sufficiently small interval sizes h_i with $h_i = (x_i'' - x_i')/N_i$ where N_i is the number of intervals in the x_i-direction. We first divide the domain D into n-blocks. Each block is of the size $h_1 \times h_2 \times \ldots \times h_n$. The boundary of each n-block can be triangulated into $2(n!)$ number of $(n-1)$-simplexes. We then take this boundary surface of an n-block as a hypersurface S and evaluate its index with respect to the given function in accordance with the procedure described in Section 2. The outcomes of such an evaluation are the following. In the discussion a higher order zero will be regarded as multiple zeros coalesced.

(*i*) The index is $+1$ or -1. This implies that the given function has a zero inside the n-block or a number of zeros with the sum of their indices equal to $+1$ or -1.

(*ii*) The index is zero. This undoubtedly will be the case for most of the n-blocks. When the index is zero, either there is no zero inside the block or there are several zeros inside with the sum of their indices equal to 0. In this case we conclude that the function has no zero or no sufficiently separated zeros inside the block and proceed to examine the next n-block.

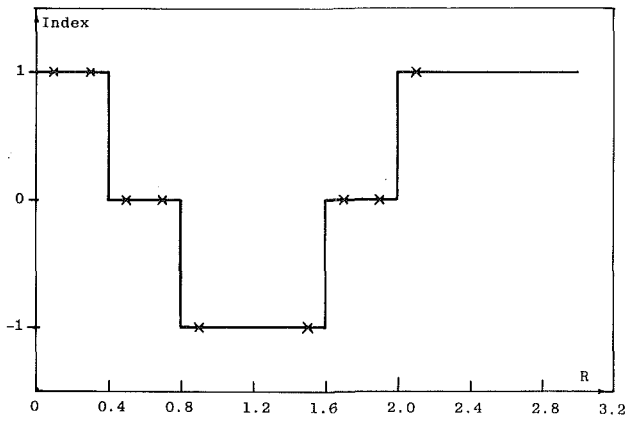


Fig. 2 Variation of the index of an expanding cube as a function of the cube size *R*, for Example (1)

(*iii*) The index is an integer other than -1, 0, $+1$. This implies there are several zeros inside the block. In this case we could divide the block into a number of smaller subblocks. For each of the subblocks we repeat the index evaluation. This subdivision can be repeated as often as necessary until the index obtained for a subblock is either ± 1 or 0.

In this manner each n-block within the domain of interest is searched for the presence of a zero. Many $(n-1)$-simplexes are shared by the adjacent blocks. Provisions are made so that any duplication of testing is avoided. If the interval sizes are chosen reasonably small, then at the end of the search we would have discovered all the simple zeros that are mutually apart by a distance larger than h_i in each x_i-direction, $i = 1,2, \ldots, n$. Here, we observe that there are two types of zeros that might not be discovered by this method. The first type involves cases where several zeros reside in one n-block and have a net index equal to zero. The second type involves higher order zeros with an index zero. The inability of the method to deal with these zeros is to be expected. The first type of zeros can, of course, still be discovered if we elect to use smaller interval sizes. On the other hand, the difficulty with the second type is inherent and cannot be circumvented by taking smaller h_i values.

After a zero-containing n-block has been found, we can follow two routes to refine the location of the discovered zero. One is simply to take the center of the n-block as the approximate location and proceed to apply any iteration method of Newton's type to refine the zero. The second route is to divide this particular n-block into smaller subblocks and to apply the index evaluation procedure to search for the subblock that contains the discovered zero. This step can be repeated to form an iteration procedure. It leads to a set of nested subblocks enclosing the desired zero. The process is terminated when the size of the subblock becomes smaller than the required accuracy.

4 Examples of Application

We present here two examples of application of the method.

(1) A Third-Order System. First we consider a nonlinear system with a *known* distribution of singular points.

$$\begin{aligned} \dot{x}_1 &= F_1(x_1,x_2,x_3) = x_2(x_2 + 0.8)(x_2 - 1) \\ \dot{x}_2 &= F_2(x_1,x_2,x_3) = x_3 \\ \dot{x}_3 &= F_3(x_1,x_2,x_3) = x_1(x_1 + 0.2)(x_1 - 0.4). \end{aligned} \tag{4.1}$$

Downloaded 02 May 2010 to 171.66.16.250. Redistribution subject to ASME license or copyright; see http://www.asme.org/terms/Terms_Use.cfm

Table 1 Example (2). $P-1$ solutions and their indices

No.	Solution	Index w.r.t. $\mathbf{F}=\mathbf{G}-\mathbf{I}$	Index w.r.t. $\mathbf{F}=\mathbf{G}^2-\mathbf{I}$
1	$(-\pi, -\pi, 0, 0)$	1	1
2	$(-\pi, 0, 0, 0)$	1	1
3	$(-\pi, \pi, 0, 0)$	1	1
4	$(-\pi/2, -\pi/2, 0, 0)$	−1	1
5	$(-\pi/2, \pi/2, 0, 0)$	−1	1
6	$(0, -\pi, 0, 0)$	1	1
7	$(0, 0, 0, 0)$	1	1
8	$(0, \pi, 0, 0)$	1	1
9	$(\pi/2, -\pi/2, 0, 0)$	−1	1
10	$(\pi/2, \pi/2, 0, 0)$	−1	1
11	$(\pi, -\pi, 0, 0)$	1	1
12	$(\pi, 0, 0, 0)$	1	1
13	$(\pi, \pi, 0, 0)$	1	1

Table 2 Example (2). P − 2 solutions and their indices

No.	Solution	Index
14	$(0.33419\pi, 0, 0.48025\pi, 0)$	1
15	$(-0.33419\pi, 0, -0.48025\pi, 0)$	1
16	$(0, 0.24702\pi, 0, 0.24699\pi)$	1
17	$(0, -0.24702\pi, 0, -0.24699\pi)$	1
18	$(0.09648\pi, 0.18318\pi, 0.13864\pi, 0.18316\pi)$	−1
19	$(-0.09648\pi, -0.18318\pi, -0.13864\pi, -0.18316\pi)$	−1
20	$(-0.09648\pi, 0.18318\pi, -0.13864\pi, 0.18316\pi)$	−1
21	$(0.09648\pi, -0.18318\pi, 0.13864\pi, -0.18316\pi)$	−1
N22	$(-0.66580\pi, -\pi, 0.48025\pi, 0)$	1
N23	$(0.66580\pi, -\pi, -0.48025\pi, 0)$	1
N24	$(-0.66580\pi, \pi, 0.48025\pi, 0)$	1
N25	$(0.66580\pi, \pi, -0.48025\pi, 0)$	1
N26	$(\pi, -0.75298\pi, 0, 0.24699\pi)$	1
N27	$(\pi, 0.75298\pi, 0, -0.24699\pi)$	1
N28	$(-\pi, -0.75298\pi, 0, 0.24699\pi)$	1
N29	$(-\pi, 0.75298\pi, 0, -0.24699\pi)$	1
N30	$(0.90352\pi, 0.81682\pi, -0.13864\pi, -0.18316\pi)$	−1
N31	$(-0.90352\pi, -0.81682\pi, 0.13864\pi, 0.18316\pi)$	−1
N32	$(0.90352\pi, -0.81682\pi, -0.13864\pi, 0.18316\pi)$	−1
N33	$(-0.90352\pi, 0.81682\pi, 0.13864\pi, -0.18316\pi)$	−1
N34	$(0.34989\pi, -0.64408\pi, -0.21572\pi, -0.14406\pi)$	−1
N35	$(0.65011\pi, -0.35592\pi, 0.21572\pi, 0.14406\pi)$	−1
N36	$(0.34989\pi, 0.64408\pi, -0.21572\pi, 0.14406\pi)$	−1
N37	$(0.65011\pi, 0.35592\pi, 0.21572\pi, -0.14406\pi)$	−1
N38	$(-0.34989\pi, -0.64408\pi, 0.21572\pi, -0.14406\pi)$	−1
N39	$(-0.65011\pi, -0.35592\pi, -0.21572\pi, 0.14406\pi)$	−1
N40	$(-0.34989\pi, 0.64408\pi, 0.21572\pi, 0.14406\pi)$	−1
N41	$(-0.65011\pi, 0.35592\pi, -0.21572\pi, -0.14406\pi)$	−1

The singular points and their indices are:

No.1: $(0,0,0), +1$; No. 2: $(-0.2,0,0), -1$;

No. 3: $(0.4,0,0), -1$; No. 4: $(0, -0.8, 0), -1$;

No. 5: $(-0.2, -0.8, 0), +1$; No. 6: $(0.4, -0.8, 0), +1$;

No. 7: $(0,1,0), -1$; No. 8: $(-0.2,1,0), +1$;

No. 9: $(0.4,1,0), +1$. (4.2)

For the hypersurface S we take an expanding three-dimensional cube with an increasing edge size R. The interval sizes in the x_1, x_2, and x_3-directions are all taken to be 0.1. The index evaluation results are shown in Fig. 2 where the variation of the index with the cube size R is shown. The solid line indicates how this relation should be and the cross points show the results of the index evaluation.

(2) A Fourth-Order System. As a second example we apply the method to a mechanical system with two degrees of freedom. The system consists of two identical rigid bars free to rotate about a common axis. The bars are connected to the stationary support as well as coupled to each other through rotational dampers. The two bodies are subjected to synchonized periodic impact loads of fixed direction at a distance

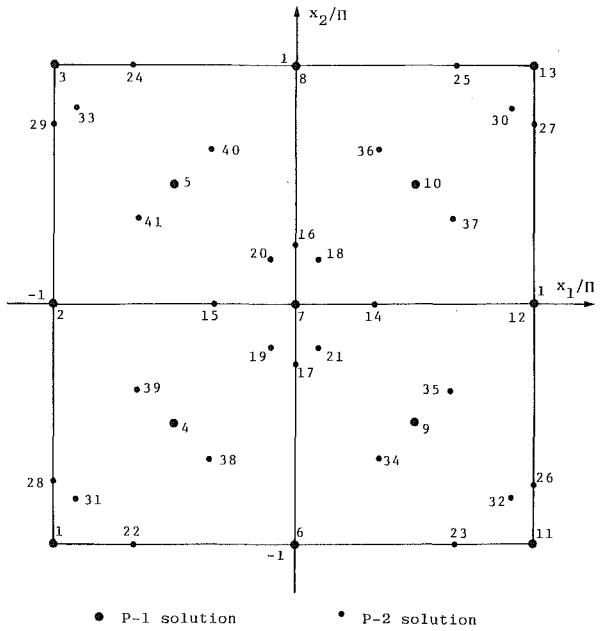


Fig. 3 Example (2). Distribution of the discovered $P-1$ and $P-2$ solutions in the x_1-x_2 plane.

l from the axis of rotation. The motion of the system can be formulated, [19], in terms of a fourth-order point mapping:

$$\begin{aligned} x_1(n+1) &= G_1(\mathbf{x}(n)) = x_1(n) + C_1[x_3(n) \\ &\quad - \alpha \sin x_1(n) \cos x_2(n)], \\ x_2(n+1) &= G_2(\mathbf{x}(n)) = x_2(n) + C_2[x_4(n) \\ &\quad - \alpha \cos x_1(n) \sin x_2(n)], \\ x_3(n+1) &= G_3(\mathbf{x}(n)) = D_1[x_3(n) \\ &\quad - \alpha \sin x_1(n) \cos x_2(n)], \\ x_4(n+1) &= G_4(\mathbf{x}(n)) = D_2[x_4(n) \\ &\quad - \alpha \cos x_1(n) \sin x_2(n)], \end{aligned} \tag{4.3}$$

where

$$D_1 = \exp(-2\mu_1),\ D_2 = \exp(-2\mu_2),\ C_1 = \frac{1-D_1}{2\mu_1},$$

$$C_2 = \frac{1-D_2}{2\mu_2}. \tag{4.4}$$

Here x_1 and x_2 are, respectively, the angular displacements of the in-phase and out-of-phase modes, and x_3 and x_4 the corresponding angular velocities. For the detail of the derivation the reader is referred to [19]. This seemingly simple system has an extremely complicated behavior pattern. In [19] some $P-1$ and $P-2$ solutions were found. However, it was not certain that all the $P-2$ solutions had been found, particularly the unstable ones. Therefore, the present method is applied to this problem. The case reported here is for $\alpha=5$, $\mu_1=0.1\pi$, $\mu_2=0.2\pi$. The domain of interest is taken to be $x_1'=x_2'=-1.02\pi$, $x_1''=x_2''=1.02\pi$, $x_3'=x_4'=-0.5\pi$, $x_3''=x_4''=0.5\pi$. In [19] it is shown that within this domain there are 13 $P-1$ solutions. They are listed in Table 1 together with their indices. Some solutions in the table represent physically one and the same solution. However, for this example of illustrating the method of finding zeros, each will be considered as a separate singular point of $\mathbf{F}(\mathbf{x})$. To locate the $P-1$ solutions we take $\mathbf{F}(\mathbf{x})=(\mathbf{G}-\mathbf{I})(\mathbf{x})$ and $N_1=N_2=N_3=N_4=15$. The computation indeed locates 13 blocks containing the 13 $P-1$ solutions listed in Table 1.

For the $P-2$ solutions $\mathbf{F}(\mathbf{x})$ is taken to be $(\mathbf{G}^2-\mathbf{I})(\mathbf{x})$ and N_1, N_2, N_3, and N_4 are all taken to be 31. Located by the

Downloaded 02 May 2010 to 171.66.16.250. Redistribution subject to ASME license or copyright; see http://www.asme.org/terms/Terms_Use.cfm

computation are 41 blocks, each containing a $P-2$ solution. Among these 41 $P-2$ solutions are the 13 solutions of Table 1, because $P-1$ solutions will also show up as $P-2$ solutions. With the approximate locations of the solutions known, it is easy to find the precise locations. The 28 true $P-2$ solutions are listed in Table 2. The solutions Nos. 14–21 have been found in [19]. The other Nos. 22–41 are 20 new $P-2$ solutions discovered by this zero-finding procedure. Some of the new 20 soutions represent physically the same solutions as Nos. 14–21. However, even after removing these, there remain eight new mixed-mode $P-2$ solutions which *were not anticipated* in [19]. In Fig. 3 we display in the x_1-x_2 plane all the discovered $P-1$ and $P-2$ solutions. The pairing of the $P-2$ solutions is as follows: Nos. (14, 15), (16, 17), (18, 19), (20, 21), (34, 35), (36, 37), (38, 39), (40, 41). The pairing solutions of Nos. 22–33 lie outside the domain shown.

Acknowledgments

This material is based on work supported by the National Science Foundation under Grant No. MEA-8217471.

References

1 Coddington, E. A., and Levinson, N., *Theory of Ordinary Differential Equations*, McGraw-Hill, New York, 1955.

2 Minorsky, N., *Nonlinear Oscillations*, D. Van Nostrand, Princeton, N.J., 1962.

3 Hagedorn, P., *Nonlinear Oscillations*, Oxford University Press, Oxford, 1981.

4 Hsu, C. S., "Theory of Index for Dynamical Systems of Order Higher Than Two," ASME JOURNAL OF APPLIED MECHANICS, Vol. 47, 1980, pp. 421–427.

5 Guttalu, R. S., and Hsu, C. S., "Index Evaluation for Nonlinear Systems of Order Higher Than Two," ASME JOURNAL OF APPLIED MECHANICS, Vol. 49, 1982, pp. 241–243.

6 Hsu, C. S., "Theory of Index and a Generalized Nyquist Criterion," *International Journal of Nonlinear Mechanics*, Vol. 15, 1980, pp. 349–354.

7 Allgower, E., and Georg, K., "Simplicial and Continuation Methods for Approximating Fixed Points and Solutions to Systems of Equations," *SIAM Review*, Vol. 22, 1980, pp. 28–85.

8 Karamardian, S., ed., *Fixed Points, Algorithms and Applications*, Academic Press, New York, 1977.

9 Peitgen, H. O., and Walther, H. O., *Functional Differential Equations and Approximation of Fixed Points*, Springer-Verlag, New York, 1979.

10 Forster, W., ed., *Numerical Solution of Highly Nonlinear Problems*, North-Holland, Amsterdam, 1980.

11 Chow, S. N., Mallet-Paret, J., and Yorke, J. A., "Homotopy Method for Locating All Zeros of a System of Polynomials," in *Functional Differential Equations and Approximation of Fixed Points*, Springer-Verlag, New York, 1979, pp. 77–88.

12 Stenger, F., "Computing the Topological Degree of a Mapping in R^n," *Numerische Mathematik*, Vol. 25, 1975, pp. 23–38.

13 Prüfer, M., and Siegberg, H. W., "On Computational Aspects of Topological Degree in R^n," in *Functional Differential Equations and Approximation of Fixed Points*, Springer-Verlag, New York, 1979, pp. 410–433.

14 Lefschetz, S., *Introduction to Topology*, Princeton University Press, Princeton, N.J., 1949.

15 Aleksandrov, P. S., *Combinatorial Topology*, Vol. 1, Graylock Press, Rochester, N.Y., 1956.

16 Nomizu, K., *Fundamentals of Linear Algebra*, McGraw-Hill, New York, 1966.

17 Arnold, V. I., *Ordinary Differential Equations*, The M. I. T. Press, Cambridge, Mass., 1973.

18 Guillemin, V., and Pollack, A., *Differential Topology*, Prentice-Hall, Englewood Cliffs, N.J., 1974.

19 Hsu, C. S., "Nonlinear Behavior of Multibody Systems Under Impulsive Parametric Excitation," *Dynamics of Multibody Systems*, Magnus K., ed; Springer-Verlag, New York, 1978, pp. 63–74.

Downloaded 02 May 2010 to 171.66.16.250. Redistribution subject to ASME license or copyright; see http://www.asme.org/terms/Terms_Use.cfm

An Alternative Analysis of the Plane Stick-Slip Problem[1]

A. Dutta[2]
Chemical Engineering Division,
National Chemical Laboratory,
Pune-411008, India

The plane stick-slip problem has been solved analytically using the separation of variable technique. The essence of the mathematical procedure is to solve the problem separately for the "stick" and the "slip" regions and then to match the two solutions at the exit plane. The present solution, which is relatively easy to evaluate, yields results that compare favorably with those obtained by the Wiener-Hopf technique. Furthermore, the stick-slip solution has been used to estimate the expansion of a two-dimensional plane Newtonian jet at very low Reynolds numbers. For capillary numbers less than 0.1, the approximate method predicts swell ratios that are in fairly good agreement with those obtained from a more elaborate numerical solution of the jet swell problem.

1 Introduction

In recent years, the phenomenon of Newtonian jet swell has received considerable attention in the literature. The flow situation, which is associated with this phenomenon, is essentially that of a low-speed Newtonian jet emerging from a conduit into an inviscid medium in the absence of gravity. Experimental investigations indicate that there occurs a rearrangement in flow from a fully developed state within the conduit to a uniform flow far downstream [1, 2], and this adjustment results in appreciable swelling of the jet [3–5]. In particular, about a 10–25 percent increase in jet dimensions has been reported for circular and plane jets.

Even though no analytical solution of the jet swell problem is available at the present time, numerical solutions based on various finite element formulations have been reported in the literature [6–12]. In addition, a considerably simpler and efficient finite difference technique has recently been developed by the author to solve the Newtonian jet swell problem [13, 14]. The latter study, which employs an iterative solution scheme, indicates that considerable savings in computational effort can be achieved by feeding the (numerical) stick-slip solution as the initial guess in order to start the numerical solution procedure. It therefore follows that an analytical solution of the stick-slip problem, which can readily be implemented for numerical calculations will significantly aid the efficiency of the computational algorithm developed for analyzing the Newtonian jet swell phenomenon.

The plane stick-slip problem, as discussed by Richardson [15], is the two-dimensional creeping flow of a Newtonian liquid between two infinite parallel planes located at $y = \pm H$. For $x < 0$, the walls are rigid and hence the fluid sticks to it, whereas for $x > 0$, the fluid slips at the boundaries thereby resulting in a zero shear stress condition. An analytical solution of this problem has been presented by Richardson using the Wiener-Hopf technique. Apart from the presence of the free-surface, the stick-slip problem closely resembles the jet swell phenomenon. Consequently, besides offering considerable insight into the hydrodynamics of the swelling phenomenon, the stick-slip problem has proved to be an ideal model case for the various numerical schemes developed for studying the more involved problem of jet swell [6, 10, 13].

In this work, an alternative solution procedure employing the separation of variables method is presented. The approach followed is similar to that developed by Vrentas and Duda [16] for describing the flow development in circular conduits. As indicated by Trogdon and Joseph [17], the present (eigenfunction) method is much easier to implement than the Wiener-Hopf technique. This is an important consideration if the solution is to be effectively used as an initial starting point for the numerical analysis of Newtonian jet swell. Moreover, the stick-slip solution itself provides valuable qualitative understanding of the complex flow process occurring within the exit region of a plane jet flow.

The present work, therefore, is concerned with the analytical solution of the plane stick-slip problem using the eigenfunction method. The solution, thus obtained, has been utilized to estimate the swelling of a plane Newtonian jet by means of an expansion procedure suggested by Richardson [15].

2 Mathematical Formulation

We consider the steady, two-dimensional, creeping flow of an incompressible Newtonian liquid in Cartesian (x, y) plane as shown schematically in Fig. 1. For convenience, the distances are nondimensionalized by H (half of die opening) and the velocities by the average velocity, V. Incompressibility implies the existence of a stream-function, ψ, such that

$$v = \frac{\partial \psi}{\partial y}, \quad u = -\frac{\partial \psi}{\partial x} \tag{1}$$

[1] NCL Communication No. 2794

[2] Present Address: Applications Research and Development (Rubber Chemicals), The Alkali and Chemical Corporation of India Ltd., Rishra, Hooghly 712248, West Bengal, India.

Contributed by the Applied Mechanics Division for publication in the JOURNAL OF APPLIED MECHANICS.

Discussion on this paper should be addressed to the Editorial Department, ASME, United Engineering Center, 345 East 47th Street, New York, N.Y. 10017, and will be accepted until two months after final publication of the paper itself in the JOURNAL OF APPLIED MECHANICS. Manuscript received by ASME Applied Mechanics Division August, 1982; final revision, February, 1983.

Copyright © 1983 by ASME
Downloaded 02 May 2010 to 171.66.16.250. Redistribution subject to ASME license or copyright; see http://www.asme.org/terms/Terms_Use.cfm

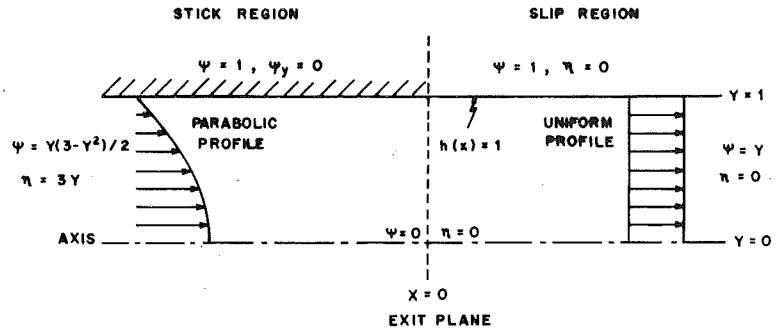


Fig. 1 Schematic representation of the plane stick-slip problem

where v and u are the velocities in the x and y directions, respectively. If vorticity, η, is defined as

$$\eta = \frac{\partial u}{\partial x} - \frac{\partial v}{\partial y} \tag{2}$$

then the stream-function equation becomes

$$\frac{\partial^2 \psi}{\partial x^2} + \frac{\partial^2 \psi}{\partial y^2} = -\eta \tag{3}$$

Neglecting the convective terms, the vorticity transport equation can be written as

$$\frac{\partial^2 \eta}{\partial x^2} + \frac{\partial^2 \eta}{\partial y^2} = 0 \tag{4}$$

The problem thus involves solution to equations (3) and (4) subject to the boundary conditions as indicated in Fig. 1. The essence of the solution procedure is to generate solutions for the stick and the slip regions separately and then to match the two solutions at the exit plane located at $x = 0$.

3 Solution for the Slip Region, $x > 0$

Within the slip region we assume that

$$\eta[x, y] = X[x]\,Y[y] \tag{5}$$

Substituting equation (5) in equation (4) and making use of the conditions that $X[\infty] = Y[0] = Y[1] = 0$, the following expression for the vorticity results

$$\eta = \sum_{n=1}^{\infty} A_n \,\mathrm{Sin}\alpha_n y \exp\left[-\alpha_n x\right] \tag{6}$$

where $\alpha_n = n\pi$, $n = 1, 2, 3 \ldots$ are the eigenvalues and A_n are unknown constants to be determined later.

For the stream function, we take $\psi = \psi^+ + y$ such that equation (3) becomes

$$\frac{\partial^2 \psi^+}{\partial x^2} + \frac{\partial^2 \psi^+}{\partial y^2} = -\eta \tag{7}$$

and $\psi^+ = 0$ at the boundaries. The nth eigenfunction for the solution of equation (7) is assumed to be of the following form:

$$\psi^+_n = X^+_n[x] \,\mathrm{Sin}\, \alpha_n y \tag{8}$$

Substitution of equation (8) in equation (7) yields the following ordinary differential equation:

$$\frac{d^2 X^+_n}{dx^2} - \alpha_n^2 X^+_n = -A_n \exp\left[-\alpha_n x\right] \tag{9}$$

Equation (9) can readily be solved to give the expression for ψ^+ as

$$\psi^+ = \sum_{n=1}^{\infty} \left(B_n + \frac{A_n x}{2\alpha_n}\right) \exp\left[-\alpha_n x\right] \mathrm{Sin}\, \alpha_n y \tag{10}$$

Thus, the stream function for the slip region can be written as

$$\psi = y + \sum_{n=1}^{\infty} \left(B_n + \frac{A_n x}{2\alpha_n}\right) \exp\left[-\alpha_n x\right] \mathrm{Sin}\, \alpha_n y \tag{11}$$

Once ψ is known, the velocities u and v can readily be obtained by appropriate differentiation of equation (11).

4 Solution for the Stick Region, $x < 0$

For the stick region of the flow field the nature of the no-slip conditions (at $y = 1$) poses certain mathematical difficulties. To circumvent these difficulties the problem in the upstream section is split into two separate problems which when combined give the desired solution. Hence, for $x < 0$, it is assumed that

$$\eta = 3y + \eta_1 + \eta_2 \tag{12}$$

and

$$\psi = \frac{3}{2} y - \frac{1}{2} y^3 + \psi_1 + \psi_2 \tag{13}$$

Substitution of equations (12) and (13) into equations (3) and (4) results in the following set of governing equations:

$$\frac{\partial^2 \psi_i}{\partial x^2} + \frac{\partial^2 \psi_i}{\partial y^2} = -\eta_i \tag{14}$$

and

$$\frac{\partial^2 \eta_i}{\partial x^2} + \frac{\partial^2 \eta_i}{\partial y^2} = 0 \tag{15}$$

where $i = 1, 2$. The appropriate boundary conditions then become

$$-\infty \le x < 0, \quad y = 0, \quad \psi_i = 0, \quad \eta_i = 0 \tag{16a}$$

$$-\infty \le x < 0, \quad y = 1, \quad \psi_i = 0, \quad \eta_1 = 0, \quad \frac{\partial \psi_2}{\partial y} = -\frac{\partial \psi_1}{\partial y} \tag{16b}$$

$$x = -\infty, \quad 0 \le y \le 1, \quad \psi_i = 0, \quad \eta_i = 0 \tag{16c}$$

A solution procedure, analogous to that employed in the preceding section to derive equations (6) and (10) can also be used to solve for η_1 and ψ_1. The solutions can be written as

$$\eta_1 = \sum_{n=1}^{\infty} C_n \exp\left[\alpha_n x\right] \mathrm{Sin}\, \alpha_n y \tag{17}$$

$$\psi_1 = \sum_{n=1}^{\infty} \left(D_n + \frac{C_n x}{2\alpha_n}\right) \exp[\alpha_n x] \,\mathrm{Sin}\, \alpha_n y \tag{18}$$

and the function $f[x] = \partial \psi_1 / \partial y|_{y=1}$ then becomes

$$f[x] = \sum_{n=1}^{\infty} \left(\alpha_n D_n + \frac{C_n x}{2}\right) \exp[\alpha_n x] \,\mathrm{Cos}\, \alpha_n \tag{19}$$

Downloaded 02 May 2010 to 171.66.16.250. Redistribution subject to ASME license or copyright; see http://www.asme.org/terms/Terms_Use.cfm

For η_2, we take the solution to be of the form $\eta_2 = X_2[x]\, Y_2[y]$. The general solution for η_2 can then be obtained as

$$\eta_2 = \int_0^\infty [E(\beta)\,\mathrm{Cos}\,\beta x + F(\beta)\,\mathrm{Sin}\,\beta x]\,\mathrm{Sinh}(\beta y)\,d\beta \tag{20}$$

where the integral represents an infinite set of solutions corresponding to all positive values of β. Similarly for ψ_2, we assume the solution to be of the form

$$\psi_2 = [E(\beta)\,\mathrm{Cos}\,\beta x + F(\beta)\,\mathrm{Sin}\,\beta x]\,S(y) \tag{21}$$

and general solution for ψ_2 can be expressed as

$$\psi_2 = \int_0^\infty [E(\beta)\,\mathrm{Cos}\,\beta x + F(\beta)\,\mathrm{Sin}\,\beta x]\,\frac{\mathrm{Cosh}(\beta)\mathrm{Sinh}(\beta y) - y\,\mathrm{Sinh}\,(\beta)\,\mathrm{Cosh}\,(\beta y)}{2\beta\,\mathrm{Sinh}\,(\beta)}\,d\beta \tag{22}$$

From equations (16*b*) and (22), the function $f[x]$ then becomes

$$-f[x] = \frac{\partial \psi_2}{\partial y}\bigg|_{y=1} = \int_0^\infty [E(\beta)\mathrm{Cos}\beta x + F(\beta)\mathrm{Sin}\beta x]\,\frac{\beta\mathrm{Cosh}^2\beta - \mathrm{Sinh}\beta\,\mathrm{Cosh}\beta - \beta\mathrm{Sinh}^2\beta}{2\beta\,\mathrm{Sinh}\,\beta}\,d\beta \tag{23}$$

We now represent the function $-f[x]$ by means of a Fourier integral as suggested by Vrentas and Duda [16]. Thus, assuming that $-f[x]$ is an even function, its Fourier integral representation becomes

$$-f[x] = \frac{2}{\pi}\int_0^\infty \mathrm{Cos}\beta x d\beta \int_0^{-\infty} f(s)\,\mathrm{Cos}\beta\, sds \tag{24}$$

Comparing equation (24) with equation (23), we get

$$F[\beta] = 0 \tag{25}$$

and

$$E[\beta] = \frac{4\beta\,\mathrm{Sinh}\,\beta}{\pi[\beta - \mathrm{Sinh}\beta\,\mathrm{Cosh}\beta]}\int_0^{-\infty} f[s]\,\mathrm{Cos}\,\beta s\,ds \tag{26}$$

Substitution of equation (19) in equation (26) gives $E[\beta]$as

$$E[\beta] = \frac{-4\beta\,\mathrm{Sinh}\,\beta}{\pi[\beta - \mathrm{Sinh}\beta\,\mathrm{Cosh}\beta]}\left[\sum_{n=1}^\infty \frac{D_n\alpha_n{}^2\mathrm{Cos}\,\alpha_n}{\alpha_n{}^2+\beta^2} + \sum_{n=1}^\infty \frac{C_n[\alpha_n{}^2-\beta^2]\mathrm{Cos}\,\alpha_n}{2[\alpha_n{}^2+\beta^2]^2}\right] \tag{27}$$

Combination of equations (12), (13), (17), (18), (20), (22), (25), and (27) yields the following expressions for the vorticity and the stream function within the stick region:

$$\eta = 3y + \sum_{n=1}^\infty C_n\,\exp[\alpha_n x]\,\mathrm{Sin}\,\alpha_n y - \sum_{n=1}^\infty D_n\alpha_n{}^2\mathrm{Cos}\,\alpha_n \int_0^\infty \frac{P[\beta]\,\mathrm{Sinh}\,\beta y\,\mathrm{Cos}\,\beta x}{\alpha_n^2+\beta^2}\,d\beta - \sum_{n=1}^\infty \frac{C_n\mathrm{Cos}\,\alpha_n}{2}\int_0^\infty \frac{[\alpha_n{}^2-\beta^2]P[\beta]\,\mathrm{Sinh}\,\beta y\,\mathrm{Cos}\,\beta x}{[\alpha_n{}^2+\beta^2]^2}\,d\beta \tag{28}$$

and

$$\psi = \frac{y}{2}[3-y^2] + \sum_{n=1}^\infty \left[D_n - \frac{C_n x}{2\alpha_n}\right]\exp[\alpha_n x]\,\mathrm{Sin}\,\alpha_n y - \sum_{n=1}^\infty D_n\alpha_n{}^2\mathrm{Cos}\,\alpha_n \int_0^\infty \frac{P[\beta]Z[\beta,y]\,\mathrm{Cos}\,\beta x}{\alpha_n{}^2+\beta^2}\,d\beta - \sum_{n=1}^\infty \frac{C_n\mathrm{Cos}\,\alpha_n}{2}\int_0^\infty \frac{P[\beta]Z[\beta,y][\alpha_n{}^2-\beta^2]\mathrm{Cos}\,\beta x}{[\alpha_n{}^2+\beta^2]^2}\,d\beta \tag{29}$$

where

$$P[\beta] = \frac{4\beta\,\mathrm{Sinh}\,\beta}{\pi[\beta - \mathrm{Sinh}\,\beta\,\mathrm{Cosh}\,\beta]} \tag{30}$$

and

$$Z[\beta, y] = \frac{\mathrm{Cosh}\,\beta\,\mathrm{Sinh}\,\beta y - y\,\mathrm{Sinh}\,\beta\,\mathrm{Cosh}\,\beta y}{2\beta\,\mathrm{Sinh}\,\beta}$$

From the preceding analysis it may not be obvious how the upstream conditions $\psi_2 = \eta_2 = 0$ at $x = -\infty$ is satisfied. This feature, however, is implicit in the assumption that the solutions could be represented by means of Fourier integrals of even functions. That is, all the integrals of the form $\int_0^\infty g[\beta, y]\,\mathrm{Cos}\,\beta x\,d\beta$ are proportional to exp $[ax]$ where g is a function of β and y and a is a positive constant. At upstream locations infinitely far away from the exit plane the integrals in equations (20), (22), and (24) vanish, which implies that $\psi_2 = \eta_2 = f[x] = 0$ at $x = -\infty$.

5 Determination of Constants

The analytical solution presented in the foregoing involves four unknown constants, namely, A_n, B_n, C_n, and D_n. These are determined by matching the solutions for the stick and the slip regions at the exit plane, $x = 0$. Since both the stream function and the vorticity need to be continuous at $x = 0$ along with their derivatives, it implies that

$$\eta(0^-, y) = \eta(0^+, y) \tag{31a}$$

$$\psi(0^-, y) = \psi(0^+, y) \tag{31b}$$

$$\frac{\partial\eta(0^-,y)}{\partial x} = \frac{\partial\eta(0^+,y)}{\partial x} \tag{31c}$$

$$\frac{\partial\psi(0^-,y)}{\partial x} = \frac{\partial\psi(0^+,y)}{\partial x} \tag{31d}$$

Equations (6), (28), and (31*c*) suggest that $A_n = -C_n$ and from equations (10), (29), and (31*d*) it can be shown that $B_n = -D_n$. Equations (31*a*) and (31*b*) are now used to determine C_n and D_n. By substituting equations (6) and (28) into equation (31*a*), multiplying by Sin $\alpha_m y$ and integrating the resulting expression with respect to y between the limits 0 and 1 yields

$$C_m - \frac{3\,\mathrm{Cos}\,\alpha_m}{\alpha_m} + \sum_{n=1}^\infty D_n\alpha_n{}^2\,\mathrm{Cos}\,\alpha_n \int_0^\infty \frac{P[\beta]\alpha_m\,\mathrm{Cos}\,\alpha_m\mathrm{Sinh}\beta}{[\alpha_m{}^2+\beta^2][\alpha_n{}^2+\beta^2]}\,d\beta + \sum_{n=1}^\infty \frac{C_n\mathrm{Cos}\,\alpha_n}{2}\int_0^\infty \frac{P[\beta][\alpha_n{}^2-\beta^2]\alpha_m\,\mathrm{Cos}\,\alpha_m\,\mathrm{Sinh}\beta}{[\alpha_m{}^2+\beta^2][\alpha_n{}^2+\beta^2]^2}\,d\beta = 0 \tag{32}$$

Similarly from equations (10), (29), and (31*b*) one gets the following expression

$$D_m - \frac{3\,\mathrm{Cos}\,\alpha_m}{\alpha_m{}^3} - \sum_{n=1}^\infty D_n\alpha_n{}^2\,\mathrm{Cos}\,\alpha_n\int_0^\infty \frac{P[\beta]I[\beta,\alpha_m]}{\alpha_n{}^2+\beta^2}\,d\beta - \sum_{n=1}^\infty \frac{C_n\,\mathrm{Cos}\,\alpha_n}{2}\int_0^\infty \frac{P[\beta][\alpha_n{}^2-\beta^2]I[\beta,\alpha_m]}{[\alpha_n{}^2+\beta^2]^2}\,d\beta = 0 \tag{33}$$

where

Downloaded 02 May 2010 to 171.66.16.250. Redistribution subject to ASME license or copyright; see http://www.asme.org/terms/Terms_Use.cfm

$$I[\beta,\alpha_m] = -\frac{\alpha_m \operatorname{Cos}\alpha_m \operatorname{Sinh}\beta}{[\alpha_m{}^2+\beta^2]} \tag{34}$$

Equations (32) and (33), which represent two infinite sets of linear algebraic equations, permit determination of the unknown constants C_n and D_n. Consequently, the solution of the plane stick-slip problem becomes formally complete.

6 Jet Swell for Large Surface Tension

We now consider the creeping flow of a two-dimensional plane jet in the absence of gravity. At the free surface, $h(x)$, the shear stress must vanish, therefore

$$4h_x\psi_{xy} + [\psi_{xx} - \psi_{yy}][1 - h_x{}^2] = 0 \tag{35}$$

and the normal stress must be balanced by the surface tension forces, which imply that

$$\frac{h_{xx}}{Ca[1+h_x{}^2]^{3/2}} = -p + \frac{2}{1+h_x{}^2}\left[(h_x{}^2-1)\psi_{xy} + h_x(\psi_{xx}-\psi_{yy})\right] \tag{36}$$

where $Ca = \mu V/\sigma$ is the capillary number, μ being the viscosity, σ the surface tension, and the subscripts denoting appropriate derivatives. For large σ, $Ca << 1$ and in the limiting case of infinite surface tension Ca becomes zero. From equation (36), it can be seen that $h_{xx} = 0$ for $Ca = 0$. Since $h[0] = 1$ and $h_x(\infty) = 0$, therefore $h[x] = 1$ when $Ca = 0$. In other words, the stick-slip problem corresponds to the Newtonian jet swell problem for liquids possessing infinitely large surface tension. Thus for large surface tension $[Ca << 1]$ it is reasonable to assume that

$$\begin{aligned} h[x] &= 1 + Ca\ h_1[x] + \ldots, \quad x > 0 \\ p[x,y] &= p_0[x,y] + Ca\ \bar{p}_1[x,y] + \ldots \\ \psi[x,y] &= \psi_0[x,y] + Ca\ \bar{\psi}_1[x,y] + \ldots \end{aligned} \tag{37}$$

where p is the pressure and the subscript 0 refers to the stick-slip solution [15].

Substituting equation [37] into equation [36] and equating the coefficients of Ca° gives

$$\frac{d^2h_1}{dx^2} = -\left[p_0 + 2\frac{\partial^2\psi_0}{\partial x\partial y}\right]_{y=1} \tag{38}$$

The right-hand side of equation (38) represents the total normal stress experienced by the slip surface. Since $\partial p/\partial x = -\partial\eta/\partial y$, therefore from equation [6] the surface pressure distribution can be expressed as

$$p_0[x,1] = -\sum_{n=1}^{\infty} C_n \operatorname{Cos}\alpha_n \exp[-\alpha_n x],\ x>0 \tag{39}$$

Note that equation (39) assumes zero surface pressure at $x = \infty$. Combination of equations (10), (38), and (39) gives the following expression for $h_1[x]$

$$h_1[x] = -\sum_{n=1}^{\infty}\frac{C_n \operatorname{Cos}\alpha_n}{\alpha_n} x\exp[-\alpha_n x] + 2\sum_{n=1}^{\infty} D_n \operatorname{Cos}\alpha_n[1-\exp(-\alpha_n x)] \tag{40}$$

Equation (40), therefore, provides an estimate of the surface shape of a creeping plane Newtonian jet for small capillary numbers.

7 Discussion

In this section, we will briefly describe the method for calculating the numerical results and discuss how these results compare with those obtained by means of other analytical and numerical techniques.

The computational procedure adopted for evaluating the constants C_n and D_n was to truncate the series by choosing an appropriate value of n, thereby converting the infinite system of equations into a finite form. Moreover, the integrations wtih respect to β were done numerically within the limits $\beta_{\min}$ and $\beta_{\max}$ as the integrands are unbounded at both the limits of integration. Table 1 summarizes the results for different values of n and $\beta_{\max}$. $\beta_{\max} > 100$ appears to be a satisfactory choice for the upper limit of integration. The values of the coefficients C_n and D_n, however, are strongly dependent on n, the number of terms considered in equations (32) and (33). It can be seen that a precise evaluation of C_n and D_n requires n to be in excess of 20. Fortunately, however, reasonably good results can be obtained by considering just the first 10 terms, that is, with $n = 10$. A more detailed and interesting discussion regarding evaluation of the coefficients and the subsequent computation of the flow variables has been provided by Trogdon and Joseph [17].

Once the coefficients C_n and D_n are determined, the flow variables can readily be evaluated from the derived ex-

Table 1 Calculated coefficients for different numerical parameters, $\beta_{\min} = 10^{-6}$

	I $\beta_{\max}=100$		*II* 200		*III* 300		*IV* 200	
n	C_n	D_n	C_n	D_n	C_n	D_n	C_n	D_n
1	−1.71757	−0.14935	−1.71740	−0.14935	−1.71584	−0.14928	−1.75600	−0.15133
2	1.04183	0.02290	1.04160	0.02289	1.04033	0.02288	1.08255	0.02338
3	−0.76730	−0.00764	−0.76702	−0.00764	−0.76210	−0.00761	−0.80878	−0.00787
4	0.61418	0.00348	0.61383	0.00348	0.61123	0.00346	0.65563	0.00362
5	−0.51284	−0.00189	−0.51237	−0.00189	−0.51106	−0.00188	−0.55342	−0.00198
6	0.44080	0.00114	0.44033	0.00114	0.43846	0.00114	0.48055	0.00121
7	−0.38643	−0.00074	−0.38589	−0.00074	−0.38442	−0.00074	−0.42517	−0.00079
8	0.34430	0.00051	0.34360	0.00051	0.34247	0.00051	0.38186	0.00055
9	−0.31028	−0.00037	−0.30964	−0.00037	−0.30887	−0.00036	−0.34683	−0.00040
10	0.28211	0.00027	0.28141	0.00027	0.28092	0.00027	0.31749	0.00030
11							−0.29360	−0.00023
12							0.27224	0.00018
13							−0.25406	−0.00014
14							0.23816	0.00012
15							−0.22413	−0.00010
16							0.21165	0.00008
17							−0.20042	−0.00007
18							0.19034	0.00006
19							−0.18122	−0.00005
20							0.17292	0.00004

Downloaded 02 May 2010 to 171.66.16.250. Redistribution subject to ASME license or copyright; see http://www.asme.org/terms/Terms_Use.cfm

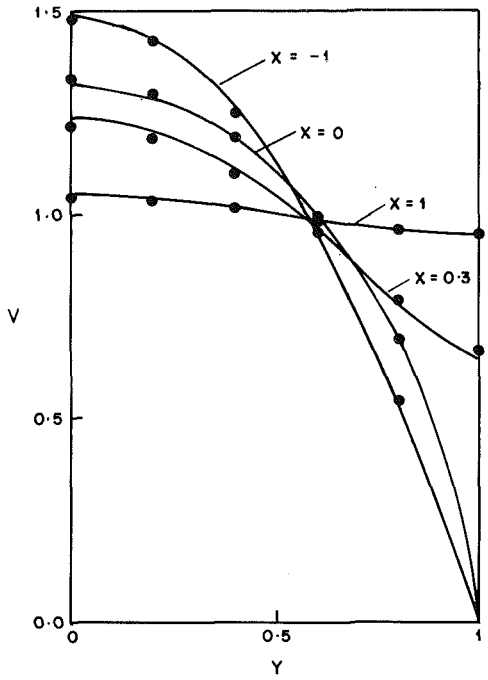


Fig. 2 Axial velocity profile —— = Analytical, [•] = numerical [13].

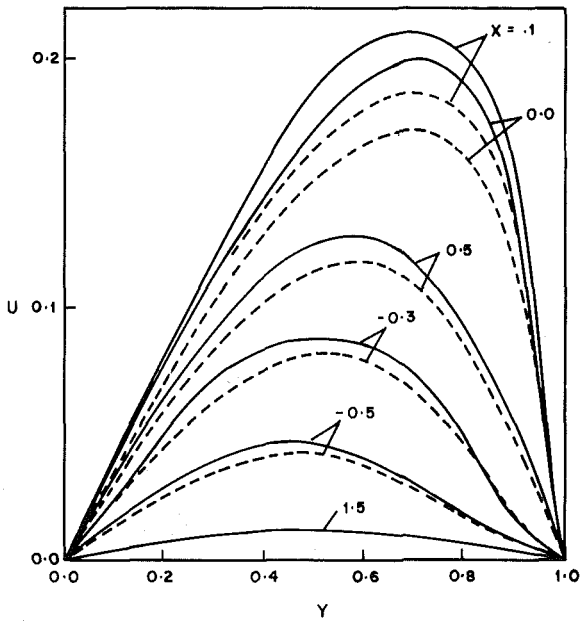


Fig. 3 Transverse velocity profiles—— = Analytical, – – – – = numerical [13].

Table 2 Axial velocity profile at the exit plane

y	0.0	0.2	0.4	0.6	0.8	1.0
Analytical: Present work	1.321	1.287	1.182	1.001	0.723	0.000
Richardson [15]	1.347	1.298	1.198	0.989	0.707	0.000
Numerical: Dutta [13]	1.332	1.295	1.184	0.992	0.695	0.000

pressions. The results presented in the subsequent sections have been calculated using the coefficients listed in column *II* of Table 1. Figures 2 and 3 illustrate the axial and transverse velocity profiles at different axial locations. It is evident that the process of velocity profile rearrangement from a fully

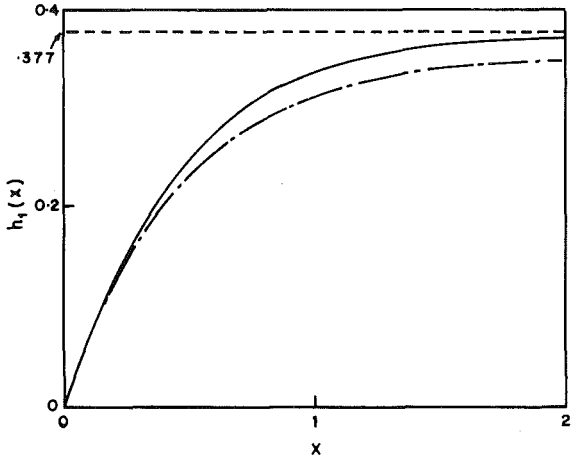


Fig. 4 Variation of h_1 with axial distance. —— = equation (40), – · – = Richardson [15].

developed parabolic flow far upstream to a uniform plug flow far downstream occurs essentially between $x = -1$ and $x = 1$. In Figs. 2 and 3, velocity profiles predicted by the analytical solution are also compared with those obtained from a complete numerical solution of the problem (13). The analytical predictions are seen to be in reasonably good agreement with their numerical counterparts. The correspondence between the analytical and numerically predicted transverse velocities, however, improves as the distance from the exit plane increases.

Table 2 presents a comparison of the axial velocities at the exit plane. Results as calculated by the present method are compared with those obtained by Richardson using the Wiener-Hopf technique. Considering the differences in the calculational procedure, the results predicted by the two methods agree quite favorably. It needs to be emphasized that the conditions represented by equations (31*a*), (31*c*), and (31*d*) are valid only within the fluid [$| y | < 1$] as the pressure, the velocities, and the stresses need to be continuous. At the surfaces along the exit plane, velocities are discontinuous owing to the sudden change in the boundary conditions. Consequently, these locations involve severe pressure and stress singularities which in turn, implies a discontinuity in the vorticity and its gradients. In fact, the calculated values at [0, ± 1] are found to depend strongly on how these locations are approached.

The singular behavior of the flow variables at the die lip can best be illustrated by considering the analytical solution presented in the foregoing. From equations (6) and (28), the pressure field can be expressed as

$$p(x,y) = -\sum_{n=1}^{\infty} C_n \operatorname{Cos}(\alpha_n y) \exp(-\alpha_n x) \quad \text{for} \quad x > 0 \qquad (41a)$$

and

$$p(x,y) = -3x - \sum_{n=1}^{\infty} C_n \operatorname{Cos}(\alpha_n y) \exp(\alpha_n x) + \sum_{n=1}^{\infty} D_n \alpha_n^2 \operatorname{Cos} \alpha_n \int_0^{\infty} P(\beta) \frac{\operatorname{Cosh} \beta y \operatorname{Sin} \beta x}{(\alpha_n^2 + \beta^2)} d\beta + \sum_{n=1}^{\infty} \frac{C_n \operatorname{Cos}\alpha_n}{2} \int_0^{\infty} \frac{(\alpha_n^2 - \beta^2) P(\beta) \operatorname{Cosh} \beta y \operatorname{Sin} \beta x}{(\alpha_n^2 + \beta^2)^2} d\beta \qquad (41b)$$

for $x < 0$. It follows from equation (41) that

$$p(0,1) = \sum_{n=1}^{\infty} C_n (-1)^{n+1} \qquad (42)$$

and

Downloaded 02 May 2010 to 171.66.16.250. Redistribution subject to ASME license or copyright; see http://www.asme.org/terms/Terms_Use.cfm

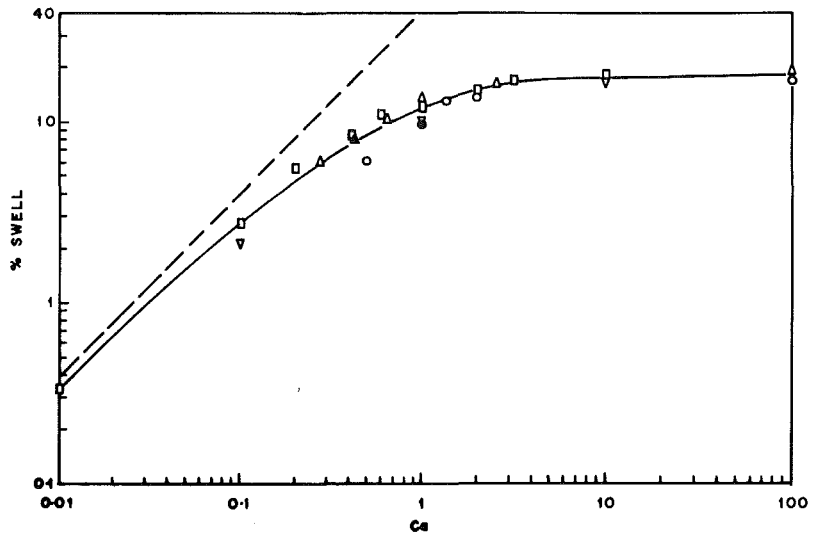


Fig. 5 Swelling of a plane Newtonian jet as a function of capillary number, – – – – – – – – = approximate method, — trend exhibited by numerical solutions: [▵] Omodei [8]; [▽] Ruschak [12]; [□] Silliman and Scriven [11]; [○] Dutta [14].

$$p(0,0) = -\sum_{n=1}^{\infty} C_n \tag{43}$$

Since C_n is negative only for odd values of n, equation (42) becomes

$$p(0,1) = -\sum_{n=1}^{\infty} | C_n | \tag{44}$$

which implies that the pressure at the die-lip goes to negative infinity. This discontinuous behavior is typical of the stick-slip problem. In comparison, the centerline pressure is a continuous monotonically decreasing function with the pressure at the exit plane being finite and positive. For n = 10, equation (43) predicts that $p(0,0) = 0.98$ which compares quite favorably with the value of 1.1 reported by Richardson [15] and others [10, 13].

The free-surface shape of a creeping, plane Newtonian jet as calculated from equation (40) is shown in Fig. 4. The surface profile is quite similar to that predicted by various numerical techniques. Here too, the surface shape predicted by the eigenfunction method is quite close to that obtained by the Wiener-Hopf method. Figure 5 illustrates the expansion of a plane jet as a function of capillary number, Ca. It is evident that the correspondence between the numerically predicted values and those obtained from equation (40) increases as Ca decreases. This is somewhat expected because the expansion procedures [see equation (37)] is only accurate for small capillary numbers. For $Ca < 0.1$, the approximate method yields a fairly good estimate of jet expansion. In all cases, however, the approximate method overestimates the swelling of a Newtonian jet.

8 Conclusions

The separation of variables technique can be effectively used to analyze the plane stick-slip problem. The eigenfunction method discussed here is easier to implement for numerical calculations and yields results comparable to those obtained by the Wiener-Hopf technique. The analytical results indicate the complex flow process of rapid velocity profile rearrangement that occurs within half a die opening both upstream and downstream from the exit plane. In addition, a perturbation of the stick-slip solution for small capillary numbers suggests that liquid-surface tension exerts an inhibiting influence on jet expansion. Finally, it appears that the solution technique can easily be extended to solve the axisymmetric [both circular (16) as well as annular] stick-slip cases and similar other problems involving mixed boundaries.

References

1 Gottlieb, M., and Bird, R. B., "Exit Effects in Non-Newtonian Liquids. An Experimental Study," *Ind. Eng. Chem. Fundam.*, Vol. 18, 1979, pp. 357–368.

2 Whipple, B. A., and Hill, C. T., "Velocity Distribution in Die Swell," *AICHE J.*, Vol. 24, 1978, pp. 664–671.

3 Middleman, S., and Gavis, J., "Expansion and Contraction of Capillary Jets of Newtonian Liquids," *Phys. Fluids*, Vol. 4, 1961, pp. 335–359.

4 Goren, S. L., and Wronski, S., "The Shape of Low-Speed Capillary Jets of Newtonian Liquids," *J. Fluid. Mech.*, Vol. 25, 1966, pp. 185–198.

5 Batchelor, J., Berry, J. P., and Horsfall, F., "Die Swell in Elastic and Viscous Fluids," *Polymer*, Vol. 14, 1973, pp. 297–299.

6 Nickell, R. E., Tanner, R. I., and Caswell, B., "The Solution of Viscous Incompressible Jet and Free-Surface Flows using Finite Element Methods," *J. Fluid Mech.*, Vol. 65, 1974, pp. 189–206.

7 Reddy, K. R., and Tanner, R. I., "Finite-Element Solution of Viscous Jet Flows With Surface Tension," *Computers and Fluids*, Vol. 6, 1978, pp. 83–91.

8 Omodei, B. J., "Computer Solution of a Plane Newtonian Jet With Surface Tension," *Computers and Fluids*, Vol. 7, 1979, pp. 79–96.

9 Omodei, B. J., "On the Die Swell of an Axisymmetric Newtonian Jet," *Computers and Fluids*, Vol. 8, 1980, pp. 275–291.

10 Chang, P. W., Patten, T. W., and Finlayson, B. A., "Collocation and Galerkin Finite-Element Methods for Viscoelastic Fluid Flow - II," *Computers and Fluids*, Vol. 7, 1979, pp. 285–293.

11 Silliman, W. J., and Scriven, L. E., "Separating Flow Near a Static Contact Line: Slip at a Wall and Shape of a Free Surface," *J. Comp. Phys.*, Vol. 34, 1980, pp. 287–313.

12 Ruschak, K. J., "A Method for Incorporating Free Boundaries With Surface Tension in Finite Element Fluid-Flow Simulators," *Int. J. Num. Meth. Eng.*, Vol. 15, 1980, 639–648.

13 Dutta, A., "A Theoretical Analysis and Experimental Study of Extrusion Blow Molding," Ph.D. Thesis, State University of New York at Buffalo, 1981.

14 Dutta, A., and Ryan, M. E., "The Dynamics of a Creeping Newtonian Jet With Gravity and Surface Tension: A Finite Difference Technique for Solving Steady Free-Surface Flows Using Orthogonal Curvilinear Coordinates," *AICHE J.*, Vol. 28, 1982, pp. 220–232.

15 Richardson, S., "A Stick-Slip Problem Related to the Motion of a Free Jet at Low Reynolds Number," *Proc. Camb. Phil. Soc.*, Vol. 67, 1970, pp. 477–489.

16 Vrentas, J. S., and Duda, J. L., "Effect of Axial Diffusion of Vorticity on Flow Development in Circular Conduits: Part II," *AIChE J.*, Vol. 13, 1966, pp. 97–101.

17 Trogdon, S. A., and Joseph, D. D., "The Stick-Slip Problem for a Round Jet I. Large Surface Tension," *Rheol. Acta.*, Vol. 19, 1980, pp. 404–420.

Downloaded 02 May 2010 to 171.66.16.250. Redistribution subject to ASME license or copyright; see http://www.asme.org/terms/Terms_Use.cfm

A New Method of Stabilization for Holonomic Constraints

J. W. Baumgarte
Mechanik-Zentrum,
Technische Universität,
D-3300 Braunschweig, Germany

A new method for the asymptotic stabilization of holonomic constraints is presented. The essential feature of this approach is the introduction of stabilizing momenta of constraint. The advantage of the method is the fact that to obtain the nonclassical Lagrangian multipliers in the equations of motion, the holonomic constraints need to be differentiated only once with respect to time.

1 Introduction

In a mechanical system with holonomic constraints only part of these constraints can be eliminated by introduction of generalized coordinates. The remaining constraints in the equations of motion have to be treated by means of forces of constraint. This is the case in most multibody systems found in engineering practice (compare Wittenburg [1, 2]). They do not have the structure of a topological tree but a connected structure with closed loops. A very simple example of this broad and important category is the crank and slider mechanism. In such systems it is always necessary to open the closed loop. The resulting constraints have to be treated mostly by introducing forces of constraint within the equations of motion.

To calculate the Lagrangian multipliers within the forces of constraint as function of coordinates, velocities, and time the usual method is to differentiate the constraints twice with respect to time. This procedure introduces additional instabilities which produce rapidly growing errors in the constraints during numerical integration. Within a short time the numerical solution becomes useless since the constraints are violated more and more. Therefore the constraints occurring in mechanical systems with closed loops cannot be handled in the usual way. The only way to eliminate these instabilities is to stabilize the equations of constraint. A stabilization procedure that reduces the error propagation drastically is described in [3].

2 Variational Problem, the Eulerian Equations

In this paper another method of stabilization will be described. The essence of this approach is the fact that to obtain *nonclassical* Lagrangian multipliers the holonomic constraints need to be differentiated *only once* with respect to time. This is only possible by abandoning the classical method of using forces of constraint. Our new approach is based on the physical idea of introduction of momenta of constraint.

The Lagrangian variational problem leading to the equations of motion with stabilized constraints is

$$\int_{t_0}^{t_1} dt\left\{\delta\left[L+\sum_{\rho=1}^{r}\lambda_\rho h_\rho\right]+\sum_{i=1}^{n}Q_i\delta q_i+\sum_{\rho=1}^{r}\gamma_\rho g_\rho\delta\gamma_\rho\right\}=0, \tag{2.1}$$

where q_i are the generalized coordinates taking into account on part of the constraints, $L = L(q_i, \dot{q}_i, t)$ is the Lagrangian, $Q_i = Q_i(q_j, \dot{q}_j, t)$ are the nonpotential forces, $g_\rho = g_\rho(q_i, t) = 0$ are the remaining holonomic constraints, and $\dot{g}_\rho = h_\rho = 0$, γ_ρ are positive constants.

The variational problem (2.1) leads to the following equations of motion:

$$-\left(\frac{\partial L}{\partial \dot{q}_i}+\sum_\rho\lambda_\rho\frac{\partial h_\rho}{\partial \dot{q}_i}\right)^{\cdot}+\frac{\partial L}{\partial q_i}+\sum_\rho\lambda_\rho\frac{\partial h_\rho}{\partial q_i}$$

$$+Q_i=0,\ i=1,\ \ldots,n \tag{2.2a}$$

$$h_\rho+\gamma_\rho g_\rho=\dot{g}_\rho+\gamma_\rho g_\rho=0,\ \rho=1,\ \ldots,r<n. \tag{2.2b}$$

The effect of the positive constants γ_ρ may be directly seen in the equations (2.2*b*). The differentiated constraints are asymptotically stable. All the constants γ_ρ can be chosen equal to γ. A suitable numerical implementation is the so-called readjustment, see [4]. Weak stability is found even for $\gamma_\rho = \gamma = 0$.

Please notice: The forces of constraint are:

$$Q_i^c=-\sum_{\rho=1}^{r}\lambda_\rho\frac{\partial g_\rho}{\partial q_i} \tag{2.3}$$

By putting

$$p_i=\frac{\partial L}{\partial \dot{q}_i}+\sum_{\rho=1}^{r}\lambda_\rho\frac{\partial g_\rho}{\partial q_i},\ \frac{\partial h_\rho}{\partial \dot{q}_i}\equiv\frac{\partial g_\rho}{\partial q_i}, \tag{2.4a}$$

we obtain the first-order system

$$\dot{p}_i=\frac{\partial L}{\partial q_i}+\sum_{\rho=1}^{r}\lambda_\rho\frac{\partial h_\rho}{\partial q_i}+Q_i, \tag{2.4b}$$

$$\dot{g}_\rho=-\gamma_\rho g_\rho. \tag{2.4c}$$

Equations (2.4*a*,*c*) are $(r + n)$ linear equations in $\dot{q}_i$ and λ_ρ. The calculation of these variables is conveniently done by numerical inversion within the integration procedure. Notice that this asymptotic stabilization of the constraints using the

Contributed by the Applied Mechanics Division for publication in the JOURNAL OF APPLIED MECHANICS.

Discussion on this paper should be addressed to the Editorial Department, ASME, United Engineering Center, 345 East 47th Street, New York, N.Y. 10017, and will be accepted until two months after final publication of the paper itself in the JOURNAL OF APPLIED MECHANICS. Manuscript received by ASME Applied Mechanics Division, June, 1982; final revision, May, 1983.

Copyright © 1983 by ASME
Downloaded 02 May 2010 to 171.66.16.250. Redistribution subject to ASME license or copyright; see http://www.asme.org/terms/Terms_Use.cfm

variables $q_i(t)$ and $\dot{q}_i(t)$ does not increase the computational effort.

The initial values $q_i(t_0)$ and $\dot{q}_i(t_0)$ satisfying the constraints $g_\rho(t_0) = \dot{g}_\rho(t_0) = 0$ are given. The transformation of $\dot{q}_i$ to p_i is not unique, i.e., without loss of generality we may choose r initial values from the $(r + n)$ needed values of p_i and λ_ρ arbitrarily. The easiest and best choice is $\lambda_\rho(t_0) = 0$.

The freedom in the initial values in $p_i(t_0)$ expresses the additional stability – in the sense of Ljapunov – with respect to the constraints in the variables $q_i(t)$ and $\dot{q}_i(t)$.

By a similar procedure even nonholonomic constraints $f_\rho(q_i, \dot{q}_i, t) = 0$ – linear in the velocities – may be stabilized [5]. In the related variational problem

$$\int_{t_0}^{t_1} dt \Big\{ \delta[L(q_i,\dot{q}_i,t) + \sum_{\rho=1}^{r} \lambda_\rho f_\rho(q_i,\dot{q}_i,t)] + \sum_{i=1}^{n} Q_i \delta q_i + \sum_{i=1}^{n} \sum_{\rho=1}^{r} \lambda_\rho \Big\{ \Big(\frac{\partial f_\rho}{\partial \dot{q}_i} \Big)^{\cdot} - \frac{\partial f_\rho}{\partial q_i} \Big\} \delta q_i \Big\} = 0 \quad (2.5)$$

additional nonconservative forces of constraint appear [5]. Based on the variational problem (2.5) it is even possible to stabilize constraints being nonlinear in the velocities. The most important application, however, is the stabilization of first integrals, e.g., the integral of energy.

3 The Numerical Integration

In general the classical Lagrangian multipliers have a nonzero mean value. Therefore the nonclassical multipliers as well as the nonclassical momenta increase with time. Since the velocities are bounded, but appear as the differences of large numbers, this method suffers from a loss of significant digits. To avoid this new numerical instability we propose a simple modification where the nonclassical multipliers and momenta remain bounded.

We first compute the classical forces of constraint by

$$Q_i^c = Q_i^c(q_j,\dot{q}_j,t) = -\sum_{\rho=1}^{r} \mu_\rho \frac{\partial g_\rho}{\partial q_i}. \quad (3.1)$$

The multilpliers $\mu_\rho = \mu_\rho(q_j,\dot{q}_j,t)$ are then obtained from the following system of equations, linear in $\ddot{q}_i$ and μ_ρ:

$$\Big(\frac{\partial L}{\partial \dot{q}_i} \Big)^{\cdot} - \frac{\partial L}{\partial q_i} = Q_i - \sum_{\rho=1}^{r} \mu_\rho \frac{\partial g_\rho}{\partial q_i}, \; i = 1, \ldots, n \quad (3.2a)$$

$$\ddot{g}_\rho = \ddot{g}_\rho(q_i,\dot{q}_i,\ddot{q}_i,t) = 0, \; \rho = 1, \ldots, r. \quad (3.2b)$$

With these classical forces of constraint the equations of motion have the r first integrals

$$\dot{g}_\rho = 0, \; \rho = 1, \ldots, r. \quad (3.3)$$

Now we stabilize these integrals with our method of momenta of constraint.

The momenta of constraint with $\lambda_\rho(t_0) = 0$ are pure control terms, i.e., they are identically zero for the exact solution *but not for the numerical solution*. These terms are always bounded during the numerical integration and guarantee the stabilizing effect. Furthermore the equations (2.4*c*) will leave a small nonzero mean value in the holonomic constraints. To reduce the mean values to zero we use the following modification of (2.4*c*):

$$\dot{g}_\rho + 2\alpha_\rho g_\rho + \beta_\rho^2 \int_{t_0}^{t} g_\rho d\tau = 0, \; \alpha_\rho > 0, \quad (3.4)$$

which is based on an idea by Ostermeyer [6] using control theoretic considerations. Now the variational problem takes the form:

$$\int_{t_0}^{t_f} dt \Big\{ \delta \Big[L + \sum_{\rho=1}^{r} \lambda_\rho h_\rho \Big] + \sum_{j=1}^{n} (Q_j + Q_j^c) \delta q_j + \sum_{\rho=1}^{r} (2\alpha_\rho g_\rho + \beta_\rho^2 w_\rho) \delta\lambda_\rho + \sum_{\rho=1}^{r} (\dot{w}_\rho - g_\rho) \delta\sigma_\rho \Big\} = 0, \quad (3.5)$$

For simplicity we choose $\alpha_\rho = \beta_\rho = \gamma > 0$. The Q_i^c are the classical forces of constraint, as mentioned in the foregoing. The Eulerian equations of motion following from the variational problem (3.5) written as a first-order system by means of the transformation (2.4*a*), are now:

$$p_i = \frac{\partial L}{\partial \dot{q}_i} + \sum_{\rho=1}^{r} \lambda_\rho \frac{\partial h_\rho}{\partial \dot{q}_i}, \quad \frac{\partial h_\rho}{\partial \dot{q}_i} = \frac{\partial g_\rho}{\partial q_i} \quad (3.6a)$$

$$\dot{p}_i = \frac{\partial L}{\partial q_i} + Q_i + Q_i^c + \sum_{\rho=1}^{r} \lambda_\rho \frac{\partial h_\rho}{\partial q_i} \quad (3.6b)$$

$$\delta\lambda_\rho : \; h_\rho + 2\gamma g_\rho + \gamma^2 w_\rho = 0 \quad (3.6c)$$

$$\delta\sigma_\rho : \; \dot{w}_\rho = g_\rho. \quad (3.6d)$$

These equations lead to a procedure with better numerical accuracy for the stabilization of constraints in the variables $q_i(t)$, $\dot{q}_i(t)$ than the system (2.4*a–c*).

All numerical experiments show the following typical error propagation in the constraints $f_\rho = 0$:

Classical equations of motion (forces of constraint): quadratic and higher.

The use of momenta of constraint without stabilization ($\alpha_\rho = 0$, $\beta_\rho \neq 0$ in (3.4)):
at least linear.

The use of momenta of constraint without stabilization ($\alpha_\rho = 0$, $\beta_\rho \neq 0$ in (3.4)):
the mean values of the constraints $f_\rho = 0$ are zero.

Acknowledgment

The author thanks the Stiftung Volkswagenwerk for the support of this work and Mr. G. P. Ostermeyer for stimulating discussions.

References

1 Wittenburg, J., *Dynamics of Systems of Rigid Bodies*, B. G. Teubner, Stuttgart, 1977.

2 Wittenburg, J., "Dynamics of Multibody Systems," *IUTAM*, 1980, pp. 197–207.

3 Baumgarte, J., "Stabilization of Constraints and Integrals of Motion in Dynamical Systems, "*Comp. meth. in Appl. Mech. and Engineering*, Vol. 1, 1972, pp. 1–16.

4 Baumgarte J., "Stabilisierung von Bindungen im Lagrangeschen Formalismus," *ZAMM*, Vol. 58, 1978, T360–T361.

5 Baumgarte J., "Stabilisierung von Bindungen über Zwangsimpulse," ZAMM, Vol. 62, 1982, pp. 447–454.

6 Ostermeyer, G. P., "Die Stabilisierung von Bindungen und ersten Integralen als Regelungsproblem und ihre Konsequenzen," to appear.

Downloaded 02 May 2010 to 171.66.16.250. Redistribution subject to ASME license or copyright; see http://www.asme.org/terms/Terms_Use.cfm

S. L. Lau
Lecturer,
Department of Civil and Structural Engineering,
Hong Kong Polytechnic,
Hong Kong
Mem. ASME

Y. K. Cheung
Professor and Head.

S. Y. Wu
Assistant Computer Officer.

Department of Civil Engineering,
University of Hong Kong,
Hong Kong,

Incremental Harmonic Balance Method With Multiple Time Scales for Aperiodic Vibration of Nonlinear Systems

An incremental harmonic balance method with multiple time scales is presented in this paper. As a general and systematic computer method, it is capable of treating aperiodic "steady-state" vibrations such as combination resonance, etc. Moreover, this method is not subjected to the limitation of weak nonlinearity. To show the essential features of the new approach, the almost periodic free vibration of a clamped-hinged beam is computed as an example.

1 Introduction

It is well known that the harmonic balance method [1] is one of the most commonly used approaches for analyzing nonlinear structural vibrations. However it has several disadvantages. First, the formulation is very tedious for a nonlinear system having many DOF and with higher harmonic terms taken into account. Second, to obtain a consistent solution, one needs to know a priori which harmonic terms ought to be included in the analysis.

To overcome such discrepancies, an incremental harmonic balance (IHB) method [2–5] was developed and successfully applied to the analysis of periodic nonlinear structural vibrations and related problems. This incremental approach is particularly simple and economical for computer implementation because only linearized equations have to be formed and solved in each incremental step. It is believed that a great deal of further research work can be done along this line.

Nevertheless, the aforementioned method is limited in application to periodic vibrations only, whereas in reality, both experimental results and theoretical analysis have shown that under certain conditions a system may exhibit nonperiodic motions, in which the amplitudes, frequencies, and relative phases vary continuously with time [6].

In this paper, the IHB method is generalized to multiple time scales whereby the solution is expanded into a multiple Fourier series containing a number of frequencies incommensurable with one another. Obviously, this form of solution is aperiodic in general. Theoretically, there is no limitation to the number of time scales used and hence a very general aperiodic solution of any accuracy can be obtained if the proper frequencies and sufficient number of corresponding harmonic terms are included, although it is obvious that the cost in implementation on computer will increase rapidly with the increasing number of frequencies and Fourier terms.

The aim of the present paper is primarily to introduce the essence of the new approach, and therefore only some particular cases of a beam problem are treated to show the effectiveness of the method. The behavior of the beam undergoing aperiodic vibration will not be dealt with in-depth at present.

2 General Procedure

Consider the modal representation of a structural system of the form

$$L_i(u_i) + f_i(u_1, u_2, \ldots, u_n) = p_i \quad (i = 1, 2, \ldots, n) \tag{1}$$

where u_i = normal mode coordinates, $f_i(u_1, u_2, \ldots, u_n)$ = the ith nonlinear restoring force component, p_i = the ith load component, which is assumed to be periodic with period Ω, and L_i a linear operator such that

$$L_i = \frac{d^2}{dt^2} + 2\, c_i \frac{d}{dt} + \Omega_i^2 \tag{2}$$

in which t = time, c_i = the ith modal damping coefficient, and Ω_i = the ith linear natural frequency.

For a nonlinear system excited by a periodic force, it is well known that two distinct types of vibration may occur, i.e., periodic and aperiodic motions.

For periodic vibration, the general solution can be written in Fourier series of the form

Contributed by the Applied Mechanics Division and presented at the Winter Annual Meeting, Boston, Mass., November 13–18 1983, of THE AMERICAN SOCIETY OF MECHANICAL ENGINEERS.

Discussion on this paper should be addressed to the Editorial Department, ASME, United Engineering Center, 345 East 47th Street, New York, N.Y. 10017, and will be accepted until two months after final publication of the paper itself in the JOURNAL OF APPLIED MECHANICS. Manuscript received by ASME Applied Mechanics Division, July, 1982; final revision, February, 1983. Paper No. 83-WA/APM-7.

Copies will be available until July, 1984.

Copyright © 1983 by ASME
Downloaded 02 May 2010 to 171.66.16.250. Redistribution subject to ASME license or copyright; see http://www.asme.org/terms/Terms_Use.cfm

$$u_i(\Omega t) = \sum_{j=0}^{\infty} (A_{j\eta}^{(i)} \cos\, j\eta\Omega t + B_{j\eta}^{(i)} \sin\, j\eta\Omega t)$$

$$(B_0^{(i)} = 0,\ i = 1,2,\ \ldots\ ,n) \tag{3}$$

where η is a rational number, e.g., η is taken as unity when the fundamental and superharmonic resonances are sought while η is taken to be 1/2, 1/3, ... , respectively, for the analysis of subharmonic resonances with orders one-half, one-third, and so on. In practice, a truncated series of (3) is used.

To determine this form of periodic solution, a systematic computer method – the incremental harmonic balance method (IHB) was developed and a number of problems have been treated [2–5] successfully.

In contrast, the present paper centers on the development of a general and systematic computer method for analyzing the aperiodic "steady-state" vibrations. The basic idea may be summarized in the following paragraph.

In periodic vibration (see equation (3)), all frequencies are commensurable, and therefore, it is reasonable to postulate that aperiodic motion should be made up of components with incommensurable frequencies. In other words, in periodic vibration, the solution u_i $(i=1,2,\ \ldots\ ,n)$ are periodic functions of $\eta\Omega t$, as expressed by equation (3), while in aperiodic vibration, u_i have to be regarded as functions of $\eta\omega_1 t, \eta\omega_2 t, \ldots\ ,\eta\omega_m t$, i.e.,

$$u_i = u_i(\eta\omega_1 t, \eta\omega_2 t, \ldots\ ,\eta\omega_m t) \quad (i=1,2,\ .\ .\ ,n) \tag{4}$$

where the frequencies ω_1, $\omega_2, \ldots\ ,\omega_m$ are incommensurable with one another.

By writing

$$\tau_k = \eta\omega_k t \quad (k=1,2,\ \ldots\ ,m) \tag{5}$$

within the hypertime domain

$$0 \le \tau_k \le 2\pi \tag{6}$$

equation (4) can be rewritten as

$$u_i = u_i(\tau_1, \tau_2, \ldots\ ,\tau_m) \quad (i=1,2,\ .\ .\ .\ ,n) \tag{7}$$

The adoption of multiple time scales leads to a general aperiodic steady-state solution expressed by multiple Fourier series in the hypertime domain (defined by equation (6)) of the following form

$$u_i = \sum_{j_1=-N}^{N} \sum_{j_2=-N}^{N} \cdots \sum_{j_m=-N}^{N} \left[A_{j_1 j_2 \ldots j_m}^{(i)} \cos\left(\sum_{k=1}^{m} j_k \tau_k \right) + B_{j_1 j_2 \ldots j_m}^{(i)} \sin\left(\sum_{k=1}^{m} j_k \tau_k \right) \right]$$

$$(i=1,2,\ .\ .\ .\ n) \tag{8}$$

with the understanding that only one of the linearly dependent terms is retained in the expression. Linear dependence may happen because, for example,

$$\cos\left(\sum_{k=1}^{m} j_k \tau_k \right) = \cos\left(-\sum_{k=1}^{m} j_k \tau_k \right)$$

$$\sin\left(\sum_{k=1}^{m} j_k \tau_k \right) = -\sin\left(-\sum_{k=1}^{m} j_k \tau_k \right)$$

and so on. In equation (8), $A_{j_1 j_2 \ldots j_m}^{(i)}$, $B_{j_1 j_2 \ldots j_m}^{(i)}$ are Fourier coefficients.

Since τ_j $(j=1,2,\ .\ .\ .\ ,m)$ are functions of t, the following operator relations can be obtained

$$\left.\begin{aligned} \frac{d}{dt} &= \sum_{j=1}^{m} \omega_j \frac{\partial}{\partial \tau_j} \\ \frac{d^2}{dt^2} &= \left(\sum_{j=1}^{m} \omega_j \frac{\partial}{\partial \tau_j} \right)^2 = \sum_{j=1}^{m} \sum_{k=1}^{m} \omega_j \omega_k \frac{\partial^2}{\partial \tau_j \partial \tau_k} \end{aligned}\right\} \tag{9}$$

$$L_i = \sum_{j=1}^{m} \sum_{k=1}^{m} \omega_j \omega_k \frac{\partial^2}{\partial \tau_j \partial \tau_k} + 2c_i \sum_{j=1}^{m} \omega_j \frac{\partial}{\partial \tau_j} + \Omega_i^2 \tag{10}$$

To determine the coefficients $A_{j_1 j_2 \ldots j_m}^{(i)}$, $B_{j_1 j_2 \ldots j_m}^{(i)}$ $(i=1,2,\ .\ .\ ,n)$, it is necessary to generalize the incremental harmonic balance method to the case of multiple time scales.

Assume that u_i, p_i, and ω_j $(i=1,2,\ .\ .\ ,n;\ j=1,2,\ .\ .\ m)$ denote the current state of vibration, and Δu_i, Δp_i, and $\Delta\omega_j$ the corresponding increments. Then a neighboring state can be written as

$$\left.\begin{aligned} u_i' &= u_i + \Delta u_i \quad (i=1,2,\ \ldots\ ,n) \\ p_i' &= p_i + \Delta p_i \\ \omega_j' &= \omega_j + \Delta\omega_j \quad (j=1,2,\ \ldots\ ,m) \end{aligned}\right\} \tag{11}$$

Inserting equation (11) into equation (1) and neglecting all the terms containing increment products, a linearized incremental equation is obtained in the form of

$$L_i(\Delta u_i) + \sum_{j=1}^{n} \frac{\partial f_i}{\partial u_j} \Delta u_j = R_i + \sum_{j=1}^{m} \Delta\omega_j F_{ij} + \Delta p_i$$

$$(i=1,2,\ .\ .\ ,n) \tag{12}$$

where R_i is a corrective term of the form

$$R_i = -[L_i(u) + f_i(u_1, u_2, .\ .\ ,u_n) - p_i] \tag{13}$$

and

$$F_{ij} = -\left(2c_i \frac{\partial u_i}{\partial \tau_j} + 2 \sum_{k=1}^{m} \omega_k \frac{\partial^2 u_i}{\partial \tau_j \partial \tau_k} \right) \tag{14}$$

It is obvious that R_i $(i=1,2,\ .\ .\ ,n)$ will vanish if the current solution is exact. In numerical analysis, the retention of the corrective terms in equation (12) is very important as it can prevent the results from drifting away from the correct solution during the process of incrementation. F_{ij} is the ith component of the unbalance force due to unit increment of ω_j.

Equation (12) is linear but with variable coefficients. Since it is difficult to obtain a general solution, the Galerkin procedure will be used. Thus equation (12) is replaced by

$$\underbrace{\int_0^{2\pi} \int_0^{2\pi} \cdots \int_0^{2\pi}}_{m} \left[L_i(\Delta u_i) + \sum_{j=1}^{n} \frac{\partial f_i}{\partial u_j} \Delta u_j - R_i - \sum_{j=1}^{m} \Delta\omega_j F_{ij} - \Delta p_i \right] \delta\Delta u_i\, d\tau_1 d\tau_2 \ldots d\tau_m = 0 \quad (i=1,2,\ \ldots\ ,n) \tag{15}$$

The increments Δu_i $(i=1,2,\ .\ .\ ,n)$ are expressed by the same expression as equation (8), but with $\Delta A_{j_1 j_2 \ldots j_m}^{(i)}$ and $\Delta B_{j_1 j_2 \ldots j_m}^{(i)}$ instead of $A_{j_1 j_2 \ldots j_m}^{(i)}$ and $B_{j_1 j_2 \ldots j_m}^{(i)}$, respectively. Substituting u_i and Δu_i into equation (15) and performing the integration exactly by making use of the orthogonal properties of trigonometric functions (see the Appendix), a linear matrix is obtained in the form of

$$[K_T]\{\Delta C\} = \{R\} + \sum_j \Delta\omega_j \{F_j\} + \{\Delta P\} \tag{16}$$

where $\{\Delta C\}$ is the vector made up of all the increments

Downloaded 02 May 2010 to 171.66.16.250. Redistribution subject to ASME license or copyright; see http://www.asme.org/terms/Terms_Use.cfm

$\Delta A^{(i)}_{j_1 j_2 \ldots j_m}, \Delta B^{(i)}_{j_1 j_2 \ldots j_m}$ $(i=1,2, \ldots, n,\ j_k = -N, -N+1, \ldots, N-1, N)$,

$[K_T]$ the corresponding tangent matrix, $\{R\}$ the corrective vector, $\{F_j\}$ the unbalance force vector due to unit change of $\Delta\omega_j$, and $\{\Delta P\}$ the exciting force increment vector. In equation (16), $[K_T]$, $\{R\}$, and $\{F_j\}$ $(j=1,2, \ldots, m)$ can be evaluated from equation (15) if the current state of vibration is known, and $\{\Delta P\}$ is usually given. Hence, say, if all the m $\Delta\omega_j$ are prescribed, then $\{\Delta C\}$ can be solved from equation (16) and a new neighboring state of vibration is then obtained by adding these corresponding increments, i.e.,

$$A^{(i)'}_{j_1 j_2 \ldots j_m} = A^{(i)}_{j_1 j_2 \ldots j_m} + \Delta A^{(i)}_{j_1 j_2 \ldots j_m} \qquad \omega'_j = \omega_j + \Delta\omega_j$$

By repeating the incremental procedure, one can finally obtain the required solution with any desired amplitudes.

It can be seen that the harmonic terms of the combined frequency

$$\sum_{k=1}^{m} j_k \omega_k$$

are contained in the general solution, which means that combination resonance can be treated by the present approach.

The solution procedure has to start from a proper known solution which might be a small amplitude (linear) solution or even any rough approximation. To achieve a satisfactory solution, the (modified) Newton-Raphson iteration is applied with an updated correction vector $\{R\}$ each time within an incremental step.

It should be pointed out that for determining the relationship among the components of $\{\Delta C\}$ and $\Delta\omega_j$ $(j=1,2, \ldots, m)$, in principle, any m increments among them may be prescribed, and remaining increments can then be solved from equation (16). However, if the increments that are prescribed are chosen properly, then the numerical problem will be well conditioned.

At this stage, it would be appropriate to discuss this problem in greater detail. For nonlinear periodic vibration, the solution is represented by a frequency response curve and as such it is only necessary to prescribe one increment (or, generally, to add one relation) to trace out the curve. For aperiodic vibration, since it is a combined vibration with $m\,(m>1)$ frequencies incommensurable with one another, the solution is therefore represented by a hypersurface spanning in the frequency-amplitude space. For scanning such a solution a vector consisting of m increments (or, generally, m relations among increments) have to be prescribed in each incremental step. In the viewpoint of numerical analysis, the prescribed vector should be chosen so that the maximum absolute value of the increments solved from equation (16) must not be much greater than the length of the prescribed vector, because in such a case the equation will not be ill-conditioned. However, in practical calculations, the prescribed increments can be chosen in a variety of ways by physical rather than purely numerical consideration so that the results can be clearly interpreted. For example, if two incommensurable frequencies ω_1 and ω_2 are involved, to reveal the behavior of the aperiodic vibration of this system clearly one of the following ways may be adopted.

(1) One of the fundamental amplitude is fixed.

(2) The ratio of the two fundamental amplitudes is fixed.

When one of these conditions is introduced, a curve on the solution surface is thus defined. Then, what it is going to do is to trace this curve by prescribing one more increment in each step. Usually this last prescribed increment is chosen as the one that varied fastest to make the numerical problem well conditioned.

3 Example of Application

The nonlinear vibration of a clamped-hinged beam is complicated by the fact that the second linear frequency ω_{L2} is nearly three times the fundamental frequency ω_{L1}, i.e.,

$$\omega_{L2} = 3.24\omega_{L1}$$

Under such circumstance, internal resonance may occur.

This problem was first analyzed by Nayfeh, Mook, and Sridhar [7, 8] using the method of multiple scales, although only periodic solutions are treated.

As an example of application of the present method it will be demonstrated that there are almost periodic vibrations existing in the neighborhood of the periodic vibration for the clamped-hinged beam problem.

The governing equation describing the transverse vibration of a beam with large slenderness and immovable ends in which large deflections are permitted is known to be [3]

$$\rho A \frac{\partial^2 w}{\partial t^2} + \mathrm{E}1 \frac{\partial^4 w}{\partial x^4} - \left[\frac{\mathrm{E}A}{2L} \int_0^L \left(\frac{\partial w}{\partial x} \right)^2 dx \right] \frac{\partial^2 w}{\partial x^2} = 0 \quad (17)$$

where ρ = density, E = Young's modulus, A = cross-sectional area, I = moment of inertia, L length of beam, x = axial axis, and t = time. The only nonlinearity that has been included is that due to the effect of the transverse deflection on the axial force developed due to end restraint. The curvatures are still restricted to be small and both shear deformations and longitudinal inertia have been neglected.

For a clamped-hinged beam the boundary conditions are

$$w=0, \quad \frac{\partial w}{\partial x} = 0 \quad \text{at} \quad x=0$$

$$w=0, \quad \frac{\partial^2 w}{\partial x^2} = 0 \quad \text{at} \quad x=L \quad (18)$$

Using a two-mode shape approximation, we can write

$$w(x,t)/r = u(t)\ \Phi_1(x) + v(t)\ \Phi_2(x) \quad (19)$$

where $\Phi_1(x)$, $\Phi_2(x)$ are free vibration mode shapes of the beam, which can be found from Blevins [9] or other texts, $u(t)$ and $v(t)$ are normal mode coordinates, and $r = \sqrt{I/A}$ = radius of gyration.

Then, by applying Galerkin's procedure as set out previously, the following set of nonlinear ordinary differential equations can be obtained

$$\left.\begin{aligned} &\frac{d^2u}{dt^2} + \Omega_1^2 u + \alpha_1 u^3 + \alpha_2 u^2 v + \alpha_3 u v^2 + \alpha_4 v^3 = 0 \\ &\frac{d^2v}{dt^2} + \Omega_2^2 v + \beta_1 u^3 + \beta_2 u^2 v + \beta_3 u v^2 + \beta_4 v^3 = 0 \end{aligned}\right\} \quad (20)$$

where $\Omega_1 = 1$, $\Omega_2 = (\lambda_2/\lambda_1)^2 = 3.24064$, $\lambda_i^2 = \omega_{L_i} L^2 (\rho A/EI)^{1/2}$ = dimensionless linear frequency of the beam, ω_{L_i} = the ith linear frequency of the beam, $t_1 = \omega_{L_1} t$ = dimensionless time, and

$$\alpha_1 = \frac{1}{\lambda_1^4} \gamma_{1111} = 0.278769$$

$$\alpha_2 = \frac{1}{\lambda_1^4} (\gamma_{1112} + \gamma_{1121} + \gamma_{1211}) = -0.311074$$

$$\alpha_3 = \frac{1}{\lambda_1^4} (\gamma_{1122} + \gamma_{1212} + \gamma_{1221}) = 1.11585$$

$$\alpha_4 = \frac{1}{\lambda_1^4} \gamma_{1222} = -0.386361$$

$$\beta_1 = \frac{1}{\lambda_1^4} \gamma_{2111} = \frac{1}{3} \alpha_2$$

Downloaded 02 May 2010 to 171.66.16.250. Redistribution subject to ASME license or copyright; see http://www.asme.org/terms/Terms_Use.cfm

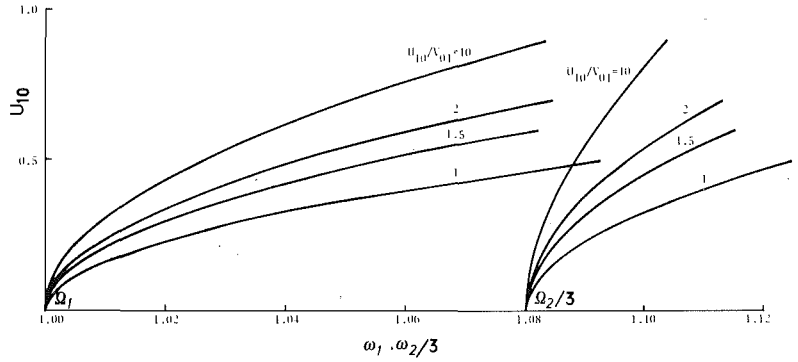


Fig. 1 Frequencies ω_1 (left-hand side family of curves) and ω_2 (right-hand side family of curves) versus amplitude component u_{10}

Table 1 Representative solutions – the values of coefficients in equation (25) ($u_{10}/v_{01} = 2$)

ω_1	1.0155588	1.0427058	1.0848488
ω_2	3.2584143	3.2898269	3.3381498
u_{10}	0.300E 0	0.500E 0	0.700E 0
u_{30}	0.228E-3	0.997E-3	0.253E-2
u_{01}	-0.323E-3	-0.151E-2	-0.483E-2
u_{03}	-0.353E-5	-0.167E-4	-0.484E-4
u_{21}	-0.389E-4	-0.174E-3	-0.451E-3
u_{12}	0.340E-4	0.155E-3	0.408E-3
$\bar{u}_{21}$	-0.224E-2	-0.143E-1	-0.995E-1
$\bar{u}_{12}$	0.647E-4	0.301E-3	0.906E-3
v_{10}	0.628E-3	0.289E-2	0.853E-2
v_{30}	0.530E-3	0.333E-2	0.238E-1
v_{01}	0.150E 0	0.250E 0	0.350E 0
v_{03}	0.386E-4	0.176E-3	0.475E-3
v_{21}	0.216E-3	0.952E-3	0.239E-2
v_{12}	-0.420E-4	-0.187E-3	-0.476E-3
$\bar{v}_{21}$	-0.417E-3	-0.192E-2	-0.589E-2
$\bar{v}_{12}$	-0.101E-3	-0.486E-3	-0.179E-2

$$\beta_2 = \frac{1}{\lambda_1^4}(\gamma_{2211}+\gamma_{2121}+\gamma_{2112}) = \alpha_3$$

$$\beta_3 = \frac{1}{\lambda_1^4}(\gamma_{2221}+\gamma_{2212}+\gamma_{2122}) = 3\alpha_4$$

$$\beta_4 = \frac{1}{\lambda_1^4}\gamma_{2222} = 3.87030$$

in which

$$\gamma_{nmpq} = \frac{1}{2}\int_0^1 \frac{\partial\phi_n}{\partial x_1}\frac{\partial\phi_m}{\partial x_1}dx_1 \int_0^1 \frac{\partial\phi_p}{\partial x_1}\frac{\partial\phi_q}{\partial x_1}dx_1 (x_1 = x/L) \tag{21}$$

and

$$\gamma_{mnpq} = \gamma_{nmpq} = \gamma_{mnqp} = \gamma_{pqmn} \tag{22}$$

It can be seen that equation (20) is a special form of equation (1), and therefore the general method developed in Section 2 can be readily applied.

Let

$$\tau_1 = \omega_1 t_1, \quad \tau_2 = \omega_2 t_1 \tag{23}$$

whereupon

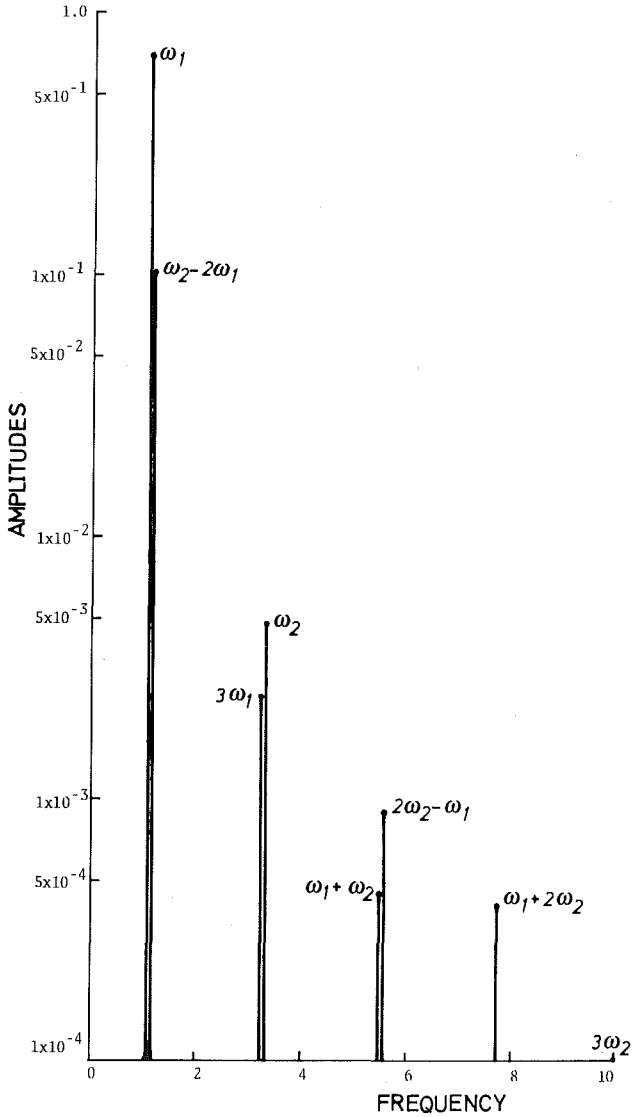


Fig. 2 Spectrum diagram of the first mode component u for the solution with $u_{10} = 0.7$, $v_{01} = 0.35$

$$\frac{d^2}{dt_1^2} = \omega_1^2\frac{\partial^2}{\partial\tau_1^2} + 2\omega_1\omega_2\frac{\partial^2}{\partial\tau_1\partial\tau_2} + \omega_2^2\frac{\partial^2}{\partial\tau_2^2} \tag{24}$$

If the incrementation procedure starts from the following particular linear solution

$$u = u_{10}^{(0)}\cos\Omega_1 t_1$$
$$v = v_{01}^{(0)}\cos\Omega_2 t_1 \tag{25}$$

Downloaded 02 May 2010 to 171.66.16.250. Redistribution subject to ASME license or copyright; see http://www.asme.org/terms/Terms_Use.cfm

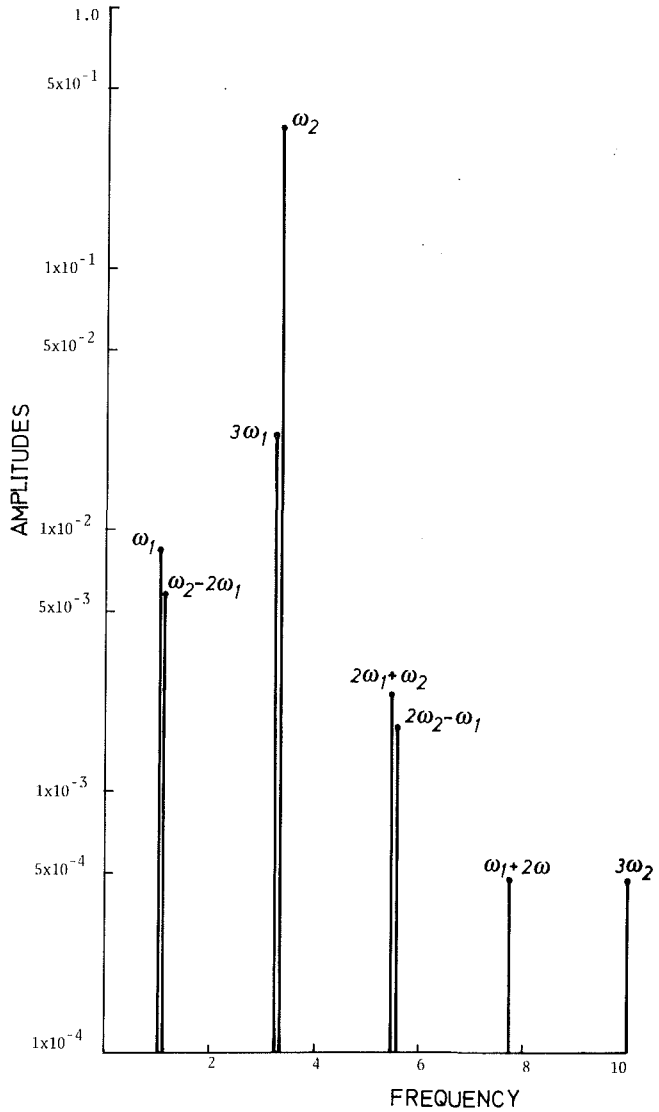


Fig. 3 Spectrum diagram of the second mode component v of the solution with $u_{10} = 0.7, v_{01} = 0.35$

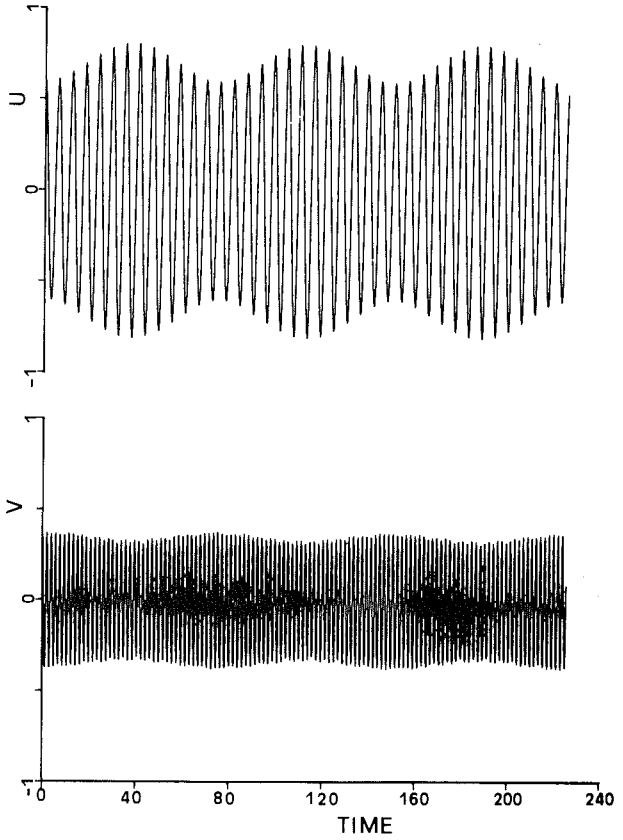


Fig. 4 Time histories of normal mode coordinates u and v for the solution with $u_{10} = 0.7, v_{01} = 0.35$

Table 2 Comparisons of inertia and restoring forces of approximate solution ($u_{10} = 0.7, v_{01} = 0.35$)

	The 1st normal mode u		The 2nd normal mode v	
Dimension-less time t_1	Inertia force $-\frac{d^2u}{dt_1^2}$	Restoring force $\Omega_1^2 u + \alpha_1 u^3 + \alpha_2 u^2 v + \alpha_3 u v^2 + \alpha_4 v^3$	Inertia force $-\frac{d^2v}{dt_1^2}$	Restoring force $\Omega_2^2 v + \beta_1 u^3 + \beta_2 u^2 v + \beta_3 u v^2 + \beta_4 v^3$
0.0	0.6953	0.6912	4.190	4.197
0.5	0.5625	0.5579	-0.374	-0.375
1.0	0.3762	0.3692	-4.107	-4.107
1.5	-0.02349	-0.02325	1.122	1.114
2.0	-0.4149	-0.4092	3.885	3.886
2.5	-0.5829	-0.5812	-1.871	-1.859
3.0	-0.6841	-0.6812	-3.487	-3.486
3.5	-0.5956	-0.5850	2.565	2.555
4.0	-0.2953	-0.2889	2.898	2.888
4.5	0.0873	0.0844	-3.081	-3.066
5.0	0.4121	0.4128	-2.344	-2.340
5.5	0.6391	0.6357	3.574	3.568
6.0	0.6711	0.6669	1.694	1.685

where $u_{10}^{(0)}$ and $v_{01}^{(0)}$ are arbitrary small amplitudes, then the approximate aperiodic solution can be taken in the form

$$\left.\begin{aligned} u = {} & u_{10}\cos\tau_1 + u_{30}\cos 3\tau_1 + u_{01}\cos\tau_2 + u_{03}\cos 3\tau_2 \\ & + u_{21}\cos(2\tau_1 + \tau_2) + u_{12}\cos(\tau_1 + 2\tau_2) \\ & + \bar{u}_{21}\cos(2\tau_1 - \tau_2) + \bar{u}_{12}\cos(\tau_1 - 2\tau_2) \\ v = {} & v_{10}\cos\tau_1 + v_{30}\cos 3\tau_1 + v_{01}\cos\tau_2 + v_{03}\cos 3\tau_2 \\ & + v_{21}\cos(2\tau_1 + \tau_2) + v_{12}\cos(\tau_1 + 2\tau_2) \\ & + \bar{v}_{21}\cos(2\tau_1 - \tau_2) + \bar{v}_{12}\cos(\tau_1 - 2\tau_2) \end{aligned}\right\} \quad (26)$$

where $u_{10}, u_{30}, \ldots, v_{10}, v_{30}, \ldots$ are unknown Fourier coefficients which, together with frequencies ω_1 and ω_2, are to be determined later.

It is worth mentioning that the form of solution can be generated by the computer program automatically. The explanation for this is follows. When the linearized incremental equations is formed by using equation (15) beginning with the linear solution, new harmonic terms will appear from the second and third terms in the brackets of equation (15) due to multiplications of harmonic terms. Of the new terms, those that fall within a specified limit (such as in equation (26), the sum of coefficients of τ_1 and τ_2 is not more than 3) will be added onto the existing terms to constitute a new form of solution. Then, this process will be repeated until none of newly appeared terms are in the specified limit.

As a matter of fact, when the IHB method is employed, the linearized incremental equations will be formed in each incremental step, and there is no difficulty to change the form

Downloaded 02 May 2010 to 171.66.16.250. Redistribution subject to ASME license or copyright; see http://www.asme.org/terms/Terms_Use.cfm

of solution in the course of incrementation procedure. Therefore, it is possible to work out a more efficient program which can select the proper harmonic terms automatically depending on the relative magnitudes of the corresponding amplitudes in various stages of solution. But this problem will not be discussed in the present paper.

Based on equations (24) and (26), a set of linearized incremental equations of the form given by equation (16) is obtained by using the procedure described in the preceding section. In the present example $\{\Delta C\}$ of equation (16) is

$$\{\Delta C\} = [\Delta u_{10}, \Delta u_{30} \ldots, \Delta \bar{u}_{12}, \Delta v_{10}, \Delta v_{30}, \ldots, \Delta \bar{v}_{12}] \quad (27)$$

By choosing Δu_{10}, Δv_{01} as the prescribed increments, the problem is solved incrementally starting form the linear solution equation (25).

A series of solutions with different ratios of u_{10}/v_{01} have been obtained. Figure 10 shows the frequency variation plotted against amplitude u_{10}. When the amplitude is small, we have $\omega_1 \doteq \Omega_1 = 1$, $\omega_2 \doteq \Omega_2 = 3.24064$ and the coupling between the two modes is very weak. While both ω_1 and ω_2 become larger and larger as the amplitude u_{10} is increased, it is however interesting to note that ω_1 increases faster than ω_2 and by the time that $\omega_1 = \omega_2/3$ the motion will be reduced to that of periodic vibration.

Some representative solutions are listed in Table 1, and the frequency spectrum for the case of $u_{10} = 0.7$ and $v_{01} = 0.35$ is presented in Figs. 2-3. It is clearly shown that components of u and v are all located near 1,3,5, . . . times ω_1 because $\omega_1 \doteq \omega_2/3$, and hence beating phenomena will be expected. Figure 4 is the computer plotting of its time histories which demonstrate the beating aperiodic motion and these indicate that energy is continuously being exchanged between the two modes.

The accuracy of the present method is checked by computing the contributions from the various terms in equation (20), based on the expressions for u and v given by equation (26) with the coefficients of a representative solution given in Table 1. The computed results for the inertia forces (d^2u/dt_1^2, and d^2v/dt_1^2) and the restoring force (the remaining terms in equation (20)) are listed in Table 2. It can be seen that the discrepancies are quite small and satisfactory approximations are obtainable by the present method.

4 Concluding Remarks

1 An incremental harmonic balance method with multiple time scales is developed and a very general form of solution is given. This general approach is capable of treating aperiodic vibrations of nonlinear systems.

2 If damping is ignored, the tangent coefficient matrix of the incremental equations will be symmetrical, as it can be derived from a variational principle, but indefinite in general.

3 Since the harmonic terms of the combined frequency

$$\sum_{k=1}^{m} j_k \omega_k$$

are contained in the general solution, combination resonance can be treated by the present approach.

References

1 Timoshenko, S. P., Young, D. H., and Weaver, Jr. W., *Vibration Problems in Engineering*, 4th ed., Wiley, New York, 1974.

2 Lau, S. L., and Cheung Y. K., "Amplitude Incremental Variational Principle for Nonlinear Vibration of Elastic Systems," ASME JOURNAL OF APPLIED MECHANICS, Vol. 48, 1981, pp. 959-964.

3 Cheung, Y. K., and Lau, S. L., "Incremental Time-space Finite Strip Method for Nonlinear Structural Vibrations," *Earthquake Engineering and Structural Dynamics*, Vol. 10, 1982, pp. 239-253.

4 Lau, S. L., Cheung, Y. K., and Wu, S. Y., "Variable Parameter Incrementation Method for Dynamic Instability of Linear and Nonlinear Elastic Systems," ASME JOURNAL OF APPLIED MECHANICS, Vol. 49, 1982, pp. 849-853.

5 Lau, S. L., Cheung, Y. K., and Wu, S. Y., "Amplitude Incremental Finite Element for Nonlinear Vibration of Thin Plates," *Proceedings of the International Conference on Finite Element Methods*, Shanghai, China, Aug. 2-6, 1982.

6 Nayfeh, A. H., and Mook, D. T., *Nonlinear Oscillations*, Wiley-Interscience, New York, 1979.

7 Nayfeh, A. H., Mook, D. T., and Sridhar, S., "Nonlinear Analysis of the Forced Response of Structural Elements," *J. Acoust. Soc. Am.*, Vol. 55, 1974, pp. 281-291.

8 Scridhar, S., Nayfeh, A. H., and Mook, D. T., "Nonlinear Resonances in a Class of Multi-Degree-of-Freedom Systems," *J. Acoust. Soc. Am.*, Vol. 58, 1975, pp. 113-123.

9 Blevins, R. D., *Formulas for Natural Frequency and Mode Shape*, VNR, 1979.

APPENDIX

Integration Formula

$$\int_0^{2\pi}\int_0^{2\pi} \ldots \int_0^{2\pi} sc\left(\sum_{i=1}^{m} j_i\tau_i\right) \cdot sc\left(\sum_{i=1}^{m} k_i\tau_i\right) d\tau_1 d\tau_2 \ldots d\tau_m$$

$$= \begin{cases} \alpha m^2 \pi^m & \text{if } j_i = k_i \quad (i = 1,2, \ldots, m) \\ 0 & \text{otherwise} \end{cases}$$

where *sc* denotes sin or cos, and

$$\alpha = \begin{cases} 1 & \text{if } j_i = k_i = 0 \quad (i = 1,2, \ldots, m) \\ 0.5 & \text{otherwise} \end{cases}$$

Downloaded 02 May 2010 to 171.66.16.250. Redistribution subject to ASME license or copyright; see http://www.asme.org/terms/Terms_Use.cfm

J. Brindley

L. Elliott

J. T. McKay

School of Mathematics,
University of Leeds,
Leeds, England LS2 9JT

The Role of Cavitation in Whirl Instability in a Rotor Bearing

1 The π-Film Model

Dynamically loaded rotor bearings are frequently observed to perform whirling motions, in which the center of the rotor describes some sort of closed orbit. In this paper we demonstrate, by using numerical computations of whirl orbits in a simple π-film model, the role of cavitation of the lubricant in enabling fluid forces alone to drive such stable orbits for certain ranges of parameter values. For other parameter values cavitation may actually enhance the instability always associated with the effects of fluid forces in a full-film bearing.

1 Introduction

We are concerned in this paper with a rotor bearing, in which an inner cylinder or rotor (usually circular) turns inside a parallel cylinder of larger radius, the space between being filled by a fluid lubricant. In such a bearing any load carried by the rotor must of course be supported by the pressure forces exerted on it by the lubricant. For the case of a static load this can be achieved by the fluid motion in a manner that requires no motion of the center of the rotor; it remains in its static equilibrium position. For the case of variable load (dynamic loading) the center of the rotor will usually need to move in some sort of closed orbit in order that the load be balanced by fluid forces.

In either case the question of stability is of fundamental importance and a type of instability of frequent occurrence is associated with the departure of the rotor center from its equilibrium position to move in an orbit of growing size, ultimately resulting, if not arrested, in a failure of the bearing. Such behavior is known as "whirl instability," and its occurrence depends on an imbalance between the fluid forces exerted by the lubricant on the rotor and the total load carried by the rotor. If the unbalanced force acts to increase the departure from the equilibrium point or orbit then instability results.

In any real situation, the load carried by the rotor, and its response to and dependence on rotor motion and position, are likely to be complicated functions of the total mechanical system. We are concerned here with the behavior of the *fluid forces*, and their capacity to cause instability, and so we will usually consider a *unidirectionally loaded bearing*. Clearly some of the cases we classify as unstable in this context could in practice be stabilized by appropriate loading forces or stiffnesses and we will occasionally comment on such possibilities.

Earlier investigations (e.g., Holmes [1], Mitchell, Holmes, and Byrne [2] suggest that, if the lubricant occupies the full space between rotor and bearing (full films), instability is universal for an unloaded rotor. However, Holmes [1] has shown that the introduction of a stiffness or damping effect is able to stabilize the rotor under appropriate conditions. The range of such conditions is not entirely understood, but it is agreed, with the exception of Tolle and Muster [3] and Reddi and Trumpler [4], that in full-film situations the fluid forces taken by themselves will cause instability.

When cavitation occurs the situation is entirely different, and it seems clear that under certain conditions the fluid forces can themselves be stabilizing. Our objectives in this paper and in the subsequent Part 2, are to identify in an appropriate parameter space such regions of stability, to establish their dependence on cavity size and position, and to examine some methods of cavity creation and control in order to optimize the stabilizing effect of fluid forces.

2 Fluid Forces and Static Equilibrium; Full Film

We relate the motion of the rotor to a fixed inertial frame and assume that its mass center behaves as a particle of mass M situated at $0'$ (Fig. 1), the center of the bearing being 0. Then if the position of $0'$ relative to 0 is specified by polar coordinates $(r, \xi + \phi_L)$ we can write its equations of motion in the radial and transverse directions as

$$M(\ddot{r} - r\dot{\phi}_L^2) = F_r + W\cos\phi_L$$

$$M(r\ddot{\phi}_L + 2\dot{r}\dot{\phi}_L) = F_n - W\sin\phi_L \qquad (2.1)$$

where (F_r, F_n) are the components in the radial and transverse directions of the fluid forces acting on the rotor and W is a force of constant magnitude and direction (for an unloaded rotor we should have $W = Mg$).

To calculate the fluid force components F_n and F_r it is convenient to start from the Reynolds equation in the form

Contributed by the Applied Mechanics Division and presented at the Winter Annual Meeting, Boston, Mass., November 13-18, 1983 of THE AMERICAN SOCIETY OF MECHANICAL ENGINEERS.

Discussion on this paper should be addressed to the Editorial Department, ASME, United Engineering Center, 345 East 47th Street, New York, N.Y. 10017, and will be accepted until two months after final publication of the paper itself in the JOURNAL OF APPLIED MECHANICS. Manuscript received by ASME Applied Mechanics Division, May, 1981; final revision, March, 1983. Paper No. 83-WA/APM-24.

Copies will be available until July, 1984.

Copyright © 1983 by ASME
Downloaded 02 May 2010 to 171.66.16.250. Redistribution subject to ASME license or copyright; see http://www.asme.org/terms/Terms_Use.cfm

$$\frac{\partial}{\partial x}\left(\frac{h^3}{\mu}\frac{\partial p}{\partial x}\right)+\frac{\partial}{\partial z}\left(\frac{h^3}{\mu}\frac{\partial p}{\partial z}\right)=6u\frac{\partial h}{\partial x}+6h\frac{\partial u}{\partial x}+12v \tag{2.2}$$

where x and z are longitudinal and transverse coordinates and u and v are tangential and normal velocity components of the moving bearing. In our case, writing,

$$r=c\epsilon$$

where c is a clearance ($R_0 - R$) and ϵ is an eccentricity parameter, we have for the tangential and normal components of the rotor at a point at angular position θ

$$\left.\begin{aligned} u&=R\bar{\omega}+c\frac{d\epsilon}{dt}\sin\theta-c\epsilon\frac{d}{dt}(\xi+\phi_L)\cos\theta \\ v&=c\frac{d\epsilon}{dt}\cos\theta+c\epsilon\frac{d}{dt}(\xi+\phi_L)\sin\theta \end{aligned}\right\} \tag{2.3}$$

Now assuming $c/R << 1$ and noting that

$$c\epsilon\sin\theta=-\frac{dh}{d\theta} \tag{2.4}$$

we can write the Reynolds equation in polar coordinates as

$$\frac{d}{d\theta}\left(h^3\frac{dp}{d\theta}\right)=6\mu R^2\left[\left(\bar{\omega}-2\omega_L-2\frac{d\phi_L}{dt}\right)\frac{dh}{d\theta}+2c\frac{d\epsilon}{dt}\cos\theta\right] \tag{2.5}$$

where we have made the long bearing approximation (i.e., neglected $\partial/\partial z$ ($h^3/\mu\ \partial p/\partial z$)) and have introduced $\omega_L \equiv d\xi/dt$ the frequency of rotation of applied load, which is later set to zero. If we now integrate (2.5) twice w.r.t. θ and apply the boundary conditions

$$p(0)=p(2\pi)=p_a,$$

we obtain

$$p-p_a=6\mu\left(\frac{R}{c}\right)^2\left\{\frac{2+\epsilon\cos\theta}{(1+\epsilon\cos\theta)^2}\left(\bar{\omega}-2\omega_L-2\frac{d\phi_L}{dt}\right)\frac{\epsilon\sin\theta}{2+\epsilon^2}+\frac{1}{\epsilon}\left[\frac{1}{(1+\epsilon\cos\theta)^2}-\frac{1}{(1+\epsilon)^2}\right]\frac{d\epsilon}{dt}\right\} \tag{2.6}$$

N.B. If $\omega_L = d\zeta/dt = d\epsilon/dt = 0$ equation (2.6) may be reduced to the classical Sommerfeld pressure distribution for the steady situation.

The fluid force components F_n and F_r are now given by

$$F_n=LR\int_0^{2\pi}p\sin\theta\,d\theta,\quad F_r=LR\int_0^{2\pi}p\cos\theta\,d\theta$$

and we obtain

$$\left.\begin{aligned} F_n&=\frac{12\pi\epsilon\mu R^3L}{(2+\epsilon^2)(1-\epsilon^2)^{1/2}c^2}\left(\bar{\omega}-2\omega_L-2\frac{d\phi_L}{dt}\right) \\ F_r&=\frac{-12\pi\mu R^3L}{(1-\epsilon^2)^{3/2}c^2}\frac{d\epsilon}{dt} \end{aligned}\right\} \tag{2.7}$$

Thus, nondimensionalizing equations (2.1) by writing $r = c\epsilon$,

$$T=t\left(\frac{W}{2Mc}\right)^{1/2},\quad \bar{\omega}_1=\bar{\omega}\left(\frac{2Mc}{W}\right)^{1/2}=2\pi N\left(\frac{2Mc}{W}\right)^{1/2} \tag{2.8}$$

substituting for F_n and F_r from (2.7) and introducing the Sommerfeld number

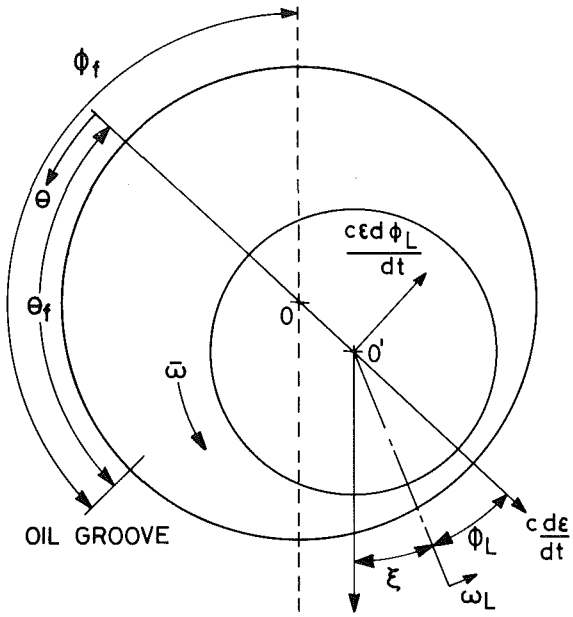


Fig. 1 Coordinate system axial groove cavitation model

$$S\equiv\frac{\mu N}{P_w}\left(\frac{D}{2c}\right)^2,\quad \text{where}\quad P_w=\frac{W}{LD}$$

we have

$$\left.\begin{aligned} \epsilon''-\epsilon\phi_L'^2&=-\frac{24\pi^2S\epsilon'}{\bar{\omega}_1(1-\epsilon^2)^{3/2}}+2\cos\phi_L \\ \epsilon\phi_L''+2\epsilon'\phi_L'&=\frac{24\pi^2\epsilon S}{(2+\epsilon^2)(1-\epsilon^2)^{1/2}}\left(1-\frac{2}{\bar{\omega}_1}\phi_L'\right)-2\sin\phi_L \end{aligned}\right\} \tag{2.9}$$

At the static equilibrium point ϵ_0, ϕ_{L_0}, we must have

$$\epsilon'=\phi_L'=\epsilon''=\phi_L''=0$$

and hence

$$\left.\begin{aligned} \frac{\epsilon_0}{(2+\epsilon_0^2)(1-\epsilon_0^2)^{1/2}}&=\frac{1}{12\pi^2S} \\ \phi_{L_0}&=\frac{\pi}{2} \end{aligned}\right\} \tag{2.10}$$

3 Numerical Computation of Orbits—Full-Film Case

The nonlinearity of equations (2.9) precludes analytic solutions; numerical computations of the whirl orbits have been carried out for a number of cases involving different values of the Sommerfeld number, and normalized angular speed $\bar{\omega}_1$, and also using different starting positions (ϵ_1, ϕ_{L_1}) relative to the static equilibrium point. Typical oribts are presented in Figs. 2(*a*), (*b*), and (*c*) showing effects of variations in S and $\bar{\omega}_1$.

The most important result to emerge is that for all values of parameters tested, every computed whirl trajectory spiralled to the bearing case and no closed orbits could be found. We are thus in agreement with Mitchell, Holmes, and Byrne [2] but differ from Reddi and Trumpler [4] who found some closed orbits. Analytic procedures carried out by Capriz [5] and one of us (J.T.M. [6]) support our numerical results, which may be summarized as follows:

Downloaded 02 May 2010 to 171.66.16.250. Redistribution subject to ASME license or copyright; see http://www.asme.org/terms/Terms_Use.cfm

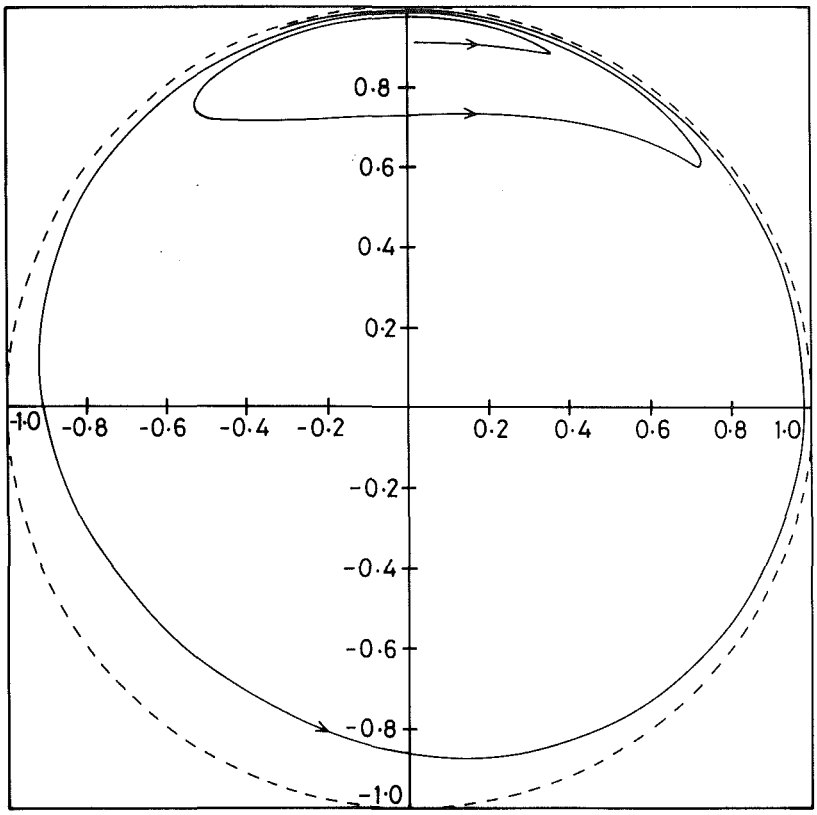


Fig. 2(*a*) $S = 0.00791, \bar{\omega}_1 = 1.6$

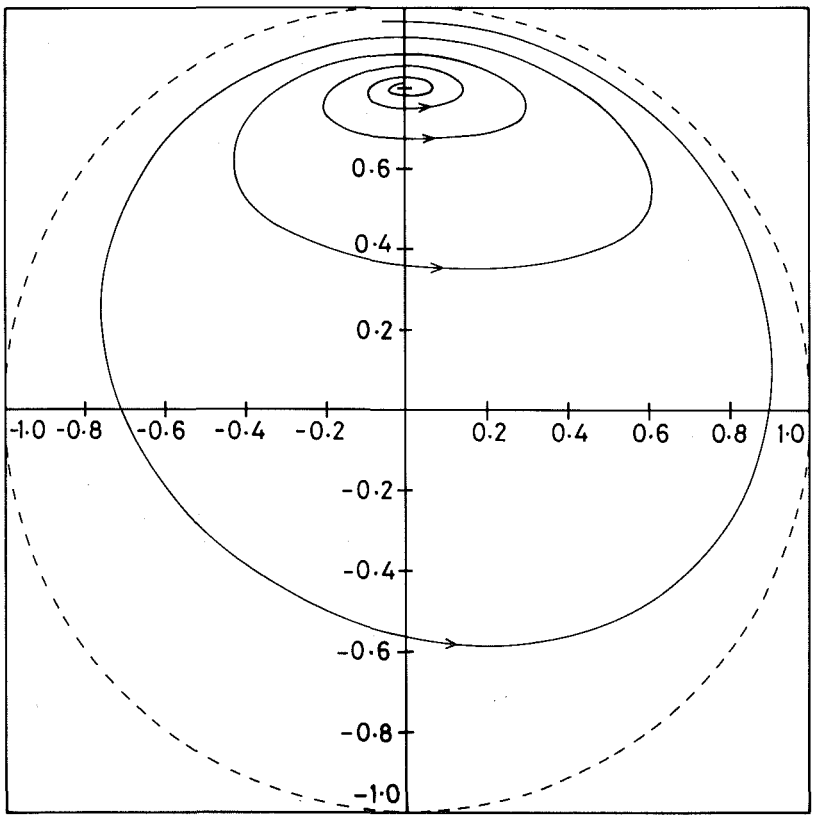


Fig. 2(*b*) $S = 0.01685, \bar{\omega}_1 = 1.6$

Downloaded 02 May 2010 to 171.66.16.250. Redistribution subject to ASME license or copyright; see http://www.asme.org/terms/Terms_Use.cfm

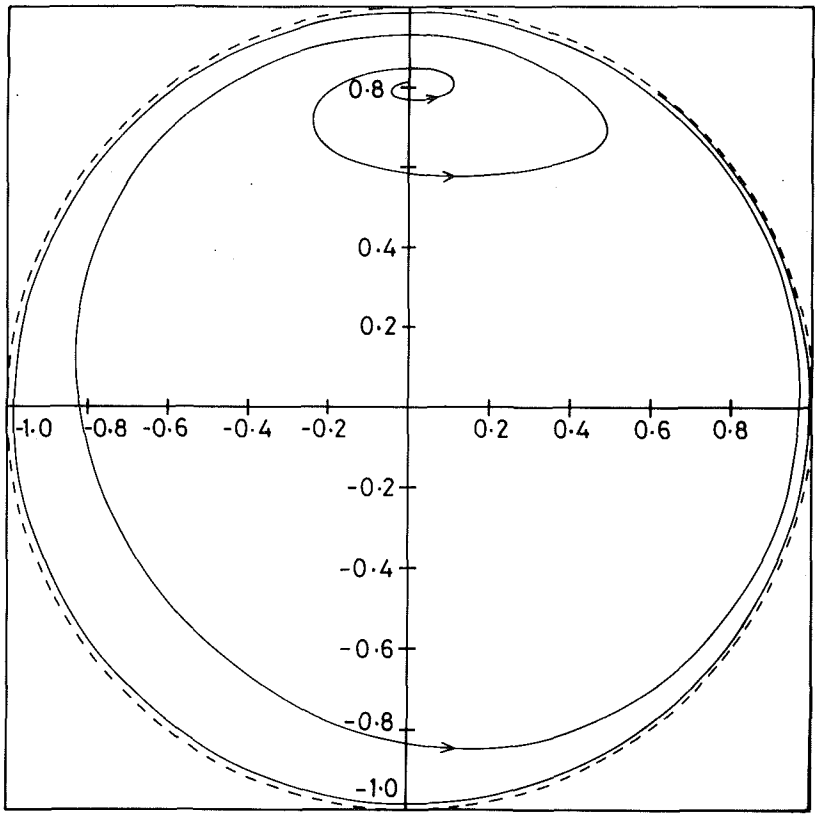


Fig. 2(c) $S = 0.01685, \bar{\omega}_1 = 2.5$

Fig. 2 Variations in Sommerfeld number and normalized angular speed (full film)

(*i*) No closed orbits were found for any of the parameters tested; all the whirl trajectories progressed to the bearing case.

(*ii*) The number of loops in the trajectories around the static equilibrium point increased as the value of the Sommerfeld number was increased. A similar effect was observed when ϵ_0 was decreased, i.e., computed trajectories with static equilibrium points nearer the bearing center produced more loops [Figs. 2(*a*), (*b*)].

(*iii*) As the Sommerfeld number was decreased the loops produced became more elongated and crescent-shaped. Conversely increases in the Sommerfeld number led to increasingly circular loops.

(*iv*) Increases in $\bar{\omega}_1$ resulted in decreases in the number of loops around the static equilibrium point [Figs. 2(*b*), (*c*)].

(*v*) Whirl speed approached half shaft speed as the journal neared the bearing case.

(*vi*) The magnitude of the initial displacement from the static equilibrium point had a noticeable effect on the whirl trajectory; as $|\epsilon_1 - \epsilon_0|$ was increased the number of loops around the static equilibrium point decreases.

4 Dynamically Loaded Journal Bearing With Cavitation

It has long been known that under many operating conditions a complete lubricating film is not maintained in a journal bearing. Instead the film ruptures and a (or perhaps several) gas/vapor cavity is formed. A recent comprehensive review by Dowson and Taylor [7] discusses the phenomenon of cavitation and describes and evaluates some of the available models. The crucial point we wish to make in this paper is that in a cavitated bearing there are regions of parameter space within which stable orbits may be described by the journal under the action of fluid forces alone. Within these regions the same loaded bearing with a full film of lubricant would be unstable, thus the presence of a cavity may be a stabilizing influence. That it may also, under certain conditions, be a destabilizing influence is also revealed by our numerical computations of orbits and we will discuss this in more detail later.

We first of all use one of the simplest models of cavitation as the basis for our computations, the so-called π-film model. This model assumes that the lubricant occupies the convergent half of the annular region between bearing and journal, whilst the divergent half is cavitated. A more realistic model considers a fixed oil feed position on the bearing case from which the cavity is assumed to form, the extent of the cavity being determined by the size of the region with apparently subambient pressure. Examination of this model in a number of forms is a substantial matter which forms the basis of a subsequent paper (Part 2).

5 Fluid Forces and Static Equilibrium—Cavitated Model

It is a quite simple matter to adapt the results of Section 3 for use in the π-film model. We again use the Reynolds equation in the form given in equation (2.5) and this time integrate it subject to the boundary conditions $p = p_a$ at $\theta = 0, \pi; \ldots\ldots$ while at the same time setting $p = p_a$ for $\pi \leq \theta \leq 2\pi$ in the calculation of total fluid forces on the journal.

Thus we find

Downloaded 02 May 2010 to 171.66.16.250. Redistribution subject to ASME license or copyright; see http://www.asme.org/terms/Terms_Use.cfm

$$\frac{p-p_a}{6\mu\left(\frac{R}{c}\right)^2} = (\bar{\omega}-2\phi_L')\frac{\epsilon\sin\theta}{2+\epsilon^2}\left\{\frac{1}{(1+\epsilon\cos\theta)^2}+\frac{1}{(1+\epsilon\cos\theta)}\right\}$$

$$+\epsilon'\left\{\frac{4}{\pi}\left[\frac{\epsilon}{(2+\epsilon^2)(1-\epsilon^2)^{1/2}}\frac{\sin\theta}{(1+\epsilon\cos\theta)^2}\right.\right.$$

$$+\frac{3\epsilon}{(2+\epsilon^2)(1-\epsilon^2)^{3/2}}\frac{\sin\theta}{(1+\epsilon\cos\theta)}$$

$$\left.-\frac{1}{(1-\epsilon^2)^2}\cos^{-1}\left(\frac{\epsilon+\cos\theta}{1+\epsilon\cos\theta}\right)\right] \tag{5.1}$$

$$\left.+\frac{1}{\epsilon}\left[\frac{1}{(1+\epsilon\cos\theta)^2}-\frac{1}{(1+\epsilon)^2}\right]\right\}$$

while the force components are now

$$F_n = LR\int_0^\pi p\sin\theta d\theta = \frac{6\mu LR\left(\frac{R}{c}\right)^2\epsilon}{(2+\epsilon^2)(1-\epsilon^2)}$$

$$\left[\pi(\bar{\omega}-2\phi_L')(1-\epsilon^2)^{1/2}+4\epsilon'\right] \tag{5.2}$$

$$F_r = LR\int_0^\pi p\cos\theta d\theta$$

$$= -6\mu LR\left(\frac{R}{c}\right)^2\left[\frac{2\epsilon^2(\bar{\omega}-2\phi_L')}{(1-\epsilon^2)(2+\epsilon^2)}\right.$$

$$\left.+\frac{\epsilon'}{(1-\epsilon^2)^{3/2}}\left(\pi-\frac{16}{\pi(2+\epsilon^2)}\right)\right] \tag{5.3}$$

The equations of motion for the journal center become

$$\epsilon\phi_L''+2\epsilon'\phi_L'+2\sin\phi_L$$

$$=\frac{12\pi S\epsilon}{(2+\epsilon^2)(1-\epsilon^2)}\left[\pi\left(1-\frac{2\phi_L'}{\bar{\omega}_1}\right)(1-\epsilon^2)^{1/2}+\frac{4\epsilon'}{\bar{\omega}_1}\right] \tag{5.4}$$

$$\epsilon''-\epsilon\phi_L'^2-2\cos\phi_L \tag{5.5}$$

$$=\frac{-12\pi S}{(1-\epsilon^2)^{3/2}}\left[\frac{2\epsilon^2(1-\epsilon^2)^{1/2}}{(2+\epsilon^2)}\left(1-\frac{2\phi_L'}{\bar{\omega}_1}\right)\right.$$

$$\left.+\frac{\epsilon'}{\bar{\omega}_1}\left(\pi-\frac{16}{\pi(2+\epsilon^2)}\right)\right]$$

and the static equilibrium point is seen to be given by

$$\frac{\epsilon_0}{(2+\epsilon^2)(1-\epsilon_0^2)^{1/2}}\left[\frac{1}{4}+\frac{\epsilon_0^2}{\pi^2(1-\epsilon_0^2)}\right]^{1/2}=\frac{1}{12\pi^2 S} \tag{5.6}$$

$$\tan\phi_{L_0}=\frac{\pi(1-\epsilon_0^2)^{1/2}}{2\epsilon_0} \tag{5.7}$$

6 Numerical Computation of Orbits, Cavitated Models

The same numerical procedures are used to solve equations (5.4) and (5.5) as in the full film case; again a number of different orbits have been computed for differing values of $\bar{\omega}_1$, S and initial position relative to static equilibrium.

We can summarize the main findings as follows:

(*i*) The presence of some form of cavitation in the fluid film permitted both stable and unstable trajectories. Trajectories that spiral to poles, limit cycles, and trajectories that progress to the bearing case were detected [Figs. 3, 4(*a*) and (*c*)].

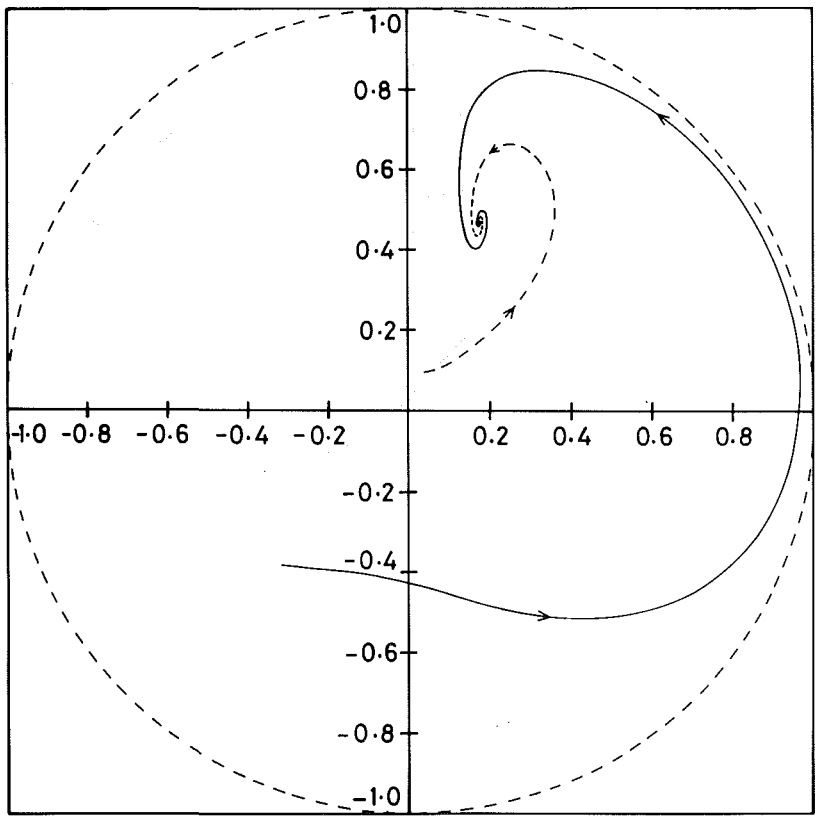


Fig. 3 $S = 0.06177$, $\bar{\omega}_1 = 1$, $\epsilon_0 = 0.50$, $\phi_{L_0} = 1.286$. (*a*)—$\epsilon_1 = 0.51$, $\phi_{L_1} = 4$;and (*b*)---$\epsilon_1 = 0.1$, $\phi_{L_1} = 1.2186$.

Downloaded 02 May 2010 to 171.66.16.250. Redistribution subject to ASME license or copyright; see http://www.asme.org/terms/Terms_Use.cfm

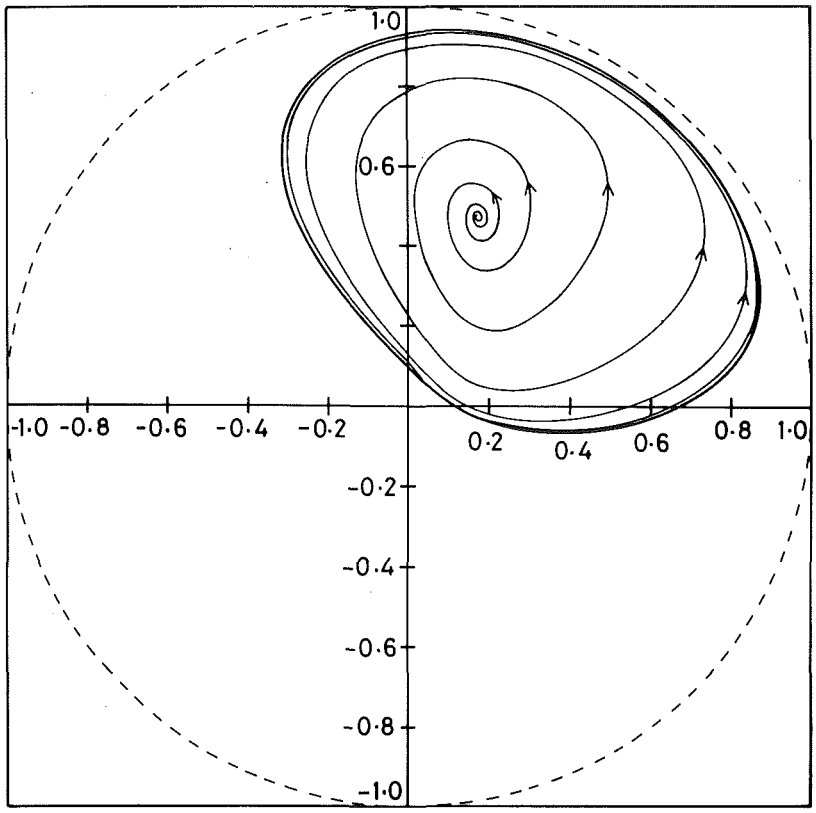


Fig. 4(a) $\bar{\omega}_1 = 2.5, \epsilon_1 = 0.51, \phi_{L_1} = 1.2186$

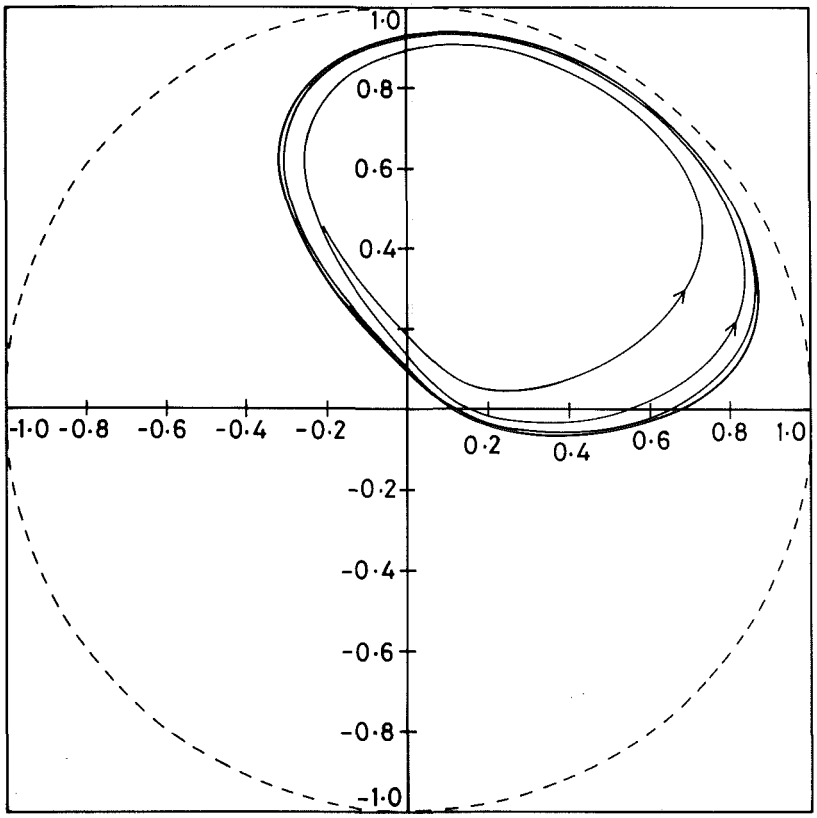


Fig. 4(b) $\bar{\omega}_1 = 2.5, \epsilon_1 = 0.51, \phi_{L_1} = 2$

Downloaded 02 May 2010 to 171.66.16.250. Redistribution subject to ASME license or copyright; see http://www.asme.org/terms/Terms_Use.cfm

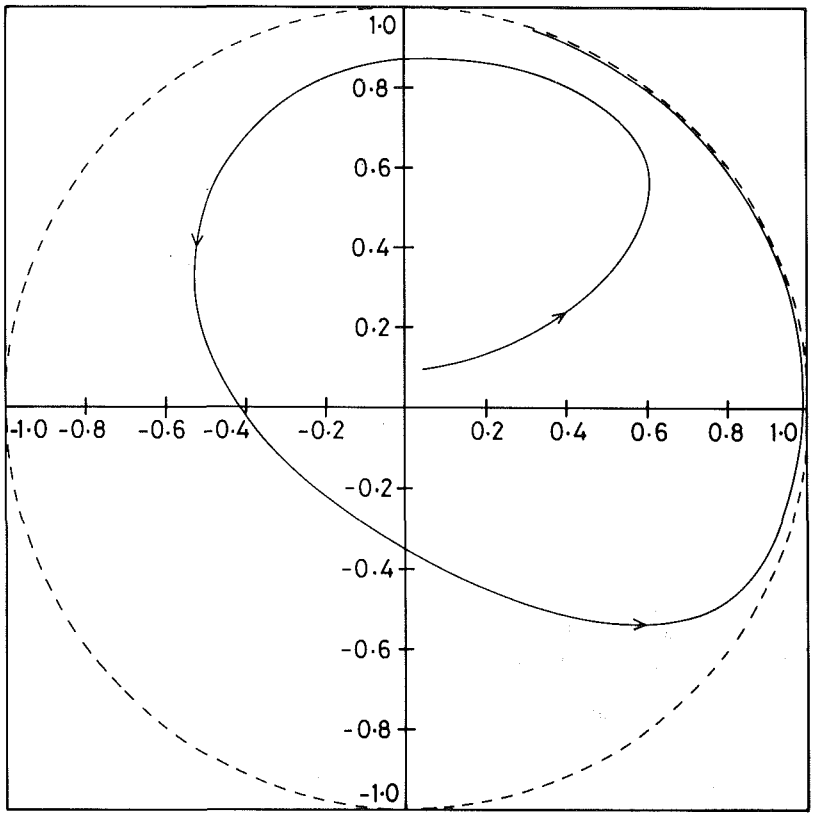


Fig. 4(c) $\bar{\omega}_1 = 4, \epsilon_1 = 0.1, \phi_{L_1} = 1.2186$

Fig. 4 $S = 0.06177, \epsilon_0 = 0.50, \phi_{L_0} = 1.2186$

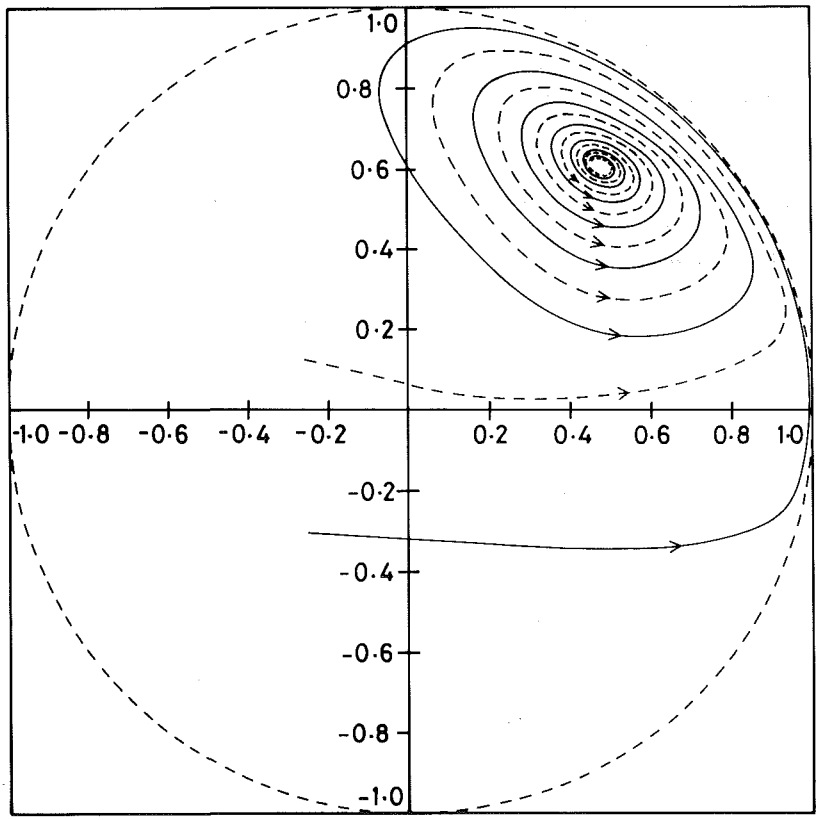


Fig. 5 $S = 0.02827, \bar{\omega}_1 = 2.5, \epsilon_0 = 0.7746, \phi_{L_0} = 0.90844$. (*a*)—$\epsilon_1 = 0.4, \phi_{L_1} = 4.0$, and (*b*)---$\epsilon_1 = 0.3, \phi_{L_1} = 2.7$

Downloaded 02 May 2010 to 171.66.16.250. Redistribution subject to ASME license or copyright; see http://www.asme.org/terms/Terms_Use.cfm

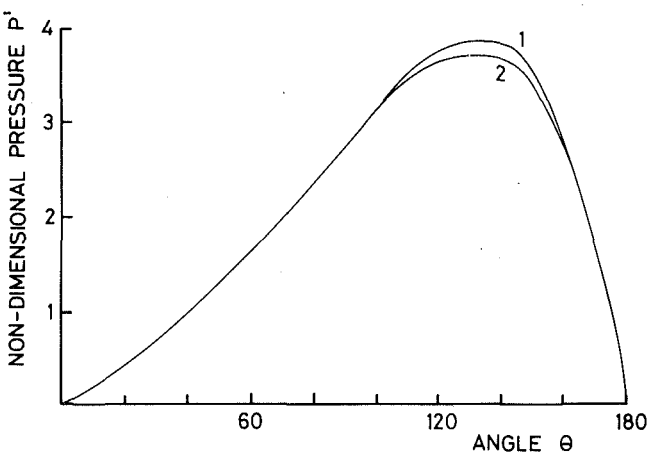


Fig. 6 Pressure distribution for stable trajectory in Fig. 3; 1 approaching pole, 2 at pole

(*ii*) Increases in the value of Sommerfeld number destabilized the resulting whirl trajectories [Figs. 5 and 4(*a*)].

(*iii*) Increases in the value of the normalized angular speed $\bar{\omega}$ destabilized the whirl trajectories [Figs. 3, 4(*a*), and (*c*)].

(*iv*) For trajectories that exhibited limit cycle or decaying orbit properties whirl speed approached half shaft speed as time progressed.

(*v*) Trajectories that spiral to a pole always have as that pole the static equilibrium point [Figs. 3, 5].

(*vi*) Changes in the value of $|\epsilon_1 - \epsilon_0|$ or of $\phi_1 - \phi_0$, had no effect on the stability behavior of the trajectory but merely altered the initial part of the whirl path. [Figs. 3, 4(*a*) and (*b*), and 5].

(Although limit cycles are stable trajectories, when viewed from the static equilibrium point they are assumed to have destabilized the system.)

The most significant result is of course the occurrence of stable orbits in the presence of cavitation. Our results agree well with the linear stability analyses of Reddi and Trumpler [4] for a long bearing, and also with that of Holmes [8] for a short bearing. An important feature of the results is that changes in $|\epsilon_1 - \epsilon_0|$, i.e., differences in initial position relative to the static equilibrium point, do not affect the stability or instability of the orbit. Such changes merely alter the initial stages of the orbit and have no effect on stability borderlines in the $\bar{\omega}_1, S$ parameter plane.

7 Pressure Distributions

The pressure distributions for the unstable situation highlight several interesting features and phases of the trajectory development. In the early part of the path the distribution is well behaved, varying little as the journal moves slowly away from the static equilibrium point. However, as the journal moves near the bearing case, the distribution begins to show a large positive pressure peak close to the point of rupture. At later positions, ever nearer the bearing shell, the distribution starts to acquire negative contributions in the assumed convergent region; the pressure may become totally negative at later stages in the trajectory, "wedge" effects challenging "squeeze" effects for dominance at such positions.

The pressure for the stable trajectory remains well behaved throughout the trajectory.

The contribution from wedge action is always dominant and squeeze effects are negligible, declining to zero as the pole is reached. We present pressure distributions for the stable trajectory

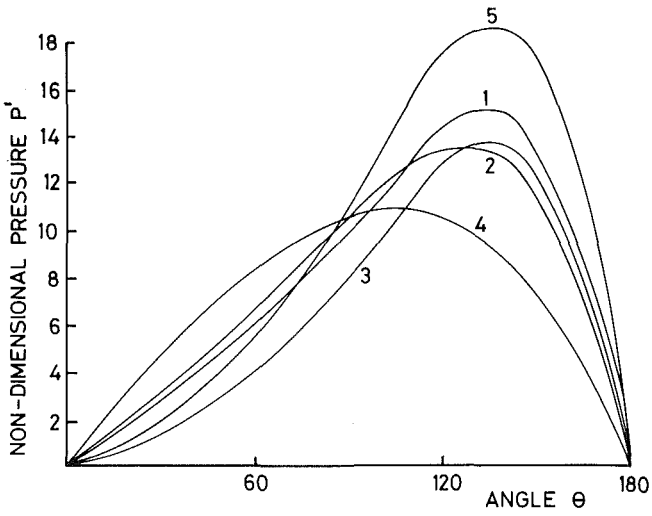


Fig. 7(*a*) Pressure distribution for unstable trajectory in Fig. 4(*c*); 1-5 corresponding to positions in initial part of trajectory

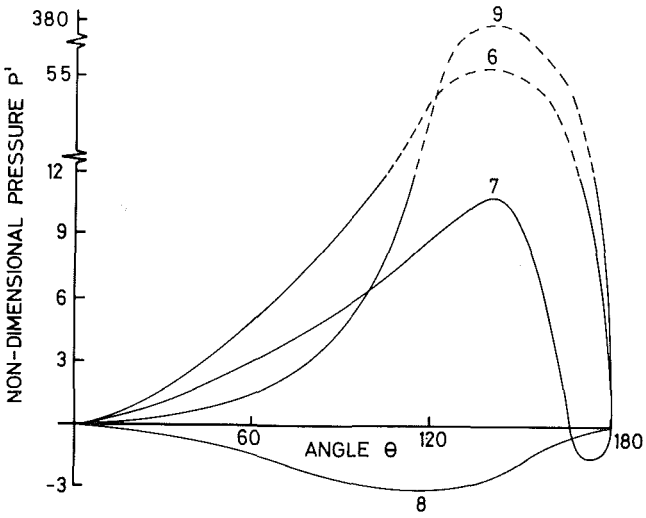


Fig. 7(*b*) Pressure distribution for unstable trajectory in Fig. 4(*c*); 6-9 corresponding to positions in later part of trajectory

Fig. 7

$S = 0.06177, \quad \bar{\omega}_1 = 1, \quad \phi_{L_0} = 1.2186, \quad \phi_{L_1} = 4,$

$\epsilon_0 = 0.50, \quad \epsilon_1 = 0.51$

and the unstable trajectory,

$S = 0.06177, \quad \bar{\omega}_1 = 4,$

$\phi_{L_0} = \phi_{L_1} = 1.2186, \quad \epsilon_0 = 0.50, \quad \epsilon_1 = 0.1.$

8 Discussion

The central result of this investigation is that, whilst in a bearing in which the lubricant film remains continuous and uncavitated the fluid forces *always* act in a destabilizing way to enlarge any small departure from the static equilibrium position, when cavitation occurs the fluid forces can be, depending on the values of the parameters S and $\bar{\omega}_1$, either stabilizing or destabilizing. It is also important to note that variations in the initial conditions, as measured by the position of the journal center relative to its static equilibrium position, have no effect on the stability or instability of the unloaded journal; they merely alter the early stages of the orbit. Thus the stability results are in this sense global, and

Downloaded 02 May 2010 to 171.66.16.250. Redistribution subject to ASME license or copyright; see http://www.asme.org/terms/Terms_Use.cfm

not confined to small initial displacements for which the linear stability analysis of Reddi and Trumpler [4] is valid; in this respect our result agrees with those of Badgeley and Booker [9].

To minimize algebra we have considered only a very simple cavitation model in which the cavity occupies the divergent half of the annular gap. Thus the cavity will or will not rotate with the whirling journal according as the whirl orbit does or does not contain the center of the bearing. Whether or not this behavior is a valid model for a real journal bearing seems to be an open question; there is a surprising dearth of direct observational evidence with which to compare our results, and the conflicting results of Cole and Hughes [10] and White [11] add to the speculation. It is, however, undoubtedly true that the assumption that the cavity always occupies just half of the total circumference of the bearing is a very crude one. Indeed the pressure distributions presented in Fig. 7 for the unstable trajectory, showing a negative total pressure at some radial positions, illustrates the weakness of the π-film model. We should certainly expect a cavity to form whenever a negative pressure is predicted, and in the later stages of the unstable trajectory we are therefore led to expect a cavity occupying the whole circumference! The pressure distributions for the stable case presented in Fig. 6 are on the other hand very realistic, and give credence to the central result that cavitation can produce fluid forces that are stabilizing.

This important result, which is in broad agreement with earlier work by Reddi and Trumpler [4], Holmes [8], and Badgeley and Booker [9] suggests that whirl stability characteristics for more realistic cavitation models should be investigated, and this we do in later papers, at the same time stressing the need for more observational evidence of real cavity behavior.

References

1 Holmes, R., "Oil-Whirl Characteristics of a Rigid Rotor in 360° Journal Bearings," *Proceedings of the Institution of Mechanical Engineers*, Vol. 177, No. *ii*, 1963, pp. 291–307.

2 Mitchell, J. R., Holmes, R., and Byrne, J., "Oil Whirl of a Rigid Rotor in 360° Journal Bearings: Further Characteristics," *Proceedings of the Institution of Mechanical Engineers*, Vol. 180, 1966, pp. 593–610.

3 Tolle, G. C., and Muster, D., "An Analytic Solution of Whirl in a Finite Journal Bearing With Continuous Lubricating Film," ASME *Journal of Engineering for Industry*, Vol. 91, 1969, pp. 1189–1195.

4 Reddi, M. M., and Trumpler, P. R., "Stability of the High Speed Journal Bearing Under Steady Load," ASME *Journal of Engineering for Industry*, Vol. 84, 1962, pp. 351–358.

5 Capriz, G., Galletti, L., and Laratta, A., "On Some Dynamical Problems Arising in the Theory of Lubrication," *Rivista Matematica Universita di Parma*, Vol. 4, 1963.

6 McKay, J. T., "Fluid Flow and Whirl Orbits in a Whirling Rotor Bearing," PhD Thesis, Leeds University, UK, 1980.

7 Dowson, D., and Taylor, C. M., "Cavitation in Bearings," *Annual Review of Fluid Mechanics*, Vol. 11, 1979, pp. 35–66.

8 Holmes, R., "The Vibration of a Rigid Shaft on Short Sleeve Bearings," *Journal of Mechanical Engineering Science*, Vol. 2, 1960, pp. 237–241.

9 Badgeley, R. H., and Booker, J. F., "Turborotor Instability: Effect of Initial Transients on Plane Motion," ASME *Journal of Lubrication Technology*, Vol. 91, 1969, pp. 625–633.

10 Cole, J. A., and Hughes, C. J., "Oil Flow and Film Extent in Complete Journal Bearings," *Proceedings of the Institution of Mechanical Engineers*, Vol. 170, 1957, pp. 499–510.

11 White, D. C., "Squeeze Film Journal Bearings," PhD Thesis, Cambridge University, UK, 1970.

Downloaded 02 May 2010 to 171.66.16.250. Redistribution subject to ASME license or copyright; see http://www.asme.org/terms/Terms_Use.cfm

J. Brindley

L. Elliott

J. T. McKay

School of Mathematics,
University of Leeds,
Leeds, England LS2 9JT

The Role of Cavitation in Whirl Instability in a Rotor Bearing:

2 Effect of Oil Inlet Position and Supply Pressure

Whirl orbits have been calculated for a cavitated rotor bearing in which the cavity is assumed to form at an oil inlet groove and occupy the region in which subambient pressure is predicted from the equations of motion. Variations in position of the inlet groove and in the oil supply pressure have a profound influence on the behavior of the journal, largely through the variations in cavity size and position that are produced.

1 Introduction

Whilst the cavitation model in Part 1 (based on the assumption of π-film) is a more accurate representation than is a full-film model of the situation found in real bearings, it is nevertheless a poor approximation. Just how realistic a model is provided by the π-film is debatable since there is conflicting evidence by Coles and Hughes [1] and White [2] as to whether or not the cavity rotates with the journal.

Lundholm [3] avoided this controversy by assuming the cavity to form at one of the oil inlet grooves, and applying Reynolds boundary condition to calculate the reformation position. The resulting pressure and force expressions were used in a linear stability analysis, from which effects of oil groove position on the stability curves were determined; actual trajectories were, however, not presented.

In the present investigation a dynamically loaded journal bearing, having an axial groove inlet at ϕ_f, is examined on the assumption that cavitation occurs wherever the pressure is subambient; at such positions the pressure is set to its ambient value; although such an assumption results in a violation of the continuity of flow at the cavity/fluid interface its use can be justified by the acceptable error bounds it gives, especially for heavily loaded situations, and it yields a problem that is relatively modest in its demands on computer time. We consider several values of Sommerfeld number S and normalized angular speed $\bar{\omega}_1$ for various positions of the oil inlet groove and values of the supply pressure p_f.

2 Pressure Distribution and Fluid Forces

As with the full-film model the pressure boundary conditions are

$$p(0)=p(2\pi)=p_a,$$

which lead to

$$p-p_a=6\mu\left(\frac{R}{c}\right)^2\left[\frac{2+\epsilon\cos\theta}{(1+\epsilon\cos\theta)^2}(\bar{\omega}-2\dot{\phi}_L)\frac{\epsilon}{2+\epsilon^2}\sin\theta+\frac{1}{\epsilon}\left[\frac{1}{(1+\epsilon\cos\theta)^2}-\frac{1}{(1+\epsilon)^2}\right]\frac{d\epsilon}{dt}\right] \tag{2.1}$$

The position of the oil supply groove is specified by the angle ϕ_f (Part 1, Fig. 1), measured counterclockwise from the vertical load line, which corresponds to an angle θ_f from the maximum film thickness, where $\theta_f=\phi_f-\phi_L$.

Substituting this value of θ_f into expression (2.1) enables us to calculate the oil inlet pressure. When this is removed from the pressure throughout the bearing, the inlet pressure becomes p_a and the size of cavity is determined by the region of subambient pressure. (Pressure at inlet may equally well be set to any supply pressure p_f.)

Because of the variations in cavity size induced by changes in ϵ, ϕ_L, $\dot{\epsilon}$, and $\dot{\phi}_L$ expressions for the fluid forces at any general position may not be obtained in analytical form, as they were in the full and π-films models in Part 1. Values are however obtainable for any journal position by numerical evaluation of the integrals representing the force components, the range of integration of course being restricted to the fluid region.

3 Equations of Motion and Numerical Procedure

The equations of motion are identical to those derived in Part 1, except for different force expressions. Hence in nondimensional form

$$\begin{aligned}\ddot{\epsilon}-\epsilon\dot{\phi}_L^2&=2\pi SF_r'+2\cos\phi_L\\ \epsilon\ddot{\phi}_L+2\dot{\epsilon}\dot{\phi}_L&=2\pi SF_n'-2\sin\phi_L\end{aligned} \tag{3.1}$$

Contributed by the Applied Mechanics Division and presented at the Winter Annual Meeting, Boston, Mass., November 13-18, 1983 of THE AMERICAN SOCIETY OF MECHANICAL ENGINEERS.

Discussion on this paper should be addressed to the Editorial Department, ASME, United Engineering Center, 345 East 47th Street, New York, N.Y. 10017, and will be accepted until two months after final publication of the paper itself in the JOURNAL OF APPLIED MECHANICS. Manuscript received by ASME Applied Mechanics Division, May, 1981; final revision, March, 1983. Paper No. 83-WA/APM-25.

Copies will be available until July, 1984.

Copyright © 1983 by ASME

Downloaded 02 May 2010 to 171.66.16.250. Redistribution subject to ASME license or copyright; see http://www.asme.org/terms/Terms_Use.cfm

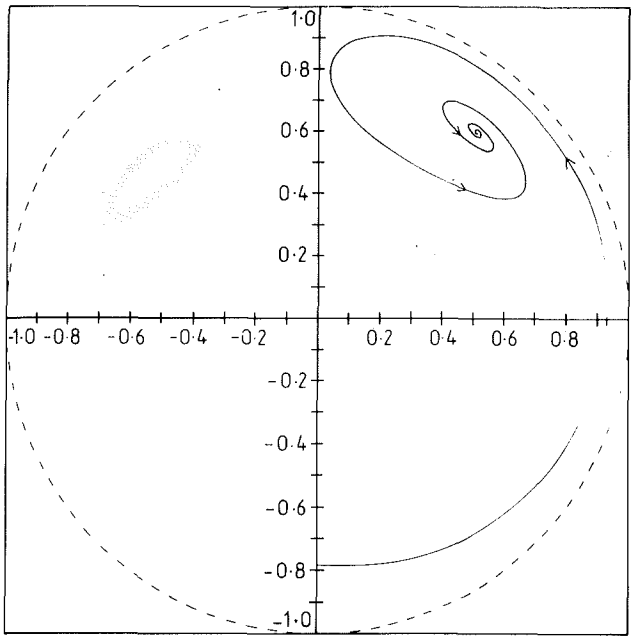


Fig. 1(*a*) $\phi_f = \pi/3, \phi_{L_1} = 4.72$

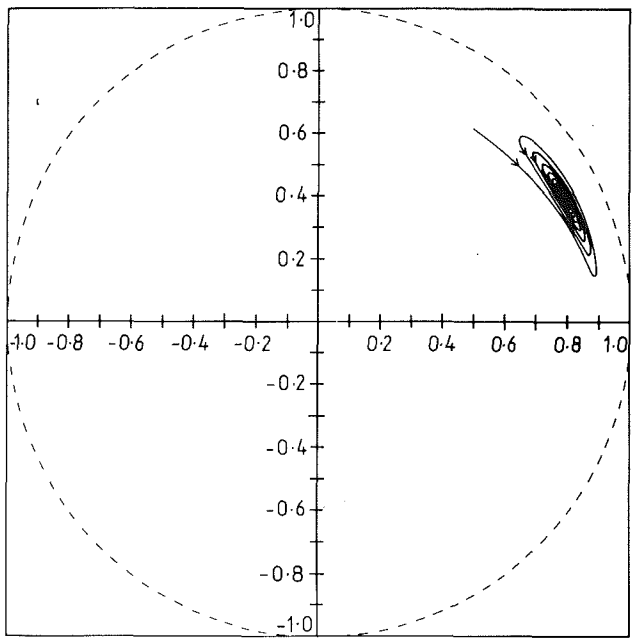


Fig. 1(*b*) $\phi_f = 3\pi/4, \phi_{L_1} = 0.90844$

where

$$F_r' = \frac{F_r}{\left(\mu L \frac{R^3}{C^2}\bar{\omega}\right)} \quad \text{and} \quad F_n' = \frac{F_n}{\left(\mu L \frac{R^3}{C^2}\bar{\omega}\right)}$$

The numerical techniques used to solve equations (3.1) are identical to those in Part 1 for a full film and a π-film except that we now need to use numerically obtained values for the force expressions instead of the analytical forms used there.

The static equilibrium point ϵ_0 and altitude angle ϕ_{L_0} are no longer as simple to determine as in the earlier full and π-film analyses because of the method employed to calculate the fluid forces. The values referred to in this part for these quantities are therefore those determined for the π-film model. This is justified by results obtained from the π-film analysis (and confirmed here), which indicate that the magnitude $|\epsilon_1 - \epsilon_0|$ and $|\phi_{L_1} - \phi_{L_0}|$, where ϵ_1 and ϕ_{L_1} are

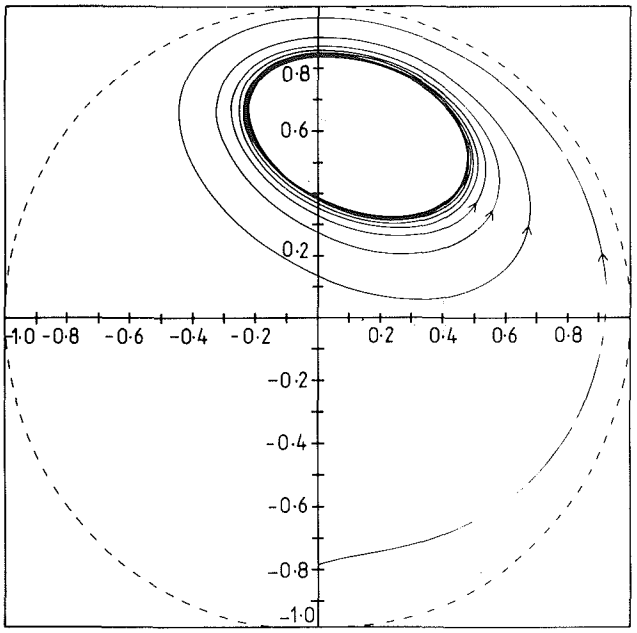


Fig. 1(*c*) $\phi_f = 3\pi/2, \phi_{L_1} = 4.72$

Fig. 1 $S = 0.02827$, $\bar{\omega}_1 = 2.5$, $p_f = 0$, $\epsilon_0 = 0.7746$, $\epsilon_1 = 0.7846$, $\phi_{L_0} = 0.90844$

the starting eccentricity ratio and altitude angle, respectively, do not affect the stability of the trajectory. In addition to variations in Sommerfeld number and normalized angular speed, we have also considered changes in the position of the oil inlet and the value of the supply pressure. Whirl trajectories for a variety of conditions have been calculated and a summary of the results follows.

4 General Observations

(*i*) The introduction of a cavity at the oil groove permits the existence of a variety of different motions (poles, limit cycles, or unstable trajectories) (Figs. 1(*a*), (*c*)).

(*ii*) The position of the groove has a great influence on the trajectories (Figs. 1(*a*), (*b*), (*c*), or 2(*a*), (*b*), (*c*)).

(*iii*) Two separate ranges of oil groove positions were detected: a large range that yielded stable orbits for groove positions to the left of the load line, with a much smaller one to the right (Fig. 3).

(*iv*) Groove positions close to edges of these regions produce a variety of different trajectories depending on the values of S, $\bar{\omega}_1$, and p_f (see (*vii*), (*viii*), and (*ix*)).

(*v*) Different groove positions within a stable region produce different behavior (Figs. 1(*a*), (*b*), or 2(*a*), (*b*)).

(*vi*) Variation in initial conditions (i.e., ϵ_1, $\dot{\epsilon}_1$, ϕ_{L_1}, $\dot{\phi}_{L_1}$) has no effect on stability.

(*vii*) Increasing the Sommerfeld number may affect the stable trajectory, poles changing to limit cycles (Figs. 1(*a*), 2(*a*)) or large limit cycles becoming small (Figs. 1(*c*), 2(*c*)) according to the groove position. A fuller pattern of these modifications is seen in Fig. 4. (Although limit cycles are stable trajectories, when viewed from the static equilibrium point they are assumed to have destabilized the system.)

(*viii*) Similar behavior to (*vii*) occurs when the inlet pressure is changed (Fig. 5).

Downloaded 02 May 2010 to 171.66.16.250. Redistribution subject to ASME license or copyright; see http://www.asme.org/terms/Terms_Use.cfm

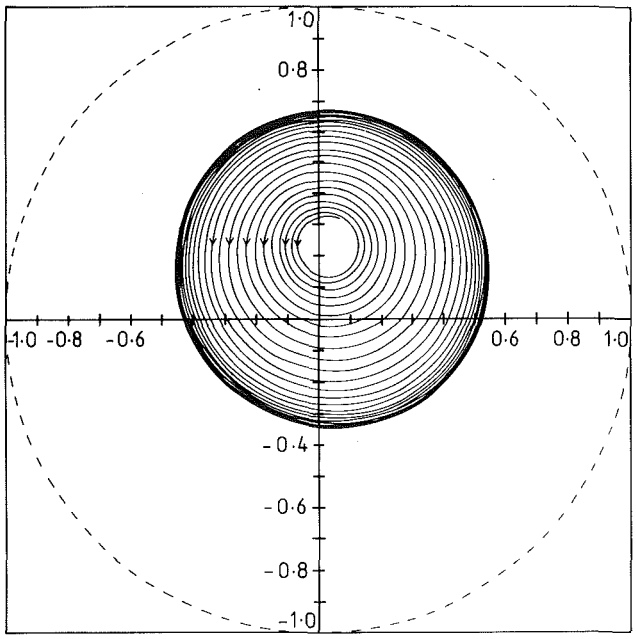


Fig. 2 (*a*) $\phi_f = \pi/3$,

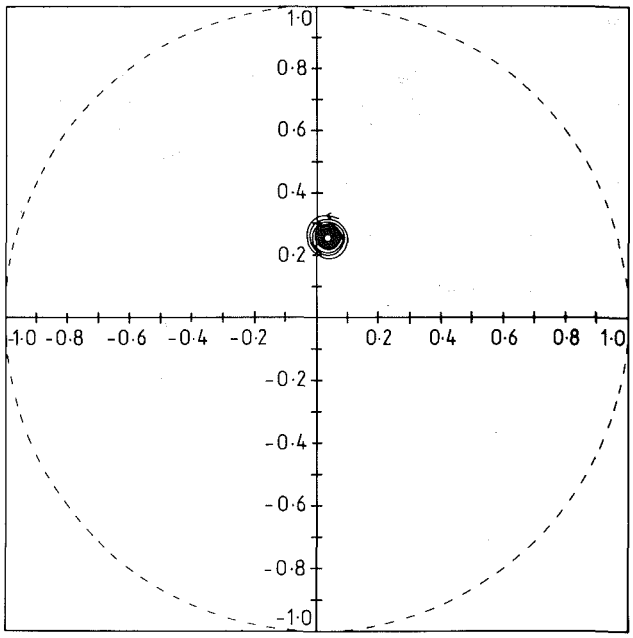


Fig. 2(*b*) $\phi_f = 3\pi/4$

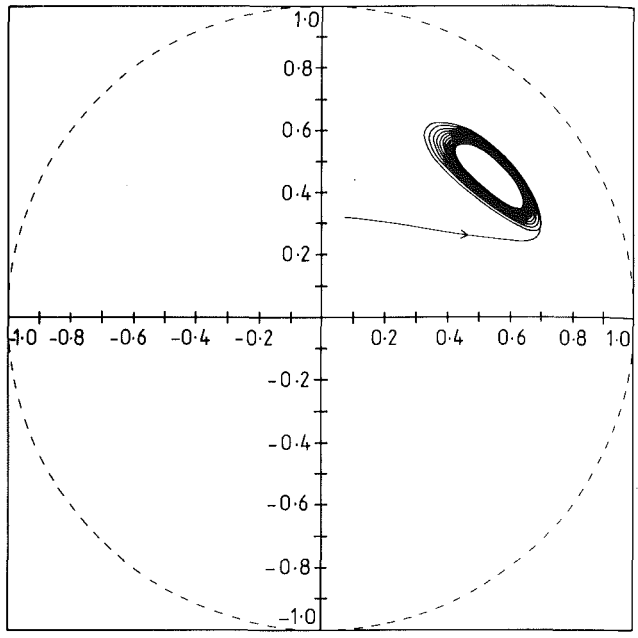


Fig. 2(*c*) $\phi_f = 3\pi/2$

Fig. 2 $S = 0.1041$, $\bar{\omega}_1 = 2.5$, $p_f = 0$, $\epsilon_0 = \epsilon_1 = 0.3162$, $\phi_{L_0} = 1.3617$, $\phi_{L_1} = 1.3617$

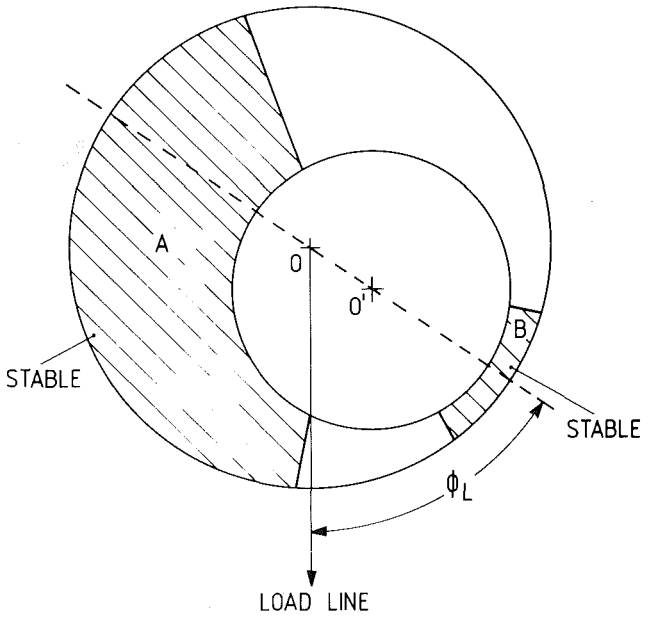


Fig. 3 Regions of stability for various groove positions

(*ix*) Increases in the normalized angular speed always destabilize the trajectories irrespective of groove position (poles becoming limit cycles, which in turn change into unstable trajectories).

5 Discussion of Results

The present calculations indicate (as observed for the π-film) that initial conditions ϵ_1, $\dot{\epsilon}_1$, ϕ_{L_1}, and $\dot{\phi}_{L_1}$ have no influence on the final stability situation, and only make small changes at the start of the trajectory. Likewise, the behavior observed on increasing the normalized angular speed follows that for the π-film and eventually results in an unstable situation regardless of the groove position.

The groove model permits the existence of both stable and unstable solutions but without doubt the most important feature to emerge is the influence of groove position and supply pressure on the journal's behavior. This influence is transmitted via the cavity size and in general results in two distinct stable regions *A* and *B* (Fig. 3), the exact boundaries of which vary according to the governing parameters.

Lundholm [3] presented several stability curves for the case of a single axial groove whose position was allowed to vary with respect to some fixed load line. For positions in region *A* (Fig. 3) the curves were similar to those denoted by *A* (Fig. 6), which in turn relate closely to those found using a π-film model. (Increasing the Sommerfeld number, i.e., decreasing ϵ_0, destabilizes the trajectory.) On the other hand, for positions in region *B* (Fig. 3) a multivalue curve denoted by *B* (Fig. 6) was found, showing that for a given stability parameter two possible neutral states may exist. (Increasing

Downloaded 02 May 2010 to 171.66.16.250. Redistribution subject to ASME license or copyright; see http://www.asme.org/terms/Terms_Use.cfm

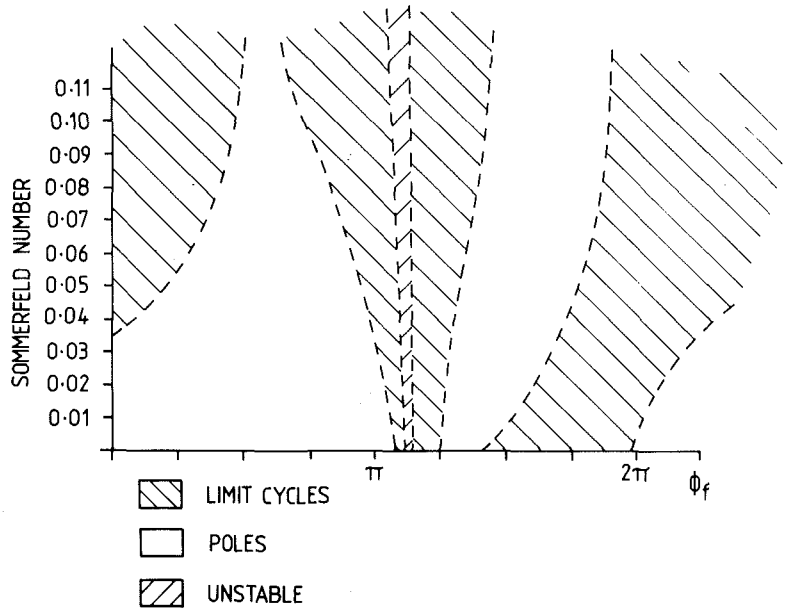


Fig. 4

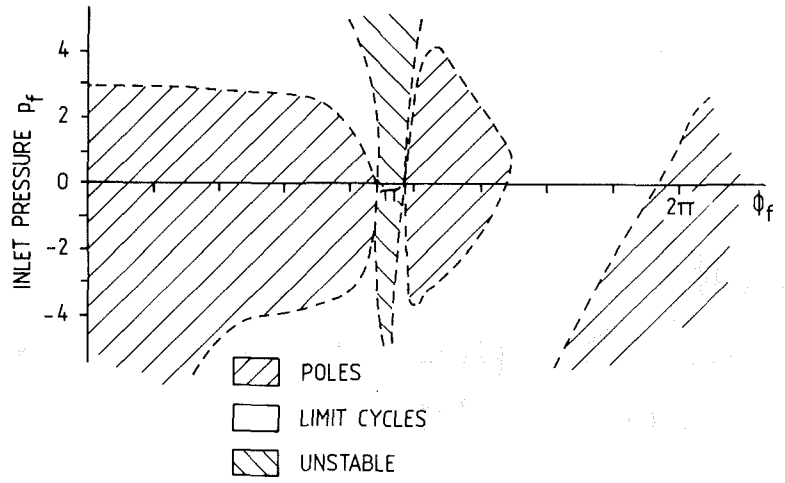


Fig. 5

the Sommerfeld number, although it initially destabilizes the trajectory, eventually produces a stable situation.) Evidence to support these statements is provided in the present results, for region A by Figs. 1(a), 2(a), and 1(b), 2(b), and for region B by Figs. 1(c) and 2(c). In general the results of the present investigation highlight the complex dependence on parameter values of the stability of the journal bearing, although for a fixed normalized angular speed and $p_f = 0$ it appears that a stability surface similar to that in Fig. 7 is appropriate.

The influence of supply pressure on the situation is not easy to summarize as decreasing p_f sometimes stabilizes yet in other cases the reverse is true. To some extent this can be explained by close examination of the pressure distributions throughout the journal's trajectory, where

(*i*) for a pole type behavior the cavity size settles to around its π-film size;

(*ii*) for a limit cycle the cavity size, although varying continuously throughout the cycle, remains small;

(*iii*) for unstable trajectories the value of p_f (varying according to ϕ_f) is:

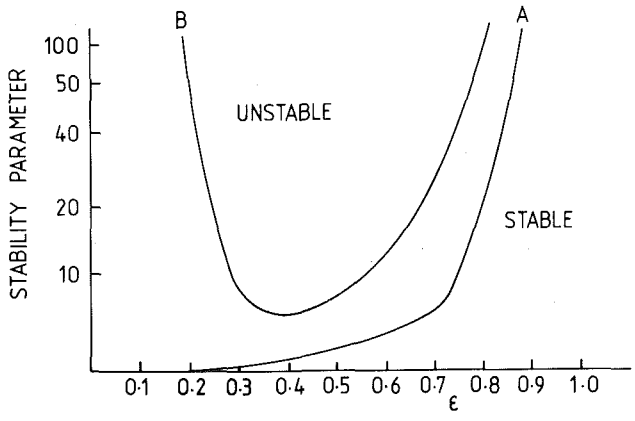


Fig. 6 Stability curves for a single axial groove

either too large to allow the cavitation sufficient for a stable situation (tending toward full-film situation),

or too small, hence producing an excess of cavitation and insufficient fluid forces at certain positions in the trajectory.

Downloaded 02 May 2010 to 171.66.16.250. Redistribution subject to ASME license or copyright; see http://www.asme.org/terms/Terms_Use.cfm

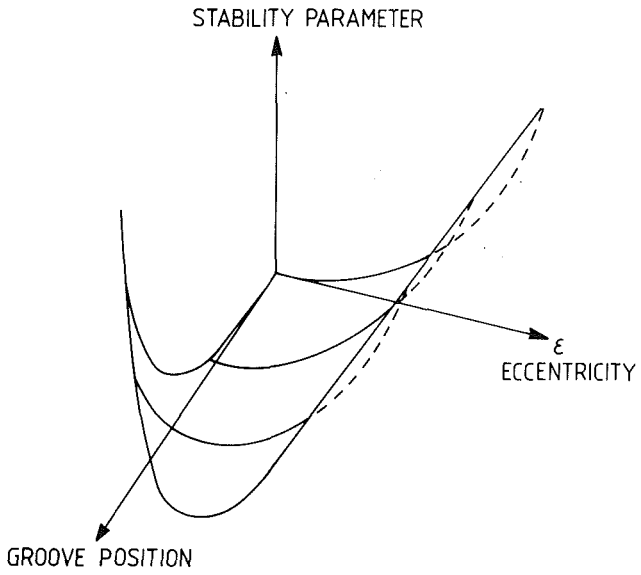


Fig. 7 Possible stability surface for fixed inlet pressure

This influence of inlet pressure and inlet position appears to provide a reasonable explanation as to why cavitation affects stability so greatly. Cole [4] has found stability to be closely related to film extent within the annulus, complete films being associated with instability, but cavitation (governed by the pressure distribution) allowing for stable situations. The present results support these findings that stability may be brought about by the introduction of an adequate sized cavity, different sized cavities producing different poles; it is important to note, however, that too little or too much cavitation results in instability.

Further support for these findings is available from the observations of Özdas [5] who draw attention to the influence that Sommerfeld number, oil inlet pressure, and the type and position of oil groove could have on cavity size and film extent.

References

1 Coles, J. A., and Hughes, C. J., "Oil Flow and Film Extent in Complete Journal Bearings," *Proceedings of the Institution of Mechanical Engineers*, Vol. 170, 1957, pp. 499–510.

2 White, D. C., "Squeeze Film Journal Bearings," Ph.D. Thesis, Cambridge University, UK, 1970.

3 Lundholm, G., "The Axial Groove Journal Bearing Considering Cavitation and Dynamic Stability," *Acta Polytechnica Scandinavia Mechanical Engineering Series*, Vol. 58, 1971, p. 111.

4 Cole, J. A., "Film Extent and Whirl in Complete Journal Bearings," *Proceedings of Conference on Lubrication and Wear, Institution of Mechanical Engineers*, London, 1957, pp. 186–190.

5 Özdas, M. N., "The Behaviour of the Lubricating Film and Side Leakage in Dynamically Loaded Bearings," Transactions ASME, Vol. 80, 1957, pp. 826–832.

Downloaded 02 May 2010 to 171.66.16.250. Redistribution subject to ASME license or copyright; see http://www.asme.org/terms/Terms_Use.cfm

Journal of Applied Mechanics

Brief Notes

A Brief Note is a short paper that presents a specific solution of technical interest in mechanics but which does not necessarily contain new general methods or results. A Brief Note should not exceed 1500 words *or equivalent* (a typical one-column figure or table is equivalent to 250 words; a one line equation to 30 words). Brief Notes will be subject to the usual review procedures prior to publication. After approval such Notes will be published as soon as possible. The Notes should be submitted to the Technical Editor of the JOURNAL OF APPLIED MECHANICS. Discussions on the Brief Notes should be addressed to the Editorial Department, ASME, United Engineering Center, 345 East 47th Street, New York, N. Y. 10017, or to the Technical Editor of the JOURNAL OF APPLIED MECHANICS. Discussions on Brief Notes appearing in this issue will be accepted until two months after publication. Readers who need more time to prepare a Discussion should request an extension of the deadline from the Editorial Department.

Optimum Quasi-Rectangular Holes in Infinite Orthotropic Plates Under Inplane Loading

K. Rajaiah[1] and N. K. Naik[1]

Introduction

Structural components with circular and elliptical holes have innumerable applications in engineering and the stress distributions around these openings are well known. Some recent studies have concentrated attention on the determination of quasi-square optimum hole shapes in infinite isotropic [1, 2] and orthotropic [1] plates yielding minimum stress concentrations using conformal transformation techniques. For isotropic plates, the stress concentration factor (s.c.f.), the stress distribution around the hole, and the optimized hole shape have been found to agree closely with photoelastically determined information reported earlier [3]. It is the purpose of this paper to show that the conformal transformation technique used earlier in reference [1] can be extended to analytically determine quasi-rectangular optimum hole shapes yielding minimum stress concentrations in infinite isotropic and orthotropic plates under uniaxial and biaxial loading conditions.

Analysis

Consider an infinite plate with an opening the contour of which is given by the equations

$$x = a(\cos\theta + \epsilon \cos 3\theta), \quad y = a(c \sin\theta - \epsilon \sin 3\theta) \tag{1}$$

where x,y = rectangular cartesian coordinates, θ = polar angle, a = semimajor axis of the hole, ϵ = hole shape parameter, and $0 < c \leq 1$.

Equations (1) are very general and can be utilized to generate a class of quasi-rectangular holes by varying the parameter ϵ for a given value of c.

Following Lekhnitskii's method [1, 4] and using the transformation function

$$z = a[(1+c)\zeta/2 + (1-c)/2\zeta + \epsilon/\zeta^3] \tag{2}$$

the tangential stress σ_θ at the opening for uniaxial applied stress of σ_0 is given by the following expressions [4]:

Case 1. Plate is subjected to tension along the major axis of the opening.

$$\begin{aligned}\sigma_\theta/\sigma_0 = {} & (B^2/C_0{}^2) + (1/L\,C_0{}^2)\{c(AD^4\cos\theta + BC_0{}^4\, n\sin\theta) \\ & + \epsilon[2AC_0{}^4\, b_{11}\, ckn\cos\theta - 3AD^4\cos 3\theta \\ & - BC_0{}^4\, n\,(2\,a_{11}\, c\sin\theta + 3\sin 3\theta)] \\ & + 2\epsilon^2\, C_0{}^4\, c\, n[-Ak\,(b_{21}\cos\theta + 3\,b_{23}\cos 3\theta) \\ & + B\,(a_{21}\sin\theta + 3\,a_{23}\sin 3\theta)]\}\end{aligned} \tag{3}$$

Case 2. Plate is subjected to tension along the minor axis of the opening.

$$\begin{aligned}\sigma_\theta/\sigma_0 = {} & (A^2/C_0{}^2) + (1/LC_0{}^2)\{AC_0{}^4 kn\cos\theta + BE^4\sin\theta \\ & + \epsilon[AC_0{}^4\, kn(-2\,c_{11}\cos\theta + 3\cos 3\theta + 2BC_0{}^4\, b_{11}\, kn\sin\theta \\ & + 3BE^4\sin 3\theta] + 2\epsilon^2\, C_0{}^4\, kn\,[A(c_{21}\cos\theta + 3c_{23}\cos 3\theta) \\ & - B(b_{21}\sin\theta + 3b_{23}\sin 3\theta)]\}\end{aligned} \tag{4}$$

Here $A = c\cos\theta - 3\epsilon\cos 3\theta$, $B = \sin\theta + 3\epsilon\sin 3\theta$, $C_0{}^2 = A^2 + B^2$

$k = -\mu_1\mu_2$, $n = -i(\mu_1 + \mu_2)$, $L = (B^2 - \mu_1{}^2A^2)(B^2 - \mu_2{}^2A^2)$, where μ_1 and μ_2 are the roots of the characteristics equation

$$\mu^4 + (E_1/G_{12} - 2\nu_{12})\mu^2 + (E_1/E_2) = 0 \tag{5}$$

And E_1, E_2, G_{12}, and ν_{12} are the elastic constants.

$$\lambda_j = (1 + i\mu_j)/(1 - i\mu_j), \quad (j = 1, 2)$$

$$D^4 = -A^4k + A^2B^2(1 - 2k - k^2) + B^4(2 + k - n^2)$$

$$E^4 = A^4(2k^2 - n^2 + k) + A^2B^2(k^2 - 2k - 1) - B^4k.$$

For orthotropic plates,

$$w_i = \frac{2}{1 + c + \lambda_i(1-c)}, \beta_i = w_i\lambda_i, \alpha_i = \frac{1 - c + \lambda_i(1+c)}{1 + c + \lambda_i(1-c)}, \quad (i = 1, 2),$$

$$a_{11} = \frac{\beta_1\mu_1 - \beta_2\mu_2}{\mu_1 - \mu_2}, b_{11} = i\,\frac{\beta_i - \beta_2}{\mu_1 - \mu_2}, c_{11} = \frac{\beta_1\mu_2 - \beta_2\mu_1}{\mu_1 - \mu_2}$$

[1] Professor, and Lecturer, respectively, Aeronautical Engineering Department, Indian Institute of Technology, Bombay 400 076, India.

Manuscript received by ASME Applied Mechanics Division, October, 1982; final revision March, 1983.

Copyright © 1983 by ASME
Downloaded 02 May 2010 to 171.66.16.250. Redistribution subject to ASME license or copyright; see http://www.asme.org/terms/Terms_Use.cfm

Table 1 Material constants (unidirectional glass/epoxy composites in orthogonal orientations)

(*i*) $E_1/E_2 = 3.41$, $E_1/G_{12} = 9.81$, $\nu_{12} = 0.27$ along fiber direction
(*ii*) $E_1/E_2 = 0.293$, $E_1/G_{12} = 2.88$, $\nu_{12} = 0.079$ across fiber direction
$\mathbf{c} = 0.5$, $a/b = 2$ for ellipse, $a/b = 2.10$ for rectangle

Loading	Stress Concentration Factor				Percent reduction in s.c.f. for optimized hole compared with	
	Optimized hole		Elliptical hole	Rectangular hole	Elliptical hole	Rectangular hole
	s.c.f.	ϵ	$\epsilon = 0.0$	$\epsilon = -0.09$		
			Isotropic			
Uniaxial[1]	1.85	−0.02	2.00	2.65	8	30
Uniaxial[2]	3.32	−0.07	5.00	3.46	34	4
Biaxial σ_0: σ_0	3.10	−0.035	4.00	4.39	23	29
Biaxial σ_0: $-\sigma_0$	3.77	−0.10	6.00	3.78	37	0.3
			Orthotropic			
Uniaxial[1,3]	2.26	−0.035	2.80	3.14	19	28
Uniaxial[2,4]	4.02	−0.09	8.20	4.02	51	0
Biaxial[3] σ_0: σ_0	2.95	−0.055	4.36	3.83	32	23
Biaxial[4] σ_0: σ_0	3.23	−0.065	6.35	3.68	49	12
Biaxial[3] σ_0: $-\sigma_0$	3.64	−0.06	5.44	4.05	33	10
Biaxial[4] σ_0: $-\sigma_0$	5.12	−0.11	10.05	5.27	49	3

[1]Loading along major axis
[2]Loading along minor axis
[3]Fiber direction along major axis
[4]Fiber direction along minor axis

$$a_{21} = a_{11}^2 + kb_{11}^2 + 2\frac{\alpha_1\beta_1^2\mu_1 - \alpha_2\beta_2^2\mu_2}{\mu_1 - \mu_2}$$

$$b_{21} = n\,b_{11}^2 + 2i\frac{\alpha_1\beta_1^2 - \alpha_2\beta_2^2}{\mu_1 - \mu_2}$$

$$c_{21} = c_{11}^2 + kb_{11}^2 + 2\frac{\alpha_1\beta_1^2\mu_2 - \alpha_2\beta_2^2\mu_1}{\mu_1 - \mu_2}$$

$$a_{23} = \frac{\beta_1^2\mu_1 - \beta_2^2\mu_2}{\mu_1 - \mu_2}, b_{23} = i\frac{\beta_1^2 - \beta_2^2}{\mu_1 - \mu_2},$$

$$c_{23} = \frac{\beta_1^2\mu_2^2 - \beta_2^2\mu_1^2}{\mu_1 - \mu_2}$$

For isotropic plates, $a_{11} = b_{11} = c_{11} = -1/(1+c)$

$$a_{21} = b_{21} = c_{21} = 2/(1+c)^2, \quad a_{23} = b_{23} = c_{23} = 0$$

For biaxial loading the stress distributions are obtained by the principle of superposition using the information from the case of uniaxial loading.

Using the preceeding equations and by changing the value of the hole shape parameter ϵ for different values of c, it is possible to determine the quasi-rectangular hole shapes and the corresponding stress distributions.

Results and Discussion

Based on the foregoing analysis, numerical results in terms of hole shape parameter ϵ to obtain the optimum quasi-rectangular hole shapes that yield minimum s.c.f. have been generated for $c = 0.5$. Here, $\epsilon = -0.09$ corresponds to a near rectangular shape with rounded corners and $\epsilon = 0$ refers to an ellipse.

For the typical glass/epoxy composite considered (Table 1), the roots of the characteristic equation (5) are given by $\mu_1 = \pm 2.9805\,i$, $\mu_2 = \pm 0.62\,i$ for case (*i*) and $\mu_1 = \pm 1.6128\,i$, $\mu_2 = \pm 0.3355\,i$ for case (*ii*). For isotropic plates $\mu_1 = \mu_2 = i$. The s.c.f. values for isotropic and orthotropic cases are given in Table 1.

It is seen from Table 1 that, with the hole shape optimization, the reduction in s.c.f., as high as 37 percent has been reached for isotropic plates. In general, the gains are much higher for the orthotropic plate considered.

References

1 Rajaiah K., and Naik, N. K., "Optimum Hole Shape Determination in Infinite Orthotropic Plates Under Inplane Loading by Conformal Transformation," *Mech. Res. Com.*, Vol. 9, No. 3, 1982, pp. 179–185.

2 Dhir, S. K., "Optimization in a Class of Hole Shapes in Plate Structures," ASME JOURNAL OF APPLIED MECHANICS, Vol. 48, 1981, pp. 905–908. (Also see Discussion on this paper by K. Rajaiah and N. K. Naik, ASME JOURNAL OF APPLIED MECHANICS, Vol. 49, 1982, p. 927.)

3 Durelli, A. J., and Rajaiah, K., "Quasi-Square Hole with Optimum Shape in an Infinite Plate Subjected to In-Plane Loading," ASME *Journal of Mechanical Design*, Vol. 103, 1981, pp. 866–870.

4 Lekhnitskii, S. G., "Anisotropic Plates," Gordon and Breach, New York 1968.

Minimum-Weight Thin-Walled Cylinders of Given Torsional and Flexural Rigidity

B. L. Karihaloo[1] and W. S. Hemp[2]

Introduction

In a recent paper [1], Parbery and Karihaloo solved the following shape optimization problem: "Find the cross section of a doubly symmetrical thin-walled cylinder of

[1]Department of Civil Engineering and Surveying, University of Newcastle, N.S.W., 2308 Australia.
[2]Department of Engineering Science, University of Oxford, Parks Road, Oxford, England.

Manuscript received by ASME Applied Mechanics Division, December, 1982; final revision, March, 1983.

Downloaded 02 May 2010 to 171.66.16.250. Redistribution subject to ASME license or copyright; see http://www.asme.org/terms/Terms_Use.cfm

Table 1 Material constants (unidirectional glass/epoxy composites in orthogonal orientations)

(*i*) $E_1/E_2 = 3.41$, $E_1/G_{12} = 9.81$, $\nu_{12} = 0.27$ along fiber direction
(*ii*) $E_1/E_2 = 0.293$, $E_1/G_{12} = 2.88$, $\nu_{12} = 0.079$ across fiber direction
$\mathbf{c} = 0.5$, $a/b = 2$ for ellipse, $a/b = 2.10$ for rectangle

Loading	Stress Concentration Factor				Percent reduction in s.c.f. for optimized hole compared with	
	Optimized hole		Elliptical hole	Rectangular hole	Elliptical hole	Rectangular hole
	s.c.f.	ϵ	$\epsilon = 0.0$	$\epsilon = -0.09$		
			Isotropic			
Uniaxial[1]	1.85	−0.02	2.00	2.65	8	30
Uniaxial[2]	3.32	−0.07	5.00	3.46	34	4
Biaxial σ_0: σ_0	3.10	−0.035	4.00	4.39	23	29
Biaxial σ_0: $-\sigma_0$	3.77	−0.10	6.00	3.78	37	0.3
			Orthotropic			
Uniaxial[1,3]	2.26	−0.035	2.80	3.14	19	28
Uniaxial[2,4]	4.02	−0.09	8.20	4.02	51	0
Biaxial[3] σ_0: σ_0	2.95	−0.055	4.36	3.83	32	23
Biaxial[4] σ_0: σ_0	3.23	−0.065	6.35	3.68	49	12
Biaxial[3] σ_0: $-\sigma_0$	3.64	−0.06	5.44	4.05	33	10
Biaxial[4] σ_0: $-\sigma_0$	5.12	−0.11	10.05	5.27	49	3

[1]Loading along major axis
[2]Loading along minor axis
[3]Fiber direction along major axis
[4]Fiber direction along minor axis

$$a_{21} = a_{11}^2 + kb_{11}^2 + 2\frac{\alpha_1\beta_1^2\mu_1 - \alpha_2\beta_2^2\mu_2}{\mu_1 - \mu_2}$$

$$b_{21} = n\,b_{11}^2 + 2i\frac{\alpha_1\beta_1^2 - \alpha_2\beta_2^2}{\mu_1 - \mu_2}$$

$$c_{21} = c_{11}^2 + kb_{11}^2 + 2\frac{\alpha_1\beta_1^2\mu_2 - \alpha_2\beta_2^2\mu_1}{\mu_1 - \mu_2}$$

$$a_{23} = \frac{\beta_1^2\mu_1 - \beta_2^2\mu_2}{\mu_1 - \mu_2}, b_{23} = i\frac{\beta_1^2 - \beta_2^2}{\mu_1 - \mu_2},$$

$$c_{23} = \frac{\beta_1^2\mu_2^2 - \beta_2^2\mu_1^2}{\mu_1 - \mu_2}$$

For isotropic plates, $a_{11} = b_{11} = c_{11} = -1/(1+c)$

$$a_{21} = b_{21} = c_{21} = 2/(1+c)^2, \quad a_{23} = b_{23} = c_{23} = 0$$

For biaxial loading the stress distributions are obtained by the principle of superposition using the information from the case of uniaxial loading.

Using the preceeding equations and by changing the value of the hole shape parameter ϵ for different values of c, it is possible to determine the quasi-rectangular hole shapes and the corresponding stress distributions.

Results and Discussion

Based on the foregoing analysis, numerical results in terms of hole shape parameter ϵ to obtain the optimum quasi-rectangular hole shapes that yield minimum s.c.f. have been generated for $c = 0.5$. Here, $\epsilon = -0.09$ corresponds to a near rectangular shape with rounded corners and $\epsilon = 0$ refers to an ellipse.

For the typical glass/epoxy composite considered (Table 1), the roots of the characteristic equation (5) are given by $\mu_1 = \pm 2.9805\,i$, $\mu_2 = \pm 0.62\,i$ for case (*i*) and $\mu_1 = \pm 1.6128\,i$, $\mu_2 = \pm 0.3355\,i$ for case (*ii*). For isotropic plates $\mu_1 = \mu_2 = i$. The s.c.f. values for isotropic and orthotropic cases are given in Table 1.

It is seen from Table 1 that, with the hole shape optimization, the reduction in s.c.f., as high as 37 percent has been reached for isotropic plates. In general, the gains are much higher for the orthotropic plate considered.

References

1 Rajaiah K., and Naik, N. K., "Optimum Hole Shape Determination in Infinite Orthotropic Plates Under Inplane Loading by Conformal Transformation," *Mech. Res. Com.*, Vol. 9, No. 3, 1982, pp. 179–185.

2 Dhir, S. K., "Optimization in a Class of Hole Shapes in Plate Structures," ASME JOURNAL OF APPLIED MECHANICS, Vol. 48, 1981, pp. 905–908. (Also see Discussion on this paper by K. Rajaiah and N. K. Naik, ASME JOURNAL OF APPLIED MECHANICS, Vol. 49, 1982, p. 927.)

3 Durelli, A. J., and Rajaiah, K., "Quasi-Square Hole with Optimum Shape in an Infinite Plate Subjected to In-Plane Loading," ASME *Journal of Mechanical Design*, Vol. 103, 1981, pp. 866–870.

4 Lekhnitskii, S. G., "Anisotropic Plates," Gordon and Breach, New York 1968.

Minimum-Weight Thin-Walled Cylinders of Given Torsional and Flexural Rigidity

B. L. Karihaloo[1] and W. S. Hemp[2]

Introduction

In a recent paper [1], Parbery and Karihaloo solved the following shape optimization problem: "Find the cross section of a doubly symmetrical thin-walled cylinder of

[1]Department of Civil Engineering and Surveying, University of Newcastle, N.S.W., 2308 Australia.
[2]Department of Engineering Science, University of Oxford, Parks Road, Oxford, England.

Manuscript received by ASME Applied Mechanics Division, December, 1982; final revision, March, 1983.

Copyright © 1983 by ASME
Downloaded 02 May 2010 to 171.66.16.250. Redistribution subject to ASME license or copyright; see http://www.asme.org/terms/Terms_Use.cfm

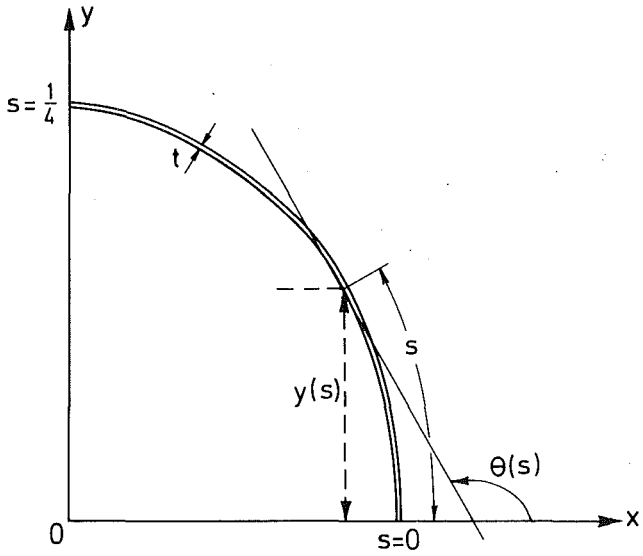


Fig. 1 A quadrant of a thin-walled section showing the coordinate systems

Table 1 Values for B, K, λ, and t/I_0 for various I_0/J_0

I_0/J_0	B	K	λ	t/I_0
0.75	4.333	6.848	0.6024	60.950
1.00	11.594	12.416	0.7688	55.825
1.50	32.968	22.111	0.8821	52.165
2.00	61.598	30.548	0.9240	50.755
2.50	95.811	38.645	0.9452	50.025
3.00	135.251	46.094	0.9578	49.588

constant wall thickness and given contour length, which uses the smallest possible wall thickness to provide, at least, certain given rigidities in torsion and in bending in a principal plane." It was shown that the form of this section depended on the ratio of the given bending rigidity, I_0, to the given torsional rigidity, J_0. For values of this ratio not exceeding one-half the optimum section was circular. For greater values the optimum sections were calculated by numerical integration of the necessary conditions for the optimum. The present Note complements the work reported in [1] by solving the latter problem ($I_0/J_0 > \frac{1}{2}$) in an analytical form. Furthermore, a simpler proof of the corresponding necessary optimality condition is given.

Formulation

If t is the wall thickness, L is the contour length, J_0 is the least value of the torsion constant, I_0 is the least value of the second moment of area, and A is the area enclosed by the center line of the cross section (Fig. 1), then the optimization problem for $I_0/J_0 > \frac{1}{2}$ may be stated as the following Mayer problem [2]:

$$\max \frac{1}{t} = [f_1(x_0)]^2 \tag{1}$$

subject to

$$[f_1(x_0)]^2 = f_2(x_0), \quad f_3(x_0) = L, \tag{2}$$

where

$$f_1(x) = \frac{8}{\sqrt{(J_0 L)}} \int_0^x y\,dx, \quad f_1(x_0) = F_1, \quad f_{1x} = \frac{8}{\sqrt{(J_0 L)}} y, \tag{3}$$

$$f_2(x) = \frac{4}{I_0} \int_0^x y^2 \sqrt{(1 + y_x^2)}\,dx, \quad f_2(x_0) = F_2,$$

$$f_{2x} = \frac{4}{I_0} y^2 \sqrt{(1 + y_x^2)}, \tag{4}$$

$$f_3(x) = 4 \int_0^x \sqrt{(1 + y_x^2)}\,dx, \quad f_3(x_0) = F_3, \quad f_{3x} = 4\sqrt{(1 + y_x^2)} \tag{5}$$

$$f_1(0) = f_2(0) = f_3(0) = y(x_0) = 0 \tag{6}$$

Subscript x denotes differentiation with respect to x. An auxiliary functional Π is constructed by adjoining (2)–(5) to (1), introducing Lagrange multipliers λ, μ, k_1, k_2, and k_3, and giving

$$\Pi = [f_1(x_0)]^2 - \lambda\{[f_1(x_0)]^2 - f_2(x_0)\} + \mu\{f_3(x_0) - L\} + \int_0^{x_0} \left\{k_1\left[f_{1x} - \frac{8y}{\sqrt{(J_0 L)}}\right] + k_2\left[f_{2x} - \frac{4y^2}{I_0} \sqrt{(1 + y_x^2)}\right] + k_3(f_{3x} - 4\sqrt{(1 + y_x^2)})\right\} dx. \tag{7}$$

The variations of Π due to f_1, f_2, and f_3 show that k_1, k_2, and k_3 are constants and that

$$2(1 - \lambda) f_1(x_0) + k_1 = 0; \quad \lambda + k_2 = 0, \quad \mu + k_3 = 0 \tag{8}$$

The variation due to x_0 gives the transversality condition $|y_x| = \infty$ at $x = x_0$. Finally, the variation due to y gives the transversality condition $y_x(0) = 0$ and

$$\frac{d}{dx}\left\{-4\left(\frac{k_2 y^2}{I_0} + k_3\right) \frac{y_x}{\sqrt{(1 + y_x^2)}}\right\} = -\frac{8k_1}{\sqrt{(J_0 L)}} - \frac{8k_2 y}{I_0} \sqrt{(1 + y_x^2)}. \tag{9}$$

Eliminating k_1, k_2, and k_3 from (9) using (8), we get the necessary optimality condition reported in [1]

$$32(1 - \lambda) \frac{I_0}{J_0 L} \int_0^{x_0} y\,dx + \frac{2\lambda y}{\sqrt{(1 + y_x^2)}} - \frac{y_{xx}(\lambda y^2 + \nu)}{(1 + y_x^2)^{3/2}} = 0, \tag{10}$$

where $\nu = \mu I_0$.

Solution

The integrodifferential equation (10) was integrated numerically in [1] by transforming it into the parametric form $y = y(s)$, $\theta = \theta(s)$ (Fig. 1) and normalizing the contour length to unity

$$\frac{d\theta}{ds} = \frac{2\lambda y \cos\theta - C}{(\lambda y^2 + \nu)}, \quad \frac{dy}{ds} = \sin\theta, \tag{11}$$

where C represents the integral term of (10).

In this Note we present an analytical solution to (11). Let us rewrite (11) as

$$\frac{d\theta}{dy} \sin\theta = -\frac{d}{dy}(\cos\theta) = \frac{2\lambda y \cos\theta - C}{(\lambda y^2 + \nu)} \tag{12}$$

The homogeneous equation

$$\frac{d}{dy}(\cos\theta) = -\frac{2\lambda y \cos\theta}{\lambda y^2 + \nu}$$

may be integrated to give

$$\cos\theta = F/(\lambda y^2 + \nu) \tag{13}$$

where F is a constant of integration. Now, treating F as a function of y, it follows from (13) that

$$-\frac{d}{dy}(\cos\theta) = -\frac{F'}{(\lambda y^2 + \nu)} + \frac{2yF}{(\lambda y^2 + \nu)^2}, \tag{14}$$

where a prime denotes differentiation with respect to y. Substituting for F from (13) into (14) and comparing the resulting equation with (11), it is easy to identify the unknown function $F(y)$ with C,

$$F' = C; \quad F = Cy + C_0. \tag{15}$$

From (13) and (15) it follows that

Downloaded 02 May 2010 to 171.66.16.250. Redistribution subject to ASME license or copyright; see http://www.asme.org/terms/Terms_Use.cfm

$$\cos\ \theta = \frac{Cy}{\lambda y^2 + \nu}, \tag{16}$$

The constant of integration $C_0 = 0$. This follows from the boundary condition $\theta(0) = \pi/2$, $y(0) = 0$. The solution to (16) is

$$y = \frac{1 - \sqrt{1 + B\cos^2\theta}}{K\cos\theta}, \tag{17}$$

where $2\lambda/C = K$ and $-2\nu K/C = B$. In the vicinity of $\theta = \pi/2$, equation (17) reduces to

$$y = -B\cos\theta/2K. \tag{18}$$

The unknowns B and K are obtained from the given conditions of the problem (2). Note that $L = 1$ and in the parametric formulation $x_0 = 1/4$. From these conditions we get the following transcendental equation in B

$$\left(48\frac{I_0}{J_0} - B - 8\right)\psi^2(B) - 4\left(12\frac{I_0}{J_0} - 1\right)\frac{B}{\sqrt{(1+B)}}\psi(B)F(m) + 12\frac{I_0}{J_0}\frac{B^2}{(1+B)}F^2(m) = 0, \tag{19}$$

where

$$\psi(B) = \frac{4}{\sqrt{(1+B)}}\{(1+B)E(m) - F(m)\}. \tag{20}$$

Here, $m = B/(1+B)$, and $F(m)$ and $E(m)$ are complete elliptic integrals of the first and second kind, respectively. The transcendental equation was solved by a trial and error procedure for various values of $I_0/J_0 > 1/2$. Table 1 shows the values of B, K, and λ for various values of I_0/J_0. The thickness of the optimum contour is also given in the table. These results gave values of C and ν that were in excellent agreement with those reported in [1].

For completeness of analytical solution, the x-coordinate of the optimum contour calculated by integrating $dx/ds = \cos\ \theta$, $x(\pi) = 0$, is also given

$$x(\theta) = \frac{1}{K}\left\{ln\frac{\sqrt{1 + B[1 + \cos\ (\theta - \pi/2)]}}{\sqrt{[1 + B\sin^2\ (\theta - \pi/2)]} + \cos\ (\theta - \pi/2)}\right\};\quad \frac{\pi}{2} \le \theta \le \pi \tag{21}$$

Acknowledgment

The visit of B. L. Karihaloo to the University of Oxford was partly supported by a grant from the Nuffield Foundation awarded by the Royal Society, London.

References

1 Parbery, R. D., and Karihaloo, B. L., "Minimum-Weight Design of Thin-Walled Cylinders Subject to Flexural and Torsional Stiffness Constraints," ASME Journal of Applied Mechanics, Vol. 47, 1980, pp. 106–110.

2 Pars, L. A., *An Introduction to the Calculus of Variations*, Heinemann, London, 1962, p. 222.

On the Hypoelastic Formulation of Plasticity Using the Past Maximum of Stress

M. E. Gurtin[1]

1 Introduction

This Note presents a formulation of plasticity theory which utilizes a pair of hypoelastic stress-strain laws and a switching rule based on whether the current stress magnitude, $s(t)$, coincides with its past maximum. We do *not* find it necessary to introduce (a priori) the notions of elastic and plastic strain or that of a yield surface. We prove that our formulation is, modulo certain assumptions, completely equivalent to classical plasticity with von Mises yield and isotropic work hardening: the existence of the yield surface and the use of plastic work as hardening parameter are consequences of the theory rather than initial assumptions. We show further that the theory can be reduced to a single rate-type equation with no extraneous switching rules, an observation that might make this formulation amenable to the numerical solution of boundary-value problems.

Notation. For $\mathbf{a}$, $\mathbf{b}$ in $\mathfrak{R}^n$, $\mathbf{a}\cdot\mathbf{b} = \Sigma\, a_i b_i$ and $\mathbf{a}\otimes\mathbf{b}$ is the linear transformation of $\mathfrak{R}^n$ into $\mathfrak{R}^n$ defined by $(\mathbf{a}\otimes\mathbf{b})\mathbf{v} = (\mathbf{b}\cdot\mathbf{v})\mathbf{a}$.

2 Hypoelastic Formulation

We consider a theory based on hypoelastic[2] constitutive equations of the form

$$\left.\begin{aligned} &\dot{\mathbf{e}} = \mathbf{V}(\mathbf{s})\dot{\mathbf{s}} \quad \text{whenever } s = s_m \quad \text{and} \quad \dot{s} \ge 0,\\ &\dot{\mathbf{e}} = \mathbf{D}(\mathbf{s})\dot{\mathbf{s}} \quad \text{whenever } s = s_m \quad \text{and} \quad \dot{s} < 0,\\ &\qquad\quad \text{or whenever } s < s_m. \end{aligned}\right\} \tag{1}$$

Here $\mathbf{e}(t)$ is the (infinitesimal) strain, $\mathbf{s}(t)$ is the stress,[3]

$$s = (\mathbf{s}\cdot\mathbf{s})^{\frac{1}{2}}$$

is the norm of $\mathbf{s}$,

$$s_m(t) = \max_{0 \le \tau \le t} s(\tau) \tag{2}$$

is the *past maximum* of s, and for each $\mathbf{s}$, $\mathbf{V}(\mathbf{s})$ and $\mathbf{D}(\mathbf{s})$ are *symmetric* linear transformations of $\mathfrak{R}^n$ into itself. The constitutive formulation is completed by adjoining the initial conditions

$$\mathbf{e}(0) = \mathbf{s}(0) = \mathbf{0}. \tag{3}$$

Consider a path $\mathbf{s}$ with $s(t) = s_m(t)$ and $\dot{s}(t) < 0$ at a given time t. Then, by (1), in the limit $\dot{s}(t) \to 0$ the strain rate $\dot{\mathbf{e}}(t)$ tends to $\mathbf{D}(\mathbf{s}(t))\dot{\mathbf{s}}(t)$. On the other hand, the strain rate for a path with $s(t) = s_m(t)$ and $\dot{s}(t) = 0$ is $\mathbf{V}(\mathbf{s}(t))\dot{\mathbf{s}}(t)$. This apparent discontinuity in behavior is removed by the following *continuity hypothesis*: on any path,

$$\mathbf{V}(\mathbf{s})\dot{\mathbf{s}} = \mathbf{D}(\mathbf{s})\dot{\mathbf{s}} \quad \text{whenever} \quad s = s_m \quad \text{and} \quad \dot{s} = 0. \tag{4}$$

We define elastic and plastic strain rates, $\dot{\mathbf{e}}^e$ and $\dot{\mathbf{e}}^P$, through

$$\begin{aligned} \dot{\mathbf{e}}^e &= \mathbf{D}(\mathbf{s})\dot{\mathbf{s}},\\ \dot{\mathbf{e}}^P &= \dot{\mathbf{e}} - \dot{\mathbf{e}}^e. \end{aligned} \tag{5}$$

It then follows, as a direct consequence of (1) and (4), that

$$\dot{\mathbf{e}}^P = \begin{cases} \mathbf{P}(\mathbf{s})\dot{\mathbf{s}} \text{ for } s = s_m \quad \text{and} \quad \dot{s} \ge 0,\\ \mathbf{0} \quad \text{otherwise,} \end{cases} \tag{6}$$

where

$$\mathbf{P}(\mathbf{s}) = \mathbf{V}(\mathbf{s}) - \mathbf{D}(\mathbf{s}). \tag{7}$$

[1] Department of Mathematics, Carnegie-Mellon University, Pittsburgh, Pa. 15213.

Manuscript received by ASME Applied Mechanics Division, October, 1982; final revision, April, 1983.

[2] Cf., e.g., [1] for a discussion of hypoelastic constitutive equations, [2] for a discussion of classical plasticity.

[3] $\mathbf{e}(t)$ and $\mathbf{s}(t)$ – identified with vectors in $\mathfrak{R}^n$ – are the deviatoric components of strain and stress. Our model has obvious generalizations which are beyond the scope of this Note.

Downloaded 02 May 2010 to 171.66.16.250. Redistribution subject to ASME license or copyright; see http://www.asme.org/terms/Terms_Use.cfm

$$\cos\ \theta = \frac{Cy}{\lambda y^2 + \nu}, \tag{16}$$

The constant of integration $C_0 = 0$. This follows from the boundary condition $\theta(0) = \pi/2$, $y(0) = 0$. The solution to (16) is

$$y = \frac{1 - \sqrt{1 + B\cos^2\theta}}{K\cos\theta}, \tag{17}$$

where $2\lambda/C = K$ and $-2\nu K/C = B$. In the vicinity of $\theta = \pi/2$, equation (17) reduces to

$$y = -B\cos\theta/2K. \tag{18}$$

The unknowns B and K are obtained from the given conditions of the problem (2). Note that $L = 1$ and in the parametric formulation $x_0 = 1/4$. From these conditions we get the following transcendental equation in B

$$\left(48\frac{I_0}{J_0} - B - 8\right)\psi^2(B) - 4\left(12\frac{I_0}{J_0} - 1\right)\frac{B}{\sqrt{(1+B)}}\psi(B)F(m) + 12\frac{I_0}{J_0}\frac{B^2}{(1+B)}F^2(m) = 0, \tag{19}$$

where

$$\psi(B) = \frac{4}{\sqrt{(1+B)}}\{(1+B)E(m) - F(m)\}. \tag{20}$$

Here, $m = B/(1+B)$, and $F(m)$ and $E(m)$ are complete elliptic integrals of the first and second kind, respectively. The transcendental equation was solved by a trial and error procedure for various values of $I_0/J_0 > 1/2$. Table 1 shows the values of B, K, and λ for various values of I_0/J_0. The thickness of the optimum contour is also given in the table. These results gave values of C and ν that were in excellent agreement with those reported in [1].

For completeness of analytical solution, the x-coordinate of the optimum contour calculated by integrating $dx/ds = \cos\ \theta$, $x(\pi) = 0$, is also given

$$x(\theta) = \frac{1}{K}\left\{ln\frac{\sqrt{1 + B[1 + \cos\ (\theta - \pi/2)]}}{\sqrt{[1 + B\sin^2\ (\theta - \pi/2)]} + \cos\ (\theta - \pi/2)}\right\};$$

$$\frac{\pi}{2} \le \theta \le \pi \tag{21}$$

Acknowledgment

The visit of B. L. Karihaloo to the University of Oxford was partly supported by a grant from the Nuffield Foundation awarded by the Royal Society, London.

References

1 Parbery, R. D., and Karihaloo, B. L., "Minimum-Weight Design of Thin-Walled Cylinders Subject to Flexural and Torsional Stiffness Constraints," ASME Journal of Applied Mechanics, Vol. 47, 1980, pp. 106–110.

2 Pars, L. A., *An Introduction to the Calculus of Variations*, Heinemann, London, 1962, p. 222.

On the Hypoelastic Formulation of Plasticity Using the Past Maximum of Stress

M. E. Gurtin[1]

1 Introduction

This Note presents a formulation of plasticity theory which utilizes a pair of hypoelastic stress-strain laws and a switching rule based on whether the current stress magnitude, $s(t)$, coincides with its past maximum. We do *not* find it necessary to introduce (a priori) the notions of elastic and plastic strain or that of a yield surface. We prove that our formulation is, modulo certain assumptions, completely equivalent to classical plasticity with von Mises yield and isotropic work hardening: the existence of the yield surface and the use of plastic work as hardening parameter are consequences of the theory rather than initial assumptions. We show further that the theory can be reduced to a single rate-type equation with no extraneous switching rules, an observation that might make this formulation amenable to the numerical solution of boundary-value problems.

Notation. For $\mathbf{a}$, $\mathbf{b}$ in $\mathfrak{R}^n$, $\mathbf{a}\cdot\mathbf{b} = \Sigma\, a_i b_i$ and $\mathbf{a}\otimes\mathbf{b}$ is the linear transformation of $\mathfrak{R}^n$ into $\mathfrak{R}^n$ defined by $(\mathbf{a}\otimes\mathbf{b})\mathbf{v} = (\mathbf{b}\cdot\mathbf{v})\mathbf{a}$.

2 Hypoelastic Formulation

We consider a theory based on hypoelastic[2] constitutive equations of the form

$$\left.\begin{aligned} \dot{\mathbf{e}} &= \mathbf{V}(\mathbf{s})\dot{\mathbf{s}} \quad \text{whenever } s = s_m \text{ and } \dot{s} \ge 0, \\ \dot{\mathbf{e}} &= \mathbf{D}(\mathbf{s})\dot{\mathbf{s}} \quad \text{whenever } s = s_m \text{ and } \dot{s} < 0, \\ &\quad \text{or whenever } s < s_m. \end{aligned}\right\} \tag{1}$$

Here $\mathbf{e}(t)$ is the (infinitesimal) strain, $\mathbf{s}(t)$ is the stress,[3]

$$s = (\mathbf{s}\cdot\mathbf{s})^{\frac{1}{2}}$$

is the norm of $\mathbf{s}$,

$$s_m(t) = \max_{0 \le \tau \le t} s(\tau) \tag{2}$$

is the *past maximum* of s, and for each $\mathbf{s}$, $\mathbf{V}(\mathbf{s})$ and $\mathbf{D}(\mathbf{s})$ are *symmetric* linear transformations of $\mathfrak{R}^n$ into itself. The constitutive formulation is completed by adjoining the initial conditions

$$\mathbf{e}(0) = \mathbf{s}(0) = \mathbf{0}. \tag{3}$$

Consider a path $\mathbf{s}$ with $s(t) = s_m(t)$ and $\dot{s}(t) < 0$ at a given time t. Then, by (1), in the limit $\dot{s}(t) \to 0$ the strain rate $\dot{\mathbf{e}}(t)$ tends to $\mathbf{D}(\mathbf{s}(t))\dot{\mathbf{s}}(t)$. On the other hand, the strain rate for a path with $s(t) = s_m(t)$ and $\dot{s}(t) = 0$ is $\mathbf{V}(\mathbf{s}(t))\dot{\mathbf{s}}(t)$. This apparent discontinuity in behavior is removed by the following *continuity hypothesis*: on any path,

$$\mathbf{V}(\mathbf{s})\dot{\mathbf{s}} = \mathbf{D}(\mathbf{s})\dot{\mathbf{s}} \quad \text{whenever} \quad s = s_m \quad \text{and} \quad \dot{s} = 0. \tag{4}$$

We define elastic and plastic strain rates, $\dot{\mathbf{e}}^e$ and $\dot{\mathbf{e}}^P$, through

$$\begin{aligned} \dot{\mathbf{e}}^e &= \mathbf{D}(\mathbf{s})\dot{\mathbf{s}}, \\ \dot{\mathbf{e}}^P &= \dot{\mathbf{e}} - \dot{\mathbf{e}}^e. \end{aligned} \tag{5}$$

It then follows, as a direct consequence of (1) and (4), that

$$\dot{\mathbf{e}}^P = \begin{cases} \mathbf{P}(\mathbf{s})\dot{\mathbf{s}} \text{ for } s = s_m \text{ and } \dot{s} \ge 0, \\ \mathbf{0} \quad \text{otherwise}, \end{cases} \tag{6}$$

where

$$\mathbf{P}(\mathbf{s}) = \mathbf{V}(\mathbf{s}) - \mathbf{D}(\mathbf{s}). \tag{7}$$

[1] Department of Mathematics, Carnegie-Mellon University, Pittsburgh, Pa. 15213.

Manuscript received by ASME Applied Mechanics Division, October, 1982; final revision, April, 1983.

[2] Cf., e.g., [1] for a discussion of hypoelastic constitutive equations, [2] for a discussion of classical plasticity.

[3] $\mathbf{e}(t)$ and $\mathbf{s}(t)$ – identified with vectors in $\mathfrak{R}^n$ – are the deviatoric components of strain and stress. Our model has obvious generalizations which are beyond the scope of this Note.

Copyright © 1983 by ASME
Downloaded 02 May 2010 to 171.66.16.250. Redistribution subject to ASME license or copyright; see http://www.asme.org/terms/Terms_Use.cfm

3 Normality. Reduction to a Single Constitutive Equation

The chief consequence of the continuity hypothesis is the following normality condition:

Theorem. The plastic strain rate $\dot{\mathbf{e}}^P$ is normal to the surface s = constant. In fact, there is a scalar function $\alpha(\mathbf{s})$ such that

$$\dot{\mathbf{e}}^P = \frac{1}{2}\alpha(\mathbf{s})(s_m^2)^{\cdot}\mathbf{s}. \tag{8}$$

It is important to note that we need not add the quantifier

$$\text{for} \quad s=s_m \quad \text{and} \quad \dot{s}\geq 0, \tag{9}$$

since $\dot{s}_m = 0$ whenever (9) is not satisfied. In view of (5), this observation allows us to write the consitutive equations (1) as a *single relation with no extraneous switching rule.*

Corollary. The hypoelastic formulation (1) is equivalent to the single relation.

$$\dot{\mathbf{e}} = \mathbf{D}(\mathbf{s})\dot{\mathbf{s}} + \frac{1}{2}\alpha(\mathbf{s})(s_m^2)^{\cdot}\mathbf{s}. \tag{10}$$

To prove this theorem, note first that, by (4) and (7),

$$\mathbf{P}(\mathbf{s})\dot{\mathbf{s}} = \mathbf{0} \quad \text{whenever} \quad s=s_m \quad \text{and} \quad \dot{s}=0. \tag{11}$$

For any vector $\mathbf{b}$, let $\mathcal{J}_\mathbf{b}$ denote the set of vectors perpendicular to $\mathbf{b}$. Given any vector $\mathbf{a} \neq \mathbf{0}$ and any $\mathbf{l}$ in $\mathcal{J}_\mathbf{a}$, it is possible to find a stress path $\mathbf{s}(t)$ such that, at $t = t_0$, say, $\mathbf{s}(t_0) = \mathbf{a}$, $\dot{\mathbf{s}}(t_0) = \mathbf{l}$, and $s(t_0) = s_m(t_0)$. Then, since $s\dot{s} = \mathbf{s}\cdot\dot{\mathbf{s}}$, it follows that $\dot{s}(t_0) = a^{-1}\mathbf{a}\cdot\mathbf{l} = 0$, and (11) at $t=t_0$ yields $\mathbf{P}(\mathbf{a})\mathbf{l} = 0$. Further, since $\mathbf{P}(\mathbf{s})$ is symmetric, for any vector $\mathbf{v}$,

$$\mathbf{l}\cdot\mathbf{P}(\mathbf{a})\mathbf{v} = \mathbf{v}\cdot\mathbf{P}(\mathbf{a})\mathbf{l} = 0$$

and $\mathbf{P}(\mathbf{a})\mathbf{v}$ is normal to $\mathcal{J}_\mathbf{a}$. In view of (6), this yields the requisite normality condition.

Next, since $\mathbf{s}$ is normal to $\mathcal{J}_\mathbf{s}$, for any vector $\mathbf{v}$ there is a scalar $\lambda(\mathbf{s}, \mathbf{v})$ such that

$$P(\mathbf{s})\mathbf{v} = \lambda(\mathbf{s}, \mathbf{v})\mathbf{s}. \tag{12}$$

Thus, as the left side of (12) is linear in $\mathbf{v}$, $\lambda(\mathbf{s}, \mathbf{v})$ must have the form $\mathbf{b}(\mathbf{s})\cdot\mathbf{v}$; hence

$$\mathbf{P}(\mathbf{s})\mathbf{v} = [\mathbf{b}(\mathbf{s})\cdot\mathbf{v}]\mathbf{s} = [\mathbf{s}\otimes\mathbf{b}(\mathbf{s})]\mathbf{v},$$

and since $\mathbf{v}$ is arbitrary and $\mathbf{P}(\mathbf{s})$ symmetric,

$$\mathbf{P}(\mathbf{s}) = \mathbf{s}\otimes\mathbf{b}(\mathbf{s}), \quad \mathbf{b}(\mathbf{s}) = \alpha(\mathbf{s})\mathbf{s},$$

with $\alpha(\mathbf{s})$ a scalar. Thus

$$\mathbf{P}(\mathbf{s}) = \alpha(\mathbf{s})\mathbf{s}\otimes\mathbf{s},$$

and, in view of (6) and the identity $\mathbf{s}\cdot\dot{\mathbf{s}} = \frac{1}{2}(s^2)^{\cdot}$,

$$\dot{\mathbf{e}}^P = \begin{cases} \dfrac{1}{2}\alpha(s)(s^2)^{\cdot}\mathbf{s} & \text{for} \quad s=s_m \quad \text{and} \quad \dot{s}\geq 0, \\ \mathbf{0} & \text{otherwise.} \end{cases} \tag{13}$$

In view of the remark containing (9), equation (13) yields the desired conclusion (8).

4 The Yield Function. Reduction to Classical Plasticity

Wew now assume that $\alpha(\mathbf{s})$ depends on $\mathbf{s}$ only through the norm s:

$$\alpha(\mathbf{s}) = \alpha(s). \tag{14}$$

We assume, in addition, that

$$\alpha(s) = 0 \quad \text{for} \quad s\leq s_0, \quad \alpha(s) > 0 \quad \text{for} \quad s > s_0, \tag{15}$$

with $s_0 > 0$ the initial yield stress.

For all s, $W \geq 0$ let

$$\varphi(s) = \int_0^s \alpha(\sigma)\sigma^3 d\sigma,$$
$$F(s, W) = \varphi(s) - W, \tag{16}$$

and note that, by (15),

$$\varphi(s) = 0 \quad \text{for} \quad s\leq s_0,$$
$$\varphi(s) \text{ is strictly increasing for } s > s_0. \tag{17}$$

As we will see, F represents a *yield function* with W, the hardening parameter, equal to the plastic work. More precisely, given any path, we define the *plastic work* $W(t)$ through

$$\dot{W} = \mathbf{s}\cdot\dot{\mathbf{e}}^P, \quad W(0) = 0. \tag{18}$$

For the remainder of this section $\mathbf{e}(t)$ and $\mathbf{s}(t)$ comprise a path consistent with the hypoelastic formulation (1)–(3), while $W(t)$ designates the corresponding plastic work.

Proposition. *$F(s, W) \leq 0$ and, when $s > s_0$,*

$$F(s, W) = 0 \Leftrightarrow s = s_m.$$

To establish this result, note that, by (13) and (18),

$$\dot{W} = \begin{cases} \alpha(s)s^3\dot{s} & \text{for} \quad s=s_m \quad \text{and} \quad \dot{s}\geq 0, \\ 0 & \text{otherwise,} \end{cases}$$

and hence, by (16),

$$\dot{W} = \varphi(s_m)^{\cdot} \tag{19}$$

for $s = s_m$ and $\dot{s} \geq 0$. On the other hand, for $s < s_m$ or $\dot{s} < 0$ we have $\dot{s}_m = 0$ and hence $\varphi(s_m)^{\cdot} = 0$; thus (19) is valid for all time. If we integrate (19) using $(18)_2$ and the fact that, by (3) and $(16)_1$, $\varphi(s_m(0)) = \varphi(0) = 0$, we find that $W = \varphi(s_m) \geq \varphi(s)$, where the inequality follows from (17). Thus by (16) and $(17)_2$, the proof is complete.

The next result asserts the reduction to classical plasticity.

Theorem. The strain-rate $\dot{\mathbf{e}}$ admits the decomposition

$$\dot{\mathbf{e}} = \dot{\mathbf{e}}^e + \dot{\mathbf{e}}^P$$

with elastic strain-rate

$$\dot{\mathbf{e}}^e = \mathbf{D}(\mathbf{s})\dot{\mathbf{s}}$$

and plastic strain-rate

$$\dot{\mathbf{e}}^P = \begin{cases} \alpha(s)s\dot{s}\mathbf{s} & \textit{whenever} \quad F(s, W) = 0 \quad \textit{and} \quad \dot{s}\geq 0, \\ \mathbf{0} & \textit{otherwise.} \end{cases} \tag{20}$$

The proof is an immediate consequence of the fact that, by the proposition and (15), the assertions (13) and (20) are equivalent.

Generally, the elastic strain rate is given by the linear, isotropic relation

$$\dot{\mathbf{e}}^e = \frac{1}{2\mu}\dot{\mathbf{s}},$$

with μ the shear modulus. Taking this form for $\mathbf{D}(\mathbf{s})$, and using $(16)_1$ to obtain $\alpha(s)$ in terms of $\varphi(s)$, we can write (10) as

$$\dot{\mathbf{e}} = \frac{1}{2\mu}\dot{\mathbf{s}} + \frac{\varphi'(s)}{2s^3}(s_m^2)^{\cdot}\mathbf{s}.$$

We therefore have – for classical plasticity with von Mises yield and isotropic work hardening – a formulation in terms of a single constitutive relation; what is most important is that

Downloaded 02 May 2010 to 171.66.16.250. Redistribution subject to ASME license or copyright; see http://www.asme.org/terms/Terms_Use.cfm

the yield function and concomitant switching rules are intrinsic to the relation and not separate statements. This observation might be useful in the numerical treatment of plasticity problems.

Acknowledgment

This work was supported by the Army Research Office and the Los Alamos Scientific Laboratory. I would like to thank R. Browning, D. Owen, K. Spear, and W. Williams for valuable comments.

References

1 Truesdell, C., and Noll, W., "The Non-Linear Field Theories of Mechanics," *Handbuch der Physik III/3*, Springer-Verlag, Berlin, 1965.

2 Hill, R., *The Mathematical Theory of Plasticity*, Oxford, London, 1950.

Evaluation of Finite Element Calculations in a Cracked Cylinder Under Internal Pressure by Speckle Photography

G. H. Kaufmann,[1] A. M. Lopergolo,[1] and S. Idelsohn[2]

The usefulness of using the speckle photography technique in fracture mechanics to check numerical calculations is demonstrated for an internally pressurized cylinder with a surface flaw. A pointwise technique was utilized to measure the opening displacements along the crack line and the Mode I stress-intensity factor was determined by extrapolating these results to the crack tip. Finite element calculations were performed to be compared with experimental data and good agreement was obtained.

Introduction

In recent years, extensive work was done to calculate stress-intensity factors in cracked cylinders under internal pressure, a problem of particular interest to demonstrate the structural integrity of nuclear piping systems. Recently, Cesari and Hellen [1] reviewed and compared different analytical and numerical methods. However, for a given situation the most pertinent choice of analysis is not clearly established. Although experimental evaluation of numerical methods is of considerable importance, only few works were done in this area.

The purpose of this Brief Note is two-fold: First, to show the usefulness of utilizing the speckle photography technique in fracture mechanics to evaluate numerical calculations obtained by means of approximate methods, such as finite elements. This optical technique is a noncontact one and in recent years it has been applied to the measurement of fracture parameters in plane specimens [2, 3]. The second purpose is to show the feasibility of utilizing this technique to determine Mode *I* stress-intensity factors in cracked cylinders under internal pressure.

[1] Instituto de Física Rosario (CONICET-UNR), Av. Pellegrini 250, 2000 Rosario, Argentina.

[2] Instituto de Desarrollo Tecnológico para la Industria Química (CONICET-UNL), Güemes 3450, 3000 Santa Fe, Argentina.

Part of this work was presented at the Seventh International Conference on Experimental Stress Analysis held in Haifa, Israel, Aug. 23-27, 1982.

Manuscript received by ASME Applied Mechanics Division, April, 1983.

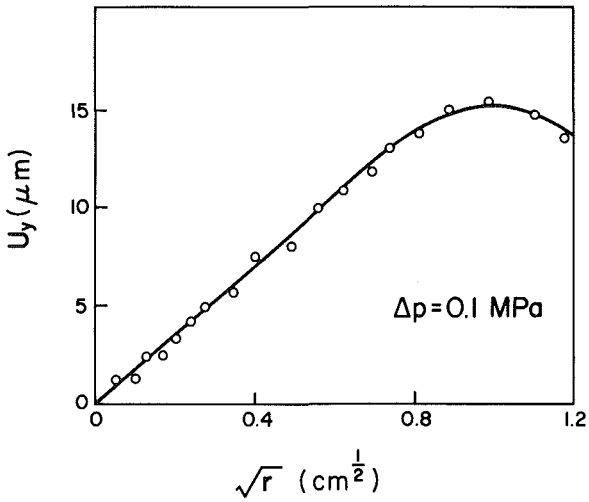


Fig. 1 Opening displacements u_y along the crack line: ○, experimental points; ——, finite element curve

Experimental Procedure

The circular cylinder used in this study was made of PMMA (E = 2020 MPa and ν = 0.33). This material was chosen because it is a brittle one, so the experimental results could be compared with those calculated using linear-elastic fracture mechanics. The cylinder had a thickness of 0.3 cm and its outside diameter was 7 cm. Its length was 20 cm, with a 1 cm clamping on both edges. It has a central axial slot through its thickness of 0.08 cm wide and 2 cm long, which terminated in a vee notch. A soft liner was placed inside the bore of the cylinder to seal the crack.

To clamp the edges of the cylinder, two square-ended steel plates were made. On each end plate there was a circular groove of 1 cm depth which fitted nicely with the cylinder. Before the two ends of the specimen were slid into the groove, a cyanoacrylate cement was poured thus clamping the ends of the cylinder to the end plates. Four rods parallel to the cylinder and fastened to both end plates made sure the clamping did not come unglued. Pressure was applied by means of a hydraulic system.

Displacements observed around the crack tip were very small, about 1 μm which was outside the basic sensitivity of the technique. This could be increased, however, by superimposing a small known artificial displacement. For our application, a rigid body displacement of about three times the speckle diameter was produced by mounting the cylinder on an x vernier table.

Specklegrams were recorded by means of a 120 mm focal length lens of F = 8 aperture used at m = 5 magnification and a He-Ne laser was used to illuminate the specimen surface. Specklegrams were mounted on an $x-y$ coordinate slide so that displacements around the crack could be measured point by point by directing a laser beam (0.5 mm diameter) through them at normal incidence [2, 3].

Stress-Intensity Factor Determination

The opening displacements u_y along the crack line were used to calculate the Mode *I* stress-intensity factor K_I. They were obtained by measuring the crack aperture along two lines parallel to the slot direction, one at each side of the crack and at a distance of 0.25 mm from it. The u_y displacements were calculated as half of the difference between the crack apertures corresponding to a pair of points at each side of the slot for the same value of r. In this way it cancelled the effect of the rigid body movement which was superimposed to increase the sensitivity of the technique.

Downloaded 02 May 2010 to 171.66.16.250. Redistribution subject to ASME license or copyright; see http://www.asme.org/terms/Terms_Use.cfm

the yield function and concomitant switching rules are intrinsic to the relation and not separate statements. This observation might be useful in the numerical treatment of plasticity problems.

Acknowledgment

This work was supported by the Army Research Office and the Los Alamos Scientific Laboratory. I would like to thank R. Browning, D. Owen, K. Spear, and W. Williams for valuable comments.

References

1 Truesdell, C., and Noll, W., "The Non-Linear Field Theories of Mechanics," *Handbuch der Physik III/3*, Springer-Verlag, Berlin, 1965.

2 Hill, R., *The Mathematical Theory of Plasticity*, Oxford, London, 1950.

Evaluation of Finite Element Calculations in a Cracked Cylinder Under Internal Pressure by Speckle Photography

G. H. Kaufmann,[1] A. M. Lopergolo,[1] and S. Idelsohn[2]

The usefulness of using the speckle photography technique in fracture mechanics to check numerical calculations is demonstrated for an internally pressurized cylinder with a surface flaw. A pointwise technique was utilized to measure the opening displacements along the crack line and the Mode I stress-intensity factor was determined by extrapolating these results to the crack tip. Finite element calculations were performed to be compared with experimental data and good agreement was obtained.

Introduction

In recent years, extensive work was done to calculate stress-intensity factors in cracked cylinders under internal pressure, a problem of particular interest to demonstrate the structural integrity of nuclear piping systems. Recently, Cesari and Hellen [1] reviewed and compared different analytical and numerical methods. However, for a given situation the most pertinent choice of analysis is not clearly established. Although experimental evaluation of numerical methods is of considerable importance, only few works were done in this area.

The purpose of this Brief Note is two-fold: First, to show the usefulness of utilizing the speckle photography technique in fracture mechanics to evaluate numerical calculations obtained by means of approximate methods, such as finite elements. This optical technique is a noncontact one and in recent years it has been applied to the measurement of fracture parameters in plane specimens [2, 3]. The second purpose is to show the feasibility of utilizing this technique to determine Mode *I* stress-intensity factors in cracked cylinders under internal pressure.

[1] Instituto de Física Rosario (CONICET-UNR), Av. Pellegrini 250, 2000 Rosario, Argentina.

[2] Instituto de Desarrollo Tecnológico para la Industria Química (CONICET-UNL), Güemes 3450, 3000 Santa Fe, Argentina.

Part of this work was presented at the Seventh International Conference on Experimental Stress Analysis held in Haifa, Israel, Aug. 23-27, 1982.

Manuscript received by ASME Applied Mechanics Division, April, 1983.

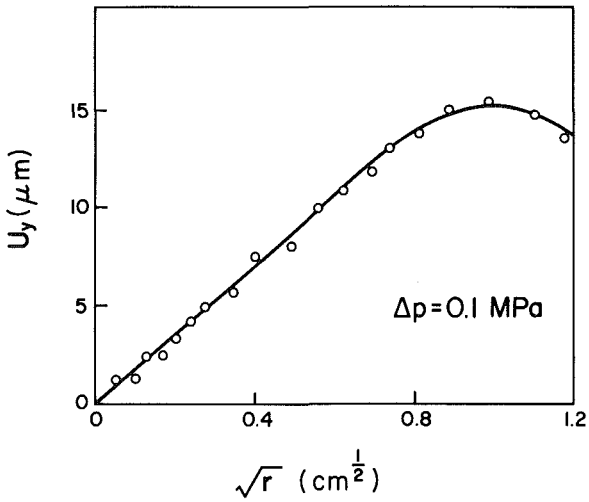


Fig. 1 Opening displacements u_y along the crack line: ○, experimental points; ——, finite element curve

Experimental Procedure

The circular cylinder used in this study was made of PMMA (E = 2020 MPa and ν = 0.33). This material was chosen because it is a brittle one, so the experimental results could be compared with those calculated using linear-elastic fracture mechanics. The cylinder had a thickness of 0.3 cm and its outside diameter was 7 cm. Its length was 20 cm, with a 1 cm clamping on both edges. It has a central axial slot through its thickness of 0.08 cm wide and 2 cm long, which terminated in a vee notch. A soft liner was placed inside the bore of the cylinder to seal the crack.

To clamp the edges of the cylinder, two square-ended steel plates were made. On each end plate there was a circular groove of 1 cm depth which fitted nicely with the cylinder. Before the two ends of the specimen were slid into the groove, a cyanoacrylate cement was poured thus clamping the ends of the cylinder to the end plates. Four rods parallel to the cylinder and fastened to both end plates made sure the clamping did not come unglued. Pressure was applied by means of a hydraulic system.

Displacements observed around the crack tip were very small, about 1 μm which was outside the basic sensitivity of the technique. This could be increased, however, by superimposing a small known artificial displacement. For our application, a rigid body displacement of about three times the speckle diameter was produced by mounting the cylinder on an x vernier table.

Specklegrams were recorded by means of a 120 mm focal length lens of F = 8 aperture used at m = 5 magnification and a He-Ne laser was used to illuminate the specimen surface. Specklegrams were mounted on an $x-y$ coordinate slide so that displacements around the crack could be measured point by point by directing a laser beam (0.5 mm diameter) through them at normal incidence [2, 3].

Stress-Intensity Factor Determination

The opening displacements u_y along the crack line were used to calculate the Mode *I* stress-intensity factor K_I. They were obtained by measuring the crack aperture along two lines parallel to the slot direction, one at each side of the crack and at a distance of 0.25 mm from it. The u_y displacements were calculated as half of the difference between the crack apertures corresponding to a pair of points at each side of the slot for the same value of r. In this way it cancelled the effect of the rigid body movement which was superimposed to increase the sensitivity of the technique.

Copyright © 1983 by ASME

Downloaded 02 May 2010 to 171.66.16.250. Redistribution subject to ASME license or copyright; see http://www.asme.org/terms/Terms_Use.cfm

If the specimen is thin, the state of deformation will approach plane stress in the immediate vicinity of the slot front. For this reason K_I was calculated from [4]

$$u_y = \frac{K_I(1+\nu)}{E}\left(\frac{r}{2\pi}\right)^{1/2}\left(\frac{4}{1+\nu}\sin\theta/2 - \sin\theta\cos\theta/2\right) \quad (1)$$

where r and θ are the polar coordinates with its origin at the crack tip ($\theta = \pi$ along the crack line).

Finite elements were used to evaluate the stress-intensity factor by calculating the plane stress state of displacement in the vicinity of the crack tip using equation (1). To represent the singular stress field in the vicinity of the crack, three-dimensional elements with the midside displaced from its nominal position were included around the crack tip [5]. Convergence of the solution was checked with a similar mesh by analyzing a known cracked plane-stress problem.

Results and Conclusions

Typical opening displacements along the crack line for an applied pressure $P = 0.1$ MPa are shown in Fig. 1. The external opening displacements obtained by finite element calculations for the same pressure are also shown in this figure. It is seen that a satisfactory agreement between experimental and numerical results was obtained. By plotting u_y against $\sqrt{r}$ and fitting a least square straight line into data points for values of r less than 10 percent of the crack length, a value $K_I = 0.287$ MPa $m^{1/2}$ was calculated. A value of 0.302 MPa $m^{1/2}$ was obtained by means of the finite element analysis. They compare reasonably well with the compendium value (Erdogan-Kibler's solution) of 0.29 MPa $m^{1/2}$ [6].

It is interesting to compare this result with that obtained assuming an infinite plane plate with a 20 mm long crack subjected to a tensile field equal in magnitude to the pipe hoop stress. For this problem the stress-intensity factor is $K_I = 0.189$ MPa $m^{1/2}$ [7] which shows the important difference of considering the curvature of the pipe, the double stress state, the Poisson's ratio, and the not infinite boundary conditions.

Concluding, this work demonstrated the practicability of using the speckle photography technique in the area of fracture mechanics to evaluate calculations obtained by means of numerical methods.

Acknowledgment

The authors wish to recognize the helpful comments made by one of the reviewers. One of the authors (A.M.L.) expresses thanks to Consejo de Investigaciones of the Universidad Nacional de Rosario for the support of a Research Fellowship.

References

1 Cesari, F., and Hellen, K. T., "Evaluation of Stress-Intensity Factors for Internally Pressurized Cylinder With Surface Flaws," *International Journal of Pressure Vessels and Piping*, Vol. 7, 1979, pp. 199–227.

2 Evans, E. T., and Luxmoore, A., "Measurement of In-Plane Displacements Around Crack Tips by a Laser Speckle Method," *Engineering Fracture Mechanics*, Vol. 6, 1974, pp. 735–743.

3 Kaufmann, G. H., Idelsohn, S. R., and López, M. J., "Measurements of Magnification Factors for Interactive Surface Flaws by Speckle Photography," *Proceedings of the Seventh International Conference on Experimental Stress Analysis*, Haifa, Israel, Aug. 1982, pp. 580–590.

4 Paris, P. C., and Sih, G., "Stress Analysis of Cracks" *ASTM Special Technical Publication* 381, 1965, pp. 30–83.

5 Henshell, R. D., and Shaw, K. G., "Crack Tip Finite Elements are Unnecessary," *International Journal of Numerical Methods in Engineering*, Vol. 9, 1975, p. 495.

6 Rooke, D. P., and Cartwright, *Compendium of Stress Intensity Factors*, The Hillingdon Press, Uxbridge, 1976.

7 Ang, D. D., and Williams, M. L., "Combined Stresses in an Orthotropic Plate Having a Finite Crack," ASME JOURNAL OF APPLIED MECHANICS, Sept. 1961, pp. 372–382.

Closed-Form, Axisymmetric Solution of the von Karman Plate Equations for Poisson's Ratio One-Third

J. G. Simmonds[1]

Introduction

Consider an initially flat, annular membrane, its inner and outer edges under opposite, uniform vertical forces of the same *net* magnitude. If the membrane is elasticity isotropic, the strains small, and the squares of the angles of rotation negligible compared to one, Föppl's nonlinear equations apply [1]. Jahsman, Field, and Holmes [2] obtained simple, *implicit*, closed-form solutions of these equations in terms of trigonometric functions. The constants of integration were chosen for a disk membrane with a concentrated vertical load at its center and a prescribed radial edge displacement. Earlier, Schwerin [3] had studied this problem for zero edge displacement. His solution failed for Poisson's ratio $\nu > 1/3$ and he erroneously concluded that if $\nu > 1/3$ no axisymmetric solution existed, because certain constants became imaginary. As shown in [2], this objection disappears if, when $\nu > 1/3$, the circular trigonometric functions in the solution of Föppl's equations are replaced by hyperbolic trigonometric functions.

Schwerin noted that if $\nu = 1/3$, the Föppl equations have one-term power solutions that yield a radial displacement that is zero throughout the membrane [3, pp. 656–657]. Schwerin's solution was rediscovered by Stein [4] in 1963 and by Allman and Mansfield [5] in 1981.

Do analogous solutions exist for edge-loaded *plates* with $\nu = 1/3$? For an annular plate subject to vertical edge forces but no edge moments and certain radial edge displacements proportional to the bending stiffness, the answer, for the von Karman equations, is yes, as we will show. It would be convenient to have a finite, closed-form solution for a concentrated load, but the structure of the governing equations and the necessary presence of logarithmic terms precludes this. (If we allow *adjustable surface loads* then one may generate an infinity of exact solutions of axisymmetric nonlinear plate equations – be they von Karman's or Reissner's – merely by choosing any twice-differentiable radial distribution of rotation and stress function, substituting these into the two basic field equations of moment equilibrium and compatibility, and seeing what the surface loads come out to be.)

The Governing Equations

Equations governing the axisymmetric deformation of elastically isotropic plates undergoing small strains but arbitrarily large rotations have been derived by Reissner [6] as a special case of the equations for shells of revolution. Specialized to our problem, these equations read

$$Ar^2\Psi'' + r\Psi' - \Psi) = r(\cos\Phi - 1) \quad (1)$$

$$D(r^2\Phi'' + r\Phi' - \sin\Phi\cos\Phi) = (r(\Psi\sin\Phi - P\cos\Phi). \quad (2)$$

Here, $D = Eh^3/12(1-\nu^2)$ is the bending stiffness and $A = 1/Eh$ is the stretching compliance, where E is Young's modulus and h is the constant plate thickness: Ψ is a stress function and Φ is the angle of rotation of radial midplane fibers; r is radial distance and $\Phi' = d\Phi/dr$. etc.; $2\pi P$ is the net vertical load applied at the edges. The hoop strain and radial stress couple are given, respectively, by

[1]Department of Applied Mathematics and Computer Science, University of Virginia, Charlottesville, Va. 22901. Mem. ASME

Manuscript received by ASME Applied Mechanics Division, January, 1983; final revision, June 1983.

Downloaded 02 May 2010 to 171.66.16.250. Redistribution subject to ASME license or copyright; see http://www.asme.org/terms/Terms_Use.cfm

If the specimen is thin, the state of deformation will approach plane stress in the immediate vicinity of the slot front. For this reason K_I was calculated from [4]

$$u_y = \frac{K_I(1+\nu)}{E}\left(\frac{r}{2\pi}\right)^{1/2}\left(\frac{4}{1+\nu}\sin\theta/2 - \sin\theta\cos\theta/2\right) \quad (1)$$

where r and θ are the polar coordinates with its origin at the crack tip ($\theta = \pi$ along the crack line).

Finite elements were used to evaluate the stress-intensity factor by calculating the plane stress state of displacement in the vicinity of the crack tip using equation (1). To represent the singular stress field in the vicinity of the crack, three-dimensional elements with the midside displaced from its nominal position were included around the crack tip [5]. Convergence of the solution was checked with a similar mesh by analyzing a known cracked plane-stress problem.

Results and Conclusions

Typical opening displacements along the crack line for an applied pressure $P = 0.1$ MPa are shown in Fig. 1. The external opening displacements obtained by finite element calculations for the same pressure are also shown in this figure. It is seen that a satisfactory agreement between experimental and numerical results was obtained. By plotting u_y against $\sqrt{r}$ and fitting a least square straight line into data points for values of r less than 10 percent of the crack length, a value $K_I = 0.287$ MPa $m^{1/2}$ was calculated. A value of 0.302 MPa $m^{1/2}$ was obtained by means of the finite element analysis. They compare reasonably well with the compendium value (Erdogan-Kibler's solution) of 0.29 MPa $m^{1/2}$ [6].

It is interesting to compare this result with that obtained assuming an infinite plane plate with a 20 mm long crack subjected to a tensile field equal in magnitude to the pipe hoop stress. For this problem the stress-intensity factor is $K_I = 0.189$ MPa $m^{1/2}$ [7] which shows the important difference of considering the curvature of the pipe, the double stress state, the Poisson's ratio, and the not infinite boundary conditions.

Concluding, this work demonstrated the practicability of using the speckle photography technique in the area of fracture mechanics to evaluate calculations obtained by means of numerical methods.

Acknowledgment

The authors wish to recognize the helpful comments made by one of the reviewers. One of the authors (A.M.L.) expresses thanks to Consejo de Investigaciones of the Universidad Nacional de Rosario for the support of a Research Fellowship.

References

1 Cesari, F., and Hellen, K. T., "Evaluation of Stress-Intensity Factors for Internally Pressurized Cylinder With Surface Flaws," *International Journal of Pressure Vessels and Piping*, Vol. 7, 1979, pp. 199–227.

2 Evans, E. T., and Luxmoore, A., "Measurement of In-Plane Displacements Around Crack Tips by a Laser Speckle Method," *Engineering Fracture Mechanics*, Vol. 6, 1974, pp. 735–743.

3 Kaufmann, G. H., Idelsohn, S. R., and López, M. J., "Measurements of Magnification Factors for Interactive Surface Flaws by Speckle Photography," *Proceedings of the Seventh International Conference on Experimental Stress Analysis*, Haifa, Israel, Aug. 1982, pp. 580–590.

4 Paris, P. C., and Sih, G., "Stress Analysis of Cracks" *ASTM Special Technical Publication* 381, 1965, pp. 30–83.

5 Henshell, R. D., and Shaw, K. G., "Crack Tip Finite Elements are Unnecessary," *International Journal of Numerical Methods in Engineering*, Vol. 9, 1975, p. 495.

6 Rooke, D. P., and Cartwright, *Compendium of Stress Intensity Factors*, The Hillingdon Press, Uxbridge, 1976.

7 Ang, D. D., and Williams, M. L., "Combined Stresses in an Orthotropic Plate Having a Finite Crack," ASME JOURNAL OF APPLIED MECHANICS, Sept. 1961, pp. 372–382.

Closed-Form, Axisymmetric Solution of the von Karman Plate Equations for Poisson's Ratio One-Third

J. G. Simmonds[1]

Introduction

Consider an initially flat, annular membrane, its inner and outer edges under opposite, uniform vertical forces of the same *net* magnitude. If the membrane is elasticity isotropic, the strains small, and the squares of the angles of rotation negligible compared to one, Föppl's nonlinear equations apply [1]. Jahsman, Field, and Holmes [2] obtained simple, *implicit*, closed-form solutions of these equations in terms of trigonometric functions. The constants of integration were chosen for a disk membrane with a concentrated vertical load at its center and a prescribed radial edge displacement. Earlier, Schwerin [3] had studied this problem for zero edge displacement. His solution failed for Poisson's ratio $\nu > 1/3$ and he erroneously concluded that if $\nu > 1/3$ no axisymmetric solution existed, because certain constants became imaginary. As shown in [2], this objection disappears if, when $\nu > 1/3$, the circular trigonometric functions in the solution of Föppl's equations are replaced by hyperbolic trigonometric functions.

Schwerin noted that if $\nu = 1/3$, the Föppl equations have one-term power solutions that yield a radial displacement that is zero throughout the membrane [3, pp. 656–657]. Schwerin's solution was rediscovered by Stein [4] in 1963 and by Allman and Mansfield [5] in 1981.

Do analogous solutions exist for edge-loaded *plates* with $\nu = 1/3$? For an annular plate subject to vertical edge forces but no edge moments and certain radial edge displacements proportional to the bending stiffness, the answer, for the von Karman equations, is yes, as we will show. It would be convenient to have a finite, closed-form solution for a concentrated load, but the structure of the governing equations and the necessary presence of logarithmic terms precludes this. (If we allow *adjustable surface loads* then one may generate an infinity of exact solutions of axisymmetric nonlinear plate equations – be they von Karman's or Reissner's – merely by choosing any twice-differentiable radial distribution of rotation and stress function, substituting these into the two basic field equations of moment equilibrium and compatibility, and seeing what the surface loads come out to be.)

The Governing Equations

Equations governing the axisymmetric deformation of elastically isotropic plates undergoing small strains but arbitrarily large rotations have been derived by Reissner [6] as a special case of the equations for shells of revolution. Specialized to our problem, these equations read

$$Ar^2\Psi'' + r\Psi' - \Psi) = r(\cos\Phi - 1) \quad (1)$$

$$D(r^2\Phi'' + r\Phi' - \sin\Phi\cos\Phi) = (r(\Psi\sin\Phi - P\cos\Phi). \quad (2)$$

Here, $D = Eh^3/12(1-\nu^2)$ is the bending stiffness and $A = 1/Eh$ is the stretching compliance, where E is Young's modulus and h is the constant plate thickness: Ψ is a stress function and Φ is the angle of rotation of radial midplane fibers; r is radial distance and $\Phi' = d\Phi/dr$. etc.; $2\pi P$ is the net vertical load applied at the edges. The hoop strain and radial stress couple are given, respectively, by

[1]Department of Applied Mathematics and Computer Science, University of Virginia, Charlottesville, Va. 22901. Mem. ASME

Manuscript received by ASME Applied Mechanics Division, January, 1983; final revision, June 1983.

Copyright © 1983 by ASME
Downloaded 02 May 2010 to 171.66.16.250. Redistribution subject to ASME license or copyright; see http://www.asme.org/terms/Terms_Use.cfm

$$\epsilon_\theta = r^{-1}U = A[\Psi' - \nu r^{-1}(\Psi \cos\Phi + P \sin\Phi] \quad (3)$$

$$M_r = -D(\Phi' + \nu r^{-1} \sin\Phi). \quad (4)$$

where U is the horizontal displacement. Boundary conditions at the inner and outer egdes, $r=a,b$, are that $M_r=0$ and that ϵ_θ (or U) take on prescribed values.

Nondimensionalization

To measure the influence of large rotations and bending stiffness, we introduce the dimensionless "angle" and "bending" parameters

$$\alpha = 2\left(\frac{AP}{b}\right)^{1/3} = 2\left(\frac{P}{Ehb}\right)^{1/3} \quad (5)$$

$$\beta^2 = \frac{4D\alpha}{Pb} = \frac{2}{3(1-\nu^2)}\left(\frac{Ehb}{P}\right)^{2/3}\left(\frac{h}{b}\right)^2. \quad (6)$$

If we then set

$$r^2 = b^2 x, \quad \Psi = \left(\frac{P}{\alpha}\right)x^{-1/2} f, \quad \Phi = \alpha x^{1/2} g \quad (7)$$

and

$$\epsilon_\theta = \left(\frac{AP}{\alpha b}\right)e, \quad U = \left(\frac{AP}{\alpha}\right)u, \quad M_r = -\left(\frac{D\alpha}{b}\right)m. \quad (8)$$

Equations (1) to (4) reduce to

$$f'' = 2(\alpha x^{1/2})^{-2}[\cos(\alpha x^{1/2} g) - 1] \quad (9)$$

$$\beta^2\{(xg)'' + \frac{1}{4}x^{-1}[g - (\alpha x^{1/2})^{-1}\sin(\alpha x^{1/2} g)\cos(\alpha x^{1/2} g)]\}$$
$$= f(\alpha x^{1/2})^{-1}\sin(\alpha x^{1/2} g) - \cos(\alpha x^{1/2} g) \quad (10)$$

$$e = x^{-1/2}u = 2f' - x^{-1}\{f + \nu[f\cos(\alpha x^{1/2} g) + (\alpha x^{1/2})\sin(\alpha x^{1/2} g)]\} \quad (11)$$

$$m = 2xg' + g + \nu(\alpha x^{1/2})^{-1}\sin(\alpha x^{1/2} g). \quad (12)$$

where, now, a prime denotes differentiation with respect to x.

Exact Solution for $\alpha \to 0$

In the limit as $\alpha \to 0$, equations (9) to (12) reduce to

$$f'' = -g^2 \quad (13)$$

$$\beta^2 x(xg)'' = fg - 1 \quad (14)$$

$$e = x^{-1/2}u = 2f' - x^{-1}(1+\nu)f \quad (15)$$

$$m = 2xg' + (1+\nu)g, \quad (16)$$

the twice-integrated, axisymmetric form of the von Karman equations.

Let $\nu = 1/3$. By inspection, we see that

$$f = (9/2)^{1/3} x^{2/3} - (2/9)\beta^2, \quad g = (2/9)^{1/3} x^{-2/3} \quad (17)$$

satisfy (13) and (14) and yield $m \equiv 0$, while (15) reduces to

$$e = x^{-1/2}u = (8/27x)\beta^2. \quad (18)$$

Thus (17) is an exact solution of the von Karman equations for an annular plate under vertical edge loads only and the prescribed radial displacement

$$u(a/b,\beta) = (8/27)(b/a)^{1/2}\beta^2, \quad u(1,\beta) = (8/27)\beta^2. \quad (19)$$

As $\beta \to 0$, our solution reduces to that of Schwerin [3] for a membrane.

Acknowledgment

This research was supported by the National Science Foundation under grant CEE-8117103.

References

1 Foppel, A., *Vorlesungen über technische Mechanik*, Vol. 3, Teubner, Leipzig, 1905, pp. 298–299.

2 Jahsman, W. E., Field, F. A., and Holmes, A. M. C., "Finite Deformations in a Prestressed, Centrally Loaded Circular Elastic Membrane," *Proc. 4th Nat. Cong. Appl. Mechs.*, Vol. 1, 1962, pp. 585–594.

3 Schwerin, E., "Über Spannungen und Formanderungen kreisringformiger Membranen," *Z f. Tech. Physik*, Vol. 12, 1929, pp. 651–659.

4 Stein, M., "Arrest of a Moving Mass by an Attached Membrane," NASA Tech. Note D-1928, 1963.

5 Allman, D. J., and Mansfield, E. M., "The Annular Membrane Under Axial Load," ASME JOURNAL OF APPLIED MECHANICS, Vol. 48, 1981, pp. 975–976.

6 Reissner, E., "On the Equations for Finite Symmetrical Deflections of Thin Shells of Revolution," *Progress in Applied Mechanics* (The Prager Anniversary Vol., Drucker, D. C., ed.,) MacMillan, 1963, pp. 171–178.

On The Elastoplastic Stress Concentration At Reentrant Corners of Thin-Walled Cross Sections Subjected to Pure Torsion

D. Durban[1]

Introduction

An approximate solution for the *elastic* stress concentration at reentrant corners, of thin-walled cross sections subjected to pure torsion, has been suggested by Timoshenko [1]. His derivation is based on the assumption of a *local axisymmetric field* near the corner (Fig. 1(*a*)), and on pragmatic conditions of *matching* with the remote stress field in the straight arms. By that he was able to obtain elegant expressions for the stress concentration factors for both open and closed, thin-walled cross sections. The validity of Timoshenko's results, for sufficiently small values of a/c, was confirmed later by Huth [2] via a more accurate finite differences solution. A further discussion of the matter has been given by Conway in [3].

Here, we propose an approximate solution for the corresponding *elastoplastic* stress concentration problems. The analysis employs the standard formulation of small strain torsion in conjunction with the deformation theory of plasticity [4]. No restriction is placed on the stress-strain characteristic, but useful asymptotic relations are derived for power-hardening materials. The dependence of the stress concentration factors, and maximum shear strain, on cross section geometry and remote shear stress is illustrated for a typical aluminium alloy.

Governing Equations

Consider a right-handed cylinder, with arbitrary cross section, subjected to pure torsion. Locate a Cartesian system (x,y,z) at the lower surface $(z=0)$ so that the cylinder's axis coincides with the positive z direction, and (x,y) are the plane coordinates of each cross section. The corresponding displacements are then given by $u = -\theta zy$, $v = \theta zx$, $w = w(x,y,\theta)$, where θ is the twist per unit length and w is the warping function. The two associated shear strain components

$$\gamma_{xz} = w_{,x} - \theta y \quad \gamma_{yz} = w_{,y} + \theta x \quad (1)$$

can be conjoined to form the compatibility equation

[1]Permanent address: Department of Aeronautical Engineering, Technion, Haifa, Israel. Present address (until October 1983): University Engineering Department, Trumpington Street, Cambridge, England CB2 1PZ.

Manuscript received by ASME Applied Mechanics Division, November, 1982; final revision, June, 1983.

Downloaded 02 May 2010 to 171.66.16.250. Redistribution subject to ASME license or copyright; see http://www.asme.org/terms/Terms_Use.cfm

$$\epsilon_\theta = r^{-1}U = A[\Psi' - \nu r^{-1}(\Psi \cos\Phi + P \sin\Phi] \quad (3)$$

$$M_r = -D(\Phi' + \nu r^{-1} \sin\Phi). \quad (4)$$

where U is the horizontal displacement. Boundary conditions at the inner and outer egdes, $r=a,b$, are that $M_r=0$ and that ϵ_θ (or U) take on prescribed values.

Nondimensionalization

To measure the influence of large rotations and bending stiffness, we introduce the dimensionless "angle" and "bending" parameters

$$\alpha = 2\left(\frac{AP}{b}\right)^{1/3} = 2\left(\frac{P}{Ehb}\right)^{1/3} \quad (5)$$

$$\beta^2 = \frac{4D\alpha}{Pb} = \frac{2}{3(1-\nu^2)}\left(\frac{Ehb}{P}\right)^{2/3}\left(\frac{h}{b}\right)^2. \quad (6)$$

If we then set

$$r^2 = b^2 x, \quad \Psi = \left(\frac{P}{\alpha}\right)x^{-1/2} f, \quad \Phi = \alpha x^{1/2} g \quad (7)$$

and

$$\epsilon_\theta = \left(\frac{AP}{\alpha b}\right)e, \quad U = \left(\frac{AP}{\alpha}\right)u, \quad M_r = -\left(\frac{D\alpha}{b}\right)m. \quad (8)$$

Equations (1) to (4) reduce to

$$f'' = 2(\alpha x^{1/2})^{-2}[\cos(\alpha x^{1/2} g) - 1] \quad (9)$$

$$\beta^2\{(xg)'' + \frac{1}{4}x^{-1}[g - (\alpha x^{1/2})^{-1}\sin(\alpha x^{1/2} g)\cos(\alpha x^{1/2} g)]\}$$
$$= f(\alpha x^{1/2})^{-1}\sin(\alpha x^{1/2} g) - \cos(\alpha x^{1/2} g) \quad (10)$$

$$e = x^{-1/2}u = 2f' - x^{-1}\{f + \nu[f\cos(\alpha x^{1/2} g) + (\alpha x^{1/2})\sin(\alpha x^{1/2} g)]\} \quad (11)$$

$$m = 2xg' + g + \nu(\alpha x^{1/2})^{-1}\sin(\alpha x^{1/2} g). \quad (12)$$

where, now, a prime denotes differentiation with respect to x.

Exact Solution for $\alpha \to 0$

In the limit as $\alpha \to 0$, equations (9) to (12) reduce to

$$f'' = -g^2 \quad (13)$$

$$\beta^2 x(xg)'' = fg - 1 \quad (14)$$

$$e = x^{-1/2}u = 2f' - x^{-1}(1+\nu)f \quad (15)$$

$$m = 2xg' + (1+\nu)g, \quad (16)$$

the twice-integrated, axisymmetric form of the von Karman equations.

Let $\nu = 1/3$. By inspection, we see that

$$f = (9/2)^{1/3} x^{2/3} - (2/9)\beta^2, \quad g = (2/9)^{1/3} x^{-2/3} \quad (17)$$

satisfy (13) and (14) and yield $m \equiv 0$, while (15) reduces to

$$e = x^{-1/2}u = (8/27x)\beta^2. \quad (18)$$

Thus (17) is an exact solution of the von Karman equations for an annular plate under vertical edge loads only and the prescribed radial displacement

$$u(a/b,\beta) = (8/27)(b/a)^{1/2}\beta^2, \quad u(1,\beta) = (8/27)\beta^2. \quad (19)$$

As $\beta \to 0$, our solution reduces to that of Schwerin [3] for a membrane.

Acknowledgment

This research was supported by the National Science Foundation under grant CEE-8117103.

References

1 Foppel, A., *Vorlesungen über technische Mechanik*, Vol. 3, Teubner, Leipzig, 1905, pp. 298–299.

2 Jahsman, W. E., Field, F. A., and Holmes, A. M. C., "Finite Deformations in a Prestressed, Centrally Loaded Circular Elastic Membrane," *Proc. 4th Nat. Cong. Appl. Mechs.*, Vol. 1, 1962, pp. 585–594.

3 Schwerin, E., "Über Spannungen und Formanderungen kreisringformiger Membranen," *Z f. Tech. Physik*, Vol. 12, 1929, pp. 651–659.

4 Stein, M., "Arrest of a Moving Mass by an Attached Membrane," NASA Tech. Note D-1928, 1963.

5 Allman, D. J., and Mansfield, E. M., "The Annular Membrane Under Axial Load," ASME JOURNAL OF APPLIED MECHANICS, Vol. 48, 1981, pp. 975–976.

6 Reissner, E., "On the Equations for Finite Symmetrical Deflections of Thin Shells of Revolution," *Progress in Applied Mechanics* (The Prager Anniversary Vol., Drucker, D. C., ed.,) MacMillan, 1963, pp. 171–178.

On The Elastoplastic Stress Concentration At Reentrant Corners of Thin-Walled Cross Sections Subjected to Pure Torsion

D. Durban[1]

Introduction

An approximate solution for the *elastic* stress concentration at reentrant corners, of thin-walled cross sections subjected to pure torsion, has been suggested by Timoshenko [1]. His derivation is based on the assumption of a *local axisymmetric field* near the corner (Fig. 1(*a*)), and on pragmatic conditions of *matching* with the remote stress field in the straight arms. By that he was able to obtain elegant expressions for the stress concentration factors for both open and closed, thin-walled cross sections. The validity of Timoshenko's results, for sufficiently small values of a/c, was confirmed later by Huth [2] via a more accurate finite differences solution. A further discussion of the matter has been given by Conway in [3].

Here, we propose an approximate solution for the corresponding *elastoplastic* stress concentration problems. The analysis employs the standard formulation of small strain torsion in conjunction with the deformation theory of plasticity [4]. No restriction is placed on the stress-strain characteristic, but useful asymptotic relations are derived for power-hardening materials. The dependence of the stress concentration factors, and maximum shear strain, on cross section geometry and remote shear stress is illustrated for a typical aluminium alloy.

Governing Equations

Consider a right-handed cylinder, with arbitrary cross section, subjected to pure torsion. Locate a Cartesian system (x,y,z) at the lower surface $(z=0)$ so that the cylinder's axis coincides with the positive z direction, and (x,y) are the plane coordinates of each cross section. The corresponding displacements are then given by $u = -\theta zy$, $v = \theta zx$, $w = w(x,y,\theta)$, where θ is the twist per unit length and w is the warping function. The two associated shear strain components

$$\gamma_{xz} = w_{,x} - \theta y \quad \gamma_{yz} = w_{,y} + \theta x \quad (1)$$

can be conjoined to form the compatibility equation

[1]Permanent address: Department of Aeronautical Engineering, Technion, Haifa, Israel. Present address (until October 1983): University Engineering Department, Trumpington Street, Cambridge, England CB2 1PZ.

Manuscript received by ASME Applied Mechanics Division, November, 1982; final revision, June, 1983.

Copyright © 1983 by ASME
Downloaded 02 May 2010 to 171.66.16.250. Redistribution subject to ASME license or copyright; see http://www.asme.org/terms/Terms_Use.cfm

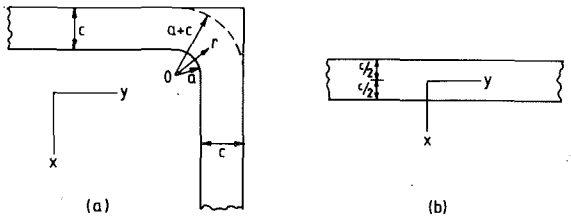


Fig. 1 Notation: (*a*) the corner, and (*b*) thin rectangular profile

$$\gamma_{xz,y} - \gamma_{yz,x} = -2\theta \tag{2}$$

The constitutive relations, according to the J_2 deformation theory, are simply

$$\gamma_{xz} = g\tau_{xz} \quad \gamma_{yz} = g\tau_{yz}, \quad \text{with} \quad g = \frac{2(1+\nu)}{E} + 3\frac{\epsilon_p}{\sigma_e}, \tag{3}$$

where (τ_{xz}, τ_{yz}) are the shear stresses, (ν, E) are the usual elastic constants, σ_e is the effective plastic stress, and ϵ_p is the effective plastic strain and a known function of σ_e. Note that here $\sigma_e = \sqrt{3}\sqrt{\tau_{xz}^2 + \tau_{yz}^2}$.

The equilibrium equation $\tau_{xz,x} + \tau_{yz,y} = 0$ is identically satisfied if the stresses are derived from a function F, viz $\tau_{xz} = F_{,y}$ and $\tau_{yz} = -F_{,x}$. Combining these with (2) and (3) we arrive at the basic differential equation

$$\underset{\sim}{\nabla} \cdot (g \underset{\sim}{\nabla} F) = -2\theta \tag{4}$$

where $\underset{\sim}{\nabla}$ stands for the plane gradient operator. The compliance g, defined in (3), is now a known function of F since the effective stress becomes $\sigma_e = \sqrt{3}\,|\underset{\sim}{\nabla} F|$.

Equation (4) is supplemented by the condition that function F should be constant along the boundary. That constant has different values on each boundary contour when the cross section is multiply connected, but can be taken as zero on the boundary of a simply connected cross section.

Open Cross Sections

For open, thin-walled cross sections we may assume that the stress distribution in the straight arms, away from the corner, is that of a thin rectangular profile. With the notation of Fig. 1(*b*) we take $|F_{,x}| >> |F_{,y}|$, neglecting the gradients in the y direction. Also, due to symmetry it is sufficient to consider the half region $0 \le x \le c/2$. The only active shear stress component is now $dF/dx = -\tau (\tau > 0$ for $x > 0)$ so that the effective stress is $\sigma_e = \sqrt{3}\tau$. Equation (4) reduces to $d(g\tau)/dx = 2\theta$ or, after one integration,

$$e = \frac{2}{\sqrt{3}}\theta x + \text{constant} \quad x \ge 0 \tag{5}$$

where

$$e = mT + \epsilon_p, \quad \text{with} \quad m = \frac{2}{3}(1+\nu) \quad T = \frac{\sqrt{3}\tau}{E}, \tag{6}$$

is the total shear strain. Observing that the shear stress vanishes along the center line $x = 0$ we find that the integration constant in (5) should vanish as well. Thus $e = (2/\sqrt{3})\theta x$ and at the boundary $x = c/2$ we have

$$e_\infty = \frac{\theta c}{\sqrt{3}} \tag{7}$$

which serves as the stress (strain) reference level.

Near the corner we assume a local axisymmetric stress field with $\tau = dF/dr$. The effective stress is again $\sigma_e = \sqrt{3}\tau$ (for $\tau \ge 0$), and equation (4) becomes

$$\frac{d}{dr}(g\tau) + \frac{1}{r}(g\tau) = -2\theta \quad \tau \ge 0 \tag{8}$$

with the solution

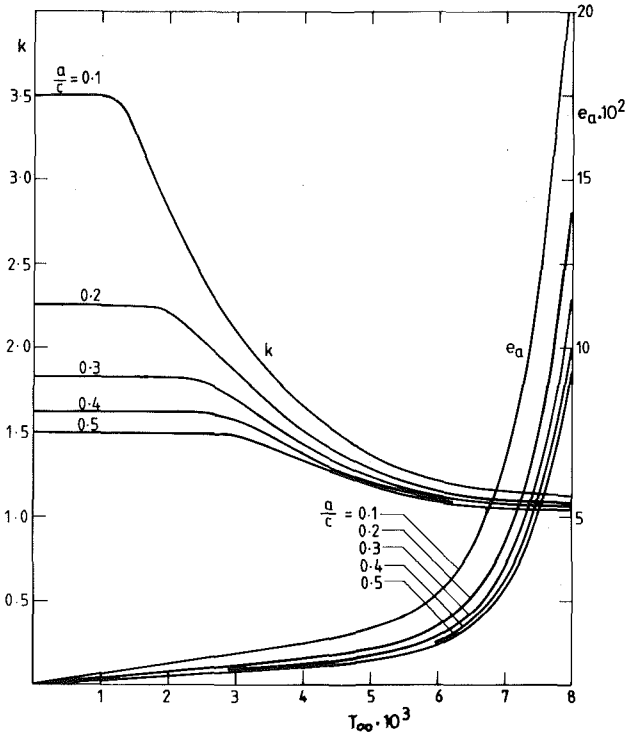


Fig. 2 Open cross sections. Variation of the stress concentration factor k, and maximum shear strain e_a, with cross section geometry and remote shear stress for aluminium 7075 T6. $\nu = 0.32$, $E = 7.24 \cdot 10^{10}$ Ne/m^2, $K = 3.94 \cdot 10^{21}$, $n = 10.9$.

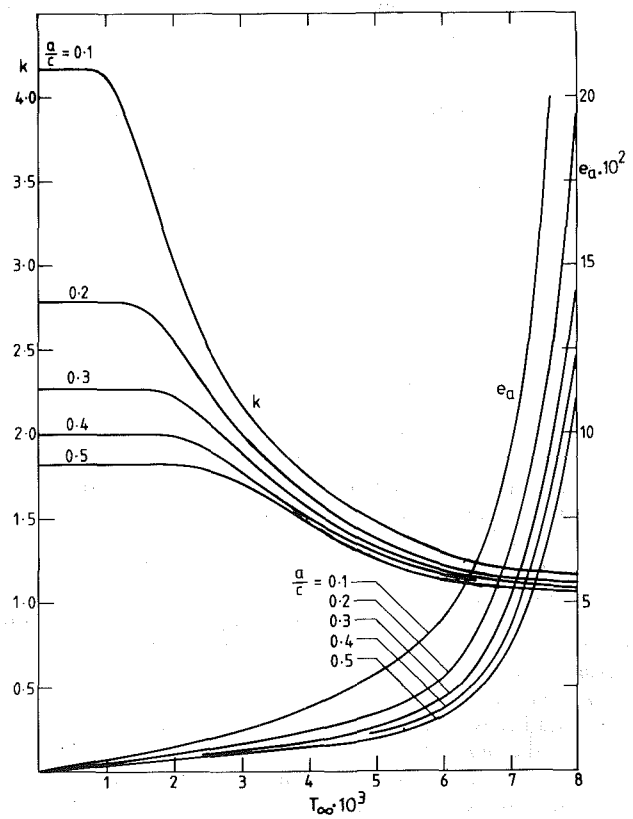


Fig. 3 Closed cross sections. Variation of the stress concentration factor k, and maximum shear strain e_a, with cross section geometry and remote shear stress for aluminium 7075 T6.

Downloaded 02 May 2010 to 171.66.16.250. Redistribution subject to ASME license or copyright; see http://www.asme.org/terms/Terms_Use.cfm

$$e=-\frac{\theta}{\sqrt{3}}\left(r+\frac{A}{r}\right) \quad e\geq 0 \tag{9}$$

Constant A is determined here by the matching condition that the shear stress should vanish at $r = a+c/2$, in agreement with the remote stress distribution in the straight arms. Since $e(\tau=0)=0$ we obtain from (9) $A = -(a+c/2)^2$. Inserting A back in (9), and using (7) to eliminate θ, gives the expression for the total shear strain near the corner. It follows that the highest value of e, which occurs at $r=a$, is given by

$$e_a=\left(1+\frac{c}{4a}\right)e_\infty \tag{10}$$

The total shear strain concentration is therefore independent of the hardening rule. Relation (10) enables a direct evaluation of the stress concentration factor defined as $k=\tau(r=a)/\tau_\infty$, where τ_∞ is the reference value of the remote shear stress along the boundaries of the straight arms. With the Ramberg-Osgood hardening rule $\epsilon_p = K(\sigma_e/E)^n$, where K,n are material constants, we get the transcendental equation

$$mkT_\infty+K(kT_\infty)^n=\left(1+\frac{c}{4a}\right)(mT_\infty+KT_\infty{}^n) \tag{11}$$

When $K=0$ we recover Timoshenko's result for an elastic material $k=(1+c/4a)$. In the deep plastic range we may neglect the elastic terms from (11) and obtain the asymptotic formula

$$k=\left(1+\frac{c}{4a}\right)^{\frac{1}{n}} \tag{12}$$

Note that for a rigid/perfectly-plastic material $n\to\infty$ and $k\to 1$.

Figure 2 shows the dependence of k on cross section geometry and remote shear stress, as calculated from (11), for a typical aluminium alloy. Also shown in Fig. 2 is the amount of total shear strain e_a at the corner. It is worth noting in that context that, [5], in the deep plastic domain fatigue is governed by the strain amplitude.

An interesting question which arises here concerns Timoshenko's original matching condition $\tau(r=a+c/2)=0$. A seemingly reasonable alternative is the equilibrium requirement $\int_a^{a+c}\tau dr=0$. In the elastic range this condition leads to the result

$$k=\frac{\left(1+\frac{c}{2a}\right)}{Ln\left(1+\frac{c}{a}\right)}-\frac{a}{c} \tag{12a}$$

which yields stress concentration values considerably lower as compared to those obtained by Timoshenko and confirmed later by Huth. Just to give a few examples, Timoshenko's formula $k = (1+c/4a)$ gives $k(a/c=0.3) = 1.83$, $k(0.2) = 2.25$, and $k(0.1) = 3.5$; while the analogous values from (12a) are $k(0.3) = 1.52$, $k(0.2) = 1.75$, and $k(0.1) = 2.4$. A possible explanation for the poor results obtained from (12a) is that, for open cross sections, the assumed axisymmetric field remains close to the real field only in the vicinity of the corner (say for $a\leq r\leq a+c/2$). With increasing radial distance from the corner the assumed axially symmetric pattern severely deviates from the actual field (particularly for low values of a/c). That deviation is apparently reflected in the low values of k obtained with the integral matching condition.

An additional difficulty arises in applying this alternative condition in the elastoplastic range: The integral has to be split into two parts divided by the strainless fiber $r=r_0$ where $e=\tau=0$. However, the location of that fiber would in general depend on the applied load and this in turn can raise problems associated with possible stress reversals near $r=r_0$.

Closed Cross Sections

For closed (single cell) cross sections the solution centers on the integral

$$I=\oint_{(c)}\gamma_{xz}dx+\gamma_{yz}dy \tag{13}$$

evaluated along the closed path (c) formed by the center line of the wall. This integral is evaluated in two different ways. First, by direct substitution of the strains from (1) we get $I = 2\theta S$, where S is the area enclosed by the contour (c). Next, we use relations (3) with the definition of the stress function to obtain $I = \oint_{(c)} g(-F_{,n})ds$ where n is the outward normal direction to (c) and ds is the line element along (c). For thin-walled cross sections we may assume a linear variation, of function F, over the thickness in the straight arms. Thus $(-F_{,n})$ is identified with the remote uniform shear stress τ_∞ and (13) gives $I = \sqrt{3}Le_\infty$ where L is the length of (c). Equating the two results for integral I we find that the remote reference stress (strain) level is $e_\infty = 2\theta S/\sqrt{3}L$.

The local axisymmetric field near the corner is still given by (9). Denoting by e_a the value of e at $r=a$, and eliminating θ with the aid of the expression for e_∞, gives

$$e=\frac{ae_a}{r}-\frac{aL}{2S}e_\infty\left(\frac{r}{a}-\frac{a}{r}\right) \tag{14}$$

For practical purposes, however, we may ignore the second term in (14) since aL/S is usually very small. This leaves us with the simplified relation $e = ae_a/r$.

Finally, we implement the matching condition which requires here that the shear flux at the corner ($\int_a^{a+c}\tau dr$) should be equal to the remote shear flux ($\tau_\infty c$). Using the simplified version of (14), with $aL/S\to 0$, and transforming to T as the independent variable, we can put the matching condition in the form

$$e_a\int_{T_c}^{kT_\infty}\frac{T}{e^2}\left(\frac{de}{dT}\right)dT=T_\infty\frac{c}{a} \tag{15}$$

where $T_c = T(r=a+c)$. Equation (15) together with the relation $e_a = (1+c/a)e_c$ can be solved, for a given hardening characteristic $e = e(T)$, to obtain the stress concentration factor k as a function of c/a and T. With the Ramberg-Osgood rule we get the system

$$[mkT_\infty+K(kT_\infty)^n]\int_{T_c}^{kT_\infty}\frac{mT+nKT^n}{(mT+KT^n)^2}dT=T_\infty\frac{c}{a} \tag{16}$$

$$mkT_\infty+K(kT_\infty)^n=\left(1+\frac{c}{a}\right)(mT_c+KT_c{}^n) \tag{17}$$

When $K=0$ we obtain from (16) and (17) the elastic stress concentration factor $k = c/a/Ln(1+c/a)$, while the asymptotic result for the deep plastic range reads

$$k=\frac{\left(\frac{n-1}{n}\right)\frac{c}{a}}{\left(1+\frac{c}{a}\right)^{\frac{n-1}{n}}-1} \tag{18}$$

Again, $k\to 1$ for a rigid/perfectly-plastic material ($n\to\infty$).

The solution to (16) and (17) is displayed in Fig. 3 for aluminium 7075 T6. The numerical scheme used is based on a semi-inverse method; assuming a value for kT_∞ equation (17) is solved for T_c, then find from (16) the corresponding value of T_∞ which in turn determines k. The procedure is then repeated with a new value of kT_∞. Also shown in Fig. 3 is the growth of the total shear strain e_a at the corner.

It is worth mentioning that a similar technique can be applied in cases where aL/S cannot be neglected from (14).

Of course, the present analysis is limited by the requirement that stress reversal does not occur. The possibility of stress

Downloaded 02 May 2010 to 171.66.16.250. Redistribution subject to ASME license or copyright; see http://www.asme.org/terms/Terms_Use.cfm

reversal in closed cross sections of perfectly-plastic materials has been demonstrated by Hodge in [6]. While no elastic unloading was discovered in the example of Fig. 3, or for that matter in several more cases not shown in the paper, it should be useful to state the continuous plastic loading condition at $r=a$.

To this end we write (15) as $e_a\int_{e_c}^{e_a}(T/e^2)de = T_\infty c/a$, where $e_c = ae_a/(c+a)$ (from (14) with $aL/S\to 0$). Now, continuous plastic loading at $r=a$ is assured as long as $\partial e_a/\partial T_\infty > 0$. Differentiating the aforementioned equation and arranging we get

$$\left(k+\frac{c}{a}\right)T_\infty - \left(1+\frac{c}{a}\right)T_c > 0 \tag{19}$$

This is the condition, independent of any particular stress-strain characteristic that should be observed during the analysis.

Acknowledgment

Thanks are due to the kind support of the Lord Marks Fellowship. The author would also like to acknowledge the kind assistance of the University Engineering Department, and the hospitality of Churchill College, Cambridge.

References

1 Timoshenko, S., *Theory of Elasticity*, McGraw-Hill, New York and London, 1934, pp. 258–260; 271–272.

2 Huth, J. H., "Torsional Stress Concentration in Angle and Square Tube Fillets," ASME JOURNAL OF APPLIED MECHANICS, Vol. 17, 1950, pp. 388–390.

3 Conway, H. D., "A Simple Formula for the Maximum Stress in a Twisted Angle or Channel," *Int. J. Mech. Sci.*, Vol. 14, 1972, pp. 615–617.

4 Kachanov, L. M., *Foundations of the Theory of Plasticity*, North-Holland, 1971, pp. 139–143.

5 McClintok, F. A., and Argon, A. S., *Mechanical Behavior of Materials*, Addison-Wesley, Reading, Mass., 1966.

6 Hodge, P. G., Jr., "On the Soap-Film Sand-Hill Analogy for Elastic-Plastic Torsion," in *Progress in Applied Mechanics—The Prager Anniversary Volume*, MacMillan, 1963, pp. 251–259.

Spectral Moments Calculation of Linear System Output

P-T. D. Spanos[1]

The stationary output of a stable linear dynamic system to white noise input is considered. It is shown that the spectral moments of the output can be determined as the solution of a set of linear equations. The corresponding solutions are utilized for determining an improper integral which can be quite useful in random vibration analyses of linear dynamic systems.

Introduction

The proper spectra of stationary stochastic models used in analyzing many physical problems are often identically equal to or can be approximated with acceptable accuracy by the spectral density of a linear system output to white noise input. Characteristic examples are atmospheric turbulence spectra [1], the Kanai-Tajimi spectrum for earthquakes [2], and the Pierson-Moskowitz spectrum for ocean waves [3]. In calculating response statistics of oscillating systems to excitations with power spectra of this mathematical form, it is necessary to calculate integrals of the form

$$I_m \equiv \int_{-\infty}^{\infty} \frac{\equiv_m(\omega)\,d\omega}{\Lambda_m(-i\omega)\,\Lambda_m(i\omega)}; \quad i=\sqrt{-1} \tag{1}$$

[1]The P. D. Henderson Associate Professor of Engineering, Department of Aerospace Engineering and Engineering Mechanics, University of Texas, Austin, Texas, 78712. Mem. ASME.

Manuscript received by ASME Applied Mechanics Division, April, 1983.

where

$$\equiv_m(\omega) = \xi_{m-1}\omega^{2m-2} + \xi_{m-2}\omega^{2m-4} + \ldots + \xi_0 \tag{2}$$

$$\Lambda_m(\omega) = \lambda_m\omega^m + \lambda_{m-1}\omega^{m-1} + \ldots + \lambda_0 \tag{3}$$

and ξ_r, λ_r are arbitrary constants. This Note aims at presenting a formula that can be used in determining I_m in a closed form. This formula is derived indirectly by considering certain properties of the spectrum of the stationary ouptut of a linear time-invariant system to white noise input.

Equations for Autocorrelation and Crosscorrelation Functions

Consider the output of a linear system of order m to white noise input described by the equation

$$[\lambda_m D^m + \lambda_{m-1}D^{m-1} + \lambda_{m-2}D^{m-2} + \ldots + \lambda_0]x(t) = w(t) \tag{4}$$

In equation (4) D^r; $r = 0, \ldots, m$ denotes the rth order differential operator, λ_i, $i = 1, \ldots, m$ are time invariant constants, and $w(t)$ represents a white noise process with autocorrelation function

$$R_w(\tau) \equiv <w(t)\,w(t-\tau)> = 2\pi\delta(\tau), \tag{5}$$

where $\delta(\tau)$ is a two-sided Dirac delta function, and $<\ >$ is the operator of mathematical expectation. It is assumed that the Routh-Hurwicz criterion [4] is satisfied and the characteristic equation that corresponds to equation (4) has roots with negative real parts. That is, the homogeneous part of equation (4) is stable. Stochastic stability aspects of the inhomogeneous equation (4) can be rigorously addressed by using references such as [5]. Herein, it is assumed that $x(t)$ eventually becomes a stationary process with autocorrelation function $R_x(\tau)$ and two-sided spectral density $S_x(\omega)$. Clearly, $S_x(\omega)$ is given by the equation

$$S_x(\omega) = \frac{1}{\Lambda_m(s)\,\Lambda_m(-s)}; \quad s=i\omega. \tag{6}$$

Furthermore, denote by $R_{xw}(\tau)$ the crosscorrelation of $x(t)$ and $w(t-\tau)$; $\tau \geq 0$. Then, two ordinary differential equations governing the dependence of $R_x(\tau)$ and $R_{xw}(\tau)$ on the time lag variable τ can be derived. For this, the following formulas can be used:

$$<x(t)D^r x(t-\tau)> = (-1)^r D^r R_x(\tau) \tag{7}$$

and

$$<w(t-\tau)D^r x(t)> = D^r R_{xw}(\tau). \tag{8}$$

These formulas can be readily proved by relying on the definition of the derivative of a real function. Replacing t by $t-\tau$ in equation (4), then multiplying by $x(t)$ and ensemble averaging yields

$$[\hat{\lambda}_m D^m + \hat{\lambda}_{m-1}D^{m-1} + \ldots + \hat{\lambda}_0]R_x(\tau) = R_{xw}(\tau); \quad \tau\geq 0, \tag{9}$$

where

$$\hat{\lambda}_r = (-1)^r\lambda_r \tag{10}$$

Similarly, multiplying equation (4) by $w(t-\tau)$ and ensemble averaging yields

$$[\lambda_m D^m + \lambda_{m-1}D^{m-1} + \ldots + \lambda_0]R_{xw}(\tau) = \pi\hat{\delta}(\tau); \quad \tau\geq 0 \tag{11}$$

where $\hat{\delta}(\tau)$ is a one-sided delta function. Strictly speaking, equation (11) is only a formal expression of the differential equation

$$[\lambda_m D^{m-1} + \lambda_{m-1}D^{m-2} + \ldots + \lambda_0 D^{-1}]\,R_{xw}(\tau) = \pi; \quad \tau\geq 0. \tag{12}$$

Equation (12) shows that the derivatives $D^r R_{xw}(\tau)$; $r = 1,$

Downloaded 02 May 2010 to 171.66.16.250. Redistribution subject to ASME license or copyright; see http://www.asme.org/terms/Terms_Use.cfm

reversal in closed cross sections of perfectly-plastic materials has been demonstrated by Hodge in [6]. While no elastic unloading was discovered in the example of Fig. 3, or for that matter in several more cases not shown in the paper, it should be useful to state the continuous plastic loading condition at $r=a$.

To this end we write (15) as $e_a\int_{e_c}^{e_a}(T/e^2)de = T_\infty c/a$, where $e_c = ae_a/(c+a)$ (from (14) with $aL/S\to 0$). Now, continuous plastic loading at $r=a$ is assured as long as $\partial e_a/\partial T_\infty > 0$. Differentiating the aforementioned equation and arranging we get

$$\left(k+\frac{c}{a}\right)T_\infty - \left(1+\frac{c}{a}\right)T_c > 0 \tag{19}$$

This is the condition, independent of any particular stress-strain characteristic that should be observed during the analysis.

Acknowledgment

Thanks are due to the kind support of the Lord Marks Fellowship. The author would also like to acknowledge the kind assistance of the University Engineering Department, and the hospitality of Churchill College, Cambridge.

References

1 Timoshenko, S., *Theory of Elasticity*, McGraw-Hill, New York and London, 1934, pp. 258–260; 271–272.

2 Huth, J. H., "Torsional Stress Concentration in Angle and Square Tube Fillets," ASME JOURNAL OF APPLIED MECHANICS, Vol. 17, 1950, pp. 388–390.

3 Conway, H. D., "A Simple Formula for the Maximum Stress in a Twisted Angle or Channel," *Int. J. Mech. Sci.*, Vol. 14, 1972, pp. 615–617.

4 Kachanov, L. M., *Foundations of the Theory of Plasticity*, North-Holland, 1971, pp. 139–143.

5 McClintok, F. A., and Argon, A. S., *Mechanical Behavior of Materials*, Addison-Wesley, Reading, Mass., 1966.

6 Hodge, P. G., Jr., "On the Soap-Film Sand-Hill Analogy for Elastic-Plastic Torsion," in *Progress in Applied Mechanics—The Prager Anniversary Volume*, MacMillan, 1963, pp. 251–259.

Spectral Moments Calculation of Linear System Output

P-T. D. Spanos[1]

The stationary output of a stable linear dynamic system to white noise input is considered. It is shown that the spectral moments of the output can be determined as the solution of a set of linear equations. The corresponding solutions are utilized for determining an improper integral which can be quite useful in random vibration analyses of linear dynamic systems.

Introduction

The proper spectra of stationary stochastic models used in analyzing many physical problems are often identically equal to or can be approximated with acceptable accuracy by the spectral density of a linear system output to white noise input. Characteristic examples are atmospheric turbulence spectra [1], the Kanai-Tajimi spectrum for earthquakes [2], and the Pierson-Moskowitz spectrum for ocean waves [3]. In calculating response statistics of oscillating systems to excitations with power spectra of this mathematical form, it is necessary to calculate integrals of the form

$$I_m \equiv \int_{-\infty}^{\infty} \frac{\equiv_m(\omega)\,d\omega}{\Lambda_m(-i\omega)\,\Lambda_m(i\omega)}; \quad i=\sqrt{-1} \tag{1}$$

[1]The P. D. Henderson Associate Professor of Engineering, Department of Aerospace Engineering and Engineering Mechanics, University of Texas, Austin, Texas, 78712. Mem. ASME.

Manuscript received by ASME Applied Mechanics Division, April, 1983.

where

$$\equiv_m(\omega) = \xi_{m-1}\omega^{2m-2} + \xi_{m-2}\omega^{2m-4} + \ldots + \xi_0 \tag{2}$$

$$\Lambda_m(\omega) = \lambda_m\omega^m + \lambda_{m-1}\omega^{m-1} + \ldots + \lambda_0 \tag{3}$$

and ξ_r, λ_r are arbitrary constants. This Note aims at presenting a formula that can be used in determining I_m in a closed form. This formula is derived indirectly by considering certain properties of the spectrum of the stationary ouptut of a linear time-invariant system to white noise input.

Equations for Autocorrelation and Crosscorrelation Functions

Consider the output of a linear system of order m to white noise input described by the equation

$$[\lambda_m D^m + \lambda_{m-1}D^{m-1} + \lambda_{m-2}D^{m-2} + \ldots + \lambda_0]x(t) = w(t) \tag{4}$$

In equation (4) D^r; $r = 0, \ldots, m$ denotes the rth order differential operator, λ_i, $i = 1, \ldots, m$ are time invariant constants, and $w(t)$ represents a white noise process with autocorrelation function

$$R_w(\tau) \equiv <w(t)\,w(t-\tau)> = 2\pi\delta(\tau), \tag{5}$$

where $\delta(\tau)$ is a two-sided Dirac delta function, and $<\ >$ is the operator of mathematical expectation. It is assumed that the Routh-Hurwicz criterion [4] is satisfied and the characteristic equation that corresponds to equation (4) has roots with negative real parts. That is, the homogeneous part of equation (4) is stable. Stochastic stability aspects of the inhomogeneous equation (4) can be rigorously addressed by using references such as [5]. Herein, it is assumed that $x(t)$ eventually becomes a stationary process with autocorrelation function $R_x(\tau)$ and two-sided spectral density $S_x(\omega)$. Clearly, $S_x(\omega)$ is given by the equation

$$S_x(\omega) = \frac{1}{\Lambda_m(s)\,\Lambda_m(-s)}; \quad s=i\omega. \tag{6}$$

Furthermore, denote by $R_{xw}(\tau)$ the crosscorrelation of $x(t)$ and $w(t-\tau)$; $\tau \geq 0$. Then, two ordinary differential equations governing the dependence of $R_x(\tau)$ and $R_{xw}(\tau)$ on the time lag variable τ can be derived. For this, the following formulas can be used:

$$<x(t)D^r x(t-\tau)> = (-1)^r D^r R_x(\tau) \tag{7}$$

and

$$<w(t-\tau)D^r x(t)> = D^r R_{xw}(\tau). \tag{8}$$

These formulas can be readily proved by relying on the definition of the derivative of a real function. Replacing t by $t-\tau$ in equation (4), then multiplying by $x(t)$ and ensemble averaging yields

$$[\hat{\lambda}_m D^m + \hat{\lambda}_{m-1}D^{m-1} + \ldots + \hat{\lambda}_0]R_x(\tau) = R_{xw}(\tau); \quad \tau\geq 0, \tag{9}$$

where

$$\hat{\lambda}_r = (-1)^r\lambda_r \tag{10}$$

Similarly, multiplying equation (4) by $w(t-\tau)$ and ensemble averaging yields

$$[\lambda_m D^m + \lambda_{m-1}D^{m-1} + \ldots + \lambda_0]R_{xw}(\tau) = \pi\hat{\delta}(\tau); \quad \tau\geq 0 \tag{11}$$

where $\hat{\delta}(\tau)$ is a one-sided delta function. Strictly speaking, equation (11) is only a formal expression of the differential equation

$$[\lambda_m D^{m-1} + \lambda_{m-1}D^{m-2} + \ldots + \lambda_0 D^{-1}]\,R_{xw}(\tau) = \pi; \quad \tau\geq 0. \tag{12}$$

Equation (12) shows that the derivatives $D^r R_{xw}(\tau)$; $r = 1,$

Copyright © 1983 by ASME

Downloaded 02 May 2010 to 171.66.16.250. Redistribution subject to ASME license or copyright; see http://www.asme.org/terms/Terms_Use.cfm

. . . , $m-1$ are finite for $0 \le \tau < \infty$. Thus, equation (9) can be differentiated r times; $0 \le r \le m-1$, to yield

$$[\hat{\lambda}_m D^{m+r} + \hat{\lambda}_{m-1} D^{m+r-1} + \ldots + \hat{\lambda}_0 D^r] R_x(\tau) = D^r R_{xw}(\tau); \quad \tau \ge 0, \quad 0 \le r \le m-1. \tag{13}$$

Determine initial conditions at $\tau = 0$ for $R_{xw}(\tau)$. Toward this end consider the response $h(t)$ of the linear system described by equation (4) to one-sided delta function. Then, the stationary system output can be expressed as

$$x(t) = \int_{-\infty}^{\infty} h(t-u)\, w(u)\, du, \tag{14}$$

where u is a dummy variable. Multiplying equation (14) by $w(t-\tau)$ and ensemble averaging yields

$$R_{xw}(\tau) = \pi h(\tau); \quad \tau \ge 0 \tag{15}$$

Clearly, $R_{xw}(\tau)$ is not an even function of τ, in fact $R_{xw}(\tau) = 0$ for $\tau < 0$. Furthermore, equation (15) can be generalized in the following form

$$D^r R_{xw}(\tau) = \pi D^r h(\tau); \quad r = 0, \ldots, m-1 \tag{16}$$

Equation (16) can be used in conjunction with equation (8) to determine the crosscorrelation between $w(t-\tau)$ and any of the derivatives of the stationary system output. At zero time lag, using the properties of $h(t)$, for example see [6], equation (16) yields

$$D^r R_{xw}(0) = 0; \quad r = 0, \ldots, m-2 \tag{17}$$

and

$$D^{m-1} R_{xw}(0) = \frac{\pi}{\lambda_m}. \tag{18}$$

Spectral Moments Calculation

Equation (13) in conjunction with equations (17) and (18) can be used to derive a formula regarding the spectral moments of the stationary output of the system. Define the spectral moment

$$M_{2r} \equiv \int_{-\infty}^{\infty} \omega^{2r} S_x(\omega)\, d\omega, \tag{19}$$

where $S_x(\omega)$ is given by equation (6). Note that $S_x(\omega)$ is related to $R_x(\tau)$ by the equation

$$R_x(\tau) = \int_{-\infty}^{\infty} e^{s\tau} S_x(\omega)\, d\omega. \tag{20}$$

Thus, differentiating equation (20) up to $2m-1$ times and taking into consideration equation (19) yields

$$M_{2r-1} = 0; \quad 0 \le r \le m \tag{21}$$

and

$$M_{2r} = (-1)^r D^{2r} R_x(0); \quad 0 \le r \le m-1 \tag{22}$$

Clearly, M_r; $r \ge 2m$, is unbounded. Substituting equations (21) and (22) into equation (13) and setting $r = m-1, m-2, \ldots, 0$ yields

$$\begin{aligned}
\lambda_{m-1} M_{2m-2} - \lambda_{m-3} M_{2m-4} + \lambda_{m-5} M_{2m-6} - \ldots &= \frac{\pi}{\lambda_m} \\
-\lambda_m M_{2m-2} + \lambda_{m-2} M_{2m-4} - \lambda_{m-4} M_{2m-6} + \ldots &= 0 \\
0 - \lambda_{m-1} M_{2m-4} + \lambda_{m-3} M_{2m-6} - \ldots &= 0 \\
\ldots \quad \ldots \quad \ldots \quad \ldots \quad \ldots &= 0 \\
\ldots \quad \ldots \quad \ldots \quad \ldots \quad -\lambda_2 M_2 + \lambda_0 M_0 &= 0
\end{aligned} \tag{23}$$

It is seen that the spectral moments M_{2r}; $r = 0, \ldots, m-1$ satisfy m linear algebraic equations. Thus, they can be determined by the classical Cramer's formula. For example the moment M_{2r} is determined by replacing the $(m-r)$th column of the coefficients determinant by the right-hand side of equation (23). That is,

$$M_{2r} = \frac{\begin{vmatrix}
\lambda_{m-1} & -\lambda_{m-3} & \lambda_{m-5} & -\lambda_{m-7} & \ldots \pi/\lambda_m & \ldots \\
-\lambda_m & \lambda_{m-2} & -\lambda_{m-4} & \lambda_{m-6} & \ldots 0 & \ldots \\
0 & -\lambda_{m-1} & \lambda_{m-3} & -\lambda_{m-5} & \ldots 0 & \ldots \\
0 & \lambda_m & -\lambda_{m-2} & \lambda_{m-4} & \ldots 0 & \ldots \\
0 & 0 & . & . & \ldots 0 & \ldots \\
0 & 0 & . & . & \ldots & \ldots -\lambda_2 \; \lambda_0
\end{vmatrix}}{\begin{vmatrix}
\lambda_{m-1} & -\lambda_{m-3} & \lambda_{m-5} & -\lambda_{m-7} & \ldots & \ldots \\
-\lambda_m & \lambda_{m-2} & -\lambda_{m-4} & \lambda_{m-6} & \ldots & \ldots \\
0 & -\lambda_{m-1} & \lambda_{m-3} & -\lambda_{m-5} & \ldots & \ldots \\
0 & \lambda_m & -\lambda_{m-2} & \lambda_{m-4} & \ldots & \ldots \\
. & . & . & . & \ldots & \ldots \\
0 & 0 & . & . & \ldots & \ldots -\lambda_2 \; \lambda_0
\end{vmatrix}}; \quad r = 0, \ldots m-1 \tag{24}$$

Examining equations (1)–(3) and (19) it is recognized that

$$I_m = \xi_{m-1} M_{2m-2} + \xi_{m-2} M_{2m-4} + \ldots + \xi_0 \tag{25}$$

Substituting into equation (25) the values for M_{2r} which are given by equation (24), and manipulating yields

Downloaded 02 May 2010 to 171.66.16.250. Redistribution subject to ASME license or copyright; see http://www.asme.org/terms/Terms_Use.cfm

$$I_m = \begin{vmatrix} \xi_{m-1} & \xi_{m-3} & & & & & & \xi_0 \\ -\lambda_m & \lambda_{m-2} & -\lambda_{m-4} & \lambda_{m-6} & . . 0 & . & . & . \\ 0 & -\lambda_{m-1} & \lambda_{m-3} & -\lambda_{m-5} & . . 0 & . & . & . \\ 0 & \lambda_m & -\lambda_{m-2} & \lambda_{m-4} & . . 0 & . & . & . \\ 0 & 0 & & & . . 0 & . & . & . \\ 0 & 0 & . & . & . . . & . & -\lambda_2 & \lambda_0 \\ \hline \lambda_{m-1} & -\lambda_{m-3} & \lambda_{m-5} & -\lambda_{m-7} & . & . & . & . \\ -\lambda_m & \lambda_{m-2} & -\lambda_{m-4} & \lambda_{m-6} & . & . & . & . \\ 0 & -\lambda_{m-1} & \lambda_{m-3} & -\lambda_{m-5} & . & . & . & . \\ 0 & \lambda_m & -\lambda_{m-2} & \lambda_{m-4} & . & . & . & . \\ . & . & . & . & . & . & . & . \\ 0 & 0 & . & . & . & . & -\lambda_2 & \lambda_0 \end{vmatrix} \frac{\pi}{\lambda_m} \quad (26)$$

Concluding Remarks

It is believed that equations (24) and (26) can simplify significantly certain calculations that are necessary in conducting random vibration analyses of linear systems; calling attention to this fact is the primary objective of this Note. For example, consider the case of a single-degree-of-freedom linear oscillator with natural frequency ω_0 and ratio of critical damping ζ, which is exposed to white noise with two-sided spectral density equal to unity. Clearly, in this case $m = 2$, $\lambda_2 = 1$, $\lambda_1 = 2\zeta\omega_0$, and $\lambda_0 = \omega_0^2$. Using these values, the stationary variances σ_x and $\sigma_{\dot{x}}$ of the oscillatory response can be conveniently determined by relying on equation (24) or equation (26). Specifically, it is found that

$$\sigma_x^2 = M_2 = \frac{\pi}{2\zeta\omega_0} \quad (27)$$

$$\sigma_{\dot{x}}^2 = M_0 = \frac{M_2}{\omega_0^2} = \frac{\pi}{2\zeta\omega_0^3} \quad (28)$$

Note that traditionally equations (27) and (28) are derived by using the theory of residues of complex functions [6]. In fact, this theory can be used, as well, to determine the general integral I_m [7],

Acknowledgments

The financial support of this research from the grant NAG 3-210 from the NASA Lewis Research Center is gratefully acknowledged.

References

1 Taylor, J., *Manual on Aircraft Loads*, Pergamon Press, New York, 1965.
2 Rosenblueth, T., ed., *Design of Earthquake Resistant Structures*, Wiley, New York, 1980.
3 Spanos, P-T. D., "ARMA Algorithms for Ocean Wave Modeling," ASME *Journal of Energy Resources Technology*, Vol. 105, Sept. 1983, pp. 302-309.
4 Casti, J. L., *Dynamical Systems and Their Applications: Linear Theory*, Academic Press, New York, 1977.
5 Kushner, H. J., *Stochastic Stability and Control*, Academic Press, New York, 1967.
6 Lin, Y. K. *Probabilistic Theory of Structural Dynamics*, R. E. Krieger, New York, 1976.
7 James, H. M., Nichols, N. B., and Philips, R. S., eds., *Theory of Servomechanisms*, Dover, New York, 1965.

Exact Periodic Solutions of Long Wave Equations for a Rotating Fluid

P. L. Sachdev[1] and M. C. Singh[2]

1 Introduction

In a previous paper, Seshadri and Sachdev [1] found exact periodic solutions of the nonlinear acoustic-gravity wave equations for an isothermal atmosphere. In the present Note, we describe exact periodic solutions for the equations describing long waves in a rotating homogeneous fluid.

2 Equations and Their Reductions

Starting from the basic system of two-dimensional equations for a fluid in hydrostatic approximation, Leblond and Mysak [2] derived, using kinematic conditions at the bottom and the free surface, the following system of equations:

$$u_t + uu_x + vu_y + gh_x = fv, \quad (1)$$

$$v_t + uv_x + vv_y + gh_y = -fu, \quad (2)$$

$$h_t + (uh)_x + (vh)_y = 0. \quad (3)$$

The hydrostatic approximation implies that the long wave limit has already been taken in deriving (1)-(3). Here u and v are the horizontal velocity components in the x and y directions, h is the total surface height, and f is the (constant) Coriolis parameter. If we look for solutions depending on the phase function $\xi = lx + my - \sigma t$ only, that is,

$$u = U(\xi), v = V(\xi), h = H(\xi),$$

the system (1)-(3) can be reduced to

[1]Department of Mechanical Engineering, University of Calgary, Calgary, Alberta, Canada. On leave from Indian Institute of Science, Bangalore, 560012 India.
[2]Department of Mechanical Engineering, University of Calgary, Calgary, Alberta, Canada.

Manuscript received by ASME Applied Mechanics Division, February, 1983; final revision, June 1983.

Downloaded 02 May 2010 to 171.66.16.250. Redistribution subject to ASME license or copyright; see http://www.asme.org/terms/Terms_Use.cfm

$$I_m = \begin{vmatrix} \xi_{m-1} & \xi_{m-3} & & & & & & \xi_0 \\ -\lambda_m & \lambda_{m-2} & -\lambda_{m-4} & \lambda_{m-6} & . . 0 & . & . & . \\ 0 & -\lambda_{m-1} & \lambda_{m-3} & -\lambda_{m-5} & . . 0 & . & . & . \\ 0 & \lambda_m & -\lambda_{m-2} & \lambda_{m-4} & . . 0 & . & . & . \\ 0 & 0 & & & . . 0 & . & . & . \\ 0 & 0 & . & . & . . . & . & -\lambda_2 & \lambda_0 \\ \hline \lambda_{m-1} & -\lambda_{m-3} & \lambda_{m-5} & -\lambda_{m-7} & . & . & . & . \\ -\lambda_m & \lambda_{m-2} & -\lambda_{m-4} & \lambda_{m-6} & . & . & . & . \\ 0 & -\lambda_{m-1} & \lambda_{m-3} & -\lambda_{m-5} & . & . & . & . \\ 0 & \lambda_m & -\lambda_{m-2} & \lambda_{m-4} & . & . & . & . \\ . & . & . & . & . & . & . & . \\ 0 & 0 & . & . & . & . & -\lambda_2 & \lambda_0 \end{vmatrix} \frac{\pi}{\lambda_m} \quad (26)$$

Concluding Remarks

It is believed that equations (24) and (26) can simplify significantly certain calculations that are necessary in conducting random vibration analyses of linear systems; calling attention to this fact is the primary objective of this Note. For example, consider the case of a single-degree-of-freedom linear oscillator with natural frequency ω_0 and ratio of critical damping ζ, which is exposed to white noise with two-sided spectral density equal to unity. Clearly, in this case $m = 2$, $\lambda_2 = 1$, $\lambda_1 = 2\zeta\omega_0$, and $\lambda_0 = \omega_0^2$. Using these values, the stationary variances σ_x and $\sigma_{\dot{x}}$ of the oscillatory response can be conveniently determined by relying on equation (24) or equation (26). Specifically, it is found that

$$\sigma_x^2 = M_2 = \frac{\pi}{2\zeta\omega_0} \quad (27)$$

$$\sigma_{\dot{x}}^2 = M_0 = \frac{M_2}{\omega_0^2} = \frac{\pi}{2\zeta\omega_0^3} \quad (28)$$

Note that traditionally equations (27) and (28) are derived by using the theory of residues of complex functions [6]. In fact, this theory can be used, as well, to determine the general integral I_m [7],

Acknowledgments

The financial support of this research from the grant NAG 3-210 from the NASA Lewis Research Center is gratefully acknowledged.

References

1 Taylor, J., *Manual on Aircraft Loads*, Pergamon Press, New York, 1965.
2 Rosenblueth, T., ed., *Design of Earthquake Resistant Structures*, Wiley, New York, 1980.
3 Spanos, P-T. D., "ARMA Algorithms for Ocean Wave Modeling," ASME *Journal of Energy Resources Technology*, Vol. 105, Sept. 1983, pp. 302-309.
4 Casti, J. L., *Dynamical Systems and Their Applications: Linear Theory*, Academic Press, New York, 1977.
5 Kushner, H. J., *Stochastic Stability and Control*, Academic Press, New York, 1967.
6 Lin, Y. K. *Probabilistic Theory of Structural Dynamics*, R. E. Krieger, New York, 1976.
7 James, H. M., Nichols, N. B., and Philips, R. S., eds., *Theory of Servomechanisms*, Dover, New York, 1965.

Exact Periodic Solutions of Long Wave Equations for a Rotating Fluid

P. L. Sachdev[1] and M. C. Singh[2]

1 Introduction

In a previous paper, Seshadri and Sachdev [1] found exact periodic solutions of the nonlinear acoustic-gravity wave equations for an isothermal atmosphere. In the present Note, we describe exact periodic solutions for the equations describing long waves in a rotating homogeneous fluid.

2 Equations and Their Reductions

Starting from the basic system of two-dimensional equations for a fluid in hydrostatic approximation, Leblond and Mysak [2] derived, using kinematic conditions at the bottom and the free surface, the following system of equations:

$$u_t + uu_x + vu_y + gh_x = fv, \quad (1)$$

$$v_t + uv_x + vv_y + gh_y = -fu, \quad (2)$$

$$h_t + (uh)_x + (vh)_y = 0. \quad (3)$$

The hydrostatic approximation implies that the long wave limit has already been taken in deriving (1)-(3). Here u and v are the horizontal velocity components in the x and y directions, h is the total surface height, and f is the (constant) Coriolis parameter. If we look for solutions depending on the phase function $\xi = lx + my - \sigma t$ only, that is,

$$u = U(\xi), v = V(\xi), h = H(\xi),$$

the system (1)-(3) can be reduced to

[1] Department of Mechanical Engineering, University of Calgary, Calgary, Alberta, Canada. On leave from Indian Institute of Science, Bangalore, 560012 India.
[2] Department of Mechanical Engineering, University of Calgary, Calgary, Alberta, Canada.

Manuscript received by ASME Applied Mechanics Division, February, 1983; final revision, June 1983.

Copyright © 1983 by ASME
Downloaded 02 May 2010 to 171.66.16.250. Redistribution subject to ASME license or copyright; see http://www.asme.org/terms/Terms_Use.cfm

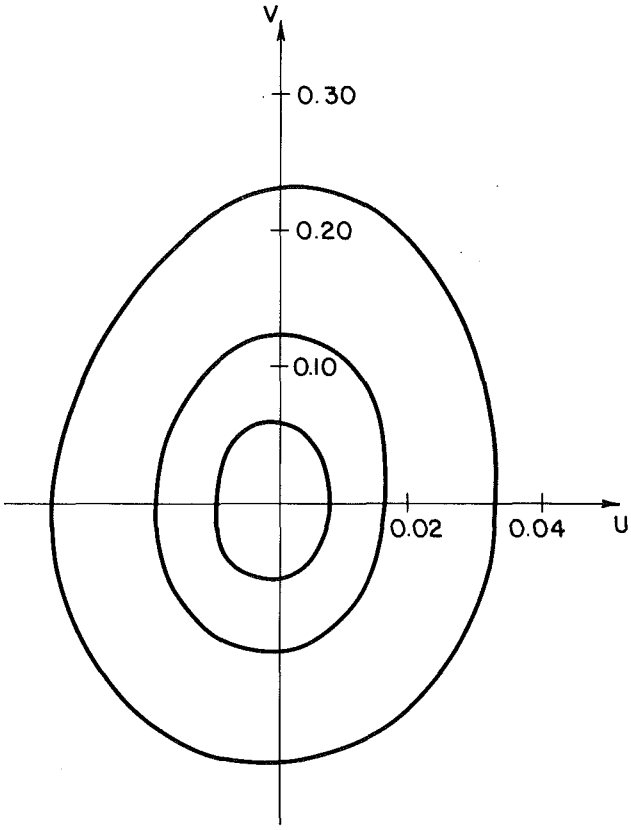


Fig. 1 Periodic solutions to equation (12) for $c = 0.01$ and $a = 5.0$

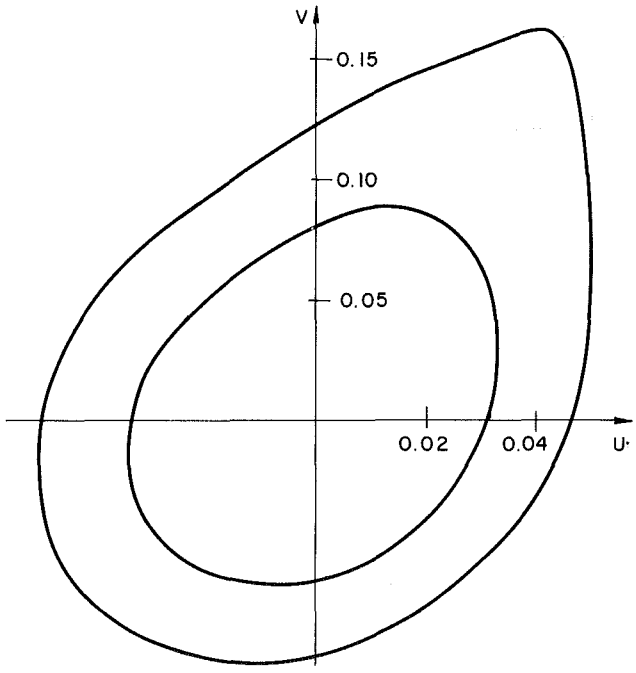


Fig. 2 Periodic solutions to equation (12) for $c = 0.1$ and $a = 2.0$

$$\frac{dU}{d\xi} = \frac{f}{K}\frac{[K^2V - gm\,H\,(lU+mV)]}{[K^2 - g(l^2+m^2)H]}, \tag{4}$$

$$\frac{dV}{d\xi} = \frac{-f}{K}\frac{[K^2U - glH\,(lU+m\,V)]}{[K^2 - g(l^2+m^2)\,H]}, \tag{5}$$

$$\frac{dH}{d\xi} = \frac{f\,H(mU-lV)}{K^2 - g(l^2+m^2)H}, \tag{6}$$

where

$$K = lU + mV - \sigma. \tag{7}$$

This system can be shown to possess an intermediate integral

$$KH = -B = -\sigma H_0, \tag{8}$$

provided

$$K \neq 0,$$

where $B = \sigma H_0 > 0$ is a constant depending on the equilibrium conditions $U = 0$, $V = 0$, $H = H_0$ (say). Introducing the nondimensional quantities

$$\bar{U} = \frac{l}{\sigma}U,\ \bar{V} = \frac{mV}{\sigma},\ \bar{\xi} = \frac{f}{\sigma}\xi,$$

with the help of the wave numbers l and m, and the frequency σ, we get the system

$$\frac{d\bar{U}}{d\bar{\xi}} = \frac{1}{a}\frac{(\bar{U}+\bar{V}-1)^3\bar{V} + ca^2(\bar{U}+\bar{V})}{(\bar{U}+\bar{V}-1)[(\bar{U}+\bar{V}-1)^3 + c(1+a^2)]}, \tag{9}$$

$$\frac{d\bar{V}}{d\bar{\xi}} = (-a)\frac{(\bar{U}+\bar{V}-1)^3\bar{U} + c(\bar{U}+\bar{V})}{(\bar{U}+\bar{V}-1)[(\bar{U}+\bar{V}-1)^3 + c(1+a^2)]}, \tag{10}$$

where $a = m/l$ is the ratio of wave numbers and $c = gl^2B/\sigma^3$ is another nondimensional parameter. In deriving (9) and (10), use has been made of (7) to eliminate K in favor of U and V. If we do not cross the critical lines

$$\bar{U}+\bar{V} = 1,\ (\bar{U}+\bar{V}-1)^3 + c(1+a^2) = 0, \tag{11}$$

and, of course, affirm that $a \neq 0$, we have the equation in $(\bar{V}, \bar{U})$ phase plane:

$$\frac{d\bar{V}}{d\bar{U}} = -a^2\frac{(\bar{U}+\bar{V}-1)^3\bar{U} + c(\bar{U}+\bar{V})}{(\bar{U}+\bar{V}-1)^3\bar{V} + ca^2(\bar{U}+\bar{V})}. \tag{12}$$

A local singular point analysis shows that the equilibrium point (0,0) is a center provided that

$$c < \frac{1}{1+a^2}. \tag{13}$$

In the physical variables, this condition is equivalent to

$$\sigma > (gH_0)^{1/2}(l^2+m^2)^{1/2} \equiv \sigma_L, \tag{14}$$

where σ_L is the frequency of the infinitely long waves in the linear approximations, [3].

Figures 1 and 2 show a few representative closed curves for some chosen values of the parameters a and c. The periodic solutions exist until the closed curves touch the critical line

$$U+V = 1 - \{c(1+a^2)\}^{1/3} = U_0, \tag{15}$$

where obviously

$$0 < U_0 < 1, \tag{16}$$

the first part of the inequality follows from (13). This line will touch the solution earlier than the other critical line in (11).

References

1 Seshadri, V. S., and Sachdev, P. L., "Quasi-Simple Wave Solutions for Acoustic Gravity Waves," *Physics of Fluids*, Vol. 20, 1977, pp. 888–894.

2 Leblond, P. H., and Mysak, L. A., *Waves in the Ocean*, Elsevier, New York, 1978, pp. 178–181.

3 Whitham, G. B., *Linear and Nonlinear Waves*, J. Wiley, New York, 1974, pp. 403–404.

Downloaded 02 May 2010 to 171.66.16.250. Redistribution subject to ASME license or copyright; see http://www.asme.org/terms/Terms_Use.cfm

A Treatment of Rigid Body Dynamics

J. Casey[1]

Introduction

The purpose of this Note is to present a derivation of the equations of rigid body dynamics that is based on the concepts of continuum mechanics. Explicit use of a reference configuration is made in constructing corotational bases, and corotational rates of vectors and tensors are discussed. It is shown by means of a simple argument that one can always choose a corotational basis that diagonalizes the inertia tensor. Also, the Euler angles are introduced through a tensorial approach that highlights the multiplicative decomposition of the rotation tensor. Finally, the work-energy theorem is proved using the integral expression for the rate of work of body forces and contact forces.

Necessary mathematical background may be found in [1, Chapter 1], in which a useful representation for the rotation tensor is also established. Related kinematical developments are discussed in [2, 3], where extensive lists of references are given.

In what follows, the transpose of a tensor is denoted by a superscript T, $\mathbf{I}$ is the identity second-order tensor, and a superposed dot signifies material time differentiation.

Basic Equations

Let X be a particle belonging to a rigid three-dimensional continuum $\mathcal{B}$ and denote by $\mathbf{X}$ and $\mathbf{x}$ the position vectors of X in a fixed reference configuration κ_0 and in the current configuration κ at time t, respectively. Every motion of $\mathcal{B}$ is of the form[2]

$$\mathbf{x} = \mathbf{Q}\,\mathbf{X} + \mathbf{a}, \tag{1}$$

where $\mathbf{Q}$ is a proper orthogonal tensor function and $\mathbf{a}$ a vector function, both depending on t only. Let $\mathcal{R}_0$ stand for the region of space that $\mathcal{B}$ occupies in the configuration κ_0, and $\mathcal{R}$ the corresponding region in κ. Denote the elements of volume in $\mathcal{R}_0$ and $\mathcal{R}$ by dV and dv, respectively. The (constant) mass of $\mathcal{B}$ is $m = \int_{\mathcal{R}} \rho\, dv = \int_{\mathcal{R}_0} \rho\, dV$, the mass density ρ being independent of t. Introducing vectors $\bar{\mathbf{x}}$ and $\bar{\mathbf{X}}$ by $m\bar{\mathbf{x}} = \int_{\mathcal{R}} \rho \mathbf{x} dv$, $m\bar{\mathbf{X}} = \int_{\mathcal{R}_0} \rho \mathbf{X} dV$, one immediately sees that $\bar{\mathbf{x}} = \mathbf{Q}\bar{\mathbf{X}} + \mathbf{a}$, so that $\bar{\mathbf{x}}$ and $\bar{\mathbf{X}}$ may be regarded as position vectors of a particle $\bar{\mathbf{X}}$ either of $\mathcal{B}$ or of a rigid extension of $\mathcal{B}$; $\bar{X}$ is the mass center of $\mathcal{B}$. The relative position vector $\boldsymbol{\pi} = \mathbf{x} - \bar{\mathbf{x}}$ satisfies

$$\int_{\mathcal{R}} \rho\, \boldsymbol{\pi}\, dV = \mathbf{0} \tag{2}$$

and a similar relation holds for the vector $\boldsymbol{\Pi} = \mathbf{X} - \bar{\mathbf{X}}$.

The velocity of X has the representations

$$\dot{\mathbf{x}} = \boldsymbol{\Omega}\,\mathbf{Q}\,\mathbf{X} + \dot{\mathbf{a}} = \boldsymbol{\Omega}\,(\mathbf{x} - \mathbf{a}) + \dot{\mathbf{a}}, \tag{3}$$

with the angular velocity tensor being defined by $\boldsymbol{\Omega} = \dot{\mathbf{Q}}\mathbf{Q}^T$. The skew-symmetry of $\boldsymbol{\Omega}$ implies the existence of an axial angular velocity vector $\boldsymbol{\omega}$ such that $\boldsymbol{\Omega}\boldsymbol{\alpha} = \boldsymbol{\omega} \times \boldsymbol{\alpha}$ for any $\boldsymbol{\alpha}$. Explicitly,

$$\boldsymbol{\omega} = -\tfrac{1}{2}\boldsymbol{\epsilon}[\boldsymbol{\Omega}], \quad \boldsymbol{\Omega} = -\boldsymbol{\epsilon}\boldsymbol{\omega},$$

where $\boldsymbol{\epsilon}$ is the alternator, and the tensor products $(\boldsymbol{\alpha} \otimes \boldsymbol{\beta} \otimes \boldsymbol{\gamma})[\boldsymbol{\eta} \otimes \boldsymbol{\xi}] = \boldsymbol{\alpha}\boldsymbol{\beta}\cdot\boldsymbol{\eta}\,\boldsymbol{\gamma}\cdot\boldsymbol{\xi}$, $(\boldsymbol{\alpha} \otimes \boldsymbol{\beta} \otimes \boldsymbol{\gamma})\boldsymbol{\eta} = \boldsymbol{\alpha} \otimes \boldsymbol{\beta}\boldsymbol{\gamma}\cdot\boldsymbol{\eta}$, $(\boldsymbol{\alpha} \otimes \boldsymbol{\beta})\boldsymbol{\eta} = \boldsymbol{\alpha}\boldsymbol{\beta}\cdot\boldsymbol{\eta}$ are defined for arbitrary vectors $\boldsymbol{\alpha}, \boldsymbol{\beta}, \boldsymbol{\gamma}, \boldsymbol{\eta}, \boldsymbol{\xi}$. It is clear that

$$\boldsymbol{\pi} = \mathbf{Q}\,\boldsymbol{\Pi}, \quad \dot{\boldsymbol{\pi}} = \boldsymbol{\Omega}\boldsymbol{\pi} = \boldsymbol{\omega} \times \boldsymbol{\pi}, \quad \dot{\boldsymbol{\pi}} \cdot \boldsymbol{\pi} = 0. \tag{4}$$

Also, grad $\dot{\mathbf{v}} = \boldsymbol{\Omega}$, curl $\dot{\mathbf{v}} = 2\boldsymbol{\omega}$ and div $\dot{\mathbf{v}} = 0$, where $\mathbf{v} = \dot{\mathbf{x}}$.

In the configuration κ, the liner momentum $\mathbf{G}$ of $\mathcal{B}$, and the angular momentum $\mathbf{H}$ of $\mathcal{B}$ relative to $\bar{X}$, are

$$\mathbf{G} = \int_{\mathcal{R}} \rho \dot{\mathbf{x}}\, dv, \quad \mathbf{H} = \int_{\mathcal{R}} \rho \boldsymbol{\pi} \times \dot{\boldsymbol{\pi}} dv. \tag{5}$$

With the help of $(4)_2$, $\mathbf{H}$ may be expressed as

$$\mathbf{H} = \mathbf{J}\boldsymbol{\omega}, \tag{6}$$

where the inertia tensor $\mathbf{J}$ is defined by

$$\mathbf{J} = \int_{\mathcal{R}} \rho\,(\boldsymbol{\pi} \cdot \boldsymbol{\pi}\,\mathbf{I} - \boldsymbol{\pi} \otimes \boldsymbol{\pi})\, dv, \tag{7}$$

and is symmetric positive definite. The value of $\mathbf{J}$ in the configuration κ_0 is

$$\mathbf{J}_0 = \int_{\mathcal{R}_0} \rho\,(\boldsymbol{\Pi} \cdot \boldsymbol{\Pi}\,\mathbf{I} - \boldsymbol{\Pi} \otimes \boldsymbol{\Pi})\, dV. \tag{8}$$

In view of $(4)_1$, (7) and (8)

$$\mathbf{J} = \mathbf{Q}\,\mathbf{J}_0\mathbf{Q}^T, \tag{9}$$

where use has been made of the identities $(\mathbf{Q}\boldsymbol{\Pi}) \otimes \boldsymbol{\Pi} = \mathbf{Q}(\boldsymbol{\Pi} \otimes \boldsymbol{\Pi})$, $\boldsymbol{\Pi} \otimes (\mathbf{Q}\boldsymbol{\Pi}) = (\boldsymbol{\Pi} \otimes \boldsymbol{\Pi})\, Q^T$.

Assume that in the configuration κ the body is acted on by externally applied body forces and contact forces, specified by a vector field $\mathbf{b}$ per unit mass, and a vector field $\mathbf{t}$ per unit area of $\partial\mathcal{R}$, the boundary of $\mathcal{R}$. The resultant, and the moment relative to $\bar{X}$, of these forces are

$$\mathbf{F} = \int_{\mathcal{R}} \rho \mathbf{b} dv + \int_{\partial\mathcal{R}} \mathbf{t} da, \quad \mathbf{M} = \int_{\mathcal{R}} \rho \boldsymbol{\pi} \times \mathbf{b} dv + \int_{\partial\mathcal{R}} \boldsymbol{\pi} \times \mathbf{t} da, \tag{10}$$

where da is the element of area of $\partial\mathcal{R}$. The balance principles of linear and angular momentum imply that

$$\mathbf{F} = \dot{\mathbf{G}} = m\,\ddot{\bar{\mathbf{x}}}, \quad \mathbf{M} = \dot{\mathbf{H}} = \dot{\mathbf{J}}\boldsymbol{\omega} + \mathbf{J}\dot{\boldsymbol{\omega}}, \tag{11}$$

where use has been made of (2), (4), (5), and (6).

The relation (6) has important consequences. Thus, for $\boldsymbol{\omega} \neq \mathbf{0}$, equation (6) implies that $\mathbf{H}$ is parallel to $\boldsymbol{\omega}$ if and only if $\boldsymbol{\omega}$ is an eigenvector of $\mathbf{J}$. Similarly, on account of the invertibility of $\mathbf{J}$, it is easy to see that if $\mathbf{H}$ is an eigenvector of $\mathbf{J}$, then $\mathbf{H}$ is parallel to $\boldsymbol{\omega}$[3].

Corotational Bases. Corotational Rates

Consider four particles X_i $(i = 0,1,2,3)$ belonging to $\mathcal{B}$ (or its extension). As in (1), the motion of these particles is described by

$$\mathbf{x}_i = \mathbf{Q}\,\mathbf{X}_i + \mathbf{a}, \quad (i = 0,1,2,3), \tag{12}$$

Now let the four particles be chosen such that the three vectors $\mathbf{E}_i = \mathbf{X}_i - \mathbf{X}_0$ $(i = 1,2,3)$ form a right-handed orthonormal basis. The images of $\mathbf{E}_i$ in the current configuration are

$$\mathbf{e}_i = \mathbf{x}_i - \mathbf{x}_0 = \mathbf{Q}\,\mathbf{E}_i, \quad (i = 1,2,3), \tag{13}$$

and, due to the proper orthogonality of $\mathbf{Q}$, also constitute a right-handed orthonormal basis. This basis is carried along by the rigid body and is called *cororational*. Differentiating (13), one obtains

$$\dot{\mathbf{e}}_i = \boldsymbol{\Omega}\,\mathbf{e}_i = \boldsymbol{\omega} \times \mathbf{e}_i, \tag{14}$$

where, as in all subsequent equations, subscripts take on values 1,2,3.

Let $\boldsymbol{\beta}$ and $\mathbf{B}$, respectively, be any vector and tensor fields associated with the rigid body. Representing these fields as $\boldsymbol{\beta} = \beta_i \mathbf{e}_i$, $\mathbf{B} = B_{ij}\,\mathbf{e}_i \otimes \mathbf{e}_j$, one may define *corotational rates*

$$\mathring{\boldsymbol{\beta}} = \dot{\beta}_i \mathbf{e}_i, \quad \mathring{\mathbf{B}} = \dot{B}_{ij} \mathbf{e}_i \otimes \mathbf{e}_j, \tag{15}$$

summation being implied over indices that are repeated once. From (14) and (15), one observes that

[1] Department of Mechanical Engineering, University of Houston, 4800 Calhoun, Houston, Texas 77004. Assoc. Mem. ASME.

[2] This can be shown by an elementary argument along the same lines as [4, Chapter 3], or by using somewhat more restrictive assumptions as in [5].

Manuscript received by ASME Applied Mechanics Division, May 1983; Final revision July, 1983.

[3] For a number of results of this type, see [6, Sections 20 and 13].

Copyright © 1983 by ASME
Downloaded 02 May 2010 to 171.66.16.250. Redistribution subject to ASME license or copyright; see http://www.asme.org/terms/Terms_Use.cfm

$$\dot{\boldsymbol{\beta}} = \mathring{\boldsymbol{\beta}} + \boldsymbol{\Omega}\boldsymbol{\beta} = \mathring{\boldsymbol{\beta}} + \boldsymbol{\omega} \times \boldsymbol{\beta}, \quad \dot{\mathbf{B}} = \mathring{\mathbf{B}} + \boldsymbol{\Omega}\mathbf{B} - \mathbf{B}\boldsymbol{\Omega}. \tag{16}$$

Similarly, one may define a second corotational rate of $\boldsymbol{\beta}$ by $\boldsymbol{\beta} = \ddot{\beta}_i \, \mathbf{e}_i$. It then follows that

$$\ddot{\boldsymbol{\beta}} = \boldsymbol{\beta} + 2\boldsymbol{\omega} \times \mathring{\boldsymbol{\beta}} + \dot{\boldsymbol{\omega}} \times \boldsymbol{\beta} + \boldsymbol{\omega} \times (\boldsymbol{\omega} \times \boldsymbol{\beta}). \tag{17}$$

From (14), $(4)_2$, and $(16)_1$, it is clear that

$$\mathring{\mathbf{e}}_i = \mathbf{0}, \quad \mathring{\boldsymbol{\pi}} = \mathbf{0}, \quad \dot{\boldsymbol{\omega}} = \mathring{\boldsymbol{\omega}}, \tag{18}$$

while it follows from (7) and (4), or alternatively from (9), that

$$\dot{\mathbf{J}} = \boldsymbol{\Omega}\,\mathbf{J} - \mathbf{J}\boldsymbol{\Omega}, \tag{19}$$

and hence by $(16)_2$

$$\mathring{\mathbf{J}} = \mathbf{0}. \tag{20}$$

Thus, the components of $\mathbf{J}$ relative to a corotational basis are constants, and may be evaluated in the reference configuration. This may also be deduced from (9) and (13), as indicated in an exercise in [7, p. 94].

Euler's Equations

In view of (19) and $(18)_3$, $(11)_2$ may be written as

$$\mathbf{M} = (\boldsymbol{\Omega}\mathbf{J} - \mathbf{J}\boldsymbol{\Omega})\boldsymbol{\omega} + \mathring{\mathbf{J}}\boldsymbol{\omega} = \boldsymbol{\omega} \times (\mathbf{J}\boldsymbol{\omega}) + \mathring{\mathbf{J}}\boldsymbol{\omega}, \tag{21}$$

a component form of which may be found in [8, equation (8–11)].

Since $\mathbf{J}$ is symmetric, it possesses at each instant t a basis of eigenvectors relative to which it is diagonal. It will now be shown that a *corotational basis of eigenvectors* always exists. Thus, choosing an orthonormal basis of eigenvectors for the tensor $\mathbf{J}_0$, one has the spectral representation

$$\mathbf{J}_0 = \sum_{i=1}^{3} \lambda_i \bar{\mathbf{E}}_i \otimes \bar{\mathbf{E}}_i, \tag{22}$$

where λ_i is the eigenvalue corresponding to $\bar{\mathbf{E}}_i$. Next. construct a corotational basis from $\bar{\mathbf{E}}_i$ by the method described in the preceding section. Thus let $\bar{\mathbf{e}}_i = \mathbf{Q}\bar{\mathbf{E}}_i$. Then, by virtue of (20), the only nonzero components of $\mathbf{J}$ are the eigenvalues in (22), and

$$\mathbf{J} = \sum_{i=1}^{3} \lambda_i \bar{\mathbf{e}}_i \otimes \bar{\mathbf{e}}_i, \tag{23}$$

so that $\mathbf{J}$ is diagonal. Relative to the basis $\{\bar{\mathbf{e}}_i\}$, the combination (21) and (23) yields Euler's equation for rigid body motions:

$$M_1 = \lambda_1 \dot{\omega}_1 + (\lambda_3 - \lambda_2)\omega_2\omega_2,$$
$$M_2 = \lambda_2 \dot{\omega}_2 + (\lambda_1 - \lambda_3)\omega_1\omega_3,$$
$$M_3 = \lambda_3 \dot{\omega}_3 + (\lambda_2 - \lambda_1)\omega_2\omega_1.$$

Equations of Motion for the Mass Center

With the use of $(16)_1$, one may write $(11)_1$ in the form

$$\mathbf{F} = m(\mathring{\bar{\mathbf{v}}} + \boldsymbol{\omega} \times \bar{\mathbf{v}}) \tag{24}$$

with $\bar{\mathbf{v}} = \dot{\bar{\mathbf{x}}}$. A component form of (24) is given in [8, equation (8–19)]. The corresponding equation for $\bar{\mathbf{x}}$ is

$$\mathbf{F} = m\{\ddot{\bar{\mathbf{x}}} + 2\boldsymbol{\omega} \times \mathring{\bar{\mathbf{x}}} + \mathring{\boldsymbol{\omega}} \times \bar{\mathbf{x}} + \boldsymbol{\omega} \times (\boldsymbol{\omega} \times \bar{\mathbf{x}})\}, \tag{25}$$

which follows from (17) and $(18)_3$. It may be observed that in view of (3) as well as similar equation for $\bar{X}$, $(16)_1$ and (17),

$$\mathring{\bar{\mathbf{x}}} = \dot{\bar{\mathbf{x}}} = \mathring{\mathbf{a}}, \quad \ddot{\bar{\mathbf{x}}} = \mathbf{x} = \mathbf{a}$$

Therefore, (25) may also be written as

$$\mathbf{F} = m\{\mathbf{a} + 2\,\boldsymbol{\omega} \times \mathring{\mathbf{a}} + \mathring{\boldsymbol{\omega}} \times \bar{\mathbf{x}} + \boldsymbol{\omega} \times (\boldsymbol{\omega} \times \bar{\mathbf{x}})\}.$$

Euler Angles

The basis $\{\mathbf{e}_i\}$ may be constructed in three successive steps, viz.,

$$\mathbf{e}_i = \mathbf{Q}(\phi)\mathbf{e}_i'', \quad \mathbf{e}_i'' = \mathbf{Q}(\theta)\mathbf{e}_i', \quad \mathbf{e}_i' = \mathbf{Q}(\psi)\mathbf{E}_i, \tag{26}$$

through the proper orthogonal tensors

$$\mathbf{Q}(\psi) = \cos\,\psi(\mathbf{E}_1 \otimes \mathbf{E}_1 + \mathbf{E}_2 \otimes \mathbf{E}_2) + \sin\,\psi(\mathbf{E}_2 \otimes \mathbf{E}_1 - \mathbf{E}_1 \otimes \mathbf{E}_2) + \mathbf{E}_3 \otimes \mathbf{E}_3,$$

$$\mathbf{Q}(\theta) = \cos\,\theta(\mathbf{e}_1' \otimes \mathbf{e}_1' + \mathbf{e}_3' \otimes \mathbf{e}_3') + \sin\,\theta(\mathbf{e}_1' \otimes \mathbf{e}_3' - \mathbf{e}_3' \otimes \mathbf{e}_1') + \mathbf{e}_2' \otimes \mathbf{e}_2',$$

$$\mathbf{Q}(\phi) = \cos\,\phi(\mathbf{e}_2'' \otimes \mathbf{e}_2'' + \mathbf{e}_3'' \otimes \mathbf{e}_3'') + \sin\,\phi(\mathbf{e}_3'' \otimes \mathbf{e}_2'' - \mathbf{e}_2'' \otimes \mathbf{e}_3'') + \mathbf{e}_1'' \otimes \mathbf{e}_1''.$$

The intermediate bases are orthonormal and are uniquely defined except when θ is a nonzero multiple of $\pi/2$. From (13) and (26) follows the multiplicative decomposition

$$\mathbf{Q} = \mathbf{Q}(\phi)\mathbf{Q}(\theta)\mathbf{Q}(\psi),$$

which is the essential content of the Eulerian construction. A lengthy calculation leads to

$$\boldsymbol{\omega} = (\dot{\phi} - \dot{\psi}\,\sin\theta)\mathbf{e}_1 + (\dot{\theta}\,\cos\phi + \dot{\psi}\,\sin\phi\,\cos\theta)\mathbf{e}_2 + (\dot{\psi}\,\cos\phi\,\cos\theta - \dot{\theta}\,\sin\phi)\mathbf{e}_3$$
$$= \dot{\phi}\,\mathbf{e}_1'' + \dot{\theta}\,\mathbf{e}_2' + \dot{\psi}\,\mathbf{E}_3.$$

The system $\{\psi, \theta, \phi\}$ of Euler angles used in the foregoing is the same as in [8], where a matrix method is employed.

Work-Energy Theorem

The kinetic energy of $\mathfrak{B}$ in the configuration κ is

$$K = \int_{\mathfrak{R}} \tfrac{1}{2}\,\rho\,\dot{\mathbf{x}} \cdot \dot{\mathbf{x}}\,dv$$

By virtue of (2) and (7) one obtains the König decomposition[4]

$$K = \bar{K} + K^*, \tag{27}$$

with

$$\bar{K} = \tfrac{1}{2}\,m\,\bar{\mathbf{v}} \cdot \bar{\mathbf{v}}, \quad K^* = \int_{\mathfrak{R}} \tfrac{1}{2}\,\rho\dot{\boldsymbol{\pi}} \cdot \dot{\boldsymbol{\pi}}\,dv = \tfrac{1}{2}\,\boldsymbol{\omega} \cdot \mathbf{J}\boldsymbol{\omega}, \tag{28}$$

where use has also been made of the identity $(\boldsymbol{\omega} \times \boldsymbol{\pi}) \cdot (\boldsymbol{\omega} \times \boldsymbol{\pi}) = \boldsymbol{\omega} \cdot \boldsymbol{\omega}\,\boldsymbol{\pi} \cdot \boldsymbol{\pi} - \boldsymbol{\omega} \cdot \boldsymbol{\pi}\,\boldsymbol{\omega} \cdot \boldsymbol{\pi}$.

The rate of work of the external forces is

$$R = \int_{\mathfrak{R}} \rho\,\mathbf{b} \cdot \mathbf{v}\,dv + \int_{\partial\mathfrak{R}} \mathbf{t} \cdot \mathbf{v}\,da. \tag{29}$$

From (29), $(4)_2$, and (10) it may be deduced that

$$R = \mathbf{F} \cdot \bar{\mathbf{v}} + \mathbf{M} \cdot \boldsymbol{\omega}. \tag{30}$$

Noting that in view of (19) and (6) $\boldsymbol{\omega} \cdot \dot{\mathbf{J}}\boldsymbol{\omega} = \boldsymbol{\omega} \cdot (\boldsymbol{\omega} \times \mathbf{H}) = 0$, one may conclude from (27), (28), and (30) that

$$R = \dot{K}. \tag{31}$$

The work done on $\mathfrak{B}$ as it undergoes a rigid motion in the time interval $t_1 \leqq t \leqq t_2$ is

$$W_{12} = \int_{t_1}^{t_2} R\,dt. \tag{32}$$

From (31) and (32) follows the work-energy theorem for a rigid body, namely

$$W_{12} = K_2 - K_1, \tag{33}$$

where K_1 and K_2 are the values of K at t_1 and t_2, respectively. It is worth observing that in a cycle of motion, in which $\mathbf{x}$ and $\mathbf{v}$ take on the same values at times t_1 and t_2, equation (33) implies that $W_{12} = 0$.

[4] For a discussion of this and related results, see [9, Section 167].

Downloaded 02 May 2010 to 171.66.16.250. Redistribution subject to ASME license or copyright; see http://www.asme.org/terms/Terms_Use.cfm

References

1 Chadwick, P., *Continuum Mechanics*, Wiley, New York.
2 Beatty, M. F., "Vector Analysis of Finite Rigid Rotations," ASME JOURNAL OF APPLIED MECHANICS, Vol. 44, 1977, pp. 501–502.
3 Beatty, M. F., "Kinematics of Finite, Rigid-Body Displacements," *American Journal of Physics*, Vol. 34, 1966, pp. 949–954.
4 O'Neill, B., *Elementary Differential Geometry*, Academic Press, New York, 1966.
5 Gurtin, M. E., and Williams, W. O., "A Note on Rigid Fields," *Journal of Elasticity*, Vol. 6, 1976, pp. 331–333.
6 Truesdell, C., *A First Course in Rational Continuum Mechanics*, Vol. 1, Academic Press, New York, 1977.
7 Gurtin, M. E., *An Introduction to Continuum Mechanics*, Academic Press, New York, 1981.
8 Greenwood, D. T., *Principles of Dynamics*, Prentice-Hall, Englewood Cliffs, N.J., 1965.
9 Truesdell, C., and Toupin, R. A., "The Classical Field Theories," in *S. Flügge's Handbuch der Physik*, Vol. IIII/1, Springer-Verlag, 1960, pp. 226–902.

An Extended Weight Function Method for Mixed-Mode Elastic Crack Analysis

Y. Bortman[1] and L. Banks-Sills[1]

1 Introduction

The weight function mehtod as presented by Bueckner [1] and adapted by Rice [2] may be used to compute stress intensity factors of symmetric, cracked, linear elastic bodies with symmetric loading. In this study, the method wil be extended so that mode *I* and *II* stress intensity factors may be computed in the most general mixed-mode case in unsymmetric bodies.

Rice [2] showed that if the displacements field $\mathbf{u}(x,y,l)$, where l is the crack length, and the stress intensity factor $K_I^{(1)}(l)$ for any one symmetrical load system acting on a linear elastic body is known, then the stress intensity factor $K_I^{(2)}$ for any other symmetric loading applied to that body may be found as

$$K_I^{(2)} = \int_\Gamma \mathbf{T}\cdot\mathbf{h}_I\, ds + \int_A \mathbf{f}\cdot\mathbf{h}_I\, dA \tag{1.1}$$

where Γ is the boundary on which the surface tractions $\mathbf{T}$ are applied and $\mathbf{f}$ are the body forces within the region A. The weight function $\mathbf{h}_I$ is expressed as

$$\mathbf{h}_I = \frac{H}{2K_I^{(1)}} \frac{\partial \mathbf{u}(x,y,l)}{\partial l} \tag{1.2}$$

where $H = E/(1-\nu^2)$ for plane strain and $H = E$ for generalized plane stress, E is Young's modulus, and ν is Poisson's ratio. The subscript I in $\mathbf{h}_I$ is used to denote the mode *I* weight function since in the sequel a mode *II* weight function will be defined, as well. Rice showed that $\mathbf{h}_I$ is a universal function of geometry, meaning that it is independent of applied loads and material properties. It may be thought of as the Green's function for the stress intensity factor. The method has been employed successfully to calculate stress intensity factors both numerically [3, 4] and from experiments [5].

Paris, McMeeking, and Tada [6] extended this method to include modes *I*, *II*, and *III*. With this extension, the displacement field and stress intensity factor must be found for three special load configurations consisting of point forces applied a small distance from the crack tip; the body need not be symmetric. Thus, a numerical solution of these particular cases must always be obtained instead of taking advantage of solutions already existing in the literature. Vainshtok [7] also presented an extension of the weight function method for mixed-mode problems. He derives two weight functions based on the expression

$$-\delta\Pi = J_1\,\delta x_1 + J_2\,\delta x_2$$

where Π is the potential energy of the body, δx_i is the virtual displacement of the crack tip, and J_i is the energy release rate in the x_i direction. His interpretation of the J_2-integral as the energy release rate for a unit crack extension in a direction perpendicular to the parent crack is incorrect [8, 9]. The J_2-integral is the energy release rate per unit translation of the crack in a perpendicular direction. Employing the correct interpretation in calculating the weight functions becomes cumbersome. Thus there is a motivation to find a less complicated method.

In this study, a general method for calculating the stress intensity factors K_I and K_{II} from any two independent reference solutions is developed in Section 2. In Section 3, as a check, the solution to a simple case from the literature is determined.

2 Analysis

Consider a two-dimensional linear elastic cracked body subjected to several independent in-plane forces acting in arbitrary locations and directions. In general, these forces will cause mixed-mode deformation so that both K_I and K_{II} are to be considered. The energy release rate G may be written as

$$G = \frac{1}{H}(K_I^2 + K_{II}^2). \tag{2.1}$$

Since the material is linear elastic, it is possible to define unit stress intensity factors $k_I^{(i)}$ and $k_{II}^{(i)}$ as

$$k_I^{(i)} = K_I^{(i)}/P_i$$

and (2.2)

$$k_{II}^{(i)} = K_{II}^{(i)}/P_i$$

where the applied force P_i induces stress intensity factors $K_I^{(i)}$ and $K_{II}^{(i)}$. By means of superposition, equation (2.1) becomes

$$G = \frac{1}{H}\sum_{i=1}^{N}\sum_{j=1}^{N}[k_I^{(i)}\,k_I^{(j)} + k_{II}^{(i)}\,k_{II}^{(j)}]\,P_i\,P_j \tag{2.3}$$

where N is the number of applied forces. On the other hand, it is possible to express G in terms of the elastic strain energy U as

$$G = \left.\frac{\partial U}{\partial l}\right|_P \tag{2.4}$$

where l is the crack length and the force P is held constant. Writing the elastic strain energy in terms of the compliance coefficient C_{ij} as

$$U = \frac{1}{2}\sum_{i=1}^{N}\sum_{j=1}^{N} C_{ij}\,P_i\,P_j \tag{2.5}$$

where the displacements $u_i = C_{ij}\,P_j$, leads to

$$G = \frac{1}{2}\sum_{i=1}^{N}\sum_{j=1}^{N}\frac{\partial C_{ij}}{\partial l}\,P_i\,P_j. \tag{2.6}$$

Since the loads P_i and P_j are arbitrary, it follows that

$$\frac{1}{2}\frac{\partial C_{ij}}{\partial l} = \frac{1}{H}(k_I^{(i)}\,k_I^{(j)} + k_{II}^{(i)}\,k_{II}^{(j)}). \tag{2.7}$$

A similar result was obtained in [6] for mode *I* alone.

[1]Department of Mechanics, Materials and Structures, Faculty of Engineering, Tel-Aviv University, Ramat-Aviv, Tel-Aviv 69978, Israel. L. Banks-Sills is an Assoc. Mem. ASME.

Manuscript received by ASME Applied Mechanics Division, May, 1983; final revision, August, 1983.

Downloaded 02 May 2010 to 171.66.16.250. Redistribution subject to ASME license or copyright; see http://www.asme.org/terms/Terms_Use.cfm

References

1 Chadwick, P., *Continuum Mechanics*, Wiley, New York.
2 Beatty, M. F., "Vector Analysis of Finite Rigid Rotations," ASME JOURNAL OF APPLIED MECHANICS, Vol. 44, 1977, pp. 501–502.
3 Beatty, M. F., "Kinematics of Finite, Rigid-Body Displacements," *American Journal of Physics*, Vol. 34, 1966, pp. 949–954.
4 O'Neill, B., *Elementary Differential Geometry*, Academic Press, New York, 1966.
5 Gurtin, M. E., and Williams, W. O., "A Note on Rigid Fields," *Journal of Elasticity*, Vol. 6, 1976, pp. 331–333.
6 Truesdell, C., *A First Course in Rational Continuum Mechanics*, Vol. 1, Academic Press, New York, 1977.
7 Gurtin, M. E., *An Introduction to Continuum Mechanics*, Academic Press, New York, 1981.
8 Greenwood, D. T., *Principles of Dynamics*, Prentice-Hall, Englewood Cliffs, N.J., 1965.
9 Truesdell, C., and Toupin, R. A., "The Classical Field Theories," in *S. Flügge's Handbuch der Physik*, Vol. IIII/1, Springer-Verlag, 1960, pp. 226–902.

An Extended Weight Function Method for Mixed-Mode Elastic Crack Analysis

Y. Bortman[1] and L. Banks-Sills[1]

1 Introduction

The weight function mehtod as presented by Bueckner [1] and adapted by Rice [2] may be used to compute stress intensity factors of symmetric, cracked, linear elastic bodies with symmetric loading. In this study, the method wil be extended so that mode *I* and *II* stress intensity factors may be computed in the most general mixed-mode case in unsymmetric bodies.

Rice [2] showed that if the displacements field $\mathbf{u}(x,y,l)$, where l is the crack length, and the stress intensity factor $K_I^{(1)}(l)$ for any one symmetrical load system acting on a linear elastic body is known, then the stress intensity factor $K_I^{(2)}$ for any other symmetric loading applied to that body may be found as

$$K_I^{(2)} = \int_\Gamma \mathbf{T}\cdot\mathbf{h}_I\, ds + \int_A \mathbf{f}\cdot\mathbf{h}_I\, dA \tag{1.1}$$

where Γ is the boundary on which the surface tractions $\mathbf{T}$ are applied and $\mathbf{f}$ are the body forces within the region A. The weight function $\mathbf{h}_I$ is expressed as

$$\mathbf{h}_I = \frac{H}{2K_I^{(1)}} \frac{\partial \mathbf{u}(x,y,l)}{\partial l} \tag{1.2}$$

where $H = E/(1-\nu^2)$ for plane strain and $H = E$ for generalized plane stress, E is Young's modulus, and ν is Poisson's ratio. The subscript I in $\mathbf{h}_I$ is used to denote the mode *I* weight function since in the sequel a mode *II* weight function will be defined, as well. Rice showed that $\mathbf{h}_I$ is a universal function of geometry, meaning that it is independent of applied loads and material properties. It may be thought of as the Green's function for the stress intensity factor. The method has been employed successfully to calculate stress intensity factors both numerically [3, 4] and from experiments [5].

Paris, McMeeking, and Tada [6] extended this method to include modes *I*, *II*, and *III*. With this extension, the displacement field and stress intensity factor must be found for three special load configurations consisting of point forces applied a small distance from the crack tip; the body need not be symmetric. Thus, a numerical solution of these particular cases must always be obtained instead of taking advantage of solutions already existing in the literature. Vainshtok [7] also presented an extension of the weight function method for mixed-mode problems. He derives two weight functions based on the expression

$$-\delta\Pi = J_1\,\delta x_1 + J_2\,\delta x_2$$

where Π is the potential energy of the body, δx_i is the virtual displacement of the crack tip, and J_i is the energy release rate in the x_i direction. His interpretation of the J_2-integral as the energy release rate for a unit crack extension in a direction perpendicular to the parent crack is incorrect [8, 9]. The J_2-integral is the energy release rate per unit translation of the crack in a perpendicular direction. Employing the correct interpretation in calculating the weight functions becomes cumbersome. Thus there is a motivation to find a less complicated method.

In this study, a general method for calculating the stress intensity factors K_I and K_{II} from any two independent reference solutions is developed in Section 2. In Section 3, as a check, the solution to a simple case from the literature is determined.

2 Analysis

Consider a two-dimensional linear elastic cracked body subjected to several independent in-plane forces acting in arbitrary locations and directions. In general, these forces will cause mixed-mode deformation so that both K_I and K_{II} are to be considered. The energy release rate G may be written as

$$G = \frac{1}{H}(K_I^2 + K_{II}^2). \tag{2.1}$$

Since the material is linear elastic, it is possible to define unit stress intensity factors $k_I^{(i)}$ and $k_{II}^{(i)}$ as

$$k_I^{(i)} = K_I^{(i)}/P_i$$

and (2.2)

$$k_{II}^{(i)} = K_{II}^{(i)}/P_i$$

where the applied force P_i induces stress intensity factors $K_I^{(i)}$ and $K_{II}^{(i)}$. By means of superposition, equation (2.1) becomes

$$G = \frac{1}{H}\sum_{i=1}^{N}\sum_{j=1}^{N}[k_I^{(i)}\,k_I^{(j)} + k_{II}^{(i)}\,k_{II}^{(j)}]\,P_i\,P_j \tag{2.3}$$

where N is the number of applied forces. On the other hand, it is possible to express G in terms of the elastic strain energy U as

$$G = \left.\frac{\partial U}{\partial l}\right|_P \tag{2.4}$$

where l is the crack length and the force P is held constant. Writing the elastic strain energy in terms of the compliance coefficient C_{ij} as

$$U = \frac{1}{2}\sum_{i=1}^{N}\sum_{j=1}^{N} C_{ij}\,P_i\,P_j \tag{2.5}$$

where the displacements $u_i = C_{ij}\,P_j$, leads to

$$G = \frac{1}{2}\sum_{i=1}^{N}\sum_{j=1}^{N}\frac{\partial C_{ij}}{\partial l}\,P_i\,P_j. \tag{2.6}$$

Since the loads P_i and P_j are arbitrary, it follows that

$$\frac{1}{2}\frac{\partial C_{ij}}{\partial l} = \frac{1}{H}(k_I^{(i)}\,k_I^{(j)} + k_{II}^{(i)}\,k_{II}^{(j)}). \tag{2.7}$$

A similar result was obtained in [6] for mode *I* alone.

[1]Department of Mechanics, Materials and Structures, Faculty of Engineering, Tel-Aviv University, Ramat-Aviv, Tel-Aviv 69978, Israel. L. Banks-Sills is an Assoc. Mem. ASME.

Manuscript received by ASME Applied Mechanics Division, May, 1983; final revision, August, 1983.

Copyright © 1983 by ASME
Downloaded 02 May 2010 to 171.66.16.250. Redistribution subject to ASME license or copyright; see http://www.asme.org/terms/Terms_Use.cfm

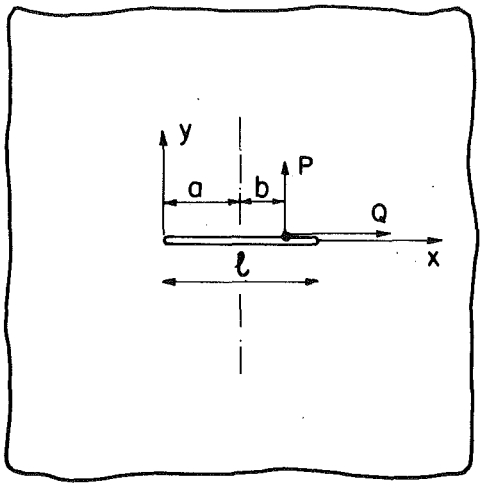


Fig. 1 Two point forces acting on the face of a Griffith crack

If the stress intensity factors and displacements field are known for two representative loading systems applied to the same cracked body and denoted by m and n, it is possible to write from equation (2.7)

$$k_I^{(i)}\, k_I^{(m)} + k_{II}^{(i)}\, k_{II}^{(m)} = \frac{H}{2}\frac{\partial C_{im}}{\partial l}$$

$$k_I^{(i)}\, k_I^{(n)} + k_{II}^{(i)}\, k_{II}^{(n)} = \frac{H}{2}\frac{\partial C_{in}}{\partial l}. \tag{2.8}$$

Solving equations (2.8) for $k_I^{(i)}$ and $k_{II}^{(i)}$ yields

$$\begin{bmatrix} k_I^{(i)} \\ k_{II}^{(i)} \end{bmatrix} = \frac{H}{2(k_I^{(m)}\, k_{II}^{(n)} - k_{II}^{(m)}\, k_I^{(n)})} \times \begin{bmatrix} k_{II}^{(n)}\frac{\partial C_{im}}{\partial l} - k_{II}^{(m)}\frac{\partial C_{in}}{\partial l} \\ k_I^{(m)}\frac{\partial C_{in}}{\partial l} - k_I^{(n)}\frac{\partial C_{im}}{\partial l} \end{bmatrix}$$

where $k_I^{(m)}/k_{II}^{(m)} \neq k_I^{(n)}/k_{II}^{(n)}$. Clearly the two reference cases may not both be either mode I or mode II. Finally, the desired stress intensity factors are obtained by means of equations (2.2), (2.9), and the definition of compliance as

$$K_I = \frac{H}{2K^2}\sum_{i=1}^{N}\left(K_{II}^{(n)}\frac{\partial u_i^{(m)}}{\partial l} - K_{II}^{(m)}\frac{\partial u_i^{(n)}}{\partial l}\right)P_i$$

$$K_{II} = \frac{H}{2K^2}\sum_{i=1}^{N}\left(K_I^{(m)}\frac{\partial u_i^{(n)}}{\partial l} - K_I^{(n)}\frac{\partial u_i^{(m)}}{\partial l}\right)P_i \tag{2.10}$$

where $K^2 = K_I^{(m)}\, K_{II}^{(n)} - K_{II}^{(m)}\, K_I^{(n)}$.

For arbitrarily distributed tractions $\mathbf{T}$ applied on the boundary Γ, relations (2.10) become

$$K_I = \int_\Gamma \mathbf{h}_I \cdot \mathbf{T}\, ds$$

and

$$K_{II} = \int_\Gamma \mathbf{h}_{II} \cdot \mathbf{T}\, ds \tag{2.11}$$

where the weight functions are given by

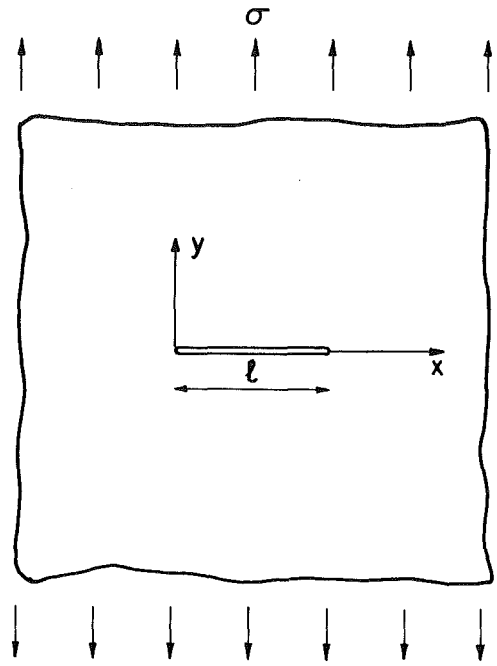


Fig. 2(a) Mode I

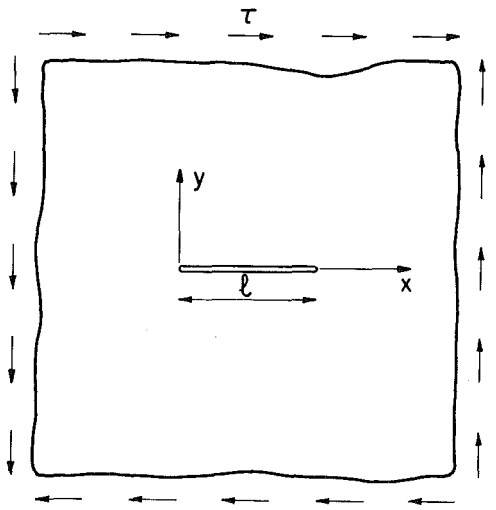


Fig. 2(b) Mode II

Fig. 2 Crack in an infinite plate

$$\mathbf{h}_I = \frac{H}{2K^2}\left(K_{II}^{(n)}\frac{\partial \mathbf{u}_m}{\partial l} - K_{II}^{(m)}\frac{\partial \mathbf{u}_n}{\partial l}\right)$$

$$\mathbf{h}_{II} = \frac{H}{2K^2}\left(K_I^{(m)}\frac{\partial \mathbf{u}_n}{\partial l} - K_I^{(n)}\frac{\partial \mathbf{u}_m}{\partial l}\right) \tag{2.12}$$

and assuming that there are no body forces.

It is also possible to determine a weight function $\mathbf{h}_{III}$, if mode III deformation is to be included as well. Equation (2.1) may be written so as to include K_{III}. Following the same procedure with three known reference cases instead of two, yields three equations (2.8), and in a straightforward manner three weight functions.

3 Application

The method presented is illustrated and checked by means of a mixed-mode example whose solution may be found in the literature. The problem is that of a Griffith crack with point forces applied to the crack faces (Fig. 1); hence the weight

Downloaded 02 May 2010 to 171.66.16.250. Redistribution subject to ASME license or copyright; see http://www.asme.org/terms/Terms_Use.cfm

fuctions of equations (2.12) are calculated along these boundaries.

To determine the weight function, the two reference cases considered are that of a Griffith crack of length l subjected first to remotely applied tension σ, denoted as case m (Fig. 2(a)), and then to remotely applied shear τ, denoted as case n (Fig. 2(b)). The stress intensity factors are given as

$$K_I^{(m)} = \sigma\sqrt{\pi l/2}, \quad K_{II}^{(m)} = 0 \tag{3.1a}$$

$$K_I^{(n)} = 0, \quad K_{II}^{(n)} = \tau\sqrt{\pi l/2}. \tag{3.1b}$$

Employing the coordinate sytem shown in Figs. 2, the corresponding crack face displacements may be written as

$$\mathbf{u}_m(x,0,l) = (1+\nu)\,\sigma[-(1-2\nu)(x-l/2)\hat{i} \pm 2(1-\nu)\sqrt{x(l-x)}\,\hat{j}]/E \tag{3.2a}$$

$$\mathbf{u}_n(x,0,l) = (1+\nu)\,\tau[\pm 2(1-\nu)\sqrt{x(l-x)}\,\hat{i} + (1-2\nu)(x-l/2)\hat{j}\,]/E \tag{3.2b}$$

where $\hat{i}$ and $\hat{j}$ are unit vectors in the x and y directions, respectively, and the plus and minus signs apply to the upper and lower crack faces, respectively. Carrying out the required differentiation and substituting into equations (2.12) leads to

$$\mathbf{h}_I = \frac{1}{\sqrt{2\pi l}}\left[\frac{1-2\nu}{2(1-\nu)}\hat{i} \pm \sqrt{\frac{x}{l-x}}\,\hat{j}\right]$$

$$\mathbf{h}_{II} = \frac{1}{\sqrt{2\pi l}}\left[\pm\sqrt{\frac{x}{l-x}}\,\hat{i} - \frac{1-2\nu}{2(1-\nu)}\,\hat{j}\right] \tag{3.3}$$

where H is taken as $E/(1-\nu^2)$ for plane strain. Thus the stress intensity factors may be written from equations (2.11) as

$$K_I = \frac{1}{\sqrt{2\pi l}}\int_0^l \left\{\frac{1-2\nu}{2(1-\nu)}\tilde{T}_x + \sqrt{\frac{x}{l-x}}\,\tilde{T}_y\right\}dx$$

$$K_{II} = \frac{1}{\sqrt{2\pi l}}\int_0^l \left\{\sqrt{\frac{x}{l-x}}\,\hat{T}_x - \frac{1-2\nu}{2(1-\nu)}\tilde{T}_y\right\}dx \tag{3.4}$$

where $\tilde{T}_i = T_i^{(+)} = T_i^{(-)}$, $\hat{T}_i = T_i^{(+)} = T_i^{(-)}$, $i = x, y$, and the superscripts $(+)$ and $(-)$ denote the upper and lower crack faces, respectively.

Now consider the problem of the Griffith crack with point faces P and Q applied to the upper crack face at a distance b from the crack center, perpendicular and parallel to the crack, respectively (Fig. 1). The tractions may be written in terms of the Driac Delta function as

$$T_x = Q\ \delta[x-(a+b)]$$

and

$$T_y = P\ \delta[x-(a+b)] \tag{3.5}$$

where a is half the crack length. Substitution of (3.5) into equations (3.4), and noting that $l = 2a$, yields the known results [10, p. 1.2. 1-4]

$$K_I = \frac{P}{2\sqrt{\pi a}}\,\frac{a+b}{a-b} + \frac{Q}{4\sqrt{\pi a}}\,\frac{1-2\nu}{1-\nu}$$

and

$$K_{II} = \frac{Q}{2\sqrt{\pi a}}\,\frac{a+b}{a-b} + \frac{P}{4\sqrt{\pi a}}\,\frac{1-2\nu}{1-\nu}. \tag{3.6}$$

Note that when Q is zero, the tensile load P induces mode I, as well as mode II deformation. This is a result of the lack of symmetry in the loading.

Acknowledgment

We wish to thank Professor Bernard Budiansky for reading the manuscript and making several helpful suggestions. This work was supported by the Israel Council for Research and Development and by the Department of Solid Mechanics, Materials and Structures, Tel-Aviv University.

References

1 Bueckner, H. F., "A Novel Principle for the Computation of Stress Intensity Factor," *Zenschrift fur Angewandte Mathematick und Mechanik*, Vo. 50, 1970, pp. 529-546.

2 Rice, J. R., "Some Remarks on Elastic Crack Tip Stress Fields," *International Journal of Solids and Structures*, Vol. 8, 1972, pp. 751-2758.

3 Grandt, A. F., Jr., "Stress Intensity Factors for Some Through-Cracked Fastener Holes," *International Journal of Fracture*, Vol. 11, 1975, pp. 283-294.

4 Grandt, A. F., Jr., "Stress Intensity Factors for Cracked Holes and Rings Loaded With Polynomial Crack Face Pressure Distributions," *International Journal of Fracture*, Vol. 14, 1978, pp. 221-229.

5 Bar-Tikva, D., Grandt, A. F., Jr., and Palazotto, A. N., "An Experimental Weight Function for Stress-Intensity-Factor Calibrations," *Experimental Mechanics*, Vol. 21, 1981, pp. 371-378.

6 Paris, P. C., McMeeking, R. M., and Tada, H., "The Weight Function Method for Determining Stresss Intensity Factors," *Cracks and Fracture*, ASTM-STP 601, 1976, pp. 471-489.

7 Vainshtok, V. A., "A Modified Virtual Crack Extensin Method of the Weight Functions Calculation for Mixed Mode Fracture Problem," *International Journal of Fracture*, Vol. 19, 1982, pp. Rp-R15.

8 Budiansky, B., and Rice, J. R., "Conservation Laws and Energy-Release Rates," ASME JOURNAL OF APPLIED MECHANICS, Vol. 40, 1973, pp. 201-203.

9 Golebiewska Herrmann, A., and Herrmann, G., "On Energy-Release Rates for a Plane Crack," ASME JOURNAL OF APPLIED MECHANICS, Vol. 48, 1981, pp. 525-528.

10 Sih, G. C., *Handbook of Stress-Intensity Factors*, Lehigh University, Bethlehem, Pa., 1973.

Downloaded 02 May 2010 to 171.66.16.250. Redistribution subject to ASME license or copyright; see http://www.asme.org/terms/Terms_Use.cfm

Journal of Applied Mechanics

Discussion

Delamination Buckling and Growth in Laminates[1]

W.-L. Yin[2]. The authors have investigated the phenomenon of delamination buckling and growth in a compressively loaded, two-layer circular plate. The postbuckling problem is solved by an "asymptotic analysis" in which the solution is expanded in powers of a parameter $\epsilon = w_0/R$, where w_0 is the central deflection and R is the radius of the plate. Solutions based on an expansion up to the second order in ϵ are used to determine the delamination growth path associated with a given critical energy release rate. Along this path, the dependence of the nondimensionalized boundary load N and boundary displacement U_R upon the nondimensionalized initial delamination radius a_0 is determined. Besides other things, the authors draw the following conclusion from their results, ". . . it can be seen from Fig. 2 that growth in a plate with initial delamination radius $a_0 = 0.8$ will be stable whether the loading is force controlled or deformation controlled."

In this discussion, I wish to point out that the perturbation method as used by Bottega and Maewal loses its validity in the range of loading corresponding to their delamination growth path because the value of the parameter ϵ in the perturbation series becomes unduly large. The perturbation method was used earlier by Friedrichs and Stoker [1] in studying the postbuckling behavior of a simply supported circular plate. They pointed out that the convergence of the method was satisfactory only for a small range of the expansion parameter. Indeed, the second-order perturbation series was considered satisfactory only if $N < 1.4$. The delamination growth path shown in Fig. 2 of the paper under discussion, however, has N values larger than 4.0. Although the difference in boundary condition (clamped versus simply supported) can change the allowable range of N to some extent, the values indicated in Fig. 2 are still too high to justify the use of a second-order perturbation series.

A postbuckling path in Fig. 2 intersects the delamination growth path at a point where the value of the expansion parameter ϵ used in Bottega and Maewal's analysis is

$$\epsilon = (23.83\ \gamma)^{1/2} a_0^2 = (23.83 \times 14.68 \times 10)^{1/2} \frac{t}{R} a_0^2.$$

For $a_0 = 0.8$, this yields an exceedingly large ratio of the central deflection versus the thickness of delamination:

$$w_0/t = \frac{w_0}{R}\frac{R}{t} = \epsilon \frac{R}{t} = 59.15\ a_0^2 = 37.86.$$

At this level of w_0/t, the second-order perturbation solution is likely to be in serious error.

In fact, by integrating von Karman's equations using the fourth-order Runge-Kutta formula, I have obtained results quite different from Figs. 2 and 4 of the paper under discussion. It was found that, along the delamination growth path, N decreases monotonically until delamination reaches the boundary of the plate. Hence the growth of delamination in a force-controlled loading, once started, is always catastrophic. While this conclusion directly contradicts the previously quoted conclusion of Bottega and Maewal, it is in qualitative agreement with an earlier conclusion of Chai [2] for the growth of a thin-film circular delamination under *uniaxial* compressive loading. The details of my analysis cannot be included here and will be presented in a forthcoming paper [3].

Finally, it is easy to verify that the combined buckling load of the two delaminated layers exceeds the buckling load of the whole plate whenever $a_0 < 0.5$. For the case $a_0 = 0.4$ considered in the paper, the two-layer plate would have buckled as a whole before symmetric buckling of the two delaminated layers could take place. Hence postbuckling and ensuing growth of delamination cannot proceed according to the manner described by the authors.

References

1 Friedrichs, K. O., and Stoker, J. J., "Buckling of the Circular Plate Beyond the Critical Thrust," ASME Journal of Applied Mechanics, Vol. 9, 1942, pp. 7-14.

2 Chai, H., "The Growth of Impact Damage in Compressively Loaded Laminates," California Institute of Technology, Pasadena, Calif., Ph.D. Thesis, 1982.

3 Yin, W.-L., "Axisymmetric Buckling and Growth of a Circular Delamination in a Compressed Laminate," forthcoming.

Authors' Closure

Professor Yin's point that our asymptotic analysis suffers from the limited range of validity of its results is almost axiomatic. We believe, however, that our results do provide a simple description of the phenomenon of delamination buckling and growth, especially with respect to the effect of geometrical nonlinearity on the process.

We would like to take this opportunity to correct the equation (28*b*) of our paper which should read

$$\epsilon^2 = 0.1124\ a^4\gamma \equiv q_0 a^4 \gamma, \qquad (28b)'$$

[1] By W. J. Bottega and A. Maewal, and published in the March 1983 issue of ASME Journal of Applied Mechanics, Vol. 50, pp. 184-189.

[2] Associate Professor, School of Engineering Science and Mechanics, Georgia Institute of Technology, Atlanta, Ga. 30332.

Copyright © 1983 by ASME
Downloaded 02 May 2010 to 171.66.16.250. Redistribution subject to ASME license or copyright; see http://www.asme.org/terms/Terms_Use.cfm

as in a companion paper [1]. The error in (28*b*) was inadvertently committed at the time of writing the paper in terms of scaled variables. All the calculations and figures, we hasten to add, are, however, correct.

With corrected (28*b*)′, the quantity w_0/t calculated by Professor Yin comes out to be 2.60, substantially lower than the value based on the incorrect equation (28*b*) of the paper. This, we hope, diminishes the concerns about the range of validity of the results for their use in the growth criterion. In any case it is evident from (28*b*)′ that it should always be possible to find a sufficiently small γ that is consistent with the asymptotic nature of the results. That asymptotic results are not valid for all the values of γ is hardly a revelation.

The fact that our analysis of symmetric delamination buckling and growth assumes that the delamination size is sufficiently large was also mentioned in the paper. Our object in the paper was only to delineate the significant features of the phenomenon by means of simple anlaysis, unencumbered by the complications that arise due to overall buckling of the plate.

Although Professor Yin's numerical results are inaccessible to us, he cites Chai's thesis [2] to support them. Whether results of [2] are applicable to our problem is an open question.

References

1 Bottega, W. J., and Maewal, A., "Dynamics of Delamination Buckling," to appear in *Int. J. Nonlinear Mechanics*.

2 Chai, H., "The Growth of Impact Damage in Compressively Loaded Lamiantes," Ph.D. Thesis, California Institute of Technology, Pasadena, Calif., 1982.

Downloaded 02 May 2010 to 171.66.16.250. Redistribution subject to ASME license or copyright; see http://www.asme.org/terms/Terms_Use.cfm

Journal of Applied Mechanics

Book Reviews

Introduction to the Theory of Thin Shells. By H. Mollman. Wiley, New York, 1983. 181 Pages. Price $41.00

REVIEWED BY A. KALNINS[1]

Shell theory originated as a discipline of mechanics late in the 19th century when it attracted the attention of some prominent scientists. Then it passed into the hands of engineers who were actually building things and had to do some analysis in order to shorten design. In the 1920s and 1930s, many structures were built on this basis and, within its limitations, shell theory became a useful designer's tool. In the late 1950s, the needs of the U.S. space program produced a flurry of activity among the shell theorists that lasted to the end of the 1960s. Looking back at this period, in which the reviewer participated with great enthusiasm, the goals do not appear now to have been clearly identified. Much of the activity seemed to center on the search for the "best" theory. The question: "What is wrong with the old theory?" did not receive a sufficiently wide and open debate. It is fair to say that the main thrust of this work has not as yet been fully understood and exploited by the consumer—the shell analyst. It is the reviewer's opinion, that the permanent impact of the 1960s on shell theory is still debatable. Unfortunately, the need to assess the impact has diminished, because, starting with the 1970s, the finite elements gained favor and the search for the "best" element moved to the center court.

Viewed against this background, it is a pleasure to see a book appear that is willing to base the development of the mathematical model for a shell on the advances of the 1960s, thus opening this work for further scrutiny and debate, which it deserves, but did not receive in the past. This book is based on lecture notes that have been written by the author and used for a one-semester course on shell theory, intended for seniors or first-year graduate students. It is limited to this objective and does not intend to compete with reference books, such as Timoshenko and Woinowsky-Krieger, and Kraus. In four chapters, it covers these subjects: Foundations of Shell Theory (54 pages), Shells of Revolution (43 pages), Shallow Shells (46 pages), and Shell Equations in Tensor Notation (26 pages). The book begins with the standard treatment of differential geometry of a surface. The author makes a point to include in the expression for twist an additional term to make the twist vanish upon rigid-body rotation about the normal. [W. Flügge, *Stresses in Shells*, 1962, p. 319, also discusses this point and shows how to treat it.] The geometry is followed by the derivation of the equilibrium equations of a surface element in terms of resultant forces and couples. [This is the clearest and shortest derivation that the reviewer knows. Reviewer first saw it done by Eric Reissner, *American Journal of Mathematics*, Vol. 63, 1941, pp. 177–184.] The purpose of the pages 34–54 is to obtain the relations between the resultant forces and couples and the strain measures. The reviewer believes that this section will disappoint most readers. The forces and couples are redefined twice, and the reader is asked to keep track of five different symbols that describe variations of the resultant force per unit length of the edge. Two of these symbols differ only by being straight or slanted. [There are contact (p. 29), effective contact (p. 37), complete contact (p. 39), and reduced (p. 49) forces and couples. The reviewer was not the only one confused by this. The printer was too, in the first of equations (1.136)]. The presentation of Chapter 1 makes the reviewer wish to return to the simplicity and clarity achieved by Reissner in 1941. Perhaps, if needed, the limits of validity of his equations could be rewritten, and then those cases where they fail, identified and treated separately. After reading Chapter 1, that looks like an attractive option.

Once one gets through Chapter 1, it is smooth sailing through the next two chapters. Chapter 2 includes the classical treatment of axisymmetric deformation of shells of revolution and finishes with Geckeler's method. The coverage of shallow shells in Chapter 3 appears to be more extensive than usual, which the reviewer likes very much. There are many applications, such as the analysis of small defects (cracks), or even finite elements, for which shallow shells play an important role.

In summary, I recommend the book to anyone who wants to understand better what a mathematical model for a shell can, and cannot, predict. Whether the development in Chapter 1 is to be followed, is for the reader to decide. I recommend it as a textbook, with one reservation. The course content should be supplemented by some discussion of numerical solutions, because that is how shell problems are now solved.

Nonlinear Problems: Present and Future. Edited by A. Bishop, D. Campbell, and B. Nicolaenko. North-Holland, The Netherlands, 1982. 482 Pages. Price $69.75.

REVIEWED BY P. HOLMES[2]

Conference proceedings are generally most useful for the

[1] Professor, Department of Mechanical Engineering and Mechanics, Lehigh University, Bethlehem, Pa. 18015. Mem. ASME.

[2] Associate Professor, Department of Theoretical and Applied Mechanics, Cornell University, Ithaca, N.Y. 14853.

Copyright © 1983 by ASME
Downloaded 02 May 2010 to 171.66.16.250. Redistribution subject to ASME license or copyright; see http://www.asme.org/terms/Terms_Use.cfm

reader who wishes to obtain an overview of research in a particular area. They are seldom adequate for the serious study of new techniques or applications. The present volume is no exception to this rule. The editors, all of the Center for Nonlinear Studies at Los Alamos National Laboratory, have collected 34 papers representing four areas of Nonlinear Problems. The papers were invited for, and in some case contributed to, a conference held at the Center in 1981. The areas are *I*: New Methods and Results in Nonlinear Analysis (11 papers), *II*: Nonlinearity in Field Theories and Low Dimensional Solids (8 papers), *III*: Reaction Diffusion Systems (2 papers), and *IV*: Nonlinear Phenomena in Fluids and Solids (13 papers).

The first and last two areas are probably of most interest to the readers of this journal, and I will therefore concentrate on them.

In the first, the rapidly expanding research area of integrable partial differential equations is represented by the contributions of Flashka/Newell and Sattinger. Finite dimensional Hamiltonians, including problems of the motions of point vortices, integrability and stellar dynamics within a galaxy, are discussed by Palmore, Lewis/Leach, and Newman. A survey of numerical methods for nonlinear equations is provided by Hyman, and papers on optimal control of distributed systems (J.-L. Lions), Variational Problems (P. L. Lions), Limit analysis (Fremond et. al.), Hamilton Jacobi equations (Crandall), and Yang Mills Fields (Singer) complete this rather diverse section. The second section is concerned mainly with problems in the physics of solids and includes several papers on the physical applications of soliton theory. The two excellent papers in Section *III*, by R. Aris and P. C. Fife, deal with models of chemical kinetics and propagating reaction fronts, respectively.

In the final section Gollub and Roux et. al. describe experimental evidence for periodic and chaotic motions in convection and chemical reactions. Bardos, Foias/Temam, Howes, and Mathieu et. al. consider various aspects of the Navier Stokes equations, including the existence of an attracting infinite dimensional manifold in phase space for finite viscosity, boundary layers, and the closure problem in turbulence theory. Patera and Orzag summarize their meticulous and extensive nonlinear stability studies of pipe flow. Two papers on the dynamics of one-dimensional mappings and universal bifurcation structures, by Feigenbaum and Chang et. al., follow. The section concludes with two papers on instability and turbulence in plasmas, by Greene and Pesme/Dubois, and papers on the nonlinear Schrodinger and related equations occurring in nonlinear stability studies (Rose/Dubois and Wang).

As this brief list shows, this is a very diverse collection and the coverage is, consequently, uneven and sometimes cursory. The papers range from Fife's fairly complete review on propagating fronts and Foias and Temam's detailed proof of existence of an "approximative stationary (finite dimensional) manifold" which attracts all solutions of the Navier Stokes equations, to relatively slight notes on special problems. However, as a whole, the editors have collected papers that do provide a good cross section of current research in nonlinear analysis, and which certainly illustrate the diverse applications that the methods of global analysis and bifurcation theory are now finding. The volume is therefore a useful survey and a reasonable starting point for someone wishing to explore a new and exciting field.

In closing this review I would like to mention two further conference proceedings which cover similar ground, with somewhat different emphasis, namely, *Bifurcation Theory and Applications in Scientific Disciplines* (edited by O. Gurel and O. Rössler, *Ann. N. Y. Acad. Sci.*, Vol. 316, 1979) and *Nonlinear Dynamics* (edited by R. H. G. Helleman, *Ann. N. Y. Acad. Sci.*, Vol. 357, 1980). I also draw the reader's attention to the forthcoming Proceedings of the 1982 "Order in Chaos" meeting held at Los Alamos. The latter will appear as an issue of *Physica D*, and also as a volume in the same North Holland Series as the present one.

Finite Element Flow Analysis. Edited by T. Kawai. North-Holland, The Netherlands, 1982. 1096 Pages. Price $95.00.

REVIEWED BY P. M. PINSKY[3]

This book, 1096 pages long, contains the proceedings of the Fourth International Symposium on Finite Element Methods in Flow Problems held at Chuo University, Tokyo, on July 26–29, 1982. The proceedings are dedicated to the memory of Professor Kyuichiro Washizu who was a member of the Japanese Organizing Committee until his death in November 1981. The proceedings of the conference, the fourth in a series which was first held at the University of Wales, Swansea, in 1974, consist of 131 papers and one abstract dealing with recent developments and applications in the finite element method as well as boundary integral techniques, to a wide range of fluid mechanics problems. The contents of the book are divided into 14 chapters, the titles of which illustrate the considerable scope of this conference. These are: General Lecture, Mathematical Analysis, Viscous Flow, Thermal Convection, Polymer Flow, Compressible Flow, Wave, Free Surface Flow, Shallow Water Flow, Seepage Flow, Sediment Transport, Further Application, Boundary Element Method, and Computational Techniques.

Chapter 1 presents four general lectures, the first of which is a paper by K. Washizu in which finite element, boundary element, and modified fluid-in-cell techniques are applied to solve several nonlinear free surface fluid flow problems. The next general lecture by O. C. Zienkiewicz et al., of which only an abstract is printed, presents a survey of the recent development of the finite element method applied to the time-dependent problems of Navier-Stokes and shallow water wave flow. J. T. Oden and O. Jacquotte present an abbreviated paper on the convergence of RIP (reduced integration-penalty) methods for two-dimensional incompressible viscous flows. Chapter 1 is concluded by a survey of numerical procedures for weather prediction in a paper by Y. K. Sasaki and L. P. Chang. The remaining 13 chapters, containing a total of 128 papers, bring together the work of major researchers and contain many notable contributions dealing with new results for subsonic and transonic fluids as well as topics as diverse as geothermal heat storage, thermal analysis in biomechanics, and the circulation of lakes.

Both the variety of problems now capable of solution and the rapid development of new techniques, as exemplified by the contents of these proceedings, clearly demonstrate that the extraordinary rate of progress that this branch of computational fluid mechanics has been experiencing over the last 10 years is continuing in full force. Much of the latest research on the development and application of the finite element method and boundary integral procedures is collected on a worldwide scale in this volume and it is highly recommended as a reference book to libraries of universities as well as research organizations dealing with any aspect of computational fluid mechanics.

[3]Assistant Professor, Division of Engineering, Brown University, Providence, R.I. 02912.

Copyright © 1983 by ASME
Downloaded 02 May 2010 to 171.66.16.250. Redistribution subject to ASME license or copyright; see http://www.asme.org/terms/Terms_Use.cfm

Viscoplasticity. By N. Cristescu and I. Suliciu. Martinus Nijhoff, The Netherlands, 1982. 307 Pages. Price $64.40.

REVIEWED BY J. L. BASSANI[4]

This is a revised and reorganized translation of the 1976 Romanian edition. From the title the reader may expect a more general monograph but the emphasis throughout is on the development of rate-type constitutive equations that are appropriate for the analysis of inelastic wave propagation problems. This book incorporates an interesting and refreshing blend of physical and mathematical detail. For example, some observable, if not critical, features of dynamic experiments (mostly uniaxial impact) are reviewed and then interpreted in terms of the restrictions they impose on the rate-type constitutive equations.

Except for a general discussion of wave propagation theory the book is based mostly on the authors' research although nearly 200 references to other works are included. Often results are excerpted directly from journal papers with some details omitted; figures taken from papers too often lack adequate labels or captions. Overall the book is well organized. The four chapters written by N.C. tend to emphasize the physical phenomenon and the six chapters written by I.S. tend to be more mathematical. Occasionally the transition from one point of view to the other is abrupt.

The first five chapters form a coherent presentation of both the physical and mathematical aspects of one-dimensional wave propagation in solids that are capable of simultaneous elastic, instantaneous plastic, and viscous deformations. Chapter I covers some preliminaries. Chapter II introduces several one-dimensional rate-type constitutive equations followed by the characteristic fields and domains of hyperbolicity associated with mechanical phenomena in solids described by these equations. Chapter III describes critical features of some experiments on metals, plastics, rocks, and soils at various strain rates. Particular attention is given to the observed short-time stress peak followed by a long-time plateau near the impacted end of a bar and to the observed wave speed corresponding to a dynamic reloading event. Classical plasticity is shown to be inconsistent with these observations.

Numerical simulations of impacting bars are presented in Chapter IV (with details of the numerical analysis given in the Appendix) and these simulations are used to determine the best choice for the constants in the elastic-viscoplastic constitutive equations. The importance of the relaxation boundary, which gives the magnitude of stress $\sigma(\epsilon)$ that corresponds to a zero viscous strain rate, is emphasized in terms of reproducing the experimental observations. Based on three constitutive assumptions several theorems concerning the existence and uniqueness of the relaxation curve as well as certain features (e.g., wave speeds and stress plateaus) of solutions to dynamic problems are presented in Chapter V. A few examples from two-dimensional wave propagation would have enhanced the first half of this book.

Multidimensional inelastic constitutive equations with internal state variables are considered in Chapter VI. Restrictions on the growth law for the internal state variables are developed in terms of consequences of the first and second laws of thermodynamics and consequences of the principle of frame indifference. Chapter VII considers the existence of real acceleration waves in materials with internal state variables.

A short chapter (VIII) follows that summarizes some classical multiaxial viscoplastic constitutive equations based on the von Mises effective stress. Chapter IX, which is also rather brief, proposes some uniaxial constitutive equations that describe creep of rocks. Chapter X introduces the analogy between the constitutive equations of one-dimensional viscoplasticity and those of electric lines. Numerical examples of wave propagations in electric lines and comparisons with experimental results concludes this chapter. The book closes with an appendix on the numerical methods that have been employed by the authors for solving one-dimensional elastic-viscoplastic wave propagation problems.

This book should be both interesting and useful for researchers working in the areas of plasticity and wave propagation in solids. It also can provide supplemental material for graduate courses in these areas.

The Finite Element Method in Engineering. By S. S. Rao. Pergamon Press, New York, 1982. 400 Pages. Price $20.00 (soft cover).

REVIEWED BY S. N. ATLURI[5]

This is a textbook written for senior undergraduates or first-year graduate students. It contains eight chapters, in the order: (*i*) Introduction to Finite Element Method, (*ii*) Solution of Finite Element Equations, (*iii*) General Procedure of Finite Element Method, (*iv*) Higher Order and Isoparametric Element Formulations, (*v*) Solid and Structural Mechanics, (*vi*) Heat Transfer, (*vii*) Fluid Mechanics, (*viii*) Additional Applications and Generalizations of the Finite Element Method, and a brief appendix on the Green-Gauss theorem. The book contains several simple examples and listings of computer programs. The book is written in a clear and simple style and should be easily accessible to the students for whom it is intended. The book is reproduced directly from the author's typescript. This soft cover volume is relatively inexpensive – another attractive feature if this were to be used as an undergraduate or first-year graduate text book.

Fracture of Composite Materials. Edited by G. C. Sih and V. P. Tamuzs. Martinus Nijhoff, The Netherlands, 1981. 488 Pages. Price $69.00.

REVIEWED BY C. T. HERAKOVICH[6]

This book is unique in the Western World in that it is a collection of 37 papers, all written in English, with more than half (20) of the papers written by authors from the Soviet Union. Of the remaining 17 papers, 14 are by American authors, two Canadian, and one Polish. The high percentage of papers from the Eastern countries is rare in a proceeding of this type and thus the book presents the reader with an unusual opportunity to compare areas of interest and methods of solution between East and West. The papers were presented during a symposium at Lehigh University, March 9–12, 1981. This was the second symposium of a series which was initiated at Jurmala, Latvia, USSR in 1978. A third symposium to be held in the Soviet Union is now in the planning stages.

The book is divided into seven major sections: (1) Analytical Modeling (six papers); (2) Crack and Fracture

[4] Assistant Professor, Department of Mechanical Engineering and Applied Mechanics, University of Pennsylvania, Philadelphia, Penn. 19104. Assoc. Mem. ASME

[5] Regents' Professor of Mechanics, Center for the Advancement of Computational Mechanics, School of Civil Engineering, Georgia Institute of Technology, Atlanta, Ga. 30332.

[6] Professor, Engineering Science and Mechanics, College of Engineering, Virginia Polytechnic Institute and State University, Blacksburg, Va. 24061.

Copyright © 1983 by ASME
Downloaded 02 May 2010 to 171.66.16.250. Redistribution subject to ASME license or copyright; see http://www.asme.org/terms/Terms_Use.cfm

Analysis (four papers); (3) Micromechanics (four papers); (4) Unidirectional Composites (five papers); (5) Laminates (five papers); (6) Stress and Strength Analysis (six papers); and (7) Experiments and Tests (seven papers).

In general, the papers emphasize the analytical aspects of fracture mechanics. Relatively little experimental data are presented for modern advanced composite materials. Most papers are well written. It is interesting to note that the papers by Russian authors often reference western authors, but the western authors only rarely reference Russian works. This seems to be a clear indication that more effort should be given in the western world to the study of Russian papers. This volume provides the western reader with an opportunity to make a positive step forward in the direction with a minimum of effort.

Strömungsmechanik Nicht-Newtonscher Fluide. By G. Bohme. B. G. Teubner, Stuttgart, 1981. 280 Pages. Price DM 34.

REVIEWED BY D. D. JOSEPH[7]

This book is a contribution to the literature on the mechanics of Non-newtonian fluids. Many books, at least six, on non-Newtonian fluids have been published in the last 10 years. Most of these emphasize rheological aspects of the subject, with emphasis on constitutive equations derived either from molecular theories or from continuum mechanics or on the simple flows that define instruments used in rheological measurements. Böhme's book differs from others. It treats the subject in the tradition of fluid mechanics. The mathematical level expected of readers of this book is slightly less than what is required for Lamb's book on hydrodynamics or Batchelor's book on fluid dynamics. This level is well suited for graduate courses in engineering. In addition to standard topics, like kinematics, elementary constitutive theory, and the theory of viscometric flow, many new topics are treated in this book and some old topics are treated in a new way. The chapters on simple unsteady flows, almost viscometric flows, and secondary flows all contain some new material. The analysis of the linearized dynamics of the step jump in velocity problem (Rayleigh's problem) for shear flow between parallel plates differs from that given in other rheology books in that the solution is derived rather than assumed. Böhme's book shows that the evolution of the wall shear stress is different than is generally assumed, particularly at early times when transients are important. The section of tuning of a vibration damping device has a good example of analysis of problems with industrial applications. The theory of almost viscometric flow has applications in lubrication theory, boundary layer theory, and in the theory of hydrodynamic stability. Böhme's book is the only one to treat such applications.

Böhme's book does not go deeply into the theory of constitutive equations. He uses asymptotic expressions for the constitutive equations near slow motions or viscometric motions. There is no discussion of molecular models. This is perhaps desirable in a mechanics textbook since the theory for such modeling is represented in other books and is quite confusing, with as many models as there are rheologists.

I think that a serious defect of the book is a lack of references. Böhme says that he decided against including references to works that influenced his because he could not make such a list complete, and some deserving works would not be cited. The decision not to give any specific references and only to give a small list of general references is a bad one. Students of the subject who get interested in some topics need some leads for further study. The teaching that is done by a book is more important than assuaging egos of authors not mentioned.

I would like to see Böhme's book published in English after he adds a useful list of current references for each live subject.

[7]Professor, Department of Aerospace Engineering and Mechanics, University of Minnesota, Minneapolis, Minn. 55455.

Copyright © 1983 by ASME
Downloaded 02 May 2010 to 171.66.16.250. Redistribution subject to ASME license or copyright; see http://www.asme.org/terms/Terms_Use.cfm